Hippocampal ripple oscillations in inhibitory network models

Analyses at microscopic, mesoscopic, and mean-field scales

DISSERTATION

zur Erlangung des akademischen Grades

Doctor rerum naturalium
(Dr. rer. nat.)

eingereicht an der
Lebenswissenschaftlichen Fakultät
der Humboldt-Universität zu Berlin

von

M.Sc. Natalie Schieferstein

Präsidentin der Humboldt-Universität zu Berlin:
Prof. Dr. Julia von Blumenthal

Dekan der Lebenswissenschaftlichen Fakultät:
Prof. Dr. Dr. Christian Ulrichs

Gutachter:

1. Prof. Dr. Richard Kempter
2. Prof. Dr. Benjamin Lindner
3. Prof. PhD Nicolas Brunel

Tag der mündlichen Prüfung: 20. Januar 2023

Abstract

Brain activity is organized by a variety of rhythms that correlate with cognitive functions. During slow wave sleep or quiet rest, hippocampal activity is characterized by sharp wave-ripples (SPW-Rs): transient (∼50–100 ms) periods of elevated neuronal activity modulated by a fast oscillation — the ripple (∼140–220 Hz). SPW-Rs have been linked to memory consolidation as they co-occur with the replay of behaviorally relevant neuronal activity. Yet, the generation mechanism of ripple oscillations remains unclear. Multiple potential mechanisms have been proposed, relying on excitation and/or inhibition as the main pacemaker. A prominent model for ripple generation is based on delayed inhibitory feedback in a population of interneurons. Recent support for this model has come from the observation that it can reproduce the experimentally observed intra-ripple frequency accommodation (IFA) — a decrease in the instantaneous ripple frequency over the course of a ripple event triggered by transient, sharp wave-like stimulation. A mechanistic understanding of IFA could thus advance model selection.

This thesis analyses ripple oscillations in inhibitory network models at micro-, meso-, and macroscopic scales and elucidates how the ripple dynamics and IFA depend on the excitatory drive, inhibitory coupling strength, and the noise model.

To this end, a theory for the oscillation dynamics in interneuron networks under strong drive is developed, capturing drift-mediated spiking in the mean-field limit. For constant drive, the ripple frequency and the amplitude of the subthreshold membrane potential oscillation are approximated as a function of the drive, the coupling strength, and the noise intensity. For a transient increase of the external drive, the theory predicts a speed-dependent hysteresis in the membrane potential dynamics that leads to an IFA-like decrease in oscillation frequency over time. IFA is thus a robust feature of the model, relying solely on the sharp wave-induced change in the excitatory drive to the interneurons. In contrast, numerical analysis shows that an alternative inhibitory ripple model, based on a transient ringing effect in a weakly coupled population of interneurons, can only account for IFA in response to an asymmetric input profile. IFA can thus guide model selection and provides new support for delayed inhibitory coupling as a mechanism for ripple generation. The speed-dependence of IFA is a novel prediction that can be tested in optogenetic experiments.

Studying the propagation of ripples and replay across brain regions, requires larger-scale models and thus poses a challenge to microscopic simulation schemes. A recently proposed mesoscopic description of the population dynamics combines computational efficiency with an account for finite size effects. This approach, however, requires a switch of the noise model, from noisy input to stochastic output spiking mediated by a hazard function. I demonstrate how the choice of hazard function affects the linear response of single neurons, and therefore the ripple dynamics in a recurrent interneuron network. In principle, a mesoscopic description of ripple oscillations is possible, and approximates the microscopic dynamics under noisy input best, when the hazard takes into account the slope of the membrane potential.

Altogether, this thesis presents a novel analysis of rhythmic neuronal activity paced by inhibition, and outlines new ways towards understanding ripple oscillations and their potential role in cognitive functions such as memory consolidation.

Zusammenfassung

Die Aktivität unseres Gehirns ist geprägt von einer Vielzahl von Rhythmen, die mit kognitiven Funktionen korrelieren. Ein charakteristisches Muster hippocampaler Aktivität im Tiefschlaf sind Sharp Wave-Ripple Komplexe (SPW-R): kurze (∼50–100 ms) Phasen mit erhöhter neuronaler Aktivität, moduliert durch eine schnelle Schwingung — die Ripple Oszillation (∼140–220 Hz). SPW-R werden mit Gedächtniskonsolidierung in Verbindung gebracht, da sie zusammen mit der Reaktivierung von verhaltensrelevanter neuronaler Aktivität auftreten. Dennoch bleibt weiterhin unklar, wie Ripples erzeugt werden. Sowohl exzitatorische als auch inhibitorische Populationen könnten die Oszillation generieren. Ein möglicher Mechanismus basiert auf verzögertem inhibitorischen Feedback in einer Interneuron-Population. Dieses Modell wurde neu bestärkt durch die Beobachtung, dass es den experimentell beobachteten Effekt der Intra-Ripple Frequency Accommodation (IFA) reproduziert — ein Abfall der instantanen Ripple-Frequenz im Verlauf eines SPW-R Ereignisses, ausgelöst durch transiente, Sharp Wave-artige Stimulation. Ein Verständnis des IFA Mechanismus könnte daher die Modellauswahl vorantreiben.

Diese Arbeit analysiert Ripple-Oszillationen in inhibitorischen Netzwerkmodellen auf mikro-, meso- und makroskopischer Ebene und zeigt auf, wie die Ripple-Dynamik und IFA vom exzitatorischen Input, der inhibitorischen Kopplungsstärke, und dem Rauschmodell abhängen.

Es wird eine Theorie entwickelt, die die Oszillationsdynamik in Interneuron Netzwerken unter starkem Input beschreibt, basierend auf der Drift-bedingten Feuerdynamik im Mean-field Grenzfall. Für konstanten Input können die Ripple-Frequenz und die Amplitude der unterschwelligen Oszillation im Membranpotential als Funktion des Inputs, der Kopplungsstärke und der Stärke des Rauschens angenähert werden. Im Falle eines transienten Anstiegs und Abfalls des Inputs, erklärt die Theorie den Abfall der instantanen Ripple-Frequenz (IFA) durch eine geschwindigkeitsabhängige Hysterese in der Dynamik des Membranpotentials. IFA ist daher eine weitgehend parameterunabhängige Eigenschaft des Modells, die allein von der Sharp Wave-abhängigen Änderung des Inputs abhängt. Im Gegensatz dazu zeigt eine numerische Analyse, dass ein alternatives inhibitorisches Ripple-Modell, basierend auf einem transienten Störungseffekt in einer schwach gekoppelten Interneuron Population, nur für asymmetrische Inputverläufe IFA erzeugen kann. IFA kann somit zur Modellauswahl beitragen und deutet auf verzögerte inhibitorische Kopplung als plausiblen Mechanismus hin. Die Abhängigkeit der IFA von der Änderungsrate des Inputs ist eine neue Vorhersage und kann experimentell mit Hilfe optogenetischer Techniken überprüft werden.

Eine Analyse der Ausbreitung von Ripple-Oszillationen und neuronalem *replay* über mehrere Hirnregionen, erfordert Simulationen größeren Maßstabs, was eine Herausforderung für mikroskopische Modelle darstellt. Eine kürzlich entwickelte mesoskopische Beschreibung der Netzwerkaktivität ist effizienter und berücksichtigt gleichzeitig die endliche Größe der Netzwerke. Dieser Ansatz erfordert allerdings einen Wechsel des Rauschmodells: das Rauschen wird nicht im Input der Neurone beschrieben, sondern als stochastisches Feuern entsprechend einer Hazard Rate. Ich zeige, wie die Wahl der Hazard Rate die dynamische Suszeptibilität einzelner Neurone, und damit die Ripple-Dynamik in rekurrenten Interneuron Netzwerken beeinflusst. Eine mesoskopische Beschreibung von Ripple-Oszillationen ist grundsätzlich möglich und bildet die mikroskopische Dynamik unter verrauschtem Input am besten ab, wenn die Hazard Rate die momentane Änderung des Membranpotentials berücksichtigt.

Insgesamt stellt diese Arbeit eine neue Analyse von inhibitorisch verursachter, rhythmischer neuronaler Aktivität vor, und zeigt neue Wege auf um Ripple-Oszillationen und ihre mögliche Rolle für kognitive Funktionen wie Gedächtniskonsolidierung zu verstehen.

Contents

Abstract i

Zusammenfassung iii

List of abbreviations viii

1 Overview 1
- 1.1 Motivation 1
- 1.2 Structure of the thesis 1

2 Introduction and background 3
- 2.1 Memory 3
  - 2.1.1 The engram 3
  - 2.1.2 Memory consolidation 4
  - 2.1.3 Replay 4
- 2.2 Rhythms in the brain 6
  - 2.2.1 Rhythms during awake exploration 6
  - 2.2.2 Rhythms during offline states and sleep 6
- 2.3 A functional role for sharp wave-ripples in memory consolidation 7
  - 2.3.1 Sharp wave-ripples for active memory consolidation 8
  - 2.3.2 Sharp wave-ripples for synaptic homeostasis 10
- 2.4 Hippocampal anatomy 10
  - 2.4.1 Circuitry and cell types of CA1 12
- 2.5 Hippocampal sharp-wave ripple 14
  - 2.5.1 Measuring sharp-wave ripples in the LFP 16
  - 2.5.2 Intra-ripple frequency accommodation 16
  - 2.5.3 Recruitment of hippocampal cell types during SPW-Rs 17
- 2.6 Models of hippocampal ripple oscillations 19
  - 2.6.1 Inhibition-first models 20
  - 2.6.2 Excitation-first models 21
  - 2.6.3 Mixed models 22
- 2.7 Basic ingredients of ripple models 23
  - 2.7.1 Axo-axonic gap junctions between CA1 pyramidal cells 23
  - 2.7.2 Antidromic spikes and spikelets in CA1 pyramidal cells 24
  - 2.7.3 Dendritic spikes in CA1 pyramidal cells 24
  - 2.7.4 Properties of inhibitory synaptic coupling in CA1 25

2.8 Experimental tests of model predictions 25
    2.8.1 Pharmacology 25
    2.8.2 Optogenetics 28
    2.8.3 Summary 29

3 Research aims **31**

4 The bifurcation-based inhibitory ripple model **33**

4.1 Introduction 33
4.2 Simulation of ripple dynamics in a spiking network 34
    4.2.1 The detailed model 34
    4.2.2 The reduced model 37
4.3 Theory of ripple dynamics in the mean-field limit 41
    4.3.1 Linear approaches and their limitations 42
    4.3.2 A drift-based approximation of oscillation dynamics under strong drive 44
    4.3.3 Oscillation dynamics for constant drive 46
    4.3.4 Oscillation dynamics and IFA for time-dependent drive 49
    4.3.5 The role of the inhibitory reversal potential 56
    4.3.6 The role of the refractory period 58
4.4 Discussion 59
4.5 Methods 62
    4.5.1 Spiking network simulations 62
    4.5.2 Mean-field dynamics for constant drive 77
    4.5.3 Derivation of drift-based approximation of oscillation dynamics 87
    4.5.4 Analytical approximation of drift-based oscillations for constant drive 91
    4.5.5 Analytical approximation of drift-based oscillations for linear drive 101
4.A Parameter-dependencies of drift-based oscillation dynamics 106
    4.A.1 The role of noise and coupling strength 106
    4.A.2 The role of the reset potential 109
    4.A.3 The role of the synaptic delay 111
4.B Drift-based approximation in a network of pulse-coupled oscillators (PCO) 114
    4.B.1 Ripples in a PCO network with linear phase response curve . . . 114
    4.B.2 Mean-field dynamics of the PCO network 116
    4.B.3 Drift-based approximation of ripples and IFA in the PCO network 117
4.C Auxiliary calculations for piecewise linear drive 124
    4.C.1 Comparison of $\mu_{\max}$ for constant and linear drive 124
    4.C.2 A solvability condition for the initial mean membrane potential 125
    4.C.3 Decomposition of total input current under linear drive 125
4.D Background on Fokker-Planck Equations and linear response 127
    4.D.1 The Fokker-Planck Equation for leaky integrate-and-fire (LIF) neurons 127
    4.D.2 The Fokker-Planck Equation for pulse-coupled oscillators with linear phase response curve 134
    4.D.3 Linear response 135

4.D.4 Two “flavors” of linear stability analysis 144
4.E Supplementary figures 153

5 The perturbation-based inhibitory ripple model 155
5.1 Introduction 155
5.2 Analysis of the perturbation-based inhibitory ripple model 155
5.2.1 The default ripple event 156
5.2.2 Parameter dependencies 157
5.2.3 Ripple properties summarized 160
5.3 IFA in the perturbation-based model 163
5.3.1 IFA for asymmetric ramp input 163
5.3.2 “Anti-IFA” for symmetric input 164
5.3.3 IFA via adaptation 165
5.4 Differentiation of inhibition-first ripple models 166
5.4.1 No persistent oscillations in the perturbation-based ripple model. 167
5.4.2 From perturbation- to bifurcation-based ripples 167
5.5 Discussion 172
5.6 Methods 175
5.6.1 Model summary 175
5.6.2 Simulation and analysis 177
5.A Appendix: Replicating (Malerba et al., 2016) 178
5.A.1 Parameter corrections 178
5.A.2 The role of random connectivity 181
5.A.3 Parameter explorations 183
5.B Supplementary figures 186

6 Mesoscopic models of ripple oscillations 189
6.1 Introduction 189
6.2 Microscopic reference model with noisy input 190
6.3 Escape-noise models: Mapping input to output noise 191
6.3.1 Hazard functions 192
6.3.2 Dependence of the linear response on the hazard 196
6.3.3 Ripple oscillations in networks of escape-noise units at microscopic level 198
6.4 Mesoscopic models of network dynamics 200
6.4.1 Ripples in networks of escape-noise units on mesocopic level . . 202
6.4.2 A note on computational efficiency 203
6.5 Discussion 204
6.6 Methods 206
6.6.1 Numerical estimate of linear response 206
6.A Derivation of Chizhov-Graham hazard 206
6.A.1 Subthreshold regime ($H = A$) 208
6.A.2 Subthreshold regime ($H = B$) 208
6.B f-I curves 209
6.B.1 f-I curve for LIF units 209
6.B.2 f-I curve for GIF neurons 209

6.C Susceptibility for GIF units 211
6.C.1 Derivation of kernel $\mathcal{L}$ 213
6.C.2 Susceptibility for exponential hazard 216
6.D Supplementary figures 218

7 Discussion and outlook **219**
7.1 Summary of the thesis 219
7.2 Outlook and future research 220
7.2.1 Understanding ripple generation 220
7.2.2 Mesoscopic models of ripple oscillations 223

Bibliography **225**

List of Figures **257**

List of Tables **261**

Abbreviations

aEIF	adaptive exponential integrate-and-fire
AMPA	α-amino-3-hydroxy-5-methyl-4-isoxazolepropionic, receptor
CA	cornu ammonis (with subfields CA1, CA2, CA3)
BC	basket cell
CCK$^+$	Cholecystokinin-positive
CV	coefficient of variation
DDE	delay differential equation
EC	entorhinal cortex (MEC/LEC: medial/lateral entorhinal cortex)
EIF	exponential integrate-and-fire
EPSP	excitatory postsynaptic potential
GIF	generalized integrate-and-fire
IFA	intra-ripple frequency accommodation
IPSP	inhibitory postsynaptic potential
ISI	interspike interval
LFP	local field potential
LIF	leaky integrate-and-fire
LTP	long-term potentiation
NMDA	N-methyl-D-aspartate, receptor
ODE	ordinary differential equation
O-LM	oriens lacunosum-moleculare
PCO	pulse-coupled oscillator
PIF	perfect integrate-and-fire
PV$^+$	parvalbumin-positive
REM	rapid eye movement (sleep)
SC	Schaffer Collateral
SD	standard deviation
SDE	stochastic differential equation
SOM$^+$	somatostatin-positive

STDP	spike-timing dependent plasticity
str. lac. mol.	stratum lacunosum moleculare
str. or.	stratum oriens
str. pyr.	stratum pyramidale
str. rad.	stratum radiatum
SPW	sharp wave
SPW-R	sharp wave-ripple
SWS	slow-wave sleep

1 | Overview

1.1 Motivation

The brain is a structure of great complexity. Billions of neurons — each a complex structure in itself — interact within and across brain regions and on various time scales. Yet, observing the brain we do not find pure chaos but a variety of rhythms and patterns that seem to coordinate brain activity and have been shown to correlate with cognitive functions such as memory consolidation. One of the rhythms for which this link is particularly evident is the hippocampal sharp wave-ripple. This thesis aims to contribute to our understanding of the generating mechanism of sharp wave-ripples, focusing in particular on inhibitory interneurons as a potential pacemaker for ripple oscillations.

1.2 Structure of the thesis

In Chapter 2 I will review the most important concepts that are necessary to motivate and understand the work presented in this thesis. I begin with a short introduction to the two hallmarks of computation and dynamics in the brain that I mentioned above: The brain's ability to support memory (Sec. 2.1), and the diversity of rhythms that characterize its activity (Sec. 2.2). Section 2.3 then summarizes how the sharp wave-ripple rhythm in particular may be linked to computational function, such as memory consolidation. Section 2.4 provides an overview of the anatomy and neuronal circuits of the hippocampus — the primary region of origin of sharp wave-ripples. I will then introduce sharp wave-ripples in detail (Sec. 2.5) and summarize their dynamical features. Section 2.6 introduces the variety of models that have been proposed to explain the generation of the ripple oscillation in particular. In a discussion of the current experimental evidence, I will point out the gaps in our understanding of the sharp wave-ripple rhythm and summarize why there is still no consensus about its generating mechanism (Sec. 2.7, 2.8). In light of this background, the research aims of this thesis will be stated more precisely in Chapter 3.

The main body of this thesis then contains three chapters: In Chapter 4, I develop a mean-field approximation for the ripple oscillation dynamics in an interneuron network with strong, delayed coupling under strong drive. The theory uncovers new parameter dependencies of the ripple frequency at strong, constant drive, and allows a mechanistic understanding of the emergence of IFA under time-dependent drive. Chapter 5 studies the alternative, inhibition-based ripple model based on an transient ringing effect in a weakly coupled population of interneurons. I demonstrate that this model has different prerequisites for the emergence of IFA, and highlight further crucial differences between the two inhibiton-first models that may advance model selection. Chapter 6 studies the linear response of escape noise models that receive deterministic input but spike stochastically according to a hazard function. I demonstrate that the choice of hazard function affects the single neuron linear response, and thus the oscillation dynamics in a network of such units with delayed inhibitory coupling. The mapping from input to output noise on the microscopic, single neuron level, is then used to apply a recently proposed mesoscopic integration scheme to efficiently simulate ripple oscillations on a population level. I will conclude with an overall discussion and outlook in Chapter 7.

2 | Introduction and background

2.1 Memory

2.1.1 The engram

What is a “memory”? In principle this is an unresolved question. A basic assumption in memory research is that the brain forms *representations* of the outside world (Semon, 1921; Josselyn et al., 2017). We define these representations by observing brain activity, often averaged over many trials, and correlating it with selected aspects of the environment (a *stimulus*), from our perspective of an outside observer. This is a dangerous concept since there is no inherent reason to assume that neural “representations” found in this way reflect how the brain actually represents, stores and processes information (Buzsáki, 2019).

Nevertheless, tracing the activity of such neuronal representations (also called *assemblies* or *engrams*) has yielded interesting insights into the workings of the brain (Tonegawa et al., 2015a; Barron et al., 2017; Josselyn and Tonegawa, 2020). The behavioral relevance of the engram has recently been demonstrated using transgenic and optogenetic tools: When mice learn to associate a specific context (cage) with a fearful experience (footshock) in a classical contextual fear conditioning task, the cells that are activated during the experience can be tagged genetically. After training, an optogenetic reactivation of these “engram” cells in a neutral cage (*i.e.* without presentation of the conditioned context) is sufficient to induce a fear response (Liu et al., 2012). It thus appears that the activity of the engram cells does indeed carry memory content and can support memory reactivation.

Current research is tracking engrams across brain regions and time to advance our understanding of memory consolidation (Tonegawa et al., 2015b,a; Kitamura et al., 2017; Tonegawa et al., 2018; Roy et al., 2022) (but see Lamothe-Molina et al., 2020).

2.1.1.1 Spatial memory in rodents

Memory studies in rodents are often based on spatial memory tasks for several reasons: Animals can easily be trained to perform different tasks in space, there is a clear readout of memory performance, and a lot is already known about how the brain, and specifically the hippocampus, represents space. It has been shown that the firing rate of pyramidal cells in the hippocampus can be tuned to a specific location in space. These so called *place cells* fire spikes whenever the animal traverses a particular region in space (the *place field*) (O’Keefe et al., 1971; O’Keefe, 1976). Place cells are complemented by *grid cells* in entorhinal cortex (Hafting et al., 2005), that fire in regular, hexagonal patterns across space, and *head direction cells* in various brain areas, such as the postsubiculum, thalamus and entorhinal cortex (Taube et al., 1990). In spatial memory tasks the experimenter thus already knows “where to look for the engram”.

2.1.2 Memory consolidation

The standard model for memory consolidation posits that new memories are first formed in the hippocampus and then gradually transferred to the neocortex (McClelland et al., 1995; Squire, 2004). Such a separation into a fast and a slow learning system is advantageous in that the hippocampus can capture newly incoming information fast on a one-shot basis, while the cortex can integrate the new information into the existing knowledge base in a slow, interleaved learning process avoiding catastrophic interference (McClelland et al., 1995).

There is plenty of evidence that the standard model is too simplified: Some memories may never become hippocampus-independent (Sutherland et al., 2008; Sutherland and Lehmann, 2011; Broadbent and Clark, 2013). On the other hand there are certain memories that can be newly acquired by the cortex alone, without hippocampal contribution (Sharon et al., 2011; Merhav et al., 2015). Effects such as reconsolidation (Nader, 2015; Kastner et al., 2016) and the formation of false episodic memories (Straube, 2012) suggest that memory is most likely not a mere storage process of static content but that each recall of an episodic memory also involves a generative component, potentially relying on the hippocampus (“generative episodic memory”) (Bartlett and Kintsch, 1995; Hemmer and Steyvers, 2009; Nagy et al., 2020; Fayyaz et al., 2022). The mechanisms of memory consolidation are hence subject of ongoing research, the review of which goes beyond the scope of this thesis (Nadel and Moscovitch, 1997; Winocur and Moscovitch, 2011; Dudai et al., 2015; Klinzing et al., 2019).

In general, memory consolidation is studied on two levels: Synaptic consolidation refers to the local stabilization and maintenance of previously formed assemblies by a strengthening of individual synapses via long term potentiation (LTP) (Kandel et al., 2014). Systems consolidation considers the transformation and relocation of memory assemblies across brain areas (Dudai et al., 2015; Klinzing et al., 2019).

An equally important counterpart to these “active” consolidation processes is synaptic homeostasis (Crick and Mitchison, 1983; Tononi and Cirelli, 2003; Diekelmann and Born, 2010). Pruning of irrelevant connections by a general *de*crease of synaptic strength can be just as beneficial for the signal-to-noise ratio of memory assemblies as the active strengthening of the assembly synapses.

2.1.3 Replay

The active portion of memory consolidation described above requires some form of rehearsal of previously learned information. Such *replay* can be readily observed in experimental data (Carr et al., 2011; Foster, 2017; Ólafsdóttir et al., 2018): It was first shown by Wilson and McNaughton (1994) that if hippocampal place cells were active during a spatial behavioral task, they would be reactivated with a similar correlation structure during subsequent sleep. When the behavioral task imposes a sequential structure, such as the repeated traversal of a linear track, place cells activate sequentially, with different place cells tuned to different locations along the track. The same sequential activation (replay) can be observed during subsequent slow wave sleep (Lee and Wilson, 2002) or periods of awake immobility (Diba and Buzsáki, 2007) (see Fig. 2.1).

Replay can even be observed in human brain activity: either directly based on spiking activity extracted from microelectrode array recordings in epileptic patients (Vaz et al., 2020); or more indirectly based on a decoding of replay-like events from fMRI data of healthy subjects (Schuck and Niv, 2019).

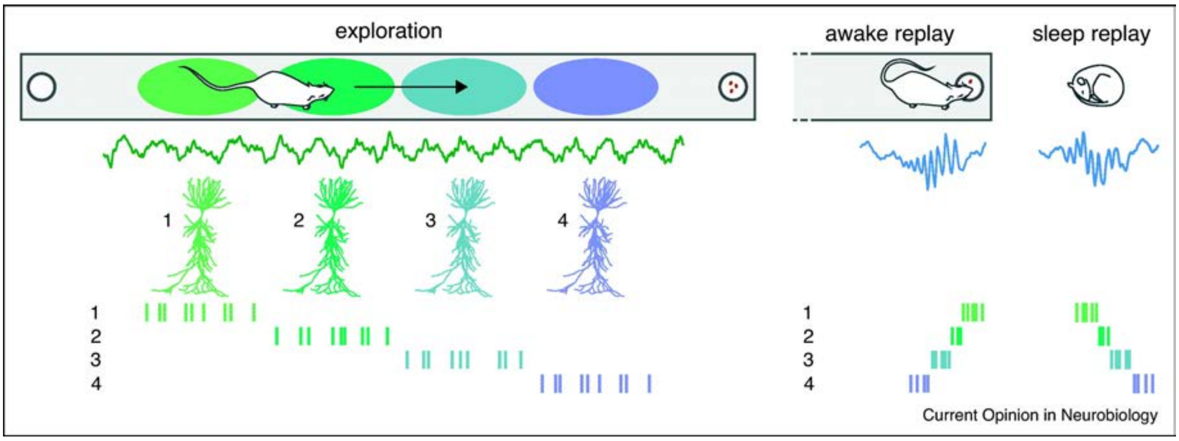

Figure 2.1: Replay. During awake exploration (left), the hippocampal LFP exhibits theta oscillations and populations of place cells (1-4) encode the animal's position in space. During quiet rest periods or SWS (right), SPW-Rs appear in the LFP while place cells are reactivated in the same order in which they fired during the prior experience (forward or reverse). Figure reprinted from Girardeau and Zugaro, 2011 with permission from Elsevier.

There are several potential functions of such replay events:

(1) Memory consolidation: Compared to the real experience which unfolds on the order of seconds, the reactivation of neuronal sequences during replay is compressed in time (∼50-100 ms), which may be beneficial for a strengthening of the respective synapses via spike-timing dependent plasticity (STDP) (Bi and Poo, 1998; Gerstner et al., 1996; Kempter et al., 1999). Replay may thus support local synaptic consolidation (King et al., 1999; Rosanova and Ulrich, 2005; Sadowski et al., 2016) (although some studies have questioned whether the neuromodulator composition in the sleep phases, during which replay occurs, can support LTP: Bramham and Srebro, 1989).

(2) Memory recall and planning: Replay goes beyond the mere rehearsal of recent experience and can be modulated by novelty (Foster and Wilson, 2006; Diba and Buzsáki, 2007), behavioral relevance (Terada et al., 2021) and the presence of rewards (Singer and Frank, 2009; Ólafsdóttir et al., 2015; Ambrose et al., 2016; Michon et al., 2019; Sterpenich et al., 2021). Awake replay can occur in both forward or reverse order (Foster and Wilson, 2006; Diba and Buzsáki, 2007; Csicsvari et al., 2007; Gupta et al., 2010). It does not require repetition but can occur after the first exposure to a novel track (Foster and Wilson, 2006) or involve the reactivation of remote memory content

(Karlsson and Frank, 2009). Awake replay (or *preplay*[1]) can also depict future paths that an animal is about to take towards a planned goal location, even if this path has never been taken before (Gupta et al., 2010; Pfeiffer and Foster, 2013; Ólafsdóttir et al., 2015). This indicates a role for awake replay in the recall of previous experience and planning of future behavior (Carr et al., 2011; Pfeiffer, 2020).

2.2 Rhythms in the brain

The investigation of memory consolidation is tightly linked to studying the various rhythms of neuronal activity which are thought to pace brain activity and potentially orchestrate cross-area communication and the transfer of information (Buzsáki, 2006).

Rhythms can be measured all over the brain, on different scales and depending on various brain states (Buzsáki, 2006; Penttonen and Buzsáki, 2003). While the macroscopic cortical rhythms can be picked up by EEG, subcortical and hippocampal rhythms are typically quantified in the local field potential (LFP) measured by intracranial electrodes. On the microscopic scale one can study the organization of the spiking activity of various neuron types with respect to the local rhythms. The rhythmic organization of the brain seems to be generally comparable across mammalian species, including humans (Colgin, 2016).

2.2.1 Rhythms during awake exploration

In the awake brain, cortical activity is dominated by transient gamma oscillations (30–100 Hz) (Adrian, 1942; Gray and Singer, 1989; Merker, 2013) and mostly desynchronized neuronal spiking (Harris and Thiele, 2011; Poulet and Crochet, 2019), potentially due to a balance of excitatory and inhibitory inputs (Van Vreeswijk and Sompolinsky, 1996; Brunel, 2000; Shu et al., 2003; Froemke, 2015; Zhou and Yu, 2018). The hippocampus exhibits a theta rhythm (4–12 Hz) (Vanderwolf, 1969; Colgin, 2016) (but see (Yartsev et al., 2011)) with nested gamma oscillations (Buzsáki et al., 1983; Bragin et al., 1995; Colgin, 2016). Hippocampal theta and cortical gamma oscillations can interact (Canolty et al., 2006; Sirota et al., 2008). During periods of quiet rest brain activity can switch and exhibit a profile more similar to slow wave sleep which will be discussed in the following.

2.2.2 Rhythms during offline states and sleep

Sleep is thought to play an important role in all aspects of memory consolidation (Born et al., 2006; Diekelmann and Born, 2010; Girardeau and Lopes-dos Santos, 2021). Sleep consists of rapid eye movement (REM) and non-REM phases that alternate cyclically (Diekelmann and Born, 2010). Non-REM sleep can be further subdivided into periods of slow wave sleep (SWS) and light sleep stages. Sleep phases vary with respect to neuromodulation and rhythmic organization. Brain activity during REM sleep is similar to the awake state with prominent theta oscillations and a high level of acetylcholine (ACh), which may promote synaptic plasticity (Diekelmann and Born, 2010). Slow wave sleep on the other hand has low cholinergic tone and is dominated by three rhythms of vastly different speeds: slow cortical oscillations, thalamic spindles and hippocampal sharp wave-ripples.

---

[1] The existence of preplay (Dragoi and Tonegawa, 2012) also raises a more fundamental question about hippocampal or brain activity in general: Is the hippocampus per se a “tabula rasa” (Buzsáki, 2019) that starts forming representations and connecting them sequentially once required by experience? Or is the hippocampus an intrinsic generator of assemblies and sequences which only acquire meaning once inputs get mapped onto them? This is a very interesting discussion that is however beyond the scope of this thesis (Grosmark and Buzsáki, 2016; Buzsáki, 2019; McKenzie et al., 2021).

During slow oscillations (0.5–1 Hz) cortical areas alternate between UP states of increased depolarization, and neuronal activity and short, intermittent DOWN states of dominant hyperpolarization and neuronal silence (Steriade et al., 1993; Sirota and Buzsáki, 2005). These UP/DOWN states are synchronized across brain areas (Volgushev et al., 2006) and also occur in the entorhinal cortex (Kajikawa et al., 2021) — one of the main input areas of the hippocampus.

Thalamo-cortical spindles are transient ($\geq$ 500 ms) bouts of mid-range oscillations (7–15 Hz) (Berger, 1933; Loomis et al., 1935; Steriade and Deschenes, 1984; Steriade et al., 1987). They are thought to be generated by bursting neurons in the thalamic reticular nucleus, but the spindle component is picked up even in the cortical EEG.

Hippocampal sharp wave-ripples (SPW-R) are short transient events (50–100 ms) of elevated neuronal firing, modulated by a fast oscillation (140–220 Hz). They are the main subject of this thesis and will thus be introduced in depth in Section 2.5.

Cortical, thalamic and hippocampal rhythms are intricately linked (Oyanedel et al., 2020): Transitions from a DOWN to an UP state in the cortex are accompanied or closely followed by an increase in hippocampal SPW-R incidence (Battaglia et al., 2004; Isomura et al., 2006; Kajikawa et al., 2021). Hippocampal SPW-Rs propagate to hippocampal output structures, such as the subiculum, retrosplenial cortex and deep layers of entorhinal cortex (Chrobak and Buzsaki, 1996; Nitzan et al., 2020), and are followed by thalamic spindles (Siapas and Wilson, 1998; Peyrache et al., 2011). Spindles and SPW-Rs can also co-occur in which case ripples tend to occur phase-locked to the spindle trough (Sirota et al., 2003; Clemens et al., 2011; Staresina et al., 2015). On the other hand, hippocampal ripples tend to be followed by an UP-DOWN transition in the cortex (Sirota et al., 2003), thus closing the loop of the cortical slow oscillation cycle.

It is worth mentioning that the classic view summarized here, with a strong separation between the rhythms during wake and sleep, is likely an oversimplification. Recent evidence has found combinations of the rhythms of distinct brain states, such as gamma oscillations during sharp wave-ripples (Carr et al., 2012) or ripples nested in theta oscillations (Seenivasan et al., 2022).

2.3 A functional role for sharp wave-ripples in memory consolidation

The connection between brain dynamics and computation is particularly evident in the case of the hippocampal sharp wave-ripple. SPW-Rs have been implicated in both the active and the passive aspects of memory consolidation described above.

2.3.1 Sharp wave-ripples for active memory consolidation

Whenever hippocampal cells "replay" previous experiences (Section 2.1.3), the local field potential exhibits sharp wave-ripples (rodents: Nádasdy et al., 1999; Lee and Wilson, 2002; Diba and Buzsáki, 2007, humans: Clemens et al., 2011; Jiang et al., 2017; Cox et al., 2019; Vaz et al., 2019, 2020). It remains unclear whether the SPW-R rhythm aids the emergence of replay and/or synaptic consolidation (Stark et al., 2015; Roux et al., 2017; Sadowski et al., 2016), or whether both phenomena just co-occur, potentially due to the same cause. A prolongation of SPW-Rs by optogenetic stimulation has been shown to also prolong the replay event (Fernández-Ruiz et al., 2019). Experiments on a particularly long linear track demonstrated that, vice versa, replay of particularly long sequences does *not* extend the SPW-R arbitrarily. Instead, long replay episodes span multiple SPW-R events, with SPW-R incidence strongly increased during the replay period (Davidson et al., 2009).

Even if SPW-Rs do not *cause* replay, their co-occurence with the neuronal reactivation may support systems memory consolidation, given that SPW-Rs are integrated into a large system of brain-wide rhythms (Sec. 2.2.2) (Todorova and Zugaro, 2020). Hippocampal SPW-Rs are followed by neuronal reactivations in deep entorhinal cortex, medial prefrontal cortex (Siapas and Wilson, 1998; Wierzynski et al., 2009; Peyrache et al., 2009; Jadhav et al., 2016) and even parietal cortex (Wilber et al., 2017). These extra-hippocampal reactivations can be coherent with hippocampal replay in their content, as was shown in the case of CA1 place cells and deep EC grid cells replaying spatially coherent trajectories (Ólafsdóttir et al., 2016, 2017, but see Kaefer et al., 2020). Such cross-area communication may be mediated by the nested hippocampal, subcortical and cortical rhythms (Todorova and Zugaro, 2020; Tukker et al., 2020; Girardeau and Lopes-dos Santos, 2021). The flow of information during these rhythmic interactions is largely unresolved. A common hypothesis, in line with the standard two-stage model of memory consolidation (McClelland et al., 1995; Buzsáki, 1989) is the following (Fig. 2.2): When the cortex transitions from a DOWN to an UP state, the resulting depolarization triggers hippocampal SPW-Rs and a relay of hippocampal information to the cortex (possibly gated by the spindle rhythm), which in turn reactivates relevant cortical memory assemblies. The subsequent thalamic spindles support cortical synaptic plasticity (Seibt et al., 2017) and hence an integration of the hippocampal information into the existing cortical knowledge structure. Spindles might decouple cortical regions from hippocampal inputs during these periods (Peyrache et al., 2011). Maingret et al. (2016) demonstrated that artificial enhancement of cortico-hippocampal coupling can indeed enhance memory performance. Theoretical work has investigated in more detail the potential mechanisms for how oscillations could support the transfer and storage of information (Varela et al., 2001; Fries, 2005, 2015; Kirst et al., 2016; Droste and Lindner, 2017; Palmigiano et al., 2017).

There is a growing body of experimental evidence supporting a functional role of SPW-R-associated replay in memory consolidation (Buzsáki, 1989; Hasselmo and McClelland, 1999). If rats are trained on a hippocampus-dependent spatial memory task and SPW-Rs during subsequent slow wave sleep are detected and disrupted in an online-protocol, performance decreases markedly (Girardeau et al., 2009; Ego-Stengel and Wilson, 2010). On the other hand, prolongation of SWP-Rs by optogenetic stimulation extends ongoing replay and is beneficial for memory (Fernández-Ruiz et al., 2019). SWP-R incidence is increased during slow wave sleep following learning (Eschenko et al., 2008). It was shown that this upregulation is NMDA-dependent and specific to episodes of novel learning, i.e. when new information needs to be consolidated (Girardeau et al., 2014). Replay of assembly patterns representing specific goal locations during SPW-R is associated with subsequent memory performance for the respective locations (Dupret et al., 2010).

The possibilities for manipulating replay in humans to examine behavioral effects are of course limited. There have been a number of elegant experiments, however, suggesting a link between replay and memory performance: For example, providing auditory cues for specific memory items during post-learning sleep (supposedly evoking increased replay of these items) was shown to increase memory performance, selectively for the cued compared to non-cued items (Rudoy et al., 2009). Furthermore, SPW-R incidence in human rhinal cortex during post-learning sleep was shown to be correlated with subsequent memory performance (Axmacher et al., 2008).

Since awake replay is equally coupled to SPW-Rs, SPW-R may by extension also have a functional role in memory recall and planning. Disruption of awake SPW-Rs and SPW-R-associated replay has been shown to impair performance in a spatial working memory task (Jadhav et al., 2012).

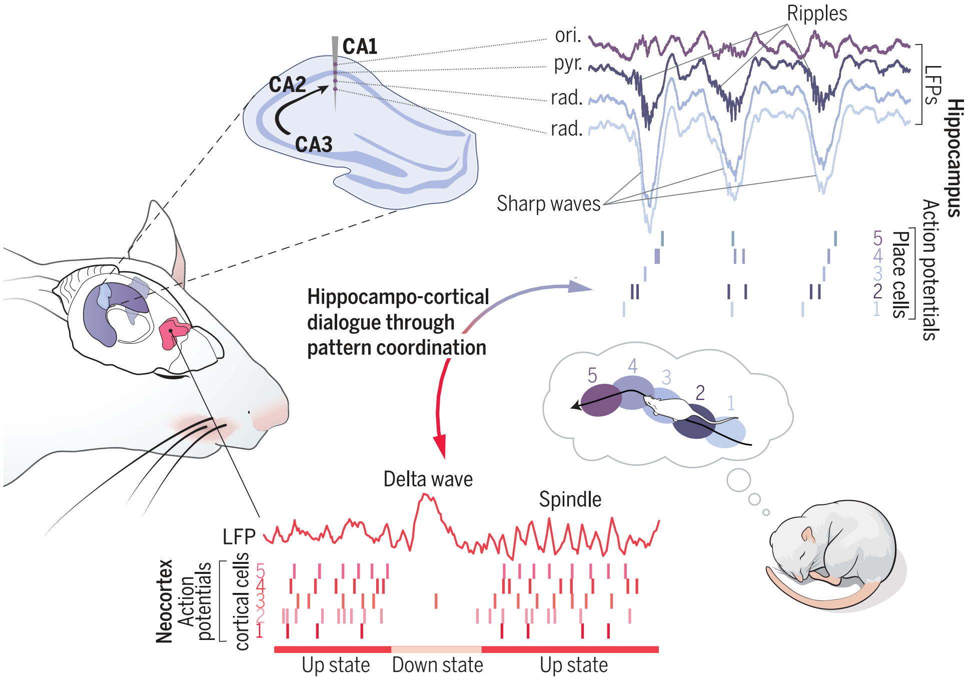
Ripples
CA1
CA2
CA3
ori.
pyr.
rad.
rad.
LFPs
Hippocampus
Sharp waves
Action potentials
Place cells
5
4
3
2
1
Hippocampo-cortical dialogue through pattern coordination
5
4
3
2
1
Delta wave
Spindle
LFP
Neocortex
Action potentials
cortical cells
5
4
3
2
1
Up state
Down state
Up state

Figure 2.2: Rhythmic cortico-hippocampal interactions and replay during slow wave sleep. The hippocampal LFP exhibits sharp wave-ripples, while individual neurons (here place cells) *replay* behaviorally relevant information (blue). The occurrence of SPW-Rs is coordinated with neocortical activity (red) that alternates between up states, with elevated neuronal activity and thalamic spindles, and silent down states. From Girardeau and Lopes-dos Santos (2021)/Reprinted with permission from AAAS.

2.3.2 Sharp wave-ripples for synaptic homeostasis

The synaptic homeostasis hypothesis assumes that, after waking periods inducing a net *in*crease in synaptic strengths all over the brain (Vyazovskiy et al., 2008; Huber et al., 2013), slow wave sleep might serve to downscale synaptic strengths (Crick and Mitchison, 1983; Tononi and Cirelli, 2003). The fact that slow waves are strongest in the early sleep phases and then progressively occur less over the course of sleep, fits nicely into this picture (Borbély, 2001).

The neuromodulatory characteristics and neuronal firing patterns during cortical slow oscillations have been suggested to favor long term synaptic depression (LTD) (Czarnecki et al., 2007; Kemp and Bashir, 2001; Vyazovskiy et al., 2008). SPW-Rs on the other hand were thought to promote LTP rather than LTD (Buzsáki et al., 1987; King et al., 1999).

Recent evidence however has also implicated SPW-Rs into the downregulation of synaptic strength (Norimoto et al., 2018): The authors disrupted hippocampal SPW-Rs by activating SOM^{+} interneurons optogenetically, while probing repeatedly the synaptic strength of the Schaffer Collateral synapses between CA3 and CA1. While synaptic strength usually decreases over the course of slow wave sleep, consistent with LTD and synaptic homeostasis, it remained constant when SPW-Rs were disrupted. As a result of this lack of depression, the encoding of new memories was impaired during subsequent waking episodes: consistent with the idea that homeostasis during slow wave epochs is needed to maintain normal brain function.

Altogether, SPW-Rs have so far been implicated in memory consolidation and planning by their *association* to the processes of replay and synaptic depression. All above experimental manipulations affect not only SPW-Rs but also the associated process: The silencing of SPW-Rs also prevents replay (Girardeau et al., 2009). It is thus difficult to draw conclusions about the functional relevance of SPW-Rs *per se* for memory consolidation/planning.

Are fast ripple oscillations beneficial for organizing the neuronal spiking activity into short time windows (Buzsáki and Chrobak, 1995; Singer, 2018)? Or are SPW-Rs a mere epiphenomenon of neuronal reactivations without any functional relevance? A detailed understanding of the generating mechanism of SPW-Rs might enable the design of more sophisticated experiments, that do not fully abolish both SPW-Rs and replay but merely *modify* SPW-R dynamics and thus allow conclusions about their role in replay, memory consolidation and the orchestration of cortical rhythms.

In the remainder of this introduction I will thus review in detail the dynamical features of sharp wave-ripples, as well as the various models that have been proposed to explain SPW-R generation, in light of current experimental evidence. I will focus specifically on the ripple oscillation. Before diving into SPW-Rs (Section 2.5) it is useful to give a short overview of the underlying circuits and cell types (Section 2.4).

2.4 Hippocampal anatomy

The hippocampus (named for its seahorse-like shape) lies in the medial temporal lobe — one in each hemisphere (Fig. 2.3A). The hippocampus proper with its distinct

Cornu Ammonis subfields CA1, CA2 and CA3, is embedded in the larger hippocampal formation that also includes the dentate gyrus (DG) and the subiculum (Fig. 2.3A,B).

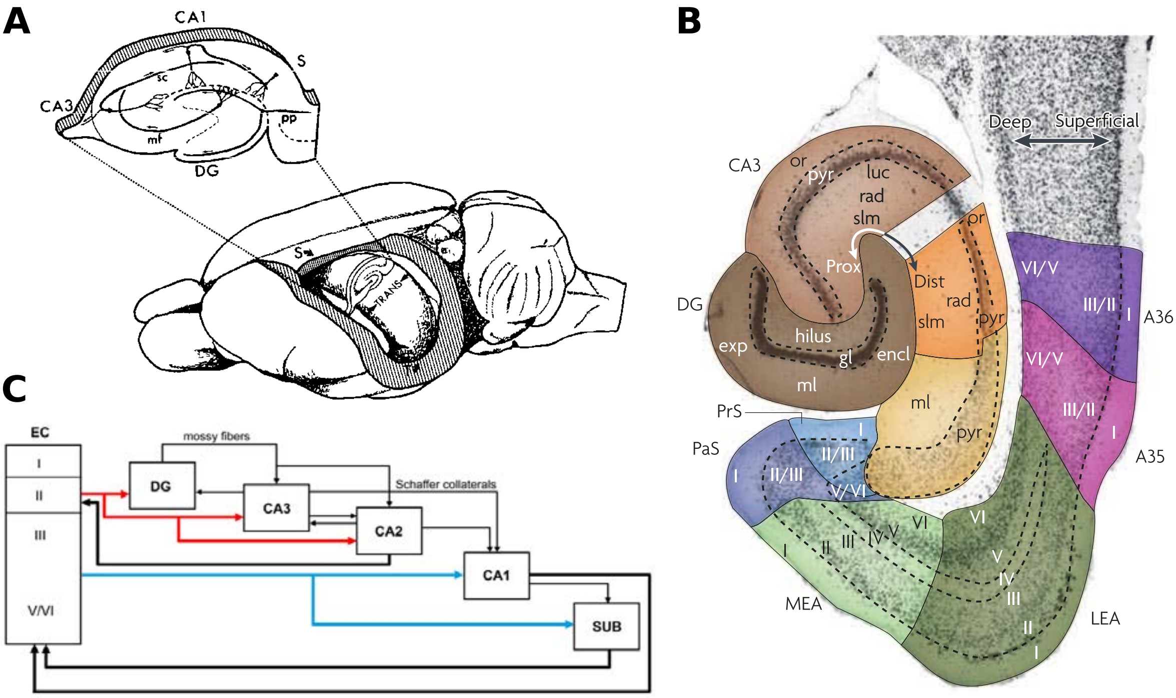
A
CA1
S
CA3
sc
pp
mf
DG
S
TRANS
B
Deep
Superficial
CA3
or
pyr
luc
rad
slm
Prox
Dist
or
rad
slm
pyr
DG
exp
hilus
gl
encl
ml
ml
pyr
PrS
PaS
I
II/III
V/VI
I
II/III
VI/V
III/II
I
A36
VI/V
III/II
I
A35
I
II
III
IV
V
VI
VI
V
IV
III
II
I
MEA
LEA
C
EC
I
II
III
V/VI
mossy fibers
DG
CA3
CA2
Schaffer collaterals
CA1
SUB

Figure 2.3: Hippocampal anatomy. A, Hippocampal formation within the rat brain. Zoom along the transverse axis shows DG, subiculum (S) and hippocampal subfields CA1-3 (reproduced from Amaral and Witter, 1989, with permission from Elsevier, top left: original image from Andersen et al., 1971). **B,** Horizontal cross section, indicating the subfields and layers of the hippocampus proper and the parahippocampal regions. DG: dentate gyrus; orange area: CA1; yellow: subiculum; PrS: presubiculum; PaS: parasubiculum; MEA, LEA: medial, lateral entorhinal aspect; Brodmann areas A35, A36: perirhinal cortex (adapted from van Strien et al., 2009, with permission from Springer Nature). **C,** Simplified diagram of the (para)hippocampal circuit structure (adapted from Llorens-Martín et al., 2014, CC BY 3.0).

The hippocampus is a complex structure that not only receives input from and projects back to cortical and thalamic structures, but is also recurrently connected to form a loop in itself (Fig. 2.3C). The entorhinal cortex (EC) is the main gateway of cortical information into and out of the hippocampus. One can distinguish two main streams of information from superficial EC via the perforant path towards CA1 (Tamamaki and Nojyo, 1993; Witter, 1993): EC layer III cells project directly onto CA1 (Kiss et al., 1996; Naber et al., 2001; Takács et al., 2012). On the other hand, EC layer II projects onto CA3, both directly and via the DG, and CA3 provides feedforward input to CA1 via the Schaffer Collaterals. All hippocampal output goes through CA1 which projects back to the deep EC layers (preferentially L5b), either directly, or via the subiculum (Sürmeli et al., 2015). The deep EC layers project back to the superficial layers, thus introducing a loop (Cajal, 1902; Dolorfo and Amaral, 1998; Köhler, 1985; Witter and Groenewegen, 1986; Hamam et al., 2002; van Haeffen et al., 2003). Furthermore, deep EC relays hippocampal output towards cortical regions such as prefrontal, parietal and retrosplenial cortex (Witter, 1993; Canto et al., 2008).

There are also direct projections from CA1 to the medial prefrontal cortex (Swanson, 1981; Jay and Witter, 1991), as well as multiple subcortical areas (Cenquizca and Swanson, 2007). In turn CA1 receives direct mPFC input via the thalamic nucleus reuniens (Wouterlood et al., 1990; Goswamee et al., 2021; Ferraris et al., 2021).

Being this highly interconnected in itself and with other cortical areas, the hippocampus may perform complex computations, integrate information from a multitude of brain areas, and broadcast its activity back to thalamic and cortical regions.

2.4.1 Circuitry and cell types of CA1

The hippocampal subfield CA1 is the most prominent site of ripple generation (see also Section 2.5). In the following I will give a brief overview of the most important cell types in CA1 and their connectivity (see also Wheeler et al., 2015).

The subareas of the hippocampal formation, as well as the entorhinal cortex, have a laminar structure (Fig. 2.3B): The cell bodies of most pyramidal cells are arranged in a dense layer, the *stratum pyramidale*. Their axons and basal dendrites extend into *str. oriens*, while their apical dendrites branch out to *str. radiatum* and *str. lacunosum-moleculare* (Andersen et al., 2006; Amaral and Witter, 1989). The various interneuron types have a more variable distribution (Freund and Buzsáki, 1996).

Region CA1 contains a total of 350,000 cells in the rat hippocampus (Bezaire and Soltesz, 2013). The cells can be subdivided into excitatory pyramidal cells, and inhibitory interneurons. The ratio of pyramidal cells to interneurons is approximately 10:1 (Bezaire and Soltesz, 2013; Traub and Miles, 1991; Andersen et al., 2006).

2.4.1.1 Pyramidal cells

The majority of CA1 cells are excitatory pyramidal cells (89-93% (Bezaire and Soltesz, 2013)). CA1 pyramids receive most of their excitatory input from ipsi- and contralateral CA3 pyramidal cells via the Schaffer Collaterals that project onto pyramidal cell dendrites in *str. radiatum* and *str. oriens* (Amaral and Witter, 1989; Bezaire and Soltesz, 2013). At the distal apical dendrites in *str. lacunosum-moleculare* most glutamatergic inputs come from lateral and medial entorhinal cortex layer III via the temporoammonic pathway (Andersen et al., 2006). The thalamic nucleus reuniens innervates the same region (Wouterlood et al., 1990). In constrast to this massive feedforward innervation, the local excitation that a CA1 pyramidal cell receives from its peers is very sparse. The connection probability between CA1 pyramids has been estimated as low as ∼1% (∼200 synapses per neuron, Knowles and Schwartzkroin, 1981; Deuchars and Thomson, 1996; Andersen et al., 2006; Bezaire and Soltesz, 2013) (but see additional longitudinal connections: Yang et al., 2014).

Disregarding ivy and neurogliaform cells, CA1 pyramidal cells receive inhibitory input mainly from local basket and axo-axonic cells (Bezaire and Soltesz, 2013). Additional inhibitory input comes from bistratified cells (at the proximal dendrites) and neurogliaform and O-LM cells (at the distal apical dendrites), among others (Buhl et al., 1994a; Megías et al., 2001; Klausberger and Somogyi, 2008; Bezaire and Soltesz, 2013). The various interneuron types can thus gate the inputs to pyramidal cells and potentially pace their spiking activity.

2.4.1.2 Interneurons

Around 7-11% of CA1 cells are GABAergic interneurons (Bezaire and Soltesz, 2013; Woodson et al., 1989). One can distinguish at least 21 different classes of interneurons based on their morphology, electrophysiological properties and sensitivity to neurochemical markers (Klausberger and Somogyi, 2008; Freund and Buzsáki, 1996; Cutsuridis et al., 2010). I will mention here only the most common interneuron types (see also Fig. 2.6):

Neurogliaform and ivy cells Neurogliaform and ivy cells do not seem to be involved in the generation of SPW-Rs, but shall be mentioned here since they form the largest class of CA1 interneurons (32.2% Bezaire and Soltesz, 2013). They are thought to be important for the maintenance of homeostasis via modulation of excitability (Klausberger and Somogyi, 2008).

Basket cells Approximately 23.8% of CA1 interneurons are basket cells. Their somata lie in *str. pyramidale* and their axonal arbor is confined to the same layer (or proximal *str. oriens/str. radiatum*) (McBain et al., 1994; Sik et al., 1995; Klausberger et al., 2003). The apical dendrites of basket cells extend to *str. radiatum* and *str. lacunosum-moleculare* where they receive excitatory input from the Schaffer Collaterals. Their basal dendrites lie in *str. oriens* and the alveus and receive input from local CA1 pyramidal cells and other interneurons (Pawelzik et al., 2002). Basket cells form synapses onto the soma or proximal dendrites of their targets.

Basket cells can express either PV (14.4% of CA1 interneurons, *i.e.* ∼5,000 cells in rat CA1) or CCK (9.4%, ∼ 3,500 cells, Bezaire and Soltesz, 2013): PV^+ BCs are fast-spiking cells that can fire up to ∼100 Hz without spike frequency adaptation (Pawelzik et al., 2002). They project only to local CA1 neurons — pyramidal cells or interneurons (Sik et al., 1995; Bezaire and Soltesz, 2013). It has been estimated that every CA1 PV^+ BC is connected to ∼40 other CA1 PV^+ BCs monosynaptically (Sik et al., 1995; Bezaire and Soltesz, 2013). CCK^+ BCs spike regularly with frequencies limited to ∼40-50 Hz (Freund, 2003). The axonal projections of CCK^+ BCs are less well studied but seem comparable to those of PV^+ BCs (Bezaire and Soltesz, 2013).

Bistratified cells The somata of bistratified cells (5.7% of CA1 interneurons) are located in *str. pyramidale* (Buhl et al., 1996; Halasy et al., 1996). Their dendrites lie mainly in *str. pyramidale* and *str. radiatum* where they receive input from the Schaffer collaterals (Halasy et al., 1996). Bistratified cells project onto the basal and apical dendrites of other CA1 cells (mostly pyramids, sometimes interneurons) in *str. oriens* and *str. radiatum* (Halasy et al., 1996; Maccaferri et al., 2000; Klausberger et al., 2004; Klausberger, 2009). Bistratified cells express both PV and SOM (Baude et al., 2007).

Axo-axonic chandelier cells Axo-axonic cells (3.8% of CA1 interneurons) have somata in *str. pyramidale* and *str. oriens* (Buhl et al., 1994a,b). They target exclusively CA1 pyramidal cells, mostly onto their axon initial segment (Somogyi et al., 1983; Li et al., 1992) and can thus gate their output (Dugladze et al., 2012). Axo-axonic cells express PV (Baude et al., 2007).

Oriens-lacunosum moleculare (O-LM) cells As suggested by their name, O-LM interneurons (4.3% of CA1 interneurons) have somata in *str. oriens* (Klausberger and Somogyi, 2008) and dendrites in the same layer or the alveus (Sik et al., 1995; Maccaferri, 2005). They hence receive excitatory input mainly from local CA1 pyramidal cells (Blasco-Ibáñez and Freund, 1995). O-LM axons mainly target the distal apical dendrites of CA1 pyramidal cells in *str. lacunosum-moleculare* (Wouterlood et al., 1990; Colbert and Levy, 1992; Empson and Heinemann, 1995), but can also extend to *str. oriens* and project onto interneurons (Sik et al., 1995). 17% of the postsynaptic targets of O-LM cells are unknown (Katona et al., 1999). O-LM cells express SOM, mGluR1α (Ferraguti et al., 2004) and up to 33% of them express PV (Varga et al., 2012, in mouse).

Inputs to CA1 interneurons To date there is not sufficient data to properly characterize the inputs to each class of CA1 interneurons separately. Instead Bezaire and Soltesz (2013) summarized the available data for different interneuron types to infer the approximate inputs to an average CA1 interneuron. For any given interneuron type one should hence expect significant variation from this hypothetical average interneuron.

In *str. radiatum* 7% of Schaffer Collateral synapses from CA3 are made onto interneurons (Takács et al., 2012; Bezaire and Soltesz, 2013). In *str. lacunosum-moleculare* 9% of the perforant path input arriving from entorhinal cortex targets interneurons (Takács et al., 2012). In addition each interneuron receives excitatory input from local CA1 pyramidal cells. Knowles and Schwartzkroin (1981) estimated the connection probability between CA1 pyramidal cells and interneurons in *str. pyramidale* as ~30%. Additional excitatory input can come from the alveus (Takács et al., 2012), septum and raphe (Gulyás et al., 1999; Bezaire and Soltesz, 2013). CA1 interneurons receive inhibition both locally and from non-CA1 sources such as the entorhinal cortex and the septum (Freund and Antal, 1988; Bezaire and Soltesz, 2013). The deviation of the input distributions of individual interneuron types from this average picture depends crucially on their lamiar position in CA1. For a review see also (Chamberland and Topolnik, 2012).

2.5 Hippocampal sharp-wave ripple

Sharp wave-ripples (SPW-R) are transient (50-100 ms) events measured in the local field potential (LFP) of the hippocampus during slow-wave sleep or episodes of quiet wakefulness (Buzsáki, 1986, 2015; Maier and Kempter, 2017). They occur spontaneously at a rate of ~1/sec and consist of a large amplitude deflection in the voltage (the sharp wave) superimposed with a fast oscillation (the ripple, ~140–220 Hz, see Fig. 2.4A).

SPW-Rs have been found in many mammalian species (rat, mouse, cat, monkey, sheep etc), including humans (Bragin et al., 1999) (for a review see Buzsáki, 2015). They occur not only in the hippocampus proper, but also in the amygdala (Ponomarenko et al., 2003; Perumal et al., 2021), dentate gyrus (Swaminathan et al., 2018; Meier et al., 2020) and hippocampal output structures such as the retrosplenial cortex (Nitzan et al., 2020), the subiculum (Chrobak and Buzsaki, 1996; Imbrosci et al., 2021), the entorhinal cortex (Chrobak and Buzsaki, 1996), and deep layers of pre- and parasubiculum (Chrobak and Buzsaki, 1996). Recently, ripple oscillations have even been observed in parietal, midline and prefrontal cortical areas (Khodagholy et al., 2017).

SPW-Rs also occur in hippocampal slices *in vitro* (Fig. 2.4B), with features that are generally comparable to *in vivo* SPW-Rs (for a comprehensive review see Maier and Kempter, 2017). Ripple oscillations *in vitro* are slightly faster (∼210 ± 16 Hz, Maier et al., 2003) than *in vivo* (150-250 Hz, Buzsáki et al., 1992). SPW-R incidence and duration, and the recruitment of various cell types, however, are similar. It is thus assumed that *in vitro* data can be used to understand SPW-R generation *in vivo.*

SPW-Rs appear coordinated with cortical and thalamic activity (Battaglia et al., 2004; Logothetis et al., 2012) and can be modulated by extra-hippocampal activity (Ishikawa et al., 2014; Vandecasteele et al., 2014). Yet, they persist after cortical lesions *in vivo* (Buzsáki et al., 1983; Suzuki and Smith, 1988; Bragin et al., 1995) and even occur spontaneously in isolated hippocampal slices *in vitro* (Wu et al., 2002; Maier et al., 2002, 2003; Hájos et al., 2009; Maier and Kempter, 2017). SPW-Rs are thus considered to originate in the hippocampus.

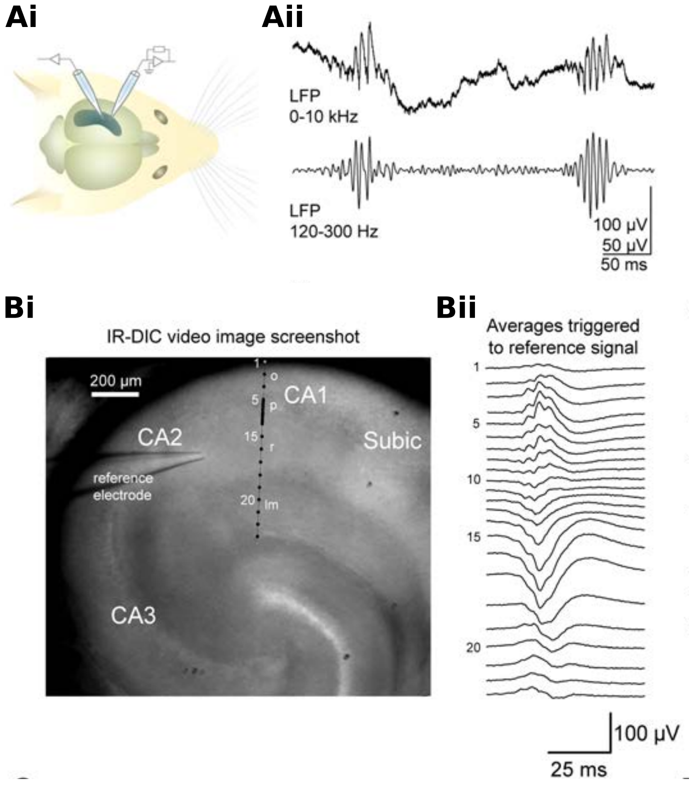

Figure 2.4: Sharp wave-ripples *in vivo* and *in vitro.* **A,** SPW-Rs in LFP of mouse CA1 *in vivo.* Ai: recording setup; Aii top: raw LFP trace with 2 SPW-R events; bottom: bandpass-filtered LFP (adapted from Maier et al., 2011, with permission from Elsevier). **B,** Laminar profile of SPW-Rs in different layers of CA1 *in vitro.* Bi: hippocampal slice with reference and recording electrode. Layers marked as o: *oriens*, p: *pyramidale*, r: *radiatum*, l: *lacunosum-moleculare.* Bii: Average LFP across CA1 layers. The SPW amplitude is positive in *str. pyramidale* and negative in *str. radiatum* (adapted from Maier et al., 2009, CC BY).

2.5.1 Measuring sharp-wave ripples in the LFP

Typically, SPW-Rs are detected in the local field potential (LFP) measured in the hippocampus. The LFP is generally thought to reflect local network activity. Its detailed composition in a given brain area depends on the arrangement and morphology of the local cells and their firing patterns (Buzsáki et al., 2016).

The amplitude and polarity of the sharp wave depend on the recording site along the somato-dendritic layers and range from large negative values in *str. radiatum* and *lacunosum-moleculare* to large positive values in *str. pyramidale* and *str. oriens*, as can be seen in Fig. 2.4Bii (Buzsáki et al., 1983; Buzsáki, 1986; Sullivan et al., 2011). In *str. radiatum* the sharp wave is thought to reflect a current sink due to increased excitatory synaptic transmission from CA3 pyramidal cells to CA1 neurons via the Schaffer Collaterals.

The ripple component is most prominent in the CA1 cell body layer *str. pyramidale* (Buzsáki, 1986; Buzsáki et al., 1992). Traditionally the LFP in *str. pyramidale* is thought to reflect synaptic transmembrane currents rather than spiking activity (Mitzdorf, 1985; Buzsáki et al., 2016; Chizhov et al., 2015). Excitatory connectivity in CA1 is sparse and pyramidal cell axons lie in *str. oriens* rather than *str. pyramidale.* There are however various CA1 interneuron types that form their synapses in *str. pyramidale*, such as basket cells and axo-axonic chandelier cells. Thus, inhibitory postsynaptic currents are thought to be the main source of the LFP signal in CA1 *str. pyramidale.*

Recent modeling studies however suggested that excitatory action potentials also contribute to the local field potential, when occuring phase-locked to the fast ripple oscillation, (Schomburg et al., 2012; Ramirez-Villegas et al., 2018). If this is indeed the case, it introduces a large confounding factor for experiments probing the role of excitation in ripple generation. I will come back to this in the discussion of experimental evidence in Section 2.8.

For now it is sufficient to keep in mind that understanding SPW-Rs observed in the LFP requires answering *two* questions: What generates the SPW-R rhythm in the neuronal circuit? And what constitutes the LFP signal? This thesis will contribute to the former question, specifically the generation of the ripple rhythm.

2.5.2 Intra-ripple frequency accommodation

While ripple frequency is usually just reported as an average over time and across many events, a few studies have quantified the instantaneous ripple frequency over the course of individual ripple events (Ponomarenko et al., 2004; Nguyen et al., 2009; Sullivan et al., 2011; Donoso et al., 2018). In most ripple events (∼75%, Nguyen et al., 2009) the instantaneous ripple frequency decreases (by ∼20–60 Hz) from high towards low frequencies over the course of the event (Fig. 2.5). This effect has been termed *intra-ripple frequency accommodation* (IFA). The exact shape of the instantaneous ripple frequency over time varies across events: the instantaneous ripple frequency can decrease monotonically (Ponomarenko et al., 2004; Nguyen et al., 2009; Sullivan et al., 2011; Hulse et al., 2016), have a peak during the first half of the ripple (Nguyen et al., 2009; Donoso et al., 2018), or a minimum during the second half of the ripple, followed by a short increase (Ponomarenko et al., 2004; Nguyen et al., 2009).

IFA has been observed both *in vivo* (Ponomarenko et al., 2004; Nguyen et al., 2009; Sullivan et al., 2011; Hulse et al., 2016) and *in vitro* (Donoso et al., 2018), in different species (rat: Ponomarenko et al., 2004; Nguyen et al., 2009; Sullivan et al., 2011, mouse: Donoso et al., 2018; Hulse et al., 2016), brain states (awake: Ponomarenko et al., 2004; Sullivan et al., 2011; Hulse et al., 2016, sleep: Nguyen et al., 2009; Sullivan et al., 2011), and both in the LFP (CA1: Ponomarenko et al., 2004; Nguyen et al., 2009; Sullivan et al., 2011; Hulse et al., 2016, CA3, DG: Sullivan et al., 2011) as well as in inhibitory postsynaptic currents of CA1 pyramidal cells (Donoso et al., 2018).

The IFA phenomenon will be a central topic of this thesis, since I propose that it can be used as a marker for model selection (see Chapter 3).

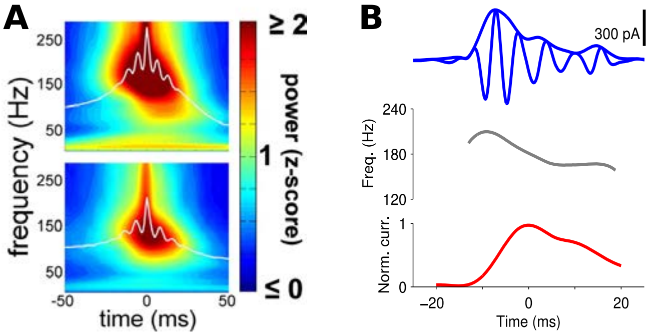

Figure 2.5: Intra-ripple frequency accommodation (IFA). A, Average wavelet spectrogram of ripple (top) or fast gamma oscillation (bottom) measured in the CA1 LFP of a freely moving rat. Power is color coded, and the LFP signal is overlaid in white. The frequency of maximal power decays over time (adapted from Sullivan et al., 2011, CC BY-NC-SA 3.0). **B,** Excitatory (red, bottom) and inhibitory (blue, top) synaptic current during ripples, measured intracellularly in pyramidal cells of mouse CA1 *in vitro.* The instantaneous frequency of the ripple-modulated inhibitory current (grey) decreases over time (adapted from Donoso et al., 2018, CC BY 4.0).

2.5.3 Recruitment of hippocampal cell types during SPW-Rs

The first step towards understanding the generation of SPW-Rs is an examination of the activity of the distinct cell types that form the substrate underlying the measured LFP signal. Approximately ∼10% of hippocampal neurons are active during SPW-Rs (Ylinen et al., 1995; Csicsvari et al., 2000; Buzsáki, 2006; Mizuseki and Buzsáki, 2013, see Fig. 2.6 for a summary). CA1 pyramidal cells increase their firing rate during SPW-Rs ∼6-9-fold to an average of ∼5-40 Hz, which is still low compared to interneuronal firing (Csicsvari et al., 1999b, 2000; Klausberger et al., 2003; English et al., 2014; Hulse et al., 2016). Their discharge probability is highest when the ripple power in the LFP reaches its peak (Klausberger et al., 2003). Pyramids fire phase-locked around the trough of the LFP ripple oscillation (∼phase 0°) (Buzsáki et al., 1992; Klausberger et al., 2003). Recent studies have shown that superficial and deep CA1 pyramidal cells are recruited differentially, since superficial cells receive net excitation while deep pyramids receive net inhibitory input during SPW-Rs (Valero et al., 2015). Note that CA1 pyramids fire at much lower rates during SPW-Rs *in vitro* compared to *in vivo* (Bähner et al., 2011).

Approximately 70% of the GABAergic interneurons in the CA1 pyramidal layer participate in SPW-Rs and increase their firing rate ∼4-fold (Csicsvari et al., 1999b, 2000). Different interneurons types are recruited differentially (Fig. 2.6):

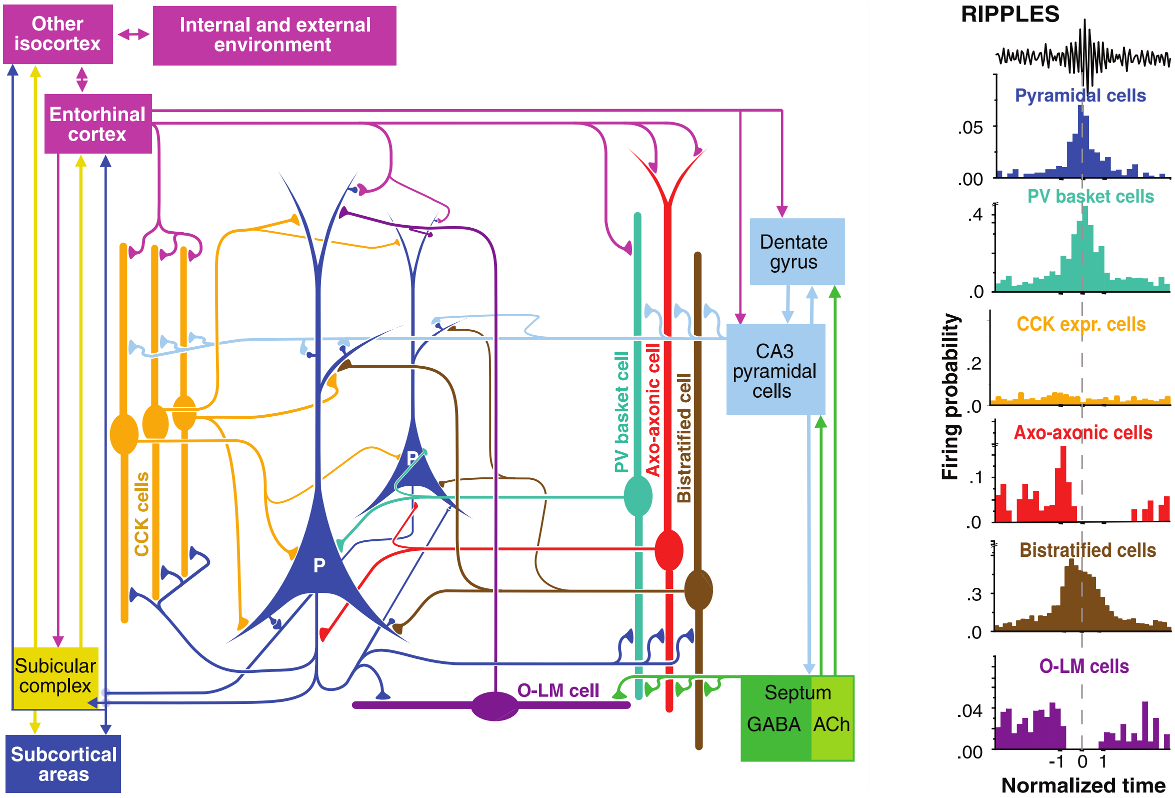
Other isocortex
Internal and external environment
Entorhinal cortex
Dentate gyrus
CA3 pyramidal cells
PV basket cell
Axo-axonic cell
Bistratified cell
CCK cells
P
P
O-LM cell
Subicular complex
Subcortical areas
Septum
GABA
ACh
RIPPLES
Pyramidal cells
.05
.00
PV basket cells
.4
.0
CCK expr. cells
.2
.0
Axo-axonic cells
.1
.0
Bistratified cells
.3
.0
O-LM cells
.04
.00
Firing probability
-1 0 1
Normalized time

Figure 2.6: Differential recruitment of hippocampal cell types during SPW-Rs. Left: simplified sketch of the CA1 circuit. Right: firing probability of pyramidal cells and 5 different interneuron types during SPW-Rs (from Klausberger and Somogyi (2008)/Adapted with permission from AAAS).

PV^+ basket cells in both CA1 and CA3 increase their firing rate during SPW-R ∼3-fold up to 40-130 Hz (Csicsvari et al., 1999a; Somogyi et al., 2014; Klausberger et al., 2003; Varga et al., 2012, 2014; Katona et al., 2014; Lapray et al., 2012). Their firing probability follows a similar profile as the pyramids with the highest discharge probability around the peak of the LFP ripple power (Klausberger et al., 2003). However, PV^+ BCs already start to increase their firing rate ∼2 ms before the onset of the LFP ripple (Klausberger et al., 2004). PV^+ BCs fire phase-locked, and ∼1-2 ms after the pyramids, during the ascending phase of each LFP ripple cycle (∼60-90°, Csicsvari et al., 1999b; Klausberger et al., 2003; Sullivan et al., 2011).

CA1 PV^+ bistratified cells fire at ∼30-60 Hz, at a similar phase as basket cells (∼80° Klausberger et al., 2004). Their spike probability is approximately the same throughout the event, less dependent on ripple power. Interestingly, bistratified cells increase their firing already ∼64 ms before the LFP ripple begins (Klausberger et al., 2004). Recent evidence has suggested that bistratified fire preferentially during fast, compared to slow ripple events Varga et al. (2014).

CA1 axo-axonic interneurons briefly increase their rate at the beginning of a SPW-R event and are then inhibited (Klausberger et al., 2003; Somogyi et al., 2014, but see: Varga et al., 2014).

The remaining GABAergic cell types are only weakly modulated by SPW-Rs: CA1

O-LM cells are either silent during SPW-Rs (Klausberger et al., 2003; Pangalos et al., 2013), or fire at low rates (Varga et al., 2012; Katona et al., 2014; Pangalos et al., 2013). Spikes occur phase-locked ∼6 ms after the ripple trough (phase ∼39°) since O-LM cells receive ripple-mouldated excitatory input (Pangalos et al., 2013). Most CCK expressing interneurons in CA1 and CA3 fire at low rates during SPW-R (Klausberger et al., 2005; Lasztóczi et al., 2011; Somogyi et al., 2014). Ivy cells do not change their firing during SPW-Rs (Somogyi et al., 2014; Lapray et al., 2012; Fuentealba et al., 2008).

Recently, a new interneuron type has been discovered that fires selectively during SPW-Rs, and not during theta epochs — hence termed "Theta-OFF-Ripple-ON (TORO)" cell (Szabo et al., 2022). TORO cells fire at high rates up to ripple frequency (∼173 Hz). Initial results suggest that TORO cells are parvalbumin-negative, but instead express muscarinic type 2 receptors (M2Rs), SOM or, in one case, calbindin (CB). Most TORO cells were found in CA1 with cell bodies scattered across different layers and axons mostly in *str. oriens*, targeting other GABAergic cells. TORO cells might also form long-range connections to the subiculum.

Rare depth electrode recordings of hippocampal spiking activity in humans (epileptic patients) have suggested that the cell-type specific recruitment during SPW-Rs is similar in humans and rodents (Le Van Quyen et al., 2008).

2.6 Models of hippocampal ripple oscillations

The generation of the sharp wave and the ripple are often studied separately, since (a) ripples appear slightly later in development (second postnatal week vs. postnatal day 3) (Leinekugel et al., 2002; Buhl and Buzsáki, 2005) and (b) ripples have been observed in CA1 without a clear sharp wave signature in the LFP (Ramirez-Villegas et al., 2015).

Sharp wave models typically focus on CA3 as the primary region of SPW generation and account for the spontaneous, transient build-up of excitatory spiking activity (Evangelista et al., 2020; Levenstein et al., 2019; Ecker et al., 2022; Hunt et al., 2018).

Multiple models have been proposed for the generation of ripple oscillations. Most of them focus on CA1 as the primary site of ripple generation, since ripples are most prominent in the LFP of CA1 *str. pyramidale* (Buzsáki, 1986; Buzsáki et al., 1992) and can be generated in isolated CA1 minislices *in vitro* (Maier et al., 2003; Nimmrich et al., 2005; Maier et al., 2011). In the intact hippocampus, SPW-Rs often do occur simultaneously in CA3 and CA1. CA3 basket cells spike phase-locked to the local CA3 ripple rhythm (Maier et al., 2003; Both et al., 2008; Tukker et al., 2013), so CA1 indeed receives feedforward oscillatory input (Sullivan et al., 2011; Schönberger et al., 2014). The ripple oscillation in CA1 is however typically faster than in CA3 (Maier et al., 2003, 2011; Sullivan et al., 2011), and does not seem to be simply inherited (see also Donoso et al., 2018).

Since ripple oscillations are coherent across large distances (∼2-5 mm *in vivo* (Buzsáki et al., 1992; Chrobak and Buzsaki, 1996), but ∼120 μm *in vitro* (Draguhn et al., 1998)), all models assume a network rather than a single unit mechanism (but see Fink et al., 2015; Gliske et al., 2017). Both pyramidal cells and some interneuron classes (see Section 2.5.3) fire phase-locked to the ripple rhythm. Most ripple models assume that either the excitatory or inhibitory population acts as the main pacemaker of ripples that entrains the other population respectively. In the following I therefore divide the ripple models into *excitation-first* and *inhibition-first*. A few “hybrid” models will be discussed in the end.

2.6.1 Inhibition-first models

Inhibition-first models account only for the generation of the fast ripple oscillation, not the sharp wave. They posit that the CA1 interneuron population generates a fast ripple oscillation in response to excitatory feedforward drive (Ylinen et al., 1995). Such drive could arise via the Schaffer Collaterals from CA3 during a sharp wave, or from other sources (Nakashiba et al., 2009) such as subcortical areas (Logothetis et al., 2012) or the entorhinal cortex, via the perforant path (Isomura et al., 2006). In experiments the drive could also be replaced by an optogenetic light stimulation (Schlingloff et al., 2014).

Of the many CA1 interneuron types PV^+ basket cells are a likely candidate to contribute to ripple generation: they increase their firing rate during SPW-Rs and fire phase-locked to the ripple rhythm. Their axons are mostly confined to *str. pyramidale*, hence their postsynaptic currents are likely reflected in the LFP. Projecting directly onto somata or proximal basal dendrites, basket cells are in an optimal position to entrain the firing of pyramidal cells to the ripple rhythm. Other synaptic terminals in this layer stem from axo-axonic chandelier interneurons, which are mostly inhibited during SPW-Rs, but have been implicated in SPW-R initiation in the basolateral amygdala (Perumal et al., 2021). PV^+ bistratified cells fire ripple-modulated but might contribute less to the LFP signal in *str. pyramidale*, since their axons are more spread out across layers (Halasy et al., 1996). Still, their involvement in ripple generation cannot be excluded and it is important to keep in mind that any experiment targeting PV^+ CA1 cells targets not only basket cells (60% of CA1 PV^+ interneurons), but also bistratified (24%), axo-axonic (16%) and potentially O-LM cells (Bezaire and Soltesz, 2013; Baude et al., 2007; Varga et al., 2012).

Inhibition-first models are the main subject of this thesis and will be discussed at length in Chapters 4 and 5, hence I will introduce the models here only briefly.

2.6.1.1 Bifurcation-based inhibition-first model

The bifurcation-based inhibition-first model assumes that the CA1 interneuron network acts as a delayed negative feedback loop which can undergo a bifurcation into a state of persistent oscillations when driven with sufficient excitation (Buzsáki et al., 1992; Ylinen et al., 1995; Brunel and Hakim, 1999; Brunel and Wang, 2003; Taxidis et al., 2012; Donoso et al., 2018). The resulting oscillations are fast, due to the short time constants involved in inhibitory synaptic transmission, and can in theory last as long as strong excitatory stimulation is provided. This model will be discussed in detail in Chapter 4.

2.6.1.2 Perturbation-based inhibition-first model

The perturbation-based inhibition-first model on the other hand (Malerba et al., 2016) assumes that the CA1 interneurons are a heterogeneous population with only weak synaptic coupling. Strong external drive (a *perturbation*) can elicit fast synchronized spiking and thus a transient ripple oscillation of inherently finite length (Gerstner et al., 2014). This model will be discussed in detail in Chapter 5.

2.6.1.3 Gap junctions between interneurons

CA1 basket cells are not only connected by chemical synapses but also via electrical gap junctions (Fukuda and Kosaka, 2000; Tamás et al., 2000; Galarreta and Hestrin, 2001a,b; Bartos et al., 2002). Theoretical work has shown that GJ coupling alone can lead to oscillations in interneuron networks (Ostojic et al., 2009). These oscillations however are fully synchronized and would hence only have ripple frequency if the underlying units fired at ripple frequency. For this reason gap junction coupling alone is unlikely as the main ripple generator. Gap junctions can however increase synchrony in the bifurcation-based inhibition-first model (Traub, 1995; Whittington et al., 1995; Kopell and Ermentrout, 2004; Holzbecher and Kempter, 2018) and lower the critical network size required to achieve ripple oscillations in that model (Holzbecher and Kempter, 2018).

2.6.2 Excitation-first models

Excitation-first models account for ripple generation based on interactions among pyramidal cells. They differ in their assumption of whether it is the chemical or electrical coupling that matters most.

2.6.2.1 Axo-axonic gap junctions and antidromic spikes

This model by Traub et al. (1999a) assumes that CA1 pyramidal cells are coupled sparsely by electrical gap junctions on their axons and that spikes can propagate antidromically from the gap junction coupling sites towards the somata, causing a somatic spikelet or full-blown action potential (Draguhn et al., 1998; Traub et al., 1999a; Traub and Bibbig, 2000; Traub et al., 2012). If there is at least one gap junction on each axon, graph theory suggests that the majority of pyramidal cells are connected into one large cluster (Erdös and Rényi, 1960; Traub et al., 1999a). Such a cluster can generate an epileptiform burst of activity modulated by fast oscillations (ripple), when pyramidal cells receive a background stimulation of ectopic spikes in their distal axons. The ripple frequency depends on the average path length between any two pyramidal cells and the gap junction transmission delay. The event is terminated by increasing afterhyperpolarization of the pyramidal cell somata. The coherence of the ripple relies on large network size (Traub et al., 1999a), which might pose a challenge to this network model when it comes to explaining ripple generation in smaller networks in hippocampal slices *in vitro*. Originally designed to account for ripple-modulated epileptiform activity (Traub et al., 1999a), this model was extended to account for non-pathological sharp wave-ripples by adding transient, feedforward input, local interneurons and chemical coupling (Traub and Bibbig, 2000).

2.6.2.2 Supralinear dendritic integration

This model by Memmesheimer (2010) suggests that supralinear dendritic integration in CA1 pyramidal cells (Kamondi et al., 1998; Ariav et al., 2003; Gasparini et al., 2004; Gasparini and Magee, 2006) can lead to a propagation and amplification of synchronized spiking activity at ripple frequency (Memmesheimer, 2010; Jahnke et al., 2015). The frequency is given by the inverse of the summed propagation delays: (i) the axonal delay, (ii) the synaptic delay, (iii) the propagation delay of the dendritic spike to the soma, and (iv) the time from somatic response onset to spike. Memmesheimer (2010) argues that the range of biologically plausible values for these delays yields an overall frequency within the ripple range ($\sim$ 200 Hz). This model accounts both for ripple and sharp wave generation. SPW-Rs can be evoked by stimulation of pyramidal cells or occur spontaneously due to fluctuations. They are terminated by the combined effect of refractoriness of the pyramidal cells and strong feedback inhibition after a characteristic duration of $\sim$ 50ms.

2.6.3 Mixed models

In addition to inhibition- and excitation-first models, some authors propose a third, mixed model class taking into account coupling between pyramidal cells and interneurons (E-I or E-I-I (Stark et al., 2014)).

2.6.3.1 Excitatory-inhibitory loop (E-I)

A large body of literature has studied oscillations in networks of mutually coupled excitatory and inhibitory neurons (Kopell and Gwendal, 1994; Jefferys et al., 1996; Xiao-Jing Wang and Buzsáki, 1996; Traub et al., 1996, 1997; Whittington et al., 2000; Börgers and Kopell, 2003, 2005; Wang, 2010; Buzsáki and Wang, 2012; Viriyopase et al., 2016, 2018; Montbrió and Pazó, 2018; Nguyen and Rubchinsky, 2021). Typically such E-I circuits are considered as a model for gamma oscillations (PING: pyramidal-interneuron gamma, Traub et al., 1999b), since a di-synaptic feedback loop as the main pacemaker tends to produce oscillations that are slower than ripple-range (Brunel and Wang, 2003). E-I network models producing ripple oscillations typically rely on the interneuron population as the pacemaker and will thus be counted here as bifurcation-based inhibition-first (Brunel and Wang, 2003; Taxidis et al., 2012; Stark et al., 2014).

2.6.3.2 GABA$_\text{A}$-mediated excitatory feedback loop

A recently proposed model for SPW-Rs in the basolateral amygdala relies on GABA$_\text{A}$-mediated excitation from axo-axonic chandelier interneurons onto the axon initial segment of pyramidal cells (Perumal et al., 2021). According to this model, a single action potential in a chandelier interneuron exciting at least two pyramidal cells can trigger an excitatory feedback loop which leads to repeated bursts of action potentials in chandelier interneurons and pyramidal cells at ripple frequency. The frequency is set by the disynaptic delay from chandelier interneurons to pyramids and back, which was experimentally estimated at ~ 4 ms (Perumal et al., 2021). The SPW-R event is terminated by accumulated feedback inhibition from basket cells.

The authors suggest that chandelier interneurons might be involved in SPW-R generation in CA1 as well, although the excitatory effect of $\mathrm{GABA_A}$on CA1 pyramidal cells is debated (Somogyi, 1977; Traub et al., 2003; Szabadics et al., 2006; Glickfeld et al., 2009; Woodruff et al., 2011; Bähner et al., 2011). Therefore, as a primarily amygdala-focused model for ripple generation, I will exclude this model from the detailed comparison below.

2.7 Basic ingredients of ripple models

Having introduced the various models for ripple generation I want to briefly review the basic components of the neural network in CA1 that they are built on. I will start with the most controversial such "basic ingredients": axo-axonal gap junctions and antidromic spike propagation in CA1 pyramidal cells.

2.7.1 Axo-axonic gap junctions between CA1 pyramidal cells

To date there is no direct anatomical evidence for the existence of axo-axonal gap junctions between CA1 pyramidal cells. Dual recordings between CA1 pyramidal cells have suggested electrical coupling (Mercer et al., 2006). Furthermore, dye-coupling (Perez-Velazquez et al., 1994; Valiante et al., 1995; Schmitz et al., 2001), the existence of gap junction protein mRNA in pyramidal cells (connexin-43: (Simbürger et al., 1997), Cx-36: (Condorelli et al., 2000), Cx-47: (Teubner et al., 2001)), the pH-dependence of CA1 pyramidal cell coupling (Church and Baimbridge, 1991), and the observation of spikelets in CA1 pyramidal cells, even in calcium-free solutions *in vitro* (Valiante et al., 1995; Draguhn et al., 1998; Schmitz et al., 2001) have been put forward as indirect evidence for a potential gap junction coupling.

Outside of CA1, gap junctions have been found on the apical dendrite or soma of CA3 pyramidal cells (Schmalbruch and Jahnsen, 1981; MacVicar and Dudek, 1981), on hippocampal mossy fiber axons (Hamzei-Sichani et al., 2007; Nagy, 2012), and between unidentified hippocampal neurons of the rat (Rash et al., 1997).

Gap junctions between axons in particular are known to exist in the mammalian retina (Vaney, 1993) or the medullary pacemaker nucleus of weakly electric fish (Tokunaga et al., 1980).

Multiple experiments have tried to address the role of gap junctions in SPW-R generation by blocking gap junctions (Ylinen et al., 1995; Draguhn et al., 1998; Maier et al., 2003; Pais et al., 2003; Traub et al., 2003; D'Antuono et al., 2005; Behrens et al., 2011). The results are mostly inconclusive since all known gap junction blockers (e.g. halothane, octanol, carbenoxolone, mefloquine) come with severe side effects (Juszczak and Swiergiel, 2009). An alternative approach are Cx36 knockout mice that are genetically modified not to express gap junctions (Hormuzdi et al., 2001; Maier et al., 2002; Pais et al., 2003; Buhl et al., 2003). Here the confounding factors are potential compensatory mechanisms during development.

If axo-axonic gap junctions between CA1 pyramids indeed exist, their sparsity ($\sim$1/axon required for the excitation-based ripple model by Traub et al. (1999a)) might be one reason why they continue to evade direct detection in electron microscopy or freeze-fracture experiments (Schmitz et al., 2001).

2.7.2 Antidromic spikes and spikelets in CA1 pyramidal cells

Evoked or spontaneous antidromic spikes have been found in CA1 pyramidal cells *in vitro* (Schmitz et al., 2001; Papatheodoropoulos, 2008; Bähner et al., 2011). On the other hand, *in vivo* studies could not confirm these findings and found only orthodromic action potential waveforms (English et al., 2014; Hulse et al., 2016). Since these action potentials were recorded somatically however, it is possible that axonal spikes which did not invade the soma were missed (Dugladze et al., 2012, see also Michalikova et al., 2017, 2019). This isolation of the soma from axonic spikes might be mediated by axo-axonic interneurons inhibiting the axon-initial segment of CA1 pyramidal cells (Dugladze et al., 2012; Traub et al., 1999a). Furthermore, recent studies suggested that a large fraction (30-70%) of CA1 pyramidal cells have their axon emerging from a basal dendrite, therefore completely circumventing the soma (Thome et al., 2014).

Spikelets have been observed during epileptiform events (Valiante et al., 1995) and SPW-Rs *in vitro* (Draguhn et al., 1998), as well as *in vivo* during active exploration — a potential state of gamma oscillations (Epsztein et al., 2010).

2.7.3 Dendritic spikes in CA1 pyramidal cells

Spontaneous dendritic spikes during SPW-Rs have been observed in the apical dendrites of CA1 pyramidal cells (Kamondi et al., 1998) and are likely the result of converging excitatory inputs from CA3. The local synaptic connections between CA1 pyramidal cells are typically formed between axons and the *basal* dendrites (Deuchars and Thomson, 1996). Experiments using artificial stimulation have shown that also the basal dendrites can generate dendritic spikes, when they receive inputs synchronously in time and clustered in space (Ariav et al., 2003; Gasparini et al., 2004; Gasparini and Magee, 2006).

An unresolved question is whether the sparse connectivity between CA1 pyramidal cells ($\sim$1%, Deuchars and Thomson, 1996) is sufficient to support dendritic spike initiation. Locally clustered synaptic boutons, a spatial dependence of the connection probability and the increased synchrony of excitatory spiking during SPW-Rs are some of the factors that may enable dendritic spike generation despite sparse connectivity (Memmesheimer, 2010; Deuchars and Thomson, 1996; Knowles and Schwartzkroin, 1981; Orman et al., 2008).

Dendritic spikes have also been observed in CA3 pyramidal cells (Kim et al., 2012; Makara and Magee, 2013), suggesting that the excitation-first model by Memmesheimer (2010) could in principle account for SPW-R generation in both CA1 and CA3.

2.7.4 Properties of inhibitory synaptic coupling in CA1

CA1 PV$^+$ basket cells are synaptically connected to about 40 other PV$^+$ basket cells, often with just a single bouton contact per target cell (Sik et al., 1995). Paired recordings from PV$^+$ BCs in CA1 showed that the coupling is strong and fast: The average peak amplitude of postsynaptic inhibitory currents (PSCs) was 208 pA. PSCs were fitted by a delayed biexponential function with latency ∼0.68 ms, a 20-80% rise time of ∼0.27 ms, and a short decay time constant of ∼1.7 ms (Bartos et al., 2002). PV$^+$ BCs also target other PV$^+$ interneurons, such as bistratified cells (Sik et al., 1995; Cobb et al., 1997).

2.8 Experimental tests of model predictions

The previous section has shown that no ripple model can be generally discarded on the basis of unrealistic assumptions about the local circuitry. The next step is thus to examine the predictions that each individual model makes and evaluate their validity. Table 2.1 gives a rough overview of the model predictions with respect to the spontaneous features of ripples, and the results of pharmacological and/or optogenetic manipulations of the circuit. The validity of each prediction has been color-coded (green: likely true, yellow: likely wrong), based on the known features of spontaneous ripples summarized in Section 2.5, and the experimental evidence discussed below. Such a binary rating needs to be taken with a grain of salt, since the interpretation of the experimental findings is often controversial and hindered by confounding factors, as will become clear in the following. The color-code does however serve to illustrate at first sight, that, even after taking into account all the experimental evidence that I will discuss in this section, there is no clear “winning” model with only correct predictions.

2.8.1 Pharmacology

2.8.1.1 Altering synaptic transmission delays

Most models predict that the ripple frequency depends primarily on the delays involved in neuronal communication, be it via gap junctions or chemical synapses (an exception is the model by Malerba et al. (2016)). Testing these predictions experimentally is hard since it requires changing the propagation delays. Multiple studies have examined the effect of altered GABAergic synaptic transmission and found that various GABA$_\text{A}$ modulators (NNC-711, diazepam, zolpidem, thiopental, etc) do not change the ripple frequency significantly (Whittington et al., 1996; Bähner et al., 2011; Koniaris et al., 2011; Viereckel et al., 2013) (see (Buzsáki, 2015) for a detailed review). These GABA$_\text{A}$ modulators however affect mainly the inhibitory synaptic peak conductance and/or decay time constant. The bifurcation-based inhibition-first model predicts little change in ripple frequency in response to such changes (Brunel and Wang, 2003; Donoso et al., 2018). To dissociate this ripple model from the others one would need to change the *fast* time constants of inhibitory synaptic transmission, i.e. the delay or the rise time constant.

	Inhibition-first models		**Excitation-first models**	
	Bifurcation based	**Perturbation based**	**Axo-axonal gap junctions**	**Supralinear dendrites**
Spontaneous ripple features				
ripple frequency	• fast inhibitory syn time const. • (inh coupling) • (exc drive)	• interneuron firing rate • exc drive	• mean pyr-pyr pathlength	exc delays: • axonal • synaptic • dendritic
ripple duration	• drive	• noise • heterogeneity	• pyr AHP	• refractoriness • inhibition
interneuron firing	• sparse	• ripple frequency	• [ripple frequency]	• sparse
pyramidal firing	—	—	• sparse (soma) • ripple (axon)	• sparse
Pharmacology (+ Optogenetics)				
ripples (sp/ev) without				
• GABA_A	✘	✔	✔	✔ (prolonged)
• AMPA	✘ | ✔	✘ | ✔	✘ | ✔	✘ | ✘
• gap junctions	✔	✔	✘	✔
Optogenetics				
ripples by stimulation of				
• CA1 PV+ BC	✔	✔	✘	✘
• CA1 pyramids	[gamma]	[✔]	✔	✔
ripples despite silencing of				
• CA1 PV+ BC	✘	✘	✔	✔ (prolonged)
• CA1 pyramids	✔	✔	✘	✘

Table 2.1: Properties and predictions of ripple models.
Predictions of 4 models for CA1 ripple generation, regarding spontaneous ripple features, and pharmacological and/or optogenetic manipulations. Each prediction is color-coded based on the current experimental evidence discussed in the main text. Green: most/all experiments confirm this prediction; yellow: most/all experiments contradict this prediction. White: not tested/not testable. *sp/ev*: spontaneous or evoked by optogenetic stimulation; *AHP*: after-hyperpolarization, (·): weak parameter dependence, [·]: prediction needs to be confirmed by further analysis of the model, see Discussion Chapter 7 for a detailed comment.

Recent paired patch clamp experiments have shown that a (reversible) toxic demyelination of PV^+ BC axons (using cuprizone) changes the precision of synaptic release, prolonging only the synaptic delay while leaving the subsequent synaptic rise and decay time constants unaltered (Vandael and Kole, 2022). This may be a promising method to test the dependence of ripple frequency on the inhibitory synaptic delay — a key prediction of the bifurcation-based inhibition-first model.

2.8.1.2 Excitatory synaptic transmission

Many studies have shown that fast excitatory synaptic transmission via AMPA receptors is necessary for the emergence of spontaneous SPW-Rs (Papatheodoropoulos and Kostopoulos, 2002; Wu et al., 2002; Maier et al., 2003; Ellender et al., 2010; Hofer et al., 2015). This is in line with all models, since neither of the potential pacemakers is stimulated in the absence of excitatory synaptic transmission. However, except for the excitation-based supralinear dendritic integration model (Memmesheimer, 2010), all other models predict that ripples can still be *evoked* in the absence of excitatory synaptic transmission by stimulating the respective pacemaker optogenetically (interneurons or pyramidal cells).

In vitro experiments in CA3 showed that SPW-Rs could indeed still be evoked by optogenetic stimulation of PV^+ interneurons, even when AMPA and NMDA receptors were blocked (Schlingloff et al., 2014, but see Stark et al., 2014). This is in line with inhibition-first ripple models.

The role of NMDA receptor-mediated excitation in SPW-R generation is not fully resolved. Several studies find that a block of NMDA receptors has no significant effect (Maier et al., 2003; Ellender et al., 2010; Hofer et al., 2015), while others find an in- or decrease of SPW-R amplitude (Colgin et al., 2005; Pöschel et al., 2003). One *in vitro* study even finds SPW-Rs supported exclusively by NMDAR-mediated excitation, with all other receptors blocked (Papatheodoropoulos, 2007). Since none of the models make specific predictions regarding the role of NMDA I omitted it in Table 2.1.

2.8.1.3 Inhibitory synaptic transmission

Generally, testing the role of inhibitory synaptic transmission is difficult since a complete block of GABAergic receptors and the resulting disinhibition can lead to pathological, epileptic activity (Maier et al., 2003; Ellender et al., 2010). A block of $GABA_A$ receptors can thus only be done locally (Stark et al., 2014), partially with low doses (Ellender et al., 2010) or in a minislice preparation of CA1, which contains only few recurrent excitatory synapses (Maier et al., 2003; Nimmrich et al., 2005).

Multiple studies have found that GABAergic synaptic transmission is necessary for spontaneous SPW-R generation (Ellender et al., 2010; Stark et al., 2014; Schlingloff et al., 2014) and that SPW-Rs cannot be induced when $GABA_A$receptors are blocked (CA1 *in vivo*: Stark et al., 2014, CA3 *in vitro*: Schlingloff et al., 2014).

There are however a few *in vitro* studies with contradictory results: Draguhn et al. (1998) found that SPW-Rs in rat brain slices *in vitro* persisted, not only in the presence of $GABA_A$receptor antagonists (bicuculline), but even in the complete absence of chemical synaptic transmission in a calcium-free solution. Nimmrich et al. (2005) found that SPW-Rs could still be evoked with a potassium chloride puff after wash-in of $GABA_A$ receptor antagonist gabazine in CA1 minislices. One could speculate whether the puff application of KCl led to a significant wash-out of gabazine, effectively rendering inhibitory synaptic transmission intact (Holzbecher, 2018). Otherwise this finding can only be explained by excitation-first models. Nimmrich et al. (2005) did however also find that gabazine blocked spontaneously occuring SPW-Rs, which would be in line with other experiments and inhibition-first models.

It is also worth noting that it is hard to draw conclusions about the excitation-based ripple models based on experiments in minisclices, since the excitatory network in a minislice may likely be too small to support ripple generation.

The role of $GABA_B$ for SPW-R generation is unresolved (Ellender et al., 2010; Hollnagel et al., 2014).

2.8.2 Optogenetics

Targeting selectively either pyramidal cells or PV^+ interneurons in CA1 one can ask two kinds of questions: Does optogenetic *stimulation* of a certain cell type evoke SPW-Rs or terminate ongoing SPW-Rs? Can SPW-Rs occur despite a certain cell type being optogenetically *silenced*? It seems like with such methods at hand it should be easy to dissociate at least between inhibition- and excitation-based ripple models. Yet, the summary in Table 2.1 already indicates that this is not the case, and the sections below provide details for why.

2.8.2.1 Activating interneurons

The question whether optogenetic activation of (PV^+) interneurons can elicit ripple oscillations is still discussed controversially. I want to argue here that the existing evidence suggests that interneuron activation *can* elicit ripples, and that the remaining controversy may be attributable to the LFP confounding factor I pointed out earlier: Most ripple experiments target two questions simultaneously, namely: What generates the ripple rhythm in the neuronal circuitry? And under which conditions is this rhythmic neuronal activity visible in the LFP signal? Thus, in experiments that observe only the LFP signal, one needs to be careful with conclusions about ripple generation.

The controversy arises mainly from two studies with seemingly contradictory findings: Schlingloff et al. (2014) found that optogenetic activation of CA3 PV^+ interneurons *in vitro* elicits ripple oscillations in the LFP signal (even in the absence of excitatory synaptic transmission). Similar observations have been made in CA1 *in vitro* [personal communication with Nikolaus Maier].

Stark et al. (2014) on the other hand found that optogenetic activation of CA1 PV^+ interneurons *in vivo* could *not* induce a ripple event in the LFP. The authors did find however that the neuronal spiking was coherent in the ripple frequency range (see Fig. 6B in Stark et al., 2014). In that sense, the PV^+ stimulation in this experiment *did* induce ripple oscillations, measurable in the interneuron population activity, as predicted by inhibition-first models. In Section 2.5.1 I mentioned that the LFP likely reflects inhibitory synaptic currents, and potentially also rhythmic excitatory spiking activity. There are hence two potential reasons why LFP ripple power may have been reduced in the experiment by Stark et al. (2014), despite ripple-modulated neuronal activity: (a) The local optogenetic stimulation activated a smaller population of interneurons than is usually involved in ripple generation. Hence the inhibitory synaptic currents underlying the LFP signal were weaker compared to spontaneous events. (b) Since only interneurons were activated, pyramidal cells fired much fewer spikes than during spontaneous events, hence reducing the LFP ripple power contributed by extracellular action potentials (Schomburg et al., 2012).

My (tentative) rating in Table 2.1 (ripples by stimulation of PV^+ BCs) is based on this reasoning. Additional optogenetic experiments targeting interneurons in CA1, both *in vivo* and *in vitro*, are needed to settle the above controversy. Measuring not only the LFP, but also neuronal spiking activity or inhibitory synaptic currents, may help resolve the LFP confounding factor described above.

2.8.2.2 Activating pyramidal cells

Optogenetic activation of CA1 pyramidal cells can induce high-frequency oscillations (Stark et al., 2014). Prolonged optogenetic stimulation can prolong SPW-R duration (Fernández-Ruiz et al., 2019). For inhibition-based models a prediction of the network activity in response to local stimulation of CA1 pyramidal cells is a complex question that requires further study (hence marked with square brackets in Table 2.1). I will revisit this question in the discussion (Chapter 7).

2.8.2.3 Silencing interneurons

Optogenetic silencing of PV^+ interneurons has been shown to disrupt ongoing SPW-Rs (Schlingloff et al., 2014; Stark et al., 2014) and even prevent the generation of spontaneous SPW-Rs (Schlingloff et al., 2014).

2.8.2.4 Silencing pyramidal cells

Online silencing of pyramidal cells terminates ongoing SPW-R events in the LFP (Stark et al., 2014). Again, the decrease in the potential contribution of excitatory spikes to the LFP signature (Schomburg et al., 2012) might be a confounding factor here, and future experiments should check ripple modulation of inhibitory spiking in addition to the LFP signal.

2.8.3 Summary

Current experimental evidence remains inconclusive as to which is the most likely generation mechanism of ripples (Table 2.1). There are many predictions that cannot be tested conclusively with current techniques (non-colored cells in Table 2.1, *e.g.* the role of gap junctions). Some experimental results are contradictory or their interpretation is controversial and subject to confounding factors. At this point, there is no model that can be clearly rejected, or clearly accepted (all yellow, or all green rating in Table 2.1).

3 | Research aims

In this thesis I want to contribute to the understanding of the generating mechanism of hippocampal ripple oscillations from a theoretical perspective. In Chapter 2 I have introduced the most important features of ripples and the various models that have been proposed to account for their generation. The field is currently facing a problem of model selection. Experimental evidence has so far been inconclusive as to which is the most likely mechanism. This is not only due to contradictory experimental results or missing experiments that yet have to be performed, but also related to shortcomings on the theoretical side. Although it seems at first sight (Table 2.1) that we should be able to dissociate the different models based on the many diverging predictions derived so far, many of these predictions are hard to test experimentally or require severe manipulations of the circuit that come with many confounding factors.

An often overlooked feature of spontaneous ripple oscillations, which could guide model selection, is intra-ripple frequency accommodation (IFA, Section 2.5.2). It was recently shown in simulations that the bifurcation-based inhibition-first ripple model can account for IFA (Donoso et al., 2018), yet the underlying mechanism remains unclear. In Chapter 4 I therefore set out to answer the following questions:

1a. What is the mechanism of IFA in the bifurcation-based inhibition-first ripple model?

1b. Is IFA a robust feature of the model or does it require parameter tuning?

Answering these questions requires a theoretical understanding of the oscillation frequency in this network model, as a function of the external input. I will develop an analytical approximation of the oscillation dynamics in the mean-field limit, that allows an understanding of the emergence of IFA under strong, time-dependent input.

Since IFA is a promising marker for model selection, I then move on to the alternative inhibition-first model by Malerba et al. (2016) and ask:

2a. Can the perturbation-based inhibition-first ripple model account for IFA as well?

2b. What separates the two inhibition-first models, and how can they be dissociated experimentally?

These questions will be answered in Chapter 5.

The final chapter is inspired by the broader underlying question of a potential role of sharp wave-ripples in memory consolidation. Studying the functional role of sharp wave-ripples will eventually require a larger scale modeling approach incorporating the propagation of ripples across brain areas and their embedding into the larger system of thalamo-cortical rhythms. Recently, a mesoscopic approach has been proposed for an efficient simulation of the activity of multiple populations accounting for finite size effects (Schwalger et al., 2017). The approach is only applicable to microscopic networks of escape noise units that receive deterministic input and account for noise phenomenologically, via stochastic spiking govererned by a hazard function. I therefore ask the following questions:

3a. Can ripple oscillations be captured in an efficient, mesoscopic integration scheme?

3b. How does a phenomenological account for noise in an escape noise model affect the single neuron linear response, and thus the ripple dynamics in the bifurcation-based inhibition-first model?

The thesis will conclude with an overall summary of the results and an outlook in Chapter 7.

4 | The bifurcation-based inhibitory ripple model

4.1 Introduction

Negative feedback, when arriving with a delay, can introduce oscillations (Glass and Mackey, 1988; Van Vreeswijk et al., 1994; Terman et al., 1998). The bifurcation-based inhibitory ripple model is based on this principle, assuming that the synaptic connections between CA1 interneurons form a delayed negative feedback loop. When a sharp wave is generated in CA3 (Evangelista et al., 2020; Levenstein et al., 2019; Ecker et al., 2022), CA3 pyramidal cells transiently increase their firing rates, which leads to a transient increase in excitatory drive to CA1 via the Schaffer collaterals. This external drive can lead to a bifurcation in the network dynamics of the CA1 interneuron population: the population activity becomes rhythmic, with periods of increased spiking activity closely followed by reduced activity due to the self-generated, inhibitory feedback current. Since the synaptic delay is short, these oscillations can be fast — in the range of ripple frequencies (140–220 Hz) (Brunel and Hakim, 1999; Brunel and Wang, 2003). Importantly, if the network is also subject to noise — due to sparse connectivity or noisy background activity — the oscillations can be stochastic, with individual neurons firing irregularly and at a mean firing rate that is much lower than the frequency of the oscillation in the summed population activity (Brunel and Hakim, 1999; Brunel, 2000; Brunel and Hansel, 2006). The bifurcation-based model can thus account for ripple oscillations in a network of neurons that fire at much lower rates (Csicsvari et al., 1999b; Klausberger et al., 2003; Lapray et al., 2012; Varga et al., 2012, 2014).

Recently Donoso et al. (2018) showed that the bifurcation-based inhibitory ripple model can reproduce the experimentally observed intra-ripple frequency accommodation (IFA) (see Section 2.5.2). Understanding the mechanism of IFA in this model, and its robustness, is important to assess the plausibility of interneurons as the main pacemaker of ripples. In this chapter I will develop a mean-field ansatz that allows an analytical approximation of the ripple frequency for strong coupling and strong drive, far beyond the bifurcation. The approximation works both for constant, and time-dependent drive, and can be used to understand the mechanism of IFA. I show that IFA is a robust feature of the bifurcation-based inhibition-first model that relies solely on a fast change in the excitatory drive to the interneuron network.

The chapter is organized as follows: Section 4.2 presents results of numerical spiking network simulations to illustrate the main dynamical features of ripples and IFA in the bifurcation-based model. I will start from the detailed version of the model that was proposed by Donoso et al. (2018), and then introduce a reduced model that is amenable to analytical analysis. Section 4.3 starts with a review of existing mean-field approaches towards understanding oscillation dynamics in inhibitory networks, and their limitations. Then a novel approximation of the mean-field dynamics under strong drive is introduced which allows a systematic understanding of the parameter dependencies of the model and a proof of the existence of IFA for a wide parameter regime. Section 4.4 discusses open questions and directions for future work. Details of the numerical simulations and analytical derivations are given in the Methods, Section 4.5. The Appendix contains a numerical evaluation of the performance of the analytical approximation (Sec. 4.A), a derivation of an analog approximation for a network of pulse-coupled oscillators (Sec. 4.B), auxiliary calculations used in the derivation of the analytical approximation (Sec. 4.C), a background on Fokker-Planck equations and linear response (Sec. 4.D), and supplementary figures (Sec. 4.E). All of the appendix content will be referenced in the main text.

4.2 Simulation of ripple dynamics in a spiking network

4.2.1 The detailed model

The bifurcation-based inhibitory model has been formulated many times, at different levels of abstraction (Buzsáki, 1986; Buzsáki et al., 1992; Ylinen et al., 1995; Brunel and Hakim, 1999; Brunel and Wang, 2003; Geisler et al., 2005; Taxidis et al., 2012; Donoso et al., 2018). Donoso et al. (2018) formulated a biologically realistic version with parameters fitted to experimental data, in order to mimick the network of CA1 PV^+ basket cells as found in a hippocampal slice *in vitro*. I will hence refer to it here as the *detailed model*.

The detailed model consists of $N = 200$ model interneurons, which are connected sparsely among each other. The interneurons receive correlated, feedforward Poisson spiking input from a putative CA3 pyramidal cell population. Synaptic coupling is conductance-based and includes synaptic filtering such that each presynaptic spike produces a pulse with a faster exponential rise and a slower exponential decay in the postsynaptic conductance (see Methods Section 4.5.1.1 for details on model equations and parameters).

In the following, I will summarize how the network dynamics depends on the total excitatory (Poisson) drive Λ. Throughout this chapter I will distinguish two cases: constant drive and time-dependent, sharp wave-like (SPW-like) drive that rises and falls over a short time window (Eq. (4.22)). The network dynamics is quantified in terms of the population rate $r_N(t)$ and the distribution of membrane potentials $p(v,t)$. The (empirical) population rate $r_N(t)$ in a time window $[t, \Delta t]$ is defined as the number of spikes $n_{\mathrm{spk}}(t, t+\Delta t)$ emitted by the population (Eq. (4.14)), divided by the size of the population and the time step:

$$r_N(t) := \frac{n_{\mathrm{spk}}(t, t+\Delta t)}{N\Delta t} \ . \tag{4.1}$$

In all figures r_N is smoothed with a narrow Gaussian kernel (see Methods Eq. (4.15)) to facilitate visual assessment of its oscillatory modulation. An interneuron population rate that oscillates at a ripple-range frequency is taken as a proxy for a ripple-modulated LFP (see also Section 2.5.1, and Discussion).

4.2.1.1 Persistent ripple oscillations for constant drive

The dynamics of the detailed model for constant drive are illustrated in Fig. 4.1. At low drive the network is in a steady-state with units firing asynchronously and irregularly at an overall low rate f_{unit} (Fig. 4.1A, left). As the drive increases, the network begins to exhibit coherent stochastic oscillations (Fig. 4.1A, middle, right). In the following I will refer to the dominant frequency of this population oscillation as the network frequency f_{net} (see Methods, Section 4.5.1.6). The network frequency lies within the ripple-frequency range (140–220 Hz) for a large range of external drives (Fig. 4.1B, black line, gray band). Importantly, the firing rate of individual units can be much lower (Fig. 4.1B, blue line). This is because the unit spiking activity underlying the network oscillation is sparse and irregular for most intermediate levels of the drive. This type of network activity has been described before and will be referred to here as *sparse synchrony* (following Donoso et al., 2018, other terms include *stochastic oscillations*, Brunel and Hakim, 1999; Brunel and Hansel, 2006; or *synchronous irregular state*, Brunel, 2000). Sparse synchrony is defined by a *saturation* $s := f_{\text{unit}}/f_{\text{net}}$ that is well below 1 and a coefficient of variation (CV) of the interspike intervals that is high (Fig. 4.1B, bottom panels).

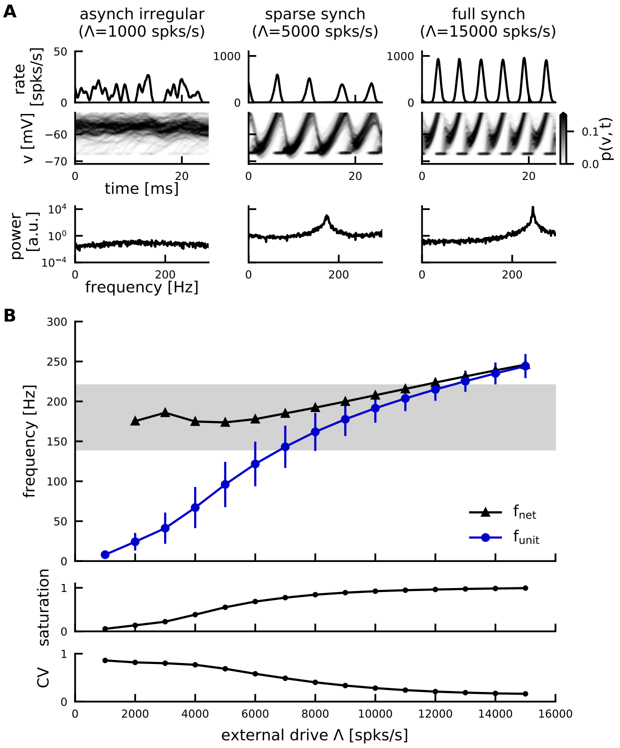

Figure 4.1: Constant-drive dynamics of the detailed spiking network. **A,** Three dynamical regimes depending on the external drive: asynchronous irregular state, sparse synchrony, full synchrony. Top: population rate; middle: histogram of membrane potentials v (normalized as density); bottom: power spectral density of the population rate. The location of the first peak is defined as the network frequency f_{net}. **B,** Top: network frequency (f_{net}, black) and unit firing rate (f_{unit}, blue, population average ± 1 SD) for a range of constant external Poisson drives Λ. Grey band: ripple-frequency range (∼140–220 Hz). Middle: saturation $s = f_{\text{unit}}/f_{\text{net}}$. Bottom: Coefficient of variation (CV) of interspike intervals.

For very strong drive, the network reaches a state of *full synchrony* ($s \approx 1$ and low CV, e.g. $\Lambda = 15000$ spks/s in Fig. 4.1A, right) in which units fire regularly at the network frequency, contributing on average one spike per cycle of the population rhythm. If the drive increases beyond this level, the network *de*synchronizes and units spike several times per cycle ($s > 1$), eventually dissolving the population rhythm (not shown). Since the firing rates in that regime are too high to be biologically plausible, I will focus in the following on the dynamical regime from the asynchronous irregular state up to the point of full synchrony.

4.2.1.2 Transient ripple oscillations and IFA for time-dependent drive

Inhibition-first ripple models do not account for the generation of the external drive and its transient variation that is associated with the sharp wave (SPW). The sharp wave is assumed to be generated by a separate mechanism and in a separate region, e.g. in region CA3 (Evangelista et al., 2020; Levenstein et al., 2019). Pyramidal cells in CA3 are known to transiently increase their firing rate during a sharp wave (Csicsvari et al., 1999b; Stark et al., 2014), resulting in a transient increase of the feedforward excitatory drive to CA1 via the Schaffer collaterals. The bifurcation-based inhibiton-first ripple model assumes that this SPW-associated drive is sufficient to elicit oscillations in the population activity of CA1 interneurons, triggering a transient ripple event.

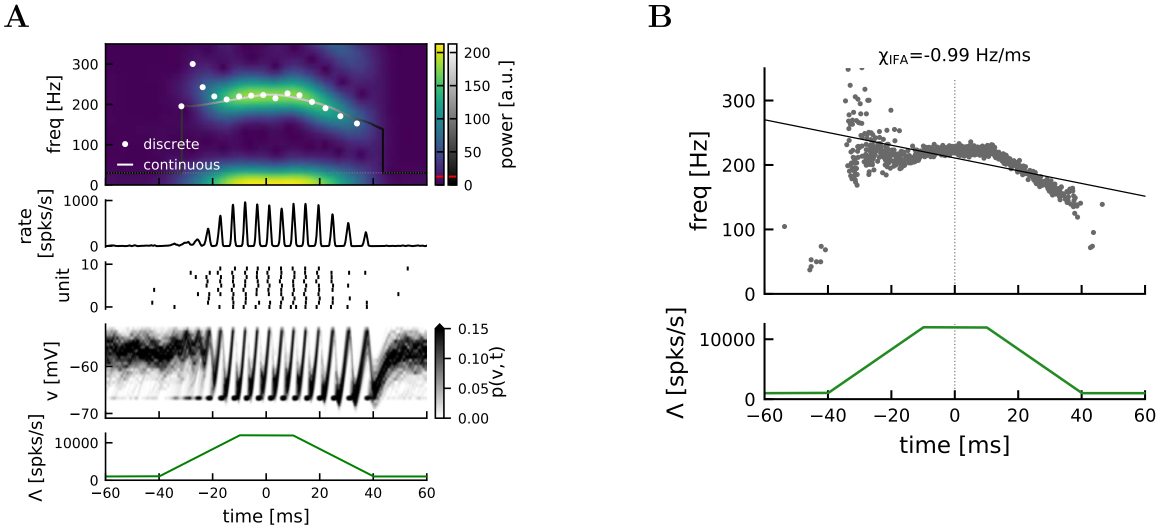

Figure 4.2: IFA in the detailed spiking network.
A, Ripple event with IFA. From bottom to top: SPW-like external drive Λ; density of membrane potentials (normalized); raster plot; population rate; wavelet spectrogram indicating instantaneous power (blue-yellow colorbar) for a frequency range of 0–350 Hz. Solid curve: continuous estimate of instantaneous frequency, gray scale: instantaneous ripple power. Dashed line: cutoff frequency $f_{\mathrm{min}} = 70\,\mathrm{Hz}$. Red line: power threshold. White dots: discrete estimate of instantaneous frequency based on peak-to-peak distances in population rate. **B,** Average transient dynamics (see Methods Section 4.5.1.6). Top: Grey dots: discrete instantaneous frequency estimates for individual cycles of 50 independent simulations. Black line: linear regression line with slope $\chi_{\mathrm{IFA}} = -0.99$ Hz/ ms (see Methods Section 4.5.1.6). Bottom: The same double-ramp drive was applied in all 50 simulations.

I model SPW-like drive in its simplest form as a symmetric, piecewise linear double-ramp, with a short plateau phase, describing the time-dependent intensity of the inhomogeneous Poisson process used to generate the excitatory input spikes (Eq. (4.21), Fig. 4.2A, bottom). The SPW-like drive elicits a transient ripple event in the network (Fig. 4.2A).

The instantaneous frequency of the rhythmic population activity can be measured either by taking the power spectrum over a sliding gaussian time window of standard deviation 5 ms and finding the first peak above 0 Hz in each time step, or by taking the inverse of the discrete peak-to-peak distances (see Methods Section 4.5.1.6, Fig. 4.2A, top). The continuous estimation of instantaneous frequency involves a hyperparameter (width of the sliding window) that can introduce unforeseen boundary effects at the beginning and end of a ripple event. The discrete estimate depends on the minimal height required for a peak in the population activity to be considered as an oscillatory modulation. The effects of changes in this hyperparameter are more transparent. I thus chose to base the analysis of instantaneous ripple frequency on the *discrete* estimate.

It is evident already in a single example simulation (Fig. 4.2A) that the instantaneous ripple frequency decays over time, i.e. the network exhibits intra-ripple frequency accommodation (IFA) (Donoso et al., 2018). IFA can be quantified systematically by repeating the same simulation for multiple, independent realizations of the Poisson spike input and computing a linear regression line for the discrete frequency estimates of all trials (Fig. 4.2B, Methods Section 4.5.1.6). A negative regression slope (here $\chi_{\mathrm{IFA}} = -0.99\ \mathrm{Hz}/\mathrm{ms}$) indicates IFA.

4.2.2 The reduced model

The detailed bifurcation-based inhibitory model has been very useful in demonstrating that it can produce ripple oscillations and even IFA in a biologically realistic parameter setting matched to the electrophysiological properties of PV$^+$ basket cells in CA1 (Donoso et al., 2018). Depending on the reader's scientific background the "detailed" model may already seem fairly simplified (point-neuron assumption, no morphology, no dendritic nonlinearities, no heterogeneity in the single-unit parameters etc). The detailed model does, however, still contain several complexities, such as conductance-based coupling, that make an analytical analysis of its dynamics difficult. I thus performed a model reduction taking away ingredients that are not essential for the ripple dynamics. I define the essential ripple dynamics as follows:

- the existence of a bifurcation from an asynchronous irregular regime to coherent stochastic oscillations at a high, ripple-like frequency for a critical amount of constant, excitatory drive
- a transition from sparse to full synchrony for increasing, constant drive
- IFA for SPW-like drive

A step-by-step description of the model reduction, describing the individual simplifying assumptions and their implications in detail, can be found in Methods Section 4.5.1.2. In the resulting reduced model the CA1 interneuron network is modeled as a homogeneous network of N leaky integrate-and-fire (LIF) units. Due to the increased level of abstraction I will no longer refer to the model interneurons as PV$^+$ BCs. The goal here is rather to show that IFA occurs largely independent of the details of the model neuron. The membrane potential v_i of a neuron i is given by the following stochastic differential equation (SDE):

$$\tau_m \dot{v}_i = -v_i + E_{\text{leak}} + \frac{\tau_m}{C} I_{\text{ext}}(t) - \frac{J}{N} \tau_m \sum_{j=1}^{N} \sum_{k} \delta(t - \Delta - t_j^k) + \sqrt{2\tau_m} \sigma_V \xi_i(t) \tag{4.2}$$

with time constant τ_m, capacitance C, and resting potential E_{leak}. Whenever the membrane potential crosses a spike threshold V_{thr}, a spike is emitted and the membrane potential is reset instantaneously to a reset potential V_{reset}. For simplicity there is no absolute refractory period. All interneurons receive the same external, excitatory drive I_{ext} and an independent Gaussian white noise input ξ_i scaled by the noise strength parameter σ_V. The network is fully connected via inhibitory pulse coupling of strength J and with a synaptic delay Δ (see Methods Section 4.5.1.3 for details, Table Table 4.3 for default parameters).

In the following I briefly illustrate that the key ripple dynamics, as defined above and illustrated in Section 4.2.1, are preserved in this reduced model, i.e., there are fast oscillations in the ripple range and there is IFA. I will furthermore demonstrate that the ripple dynamics are preserved in large networks and hence argue that IFA can be described as a mean-field effect.

4.2.2.1 Persistent ripple oscillations for constant drive

For constant drive the reduced model exhibits a range of dynamics (Fig. 4.3) that is qualitatively comparable to the detailed model (Fig. 4.1): For increasing drive the network transitions from an asynchronous irregular state to coherent stochastic oscillations that are first sparsely, and finally fully synchronised. Compared to the detailed model, the network frequency depends more strongly on the external drive and is a mostly decreasing function of the latter. Increasing the network size beyond $N \sim 10,000$ does not change the dynamics significantly (Fig. 4.3B). From here on I will thus use a simulated network of size $N = 10,000$ to compare to analytically estimated mean-field dynamics.

4.2.2.2 Transient ripple oscillations and IFA for time-dependent drive

When stimulated with transient, SPW-like drive (Eq. (4.22)) the reduced spiking network produces a transient ripple oscillation with IFA (Fig. 4.4A, B). The transient dynamics is similar to the detailed model (Fig. 4.2) except that the IFA has a slightly different shape with a small increase in frequency at the end of the event.

As I discussed in Section 2.5.2, there is no rigorous definition of IFA. The central aspect of IFA is the decrease (*accommodation*) of the instantaneous frequency over the course of a ripple event. We observe such a decrease in the central portion of this simulated ripple event, where power in the ripple band is large (Fig. 4.4A, top). In the reduced model this decay is not strictly monotonic over the entire event. The frequency increases slightly at the end of the event, albeit with low power (the underlying peaks in the population rate are small). Similar non-monotonicities have been observed in

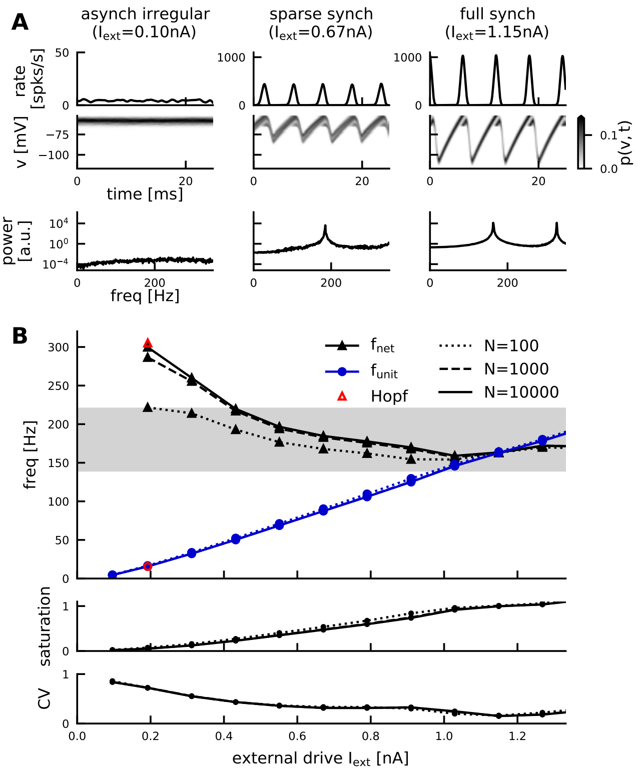

Figure 4.3: Constant-drive dynamics of the reduced spiking network. A, Examplary dynamics: asynchronous irregular state, sparse synchrony, full synchrony (left to right, $N = 10,000$). Top: population rate; middle: density of membrane potentials; bottom: power spectral density of the population rate. **B,** Top: network frequency f_{net} (black) and unit firing rate f_{unit} (blue, average ± 1 SD) for a range of constant external drives I_{ext}. Grey band: ripple frequency range (∼140–220 Hz). Red markers: Hopf bifurcation ($I_{\text{ext}}^{\text{crit}} \approx 0.19\,\text{nA}$, see Methods Section 4.5.2.4). Middle: saturation $s = f_{\text{unit}}/f_{\text{net}}$. Bottom: coefficient of variation of interspike intervals. Linestyle indicates network size ($N \in [10^2, 10^3, 10^4]$).

experimentally measured ripples and still termed IFA (Ponomarenko et al., 2004, see Discussion). Hence I define IFA here not as a strictly monotonic decay, but a more general trend from high towards lower frequencies over the course of an event.

In the model, the IFA asymmetry can be understood best by comparing the instantaneous frequencies to the asymptotic frequencies that the network would settle into if the drive remained constant at any given level indefinitely (Fig. 4.4D, black lines). Naturally, these asymptotic frequencies follow the same symmetry as the external drive and thus provide a useful reference frame. For a double-ramp drive, we observe that during the plateau phase (i.e. constant drive) the instantaneous frequency quickly approaches the asymptotic frequency. However, during the rising phase of the ramp-input the instantaneous frequency is higher than the asymptotic reference. During the falling phase it is lower, thus creating the overall IFA asymmetry.

Varying the slope of the external double-ramp drive one can see that the IFA asymmetry is speed-dependent (Fig. 4.4C,D): If the external drive changes more slowly (smaller slope), the network frequency response becomes more symmetric; for very small slopes the instantaneous frequencies approach the symmetric, asymptotic reference frequencies.

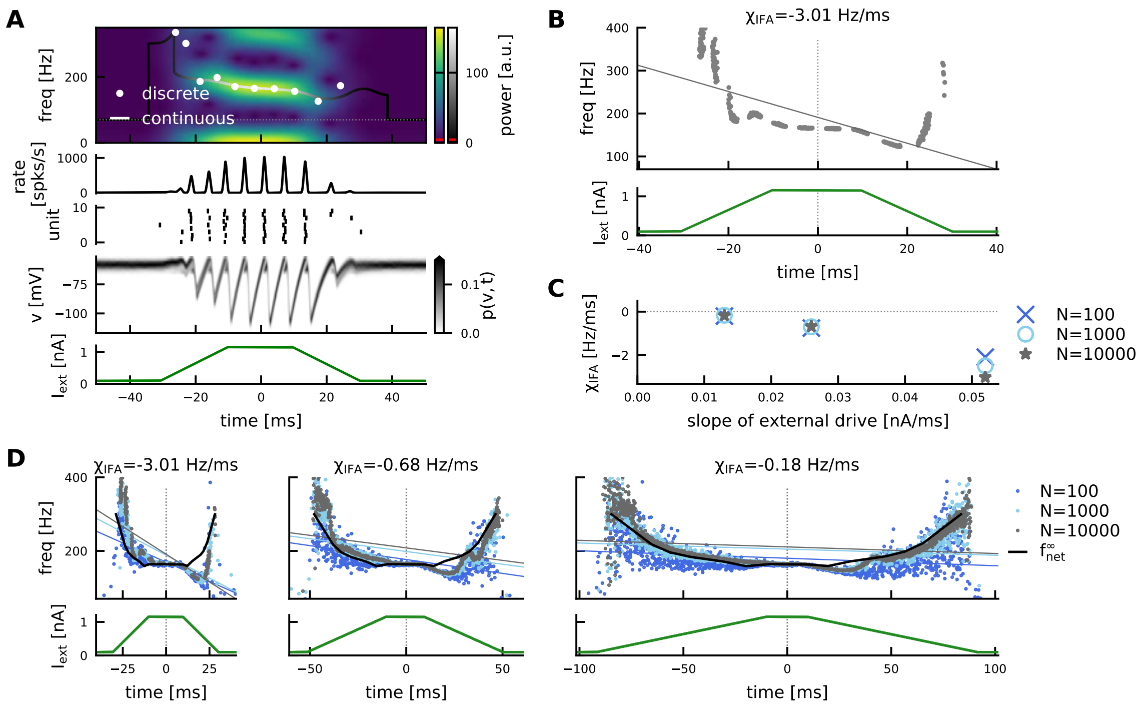

Figure 4.4: Transient dynamics and IFA in the reduced spiking network. **A,** Example simulation showing a transient ripple with IFA. From bottom to top: SPW-like drive (Eq. (4.22)); histogram of membrane potentials (normalized); raster plot showing spike times of 10 example units; population rate exhibiting transient ripple oscillation; wavelet spectrogram indicating instantaneous power (blue-yellow colorbar) for a frequency range of 0–350 Hz. Solid curve: continuous estimate of instantaneous frequency based on wavelet spectrogram with gray scale indicating maximal instantaneous power. Dotted line: cutoff frequency $f_{\min} = 70\,\text{Hz}$. Red line: power threshold (see Methods). White dots: discrete estimate of instantaneous frequency based on peak-to-peak distance in population rate. Network size $N = 10,000$. **B,** Average transient dynamics (see Methods). Top: Grey dots: discrete instantaneous frequency estimates from 50 independent simulations. Grey line: linear regression line with negative slope ($\chi_{\text{IFA}} = -3.01$ Hz/ ms) indicating IFA (see Methods, Eq. (4.23)). Bottom: The same SPW-like drive was applied in all 50 simulations. Network size $N = 10,000$. **C,** Dependency of IFA slope χ_{IFA} on the slope of the external drive for different network sizes (color coded, details see D). **D,** Instantaneous (dots) vs asymptotic (black line) network frequencies (top) for piecewise linear drives (bottom) of decreasing slopes (left to right). Color indicates network size N. Thin, colored linear regression lines illustrate decreasing strength of IFA for shallower drive. The indicated IFA slope χ_{IFA} refers to the largest network ($N = 10,000$). With decreasing slope of the drive (from left to right) the instantaneous network frequencies become more similar to the symmetric, asymptotic frequencies and IFA vanishes. Network size does not influence the IFA slope significantly (see also C). Asymptotic network frequencies are derived via interpolation of the constant-drive results shown in Fig. 4.3.

4.3 Theory of ripple dynamics in the mean-field limit

To understand the mechanism behind the network dynamics illustrated for constant drive in Fig. 4.3 and time-dependent drive in Fig. 4.4, I will resort to a mean-field ansatz. Simulations indicate that the network dynamics varies only little when the network size is increased (Fig. 4.3B, Fig. 4.4C,D). I hence hypothesize that IFA is preserved in the mean-field limit of an infinitely large network and will use a mean-field ansatz to explain its generating mechanism.

To facilitate notation in the subsequent mathematical analysis of the network dynamics, I rescale all voltages in Eq. (4.2) to units of the distance between threshold and rest such that the new spiking threshold is at $V_T = 1$ and the resting potential at $E_L = 0$ (see Methods, Section 4.5.2.1). The single unit SDE then reads

$$\tau_m \dot{V}_i = -V_i + I_{\mathrm{E}}(t) - \frac{K\tau_m}{N}\sum_{j=1}^{N}\sum_{k}\delta(t - t_j^k - \Delta) + \sqrt{2D\tau_m}\xi_i(t)\,, \tag{4.3}$$

with rescaled external excitatory current I_{E}, inhibitory synaptic strength K, and noise intensity D. In the mean-field limit, $N \to \infty$, the dynamics of the density of membrane potentials $p(V,t)$ is described by the following Fokker-Planck equation (FPE):

$$\tau_m \partial_t p(V,t) = -\partial_V\Big(\big(I(t) - V\big)p(V,t)\Big) + D\partial_V^2 p(V,t) \tag{4.4}$$

$$I(t) = I_{\mathrm{E}}(t) - I_{\mathrm{I}}(t) = I_{\mathrm{E}}(t) - K\tau_m r(t - \Delta) \tag{4.5}$$

$$r(t) = -\frac{D}{\tau_m}\partial_V p(V_T, t) \tag{4.6}$$

(see Methods, Eqs. (4.27) for a complete list of boundary conditions).

The population rate $r(t)$ is defined as the probability current through the absorbing boundary at the threshold (Eq. (4.6)) and approximates the activity of the spiking network in the mean-field limit ($N \to \infty$). Compared to the classical application of the FPE (Risken, 1989; Gardiner, 1985) there are two essential differences: First, due to the fire-and-reset rule, there is an absorbing boundary condition at the threshold (Eq. (4.27e)) and a source of probability at the reset point (Eq. (4.27g)); the latter source can be imposed by a jump condition for the derivative of the density at the reset point (see e.g. Abbott and van Vreeswijk, 1993; Brunel, 2000; Lindner and Schimansky-Geier, 2001; Brunel et al., 2003). Secondly, the current $I(t)$ (Eq. (4.5)) depends on the population rate $r(t)$, which itself depends on the probability density $p(v,t)$ (Eq. (4.6)). For such a *nonlinear* (or *nonlocal*) FPE only the stationary solution can be found analytically, with asynchronous irregular spiking and a constant population rate given low constant drive (Brunel and Hakim, 1999, Fig. 4.5). Oscillatory solutions cannot be computed exactly.

In the following I will briefly review existing linear approaches towards understanding the oscillatory regime, and their limitations. Then I will introduce a novel approximation for the oscillation dynamics at strong drive, constant or time-dependent, that allows an understanding of the IFA mechanism.

4.3.1 Linear approaches and their limitations

In the stationary state the FPE can be solved exactly (Brunel and Hakim, 1999, explained in Methods Section 4.5.2.3), yielding analytical expressions for the (constant) population rate r_0 and the distribution of membrane potentials $p_0(V)$ (Fig. 4.5).

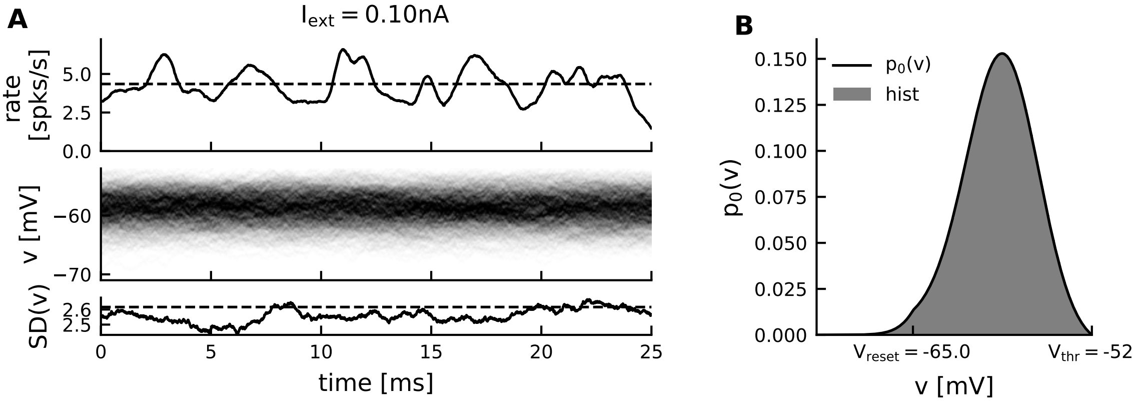

Figure 4.5: Stationary network dynamics in simulation and theory. Stationary network dynamics in the asynchronous irregular firing regime for external drive $I_{\mathrm{ext}} = 0.1\,\mathrm{nA}$ (cf. Fig. 4.3A, left). **A,** Top: The population rate $r(t)$ (solid line) in a simulation of a *finite* spiking network ($N = 10,000$) fluctuates around the constant population rate $r_0 = 4.35$ spikes/s (dashed line) that is estimated (semi-)analytically from the FPE (Fig. 4.20, Methods Section 4.5.2.3). Middle: membrane potentials in the spiking network simulation over time. Bottom: Standard deviation (SD) of membrane potentials across units at each point in time. Dashed line marks the SD expected without boundary conditions ($\sigma_V = 2.62$ mV, see also Table 4.3). **B,** The distribution of membrane potentials observed in the spiking network simulation (grey histogram, averaged over time) agrees well with the stationary solution $p_0(v)$ of the FPE (black line, Eq. (4.30)). Note the small discontinuity in the derivative of $p_0(V)$ at the reset potential, and the absorbing boundary condition at threshold. The simulation results are shown here in nA and mV (non-rescaled, cf. Eqs. (4.26)).

It has been shown that the stationary state loses stability via a supercritical Hopf bifurcation when the external drive I_{E} increases (Brunel and Hakim, 1999) (explained in Methods Section 4.5.2.5). Alternatively, the bifurcation can also be reached by an increase in inhibitory coupling strength or a decrease in noise strength (see Methods, Eq. (4.38)). In the context of SPW-Rs however, the changing external drive is assumed to act as the bifurcation parameter.

The location of the bifurcation (*i.e.* the critical drive $I_{\mathrm{E}}^{\mathrm{crit}}$) and the associated network frequency and the mean unit firing rate can be determined in a linear stability analysis (Brunel and Hakim, 1999, explained in Methods Section 4.5.2.4). This analysis involves the calculation of the linear response of a single neuron to weak oscillatory input. A self-consistent solution is found for which the synaptic and neuronal phase lags add up such that the oscillatory input and output rate of the recurrently connected network match (see Fig. 4.22).

For LIF neurons under Gaussian white noise, as in the reduced ripple model, the linear response function is known analytically (Lindner and Schimansky-Geier, 2001; Brunel et al., 2001) and the linear stability analysis thus yields accurate results: For a spiking network large enough to approximate the mean-field dynamics ($N \sim 10,000$) the simulated network frequency and the mean unit firing rate at the predicted critical input level $I_{\mathrm{E}}^{\mathrm{crit}}$ are close to the analytical approximation (Fig. 4.3B, red markers).

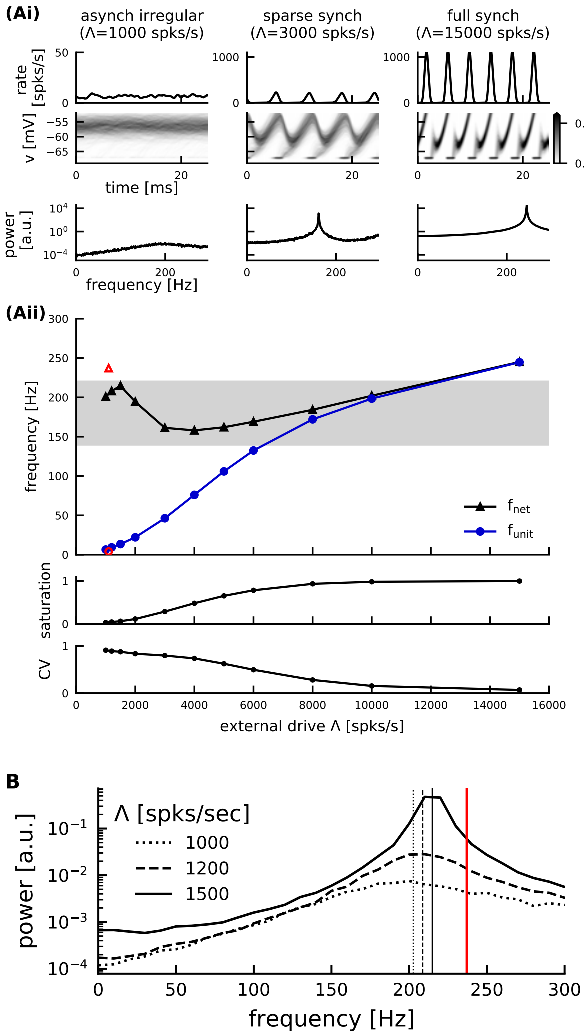

Figure 4.6: Linear stability analysis for the detailed ripple model. **A,** Oscillations in the detailed model, same outline as Fig. 4.1. Red markers: analytical estimate of bifurcation under omission of neuronal phase lag (Brunel and Wang, 2003). **B,** Power spectral densities and network frequency estimates (black vertical lines) of the simulated population activities close to the bifurcation (first 3 black triangles in Aii).

The network simulation was adjusted to optimize comparability with the mean-field result (Methods Section 4.5.2.4). The small discrepancy between the simulated and analytically estimated frequency at oscillation onset (A) seems indeed due to an error in the *analytical* estimate neglecting the neuronal phase lag, and not an inaccurate numerical estimate of the network frequency (B). A definite statement on this matter however, would require a comparison of the analytical result shown here, with the result obtained when including a (numerically estimated) neuronal phase lag.

If the neuron is subject to Gaussian colored noise, for example due to the presence of synaptic filters as in the detailed ripple model, the linear response function is not known analytically (but see Badel, 2011; Schwalger, 2021) (Methods Section 4.5.2.4). The approximation of the frequency in the bifurcation point (Eq. (4.36)) is thus either less exact (when the unknown neuronal phase lag is omitted, Fig. 4.6), or only semi-analytical (when the neuronal phase lag is estimated numerically Geisler et al., 2005; Richardson, 2007, 2008). If the synaptic decay time constant is large (compared to the membrane time constant), the neuronal phase lag is small (Brunel et al., 2001) (Methods Section 4.5.2.4). Thus it can be omitted in the linear stability analysis and still the network frequency at oscillation onset is predicted reasonably well (Fig. 4.6A, ∼237 Hz).

An important result of the analysis including synaptic filtering is that the fast synaptic time constants of inhibition (delay Δ and rise time constant τ_I^r) are much stronger determinants of the network frequency than the slow decay time constant τ_I^d (Brunel and Wang, 2003). This is relevant for the interpretation of experiments that pharmacologically alter inhibitory synaptic transmission.

Finally, linear stability analysis yields insights into how the choice of neuron model affects the network dynamics (Methods Section 4.5.2.4). In the LIF neuron, spike initiation is instantaneous. Other neuron models that account for a finite spike initiation time, such as the exponential integrate-and-fire (EIF) neuron, respond to oscillatory input with a larger phase lag than the LIF neuron. Networks of EIF neurons thus oscillate at lower frequencies than LIF networks at comparable noise levels and coupling strengths. This poses a potential constraint for the bifurcation-based ripple model, which I will come back to in the discussion.

Generally, linear stability analysis can describe the oscillation dynamics only close to the bifurcation where the oscillatory modulation of the population rate is quasi-sinusoidal and has infinitesimal amplitude. In a *weakly nonlinear analysis* Brunel and Hakim (1999) approximated the frequency and amplitude of the oscillation close at but beyond the bifurcation (Methods Section 4.5.2.5). In the limit of short synaptic delay, the network frequency *de*creases when the bifurcation parameter (here the external drive) increases beyond its critical value (Eq. (4.42)). The oscillation amplitude grows as the square root of the drive, as expected after a supercritical Hopf bifurcation (Eq. (4.41)). Both results are confirmed in the numerical simulations of the reduced ripple model (Fig. 4.3).

Further away from the bifurcation the population rate oscillation becomes strongly non-sinusoidal with brief moments of silence ($r(t) \approx 0$) inbetween population spikes (Fig. 4.3A, middle and right). In that regime all of the above approaches break down. Furthermore, all the above approaches consider *constant* external drive and do not allow a straight-forward prediction of the transient dynamics that occur for *time-dependent* ("SPW-like") drive. Thus to address the mechanism of IFA a novel theoretical approximation of the network dynamics is required, that is valid even for strong and time-dependent drive.

4.3.2 A drift-based approximation of oscillation dynamics under strong drive

In this section I will introduce a simplified approach to approximate the network dynamics at strong drive beyond the bifurcation. The approach can be motivated by two observations from the spiking network simulations: (a) In the relevant regime between sparse and full synchrony, units spike at most *once* per cycle of the population rhythm ($f_{\text{unit}} < f_{\text{net}}$, Fig. 4.3B). Hence one can approximate the time course of a single population spike using a first-passage-time ansatz, neglecting the reset mechanism. (b) Inbetween population spikes, the bulk of the membrane potential distribution is pushed significantly below threshold and the population rate approaches zero (see Fig. 4.3A). In those periods the absorbing boundary condition at threshold does not have any significant impact on the dynamics of $p(V,t)$.

These two observations motivate a considerable simplification: Without the boundary conditions at threshold and reset, the FPE can be solved analytically. In the long-time limit its solution becomes a simple Gaussian — independent of the initial condition (see Methods, Eq. (4.43)). One can thus approximate the density of membrane potentials p as

$$p(V,t) \approx \frac{1}{\sqrt{2\pi D}} \exp\left[-\frac{(V-\mu(t))^2}{2D}\right] . \tag{4.7a}$$

The only time-dependent quantity is the mean membrane potential μ, which evolves according to the single unit SDE (Eq. (4.3)) without the noise term:

$$\dot{\mu}(t) = \frac{1}{\tau_m}\Big(I(t) - \mu(t)\Big) \overset{(4.5)}{=} \frac{1}{\tau_m}\Big(I_\mathrm{E}(t) - K\tau_m r(t-\Delta) - \mu(t)\Big) . \tag{4.7b}$$

The population rate can be redefined in this framework, based solely on the drift-based spiking probability current, ignoring diffusion-mediated spiking (see Methods Eqs. (4.48), (4.49), Goedeke and Diesmann, 2008; Plesser and Gerstner, 2000; Chizhov and Graham, 2007):

$$r(t) = [\dot{\mu}(t)]_+ p(V_T,t) = \frac{[\dot{\mu}(t)]_+}{\sqrt{2\pi D}} \exp\left[-\frac{(V_T-\mu(t))^2}{2D}\right] . \tag{4.7c}$$

The rate r is given by the membrane potential density at threshold, $p(V_T,t)$, scaled by the speed $\dot{\mu}$ at which the mean membrane potential approaches the threshold. Whenever the mean membrane potential is *de*creasing, the rate is clipped to 0 ($[x]_+ := (x+|x|)/2$).

Taken together, Eqs. (4.7), which are coupled via the inhibitory feedback current $I_\mathrm{I}(t)$ (see Eq. (4.7b)), are equivalent to a single delay differential equation (DDE) describing the dynamics of the mean membrane potential and the resulting drift-based population rate under the drift-based approximation (Methods Eq. (4.51)). This DDE is of course *not* equivalent to the FPE (Eqs. (4.4)) with its orignal boundary conditions, or the spiking network (Eq. (4.2)). The main discrepancies between the spiking network dynamics and the drift-based approximation are illustrated in Fig. 4.7 for the case of constant drive (A: spiking network vs B: drift-based approximation). A quantification of the membrane potential density $p(V,t)$ in the spiking network shows that it is not strictly Gaussian (Fig. 4.7Aii-iii, Methods Section 4.5.1.7): Due to the fire-and-reset mechanism, $p(V,t)$ changes in *shape* during the oscillation cycle, becoming at times almost bimodal. Still, we see that simplifying assumption (b) is justified: When the membrane potential density is subthreshold inbetween population spikes, it becomes indeed more Gaussian and its standard deviation approaches $\sqrt{D}$ (Fig. 4.7 Aii, bottom, Aiii, first 3 snapshots).

The advantage of the drift-based approximation is that its dynamics can be approximated analytically. In the following I will first consider the dynamics for constant drive, then this ansatz is extended for time-dependent drive to allow an understanding of transient frequency responses and hence the emergence of IFA.

4.3.3 Oscillation dynamics for constant drive

A T-periodic solution of the Gaussian model (DDE (4.7b), Methods Eq. (4.51)) must have a mean membrane potential $\mu(t) = \mu(t + T)$ that oscillates between two local extrema $\mu_{\min}$ and $\mu_{\max}$ (Fig. 4.7Bi). Whenever the mean membrane potential *in*creases, a positive population rate is produced; when the mean membrane potential *de*creases the population rate is clipped to 0 (Eq. (4.7c)). The moment when μ reaches its local maximum $\mu_{\max}$ is thus of special importance as it marks the end of the population spike. I will refer to this time as t_{off}:

$$\mu(t_{\text{off}}) = \mu_{\max}\,, \quad r(t_{\text{off}}) = 0\ .$$

Since all inhibitory feedback arrives with a delay of Δ, it follows that the inhibitory feedback ceases exactly Δ after the end of the population spike, *i.e.* $I_{\text{I}}(t_{\text{off}} + \Delta) = 0$. It is convenient to define this moment as the end of a cycle, *i.e.* the beginning of the next one. The mean membrane potential at this time is close to its local minimum (see Methods Section 4.5.4.2) and will be denoted as $\mu_{\min} := \mu(t_{\text{off}} + \Delta)$. The period T can then be split into the time t_{off} needed for the mean membrane potential to rise from $\mu(0) = \mu_{\min}$ towards $\mu(t_{\text{off}}) = \mu_{\max}$ (the *upstroke*), plus a fixed interval Δ during which the mean membrane potential is pushed back down to $\mu(T) = \mu_{\min}$ due to the delayed inhibitory feedback (the *downstroke*) (Fig. 4.7Bii). In the Methods I derive, through a series of heuristic approximations, analytical expressions for the local extrema $\mu_{\max}$ (Eq. (4.58)) and $\mu_{\min}$ (Eq. (4.73)) of the mean membrane potential oscillation as a function of the external drive I_E. Using these expressions, I obtain an analytical approximation for t_{off} (Eq. (4.70)) and hence for the network frequency:

$$f_{\text{net}} = T^{-1} = (t_{\text{off}} + \Delta)^{-1}\ . \tag{4.8}$$

Apart from the network frequency the drift-based approximation also allows an intuitive understanding of the mean unit firing rate. When the population spike ends at time t_{off}, the suprathreshold portion of the Gaussian density corresponds to the fraction of units that have spiked in the given cycle (the *saturation* s, Methods Eq. (4.71)). The mean unit firing rate can thus be inferred as:

$$f_{\text{unit}} = s f_{\text{net}}\ . \tag{4.9}$$

The example in Fig. 4.7 ($I_{\text{E}} = 4.24$) shows that the dynamics of the Gaussian model can be very close to the dynamics of the spiking network: The population rate in the simulated spiking network oscillates with a period $T = 5.08$ ms, corresponding to a network frequency of f_{net} =196.9 Hz (Fig. 4.7A). The Gaussian model predicts an oscillation period $T = 5.11$ ms, corresponding to a network frequency of f_{net} =195.7 Hz (Fig. 4.7B). Such a good quantitative fit can only be achieved by including a phenomenological account for the single unit reset mechanism in the drift-based approximation (yellow marks in Fig. 4.7B, see Methods Section 4.5.4.3 for details). In the following the performance of the drift-based approximation is compared systematically for a range of external drives I_{E}.

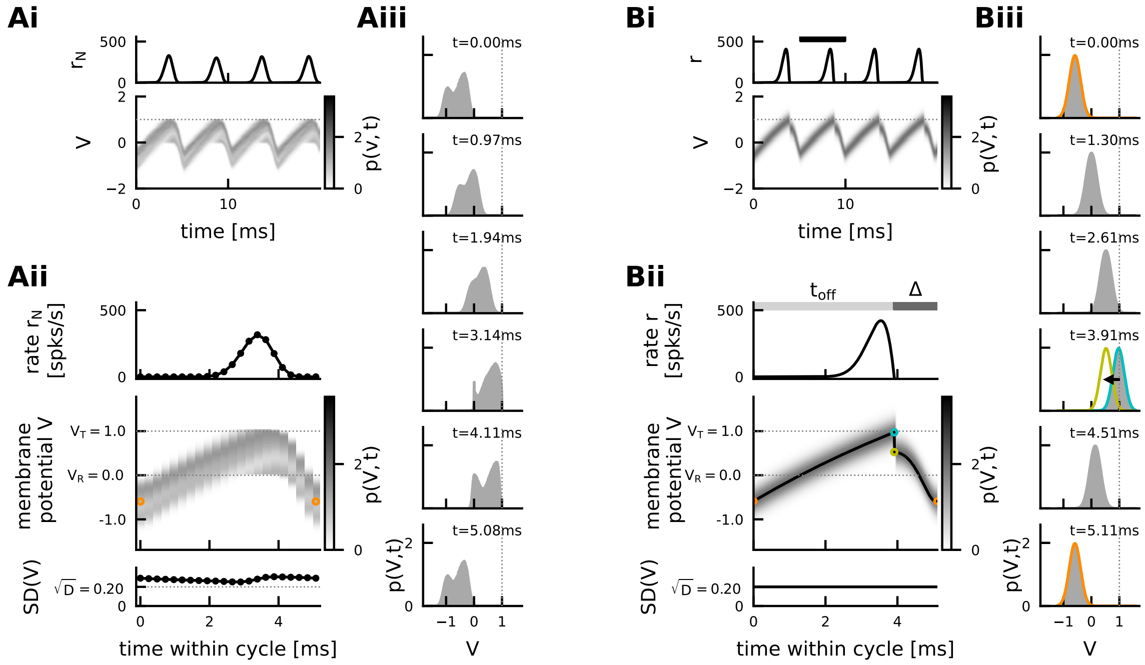

Figure 4.7: Illustration of the drift-based approximation. Comparison of oscillation dynamics in the spiking network simulation (A) and the drift-based approximation (B) at constant drive ($I_E = 4.24$). **Ai**, Spiking network simulation. Empirical population rate r_N (top), and density of membrane potentials (bottom), exhibiting coherent stochastic oscillations with (weak) finite size fluctuations. Dotted line marks spike threshold ($V_T = 1$). **Aii**, The average oscillation cycle: Top: population rate; middle: density of membrane potentials, orange marker: local minimum of mean membrane potential; bottom: standard deviation of membrane potential distribution, dotted line: theoretical asymptote $\sqrt{D}$ in the absence of boundary conditions (Eq. (4.46)). **Aiii**, Snapshots of the membrane potential density over the course of the average cycle shown in (Aii). Dotted line marks spike threshold/absorbing boundary. **Bi**, Drift-based approximation (Eqs. (4.7)). Top: population rate, bottom: Gaussian density of membrane potentials $p(V,t)$, both perfectly periodic. **Bii**, Zoom into one oscillation cycle (black bar in Bi). Top: population rate r, middle: density of membrane potentials $p(V,t)$, bottom: constant standard deviation $\sqrt{D}$. The mean membrane potential $\mu(t)$ (black line) starts each cycle in μ_{min} (orange) and rises up until μ_{max} (cyan) at time t_{off}, at which point the population spike ends. In a phenomenological account for the single unit reset, μ is reset instantaneously to μ_{reset} (yellow, Eq. (4.72)). From there μ declines back towards μ_{min}. **Biii**, Snapshots of the membrane potential density $p(V,t)$ over the course of one cycle (Bii). Note that in the theoretical approximation the spiking threshold $V_T = 1$ (dotted line) is no longer an absorbing boundary.
(For an analog illustration of the drift-based approximation in the regime of full synchrony, see Supplementary Fig. 4.41).

4.3.3.1 Evaluation of the performance of the theory

The drift-based approximation captures the dependence of network frequency f_{net} and mean unit firing rate f_{unit} on the external drive I_E, including the transition from sparse to full synchrony for increasing external drive (Fig. 4.8, top). The analytically derived expression for the saturation s predicts this transition, since s is a monotonically increasing function of μ_{max} (Eq. (4.71)), which monotonically increases as a function of the external drive I_{E} (Eq. (4.58), Fig. 4.8, middle). The Gaussian model also allows an analytical estimation of the point of full synchrony, i.e. the amount of external drive $I_{\mathrm{E}}^{\mathrm{full}}$ that is required for single units to fire approximately at the frequency of the network rhythm (Fig. 4.8, vertical dashed line, see Methods Section 4.5.4.4, Eq. (4.74)). The Gaussian model slightly overestimates the point of full synchrony, but correctly predicts its parameter dependencies: For stronger coupling and/or larger noise, stronger external drive is required to reach full synchrony (Fig. 4.28 in Appendix Section 4.A). A detailed analysis of how the drift-based ripple oscillations in the Gaussian model depend on network parameters, such as the coupling strength and the noise, can be found in Appendix Section 4.A.

The theory shows that the amplitude $\mu_{\mathrm{max}} - \mu_{\mathrm{min}}$ of the oscillatory mean membrane potential grows with increasing drive (Fig. 4.8, bottom). This is mainly due to a strong decrease of the periodic minimum μ_{min} (Fig. 4.8, bottom, solid orange line), which is also observed in the spiking network simulation (Fig. 4.8, bottom, dashed orange line). The quantities μ_{max} and μ_{reset} are pertinent to the drift-based approximation and have no direct counterpart in the spiking neural network model. The strong, monotonic increase of the oscillation amplitude for increasing drive will be of great importance in the next section, where I study hysteresis effects caused by fast changes in the drive.

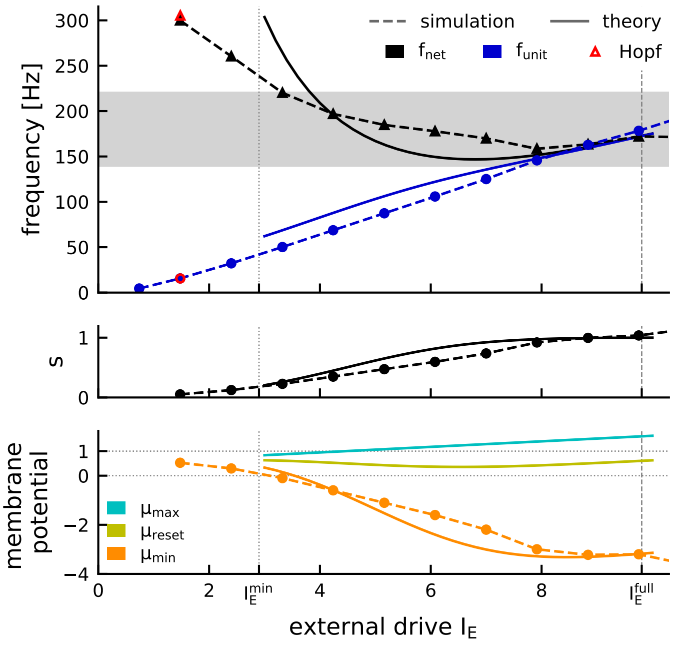

Figure 4.8: Drift-based approximation of ripple dynamics for constant drive. Theory vs spiking network simulation. Top: network frequency (black) and mean unit firing rate (blue). Red marker: Hopf bifurcation. Vertical lines indicate the range $[I_{\mathrm{E}}^{\mathrm{min}}, I_{\mathrm{E}}^{\mathrm{max}} = I_{\mathrm{E}}^{\mathrm{full}}]$ for which the theory applies. Middle: saturation s. Bottom: local maximum μ_{max} (cyan, Eq. (4.58)), local minimum μ_{min} (orange, Eq. (4.73)) and population reset μ_{reset} (yellow, Eq. (4.72)) of mean membrane potential. Default parameters (Table 4.3).

I will conclude this section with a few remarks on the limitations of the drift-based approximation and its relation to other mean-field approaches:

The range of applicability of the theory is defined by the two assumptions motivated in the beginning: (a) units should spike at most once per cycle (i.e. $I_{\mathrm{E}} \leq I_{\mathrm{E}}^{\mathrm{full}}$), (b) inbetween population spikes, the bulk of the membrane potential distribution should be subthreshold (i.e. $\mu_{\min}(I_{\mathrm{E}})+3\sqrt{D} \leq V_T$). The resulting range $[I_{\mathrm{E}}^{\min}, I_{\mathrm{E}}^{\max}]$ (see Methods Section 4.5.4.5) covers the large part of the regime of sparse synchrony up to the point of full synchrony (Fig. 4.8, area between vertical dotted and dashed line). Numerical simulations confirm that for strong enough drive, the drift-based approximation works for a wide parameter regime w.r.t. noise, coupling strength, and synaptic delay (see Appendix Section 4.A, Fig. 4.27, Fig. 4.28).

The parameter exploration in Appendix Section 4.A reveals that the network frequency beyond the Hopf bifurcation depends strongly on the inhibitory coupling strength (Fig. 4.27C). Previous studies focusing on linear stability analysis around the Hopf bifurcation (Brunel and Hakim, 1999; Brunel and Wang, 2003) have suggested that the network frequency is set primarily by the (fast) synaptic time constants and depends only weakly on other parameters, which is confirmed by the spiking network simulations shown in Fig. 4.27C (red markers). The drift-based approximation shows, however, that further away from the bifurcation other parameter dependencies *do* play a role. For strong coupling ($K = 50$, Fig. 4.27C, top row) one even observes a drop in the network frequencies to slow gamma range. The drift-based approximation captures this dependency very well and thus complements previous work focusing on the bifurcation point (Brunel and Hakim, 1999).

At low drive ($I_{\mathrm{E}} < I_{\mathrm{E}}^{\min}$) the theory breaks down (see also Methods Section 4.5.3.1). This is to be expected from a purely drift-based approximation. The dynamics of the spiking network close to its supercritical Hopf bifurcation is largely fluctuation-driven. Such dynamics cannot be captured by focusing only on the oscillation of the mean membrane potential, which has infinitesimal amplitude as the drive approaches its critical value. This limitation of the theory does not pose a problem, since (a) the fluctuation-driven dynamics around the Hopf bifurcation has already been studied in depth by Brunel and Hakim (1999) (see Methods Section 4.5.2.4) and (b) the main goal here is to explain the IFA dynamics, which happens in the strongly mean-driven regime $I_{\mathrm{E}}(t) \gg I_{\mathrm{E}}^{\min}$.

So far, I have considered the case of constant drive and described the *asymptotic* oscillatory dynamics that are observed after initial conditions have been forgotten. I will emphasize this from here on by adding a superscript "∞". I will now study how the *transient* dynamics, introduced either by a perturbation of the initial condition or a time-dependent drive, deviate from these asymptotic constant-drive dynamics.

4.3.4 Oscillation dynamics and IFA for time-dependent drive

4.3.4.1 Piecewise constant drive

Even for constant drive, there is *transient* dynamics if the initial mean membrane potential deviates from the asymptotic minimum $\mu_{\min}^{\infty}$. Let's assume that a cycle starts with an initial mean membrane potential $\mu_{\min} \neq \mu_{\min}^{\infty}(I_{\mathrm{E}})$. We only require that $\mu_{\min}$ is sufficiently subthreshold, such that the initial population rate is close to zero. What will be the period of the first cycle and how long does it take until the asymptotic dynamics is reached?

First I note that, independent of $\mu_{\min}$, the mean membrane potential will rise towards the asymptotic $\mu_{\max}^{\infty}(I_{\mathrm{E}})$, which has been shown to be independent of the initial condition (Eq. (4.58)). Thus, only the duration of the first upstroke will be influenced by the initial condition and the asymptotic dynamics is reached immediately thereafter.

The duration of the first upstroke depends on the distance that the mean membrane potential has to travel, from its initial value μ_{min} to the next peak $\mu^{\infty}_{\text{max}}(I_{\text{E}})$. For $\mu_{\text{min}} = \mu^{\infty}_{\text{min}}(I_{\text{E}})$ the upstroke has length $t^{\infty}_{\text{off}}(I_{\text{E}})$ and the first cycle has the asymptotic period T^{∞}/ instantaneous frequency f^{∞}_{net} (Fig. 4.9A, middle). Trivially, the upstroke will take *less* time, if the mean membrane potential starts at a *higher* value ($\mu_{\text{min}} > \mu^{\infty}_{\text{min}}(I_{\text{E}})$) and more otherwise (Fig. 4.9A, left vs right). Hence the period of the first cycle will be either shorter or longer, which can be rephrased as an instantaneous frequency $f^{\text{inst}}_{\text{net}}$ that is higher or lower than the asymptotic $f^{\infty}_{\text{net}}(I_{\text{E}})$. Fig. 4.9B illustrates the instantaneous frequency of the first cycle for a range of combinations of (constant) drive I_{E} and initial conditions μ_{min} (red: instantaneous frequency is higher than asymptotic frequency; blue: instantaneous frequency is lower).

Once the mean membrane potential has reached its first peak $\mu^{\infty}_{\text{max}}(I_{\text{E}})$, it will follow the asymptotic dynamics, settling into $\mu^{\infty}_{\text{min}}(I_{\text{E}})$ at the end of the first cycle, and all subsequent cycles will come at the asymptotic frequency $f^{\infty}_{\text{net}}(I_{\text{E}})$ associated to the external drive I_{E} (convergence indicated by arrows in Fig. 4.9B). A change of initial condition can thus only introduce a transient deviation from the asymptotic dynamics in a *single* cycle.

What if we change the external drive after each cycle (green line in Fig. 4.9C)? Then the initial mean membrane potential of each cycle i will be the asymptotic minimum associated to the drive of the *previous* cycle:

$$\mu^{i}_{\text{min}} = \mu^{\infty}_{\text{min}}(I^{i-1}_{\text{E}})$$

i.e. the mean membrane potential dynamics exhibits a history dependence (or *hysteresis*, see Fig. 4.9C, orange marker vs orange line). Now recall that the asymptotic minimum $\mu^{\infty}_{\text{min}}(I_{\text{E}})$ is a monotonically decaying function of the drive (except for strong drive close to $I^{\text{full}}_{\text{E}}$, Fig. 4.9B, black line). Thus, if the external drive *in*creases stepwise, each cycle will start with an initial mean membrane potential *above* the asymptotic minimum associated to that cycle's drive, hence the instantaneous frequency will be *above* its asymptotic value in every cycle (Fig. 4.9B, trajectory through red area: $f^{\text{inst,i}}_{\text{net}} > f^{\infty}_{\text{net}}(I^{i}_{\text{E}})\,\forall i$, Fig. 4.9C, cycles 1-4). Vice versa, if the external drive *de*creases stepwise, each cycle will start with an initial mean membrane potential *below* the asymptotic minimum associated to that cycle's drive, hence the instantaneous frequency will be *below* its asymptotic value in every cycle (Fig. 4.9B, trajectory through blue area: $f^{\text{inst,i}}_{\text{net}} < f^{\infty}_{\text{net}}(I^{i}_{\text{E}})\,\forall i$, Fig. 4.9C, cycles 5-7). In summary:

$$\begin{aligned}
I^{i}_{\text{E}} > I^{i-1}_{\text{E}} \quad &\Rightarrow \quad \mu^{i}_{\text{min}} = \mu^{\infty}_{\text{min}}\left(I^{i-1}_{\text{E}}\right) > \mu^{\infty}_{\text{min}}\left(I^{i}_{\text{E}}\right) \quad \Rightarrow \quad f^{\text{inst},i}_{\text{net}} > f^{\infty}_{\text{net}}\left(I^{i}_{\text{E}}\right)\\
I^{i}_{\text{E}} < I^{i-1}_{\text{E}} \quad &\Rightarrow \quad \mu^{i}_{\text{min}} = \mu^{\infty}_{\text{min}}\left(I^{i-1}_{\text{E}}\right) < \mu^{\infty}_{\text{min}}\left(I^{i}_{\text{E}}\right) \quad \Rightarrow \quad f^{\text{inst},i}_{\text{net}} < f^{\infty}_{\text{net}}\left(I^{i}_{\text{E}}\right)
\end{aligned}$$

Thus, if we approximate the transient change in drive during a sharp wave as a simple, piecewise constant function that first increases after each cycle, and then decreases (Fig. 4.9C, green line), we get IFA: The asymptotic network frequency associated to the drive in each cycle describes a reference curve that follows the same symmetry as the drive (Fig. 4.9C, top, solid black line). The instantaneous network frequency

(Fig. 4.9C, top, round markers) will be asymmetric over time, as it is *above* the asymptotic network frequencies during the rising phase of the external drive, and *below* during the falling phase. The theory thus describes the relationship between instantaneous and asymptotic frequencies that I already hinted at in the presentation of the spiking network simulations in Fig. 4.4D.

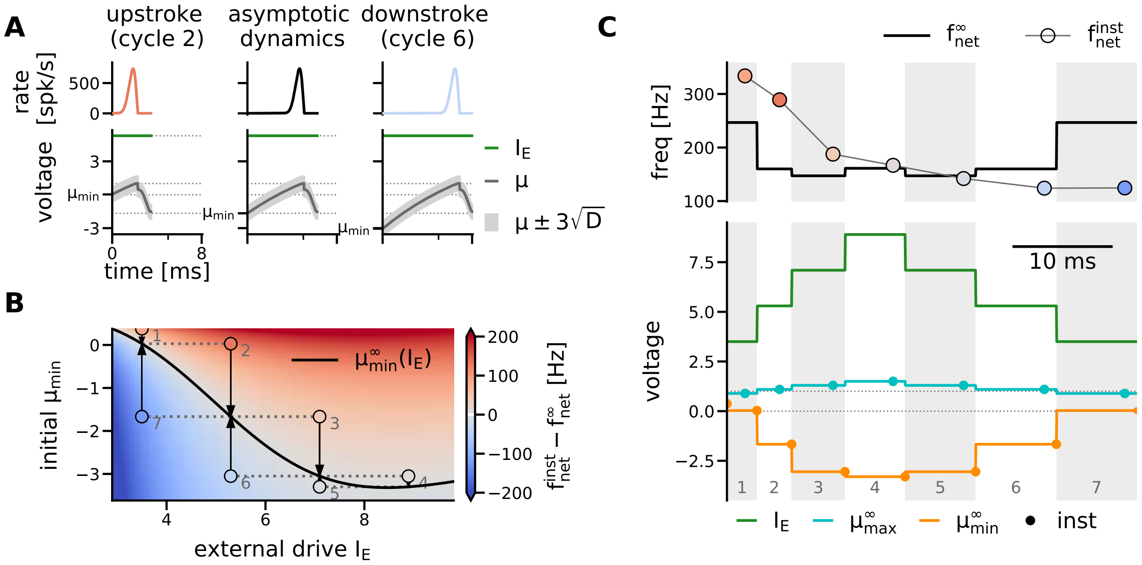

Figure 4.9: Transient dynamics and IFA for piecewise constant drive. **A,** Dependence of the length of the oscillation cycle on the initial mean membrane potential. Left: shorter period for $\mu_{\text{min}} > \mu_{\text{min}}^{\infty}(I_{\text{E}})$ (cycle 2 in C). Middle: asymptotic period for $\mu_{\text{min}} = \mu_{\text{min}}^{\infty}(I_{\text{E}})$. Right: longer period for $\mu_{\text{min}} < \mu_{\text{min}}^{\infty}(I_{\text{E}})$ (cycle 6 in C). **B,** Difference between the instantaneous frequency of a cycle with constant drive I_{E} and initial condition μ_{min}, and the asymptotic frequency $f_{\text{net}}^{\infty}(I_{\text{E}})$ for a range of external drives I_{E} and initial mean membrane potentials μ_{min}. Black line: asymptotic $\mu_{\text{min}}^{\infty}(I_{\text{E}})$ (cf. Fig. 4.8, bottom, orange line). Markers show example cycles shown in A, C. Arrows indicate convergence to the asymptotic dynamics after one cycle. If the drive changes after each cycle (dotted lines), the 7 examples combine into the trajectory shown in C. **C,** IFA for piecewise constant drive with symmetric step-heights. Shaded areas mark oscillation cycles. Bottom: The external drive is increased step-wise, up to the point of full synchrony $I_{\text{E}}^{\text{full}} \approx 8.9$ (green line). Lines in all panels indicate the asymptotic dynamics associated to the external drive of the respective cycle. Markers indicate transient behavior. Cyan: μ_{max}. Orange: μ_{min}. Top: the instantaneous network frequency (markers) is first above and then below the resp. asymptotic network frequencies (black line).

The piecewise constant shape of the drive may not be realistic, but serves to illustrate the core mechanism of IFA: a hysteresis in the oscillation amplitude of the mean membrane potential. A drawback is that this simple model for SPW-like drive is not symmetric in *time*, since the drive changes after each cycle, and the cycle length increases due to IFA. To show that the IFA asymmetry does not rely on an asymmetry in the drive, I adapted the drift-based approximation to incorporate time-dependent, linear drive (see Methods Section 4.5.5).

4.3.4.2 Piecewise linear drive

Previously I compared each transient cycle to the asymptotic dynamics associated to the (constant) external drive during that particular cycle. For a drive that changes linearly *within* one cycle, one level of drive has to be chosen for the asymptotic reference. Since all previous analytical approximations are anchored to the end of the population spike t_{off}, I decided to use the external drive reached at (the yet unknown!) time t_{off} as the reference drive, from here on referred to as $\hat{I}_{\text{E}} := I_{\text{E}}(t_{\text{off}})$ (see sketch in Methods Section 4.5.5, Fig. 4.26 for a clarification of “inputs” and “outputs” of the analytical approximation).

Following the same approach as before, I derive an approximation for the *transient* dynamics of a cycle i that starts with a mean membrane potential μ^i_{min}, given linear external drive $I_{\text{E}}(t) = \hat{I}^i_{\text{E}} + m(t - t^i_{\text{off}})$ with slope m and reference drive $\hat{I}^i_{\text{E}}$:

$$\left(\hat{I}^i_{\text{E}}, \mu^i_{\text{min}}, m\right) \longmapsto \left(f^{\text{inst,i}}_{\text{net}}, t^i_{\text{off}}, \mu^i_{\text{max}}, \mu^i_{\text{reset}}, \mu^{i+1}_{\text{min}}\right) \tag{4.10}$$

The dynamics is quantified in terms of the peak of the mean membrane potential μ^i_{max}, its reset value μ^i_{reset} and the value μ^{i+1}_{min} that is reached at the end of cycle i (and may thus be the initial membrane potential of the next cycle $i + 1$). Most importantly, the duration of the upstroke t^i_{off} is inferred, and from that the instantaneous network frequency $f^{\text{inst,i}}_{\text{net}} = \left(t^i_{\text{off}} + \Delta\right)^{-1}$ (see Methods Eqs. (4.79)-(4.87)).

The analysis is now a little more complex, since each cycle depends on three parameters ($\hat{I}^i_{\text{E}}, \mu^i_{\text{min}}, m$, see Fig. 4.26), in contrast to only two parameters ($I^i_E, \mu^i_{\text{min}}$) for piecewise constant drive. I will demonstrate, however, that the essential findings from the basic case of piecewise constant drive still hold, *i.e.* that IFA is generated by the same hysteresis in the transient dynamics of the mean membrane potential (Fig. 4.9 vs Fig. 4.10). To illustrate this in an example, I fix the slope of the linear drive to $m = \pm 0.4/\,\text{ms}$. I then compare how the transient dynamics deviates from the asymptotic dynamics depending on whether the drive is increasing ($m = +0.4/\,\text{ms}$) or decreasing ($m = -0.4/\,\text{ms}$) (Fig. 4.10).

The principal idea still holds for most combinations of reference drive $\hat{I}^i_{\text{E}}$ and initial value μ^i_{min} (Fig. 4.10A): If the drive is increasing ($m = +0.4/\,\text{ms}$) and the initial mean membrane potential is well above the asymptotic reference ($\mu^i_{\text{min}} \gg \mu^{\infty}_{\text{min}}(\hat{I}^i_{\text{E}})$), the cycle's period is shorter than the asymptotic reference, i.e. $f^{\text{inst,i}}_{\text{net}} > f^{\infty}_{\text{net}}(\hat{I}^i_{\text{E}})$ (Fig. 4.10A, left). Vice versa, if the drive is decreasing ($m = -0.4/\,\text{ms}$) and the initial mean membrane potential is well below the asymptotic reference ($\mu^i_{\text{min}} \ll \mu^{\infty}_{\text{min}}(\hat{I}^i_{\text{E}})$), the cycle's period is longer than the asymptotic reference, i.e. $f^{\text{inst,i}}_{\text{net}} < f^{\infty}_{\text{net}}(\hat{I}^i_{\text{E}})$ (Fig. 4.10A, right).

Exceptions from this “rule” can be seen in a systematic comparison of instantaneous and asymptotic frequencies depending on initial condition μ_{min} and reference drive $\hat{I}_{\text{E}}$, which now yields two plots: one for positive slope ($m = +0.4/\,\text{ms}$, Fig. 4.10B, left) and another one for negative slope ($m = -0.4/\,\text{ms}$, Fig. 4.10B, right). The white line illustrates the initial condition for which the period of the transient cycle coincides with the asymptotic period. For cycle-wise *constant* drive (Fig. 4.9B) the white line trivially coincided with the asymptotic minimum $\mu^{\infty}_{\text{min}}(\hat{I}_{\text{E}})$ (black line), but in Fig. 4.10B the two lines are different. They deviate because the drive changes linearly *within* a cycle. The small space between the white and black lines indicates the exceptions from the above "rule": if the initial mean membrane potential is close to the asymptotic reference, it no longer predicts the sign of the deviation of the instantaneous from the asymptotic frequency.

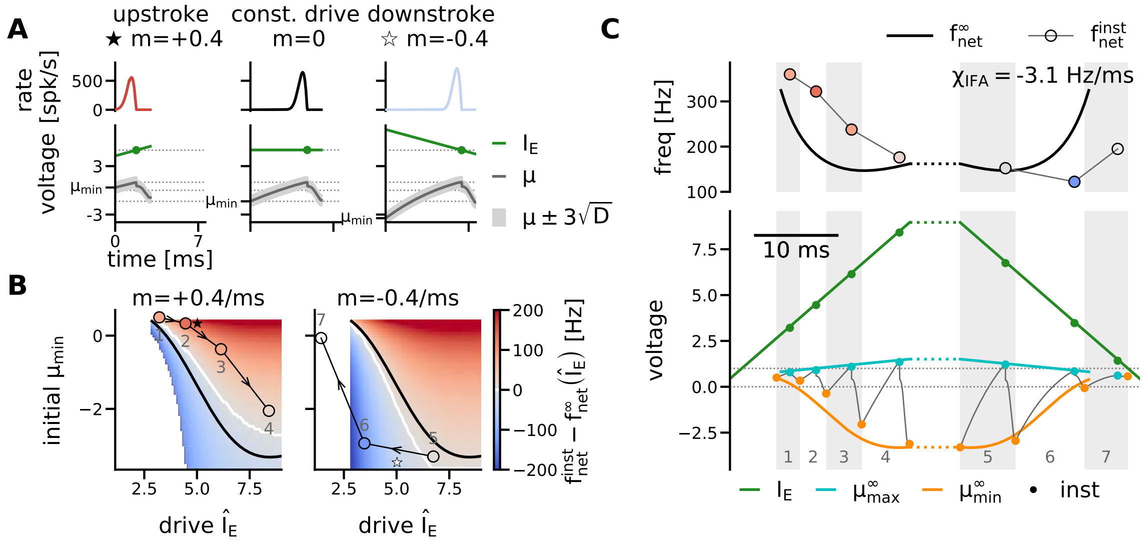

Figure 4.10: Transient dynamics and IFA for piecewise linear drive. **A,** Exemplary transients during rising vs. falling phase of the drive, green dot: $\hat{I}_\mathrm{E} = I_\mathrm{E}(t_\mathrm{off}) = 5$. Left: shorter period for $m > 0$ and $\mu_\mathrm{min} \gg \mu^\infty_\mathrm{min}(\hat{I}_\mathrm{E})$; middle: asymptotic period for constant drive ($I_\mathrm{E} \equiv \hat{I}_\mathrm{E}$, $m = 0$) and $\mu_\mathrm{min} = \mu^\infty_\mathrm{min}(\hat{I}_\mathrm{E})$; right: longer period for $m < 0$ and $\mu_\mathrm{min} < \mu^\infty_\mathrm{min}(\hat{I}_\mathrm{E})$. Dotted horizontal lines: reference drive $\hat{I}_\mathrm{E}$, threshold $V_T = 1$, reset potential $V_R = 0$ and the asymptotic $\mu^\infty_\mathrm{min}(\hat{I}_\mathrm{E})$. **B,** Difference between instantaneous and asymptotic frequency depending on $\hat{I}_\mathrm{E}$ and μ_min. Left: increasing drive ($m = +0.4/\,\mathrm{ms}$); right: decreasing drive ($m = -0.4/\,\mathrm{ms}$). Black line: asymptotic $\mu^\infty_\mathrm{min}(\hat{I}_\mathrm{E})$. White line: initial μ_min, for which $f^\mathrm{inst}_\mathrm{net} = f^\infty_\mathrm{net}(\hat{I}_\mathrm{E})$. Stars mark examples shown in A for $\hat{I}_\mathrm{E} = 5$. Round markers and arrows indicate trajectory shown in C for piecewise linear drive, numbered by cycle. White space where either: no asymptotic oscillations occur ($I_\mathrm{E} < I^\mathrm{min}_\mathrm{E}$, $\mu_\mathrm{min} > V_T - 3\sqrt{D}$), or (bottom left): no transient solution exists (Eq. (4.86)). **C,** IFA for piecewise linear (SPW-like) drive (green, Eq. (4.22)). Shaded areas mark oscillation cycles. Lines: asymptotic dynamics. Markers: transient dynamics (numerical, Eqs. (4.7)). Bottom: $\mu(t)$ (grey line), μ_max (cyan), μ_min (orange). Reset not shown for readability. Top: instantaneous network frequency (markers),asymptotic network frequencies (black line). Dashed lines: arbitrary plateau phase with $I_\mathrm{E} \equiv I^\mathrm{full}_\mathrm{E}$ IFA slope $\chi_\mathrm{IFA} = -3.1\;\,\mathrm{Hz}/\,\mathrm{ms}$ for 20 ms plateau.

Instead, the slope in the external drive is the determining factor: For increasing drive ($m > 0$) the drive during the upstroke of the membrane potential is *below* the reference $\hat{I}_\mathrm{E}$, and thus the upstroke can take *longer* than in the constant-drive case ($I_\mathrm{E} \equiv \hat{I}_\mathrm{E}$) even if μ_min is slightly *above* $\mu^\infty_\mathrm{min}(\hat{I}_\mathrm{E})$ (Fig. 4.10B, left, bluish color of region between the black and white lines); in contrast, for decreasing drive ($m < 0$; Fig. 4.10B, right, reddish color of region between the black and white lines), the drive during the upstroke of the membrane potential is *above* the reference $\hat{I}_\mathrm{E}$, and thus the upstroke can be *shorter* than in the constant-drive case ($I_\mathrm{E} \equiv \hat{I}_\mathrm{E}$) even if μ_min is slightly *below*

$\mu_{\text{min}}^{\infty}(\hat{I}_{\text{E}})$. These exceptions however occur only in a small portion of the parameter space that is rarely visited in a given ripple event, as we will see in the following.

What can we say about the dynamics of consecutive cycles $i, i+1, \ldots$ that occur if the drive rises or falls continuously with slope m? At the end of each cycle the mean membrane potential is close to the asymptotic reference $\mu_{\text{min}}^{\infty}(\hat{I}_{\text{E}})$ (see Methods, Eq. (4.90)). Thus we observe the same hysteresis as before: if the drive *increases* ($m > 0$, Fig. 4.10B, left), trajectories of consecutive cycles will lie in the upper right half of the parameter space ($\mu_{\text{min}}^{i} \gtrsim \mu_{\text{min}}^{\infty}(\hat{I}_{\text{E}}^{i-1}) > \mu_{\text{min}}^{\infty}(\hat{I}_{\text{E}}^{i})$) where instantaneous frequencies are mostly *higher* than their asymptotic reference (red color code). Vice versa, as the drive *decreases* ($m < 0$, Fig. 4.10B, right), trajectories will lie in the lower left half ($\mu_{\text{min}}^{i} \lesssim \mu_{\text{min}}^{\infty}(\hat{I}_{\text{E}}^{i-1}) < \mu_{\text{min}}^{\infty}(\hat{I}_{\text{E}}^{i})$) where instantaneous frequencies are mostly *lower* than their asymptotic reference (blue color code). Hence also a symmetric, piecewise linear double-ramp drive (Eq. (4.22)), induces IFA (Fig. 4.10C) : During the rising phase of the drive the instantantaneous frequencies are above the asymptotic reference, and during the falling phase they lie below (Fig. 4.10C, top: markers vs black line). The IFA asymmetry does *not* rely on asymmetry in the input. Linear regression over the theoretically estimated instantaneous frequencies yields an IFA slope of -3.1 Hz/ms which is very close to the spiking network simulation (Fig. 4.4B).

Interestingly, the last cycle $i = 7$ in Fig. 4.10C has a reference drive for which the constant-drive theory no longer applies ($\hat{I}_{\text{E}}^{7} = 1.42 < 2.85 = I_{\text{E}}^{\text{min}}$), hence there is no asymptotic reference for the network frequency (empty marker, Fig. 4.10C, top). This means that at the end of the sharp wave the network can sustain one more ripple cycle at a level of drive that in the beginning would be insufficient to trigger ripples (see cycle 1 in Fig. 4.10C). The transient ripple is thus not only asymmetric in its instantaneous frequency (IFA), but also with respect to the level of drive at which it starts and ends.

The extension of the drift-based approximation for linear drive has thus established that IFA does *not* depend on asymmetry in the drive, but occurs, even for a fully symmetric, double-ramp drive, due to a hysteresis effect in the amplitude of the oscillatory mean membrane potential.

In a last step I will vary the slope m of the external drive and examine the effect on the transient dynamics (Fig. 4.11). I find that the hysteresis causing IFA is *speed-dependent*, i.e. the transient dynamics approaches the asymptotic dynamics and becomes symmetric if the external drive changes more slowly. This can be seen (a) in the analytical expressions derived for the transient dynamics under linear drive ($|m| \to 0$ in Eqs. (4.79)–(4.87)), and (b) in a graphical illustration of the analytical approximation (Fig. 4.11 A-C). The theory thus explains the speed-dependence of IFA that we already observed in the spiking network simulations (Fig. 4.4D). The simulated instantaneous network frequencies shown in Fig. 4.4D (grey: $N = 10,000$) are shown again in Fig. 4.11 (Aii-Cii) to enable a direct comparison between theory and simulation. A quantitative comparison between the theory and simulations (Table 4.1, Methods Section 4.5.5.3) shows that the IFA slopes predicted by the theory are close to the IFA slopes observed in the spiking network. In both theory and simulation the IFA slope decreases for a decreasing slope $|m|$ of the external drive. The theoretically predicted instantaneous network frequencies even match the simulation results quantitatively, with an average relative error of $\sim 14\%$.

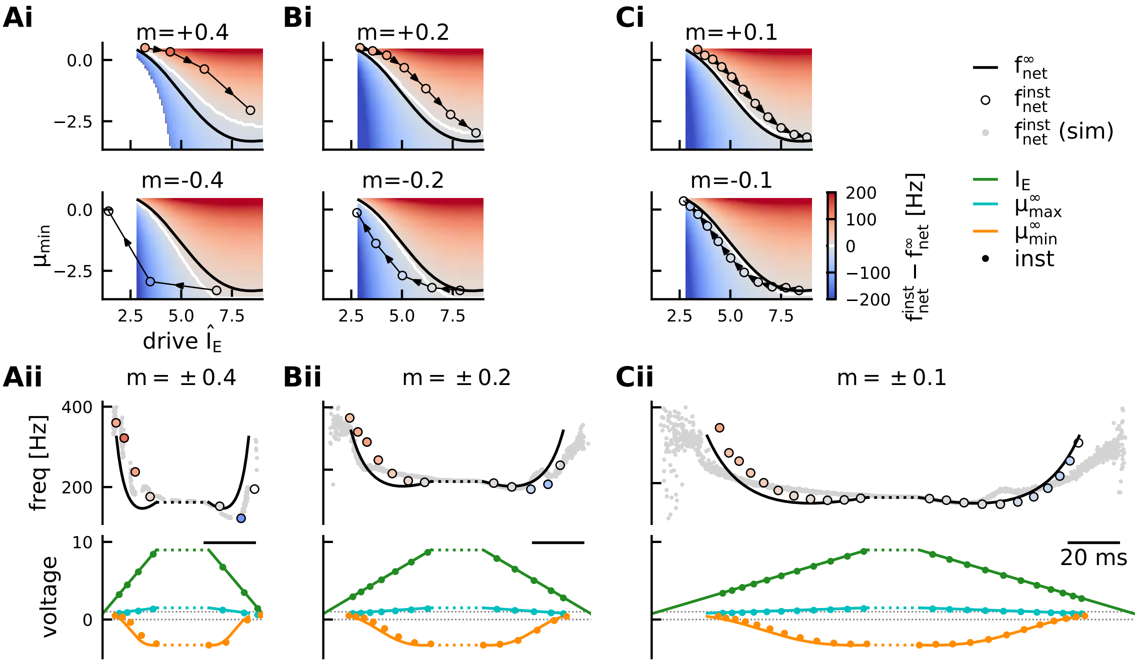

Figure 4.11: IFA is speed-dependent.
Transient dynamics for SPW-like drive with slope $m = \pm 0.4$/ms (**A**, cf. Fig. 4.10), $m = \pm 0.2$/ms (**B**), or $m = \pm 0.1$/ms (**C**). Top panel **(i)**: difference between instantaneous and asymptotic network frequency for all possible combinations of external reference drive $\hat{I}_\mathrm{E}$ and initial mean membrane potential μ_min, shown separately for positive (top) and negative (bottom) slope of the drive. Numerical trajectories shown in (ii) are overlaid. Bottom panel **(ii)**: Example trajectories through the space shown in (i) for SPW-like drive with slope $\pm m$. Top: instantaneous (colored markers) vs asymptotic (black) network frequency as predicted by the theory. Grey dots indicate instantaneous frequencies in spiking network simulations (cf. Fig. 4.4D, $N = 10,000$). See Table 4.1 for a quantitative comparison of simulation and theory. Bottom: transient vs asymptotic μ_min (orange) and μ_max (cyan). Green line shows SPW-like external drive (Eq. (4.22)), green dots mark reference drive $\hat{I}_\mathrm{E}$ of each cycle. The difference between instantaneous and asymptotic network frequencies (IFA) becomes less pronounced for smaller slope (C vs A, see also Table 4.1).

slope of SPW-like drive [1/ms]	$m = \pm 0.4$	$m = \pm 0.2$	$m = \pm 0.1$
IFA slope χ_IFA (Hz/ms, simulation)	– 3.01	– 0.68	– 0.18
IFA slope χ_IFA (Hz/ms, theory)	– 3.08	– 1.75	– 0.27
error ϵ in instantaneous frequency	14%	14%	13%

Table 4.1: IFA in theory and simulation. Quantification of the IFA slope χ_IFA in the spiking network simulations and the theoretical approximations shown in Fig. 4.11Aii-Cii for different slopes m of the external SPW-like drive. The error ϵ (Eq. (4.92)) quantifies the average relative deviation of the theoretically predicted instantaneous network frequencies (colored markers in Fig. 4.11) from the simulation results (grey dots in Fig. 4.11).

The speed-dependence of IFA is an important prediction of the bifurcation-based inhibitory ripple model that can be tested in experiments: Optogenetic stimulation of PV^+ basket cells can trigger ripple oscillations (Schlingloff et al., 2014, but see Stark et al., 2014). Increasing and decreasing the intensity of the light pulse over time could mimick the piecewise linear, double-ramp drive studied here. The model predicts that for shallower slopes the IFA asymmetry is reduced.

4.3.5 The role of the inhibitory reversal potential

I have shown that in the reduced bifurcation-based ripple model IFA occurs due to a speed-dependent hysteresis effect in the mean membrane potential dynamics. A central ingredient for this hysteresis effect is the strong increase in the oscillation amplitude ($\mu_{\mathrm{max}}^{\infty} - \mu_{\mathrm{min}}^{\infty}$) of the mean membrane potential for increasing drive. In the reduced model with current-based coupling, this increase in amplitude is mainly due to a strong decay of $\mu_{\mathrm{min}}^{\infty}(I_{\mathrm{E}})$, from close to threshold to very hyperpolarized values, for increasing drive I_{E} (shown here again in Fig. 4.12, left). The introduction of an inhibitory reversal potential $E_i = -75$ mV limits the hyperpolarizing effect of the inhibitory feedback and thus the range over which μ_{min} can decay (Fig. 4.12, right). Thus, one might expect a reduction in the hysteresis effect and hence less IFA. I want to argue here that this is *not* the case, since the reversal potential also introduces a second effect: a compression of the membrane potential density under feedback inhibition.

Fig. 4.12 shows a direct comparison between the ripple dynamics at constant drive in the reduced model with current-based delta-pulse coupling (left), and in the same network with conductance-based coupling and a double-exponential synaptic kernel (right, variant of the detailed model, see Methods Section 4.5.1.4, Eqs. (4.20)). For each level of constant drive the average oscillation cycle is extracted (Fig. 4.12A, Methods Section 4.5.1.7). The mean μ and standard deviation σ of the averaged distribution of membrane potentials can be compared to the drift-based approximation at the beginning of the cycle ($t = 0$, orange) and at the beginning of the population spike ($t = t_{\mathrm{on}}$, light blue), which is approximated as the time when a significant portion of the membrane potential distribution (mean + 3 SD, upper dashed line in Fig. 4.12A, bottom panels) has crossed the spike threshold. Note that $\mu(0)$ corresponds to μ_{min} in the drift-based approximation, but $\mu(t_{\mathrm{on}})$ is *not* equivalent to μ_{max}, which has no counterpart in the spiking network simulation. The time t_{on} is simply the latest time point we can use in the spiking network simulation to quantify the change of the (almost Gaussian) membrane potential distribution during the upstroke of its mean. During the population spike ($t \geq t_{\mathrm{on}}$), the fire-and-reset rule destroys the unimodality of the membrane potential distribution, and a quantification in terms of mean and standard deviation is no longer meaningful.

In the network with current-based coupling (Fig. 4.12, left) the distance $\mu(t_{\mathrm{on}}) - \mu(0)$, covered by the mean membrane potential during its upstroke, increases significantly for increasing drive. This is mainly due to a strong decrease of $\mu(0) = \mu_{\mathrm{min}}$ for increasing drive, over a total range of $\Delta\mu_{\mathrm{min}} \approx 60$ mV. The standard deviation σ, on the other hand, remains more or less constant and close to the asymptotic limit σ_V, both within a given cycle and across different levels of drive (Fig. 4.12B, left). The amount of variation in σ_{min} for different levels of drive is negligible, compared to the large variation in μ_{min} ($\Delta\sigma_{\text{min}}/\Delta\mu_{\text{min}} = 0.015$). This justifies once again the drift-based approximation above, that only takes into account the dynamics of the mean membrane potential μ while keeping the standard deviation $\sigma \equiv \sigma_V$ constant.

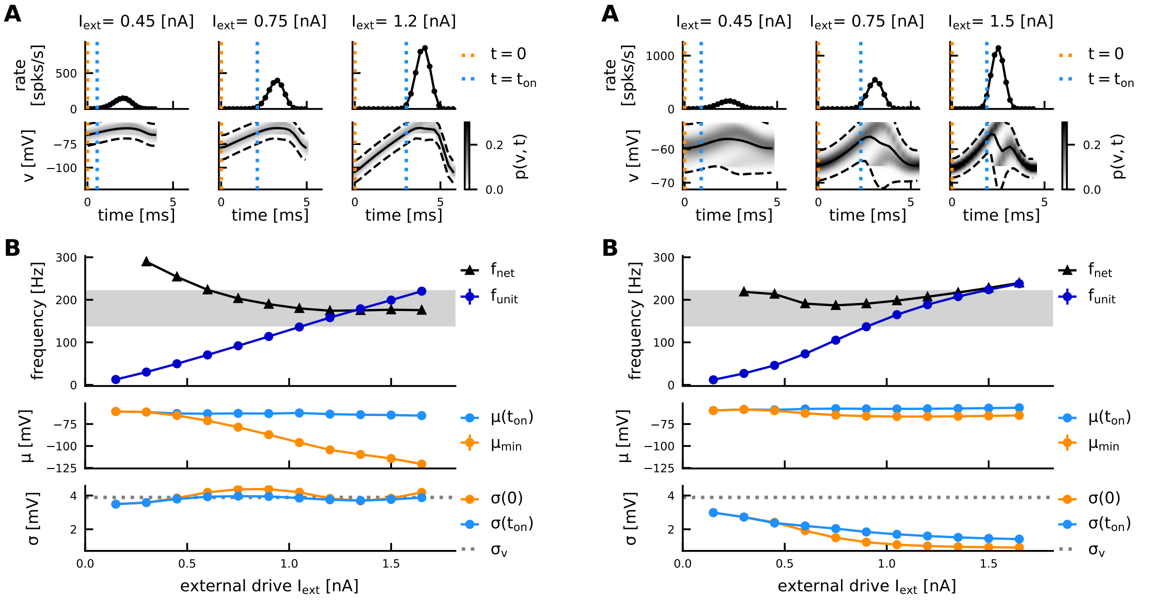

Figure 4.12: The role of the inhibitory reversal potential.
Current-based (left) vs conductance-based coupling (right). **A,** Average oscillation cycle for 3 example levels of the drive. **B,** Quantification of network dynamics for a range of external drives I_{ext}. Top: Network frequency (black) and unit firing rate (blue). Middle: Mean membrane potential μ. Bottom: Standard deviation σ of the membrane potential distribution. Both μ and σ are estimated once at the beginning of the cycle ($t = 0$, orange) and once at the beginning of the population spike ($t = t_{\text{on}}$, blue), as shown in the examples in A. Left: Reduced model with current-based delta-pulse coupling (Eq. (4.2)). Right: Reduced model with conductance-based coupling and double-exponential synaptic filter (Eqs. (4.20)). Parameters as outlined in Methods Section 4.5.1.4.

In the network with conductance-based coupling (Fig. 4.12, right) μ_{min} still decays monotonically with the drive, but over a much smaller range ($\Delta\mu_{\text{min}} \approx 8$ mV), as predicted, due to the presence of an inhibitory reversal potential at $E_I = -75$ mV. The standard deviation σ now shows a clear trend — both within a cycle and across different levels of drive. Within a cycle, the standard deviation increases from the beginning of the cycle (orange) towards the beginning of the population spike (blue), due to diffusion. The inhibitory feedback then compresses the distribution again (see examples in Fig. 4.12A). The larger the external drive, the larger the amplitude of the population spike and the resulting inhibitory feedback. Since an increase in inhibitory feedback can no longer push the mean membrane potential beyond the inhibitory reversal potential, the distribution of membrane potentials is instead increasingly compressed: Both $\sigma_{\text{min}} = \sigma(0)$ and $\sigma(t_{\text{on}})$ decrease monotonically for increasing drive. The standard deviation thus exhibits a systematic change for increasing drive that is comparable in magnitude to the change in the mean $\mu_{\min}$ ($\Delta\sigma_{\min}/\Delta\mu_{\min} = 0.26$). Capturing the dynamics of the conductance-based network thus requires an approximation of both the mean μ and the standard deviation σ of the membrane potential distribution over the course of a cycle and depending on the external drive.

This can be done in an extension of the Gaussian ansatz, which I outline in Appendix Section 4.B for a simplified network of pulse-coupled oscillators (PCO), that accounts for the effect of an inhibitory reversal potential phenomenologically with a linear phase response curve. The drift-based approximation for the PCO network can capture the monotonic dependencies of both the mean and the standard deviation of the membrane potential distribution on the external drive (Fig. 4.36). Together, these two monotonic dependencies induce again a speed-dependent hysteresis effect when the drive changes fast over time (Fig. 4.39). Thus, IFA also occurs in biologically more realistic networks incorporating an inhibitory reversal potential. Since the speed-dependent hysteresis as the fundamental mechanism of IFA is unaffected by the presence of reversal potentials, I chose to present the theory above for the simpler case of an LIF network with current-based coupling. It allows a derivation of closed-form expressions for the Gaussian dynamics (no self-consistent solution necessary) and does not require the additional simplification from an LIF to a PCO neuron model (see Appendix Section 4.B).

4.3.6 The role of the refractory period

Adding an absolute refractory period $\tau_{\text{ref}} = 1$ ms to the reduced model in its default parametrization (Table 4.3) leads to the emergence of a period-2 oscillation in the population rate (unless the external drive is very weak) (Fig. 4.13). This can be understood intuitively and is related to the somewhat artificial account for refractoriness in simulations: When units that were active in a population spike are clamped to the reset potential over a refractory period τ_{ref}, there is effectively less time left for the density of membrane potentials to diffuse back to a unimodal, gaussian shape before the beginning of the next population spike. If the synaptic delay is short, the noise low and/or the coupling is weak relative to a given τ_{ref}, a history dependence develops and units that were active in one population spike are less likely to spike in the next.

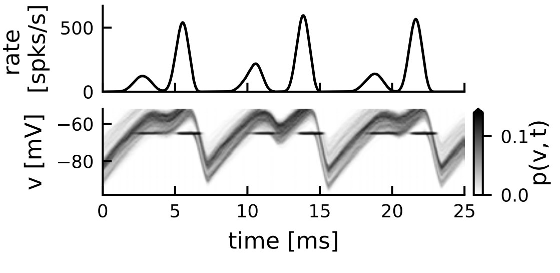

Figure 4.13: Absolute refractoriness can induce period-2 oscillations. Population rate (top) and membrane potential distribution (bottom) of the reduced model (Table 4.3) with an absolute refractory period of 1 ms under constant drive $I_{\text{ext}} = 0.79$ nA.

With sufficient noise and a long enough synaptic delay, diffusion can preserve the approximate unimodality of the membrane potential distribution. In that case the refractory period has a negligible effect on the ripple frequency (Fig. 4.14): For most of the sparse synchrony regime the network frequency is virtually independent of the refractory period. Without refractory period, the network reaches the point of full synchrony slightly earlier and is immediately desynchronized thereafter. When there is a refractory period, full synchrony is reached slightly later and can be approximately maintained, even for larger drives, since the refractory period counteracts an immediate desynchronization of the network: Note how the network frequency remains close to the mean unit firing rate even shortly after full synchrony was reached (solid black and blue curve in Fig. 4.14).

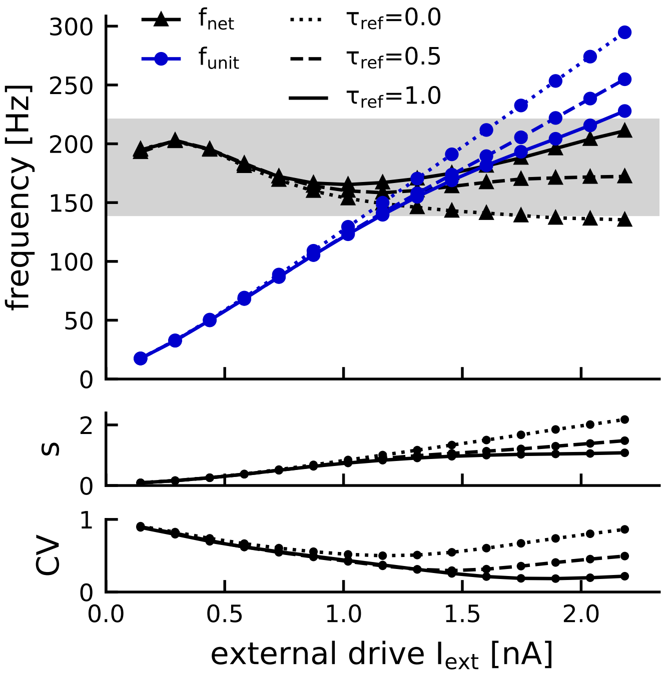

Figure 4.14: Absolute refractoriness has negligible effect on ripple frequency. Oscillation dynamics of the reduced model (Table 4.3) with increased synaptic delay ($\Delta = 1.5$ ms) and noise strength ($\sqrt{D} = 0.3$), and a variable absolute refractory period (solid lines: $\tau_{\mathrm{ref}} = 1$ ms, dashed: $\tau_{\mathrm{ref}} = 0.5$ ms, dotted: $\tau_{\mathrm{ref}} = 0$ ms). Panels from top to bottom: network frequency (blue) and mean unit firing rate; saturation s; coefficient of variation of interspike intervals.

In conclusion, neglecting the refractory period in the approximation of the ripple dynamics is justified. Instead of the artificial clamping of the membrane potential to the reset, one could explore less pathological ways of accounting for absolute refractoriness in the simulations, that would likely have a less drastic effect on the shape of the membrane potential distribution.

4.4 Discussion

In this chapter I presented a novel approximation of the mean-field dynamics of the bifurcation-based inhibitory ripple model in the regime of strong drive and strong coupling. For constant drive, the theory (1) yields an approximation of the asymptotic network frequencies and mean unit firing rates far beyond the Hopf bifurcation, (2) captures the transition from sparse to full synchrony, and (3) reveals a monotonic dependence of the mean membrane potential oscillation amplitude on the external drive. For a fast changing, sharp wave-like drive I showed that a speed-dependent hysteresis effect in the trajectory of the mean membrane potential produces an IFA-like asymmetry of the instantaneous ripple frequency compared to the asymptotic frequencies expected at constant drive. My derivation shows that IFA is an intrinsic feature of the bifurcation-based inhibitory ripple model that occurs for any fast-enough, sharp wave-like drive, independent of other parameter choices. The speed-dependence of IFA is a new prediction that can be tested experimentally.

Simplifying assumptions

To allow an analytical treatment of the spiking network dynamics, I made a number of simplifying assumptions. The resulting reduced ripple model is similar to the network studied by Brunel and Hakim (1999), except for its all-to-all connectivity, which makes the Gaussian white noise input the only source of noise in the network. The ripple dynamics in my *reduced* network model are qualitatively similar to a biologically more realistic model (Donoso et al., 2018) that includes random sparse connectivity, correlations in the background noise, synaptic filtering, refractoriness, and conductance-based synapses. In Appendix Section 4.B I showed how the effect of conductance-based coupling with an inhibitory reversal potential can be mimicked in a network of pulse-coupled oscillators with linear phase response curve. IFA in the PCO network occurs due to the same speed-dependent hysteresis uncovered in the reduced LIF network with current-based coupling. However, both the mean and the standard deviation of the membrane potential distribution need to be taken into account to describe the dynamics accurately.

Phenomenological account for the reset

The reduced network model allows a drift-based approximation of the mean-field dynamics that can be treated analytically. I added a phenomenological account for the reset mechanism on the population level, which improves the accuracy and range of applicability of the drift-based approximation. I want to stress that this phenomenological reset is not *necessary* to capture the most important *qualitative* features of the network, namely the transition from sparse to full synchrony for constant drive and the hysteresis effect leading to IFA for time-dependent drive.

The shape of IFA

The drift-based approximation predicts that instantaneous ripple frequencies for a changing drive are different from the asymptotic frequencies for constant drive: For a double-ramp drive, the instantaneous ripple frequency is higher than the asymptotic reference on the upstroke, and lower on the downstroke of the external drive. The concrete shape of the resulting intra-ripple frequency curve over time thus depends on the shape of the asymptotic frequency as a function of the external drive.

In the reduced model, the asymptotic frequencies decrease for increasing, constant drive (Fig. 4.3B, in the vicinity of the Hopf bifurcation and in the limit of small synaptic delay this decrease was already predicted by Brunel and Hakim (1999), see Methods Section 4.5.2.5). Thus, it is possible for the instantaneous frequencies in the second half of the ripple event (when the external drive decreases) to lie *below* the asymptotic reference while actually *in*creasing as a function of time (Fig. 4.4D).

In the detailed model, on the other hand, the asymptotic frequency is a mostly increasing function of the external drive (Fig. 4.1B). Thus the above asymmetry of the instantaneous frequency response w.r.t. the asymptotic reference frequencies implies a monotonic decrease of the instantaneous ripple frequency in response to a SPW-like double-ramp drive. This is indeed what we observe in simulations (Fig. 4.2).

Experimental data suggest a similar variability in the shape of IFA. Some studies reported a switch from decreasing to increasing frequency at the end of the ripple event (Ponomarenko et al., 2004); others an almost monotonic decrease or even a small peak in the beginning of the event (Nguyen et al., 2009; Sullivan et al., 2011; Donoso et al., 2018). Generally, intra-ripple frequency accommodation is robust with respect to the method used to estimate instantaneous frequencies (peak-to-peak distance vs. wavelet spectrogram, choice of time windows and smoothing kernels), even though there are quantitative differences in the instantaneous frequency estimates, especially in the low power regime at the beginning and end of each event (Fig. 4.4A, discrete vs. continuous estimate). The discrete frequency estimate was particularly useful for the comparison between simulations and the theory, which is also based on a discrete, cycle-wise approximation of period/frequency.

I used simple linear regression to quantify IFA, despite the fact that the instantaneous ripple frequency is not necessarily a linear function of time as explained above. I want to stress that linear regression still provides an adequate measure of IFA, as long as the underlying drive is symmetric: The drift-based approximation predicts that the instantaneous ripple frequency in response to symmetric, SPW-like drive (Eq. (4.22)) can be decomposed into a symmetric part (the asymptotic reference frequencies expected under constant drive, or in the limit of vanishing slope), and an asymmetric part (accounting for the speed-dependent hysteresis), which is positive as the drive increases, and negative as it decreases (cf. Fig. 4.10B):

$$f_{\mathrm{net}}^{\mathrm{inst}}(t_i) \approx f_{\mathrm{net}}^{\infty}(t_i) + \Delta f_{\mathrm{net}}(t_i)$$

The symmetric part does not influence the linear regression slope (except for small effects of the finite, discrete sampling of the instantaneous frequencies at not fully symmetric time points t_i):

$$\chi_{\mathrm{IFA}} = \frac{\mathrm{Cov}(f_{\mathrm{net}}^{\mathrm{inst}}, t)}{\mathrm{Var}(t)} = \underbrace{\frac{\mathrm{Cov}(f_{\mathrm{net}}^{\infty}, t)}{\mathrm{Var}(t)}}_{\approx 0} + \frac{\mathrm{Cov}(\Delta f_{\mathrm{net}}, t)}{\mathrm{Var}(t)} \approx \frac{\mathrm{Cov}(f_{\mathrm{net}}^{\mathrm{inst}} - f_{\mathrm{net}}^{\infty}, t)}{\mathrm{Var}(t)}$$

In the particular case of symmetric drive, linear regression thus quantifies the decrease in the *difference* between the instantaneous and the asymptotic ripple frequencies, from positive to negative values. It is thus an adequate measure for the speed-dependent hysteresis described by the theory, that works even for nonlinear instantaneous frequency responses (under symmetric drive), and can be easily applied to experimental data as well.

The shape of SPW-associated excitatory drive

I modeled the excitatory current input to CA1 during a sharp wave as a symmetric double ramp (Eq. (4.22)) to highlight that IFA in the bifurcation-based inhibition-first model does not depend on asymmetry in the input. My derivation emphasizes that the only necessary requirement for the hysteresis causing IFA is an external drive that changes sufficiently fast and first rises, then decays. Thus I predict that IFA in the bifurcation-based model will occur for any such external drive, even when it is non-linear or asymmetric.

Ripples in the LFP

Finally, understanding ripple oscillations requires not only understanding their generating mechanism but also the origin of the signal that we use to detect them (see also Section 2.5.1). The local field potential is traditionally believed to reflect synaptic currents (Mitzdorf, 1985; Buzsáki et al., 2016), but modeling studies have suggested that also extracellular action potentials of pyramidal cells can contribute in the range of ripple frequencies (Schomburg et al., 2012; Ramirez-Villegas et al., 2018; Stark et al., 2014). Here I used the population activity of interneurons as a proxy for the LFP signal. It is reasonable to assume that postsynaptic inhibitory currents would exhibit the same frequency structure as the inhibitory population activity (Donoso et al., 2018). Donoso et al. (2018) demonstrated in simulations that the inhibitory network can entrain the local pyramidal cell network, such that pyramidal cell spikes would occur phase-locked to the ripple rhythm set by the interneurons. A detailed model of the CA1 LFP is needed to confirm whether any given generating mechanism yields a ripple signature in the LFP that is consistent with experimental data.

In conclusion, the bifurcation-based inhibition-first ripple model can account for IFA naturally without adding further parameter constraints. In Chapter 5 I will study the prerequisites for IFA in the alternative, perturbation-based ripple model. Furthermore, I will give a general overview of the key differences between the two inhibition-first ripple models and discuss how they might be dissociated experimentally.

4.5 Methods

4.5.1 Spiking network simulations

4.5.1.1 The detailed model (Donoso et al., 2018)

Connectivity. The detailed model introduced by (Donoso et al., 2018) consists of $N = 200$ CA1 PV$^+$ basket cells. Every interneuron receives delayed inhibitory feedback via recurrent synaptic connections within the network. I denote by Γ_i^I the set of interneurons that project to interneuron i. The network is connected randomly with probability $p_{\text{II}} = 20\%$, hence the inhibitory indegree is on average $\langle|\Gamma_i^I|\rangle = p_{\text{II}} \cdot N = 40$. There are no autapses ($i \notin \Gamma_i^I$).

The interneuron population receives feedforward excitatory input from a population of $N_E = 8200$ CA3 pyramidal cells. The connection probability from pyramidal cells to interneurons is $p_{\text{IE}} = 9.5\%$ resulting in an average excitatory indegree of $\langle|\Gamma_i^E|\rangle = p_{\text{IE}} \cdot N_E \approx 780$. The neuronal dynamics of the pyramidal cells are not modeled in detail. Instead their activity is modeled as Poisson spike trains, with the same rate λ for all pyramidal cells. The average *total* excitatory drive to one interneuron is hence given by $\Lambda = \langle|\Gamma_i^E|\rangle \cdot \lambda \approx 780 \cdot \lambda$.

Model neuron. Every interneuron i is modeled as a leaky integrate-and-fire unit (Tuckwell, 1988) with a membrane potential v_i described by the following ordinary differential equation (ODE):

$$\dot{v}_i(t) = \frac{1}{\tau_m}(E_{\text{leak}} - v_i(t)) + \frac{1}{C}\Big(I_{\text{ext},i}(t) - I_{\text{inh},i}(t)\Big) \tag{4.11a}$$

When the membrane potential v_i reaches the spike threshold V_{thr}, a spike is recorded for unit i and v_i is reset to V_{reset} where it remains clamped for an absolute refractory period of τ_{ref}. Both excitatory and inhibitory inputs are conductance-based:

$$I_{\text{ext},i}(t) = g_{\text{exc},i}(t)\,(E_E - v_i(t)) \tag{4.11b}$$
$$I_{\text{inh},i}(t) = -g_{\text{inh},i}(t)\,(E_I - v_i(t)) \tag{4.11c}$$

The conductance in response to a *single* excitatory input spike at time $\hat{t}$ is given by a double-exponential pulse described by a rise time constant τ_E^r and a decay time constant τ_E^d:

$$g_E^{\text{peak}} s_E \left(\exp\left[-\frac{t-\hat{t}}{\tau_E^d}\right] - \exp\left[-\frac{t-\hat{t}}{\tau_E^r}\right]\right)\Theta(t-\hat{t})$$

with the normalizing factor s_E chosen such that the peak conductance equals g_E^{peak}, and $0 < \tau_E^r < \tau_E^d$.

Every interneuron receives excitatory input from a pool Γ_i^E of presynaptic pyramidal cells firing Poisson spike trains at a rate λ (see *Connectivity*). The summed excitatory Poisson spike train that an interneuron i receives can be denoted as

$$S_{\text{exc},i}(t) := \sum_{j\in\Gamma_i^E}\sum_k \delta(t_j^k - t)\ ,$$

summing over all presynaptic units $j \in \Gamma_i^E$ and their spike times $\{t_j^k\}_{k=1,2,\ldots}$.

The summed conductance in response to the excitatory input spike train can then be written as a convolution

$$g_{\text{exc},i}(t) = g_E^{\text{peak}}\Big(\kappa^{2\text{exp}} * S_{\text{exc},i}(t)\Big) \tag{4.11d}$$

with the synaptic kernel

$$\kappa^{2\text{exp}}(t) = s_E\left(\exp\left[-\frac{t}{\tau_E^d}\right] - \exp\left[-\frac{t}{\tau_E^r}\right]\right)\Theta(t)\ .$$

Likewise, the inhibitory conductance of unit i in response to recurrent spiking input

$$S_{\text{inh},i}(t) := \sum_{j\in\Gamma_i^I}\sum_k \delta(t_j^k - t)$$

from a pool of inhibitory, presynaptic units Γ_i^I is described by:

$$g_{\text{inh},i}(t) = g_I^{\text{peak}}\kappa_\Delta^{2\text{exp}} * S_{\text{inh},i}(t) \tag{4.11e}$$

with the synaptic kernel

$$\kappa_\Delta^{2\exp}(t) = s_I \left(\exp\left[-\frac{t-\Delta}{\tau_I^d}\right] - \exp\left[-\frac{t-\Delta}{\tau_I^r}\right] \right) \Theta(t-\Delta) \; . \tag{4.11f}$$

Note that the recurrent inhibitory input arrives with a synaptic delay Δ. All parameter values are summarized in Table 4.2.

Population activity The spike times of a single interneuron i are denoted as $\{t_i^k\}_{k=1,2,\ldots}$. The population activity is defined as the average single neuron spike train (written as a sum over Dirac delta distributions):

$$A_N(t) := \frac{1}{N} \sum_{i=1}^{N} \sum_k \delta\left(t - t_i^k\right) \tag{4.12}$$

(Gerstner et al., 2014). In simulations of the spiking network with a finite temporal resolution ($\Delta t = 0.01\,\text{ms}$) the *empirical* population activity is estimated as

$$r_N(t) = \frac{n_{\text{spk}}(t, t+\Delta t)}{N \Delta t} \tag{4.13}$$

where

$$n_{\text{spk}}(t, t+\Delta t) = \int_t^{t+\Delta t} \sum_{i=1}^{N} \sum_k \delta\left(s - t_i^k\right) \mathrm{d}s \tag{4.14}$$

denotes the total number of spikes that were emitted from the population in the time interval $[t, t+\Delta t]$. r_N has units of spikes per second and can also be interpreted as the instantaneous firing rate of any given neuron in the homogeneous network (Gerstner and Kistler, 2002). In the limit of an infinitely small time step one recovers:

$$\lim_{\Delta t \to 0} r_N(t) = \lim_{\Delta t \to 0} \frac{\int_t^{t+\Delta t} \sum_{i=1}^{N} \sum_k \delta\left(s - t_i^k\right) \mathrm{d}s}{N \Delta t} = \frac{1}{N} \sum_{i=1}^{N} \sum_k \delta\left(t - t_i^k\right) = A_N(t) \; .$$

In all figures the empirical population activity is smoothed with a narrow Gaussian window g of standard deviation $\sigma_t = 0.3\,\text{ms}$:

$$r_N^{\text{plot}}(t) = \left(g * r_N\right)(t) \, , \quad g(t) = \frac{1}{\sqrt{2\pi}\sigma_t} \exp\left[-\frac{t^2}{2\sigma_t^2}\right] \; . \tag{4.15}$$

To facilitate notation I omit the superscript “plot”.

4.5.1.2 Model reduction

To allow an analytical treatment of its dynamics, the detailed version of the bifurcation-based model is reduced. In the following I give a step-by-step overview of the simplifications I made.

Parameter	Value	Definition
N	200	Number of interneurons
N_E	8200	Number of pyramidal cells
p_{II}	0.2	Connection probability between interneurons
p_{IE}	0.095	Connection probability from pyramidals to interneurons
τ_m	10 ms	Membrane time constant
C_m	100 pF	Membrane capacitance
g_L	10 nS	Leak conductance
E_{leak}	-65 mV	Resting potential
V_{thr}	-52 mV	Spike threshold
V_{reset}	- 67 mV	Reset potential
E_I	-75 mV	Reversal potential for inhibition
E_E	0 mV	Reversal potential for excitation
τ_{ref}	1 ms	Refractory period
Δ	1 ms	Synaptic delay for inhibition
τ_I^r	0.45 ms	Synaptic rise time constant for inhibition
τ_I^d	1.2 ms	Synaptic decay time constant for inhibition
τ_E^r	0.5 ms	Synaptic rise time constant for excitation
τ_E^d	2 ms	Synaptic decay time constant for excitation
g_I^{peak}	5 nS	Peak conductance for inhibition
g_E^{peak}	0.8 nS	Peak conductance for excitation
dt	0.01 ms	Simulation time step (Euler)
I_I^{peak}	83 pA	IPSC amplitude at $V_{\text{hold}} = -58$ mV
I_E^{peak}	46 pA	EPSC amplitude at $V_{\text{hold}} = -58$ mV
W^{IPSP}	17.5 mVms	IPSP magnitude (integral) at $V_{\text{hold}} = -58$ mV
W^{EPSP}	14.6 mVms	EPSP magnitude (integral) at $V_{\text{hold}} = -58$ mV

Table 4.2: Default parameters of the detailed spiking network. (Donoso et al., 2018) The last four lines indicate the strength of inhibition and excitation at a holding potential of $V_{\text{hold}} = -58$ mV, that were used to match the coupling strengths for current-based coupling to the conductance-based model.

Feedforward excitation: Input correlations and noise. In the detailed model the excitatory drive to the interneuron network is provided by a population of N_E pyramidal cells that fire Poisson spike trains, each at the same rate λ. Each interneuron is targeted by a random subset of this population of average size $\langle|\Gamma_i^E|\rangle = p_{\text{IE}} \cdot N_E$ where p_{IE} is the (small) probability of a connection. Thus, each interneuron receives a total drive of $p_{\text{IE}} \cdot N_E \cdot \lambda$ on average, refered to above as the external drive Λ (see Methods, Section 4.5.1.1). Since all interneurons draw their inputs from the same population of excitatory neurons, there are overlaps in the input sets of different interneurons, which introduces correlations in the excitatory drive that the interneurons receive. Since the feedforward connectivity is sparse, these overlaps are small ($\sim p_{\text{IE}}$) and the resulting correlations are weak. I thus hypothesize that these input correlations are *not* crucial for the ripple dynamics (see Lindner et al., 2005, for a treatment of input correlations). If I assume *independent* input sets, it is no longer relevant to model the stream of excitatory input spikes arriving at one interneuron as stemming from several distinct pyramidal cells. Instead I can model the input to one interneuron i as a single, independent Poisson process with rate $\Lambda = p_{\mathrm{IE}} N_E \lambda$:

$$S_{\mathrm{exc},i}(t) = \sum_{j \in \Gamma_i^E} S_j^\lambda(t) = \sum_{j \in \Gamma_i^E} \sum_k \delta(t_j^k - t) \quad \longmapsto \quad S_i^\Lambda(t)$$

Note that this simplification also removes heterogeneity in the average excitatory input across different interneurons.

Since the coupling in the detailed model is conductance-based, the amplitude of excitatory postsynaptic potentials (EPSPs) caused by the incoming Poisson spikes depends on the momentary membrane potential of the interneuron (Methods Section 4.5.1.1, Eq. (4.11b)). I will omit this complexity and use current-based coupling instead. I will also omit the double-exponential shape of the postsynaptic pulse and use a simple delta-pulse coupling without synaptic filtering. Every excitatory input spike thus causes an immediate upwards jump of the interneuron's membrane potential of amplitude $J_E = 1.46\,\mathrm{mV}$:

$$\dot{v}_i(t) = \frac{1}{\tau_m}(E_{\mathrm{leak}} - v_i(t)) + J_E S_i^\Lambda(t) - \frac{1}{C} I_{\mathrm{inh},i}(t)$$

The amplitude was fitted such that the magnitude of a single EPSP (integral over the pulse in the postsynaptic membrane potential) is the same as in the conductance-based setting at a holding potential close to threshold ($V_{\mathrm{hold}} = -58\,\mathrm{mV}$, see Table 4.2).

I have now derived a setup where each interneuron receives many ($\tau_m \Lambda$) Poisson input spikes per membrane time constant, each causing a jump J_E in the membrane potential which is small compared to the distance from resting potential to spike threshold that has to be bridged in order to elicit a spike. These conditions justify a diffusion approximation (Tuckwell, 1988). I thus replace the Poisson spiking input by a Gaussian white noise of matching mean and variance. The first two moments of the Poisson process $S_i^\Lambda(t)$ of intensity Λ are:

$$\langle S_i^\Lambda(t) \rangle = \Lambda\,, \qquad \langle S_i^\Lambda(t) S_{\mathrm{exc},i}(t') \rangle = \Lambda\, \delta(t - t')$$

The Poisson spike train is thus approximated as

$$S_i^\Lambda(t) \approx \Lambda + \sqrt{\Lambda}\, \xi_i(t)$$

where ξ_i is Gaussian white noise with zero mean and unit variance: $\langle \xi_i(t) \rangle = 0$, and $\langle \xi_i(t) \xi_j(t') \rangle = \delta_{ij} \delta(t - t')$. The response of the neuron to the many excitatory input spikes is thus modeled as a diffusion process:

$$\dot{v}_i(t) = \frac{1}{\tau_m}(E_{\mathrm{leak}} - v_i(t)) + \frac{1}{C}\left(I_{\mathrm{ext}} - I_{\mathrm{inh}}(t)\right) + \sqrt{\frac{2}{\tau_m}} \sigma_V \xi_i(t) \tag{4.16a}$$

with mean excitatory drive

$$I_{\mathrm{ext}} = J_E \Lambda C \quad (\mathrm{nA}) \qquad \text{or} \qquad \mu = J_E \Lambda \tau_m \quad (\mathrm{mV}) \tag{4.16b}$$

and standard deviation of the noise

$$\sigma_V = J_E \sqrt{\frac{\tau_m \Lambda}{2}} \qquad (\mathrm{mV})\;. \tag{4.16c}$$

Written in this form, the parameter σ_V expresses the expected spread of the membrane potentials (standard deviation), if the spike threshold was moved to infinity. Note that this simplification still implies that the noise (σ_V) increases with the mean drive (Fig. 4.15).

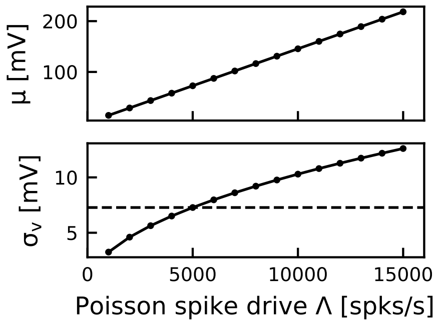

Figure 4.15: Approximating Poisson input spikes by Gaussian white noise. Mean μ and standard deviation σ of the Gaussian white noise process for different levels of Poisson spiking input Λ and fixed coupling strength $J_E = 1.46$ mV. Dashed line marks constant noise level $\sigma_V = 5J_E = 7.3\,\text{mV}$ used in Fig. 4.16 (right), corresponding to Poisson rate $\Lambda = 5$ kHz and $\tau_m = 10$ ms.

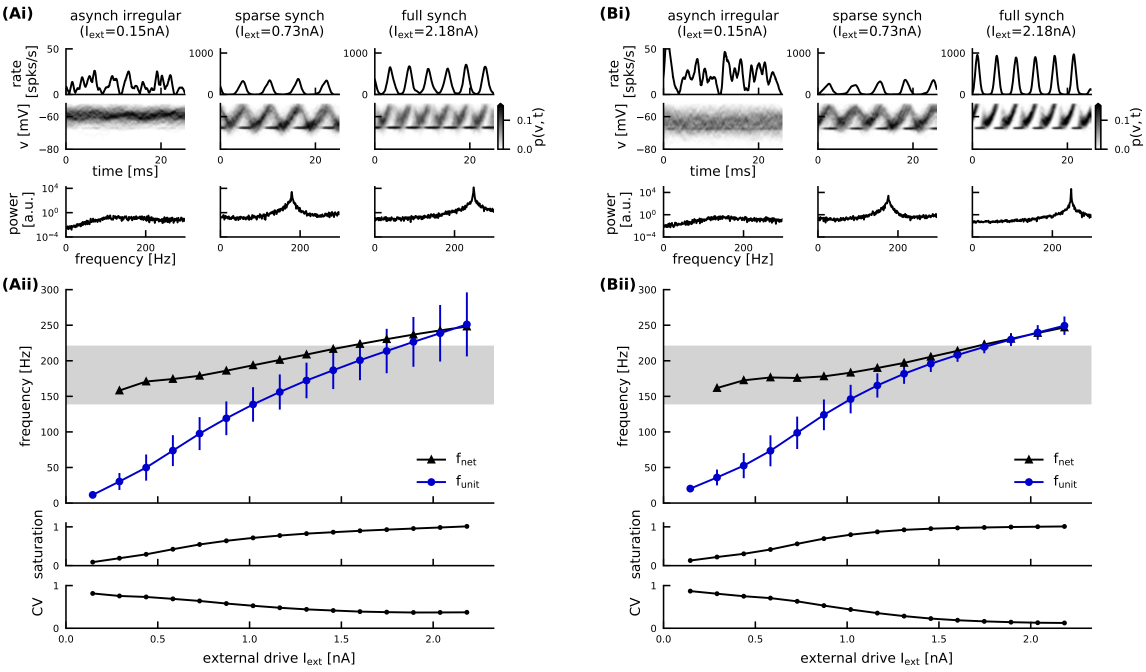

Figure 4.16: Ripple dynamics after diffusion approximation in feedforward input. Same outline as in Fig. 4.1 but correlated Poisson spiking input was replaced by independent Gaussian white noise inputs (Eqs. (4.16)). **A,** Noise increases with the mean as for Poisson spikes (see Fig. 4.15). **B,** Constant noise level corresponding to Poisson rate $\Lambda = 5$ kHz ($\sigma_V \equiv 7.3\,\text{mV}$).

The dynamics of the ripple network with this simplified account of the feedforward excitatory drive as independent Gaussian white noise input (Eqs. (4.16)) is shown in Fig. 4.16A There is no qualitative change of the dynamics compared to the original detailed model (Fig. 4.1). The dynamics of population rate and membrane potential distribution are more homogeneous across cycles (Fig. 4.16Ai) due to the removal of heterogeneity in the feedforward drive (all units receive the same average drive, there are no input correlations).

The increase in noise strength with the mean drive is not a necessary requirement for the generation of ripple oscillations. In a last simplification step I thus fix the noise level to a constant value. The exact noise level is irrelevant, as long as it is large enough to introduce some stochasticity in the network (in the limit $\sigma_V \to 0$ the network behaves like a single unit or produces a pathological cluster state). An example is shown in Fig. 4.16B for noise intensity $\sigma_V \equiv 7.3$ mV, corresponding to a Poisson drive of $\Lambda = 5$ kHz. Naturally the distribution of membrane potentials becomes relatively broader at drive levels < 5 kHz, and relatively narrower at drive levels > 5 kHz (Fig. 4.16Ai vs Bi). The reduction of noise at high drive allows the network to reach the state of full synchrony slightly earlier, with even more regular unit spiking (Fig. 4.16Bii). Other than that I find no significant change of the ripple dynamics (Fig. 4.16Bi vs Bii). I hence continue using a Gaussian white noise drive of constant variance and vary only the mean. This last simplification step is however not strictly necessary for the theory developed in Section 4.3.2, which could easily incorporate a noise intensity that depends on the mean drive.

In the next section I describe simplifications regarding the inhibitory synaptic connections. All changes are incremental, i.e. all subsequent simulations include the simplification of the feedforward drive as independent Gaussian white noise processes with fixed intensity, as it was described here.

Recurrent inhibition: Connectivity and synaptic filtering. CA1 PV$^+$ BCs are known to be connected sparsely (see Introduction), hence the recurrent connection probability was assumed as $p_{\mathrm{II}} = 0.2$ in the detailed model (Donoso et al., 2018). Computationally speaking, sparse connectivity, with a small indegree K such that $\lim_{N\to\infty} K/N = 0$ where N is the number of interneurons, ensures that correlations in the feedforward input do not influence the network dynamics in the mean field (Brunel and Hakim, 1999). Given that I have already assumed independent inputs in the previous section, it should be possible to connect the network fully without fundamentally changing the dynamics — as long as the synaptic connection strength is scaled down accordingly. In a network with conductance-based synapses, however, it is not obvious how to scale the coupling strength depending on the indegree in order to keep the mean input constant. I thus replaced the conductance-based synapses by current-based synapses such that the amplitude of IPSPs is independent of a unit's membrane potential:

$$\dot{v}_i(t) = \frac{1}{\tau_m}(E_{\mathrm{leak}} - v_i(t)) + \frac{1}{C}\left(I_{\mathrm{ext}} - I_{\mathrm{inh},i}(t)\right) + \sqrt{\frac{2}{\tau_m}}\sigma_V \xi_i(t) \tag{4.17a}$$

$$I_{\mathrm{inh},i}(t) = I_I^{\mathrm{peak}}\left(\kappa_\Delta^{\mathrm{2exp}} * S_{\mathrm{inh},i}(t)\right) \tag{4.17b}$$

(double-exponential synaptic kernel $\kappa_\Delta^{\mathrm{2exp}}$ with delay as before (Eq. (4.11f)). The peak of the inhibitory postsynaptic current pulse (IPSC) $I_I^{\mathrm{peak}} = 83\,\mathrm{pA}$ is chosen to match the IPSC amplitude of the conductance-based synapse at a holding potential of $V_{\mathrm{hold}} = -58\,\mathrm{mV}$ (Table 4.2).

The ripple dynamics for current-based inhibitory synapses is shown in Fig. 4.17A. When switching from conductance- to current-based synapses in a small, sparsely connected network, the network frequencies remain similar but the underlying unit firing rates become much more variable (Fig. 4.16Bii vs Fig. 4.17Aii, Aiii). In the absence of an inhibitory reversal potential (Fig. 4.17A) the variability introduced by the random sparse connectivity becomes visible in the increased variability of membrane potentials (now even below the inhibitory reversal potential), which results in a spread of unit firing rates: units with an above-average inhibitory indegree get strongly hyperpolarized and reach the spike threshold only rarely (see outlier voltage traces in Fig. 4.17Ai). Similarly units receiving less inhibitory inputs remain closer to threshold and fire at higher rates. This variability is quenched in the conductance-based model with an inhibitory reversal potential.

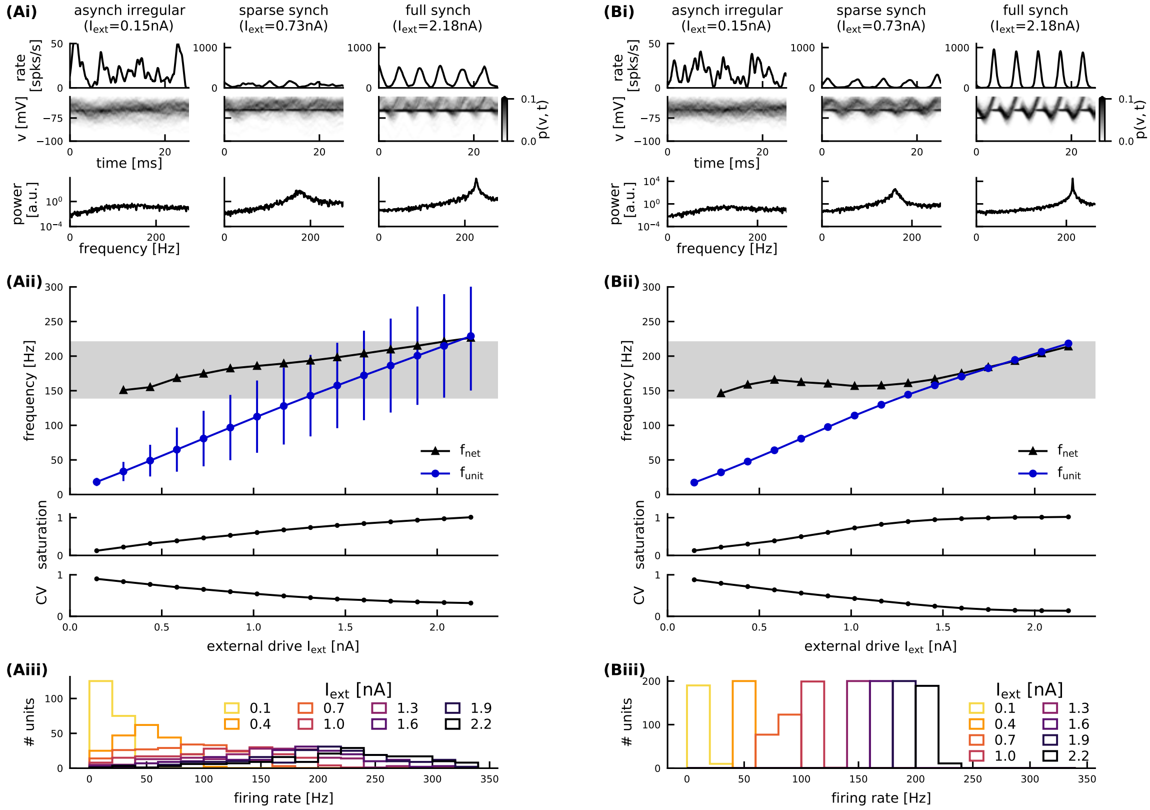

Figure 4.17: Ripple dynamics with current-based inhibitory coupling: sparse vs. full connectivity. Same outline as in Fig. 4.1 (i-ii). Conductance-based synapses are replaced by current-based coupling, still with a double-exponential synaptic filter. **A,** The network is sparsely connected ($p_{\mathrm{II}} = 0.2$, Eqs. (4.17)). **B,** The network is fully connected ($p_{\mathrm{II}} = 1$, Eqs. (4.17), (4.18)). Panel iii: Unit firing rates.

The network can be made homogeneous by connecting the interneurons all-to-all: Every interneuron receives inhibitory feedback from the entire network ($\Gamma_i^I =$

$\{1, \ldots, N\}$), instead of just sampling a random subset of average size $\langle|\Gamma_i^I|\rangle = p_{\mathrm{II}}N$:

$$S_{\mathrm{inh},i}(t) \quad \longmapsto \quad S_{\mathrm{inh}}(t) = \sum_{j=1}^{N}\sum_{k}\delta(t_j^k - t)\ . \tag{4.18a}$$

To keep the mean inhibitory input constant, the synaptic coupling strength is scaled down accordingly:

$$I_{\mathrm{peak}} \quad \longmapsto \quad p_{\mathrm{II}}^{\mathrm{orig}} \cdot I_I^{\mathrm{peak}} = 0.2 \cdot I_I^{\mathrm{peak}}\ . \tag{4.18b}$$

In the fully connected, homogeneous network (Fig. 4.17B) the variability of membrane potentials is strongly reduced (Fig. 4.17Bi vs Ai), and the individual units fire at very similar rates (Fig. 4.17Biii). The core difference that remains, due to the switch from conductance-based (Fig. 4.16) to current-based coupling, is that the oscillation amplitude of the membrane potential distribution varies more strongly with the drive (Fig. 4.17Bi). Without an inhibitory reversal potential the hyperpolarization of membrane potentials in response to increasing inhibitory feedback is unbounded. This will be discussed in more detail in Section 4.3.5.

It is known that synaptic filtering modulates the network frequency (Brunel and Wang, 2003), but that a synaptic delay alone is sufficient to generate fast network oscillations (Brunel and Hakim, 1999). I thus replaced the double-exponential synaptic filter by a simple delayed delta-pulse of amplitude $J_I = 1.75$ mV, preserving the magnitude of the IPSP of the conductance-based synapse at $V_{\mathrm{hold}} = -58\,\mathrm{mV}$ (Table 4.2). For a fully-connected network of arbitrary size N the membrane potential of a single unit is then described by:

$$\dot{v}_i(t) = \frac{1}{\tau_m}(E_{\mathrm{leak}} - v_i(t)) + \frac{1}{C}I_{\mathrm{ext}} - \frac{J}{N}\left(\kappa_\Delta^\delta * S_{\mathrm{inh}}(t)\right) + \sqrt{\frac{2}{\tau_m}}\sigma_V\xi_i(t) \tag{4.19a}$$

with inhibitory synaptic kernel

$$\kappa_\Delta^\delta(t) = \delta(t - \Delta)\ . \tag{4.19b}$$

Note that $\kappa_\Delta^\delta * S_{\mathrm{inh}}(t)$ is simply $S_{\mathrm{inh}}(t - \Delta)$. When the network size is varied, the synaptic strength is scaled by the new indegree to keep the mean feedback constant: A new parameter for inhibitory coupling strength J is introduced with

$$\frac{J}{N^{\mathrm{orig}}} = p_{\mathrm{II}}^{\mathrm{orig}}J_I \quad \Rightarrow \quad J = 200 \cdot 0.2 \cdot J_I = 82.37\,\mathrm{mV} \tag{4.19c}$$

In the fully connected network of original size $N^{\mathrm{orig}} = 200$ a single inhibitory input spike thus causes a downward jump of the postsynaptic membrane potential of amplitude $J/N^{\mathrm{orig}} = 0.41$ mV. If the network size is increased to $N = 1000$, the pulse amplitude decreases to $J/N = 0.082$ mV.

For such "$1/N$"-scaling the fluctuations in the recurrent feedback decay as $1/\sqrt{N}$ for increasing network size and vanish in the mean-field limit. This can be seen in a diffusion approximation of the recurrent inputs: If the spike trains of all interneurons are approximated as independent Poisson processes $S_j^{r(t)}(t)$ with the same rate $r(t)$, their sum is again a Poisson process of rate $Nr(t)$ that can be approximated as a Gaussian white noise with mean and variance $Nr(t)$:

$$S_{\mathrm{inh}}(t) \approx \sum_{j=1}^{N} S_j^{r(t)}(t) = S^{Nr(t)}(t) \approx Nr(t) + \sqrt{Nr(t)}\xi(t)$$

$(\langle \xi(t) \rangle = 0, \langle \xi(t)\xi(t') \rangle = \delta(t-t'))$. The inhibitory feedback is then given by:

$$\frac{J}{N}\left(\kappa_{\Delta}^{\delta} * S_{\mathrm{inh}}(t)\right) \approx Jr(t-\Delta) + \underbrace{\frac{J\sqrt{r(t-\Delta)}}{\sqrt{N}}}_{\longrightarrow 0 \text{ as } N\to\infty} \xi(t) \ .$$

A "$1/\sqrt{N}$"-scaling of the synaptic strength would keep the fluctuations constant but lead to an effective increase in coupling strength for larger networks. Since the coupling strength is one of the parameters that can influence the network oscillation frequency, I chose the $1/N$-scaling for constant mean in order to maintain the same ripple dynamics independent of network size (see Fig. 4.3B). Fig. 4.18 shows the network dynamics for delta pulse-coupling in a network of the default size $N = 200$. The removal of the double-exponential synaptic filter leads to a slight increase of the network frequency around oscillation onset and the point of full synchrony is reached slightly earlier (Fig. 4.18ii vs Fig. 4.17Bii). Qualitatively there is no significant change of the ripple dynamics.

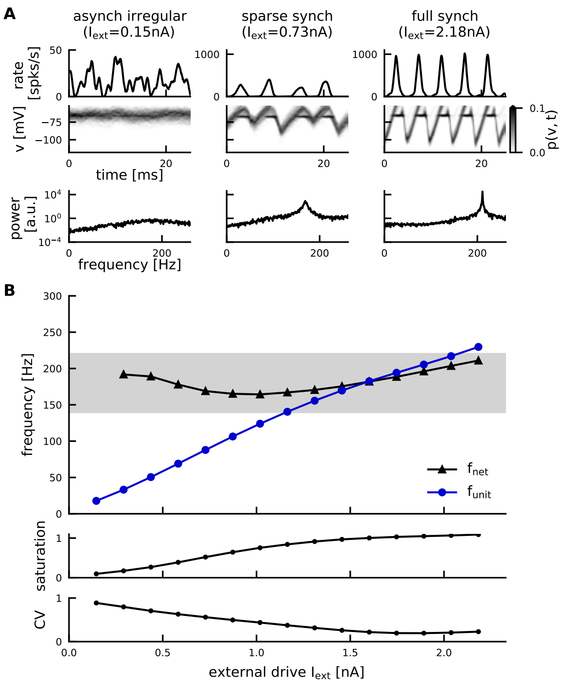

Figure 4.18: Ripple dynamics in fully connected network with delta-pulse coupling. Same outline as in Fig. 4.1. The interneurons are coupled all-to-all via simple delayed pulses (Eqs. (4.19)). The synaptic delay was increased to $\Delta = 1.8\,\mathrm{ms}$ to compensate for the absence of additional filter time constants and to keep the network frequencies in ripple range.

4.5.1.3 The reduced model

Taken together, all the above simplifications (Section 4.5.1.2) result in the reduced model described by Eqs. (4.19) (cf. Eq. (4.2) in the Results). The parameters that will be used as the default setting for the reduced model throughout the chapter are summarized in Table 4.3. For the sake of simplicity I adjusted a few parameters compared to the detailed model and its simplifications introduced above (marked with asterisks in Table 4.3): V_{reset} is changed by 2 mV such that it is equal to the resting potential ($V_R = 0$). The coupling strength is slightly decreased such that its dimensionless value is an integer ($J = 65\,\text{mV} \Rightarrow K = 5$). The synaptic delay was chosen as 1.2 ms. Since simulations of the reduced model will be compared with analytical results from a mean-field ansatz, I increased the default network size to $N = 10,000$. I found no significant changes of the simulated network dynamics when increasing the network size further. The absolute refractory period is neglected in the reduced model. I comment on the role of the refractory period and its negligible effect on the oscillation dynamics in Section 4.3.6.

The only meaningful adjustment is a reduction in noise strength ($\sigma_V = 2.62\,\text{mV}$), which will prove beneficial for the mean-driven theory that I will develop in the following. All parameters will be explored systematically and their role will be discussed in more detail in Appendix Section 4.A.

Parameter	Value	Definition
N	10,000	Number of interneurons*
τ_m	10 ms	Membrane time constant
C_m	100 pF	Membrane capacitance
E_{leak}	-65mV	Resting potential
V_{thr}	-52 mV	Spike threshold
V_{reset}	- 65 mV	Reset potential*
J	65 mV	Inhibitory coupling strength*
Δ	1.2 ms	Synaptic delay*
τ_{ref}	0 ms	No refractory period
σ_V	2.62 mV	Standard deviation of Gaussian white noise input*
V_T	1	Spike threshold, dimensionless
V_R	0	Reset potential, dimensionless
K	5	Inhibitory coupling strength, dimensionless
D	0.04	Variance of Gaussian white noise input, dimensionless

Table 4.3: Default parameters of the reduced spiking network.
Parameter values that deviate from the default values of the detailed model (Table 4.2) or the model reduction described in Section 4.5.1.2 are marked with an asterisk. The lower section indicates the main parameter values converted to dimensionless voltage.

4.5.1.4 Hybrid model (current- vs conductance-based)

For a comparison of current- and conductance-based coupling a introduce two hybrid models, derived from either the reduced or the detailed version of the bifurcation-based ripple model. For the current-based network (Fig. 4.12, left) I use the reduced model (Eq. (4.2)) with a few parameter adjustments to match it to the conductance-based model as detailed in Table 4.4.

For the conductance-based network (Fig. 4.12, right) I use the detailed model after the diffusion approximation in the feedforward input (see Eqs. (4.16)):

$$\dot{v}_i(t) = \frac{1}{\tau_m}(E_{\text{leak}} - v_i(t)) + \frac{1}{C}\left(I_{\text{ext}} - I_{\text{I}}(t)\right) + \sqrt{\frac{2}{\tau_m}}\sigma_V \xi_i(t) \tag{4.20a}$$

$$I_{\text{ext}} = CJ_E\Lambda \qquad (\text{nA}) \tag{4.20b}$$

$$I_{\text{inh},i}(t) = -g_{\text{inh},i}(t)\left(E_I - v_i(t)\right) \tag{4.20c}$$

$$g_{\text{inh},i}(t) = g_I^{\text{peak}} \kappa_\Delta^{\text{2exp}} * S_{\text{inh}}(t) \tag{4.20d}$$

To match the reduced model setup the network is increased in size ($N = 1000$) and connected all-to-all. The peak conductance is decreased accordingly by the factor 0.2/1000 (see Table 4.4). To get comparable network frequencies with the double exponential filter the synaptic delay is decreased to $\Delta = 0.5\,\text{ms}$. There is no refractory period and the reset potential is set to E_{leak} as in the reduced model.

Parameter	Value	Definition
N	1,000	Number of interneurons
p_{II}	1	Connection probability
τ_m	10 ms	Membrane time constant
C_m	100 pF	Membrane capacitance
E_{leak}	-65mV	Resting potential
V_{thr}	-52 mV	Spike threshold
V_{reset}	- 65 mV	Reset potential (reduced model)
J	82.37 mV	Coupling strength (κ_Δ^δ, detailed model)
g_I^{peak}	0.2 nS	Coupling strength ($\kappa_\Delta^{\text{2exp}}$, detailed model rescaled)
Δ	1.2 / 0.5 ms	Synaptic delay (current-based / conductance-based)
τ_{ref}	0 ms	No refractory period (reduced model)
σ_V	3.9 mV	SD of Gaussian white noise (hybrid)
K	6.34	Coupling strength, dimensionless (detailed model)
D	0.09	Var. of Gaussian white noise, dimensionless (hybrid)

Table 4.4: Default parameters of the hybrid spiking networks.
Parameter values are taken either from the detailed model (Table 4.2) or from the reduced model (Table 4.3) as indicated in the parameter description. Only the noise strength was set at an intermediate level, close to the default of the detailed model but small enough that the drift-based approximation would apply well to the hybrid networks.

4.5.1.5 Numerical implementation

Spiking network simulations were done using the Brian2 simulator (Goodman and Brette, 2009). For large parameter explorations I used the Python toolkit *pypet* for data storage and parallelization of simulations (Meyer and Obermayer, 2016).

To evaluate the oscillation dynamics for constant drive, the network activity is numerically integrated over 5.05 s (time step $\Delta t = 0.01$ ms). The initial 50 ms are excluded from analysis, to make sure that initial transients do not influence my estimate of the asymptotic network dynamics. The remaining 5 s are sufficient for a basic spectral analysis.

For time-dependent drive, I first simulate the network for 200 ms with a constant baseline drive, followed by the time-dependent stimulus. The drive that the interneuron network receives via the Schaffer Collaterals during a sharp wave ("SPW-like drive") is modeled as a piecewise linear double-ramp of slope $\pm m$ with a plateau phase of arbitrary length inbetween (here 20 ms). In the detailed model (Eqs. (4.11)) the SPW-like drive is delivered via Poisson spikes of intensity

$$\Lambda(t) = \begin{cases} \Lambda^{\text{crit}}/2, & 0 \leq t \leq t_1 = 200\,\text{ms} \\ \Lambda^{\text{crit}}/2 + m(t - t_1), & t_1 < t \leq t_2 = t_1 + \frac{\Lambda^{\text{full}} - \Lambda^{\text{crit}}/2}{m} \\ \Lambda^{\text{full}}, & t_2 < t \leq t_3 = t_2 + 20\,\text{ms} \\ \Lambda^{\text{full}} - m(t - t_3), & t_3 < t \leq t_4 = t_3 + \frac{\Lambda^{\text{full}} - \Lambda^{\text{crit}}/2}{m} \end{cases} \tag{4.21}$$

In the reduced model (Eq. (4.2)) the SPW-like drive is delivered as a time-dependent current

$$I_{\text{ext}}(t) = \begin{cases} I_{\text{ext}}^{\text{crit}}/2, & 0 \leq t \leq t_1 = 200\,\text{ms} \\ I_{\text{ext}}^{\text{crit}}/2 + m(t - t_1), & t_1 < t \leq t_2 = t_1 + \frac{I_{\text{ext}}^{\text{full}} - I_{\text{ext}}^{\text{crit}}/2}{m} \\ I_{\text{ext}}^{\text{full}}, & t_2 < t \leq t_3 = t_2 + 20\,\text{ms} \\ I_{\text{ext}}^{\text{full}} - m(t - t_3), & t_3 < t \leq t_4 = t_3 + \frac{I_{\text{ext}}^{\text{full}} - I_{\text{ext}}^{\text{crit}}/2}{m} \end{cases} \tag{4.22}$$

During the baseline period the network receives a drive $\Lambda^{\text{crit}}/2$ or $I_{\text{E}}^{\text{crit}}/2$, that is half of the critical drive required for the bifurcation towards oscillations in the mean-field, as estimated by linear stability analysis (see Methods Section 4.5.2.4). During the plateau phase the drive is at the approximate point of full synchrony Λ^{full} or $I_{\text{ext}}^{\text{full}}$ of the respective spiking network, which is determined by a range of constant-drive simulations beforehand.

4.5.1.6 Frequency analysis

The network frequency at constant drive is defined as the location of the dominant peak in the power spectral density of the population activity $r_N(t)$. The saturation s (average fraction of neurons firing in one cycle of the population rhythm) is computed by dividing the mean unit firing rate by the network frequency. The point of full synchrony in the spiking network is estimated by interpolating the simulated saturation curve and estimating the level of drive for which it becomes 1.

To define the instantaneous network frequency in response to time-dependent drive, I use both a continuous and a discrete estimate. The continuous estimate is derived from the wavelet spectrogram (windowed Fourier transform) of the population activity, which indicates instantaneous power in the frequency band from 0 to 350 Hz over time; the instantaneous frequency at each point in time is defined as the frequency above 70 Hz, that has maximal power. The lower limit is introduced to exclude the low-frequency contribution due to the sharp wave. The instantaneous frequency is considered significant, whenever it is strictly higher than 70 Hz *and* the corresponding instantaneous power exceeds a certain power threshold. The power threshold is chosen as the average instantaneous power at 0 Hz plus 4 standard deviations, computed over the initial 200 ms baseline time window.

A straightforward *discrete* estimate of the instantaneous frequency is given by the inverse of the peak-to-peak distances in the (smoothed) population activity r_N. The estimate is restricted to peaks that are more than 4 standard deviations above the average population activity during baseline stimulation. I mostly rely on the discrete estimate of instantaneous frequency since its parameter-dependencies (minimal height of oscillation peaks) are more transparent than the ones of the continuous estimate (size of time window for windowed Fourier transform, power threshold). Furthermore it is better suited for comparison with the theory developed in Section 4.5.4, which also describes instantaneous frequency as a discrete measure per cycle (see Eq. (4.87)).

To quantify the network's instantaneous frequency response to a SPW-like drive (Eq. (4.22)), I perform 50 independent simulations of the network model with the same drive but different noise realizations. Linear regression over all discrete instantaneous frequency estimates $(t_i, f_{\mathrm{net,i}}^{\mathrm{inst}})$ yields the average change of the instantaneous frequency over time:

$$f_{\mathrm{net}}^{\mathrm{inst}}(t) \approx \chi_{\mathrm{IFA}} \cdot t + \mathrm{const.} \quad , \qquad \chi_{\mathrm{IFA}} = \frac{\mathrm{Cov}(f_{\mathrm{net}}^{\mathrm{inst}}, t)}{\mathrm{Var}(t)} \tag{4.23}$$

Covariance and variance are computed over discrete oscillation cycles i, pooled together from all 50 simulations. A negative slope $\chi_{\mathrm{IFA}} < 0$ indicates IFA.

4.5.1.7 Extracting the average oscillation cycle

For constant drive, the dynamics of the spiking network can be averaged over many cycles to obtain a good estimate of the average oscillation cycle. I split the spiking network simulation into individual cycles based on the Hilbert transform of the mean membrane potential. I take a sufficient number of equally spaced samples from each cycle (here 21) and average them across cycles to derive the average trajectory of the population rate and the membrane potential histogram over the course of a ripple cycle. For each of the 21 sample times one can calculate the average membrane potential, which will be used for comparison with the theory.

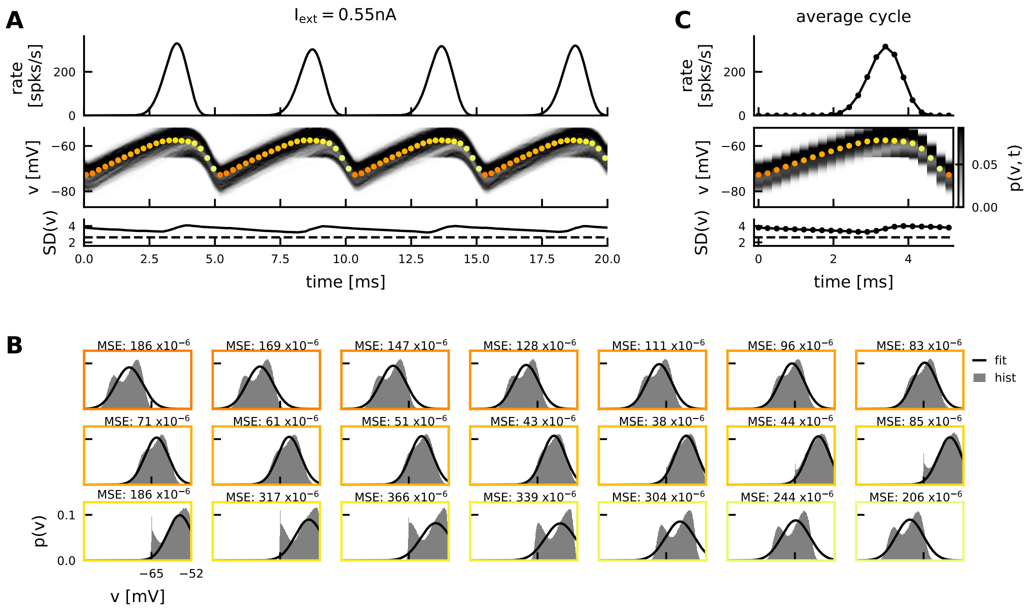

Figure 4.19: Extracting the average oscillation cycle from the spiking network simulation. **A,** Dynamics of the spiking network for constant drive. Top to bottom: population rate r_N, distribution of membrane potentials, standard deviation of membrane potential distribution. The dashed line indicates the asymptotic standard deviation $\sigma_V = 2.62$ mV expected in the absence of the absorbing boundary condition at the spike threshold. Colored dots mark the 21 equally spaced samples taken from each cycle. **B,** Distribution of membrane potentials shown for 21 sample times over the course of a ripple cycle, averaged over many cycles (as indicated in A). Black lines show the best gaussian fit of the membrane potential distribution (mean squared error indicated in top right). **C,** The average ripple cycle in terms of population rate, and membrane potential distribution.

4.5.2 Mean-field dynamics for constant drive

4.5.2.1 Dimensionless equations

To facilitate notation in the theoretical part of this chapter, all voltages are shifted and rescaled, such that the spiking threshold becomes $V_T = 1$ and the resting potential is $E_L = 0$. This corresponds to measuring voltage in units of the distance from the resting potential to the spike threshold. The single unit SDE then reads

$$\tau_m \dot{V}_i = -V_i + I(t) + \sqrt{2D\tau_m}\,\xi_i(t) \tag{4.24}$$

$$I(t) = I_{\mathrm{E}}(t) - I_{\mathrm{I}}(t) \tag{4.25}$$

where now

$$\begin{aligned} V_i &= \frac{v_i - E_{\mathrm{leak}}}{V_{\mathrm{thr}} - E_{\mathrm{leak}}} & K &= \frac{J}{V_{\mathrm{thr}} - E_{\mathrm{leak}}} \\ I_{\mathrm{E}}(t) &= \frac{\tau_m}{C(V_{\mathrm{thr}} - E_{\mathrm{leak}})} I_{\mathrm{ext}}(t) & \sqrt{D} &= \frac{\sigma_V}{V_{\mathrm{thr}} - E_{\mathrm{leak}}} \\ I_{\mathrm{I}}(t) &= K\tau_m \frac{1}{N}\sum_{i=1}^{N}\sum_{k=1}^{n_j} \delta(t - \Delta - t_j^k) & V_R &= \frac{V_{\mathrm{reset}} - E_{\mathrm{leak}}}{V_{\mathrm{thr}} - E_{\mathrm{leak}}} \end{aligned} \tag{4.26}$$

are all dimensionless quantities.

4.5.2.2 Fokker-Planck equation for a network of LIF neurons under Gaussian white noise

In the mean-field limit of an infinitely large interneuron population ($N \to \infty$) the evolution of the membrane potential density $p(V,t)$ is desribed by the following Fokker-Planck equation (FPE) (see e.g. Abbott and van Vreeswijk, 1993; Brunel and Hakim, 1999):

$$\partial_t p(V,t) = -\partial_V \left(\frac{1}{\tau_m}\Big(I(t) - V\Big)p(V,t)\right) + \frac{D}{\tau_m}\partial_V^2 p(V,t) \tag{4.27a}$$

$$I(t) = I_{\mathrm{E}}(t) - I_{\mathrm{I}}(t) = I_{\mathrm{E}}(t) - K\tau_m r(t-\Delta)\ . \tag{4.27b}$$

The FPE can also be written as a continuity equation

$$\partial_t p(V,t) = -\partial_V J(V,t) \tag{4.27c}$$

with a probability current

$$J(V,t) = \frac{1}{\tau_m}\Big(I(t) - V\Big)p(V,t) - \frac{D}{\tau_m}\partial_V p(V,t) \tag{4.27d}$$

Since units are instantaneously reset as soon as they reach the spiking threshold, the FPE has an absorbing boundary condition at threshold:

$$p(V_T, t) = 0\ . \tag{4.27e}$$

The population rate r is given by the probability current through the threshold:

$$r(t) = J(V_T, t) \overset{(4.27e)}{=} -\frac{D}{\tau_m}\partial_V p(V,t)|_{V_T} \ . \tag{4.27f}$$

The fire-and-reset mechanism introduces a derivative discontinuity at the reset potential V_R:

$$[\partial_V p(V,t)]_{V_R} := \lim_{\epsilon\to 0}\left(\partial_V p(V_R+\epsilon,t) - \partial_V p(V_R-\epsilon,t)\right) = -\frac{\tau_m}{D}r(t) \ . \tag{4.27g}$$

(Abbott and van Vreeswijk, 1993; Brunel, 2000; Lindner and Schimansky-Geier, 2001; Brunel et al., 2003). Because a probability density like $p(V,t)$ obeys the normalization condition, we have

$$\int_{-\infty}^{V_T} p(V,t)\ \mathrm{d}V = 1 \quad \forall\, t. \tag{4.27h}$$

Finally, a solution of the FPE must decay to zero fast enough in the limit of $V \to -\infty$

$$\lim_{V\to-\infty} p(V,t) = \lim_{V\to-\infty} V p(V,t) = 0 \tag{4.27i}$$

(Brunel and Hakim, 1999), see also Appendix Section 4.D.1, Eq. (4.111).

4.5.2.3 Stationary solution

In the stationary state the population rate is constant:

$$r(t) \equiv r_0 \tag{4.28}$$

and thus so is the total input current:

$$I(t) \overset{(4.27b)}{=} I_\mathrm{E} - K\tau_m r(t) \overset{(4.28)}{\equiv} I_\mathrm{E} - K\tau_m r_0 =: I_0 \ . \tag{4.29}$$

For constant input $I(t) \equiv I_0$ the stationary solution $p_0(V)$ of the FPE (Eq. (4.27a)) is given by

$$p_0(V) = \frac{\tau_m r_0}{D}\,\mathrm{e}^{-\frac{(V-I_0)^2}{2D}}\int_V^{V_T}\mathrm{e}^{\frac{(s-I_0)^2}{2D}}\,\Theta(s-V_R)\,\mathrm{d}s \tag{4.30}$$

with population rate

$$r_0(I_0) = \left(\sqrt{\pi}\tau_m\int_{\frac{I_0-V_T}{\sqrt{2D}}}^{\frac{I_0-V_R}{\sqrt{2D}}}\mathrm{e}^{x^2}\,\mathrm{erfc}(x)\,\mathrm{d}x\right)^{-1} \tag{4.31}$$

(Brunel and Hakim, 1999), see Appendix Section 4.D.1.2 for the detailed derivation.

Note that in this recurrently coupled network the total input I_0 depends on the population rate r_0 (Eq. (4.29)). The population rate r_0 and total input I_0 must thus be determined self-consistently, solving Eqs. (4.31) and (4.29):

Eq. (4.31) corresponds to the single-unit f-I curve (Holden, 1976) and describes the rate as a monotonically *in*creasing function[1] of the current I_0. On the other hand, Eq. (4.29) can be rewritten as

$$r_0(I_0) \overset{(4.29)}{=} \frac{I_\mathrm{E} - I_0}{K\tau_m} \qquad (K > 0) \; . \tag{4.32}$$

Since the coupling is inhibitory, there is a *negative* correlation between rate and total input current: The larger the rate, the larger the inhibitory feedback and thus the smaller the total current I_0. Hence there is a unique solution for I_0 and r_0 that satisfy both Eq. (4.31) and Eq. (4.32) (intersection marked in Fig. 4.20). Note that for *excitatory* coupling a stationary solution may not always exist (Abbott and van Vreeswijk, 1993).

The stationary solution of the FPE for the reduced inhibitory ripple network is shown in Fig. 4.5.

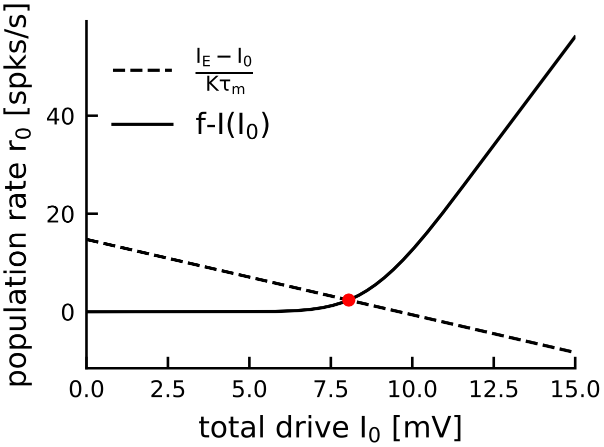

Figure 4.20: Self-consistent solution for the population rate r_0 and the total drive I_0 in steady-state. Graphical solution (red dot) of Eqs. (4.31) (solid line) and (4.32) (dashed line) in the reduced model (parameters see Table 4.3, $I_\mathrm{E} = 0.1$ nA). See Fig. 4.5 for a complete illustration fo the stationary solution of the FPE and a comparison with spiking network simulations.

4.5.2.4 Linear stability analysis

The stationary solution computed above loses stability if either (i) the external drive increases, (ii) the synaptic coupling strength increases, or (iii) the noise intensity decreases (Brunel and Hakim, 1999). In the context of SPW-Rs, and hence throughout this thesis, it is assumed that the external drive acts as the bifurcation parameter, while noise and coupling strength remain fixed. If the external drive, as the bifurcation parameter, exceeds a critical value $I_\mathrm{E}^\mathrm{crit}$, an oscillatory solution of the FPE emerges with a T-periodic density $p(V,t) = p(V, t+T)$ and a periodic population rate $r(t) = r(t+T)$. In simulations of a finite spiking network this manifests itself as coherent stochastic

---

[1] One can easily see that:

$$\frac{\mathrm{d}}{\mathrm{d}I_0} r_0(I_0) \overset{(4.31)}{=} -\left(\sqrt{\pi}\tau_m \int_{\frac{I_0-V_T}{\sqrt{2D}}}^{\frac{I_0-V_R}{\sqrt{2D}}} \mathrm{e}^{x^2}\,\mathrm{erfc}(x)\,\mathrm{d}x\right)^{-2} \cdot \frac{\sqrt{\pi}\tau_m}{\sqrt{2D}} \left[\mathrm{e}^{x^2}\,\mathrm{erfc}(x)\right]_{(I_0-V_T)/\sqrt{2D}}^{(I_0-V_R)/\sqrt{2D}} > 0$$

since $V_T > V_R$ and $\mathrm{e}^{x^2}\,\mathrm{erfc}(x) \geq 0$, $\mathrm{d}/\mathrm{d}x(\mathrm{e}^{x^2}\,\mathrm{erfc}(x)) \leq 0 \quad \forall\, x \in \mathbb{R}$.

oscillations in the population activity $r_N(t)$. The autocorrelation of these oscillations in the finite network is dampened due to phase diffusion (Brunel and Hakim, 1999) [2].

In the mean-field limit, the bifurcation point $I_\mathrm{E}^\mathrm{crit}$ and the frequency ω of the emerging oscillation can be approximated self-consistently based on the linear response of a single unit to weakly oscillatory input. I will first summarize the procedure for a general network of integrate-and-fire-type neurons, fully coupled with synaptic weight J and filter κ. In the end I show the specific result for the reduced bifurcation-based inhibitory ripple model (Eqs. (4.24)) and comment on how different model parameters affect the linear stability of the network.

At first order, the oscillatory modulation of the population rate can be approximated as a weak sinusoidal perturbation r_1 around its stationary value r_0:

$$r(t) = r_0 + \epsilon r_1(t) = r_0 + \epsilon\, \mathrm{e}^{i\omega t+\lambda t}\,, \quad (\epsilon > 0 \text{ small})\ . \tag{4.33}$$

For $\lambda < 0$ the oscillation is damped and the rate returns to its stationary value. For $\lambda > 0$ the oscillation amplitude increases over time. Hence the bifurcation corresponds to $\lambda = 0$.
In a recurrently coupled network such a perturbation of the (output) rate translates into a perturbation of the input current:

$$I(t) = \underbrace{I_\mathrm{E} + Jr_0}_{=I_0} + \epsilon \underbrace{J\Big(\kappa * r_1\Big)(t)}_{=I_1(t)} \tag{4.34}$$

To keep the derivation general, no assumptions are made yet about the synaptic filter κ, and synaptic weight J. Inhibitory coupling corresponds to $J < 0$ (see below).
The linear response of a single neuron to the weakly modulated drive $I(t)$ is given by convolution with a linear response function G:

$$r(t) = r_0 + \epsilon \int_0^\infty G(s, I_\mathrm{E}) I_1(t-s)\,\mathrm{d}s \tag{4.35}$$

I emphasize here the dependence of G on the external drive I_E, since its critical value is one of the unknowns that we want to determine. In the recurrent network this output rate $r(t)$ must match the initially assumed oscillatory rate (Eq. (4.33)) in phase and amplitude. Together, Eqs. (4.33) – (4.35) yield a self-consistent equation for the first order rate modulation r_1:

$$r_1(t) = \int_0^\infty G(s, I_\mathrm{E}) I_1(t-s)\,\mathrm{d}s \overset{(4.34)}{=} J \int_0^\infty G(s, I_\mathrm{E})(\kappa * r_1)(t-s)\,\mathrm{d}s$$

In the bifurcation ($\lambda = 0 \Rightarrow r_1(t) = \mathrm{e}^{i\omega t}$, Eq. (4.33)) this self-consistent condition is equivalent to

$$\begin{aligned} \mathrm{e}^{i\omega t} &= J \int_0^\infty G(s, I_\mathrm{E})(\kappa * \mathrm{e}^{i\omega(t-s)})\,\mathrm{d}s \\ \Leftrightarrow \quad 1 &= J \int_{-\infty}^\infty G(s, I_\mathrm{E}) \int_{-\infty}^\infty \kappa(x)\,\mathrm{e}^{-i\omega(s+x)}\,\mathrm{d}x\,\mathrm{d}s\ . \end{aligned}$$

---

[2] Hence, throughout this thesis, when I talk about oscillations in the population rate, I refer to the rate $r_N(t)$, averaged over a small time step, for a given noise realization (Eq. (4.13)), but *not* to an average over many noise realizations. Due to the phase diffusion mentioned above, averaging over many noise realizations would always yield a rate that is constant over time.

Since G is a causal filter ($G(s) = 0 \quad \forall\, s < 0$), the lower integration boundary can be extended to $-\infty$. Now substitute $s := y - x$:

$$\Leftrightarrow \quad 1 = J \int_{-\infty}^{\infty} \underbrace{\int_{-\infty}^{\infty} \kappa(x) G(y - x, I_\mathrm{E})\, \mathrm{d}x}_{=(\kappa * G)(y)}\, \mathrm{e}^{-i\omega y}\, \mathrm{d}y$$

Note that the outer integral is a Fourier transformation. According to the convolution theorem the Fourier transform of a convolution can be written as a product:

$$\Leftrightarrow \quad 1 = J\tilde{G}(\omega, I_\mathrm{E})\tilde{\kappa}(\omega)$$

$\tilde{G}$ and $\tilde{\kappa}$ indicate the (complex) Fourier transforms of the linear response function (*susceptibility*) and of the synaptic kernel respectively. The complex equation can be reformulated in terms of an amplitude- and phase-condition, *i.e.* a set of two equations determining the two unknowns $I_\mathrm{E}^\mathrm{crit}$ and ω:

$$\Leftrightarrow \quad \begin{cases} 1 = |J||\tilde{G}(\omega, I_\mathrm{E})||\tilde{\kappa}(\omega)|\,, & \text{amplitude condition} \\ 0 = \arg(J) + \arg(\tilde{G}(\omega, I_\mathrm{E})) + \arg\left(\tilde{\kappa}(\omega)\right) \quad \mod 2\pi\,, & \text{phase condition} \end{cases} \tag{4.36}$$

Let's return to the concrete case of the reduced bifurcation-based inhibitory ripple model (Eqs. (4.24)): The coupling is inhibitory ($J = -K\tau_m$) with a synaptic filter $\kappa_\Delta^\delta(t) = \delta(t - \Delta)$ that has Fourier transform $\tilde{\kappa}_\Delta^\delta(\omega) = \mathrm{e}^{-i\omega\Delta}$. For an LIF unit under Gaussian white noise the susceptibility $\tilde{G}$ can be computed analytically (Lindner and Schimansky-Geier, 2001; Brunel et al., 2001, see Eq. (4.145) and Appendix Section 4.D.3 for full derivation). The amplitude- and phase-condition can thus be solved numerically to find the critical drive $I_\mathrm{E}^\mathrm{crit}$ at which the stationary state loses stability, and the frequency ω of the emerging oscillation (Fig. 4.21). The network frequency and mean unit firing rate in the point of bifurcation are then given by $f_\mathrm{net}^\mathrm{crit} = \omega/2\pi$ and $f_\mathrm{unit}^\mathrm{crit} = r_0(I_\mathrm{E}^\mathrm{crit})$ (Eq. (4.31)). These analytical approximations match the results of a spiking network simulation very well (see red markers in Fig. 4.3B).

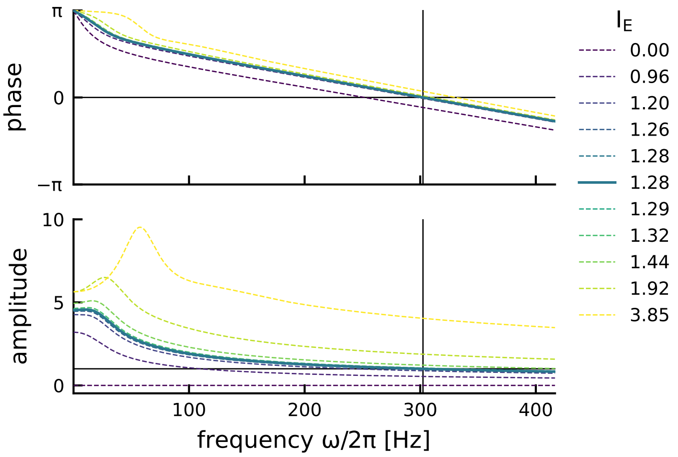

Figure 4.21: Numerical solution of the amplitude and phase condition for the reduced ripple model. Iterative variatio of external drive I_E (colored dashed lines) until the approximate solution of Eq. (4.36) is found, here: $I_\mathrm{E}^\mathrm{crit} = 1.28$ (solid blue line) and $\omega_\mathrm{crit} = 2\pi 302.4$ Hz (vertical line). Parameters: Table 4.3.

Note: The self-consistent phase condition can be understood intuitively: in the recurrent network the population rate is both input and output signal. The population rate goes through a synaptic filter introducing a phase lag $\arg(\tilde{\kappa}(\omega))$, is then sign-flipped due to the inhibitory nature of the synapses (phase lag $\arg(J) = \pi$) and then fed back into the same units which will respond with a neuronal phase lag $\arg(\tilde{G}(\omega))$. To close the cycle, the phase lags must thus add up to zero (modulo 2π). This was illustrated nicely in (Geisler et al., 2005) (see Fig. 4.22A).

Though conceptually equivalent, the ansatz described here (Brunel and Hansel, 2006; Lindner and Schimansky-Geier, 2001) is formally different from the linear stability analysis as it is presented in (Brunel and Hakim, 1999). I comment on the differences in Appendix Section 4.D.4 and confirm in a direct calculation that, in the context of the fully connected network of the reduced ripple model (Eqs. (4.24)), the results of both approaches are indeed mathematically equivalent (Eq. (4.36) shown here and Eq. (A.29) in (Brunel and Hakim, 1999)).

The amplitude and phase condition Eq. (4.36) clearly shows that the linear response properties of a single unit determine the linear stability of the network. In the following I briefly review how the noise, synaptic filtering or the choice of neuron model can affect the linear response of a single unit and thus the network dynamics.

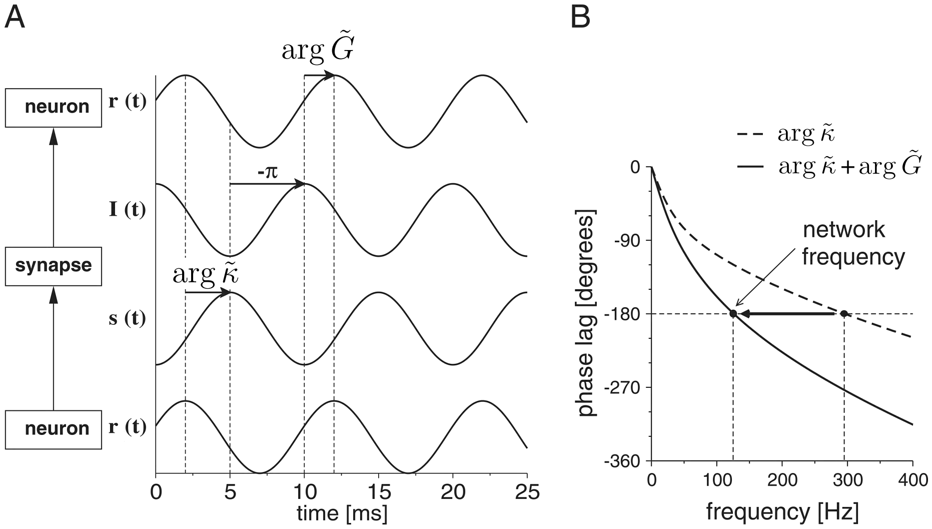

Figure 4.22: Illustration of the self-consistent phase condition. A, Conceptual sketch: Any given neuron in the network spikes with instantaneous rate $r(t)$, which is assumed to be weakly sinusoidally modulated in vicinity of the bifurcation. This rate is fed back to the network due to the recurrent inhibitory coupling: The synaptic filtering produces a phase lag $\arg(\tilde{\kappa})$. Since the synapses are inhibitory, the sign in the current is flipped, which corresponds to an additional phase lag of $-\pi$. The oscillatory current is received as an input signal and every unit responds with a neuronal phase lag $\arg(\tilde{G})$. Since these are the very same units that produced the input rate in the first place, the signals in the top and bottom row must be identical (0 phase lag as indicated by dotted line), which leads to the self-consistent phase- and amplitude-condition (Eq. (4.36)). **B,** Solution of the phase-condition with or without accounting for the neuronal phase lag $\arg(\tilde{G})$ (intersection of solid or dashed line with -180°). Ignoring the neuronal phase lag leads to an *over*estimation of the oscillation frequency. Figure adapted from Geisler et al., 2005 with permission from The American Physiological Society.

Noise correlation time constant (white vs colored noise). It has been shown that the nature of the noise influences the linear response properties of LIF units: Under Gaussian white noise, an LIF unit behaves as a low-pass filter with an amplitude $|\tilde{G}(\omega)|$ approaching 0, and a neuronal phase lag $\arg[\tilde{G}(\omega)]$ approaching 45°in the high-frequency limit (Lindner and Schimansky-Geier, 2001; Brunel et al., 2001). The linear response under Gaussian white noise can be calculated analytically as explained in Methods Section 4.D.3.1 (Lindner and Schimansky-Geier, 2001).

Under colored noise, the LIF linear response can no longer be calculated analytically. In the limit of a small noise time constant (small compared to the membrane time constant) the high-frequency limit can be estimated: The amplitude remains finite ($|\tilde{G}(\omega)| > 0$) and the phase lag $\arg[\tilde{G}(\omega)]$ approaches 0 for high frequencies (Brunel et al., 2001). Thus, under colored noise, an LIF unit can track oscillatory inputs even at arbitrarily high frequencies. Numerical simulations suggest that the linear response under colored noise generally depends both on the mean unit firing rate and on the noise time constant (Brunel et al., 2001; Geisler et al., 2005). The larger the noise time constant, the smaller the phase lag and hence the LIF unit can track an oscillatory input better. For noise correlation times on the order of the membrane time constant, the neuronal phase lag can thus be neglected in the solution of the phase-amplitude-condition (Brunel and Wang, 2003). This will however always lead to a (slight) overestimation of the oscillation frequency (see sketch in Fig. 4.22B, example for the detailed ripple model in Fig. 4.6).

Noise strength. For low noise, the neuronal phase lag $\arg(\tilde{G}(\omega))$ exhibits peaks close to multiples of the neuron's mean firing rate (Brunel and Hansel, 2006). The solution of the phase-condition (Eq. (4.36)), and hence the frequency of the collective oscillation that emerges when the stationary state in the network loses stability, may thus be close to a multiple (n) of the mean unit firing rate r_0. This corresponds to a clustering state in the spiking network, where distinct groups of neurons spike rather regularly in every n-th cycle of the population rhythm (Brunel and Hansel, 2006). Due to the low noise level units rarely switch between clusters.

Since the first peaks of the neuronal phase lag ($n = 1, 2$) of an LIF neuron are low ($|\arg(\tilde{G}(\omega))| \ll 2\pi$ for $\omega < 3r_0$), the lowest frequency solutions of the phase condition Eq. (4.36) for LIF networks appear at a higher multiple of the unit firing rate ($n > 1$) (unless the added synaptic phase lag is unrealistically large). This explains the observation of sparse synchrony at oscillation onset, with a population rhythm that is faster than the average mean unit firing rate (Fig. 4.3).

As the noise level increases, the peaks in the neuronal phase lag smoothen out until the phase lag becomes a monotonically increasing function of the input frequency (see Fig. 2B in Brunel and Hansel, 2006). The clusters thus dissolve and neurons fire sparse and irregularly (see Fig. 4.3).

Accounting for synaptic filtering. The synaptic filter κ influences both the phase- and amplitude-condition Eq. (4.36) (see also Fig. 4.22A). Different synaptic filters have different synaptic phase lags, *e.g.* for the reduced ripple model (Eqs. (4.2)):

$$\arg(\tilde{\kappa}^{\delta}_{\Delta}(\omega)) = -\omega\Delta$$

For the detailed ripple model (Eqs. (4.11)):

$$\arg(\tilde{\kappa}_{\Delta}^{2\exp}(\omega)) = -\left(\omega\Delta + \arctan(\omega\tau_I^r) + \arctan(\omega\tau_I^d)\right) \tag{4.37}$$

(cf. Eq. (8) in (Brunel and Wang, 2003)). Note that the arctangent function has the strongest slope in 0. Hence changes in the small synaptic rise time constant τ_I^r have a much stronger effect on the synaptic phase lag, and hence the oscillation frequency, than changes in the larger synaptic decay time constant τ_I^d (Brunel and Wang, 2003).

The role of the neuron model. The choice of the neuron model influences the linear response of a single neuron and hence the linear stability of a network of such neurons when they are synaptically coupled (Geisler et al., 2005; Brunel and Hansel, 2006).

A popular alternative to the LIF neuron model is the exponential integrate-and-fire (EIF) neuron. The ODE describing the membrane potential of an EIF neuron contains an exponential non-linearity mimicking spike initiation by fast sodium currents:

$$\tau_m \dot{V} = -V + \Delta_{\text{thr}} \exp\left[\frac{V - V_t}{\Delta_{\text{thr}}}\right] + I(t) \ .$$

The potential V_t determines the onset of fast spike initiation. A spike is fired and the membrane potential is reset, when V crosses a threshold V_{thr}. The *softness* of the threshold is determined by Δ_{thr}. Simple Hodgkin-Huxley-type neuron models (Hodgkin and Huxley, 1952), such as the Wang-Buzsáki neuron (Xiao-Jing Wang and Buzsáki, 1996), can be mapped onto the EIF model (Fourcaud-Trocmé et al., 2003). EIF units are thus considered a good compromise between biological realism and analytical tractability.

The linear response of EIF units to oscillatory input has been approximated analytically in the low- and high-frequency limit (Fourcaud-Trocmé et al., 2003): The EIF unit acts as a low-pass filter with an amplitude attenuating as $\sim 1/f$ in the high-frequency limit. For high frequencies, the phase lag of the EIF neuron approaches 90°, independent of the noise time constant, and is thus twice as large as the neuronal phase lag of an LIF neuron under Gaussian white noise (Fourcaud-Trocmé et al., 2003).

The linear response of EIF units is hard to study analytically for arbitrary frequencies but has been estimated numerically (Geisler et al., 2005; Brunel and Hansel, 2006; Richardson, 2007, 2008): As for LIF units, the neuronal phase lag of EIF units exhibits peaks close to (n-)multiples of the mean unit rate, that are more pronounced at low noise levels. Just like the asymptotic phase lag for high frequencies, these peaks are much larger than for an LIF unit. Solutions of the phase-condition (Eq. (4.36)) for an EIF network can thus appear close to the mean unit firing rate ($n = 1$). The frequency of the emerging oscillation is thus lower, and stronger noise is needed to bring the network out of the clustering state towards an oscillatory regime in which individual units fire irregularly (Brunel and Hansel, 2006, see also Fig. 5.10 in Chapter 5).

In summary, EIF units respond to oscillatory input with a larger phase lag than LIF units and thus produce slower oscillations when connected with inhibitory synapses. This is due to the fact that spikes are not elicited instantaneously, as in the LIF neuron, but have a finite initiation time set by the parameter Δ. In the limit $\Delta \to 0$ spike initiation becomes instantaneous and the EIF effectively becomes the LIF model.

Comparison with spiking network simulations. Comparing the result of the analytical linear stability analysis (Eq. (4.36)) with simulations of a spiking network comes with several difficulties. The analytical approximation is valid in the mean-field limit ($N \to \infty$). A simulated spiking network, however, can only have finitely many units. Apart from making the simulated network as large as possible, one can further counteract unwanted finite size effects by making the feedforward inputs fully independent and by fixing the indegree in the recurrent connectivity matrix. Thus input correlations or heterogeneity in the network will not influence the frequency of the simulated population oscillation. A second difficulty is the fact that one attempts to approximate the frequency in a supercritical Hopf bifurcation, i.e. of an oscillation that has infinitesimal amplitude. The peak in the power spectral density is therefore very small and hard to detect accurately. Increasing the bifurcation parameter (here the drive) slightly beyond the critical value should slightly increase the amplitude of the simulated oscillation and facilitate the frequency analysis. It is advisable to increase the simulation time and split the simulated time series into many shorter snippets, the Fourier transforms of which are averaged, to obtain a smooth estimate of the power spectral density (Methods Section 4.5.1.6). In Fig. 4.6, for example, I simulated a network of $N = 5000$ units with independent inputs and fixed indegree $p_{\mathrm{II}}N = 1000$ over 20 s. The simulated network frequencies around oscillation onset are much closer to the analytical estimate (237 Hz) than in the un-adjusted network (200-214 Hz in Fig. 4.6 vs. 175 Hz in Fig. 4.1). Still, a small discrepancy remains, which is likely due to the omission of the neuronal phase lag in the analytical estimate (see Main text, Section 4.3.1, Fig. 4.6).

4.5.2.5 Weakly nonlinear analysis.

The dynamics of the (small amplitude) oscillations shortly *after* the bifurcation can be studied in a *weakly nonlinear analysis* (Brunel and Hakim, 1999).

A note on network architecture. Before I summarize the main results of this analysis by Brunel and Hakim (1999), a quick note on their network architecture: The network considered in (Brunel and Hakim, 1999) is almost the same as the reduced ripple model studied here (Eq. (4.2)), except for one additional complexity: the recurrent connectivity between the interneurons is assumed to be random and sparse and the resulting fluctuations in the inhibitory feedback are taken into account. In steady state, both the feedforward and the feedback input are approximated as white-noise processes the means and variances of which add up. Two dimensionless parameters, G and H, are introduced to quantify the strength of the mean and the variance of the inhibitory feedback relative to the overall noise. The network dynamics are analyzed with respect to G and H as the bifurcation parameters. The reduced ripple model studied here thus represents a special case, where the network is fully connected (inhibitory indegree = N) and the variance of the inhibitory feedback vanishes ($H = 0$). The relative strength of the inhibitory feedback G is given by

$$G = \frac{K\tau_m r_0(I_{\mathrm{E}})}{\sqrt{2D}} \qquad \text{(cf. Eq. (3.16) in Brunel and Hakim, 1999).} \tag{4.38}$$

Recall that the stationary rate r_0 depends on all the network parameters (Eq. (4.31), Eq. (4.32)) including also the external drive I_{E}, which I highlighted here specifically.

We thus see that the bifurcation (at $G = G_c$) can be reached in several ways: an increase in external drive I_{E}, an increase in coupling strength K, or a decrease in noise D. In the context of sharp wave-ripples I assume that the external excitatory drive I_{E} serves as the bifurcation parameter.

Weakly nonlinear analysis. Brunel and Hakim (1999) analyze the network dynamics around the bifurcation by expanding the solution of the FPE around its steady-state solution (see also Appendix Section 4.D.4). The population rate is expanded as

$$r(t) = r_0 \left(1 + \hat{n}_1 e^{i\omega t/\tau_m} + \hat{n}_2 e^{i2\omega t/\tau_m} + \cdots + c.c.\right) \tag{4.39}$$

(frequency ω is denoted in units of $1/\tau_m$, time t is given in seconds).

If the network undergoes a *supercritical* Hopf bifurcation in $G = G_c$, the first order oscillation amplitude $\hat{n}_1$ is expected to grow as the square root of the distance of the bifurcation parameter from its critical value $(G - G_c)$. Under this assumption the distance of the bifurcation parameter from its critical value appears for the first time in a third order term of the FPE for the expanded solution ($\hat{n}_1 \cdot (G - G_c) \sim \mathcal{O}(\hat{n}_1^3)$ in Eq. (A.42) in Brunel and Hakim, 1999). Hence the authors push the development up to third order and show that such a solution of the FPE exists *if* the first order amplitude $\hat{n}_1$ exhibits a slow time-dependence described by the Hopf normal form:

$$\tau_m \frac{\mathrm{d}\hat{n}_1}{\mathrm{d}t} = A\hat{n}_1 - B|\hat{n}_1|^2\hat{n}_1 \qquad \text{(Eq. (3.20) in Brunel and Hakim, 1999)}\ .$$

If $\mathrm{Re}(A) > 0$, the solution is a stable limit cycle:

$$\hat{n}_1(t) = R\, \mathrm{e}^{i\Delta\omega t/\tau_m} \tag{4.40}$$

with amplitude

$$R = \sqrt{\frac{\mathrm{Re}(A)}{\mathrm{Re}(B)}}$$

and (slow) frequency

$$\Delta\omega = \mathrm{Im}(A) - \mathrm{Im}(B)\frac{\mathrm{Re}(A)}{\mathrm{Re}(B)}\ .$$

What is formulated here as a slow modulation of the amplitude can simply be rephrased as a small change in the frequency of the population rate oscillation:

$$\begin{aligned} r(t) &\overset{(4.39)}{\approx} r_0 \left(1 + \hat{n}_1 e^{i\omega t/\tau_m} + c.c.\right) \overset{(4.40)}{=} r_0 \left(1 + R\, \mathrm{e}^{i\Delta\omega t/\tau_m}\, e^{i\omega t/\tau_m} + c.c.\right) \\ &= r_0 \left(1 + R\, \mathrm{e}^{i(\omega + \Delta\omega)t/\tau_m} + c.c.\right) \end{aligned}$$

Brunel and Hakim (1999) have thus derived an analytical expression for the change in frequency and the amplitude of the oscillation shortly after the Hopf bifurcation.

The expressions for the complex numbers A and B are rather complicated (Eqs. (A.54), (A.55) in Brunel and Hakim, 1999). In the limit of small synaptic delay

$(\Delta/\tau_m \to 0)$ and for $H = 0$ the authors show that the expressions simplify and become interpretable:

$$\begin{aligned} A &\approx \frac{\tau_m}{\Delta}(1.35 + 0.29i)\frac{G - G_c}{G_c} \\ B &\approx \frac{\tau_m}{\Delta}(0.53 + 0.30i) \qquad\qquad \text{(Eq. (3.21) in Brunel and Hakim, 1999)} \end{aligned}$$

We can see several things here: As expected, the distance of the bifurcation parameter G from its critical value G_c determines the sign of $\mathrm{Re}(A)$ and hence whether or not an oscillation develops: If $G < G_c$, $\mathrm{Re}(A) < 0$ and any oscillatory rate modulation decays to zero — the network is in steady-state. If $G > G_c$, $\mathrm{Re}(A) > 0$ and a stable limit cycle develops.
The amplitude in the above limit simplifies to

$$R = \sqrt{\frac{\mathrm{Re}(A)}{\mathrm{Re}(B)}} \approx \sqrt{2.55\frac{G - G_c}{G_c}}$$

If the bifurcation parameter is the external drive, as assumed in this thesis, this corresponds to

$$R \overset{(4.38)}{\approx} \sqrt{2.55\frac{r - r_0}{r_0}} \tag{4.41}$$

where r is the mean unit firing rate at the given drive and r_0 is the mean unit rate at the critical drive in the Hopf bifurcation. Since the mean unit rate rises quasi-linearly with the external drive (Fig. 4.3B), this expression implies that the amplitude increases proportionally to the square root of the drive — as expected after a supercritical Hopf bifurcation and as observed in the spiking network simulations.
The change in network frequency shortly after the bifurcation can also be understood in the limit $\Delta/\tau_m \to 0$:

$$\Delta\omega = \mathrm{Im}(A) - \mathrm{Im}(B)\frac{\mathrm{Re}(A)}{\mathrm{Re}(B)} \approx -0.47\frac{\tau_m}{\Delta}\underbrace{\frac{G - G_c}{G_c}}_{>0} \quad < 0 \tag{4.42}$$

After the bifurcation the frequency *de*creases approximately linearly. Again, this matches the simulation results (Fig. 4.3).

4.5.3 Derivation of drift-based approximation of oscillation dynamics

If we ignore the absorbing boundary at threshold and the reset mechanism, the FPE has only natural boundary conditions and can be solved analytically. Its solution p, for an initial Dirac delta distribution $p(V, 0) = \delta(V - \mu_0)$, is a Gaussian density with time-dependent mean $\mu(t)$ and variance $\sigma^2(t)$ (Uhlenbeck and Ornstein, 1930, see Appendix Section 4.D.1.1):

$$p(V, t) = \frac{1}{\sqrt{2\pi}\sigma(t)} \exp\left[-\frac{(V - \mu(t))^2}{2\sigma^2(t)}\right] \tag{4.43}$$

The mean membrane potential μ evolves according to the single unit ODE (Eq. (4.24)) without the noise term:

$$\dot{\mu}(t) = \frac{1}{\tau_m}\Big(I(t) - \mu(t)\Big)\,, \quad \mu(0) = \mu_0\,. \tag{4.44}$$

Again, the total current I is given as the sum of the excitatory external drive and the inhibitory recurrent feedback (cf. Eq. (4.27b)):

$$I(t) = I_{\mathrm{E}} - K\tau_m r(t - \Delta) \tag{4.45}$$

(The population rate r will be redefined below for the drift-based approximation without absorbing boundary condition (Eq. (4.49)).) The variance $\sigma(t)^2$ of the membrane potential distribution approaches D with a time constant of $\tau_m/2$:

$$\sigma^2(t) := D\left(1 - \mathrm{e}^{-2t/\tau_m}\right) \overset{t\to\infty}{\longrightarrow} D\,. \tag{4.46}$$

The solution for an arbitrary initial condition can be found by convolution of the initial condition with this Gaussian solution for initial Dirac delta distributin. Hence in the long time limit ($t \to \infty$) *all* solutions of the FPE with natural boundary conditions tend towards a Gaussian with variance D — independent of the initial condition $p(V, 0)$ (which has to satisfy the boundary conditions Eqs. (4.27), see Appendix Section 4.D.1.1 for a few examples).
I will hence assume that in the ripple network, inbetween population spikes, the bulk of the membrane potential distribution spends enough time subthreshold (i.e. unaffected by the absorbing boundary condition) to become “sufficiently Gaussia” again. Thus, when the next population spike begins, the membrane potential density is approximately Gaussian with fixed variance D (see also Fig. 4.19):

$$p(V, t) \approx \frac{1}{\sqrt{2\pi D}} \exp\left[-\frac{(V - \mu(t))^2}{2D}\right] \tag{4.47}$$

This Gaussian approximation allows me to derive a simple expression for the population rate (Plesser and Gerstner, 2000; Chizhov and Graham, 2007; Goedeke and Diesmann, 2008):

$$r(t) = J(V_T, t) \overset{(4.27\mathrm{i})}{=} \int_{-\infty}^{V_T} \partial_V J(V, t)\,\mathrm{d}V \overset{(4.27\mathrm{c})}{=} -\partial_t \int_{-\infty}^{V_T} p(V, t)\,\mathrm{d}V \overset{(4.47)}{=} \dot{\mu}(t)\,p(V_T, t)\,. \tag{4.48}$$

In the last step I used the Gaussian solution of the FPE with the assumption of constant variance D to solve the integral explicitly. The rate is given by the value of the Gaussian density at threshold, scaled by the speed at which the mean membrane potential approaches the threshold. Since only upwards-crossings of the threshold should be counted as spikes, add a sign-dependence is added:

$$r(t) = [\dot{\mu}(t)]_+ p(V_T, t) \tag{4.49}$$

clipping the rate to 0 whenever the mean membrane potential decays: $[\dot{\mu}(t)]_+ := \max(0, \dot{\mu}(t))$ (Plesser and Gerstner, 2000; Chizhov and Graham, 2007; Goedeke and Diesmann, 2008).

4.5.3.1 Numerical analysis of drift-based oscillation dynamics

In its derivation above, I formulated the drift-based approximation in several equations, describing the membrane potential density p (Eq. (4.47)), mean membrane potential μ (Eq. (4.44)) and population rate r (Eq. (4.49)) separately. Note however that the mean membrane potential is the only independent variable and thus the drift-based approximation can be rephrased as a single delay differential equation (DDE) describing the dynamics of μ:

$$\begin{aligned}
\dot{\mu}(t) &\overset{(4.44)}{=} \frac{1}{\tau_m}\left(I(t)-\mu(t)\right) \overset{(4.45)}{=} \frac{1}{\tau_m}\Big(I_{\mathrm{E}} - \tau_m K r(t-\Delta) - \mu(t)\Big) && (4.50)\\
&\overset{(4.49)}{=} \frac{1}{\tau_m}\Big(I_{\mathrm{E}} - \tau_m K[\dot{\mu}(t-\Delta)]_+ p(V_T, t-\Delta) - \mu(t)\Big)\\
&\overset{(4.47)}{=} \frac{1}{\tau_m}\left(I_{\mathrm{E}} - \tau_m K[\dot{\mu}(t-\Delta)]_+ \frac{1}{\sqrt{2\pi D}}\exp\left[-\frac{(V_T-\mu(t-\Delta))^2}{2D}\right] - \mu(t)\right) && (4.51)
\end{aligned}$$

Since the population rate is the main variable of interest I will nevertheless look at the solutions in terms of both $\mu(t)$ and $r(t)$. Using a simple forward Euler method and initial conditions $\mu(0) \ll V_T$ such that $r(t) \approx 0\ \forall t \leq 0$, we can numerically integrate the DDE and find a range of potential dynamics for constant drive I_{E} (see Fig. 4.23).

There is a large regime of sufficiently strong drive, in which the solution μ exhibits persistent period-1 oscillations (Fig. 4.23, green). This is the regime of interest, the dynamics of which will be approximated analytically in the following.

At lower levels of drive there are three additional dynamical regimes that will be excluded from analysis: At low drive, the system has a stable fixed point ($\dot{\mu} = 0$) in $(\mu(t), r(t)) \equiv (I_{\mathrm{E}}, 0)$ (Eq. (4.50), Fig. 4.23, blue). The bifurcation at which the fixed point loses stability can be determined numerically. Immediately after the bifurcation the DDE solution exhibits very fast oscillations at $(2\Delta)^{-1} \sim 417\,\mathrm{Hz}$ (Fig. 4.23, red). The oscillation amplitude of the mean membrane potential is very small and a large portion of the Gaussian potential density is suprathreshold at all times. I refer to this oscillation as pathological since it is a direct result of the artificial clipping of the rate to 0 whenever the mean membrane potential decays (Eq. (4.49)). Increasing the drive further brings the system into a state of period-2 oscillations where the Gaussian density gets pushed below threshold only every other cycle (Fig. 4.23, yellow).

These regimes of pathological high frequency or period-2 oscillations exist due to the simplifying assumptions capturing only the mean-driven aspects of the network dynamics. Both regimes occur either shortly before or after the level of drive $I_{\mathrm{E}}^{\mathrm{crit}}$ at which the original spiking network undergoes a supercritical Hopf bifurcation (see tick mark in Fig. 4.23). In the vicinity of that bifurcation the spiking network dynamics are fluctuation-driven with either no ($I_{\mathrm{E}} < I_{\mathrm{E}}^{\mathrm{crit}}$) or only small-amplitude ($I_{\mathrm{E}} > I_{\mathrm{E}}^{\mathrm{crit}}$) oscillations in the mean membrane potential and population rate. These cannot be captured without taking into account the absorbing boundary at threshold and the non-Gaussian shape of the density of membrane potentials. These pathological dynamics will be excluded from analysis by introducing a lower bound $I_{\mathrm{E}}^{\mathrm{min}}$ for the theoretical approximations developed in the following (see tick mark in Fig. 4.23).

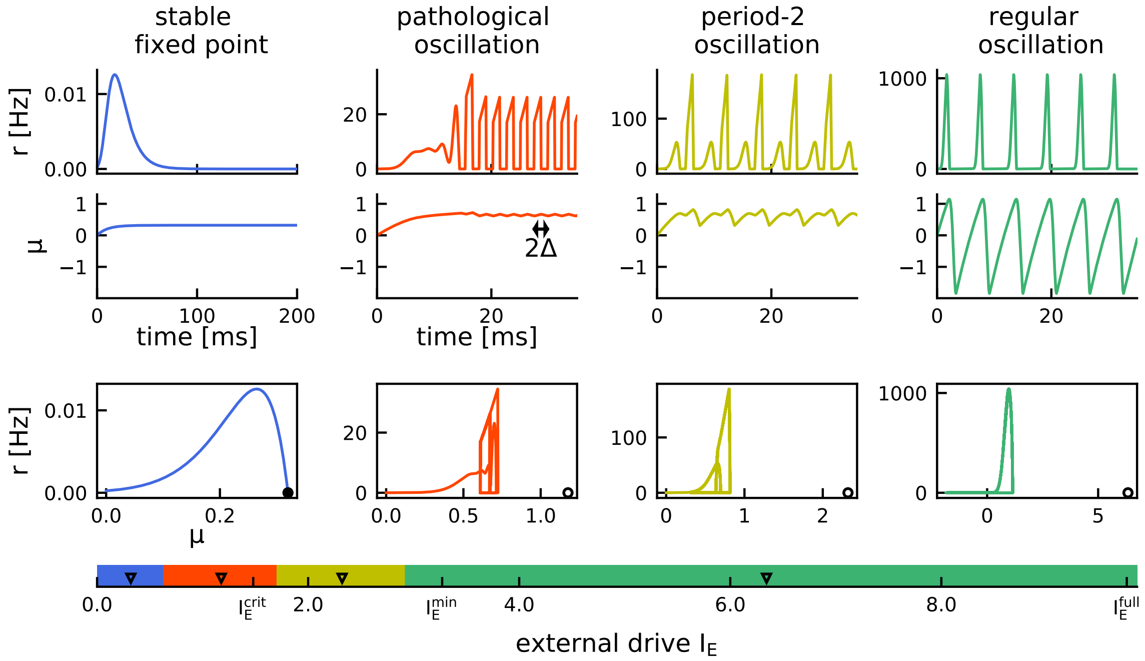

Figure 4.23: Numerical analysis of the drift-based approximation. Numerical integration of the DDE system demonstrating 4 distinct dynamical regimes for increasing external drive I_E (bottom axis). Blue: Stable fixed point with zero rate. Red: Pathological, fast oscillations. Yellow: Period-2 oscillations. Green: Regular period-1 oscillations. Top: Numerically integrated trajectories of population rate r and mean membrane potential μ over time. Note the changes in scale for the population rate. Bottom: Phase space showing the trajectory $(\mu(t), r(t))$ and the fixed point $(I_\mathrm{E}, 0)$, which is only stable in the first case (black circle) and unstable otherwise (empty circle). X-axis shows the full range of (relevant) drives from 0 to the point of full synchrony $I_\mathrm{E}^\mathrm{full}$. Black triangles mark the levels, for which the above example dynamics are shown. Extra ticks indicate: critical drive $I_\mathrm{E}^\mathrm{crit} \approx 1.28$, for which the spiking network undergoes a Hopf bifurcation (see Methods Section 4.5.2.4); lower bound $I_\mathrm{E}^\mathrm{min}$ introduced for the theory to exclude pathological dynamics (see Methods Section 4.5.4.5).

4.5.4 Analytical approximation of drift-based oscillations for constant drive

For large enough drive the mean membrane potential μ under the drift-based approximation oscillates periodically between two local extrema $\mu_{\min}$ and $\mu_{\max}$ (orange and cyan marker in Fig. 4.24A, green regime in Fig. 4.23). The population rate r oscillates at the same frequency and is positive while the mean membrane potential increases ($\dot{\mu} \geq 0$) and 0 otherwise (Eq. (4.49), Fig. 4.24A, top). The time when the mean membrane potential reaches its local maximum $\mu_{\max}$ marks the end of the population spike and will be denoted as t_{off}. The inhibitory feedback (Eq. (4.45)) thus ends at time $t_{\text{off}} + \Delta$ and I define $\mu_{\min} := \mu(t_{\text{off}} + \Delta)$ as the end of a cycle. This allows an approximation of the overall period as

$$T = t_{\text{off}}(\mu_{\min}, \mu_{\max}) + \Delta \ , \tag{4.52}$$

where t_{off} is the duration of the "upstroke", i.e. the time it takes for the mean membrane potential to rise from $\mu_{\min}$ to $\mu_{\max}$, and Δ is the duration of the subsequent "downstroke" back to $\mu_{\min}$ (Fig. 4.24A, top, gray bars). In the following I will approximate $\mu_{\max}$ (Step 1) and $\mu_{\min}$ (Step 2) and thus derive the network frequency as the inverse of the period:

$$f_{\text{net}} = T^{-1} = \Big(t_{\text{off}}(\mu_{\min}, \mu_{\max}) + \Delta\Big)^{-1} \ . \tag{4.53}$$

4.5.4.1 Step 1: approximating $\mu_{\max}$

To find the local maximum $\mu_{\max} = \mu(t_{\text{off}})$ (Fig. 4.24A, cyan marker) one needs to solve

$$0 = \dot{\mu}(t_{\text{off}}) \ . \tag{4.54}$$

Since the dynamics of the mean membrane potential are given by a delay differential equation, the term on the right-hand side is recurrent:

$$\dot{\mu}(t_{\text{off}}) \overset{(4.44)}{=} \frac{1}{\tau_m} \left(I(t_{\text{off}}) - \mu(t_{\text{off}})\right)$$

From the yet unknown time t_{off} we have to look back in time (in windows with length of the delay Δ, Fig. 4.24A, vertical dotted lines) at the history of the population rate $r(t)$:

$$\overset{(4.45)}{=} \frac{1}{\tau_m} \left(I_{\text{E}} - \tau_m K r(t_{\text{off}} - \Delta) - \mu(t_{\text{off}})\right) \ ,$$

which in turn depends on $\mu(t)$ and $\dot{\mu}(t)$:

$$\overset{(4.49)}{=} \frac{1}{\tau_m} \Big(I_{\text{E}} - \tau_m K \left[\dot{\mu}(t_{\text{off}} - \Delta)\right]_+ p(V_T, t_{\text{off}} - \Delta) - \mu(t_{\text{off}})\Big)$$

Since Eq. (4.44) is a delay differential equation, the last three steps can be repeated indefinitely:

$$\begin{aligned}
&\overset{(4.44)}{=} \frac{1}{\tau_m}\Big(I_\mathrm{E} - K\left[I(t_\mathrm{off}-\Delta) - \mu(t_\mathrm{off}-\Delta)\right]_+ p(V_T, t_\mathrm{off}-\Delta) - \mu(t_\mathrm{off})\Big)\\
&\overset{(4.45)}{=} \frac{1}{\tau_m}\Big(I_\mathrm{E} - K\Big[I_\mathrm{E} - \tau_m K r(t_\mathrm{off}-2\Delta) - \mu(t_\mathrm{off}-\Delta)\Big]_+ p(V_T, t_\mathrm{off}-\Delta) - \mu(t_\mathrm{off})\Big) \qquad (4.55)\\
&\overset{(4.49)}{=} \dots
\end{aligned}$$

We can resolve the recurrence by taking into account that the past time windows, during which the population rate is significantly above 0 and the network receives delayed feedback inhibition $I_\mathrm{I} = \tau_m K r$, are finite. In the first time window $[t_\mathrm{off}-\Delta, t_\mathrm{off}]$, right before the end of the upstroke, inhibition must be taken into account, since this is what stops the upstroke. In the second time window $[t_\mathrm{off}-2\Delta, t_\mathrm{off}-\Delta]$, further into the past, I will assume that the inhibitory feedback is negligible, i.e.

$$I(t) \approx I_\mathrm{E} \quad \forall\, 0 \leq t \leq t_\mathrm{off} - \Delta\ ,$$

which implies the assumption that the population rate was negligible in the previous time window, i.e.

$$r(t) \approx 0 \quad \forall\, 0 \leq t \leq t_\mathrm{off} - 2\Delta \qquad \text{(A1)}$$

(Eq. (4.45), arrows in Fig. 4.24A). Note that t here refers to time since the beginning of the cycle ($t = 0$). Since the population spike ends at time t_off, (A1) is equivalent to the assumption that the population spike lasts at most 2Δ. Adding the subsequent downstroke time of Δ this amounts to a maximal oscillation period of around 3Δ plus any additional upstroke time with $r \approx 0$, which is a reasonable assumption for a feedback loop with delay Δ as argued already by Brunel and Hakim (1999).
Under this assumption, I set $r(t_\mathrm{off} - 2\Delta) = 0$ in Eq. (4.55), and only a finite amount of terms remains:

$$0 = \dot{\mu}(t_\mathrm{off}) \overset{(A1)}{\approx} \frac{1}{\tau_m}\Big(I_\mathrm{E} - \mu(t_\mathrm{off}) - K\left(I_\mathrm{E} - \mu(t_\mathrm{off}-\Delta)\right) p(V_T, t_\mathrm{off}-\Delta)\Big) \qquad (4.56)$$

The rectification $[\cdot]_+$ could be dropped since the mean membrane potential can never be larger than the external drive. I approximate the past $\mu(t_\mathrm{off}-\Delta)$ during the upstroke based on the trajectory of μ as exponential relaxation towards only the *excitatory* drive (solution of Eq. (4.44) for $I(t) \equiv I_\mathrm{E}$):

$$\mu(t) \approx I_\mathrm{E} - (I_\mathrm{E} - \mu_\mathrm{min})\, \mathrm{e}^{-t/\tau_m} \qquad \forall\, 0 \leq t \leq t_\mathrm{off}$$

Looking backwards from time t_off, we can reformulate this assumption as:

$$\mu(t_\mathrm{off} - x) \approx I_\mathrm{E} - (I_\mathrm{E} - \mu_\mathrm{max})\, \mathrm{e}^{x/\tau_m} \qquad \forall\, x \geq 0 \qquad \text{(A2)}$$

The resulting error is small since the exponential relaxation of the mean membrane potential towards the total drive $I(t)$ is governed by the membrane time constant ($\tau_m = 10\,\mathrm{ms}$). The population spike on the other hand is quite synchronized (I assumed

that it lasts less than $2\Delta \ll \tau_m$, (A1)). The time window right before t_{off}, during which the units receive inhibitory feedback and the total drive deviates from I_{E}, is thus small compared to the membrane time constant and alters the trajectory of μ only slightly (Fig. 4.24A, full vs dotted line in zoom).
Eq. (4.56) thus simplifies to:

$$\begin{aligned} & 0 = \frac{1}{\tau_m}\Big(I_{\text{E}} - \mu_{\max} - K(I_{\text{E}} - \mu_{\max})\,\mathrm{e}^{\Delta/\tau_m}\,p(V_T, t_{\text{off}} - \Delta)\Big) \\ \Leftrightarrow\quad & 0 = 1 - K\,\mathrm{e}^{\Delta/\tau_m}\,p(V_T, t_{\text{off}} - \Delta) \qquad (4.57) \\ \Leftrightarrow\quad & 0 \overset{(4.47)}{=} 1 - K\,\mathrm{e}^{\Delta/\tau_m}\,\frac{1}{\sqrt{2\pi D}}\exp\left[-\frac{\Big(V_T - I_{\text{E}} - (\mu_{\max} - I_{\text{E}})\,\mathrm{e}^{\Delta/\tau_m}\Big)^2}{2D}\right] \end{aligned}$$

The simplified equation can be readily solved for $\mu_{\max}$:

$$\mu_{\max} = \Big(1 - \mathrm{e}^{-\Delta/\tau_m}\Big)\,I_{\text{E}} + \mathrm{e}^{-\Delta/\tau_m}\left[V_T - \sqrt{2D\ln\left[\frac{K}{\sqrt{2\pi D}}\,\mathrm{e}^{\Delta/\tau_m}\right]}\right]. \qquad (4.58)$$

Note that $\mu_{\max}$ does *not* depend on the initial voltage $\mu_{\min}$. This makes sense intuitively for any $\mu_{\min}$ that is sufficiently smaller than $\mu_{\max}$, since the "turning point" of the mean membrane potential depends only on the feedback inhibition resulting from the immediate history shortly before $\mu_{\max}$ is reached ($t \in [t_{\text{off}} - 2\Delta, t_{\text{off}}]$). To ensure that the argument of the logarithm in Eq. (4.58) is larger than 1, the coupling must be sufficiently strong: $K \geq \sqrt{2\pi D}\,\mathrm{e}^{-\Delta/\tau_m}$.

4.5.4.2 Step 2: approximating $\mu_{\min}$

I will now approximate the trajectory of the mean membrane potential during its inhibition-induced downstroke and infer $\mu_{\min} = \mu(t_{\text{off}} + \Delta)$, which constitutes both the end and the starting value of each cycle due to the periodic nature of the dynamics for constant drive (Fig. 4.24A, orange marker).

Note that while $\mu_{\min}$ is close to the periodic local minimum of the mean membrane potential, it is a slight overestimation: The local extrema of the mean membrane potential μ occur at its intersections with the total drive $I(t)$ (see Eq. (4.54), Fig. 4.24A, solid grey vs dashed black line). At time t_{off} the mean membrane potential reaches its local maximum and becomes larger than the total drive $I(t)$. Since the population spike ends at time t_{off}, the delayed inhibitory feedback $I_{\text{I}}(t)$ will stop at time $t_{\text{off}} + \Delta$: The total drive at this point will equal the external drive ($I(t_{\text{off}} + \Delta) = I_{\text{E}}$); note that the mean membrane potential μ can never be larger than the external drive I_{E}. Hence, if μ becomes larger than I at time t_{off} and is smaller than I at time $t_{\text{off}} + \Delta$, μ must intersect with $I(t)$ and reach its local minimum slightly *before* time $t_{\text{off}} + \Delta$ (see Fig. 4.24A, inset; even clearer in Fig. 4.42A, inset). What I define as the initial/final membrane potential of a cycle ($\mu_{\min} := \mu(t_{\text{off}} + \Delta)$) is thus close but slightly larger than the periodic local minimum. This does not affect the estimate of the period.

The definition of a fixed downstroke duration Δ is convenient as it allows us to find $\mu_{\min}$ directly by integrating the mean membrane potential ODE Eq. (4.44) up to time

$t_{\text{off}} + \Delta$, starting from the initial value $\mu(t_{\text{off}}) = \mu_{\max}$ that we have derived in Step 1 (instead of first finding the precise time point when the true local minimum is reached, which leads to a complicated equation that would require numerical evaluation).

The solution to ODE Eq. (4.44) with given intial value $\mu(t_{\text{off}}) = \mu_{\max}$ and given input $I(t)$ is well known:

$$\mu(t) = \mu_{\max}\, \mathrm{e}^{-(t-t_{\text{off}})/\tau_m} + \frac{1}{\tau_m}\int_{t_{\text{off}}}^{t} I(s)\, \mathrm{e}^{-(t-s)/\tau_m}\, \mathrm{d}s \quad \text{for} \quad t \geq t_{\text{off}}. \tag{4.59}$$

It follows

$$\mu_{\min} := \mu(t_{\text{off}} + \Delta) \quad \text{given intial value } \mu(t_{\text{off}}) = \mu_{\max} \tag{4.60}$$

$$\overset{(4.59)}{=} \mu_{\max}\, \mathrm{e}^{-\Delta/\tau_m} + \frac{1}{\tau_m}\int_{t_{\text{off}}}^{t_{\text{off}}+\Delta} I(s)\, \mathrm{e}^{-(t_{\text{off}}+\Delta-s)/\tau_m}\, \mathrm{d}s \tag{4.61}$$

The recurrence in the expression for the total current I is resolved using the same simplification as before in Step 1. To increase readability the value of the Gaussian density at threshold is abbreviated as: $p(t) := p(V_T, t)$.

$$\begin{aligned}
I(s) &\overset{(4.45)}{=} I_{\mathrm{E}} - K\tau_m r\big(s-\Delta\big) \quad , \qquad s \in [t_{\text{off}}, t_{\text{off}}+\Delta] \\
&\overset{(4.49)}{=} I_{\mathrm{E}} - K\tau_m \left[\dot{\mu}(s-\Delta)\right]_+ p\,(s-\Delta) \\
&\overset{(4.44)}{=} I_{\mathrm{E}} - K\left(I(s-\Delta) - \mu(s-\Delta)\right) p\,(s-\Delta) \\
&\overset{(4.45)}{=} I_{\mathrm{E}} - K\left(I_{\mathrm{E}} - K\tau_m r(s-2\Delta) - \mu(s-\Delta)\right) p\,(s-\Delta) \\
&\overset{(4.49)}{=} I_{\mathrm{E}} - K\Big(I_{\mathrm{E}} - K\tau_m \left[\dot{\mu}(s-2\Delta)\right]_+ p\,(s-2\Delta) - \mu(s-\Delta)\Big) p\,(s-\Delta) \\
&\overset{(4.44)}{=} I_{\mathrm{E}} - K\Big(I_{\mathrm{E}} - K\left[I(s-2\Delta) - \mu(s-2\Delta)\right] p\,(s-2\Delta) - \mu(s-\Delta)\Big) p\,(s-\Delta)
\end{aligned}$$

Note that all times $s - k\Delta = t_{\text{off}} + \tau - k\Delta = t_{\text{off}} - (k\Delta - \tau) < t_{\text{off}}$ for $\tau \in [0, \Delta],\ k \in [1, 2]$ refer to times during the *up*stroke before time t_{off}, hence I could omit all rectifications above ($[\dot{\mu}(s - k\Delta)]_+ = \dot{\mu}(s - k\Delta)$). I switch notation of time accordingly. For $\tau \in [0, \Delta]$:

$$\begin{aligned}
I(t_{\text{off}}+\tau) = I_{\mathrm{E}} - Kp\,(t_{\text{off}} - (\Delta-\tau)) \bigg(& I_{\mathrm{E}} - \mu\big(t_{\text{off}} - (\Delta-\tau)\big) \\
& - K\Big[I\big(t_{\text{off}} - (2\Delta-\tau)\big) - \mu\big(t_{\text{off}} - (2\Delta-\tau)\big)\Big] p\big(t_{\text{off}} - (2\Delta-\tau)\big)\bigg)
\end{aligned}$$

As before, I assume that the current I at time $t_{\text{off}} - (2\Delta - \tau) \leq t_{\text{off}} - \Delta$ is given exclusively by the excitatory drive (A1):

$$\begin{aligned}
I(t_{\text{off}}+\tau) \overset{(A1)}{\approx} I_{\mathrm{E}} - Kp\,(t_{\text{off}} - (\Delta-\tau)) \bigg(& I_{\mathrm{E}} - \mu(t_{\text{off}} - (\Delta-\tau)) \\
& - K\Big(I_{\mathrm{E}} - \mu(t_{\text{off}} - (2\Delta-\tau))\Big) p\Big(t_{\text{off}} - (2\Delta-\tau)\Big)\bigg)
\end{aligned} \tag{4.62}$$

We are left with a finite number of terms that depend on the trajectory of μ during the upstroke. Again, we approximate $\mu(t_\text{off}-x)$, $x \geq 0$ assuming exponential relaxation towards only the external drive, i.e. ignoring inhibition (A2). This abolishes all dependencies on the yet unknown time t_off of the end of the population spike:

$$\begin{aligned} I(t_\text{off}+\tau) \overset{\text{(A2)}}{\approx} {} & I_\text{E} - K(I_\text{E}-\mu_\text{max})\,\mathrm{e}^{(\Delta-\tau)/\tau_m}\,p\Big(t_\text{off}-(\Delta-\tau)\Big) \\ & + K^2(I_\text{E}-\mu_\text{max})\,\mathrm{e}^{(2\Delta-\tau)/\tau_m}\,p\Big(t_\text{off}-(2\Delta-\tau)\Big)p\Big(t_\text{off}-(\Delta-\tau)\Big) \end{aligned} \tag{4.63}$$

Inserting this approximation into the expression for μ_min yields:

$$\begin{aligned} \mu_\text{min} \overset{(4.61)}{=} {} & \mu_\text{max}\,\mathrm{e}^{-\Delta/\tau_m} + \frac{1}{\tau_m}\,\mathrm{e}^{-\Delta/\tau_m}\int_0^\Delta I(t_\text{off}+\tau)\,\mathrm{e}^{\tau/\tau_m}\,\mathrm{d}\tau \\ \overset{(4.63)}{\approx} {} & \mu_\text{max}\,\mathrm{e}^{-\Delta/\tau_m} + \frac{1}{\tau_m}\,\mathrm{e}^{-\Delta/\tau_m}\,I_\text{E}\int_0^\Delta \mathrm{e}^{\tau/\tau_m}\,\mathrm{d}\tau \\ & - \frac{1}{\tau_m}K(I_\text{E}-\mu_\text{max})\int_0^\Delta p\Big(V_T, t_\text{off}-(\Delta-\tau)\Big)\,\mathrm{d}\tau \\ & + \frac{1}{\tau_m}K^2(I_\text{E}-\mu_\text{max})\,\mathrm{e}^{\Delta/\tau_m}\int_0^\Delta p\Big(V_T, t_\text{off}-(2\Delta-\tau)\Big)p\Big(V_T, t_\text{off}-(\Delta-\tau)\Big)\,\mathrm{d}\tau \end{aligned} \tag{4.64}$$

The integrals over the Gaussians p can be solved analytically, if the past trajectory of the mean μ is approximated linearly (Fig. 4.24A, inset, solid vs dotted gray line):

$$\mu(t_\text{off}-x) \overset{\text{(A2)}}{\lessapprox} \mu_\text{max} - (I_\text{E}-\mu_\text{max})\frac{x}{\tau_m}\,, \quad \text{for small } 0 \leq x \leq 2\Delta \ll \tau_m \tag{4.65}$$

$$\Rightarrow \quad p\Big(V_T, t_\text{off}-(k\Delta-\tau)\Big) \approx \frac{1}{\sqrt{2\pi D}}\exp\left[-\frac{\Big(V_T-\mu_\text{max}+(I_\text{E}-\mu_\text{max})\frac{k\Delta-\tau}{\tau_m}\Big)^2}{2D}\right]$$

The solution of Eq. (4.64) is then

$$\begin{aligned} \mu_\text{min} = {} & \underbrace{\mu_\text{max}\,\mathrm{e}^{-\Delta/\tau_m}}_{\text{initial condition}} + \underbrace{I_\text{E}(1-\mathrm{e}^{-\frac{\Delta}{\tau_m}})}_{\text{excitatory drive}} \\ & \underbrace{-\frac{1}{2}K\left[\operatorname{erf}(\phi(0)) - \operatorname{erf}(\phi(\Delta)) - \frac{K}{\sqrt{2\pi D}}\,\mathrm{e}^{-\frac{c}{2D}}\,\frac{\mathrm{e}^{\frac{\Delta}{\tau_m}}}{\sqrt{\mathrm{e}^{\frac{2\Delta}{\tau_m}}+1}}\Big[\operatorname{erf}(\psi(\Delta)) - \operatorname{erf}(\psi(0))\Big]\right]}_{\text{inhibitory feedback}} \end{aligned} \tag{4.66}$$

where:

$$\phi(t) = \frac{V_T-\mu_\text{max}+(I_\text{E}-\mu_\text{max})\frac{\Delta-t}{\tau_m}}{\sqrt{2D}} \tag{4.67}$$

$$\psi(t) = \frac{-(I_\text{E}-\mu_\text{max})\left(\mathrm{e}^{\frac{2\Delta}{\tau_m}}+1\right)(\tau_m+\Delta-t)+\tau_m(I_\text{E}-V_T)\left(\mathrm{e}^{\frac{\Delta}{\tau_m}}+1\right)}{\sqrt{2D\left(\mathrm{e}^{\frac{2\Delta}{\tau_m}}+1\right)}\tau_m} \tag{4.68}$$

$$c = \frac{(V_T-I_\text{E})^2\left(1-\mathrm{e}^{\frac{\Delta}{\tau_m}}\right)^2}{\mathrm{e}^{\frac{2\Delta}{\tau_m}}+1} \tag{4.69}$$

Although lengthy, this expression can be easily evaluated numerically.

With μ_{min} I have not only determined the mean membrane potential at the end of a cycle, but also at its beginning. Hence I can now approximate the length of the upstroke t_{off} as the time it takes for the mean membrane potential to rise from μ_{min} to μ_{max}, based on exponential relaxation towards only the *excitatory* drive I_{E} (A2):

$$t_{\mathrm{off}} \overset{\text{(A2)}}{\approx} \tau_m \ln\left(\frac{I_{\mathrm{E}} - \mu_{\mathrm{min}}}{I_{\mathrm{E}} - \mu_{\mathrm{max}}}\right) \tag{4.70}$$

Together with the assumed downstroke duration of Δ I arrive at an analytical estimate for the oscillation period T and hence the network frequency $f_{\mathrm{net}} = T^{-1} = (t_{\mathrm{off}} + \Delta)^{-1}$ (see Eq. (4.53)). Overall, I have derived an analytical mapping from the external drive to various features of the oscillatory dynamics:

$$I_{\mathrm{E}} \mapsto [\mu_{\mathrm{max}}, \mu_{\mathrm{min}}, t_{\mathrm{off}}, f_{\mathrm{net}}]$$

To evaluate the accuracy of the analytical approximation, the DDE is integrated numerically (Eq. (4.51), Fig. 4.23, green regime of period-1 oscillations) to determine μ_{max}, μ_{min} and f_{net}. I find that the errors introduced by the simplifying assumptions (A1)-(4.65) are small (Fig. 4.25, dashed lines vs square markers).

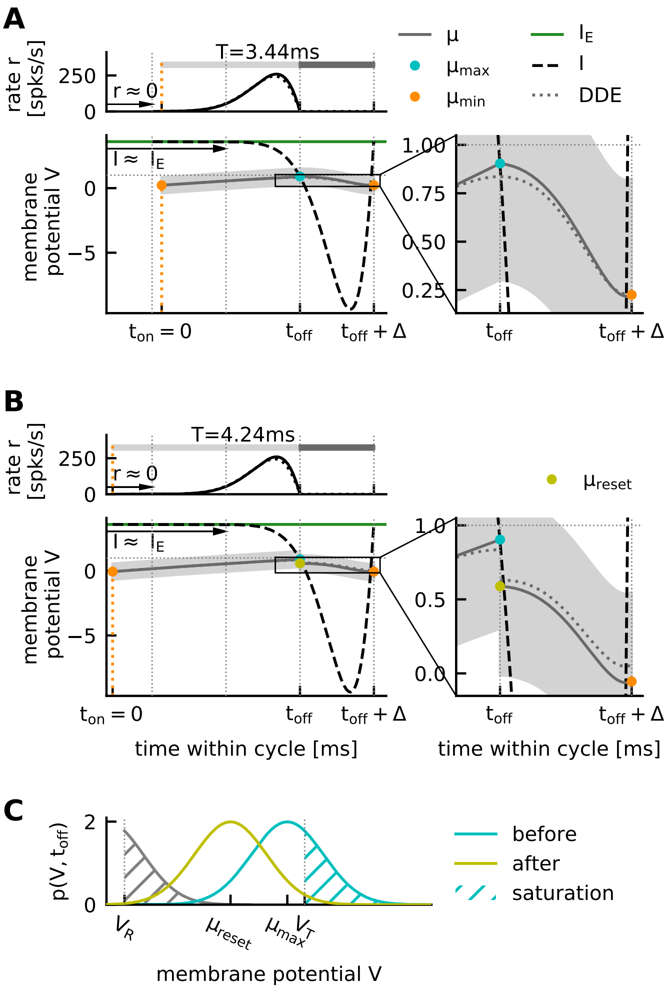

Figure 4.24: Illustration of analytical approximations. **A,** One cycle of the oscillatory solution of the DDE Eq. (4.51). Grey dotted lines: numerical solution for rate (top, Eq. (4.49)) and mean membrane potential (bottom, Eq. (4.51)). All other lines are analytical results (equation numbers in brackets): top: population rate $r(t)$ (black). Bottom: mean membrane potential $\mu(t)$ (gray, (A2), (4.59)), gray area marks $\mu(t) \pm 3\sqrt{D}$; external drive I_E (green); total input $I(t) = I_\mathrm{E} - I_\mathrm{I}(t)$ (black dashed line, (4.63)); local maximum μ_max (cyan, (4.58)); μ_min (orange, (4.66)); vertical lines mark end of population spike t_off, and intervals $t_\mathrm{off} + k\Delta$, $k \in \{-2, -1, 1\}$ before and after; arrows illustrate (A1); beginning of the cycle (orange dotted line, $t_\mathrm{on} = 0$) is determined by μ_min; grey horizontal bars mark upstroke and downstroke length, yielding a period of $t_\mathrm{off} + \Delta = T = 3.44$ms (4.70), so $f_\mathrm{net} = 291$ Hz (4.53). Zoom: Due to assumption (A2), μ_max is slightly overestimated. The true local minimum (2nd intersection of μ and I) occurs shortly *before* $t_\mathrm{off} + \Delta$ (see also Fig. 4.42). **B,** Same as A, but with an account for the reset on the population level. At the end of the population spike, μ is reset instantaneously from μ_max to μ_reset (yellow, Eq. (4.72)). This leads to a lower μ_min (orange, Eq. (4.73)) and hence a slightly longer period (T=4.24ms), i.e. slower network frequency ($f_\mathrm{net} = 235.8$Hz). **C,** Illustration of phenomenological reset. Cyan: density of membrane potentials $p(V, t_\mathrm{off})$ at the end of the population spike, centered at μ_max (before reset); cyan hatched area: fraction of active units (*saturation*, (4.71)); gray hatched area: resetting the superthreshold portion of p; yellow: $p(V, t_\mathrm{off})$ after reset, centered at μ_reset. The reset value μ_reset is calculated as the average of the density that results from summing the grey-dashed (active units), and cyan-non-hatched (silent units) density portions (4.72). Default parameters (see Table 4.3), $I_\mathrm{E} = 3.6$. See Supplementary Fig. 4.42 for the same figure with different parameter settings, for which the difference between μ_min and the true local minimum is more visible.

4.5.4.3 Accounting for the reset mechanism

To increase the quantitative accuracy of the drift-based approximation w.r.t. the original spiking network, I add a phenomenological account for the single unit fire-and-reset mechanism on the population level. During the population spike ($t < t_{\text{off}}$) the single unit reset has little influence on the population rate dynamics, since units typically spike at most once per cycle. At time t_{off} the population spike ends and the integral over the suprathreshold portion of the Gaussian potential density corresponds to the fraction of units that have spiked (the *saturation*):

$$s := \int_{V_T}^{\infty} p(v, t_{\text{off}})\, \mathrm{d}v \overset{(4.47)}{=} \frac{1}{2}\left(1 - \operatorname{erf}\left(\frac{V_T - \mu_{\max}}{\sqrt{2D}}\right)\right) \tag{4.71}$$

(see Fig. 4.24C, cyan hatched area). Taking into account the reset mechanism at this point would mean shifting the suprathreshold portion of $p(V, t_{\text{off}})$ downwards by an amount $V_T - V_R$ (Fig. 4.24C, gray hatched area), essentially splitting the voltage distribution into two pieces, corresponding to silent units (Fig. 4.24C, non-hatched area under cyan Gauss) and units that have spiked and been reset (Fig. 4.24C, gray hatched area). To preserve the simplified framework of a unimodal, Gaussian voltage distribution, I will instead assume that the Gaussian voltage distribution is reset as a whole, to a new mean membrane potential μ_{reset} given by the average of the two distribution pieces (“silent” and “spike+reset”):

$$\begin{aligned}
\mu_{\text{reset}} &:= \int_{-\infty}^{V_T} v p(v, t_{\text{off}})\, \mathrm{d}v + \int_{V_T}^{\infty} (v - (V_T - V_R)) p(v, t_{\text{off}})\, \mathrm{d}v \\
&= \int_{-\infty}^{\infty} v p(v, t_{\text{off}})\, \mathrm{d}v - (V_T - V_R) \int_{V_T}^{\infty} p(v, t_{\text{off}})\, \mathrm{d}v \\
&= \mu_{\max} - (V_T - V_R) s
\end{aligned} \tag{4.72}$$

(see Fig. 4.24C, yellow density). This phenomenological account for the reset contains the implicit assumption that inbetween population spikes the membrane potential distribution “spends enough time” subthreshold that the bimodality created by the reset mechanism vanishes due to diffusion and the distribution becomes roughly Gaussian again. This assumption is satisfied for a relatively large portion of the parameter space spanned by noise intensity, coupling strength, and reset potential (see Results).

The introduction of the population-reset requires an adjustment of the definition of $\mu_{\min}$ (Eq. (4.60)): Instead of using $\mu_{\max}$ as the initial value when integrating the feedback inhibition during the downstroke, I will now use the reset potential μ_{reset}:

$$\begin{aligned}
\mu_{\min} &= \mu(t_{\text{off}} + \Delta) \quad \text{given intial value } \mu(t_{\text{off}}) = \mu_{\text{reset}} \\
&\overset{(4.66)}{=} \underbrace{\mu_{\text{reset}}\, \mathrm{e}^{-\Delta/\tau_m}}_{\text{initial condition}} + \underbrace{I_{\mathrm{E}}(1 - \mathrm{e}^{-\frac{\Delta}{\tau_m}})}_{\text{excitatory drive}} \\
&\quad \underbrace{- \frac{1}{2} K \left[\operatorname{erf}(\phi(0)) - \operatorname{erf}(\phi(\Delta)) - \frac{K}{\sqrt{2\pi D}}\, \mathrm{e}^{-\frac{c}{2D}}\, \frac{\mathrm{e}^{\frac{\Delta}{\tau_m}}}{\sqrt{\mathrm{e}^{\frac{2\Delta}{\tau_m}} + 1}} \Big[\operatorname{erf}(\psi(\Delta)) - \operatorname{erf}(\psi(0)) \Big] \right]}_{\text{inhibitory feedback}}
\end{aligned} \tag{4.73}$$

Except for the initial condition term all other terms remain unchanged (cf. Eq. (4.66)). Since $\mu_{\mathrm{reset}} < \mu_{\mathrm{max}}$ (Eq. (4.72)), the introduction of the reset *de*creases the estimate of the local minimum μ_{min}. This leads to an *in*crease of the upstroke time t_{off} required for the mean membrane potential to rise from μ_{min} to μ_{max} (Eq. (4.70)), and hence to an increase in the overall period $T = t_{\mathrm{off}} + \Delta$, corresponding to a *de*crease in the network frequency (Eq. (4.53), see Fig. 4.25, solid vs. dashed lines).

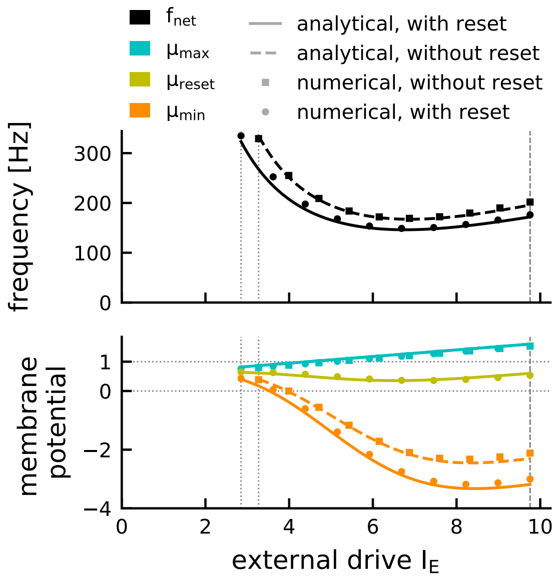

Figure 4.25: Analytical vs numerical analysis of the drift-based approximation. Network frequency (top) and dynamics of the mean membrane potential for different levels of external drive I_{E}, calculated with or without reset (yellow: μ_{reset}). Analytical approximations (lines) are very close to the results of numerical integration of the DDE (4.51) (markers). Including the reset does not affect μ_{max} but decreases μ_{min} (Eq. (4.73) vs (4.66)) and thus the network frequency. Results are shown in the relevant range of drives $[I_{\mathrm{E}}^{\mathrm{min}}, I_{\mathrm{E}}^{\mathrm{full}}]$ (dotted and dashed vertical lines). Parameters see Table 4.3.

4.5.4.4 The point of full synchrony

The drift-based approximation allows for a straightforward prediction of the point of full synchrony and its parameter dependencies. As mentioned before, the integral over the suprathreshold-portion of the membrane potential density at the end of the population spike corresponds to the fraction s of active units (*saturation*, Eq. (4.71), see Fig. 4.24C). Strictly speaking, full synchrony would correspond to

$$s = \int_{V_T}^{\infty} p(V, t_{\mathrm{off}})\, \mathrm{d}V = 1$$

which obviously can never be true, since the Gaussian probability density approaches zero only in the limit $V \to \pm\infty$. We can however define approximate full synchrony as the state where the spike threshold marks the 0.13th percentile of the membrane potential distribution at the end of the population spike, *i.e.* ~99.87% of the neurons have fired:

$$s = \int_{V_T}^{\infty} p(V, t_{\mathrm{off}})\, \mathrm{d}V = 0.9987 \quad \Leftrightarrow \quad \mu_{\mathrm{max}} - 3\sqrt{D} = V_T$$

Having derived $\mu_{\mathrm{max}}(I_{\mathrm{E}})$ as a function of the external drive (Eq. (4.58)), it is straightforward to derive a closed-form expression for the external drive that is required to achieve full synchrony:

$$I_{\mathrm{E}}^{\mathrm{full}} = V_T + \sqrt{D}\frac{3 + \mathrm{e}^{-\Delta/\tau_m}\sqrt{2\ln\left[\frac{K}{\sqrt{2\pi D}}\,\mathrm{e}^{\Delta/\tau_m}\right]}}{1 - \mathrm{e}^{-\Delta/\tau_m}} \; . \tag{4.74}$$

4.5.4.5 Range of applicability of the drift-based approximation

There are two main constraints on the applicability of the drift-based approximation: (a) Since I assume that units spike at most once per cycle, the theory is only valid up to the point of full synchrony $I_{\mathrm{E}}^{\mathrm{full}}$ where network frequency and mean unit firing rate coincide. (b) The assumption of a unimodal distribution of membrane potentials is only valid if, inbetween population spikes, the bulk of the membrane potential distribution is pushed sufficiently below threshold such that it can diffuse back to approximately Gaussian shape. I will thus require that, at its lowest point, the Gaussian density is almost entirely subthreshold:

$$\int_{-\infty}^{V_T} p(V, t_{\mathrm{on}})\,\mathrm{d}V = 0.9987 \quad \Leftrightarrow \quad \mu_{\min}(I_{\mathrm{E}}) + 3\sqrt{D} \overset{!}{\leq} V_T \tag{4.75}$$

Criteria (a) and (b) yield a finite range $[I_{\mathrm{E}}^{\min}, I_{\mathrm{E}}^{\max}]$ of external drives for which the theory applies. Since for most parameter settings $\mu_{\min}$ is an almost monotonically decaying function of the drive (see Fig. 4.25, Fig. 4.27), constraint (b) is usually only relevant for the lower boundary $I_{\mathrm{E}}^{\min}$ of the drive, while the upper boundary is determined by constraint (a): $I_{\mathrm{E}}^{\max} = I_{\mathrm{E}}^{\mathrm{full}}$ (Fig. 4.25, see Fig. 4.27D for exceptions at high noise and weak coupling).

4.5.4.6 Quantifying performance

For a given parameter setting (D, Δ, K, V_R) I quantify the performance of the drift-based approximation across the range of drives for which

(a) the theory applies ($I_{\mathrm{E}} \in [I_{\mathrm{E}}^{\min}, I_{\mathrm{E}}^{\max}]$)

(b) the spiking network has not crossed the point of full synchrony ($I_{\mathrm{E}} \leq I_{\mathrm{E}}^{\mathrm{full,sim}}$)

The size of this regime varies for different parameter settings (see Fig. 4.27). To ensure comparability I interpolate the results of all spiking network simulations to the same fine resolution:

$$I_{\mathrm{E}}^{i} = I_{\mathrm{E}}^{\min} + 0.1i \quad i = 1, 2, \ldots\, n, \qquad , \qquad I_{\mathrm{E}}^{i} \in \left[I_{\mathrm{E}}^{\min}, \min\left(I_{\mathrm{E}}^{\max}, I_{\mathrm{E}}^{\mathrm{full,sim}}\right)\right] \; .$$

I then compute the average relative error of the estimated network frequencies for each parameter setting:

$$\chi_{\mathrm{err}} := \frac{1}{n}\sum_{i} \frac{\left|f_{\mathrm{net}}^{\mathrm{sim}}(I_{\mathrm{E}}^{i}) - f_{\mathrm{net}}^{\mathrm{theory}}(I_{\mathrm{E}}^{i})\right|}{f_{\mathrm{net}}^{\mathrm{sim}}(I_{\mathrm{E}}^{i})} \quad \in [0, 1] \; . \tag{4.76}$$

A second score is introduced to quantify what portion of the relevant range of spiking network dynamics (from the Hopf bifurcation $I_{\mathrm{E}}^{\mathrm{crit,sim}}$, to the point of full synchrony $I_{\mathrm{E}}^{\mathrm{full,sim}}$) is covered by the theory:

$$\chi_{\mathrm{appl}} := \frac{\min\left(I_{\mathrm{E}}^{\max}, I_{\mathrm{E}}^{\mathrm{full,sim}}\right) - I_{\mathrm{E}}^{\min}}{I_{\mathrm{E}}^{\mathrm{full,sim}} - I_{\mathrm{E}}^{\mathrm{crit,sim}}} \quad \in [0,1] \tag{4.77}$$

I define an overall performance index as

$$\chi_{\mathrm{p}} := \chi_{\mathrm{appl}}\left(1 - \chi_{\mathrm{err}}\right) \; \in [0,1] \; . \tag{4.78}$$

The larger the performance index χ_{p} the better the drift-based approximation captures the spiking network dynamics.

4.5.5 Analytical approximation of drift-based oscillations for linear drive

To characterize the transient dynamics of a cycle i with initial mean membrane potential $\mu_{\min}^{i}$ and linear drive $I_{\mathrm{E}}(t) = \hat{I}_{\mathrm{E}} + m(t - t_{\mathrm{off}}^{i})$ I deriving a mapping

$$\left(\hat{I}_{\mathrm{E}}^{i}, \mu_{\min}^{i}, m\right) \longmapsto \left(f_{\mathrm{net}}^{\mathrm{inst,i}}, t_{\mathrm{off}}^{i}, \mu_{\max}^{i}, \mu_{\mathrm{reset}}^{i}, \mu_{\min}^{i+1}\right) \; . \tag{4.79}$$

(see Fig. 4.26, 3 inputs in blue, outputs in black/gray). Here $\mu_{\min}^{i+1}$ refers to the mean membrane potential reached at the end of cycle i, which potentially serves as the initial condition for the next cycle.

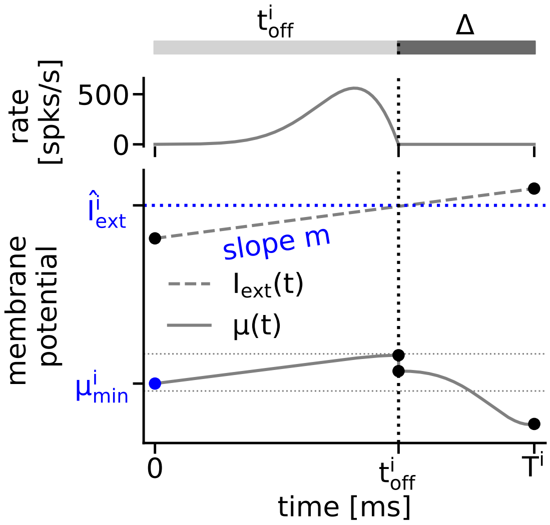

Figure 4.26: Sketch of drift-based approximation for linear drive. One hypothetical oscillation cycle i under linear drive $I_{\mathrm{E}}(t) = m(t - t_{\mathrm{off}}^{i}) + \hat{I}_{\mathrm{E}}$. Blue: the known "inputs": initial membrane potential $\mu_{\min}^{i}$, slope of the linear drive m, and one value of the drive during the cycle, here chosen as $\hat{I}_{\mathrm{E}} = I_{\mathrm{E}}(t_{\mathrm{off}}^{i})$. Note that the *time* t_{off}^{i} between the yet undefined time 0 and the end of the population spike is not known, but will be one of the *results* of the mapping. All "unknown" quantities are marked in black/grey and will be the result of the analytical approximation for piecewise linear drive.

4.5.5.1 Step 1: approximating $\mu_{\max}$

The local maximum of the mean membrane potential $\mu^i_{\max}$ can be found with the same ansatz used for constant drive:

$$\begin{aligned}
0 = \dot{\mu}(t^i_{\text{off}}) &= \frac{1}{\tau_m}\Big(I(t^i_{\text{off}}) - \mu(t^i_{\text{off}})\Big) = \frac{1}{\tau_m}\Big(\hat{I}^i_{\text{E}} - K\tau_m r(t^i_{\text{off}} - \Delta) - \mu_{\max}\Big) \\
&\overset{(4.49)}{=} \frac{1}{\tau_m}\Big(\hat{I}^i_{\text{E}} - \mu_{\max} - K\tau_m \left[\dot{\mu}(t^i_{\text{off}} - \Delta)\right]_+ p(V_T, t^i_{\text{off}} - \Delta)\Big) \\
&\overset{(4.44)}{=} \frac{1}{\tau_m}\Big(\hat{I}^i_{\text{E}} - \mu_{\max} \\
&\quad - K\Big[I_{\text{E}}(t^i_{\text{off}} - \Delta) - K\tau_m \underbrace{r(t^i_{\text{off}} - 2\Delta)}_{\approx 0,\ (\text{A1})} - \mu(t^i_{\text{off}} - \Delta)\Big]_+ p(V_T, t^i_{\text{off}} - \Delta)\Big)
\end{aligned}$$

Again, the recurrent expression for the total current I is truncated two Δ-time windows before the end of the population spike (A1):

$$\overset{(\text{A1})}{\approx} \frac{1}{\tau_m}\Big(\hat{I}^i_{\text{E}} - \mu_{\max} - K\left(\hat{I}^i_{\text{E}} - m\Delta - \mu(t^i_{\text{off}} - \Delta)\right) p(V_T, t^i_{\text{off}} - \Delta)\Big) \ . \tag{4.80}$$

Again, the trajectory of μ during the upstroke is approximated based on relaxation towards only the excitatory drive, which is now a linear function of time (cf. (A2)):

$$\begin{aligned}
\mu(t) &\overset{(4.44)}{\approx} \mu^i_{\min}\, e^{-t/\tau_m} + \frac{1}{\tau_m}\int_0^t e^{-(t-\bar{t})/\tau_m}\, I_{\text{E}}(\bar{t})\, d\bar{t} \\
&= \mu^i_{\min}\, e^{-t/\tau_m} + mt + (I_{\text{E}}(0) - m\tau_m)\left[1 - e^{-t/\tau_m}\right] \\
&= I_{\text{E}}(t) - m\tau_m + \Big(m\tau_m + \mu^i_{\min} - I_{\text{E}}(0)\Big)\, e^{-t/\tau_m}
\end{aligned} \tag{4.81}$$

Under this approximation $\mu_{\max}$ can be written as

$$\mu_{\max} = \mu(t^i_{\text{off}}) \overset{(4.81)}{\approx} \hat{I}^i_{\text{E}} - m\tau_m + \Big(m\tau_m + \mu^i_{\min} - I_{\text{E}}(0)\Big)\, e^{-t^i_{\text{off}}/\tau_m} \tag{4.82}$$

and the trajectory before time t^i_{off} is approximated linearly as:

$$\begin{aligned}
\mu(t^i_{\text{off}} - x) &\overset{(4.81)}{=} I_{\text{E}}(t^i_{\text{off}} - x) - m\tau_m + \Big(m\tau_m + \mu^i_{\min} - I_{\text{E}}(0)\Big)\, e^{-(t^i_{\text{off}} - x)/\tau_m}\,, \qquad (x \geq 0) \\
&\overset{(4.82)}{=} \Big(\mu_{\max} - \hat{I}^i_{\text{E}} + m\tau_m\Big)\, e^{x/\tau_m} + \underbrace{I_{\text{E}}(t^i_{\text{off}} - x)}_{=\hat{I}^i_{\text{E}} - mx} - m\tau_m \\
&= \mu_{\max}\, e^{x/\tau_m} + \Big(1 - e^{x/\tau_m}\Big)\,\hat{I}^i_{\text{E}} + \underbrace{m\tau_m\, e^{x/\tau_m}}_{\approx m\tau_m\left(1 + \frac{x}{\tau_m}\right)} - mx - m\tau_m \\
&\approx \mu_{\max}\, e^{x/\tau_m} + \Big(1 - e^{x/\tau_m}\Big)\,\hat{I}^i_{\text{E}} \ .
\end{aligned} \tag{4.83}$$

Inserting this expression in the local maximum condition (Eq. (4.80)) yields:

$$\begin{aligned} 0 &\approx \hat{I}_{\mathrm{E}}^{i} - \mu_{\max} - K\left(\hat{I}_{\mathrm{E}}^{i} - m\Delta - \left(\mu_{\max}\,\mathrm{e}^{\Delta/\tau_m} + \left(1-\mathrm{e}^{\Delta/\tau_m}\right)\hat{I}_{\mathrm{E}}^{i}\right)\right) p(V_T, t_{\mathrm{off}}^{i}-\Delta) \\ &= \hat{I}_{\mathrm{E}}^{i} - \mu_{\max} - K\left(\left(\hat{I}_{\mathrm{E}}^{i} - \mu_{\max}\right)\mathrm{e}^{\Delta/\tau_m} - m\Delta\right) p(V_T, t_{\mathrm{off}}^{i}-\Delta) \\ &= \hat{I}_{\mathrm{E}}^{i} - \mu_{\max} - K(\hat{I}_{\mathrm{E}}^{i} - \mu_{\max})\,\mathrm{e}^{\Delta/\tau_m} p(V_T, t_{\mathrm{off}}^{i}-\Delta) + Km\Delta p(V_T, t_{\mathrm{off}}^{i}-\Delta) \\ \Leftrightarrow \quad \frac{m\Delta K p(V_T, t_{\mathrm{off}}^{i}-\Delta)}{\hat{I}_{\mathrm{E}}^{i} - \mu_{\max}} &= K\,\mathrm{e}^{\Delta/\tau_m} p(V_T, t_{\mathrm{off}}^{i}-\Delta) - 1 \end{aligned} \tag{4.84}$$

For constant drive ($m = 0,\ I_{\mathrm{E}}(t) \equiv \hat{I}_{\mathrm{E}}$) the left-hand side of Eq. (4.84) becomes zero and we recover Eq. (4.57). For $m \neq 0$ Eq. (4.84) can be solved numerically and its solution $\mu_{\max}$ is close to the asymptotic $\mu_{\max}^{\infty}(\hat{I}_{\mathrm{E}}^{i})$ (see Appendix Section 4.C.1, Fig. 4.40). Since the reset mechanism remains unchanged (Eq. (4.72)), this implies that also μ_{reset}^{i} is close to $\mu_{\mathrm{reset}}^{\infty}(\hat{I}_{\mathrm{E}})$.

The duration of the upstroke t_{off}^{i} is inferred as the time it takes for the mean membrane potential to travel from $\mu_{\min}^{i}$ to $\mu_{\max}^{i}$, again ignoring inhibition and only considering exponential relaxation towards the external drive (Eq. (4.82)):

$$\mu(t_{\mathrm{off}}^{i}) \stackrel{!}{=} \mu_{\max}^{i} \quad \stackrel{(4.44)}{\Leftrightarrow} \quad t_{\mathrm{off}}^{i} = \tau_m \ln\left[\frac{\hat{I}_{\mathrm{E}}^{i} - m\tau_m - \mu_{\min}^{i} - m t_{\mathrm{off}}^{i}}{\hat{I}_{\mathrm{E}}^{i} - m\tau_m - \mu_{\max}^{i}}\right]$$

For $m = 0$ we recover Eq. (4.70), for $m \neq 0$ we get:

$$t_{\mathrm{off}}^{i} = -\tau_m\,\mathrm{W}\left(\frac{\hat{I}_{\mathrm{E}}^{i} - m\tau_m - \mu_{\max}^{i}}{m\tau_m}\exp\left(-1 + \frac{\hat{I}_{\mathrm{E}}^{i} - \mu_{\min}^{i}}{m\tau_m}\right)\right) + \frac{\hat{I}_{\mathrm{E}}^{i} - m\tau_m - \mu_{\min}^{i}}{m} \tag{4.85}$$

where W is the Lambert W function, which has solutions for arguments $> -\exp(-1)$. For positive slope $m > 0$ and low drive ($\hat{I}_{\mathrm{E}}^{i} - \mu_{\max}^{i} < m\tau_m$) this introduces a constraint on the initial value:

$$\mu_{\min}^{i} \stackrel{!}{>} \hat{I}_{\mathrm{E}}^{i} - m\tau_m \log\left(-\frac{m\tau_m}{\hat{I}_{\mathrm{E}}^{i} - m\tau_m - \mu_{\max}^{i}}\right) . \tag{4.86}$$

(seen in Fig. 4.10B, Fig. 4.11Ai, detailed derivation in Appendix Section 4.C.2). The instantaneous frequency of cycle i follows as

$$f_{\mathrm{net}}^{\mathrm{inst,i}} = \left(t_{\mathrm{off}}^{i} + \Delta\right)^{-1} . \tag{4.87}$$

4.5.5.2 Step 2: approximating $\mu_{\min}$

The mean membrane potential $\mu_{\min}^{i+1}$ at the end of cycle i is found by integrating the total current I during the downstroke (cf. Eq. (4.60)):

$$\mu_{\min}^{i+1} = \mu_{\mathrm{reset}}^{i}\,\mathrm{e}^{-\Delta/\tau_m} + \frac{1}{\tau_m}\int_0^{\Delta} I(s + t_{\mathrm{off}}^{i})\,\mathrm{e}^{-(\Delta-s)/\tau_m}\,\mathrm{d}s \tag{4.88}$$

The total current I can be split into two parts: I^{stat}, which is approximately equal to the feedback current for constant drive $I_{\text{E}} \equiv \hat{I}_{\text{E}}$ (Eq. (4.62), except for slight deviations in μ^i_{max}), and an additive new term I^m caused by the linear change in the external drive:

$$\begin{aligned} I(t+t^i_{\text{off}}) &= I^{\text{stat}}(t+t^i_{\text{off}}) + I^m(t+t^i_{\text{off}}) \\ I^{\text{stat}}(t+t^i_{\text{off}}) &= \hat{I}_{\text{E}} - Kp(V_T, t^i_{\text{off}} - (\Delta - t))\left(\hat{I}_{\text{E}} - \mu^i_{\text{max}}\right) \mathrm{e}^{(\Delta-t)/\tau_m} \\ &\quad + K^2 p(V_T, t^i_{\text{off}} - (\Delta - t)) p(V_T, t^i_{\text{off}} - (2\Delta - t))\left(\hat{I}_{\text{E}} - \mu^i_{\text{max}}\right) \mathrm{e}^{(2\Delta-t)/\tau_m} \\ I^m(t+t^i_{\text{off}}) &= m\Big(t + Kp(V_T, t^i_{\text{off}} - (\Delta - t))(\Delta - t) \\ &\quad - K^2 p(V_T, t^i_{\text{off}} - (\Delta - t)) p(V_T, t^i_{\text{off}} - (2\Delta - t))(2\Delta - t)\Big) \end{aligned} \tag{4.89}$$

(see derivation in Appendix Section 4.C.3). Eq. (4.88) can be integrated numerically to find that μ^{i+1}_{min} is close to the asymptotic solution for constant drive:

$$\mu^{i+1}_{\text{min}} \begin{cases} \gtrapprox \mu_{\text{min}}(\hat{I}_{\text{E}}), & m > 0 \\ \lessapprox \mu_{\text{min}}(\hat{I}_{\text{E}}), & m < 0 \end{cases} \tag{4.90}$$

The mean membrane potential μ^{i+1}_{min} at the end of cycle i would be the initial mean membrane potential for the next cycle, but does not influence the estimate of the current cycle's period $T^i = t^i_{\text{off}} + \Delta$.

Note that the transient mapping (Eq. (4.79)) can*not* be applied iteratively to infer the mean membrane potential trajectories over *multiple, consecutive* cycles under linear drive of slope m. For every cycle, an assumption has to be made about the reference drive $\hat{I}^i_{\text{E}}$ at the end of the population spike t^i_{off}, which is not known *a priori* (see Fig. 4.26, blue inputs vs black outputs of the mapping).

One could easily derive a forward mapping by anchoring the reference drive to the *beginning* of the cycle ($\hat{I}^i_{\text{E}} = I_{\text{E}}(0)$) and following the same steps as above:

$$\left(\hat{I}^i_{\text{E}}, \mu^i_{\text{min}}, m\right) \longmapsto \left(f^{\text{inst,i}}_{\text{net}}, t^i_{\text{off}}, \mu^i_{\text{max}}, \mu^i_{\text{reset}}, \mu^{i+1}_{\text{min}}, \hat{I}^{i+1}_{\text{E}}\right) \ . \tag{4.91}$$

(derivation not shown here). I chose to present here the mapping for reference drive $\hat{I}^i_{\text{E}} = I_{\text{E}}(t^i_{\text{off}})$, since the drive at time t^i_{off} is a better representative of the range of drives $[I_{\text{E}}(0), I_{\text{E}}(T)]$ covered in a cycle, than the (minimal/maximal) drive at the beginning.

4.5.5.3 Comparing theory and simulation for piecewise linear drive

Since the theory provides a cycle-wise estimate of the instantaneous network frequency, I also use a discrete estimate of instantaneous frequency for the simulation results, based on the inverse of the distances between consecutive peaks in the oscillatory population rate (see Methods Section 4.5.1.6). In the spiking network, SPW-like drive is modeled as a piecewise linear double-ramp with an intermediate plateau phase of 20 ms (Eq. (4.22)). The drift-based approximation is used to estimate the instantaneous network frequencies separately for the upstroke of the drive (linear increase with slope $m > 0$) and the downstroke of the drive (linear decrease with slope $m < 0$). The plateau phase is ignored, since the network frequencies rapidly converge to the asymptotic frequency associated to the drive during the plateau phase. In both simulation and theory IFA is quantified by computing a linear regression slope over the instantaneous frequencies. The theoretically estimated instantaneous frequencies are shifted in time to account for a hypothetical plateau phase of 20 ms inbetween up- and downstroke and allow full comparability with the simulation results.

For every theoretical instantaneous frequency estimate $(t_i, f^{\text{inst}}_{\text{theory}}(t_i))$ an error is calculated compared to the average instantaneous frequencies observed in the spiking simulation around the same time point ($t_i \pm 1.5$ ms):

$$\begin{aligned} f^{\text{inst}}_{\text{sim}}(t_i) &\approx \left\langle \{f^{\text{inst}}_{\text{sim}}(t)\}_{t\in[t_i-1.5,t_i+1.5]} \right\rangle \\ \epsilon &:= \frac{1}{n}\sum_i \frac{\left| f^{\text{inst}}_{\text{theory}}(t_i) - f^{\text{inst}}_{\text{sim}}(t_i) \right|}{f^{\text{inst}}_{\text{sim}}(t_i)} \qquad \in [0,1] \end{aligned} \tag{4.92}$$

(see Table 4.1).

4.A Parameter-dependencies of drift-based oscillation dynamics

In this section I confirm with numerical simulations that the drift-based approximation works for a wide parameter regime and captures the parameter dependencies of ripple oscillation in the spiking network. The reduced spiking network model (Eq. (4.3)) has only four parameters: the noise intensity D, the inhibitory coupling strength K, the synaptic delay Δ, and the reset potential V_R. Since time can be rescaled to units of the membrane time constant, I do not count the membrane time constant as an independent parameter. I will first show a two-dimensional parameter exploration covarying the noise intensity D and the inhibitory coupling strength K (Fig. 4.27). Subsequently I will briefly comment on the role of the synaptic delay and the reset potential.

4.A.1 The role of noise and coupling strength

To quantify the performance of the drift-based approximation, a performance index is introduced that takes into account the error in the estimate of the network frequency and the proportion of the relevant range of external drives (from the Hopf bifurcation up to the point of full synchrony) that is covered by the theory (Methods, Fig. 4.27B).

The performance of the drift-based approximation is good for a wide range of parameters (Fig. 4.27B). As expected from a drift-based approximation, the performance decreases for larger noise intensity (Fig. 4.27, large $\sqrt{D}$). At high noise and weak coupling, the range of external drives, for which the theory applies, decreases markedly. The wider the Gaussian density and the weaker the inhibitory feedback, the harder it is to satisfy requirement (b) of the bulk of the membrane potential density being pushed subthreshold inbetween population spikes (Fig. 4.27D). In the extreme case of $\sqrt{D} = 0.4,\ K = 2$ this criterion is never fulfilled (Fig. 4.27B-D, bottom right). Capturing the network dynamics in the high noise regime would require taking into account diffusion-mediated spiking.

Figure 4.27: Performance of drift-based approximation depending on noise and coupling strength. Covariation of noise intensity D and coupling strength K. **A,** Width of the Gaussian voltage density $p(V,t)$ depending on noise D. **B,** Evaluation of drift-based approximation of spiking network dynamics for different parameter combinations $\sqrt{D}, K$ shown in C. Left to right: error in network frequency approximation, applicability of the approximation, and resulting performance index (Eq. (4.78)). **C,** Network frequencies (black) and unit firing rates (blue) in theory (line) and simulation (markers). Red markers: Hopf bifurcation. Blue triangle: point of full synchrony in simulation. All theory curves shown for range $[I_\mathrm{E}^\mathrm{min}, I_\mathrm{E}^\mathrm{max}]$ (see Methods Section 4.5.4.5). **D,** Local extrema $\mu_\mathrm{max}, \mu_\mathrm{min}$, and reset μ_reset of the mean membrane potential. Full colored lines: theory applies ($I_\mathrm{E} \in [I_\mathrm{E}^\mathrm{min}, I_\mathrm{E}^\mathrm{full}]$); dashed colored lines: theory does not apply. Orange markers: estimate of μ_min in simulation ($\mu_\mathrm{max}, \mu_\mathrm{reset}$ have no counterpart in the spiking network). Note that μ_min is an almost monotonically decaying function of the drive for most parameter settings, except for very weak coupling.

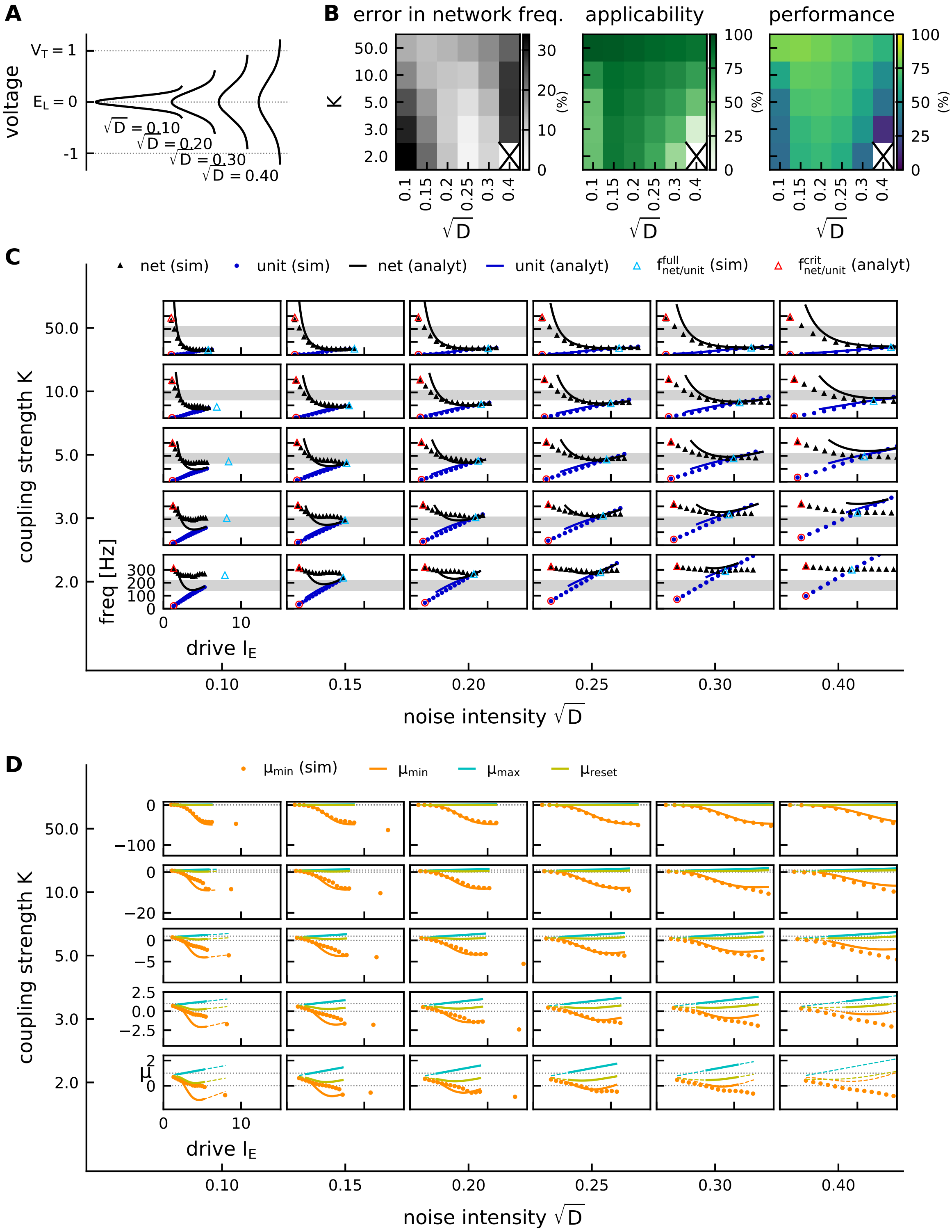

Figure 4.27: Performance of drift-based approximation depending on noise and coupling strength. Caption on previous page.

One can also observe a dip in performance for low noise and low coupling strength (Fig. 4.27B-D, bottom left). This, however, does not reflect a shortcoming of the drift-based approximation but rather a change of dynamics in the spiking network towards clustered activity, which is not our regime of interest. In Section 4.A.2 I will demonstrate how the emergence of clusters is mediated by a third parameter — the reset potential — and how a change in reset potential can recover high performance of the drift-based approximation, also at low noise and low coupling.

The point of full synchrony is predicted well for most parameter combinations shown in Fig. 4.27C. I evaluated its parameter dependencies in more detail in Fig. 4.28: while *quantitatively* the theoretical estimate produces an error that becomes larger for stronger noise (error shown in Fig. 4.28), the *qualitative* dependency of the point of full synchrony on the noise and coupling strength is captured well (Fig. 4.28, theory vs simulation). The theory predicts that stronger external drive is required to achieve full synchrony, if the noise is stronger, which is confirmed in simulations (Fig. 4.28 bottom). A similar, albeit weaker, dependence can be found for the inhibitory coupling strength: If the network is coupled more strongly, stronger external drive is required to achieve full synchrony.

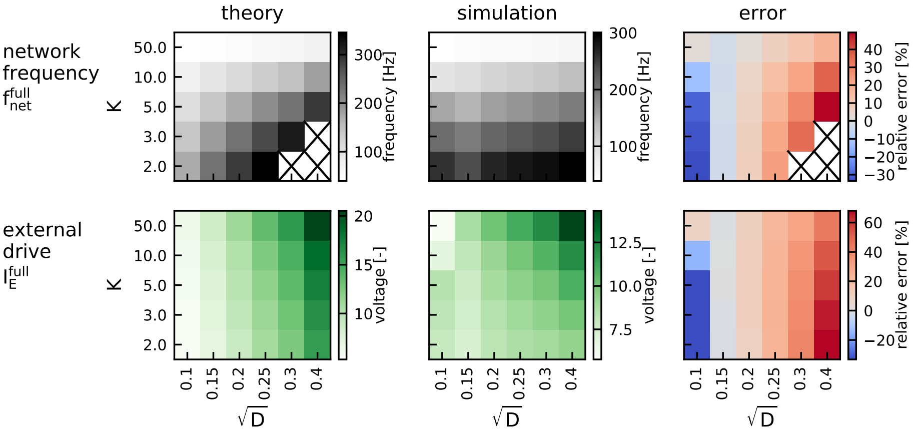

Figure 4.28: Parameter dependencies of the point of full synchrony. External drive I_E^{full} at which full synchrony is reached (bottom) and the corresponding network frequency $f_{\text{net}}^{\text{full}}$ (top), as predicted by theory (left, Eq.(4.74)) vs. as observed in spiking network simulation (middle). The right panel shows the relative deviation of the theoretical prediction from the simulation result. Same parameter exploration as in Fig. 4.27. Crosses mark the parameter settings for which the point of full synchrony lies outside the regime of applicability of the theory ($I_E^{\text{full}} > I_E^{\text{max}}$, cf. Fig. 4.27D).

Fig. 4.34 shows the same parameter exploration as Fig. 4.27C, including a *numerical* estimate of the oscillation dynamics under the drift-based approximation, derived from numerical integration of the DDE (4.51) (magenta lines). The analytical estimates are close to the numerical results for all parameter combinations (magenta vs black/blue lines). This confirms that the observed differences between drift-based approximation and spiking network dynamics (markers) are indeed due to the conceptual simplifications (neglecting diffusion-mediated spiking and the single-unit reset), and not to errors introduced by the analytical approximations in Methods Section 4.5.4.

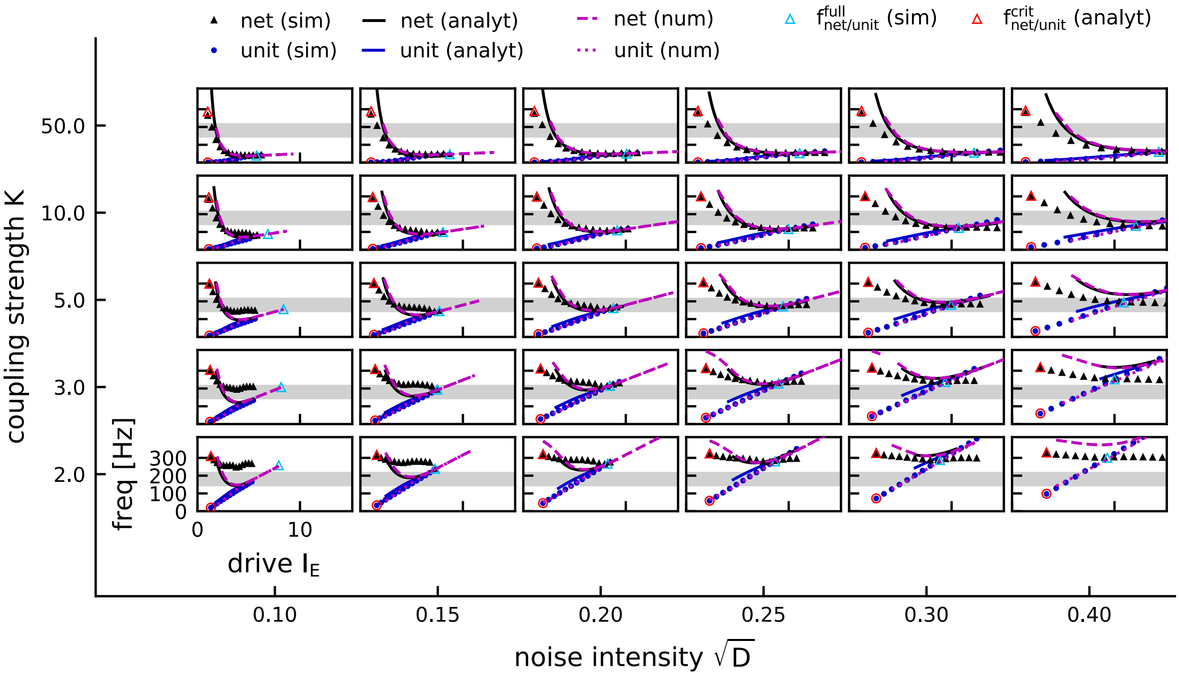

Figure 4.29: Performance of drift-based approximation — analytical vs numerical solution. Same as Fig. 4.27C, but incl. numerical evaluation of the drift-based approximation (magenta lines, dashed: network frequency, dotted: unit firing rate). The error introduced by the heuristic approximations in the analytical expressions (solid black, blue lines), compared to the numerical evaluation of DDE (4.51) is small.

4.A.2 The role of the reset potential

What about the remaining two parameters, the synaptic delay Δ and the reset potential V_R? Let's revisit the low performance region observed above for low noise and low coupling strength (Fig. 4.27B-D bottom left). In the above parameter exploration the reset potential was fixed to its default value $V_R = 0$, *i.e.* $V_{\text{reset}} = -65$ mV. If the noise is very low relative to the distance between threshold and reset, the portion of active units in a given cycle is reset far below the portion of silent units, which remain just below threshold. If, in addition, the synaptic coupling is also weak, these disjoint pieces will not merge back together before the previously silent portion hits the threshold and starts the next population spike. This leads to a membrane potential distribution that is multimodal at all times, since units that have spiked in one cycle are less likely to spike in the next (Fig. 4.30). Such a “clustered” activity does not correspond to our regime of interest and cannot be captured by the drift-based approximation, hence the low performance index in (Fig. 4.27B, bottom left). The unimodality of the membrane potential density can be restored by either increasing the reset potential (Fig. 4.31) or the inhibitory coupling strength, in which case the drift-based approximation performs well also at low noise (Fig. 4.32). As long as approximate unimodality is ensured, the reset potential does not influence the performance of the approximation much.

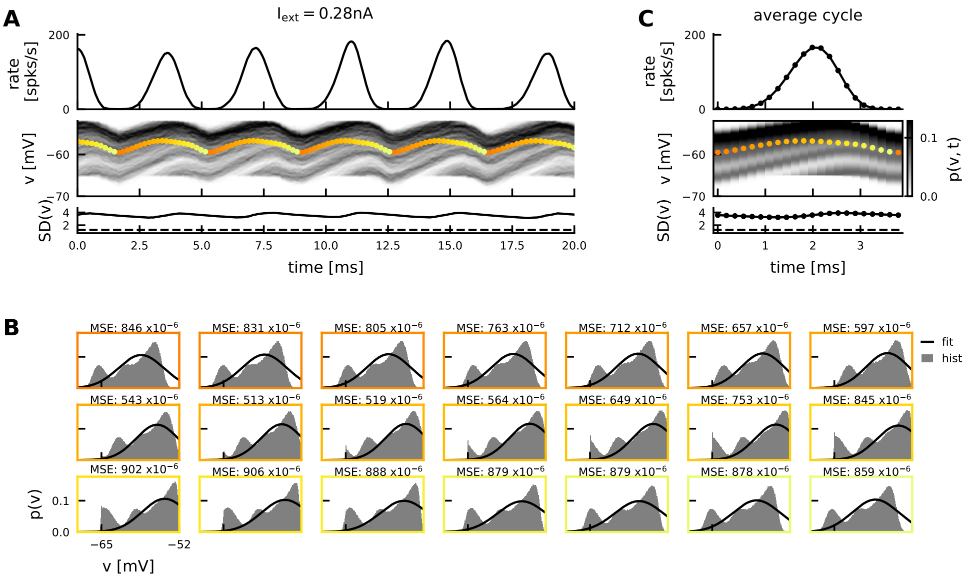

Figure 4.30: Multimodal membrane potential density for low noise, weak coupling, low reset potential. A, Spiking network simulation for $\sqrt{D} = 0.1, K = 2, V_R = 0, I_{\text{ext}} = 0.28$ nA, $N = 1000$, otherwise default parameters (Table 4.3). Top: population rate; middle: density of membrane potentials; bottom: standard deviation of membrane potentials, dashed line: theoretical asymptote $\sqrt{D}$ without boundary conditions. **B,** Snapshots of average density of membrane potentials $p(v, t)$ over the course of a cycle (see color code in A). The density is multimodal at all times: a Gaussian approximation (black line) is never a good fit. **C,** Average cycle dynamics.

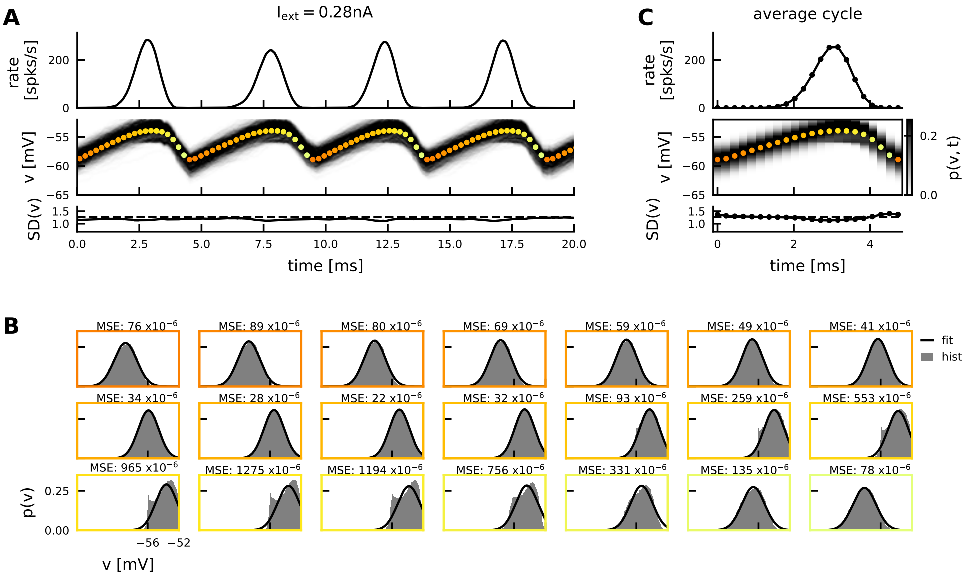

Figure 4.31: Unimodal membrane potential density for low noise, weak coupling, and increased reset potential. Same parameters and outline as Fig. 4.30, but with increased reset potential $V_R = 0.7$ ($V_{\text{reset}} = -56$ mV).

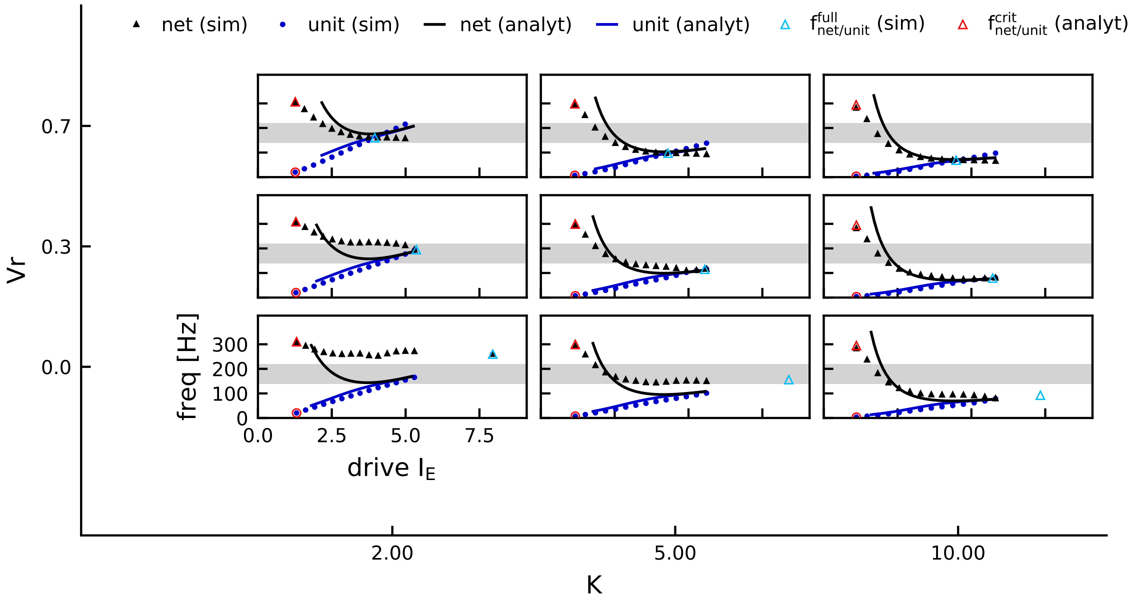

Figure 4.32: Drift-based approximation at low noise, depending on coupling strength and reset potential. Same outline as Fig. 4.27C. Bottom left: Same network configuration as bottom left in Fig. 4.27C: weak noise ($\sqrt{D} = 0.1$) and weak coupling ($K = 2$), otherwise default parameters (Table 4.3). Increasing either the reset potential V_R (vertical axis) or the coupling strength K (horizontal axis) enhances the fit between the drift-based approximation and the spiking network simulations. It is mainly the simulated network dynamics that changes qualitatively (see black triangles), due to a decrease of the reset-induced multimodality of the membrane potential density (see examples shown in Fig. 4.30 vs Fig. 4.31 for increasing V_R).

4.A.3 The role of the synaptic delay

I covaried the synaptic delay ($\Delta \in [0.5, 2]$ ms) with either the noise intensity or the coupling strength (Fig. 4.33, 4.33). The performance of the drift-based approximation is largely unaffected by the synaptic delay, which merely shifts the overall network frequencies to higher or lower values as predicted by Brunel and Hakim (1999).

Figure 4.33: Performance of drift-based approximation depending on synaptic delay and coupling strength. Same outline as Fig. 4.27. Covariation of K (vertical axis) and Δ (horizontal axis), all other parameters are at their default value (Table 4.3). Performance depends only weakly on the synaptic delay. The quantitative approximation of the network frequency slightly improves for larger delay. Figure on next page.

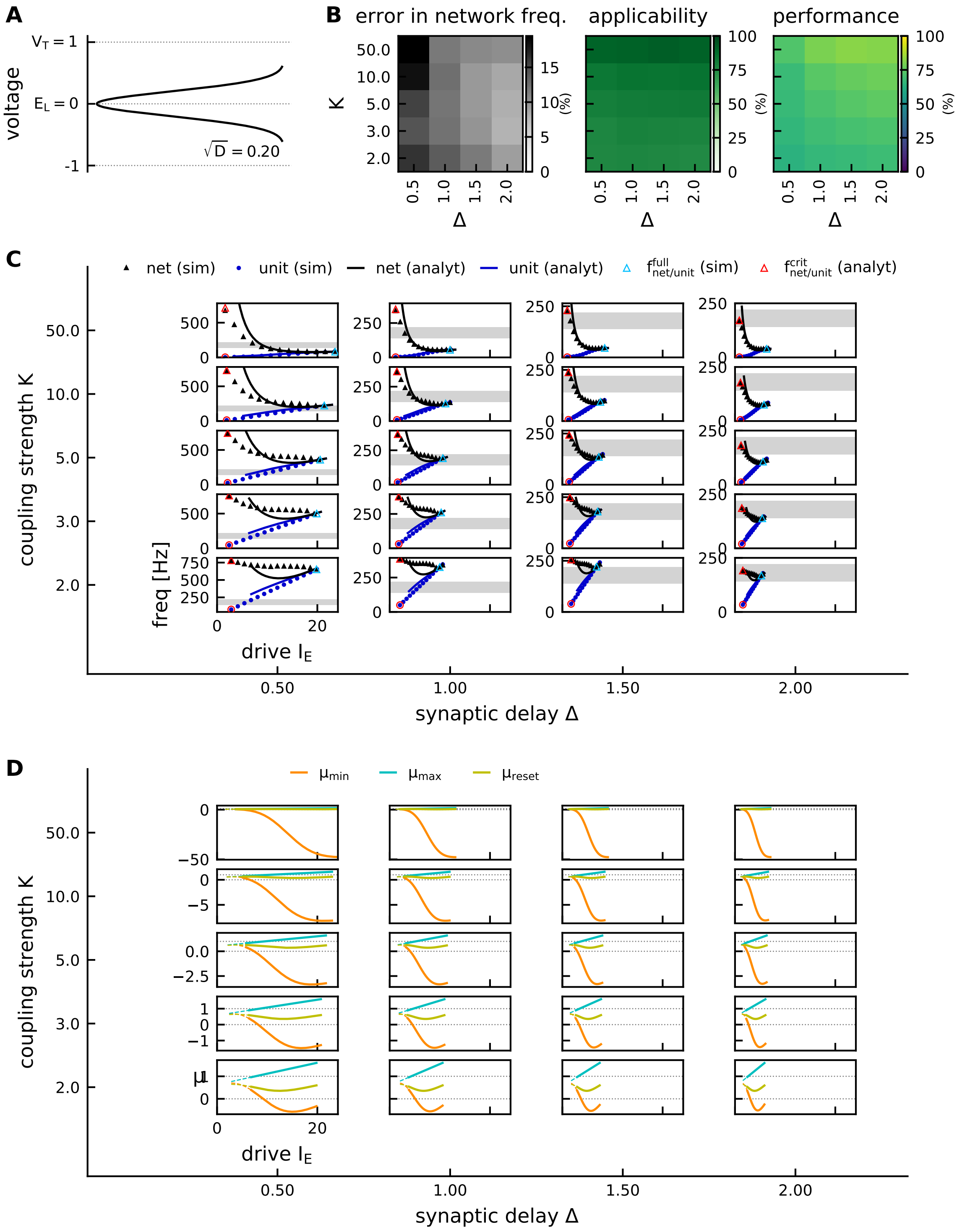

Figure 4.33: Performance of drift-based approximation depending on synaptic delay and coupling strength. Caption on previous page.

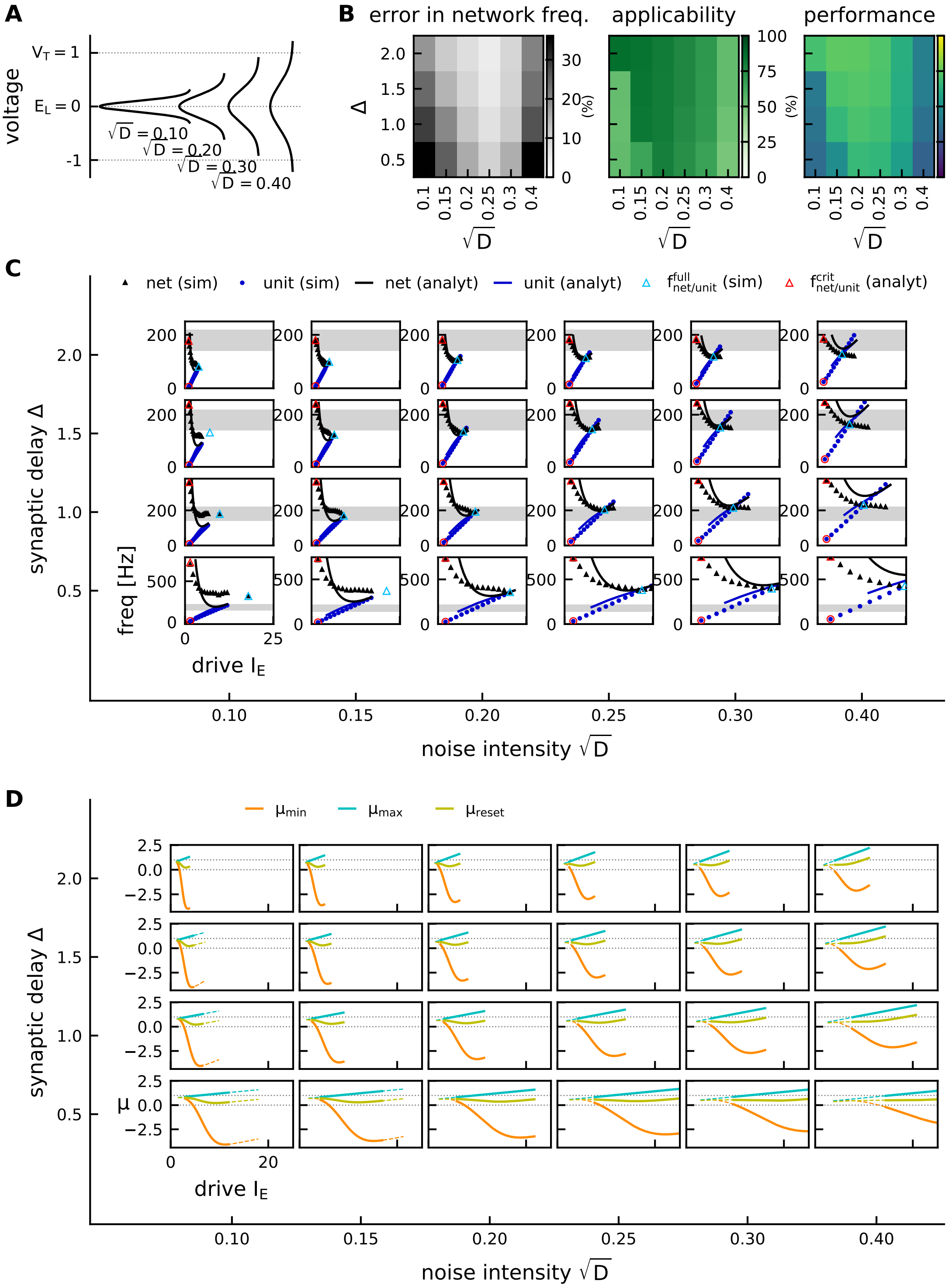

Figure 4.34: Performance of drift-based approximation depending on synaptic delay and noise intensity. Same outline as Fig. 4.27. Covariation of Δ (vertical axis) and $\sqrt{D}$ (horizontal axis), all other parameters are at their default value (Table 4.3). Performance depends only weakly on the synaptic delay. The quantitative approximation of the network frequency slightly improves for larger delay. The noise strength is however a larger determinant of performance.

4.B Drift-based approximation in a network of pulse-coupled oscillators (PCO)

In this section I want to outline how the drift-based approximation introduced in Section 4.3.2 can be used to approximate the oscillation dynamics in a network of pulse-coupled oscillators with a linear phase response curve mimicking the effect of an inhibitory reversal potential.

4.B.1 Ripples in a PCO network with linear phase response curve

The analysis in Section 4.3.4 has shown that IFA occurs for a range of external drives that are strongly superthreshold: For any such level of drive I_E individual units would fire regularly with an intrinsic frequency $\omega(I_\mathrm{E})$ if they were uncoupled. Instead of representing each neuron by its membrane potential, one can thus use a more abstract model and describe the state of each neuron i by a phase variable $\theta_i \in [0, 2\pi)$ that rises linearly with speed ω.

$$\dot{\theta}_i(t) = \omega$$

(Mirollo and Strogatz, 1990; Abbott and van Vreeswijk, 1993; Memmesheimer and Timme, 2006). Whenever the phase variable reaches a spike threshold of 2π a spike is recorded and the phase is reset to 0. A Gaussian white noise is added to account for the stochasticitiy of spiking due to background noise:

$$\dot{\theta}_i(t) = \omega + \sqrt{2D}\xi_i(t)$$

$\langle \xi_i(t) \rangle = 0, \langle \xi_i(t)\xi_j(t') \rangle = \delta_{i,j}\delta(t-t')$ for neurons i and j. When noise is included, phases can become negative ($\theta \in (-\infty, 2\pi)$, see zero-crossings in Fig. 4.36A, bottom). One could also think of the oscillator phase θ as the membrane potential of a perfect integrate-and-fire (PIF) unit. Consider a network of phase oscillators coupled via delayed inhibitory pulses:

$$\dot{\theta}_i(t) = \omega - \frac{K}{N} Z(\theta_i(t)) \sum_j \sum_k \delta(t - \Delta - t_j^k) + \sqrt{2D}\xi_i(t) \ .$$

The effect of presynaptic spikes onto a postsynaptic unit i is scaled by a linear phase response curve (PRC)

$$Z(\theta) = \theta - \theta_R \quad , \quad \theta_R = \pi/2 \ .$$

The choice of reversal phase θ_R is arbitrary and chosen here as a small positive phase. The phase response curve reverses the sign of the input depending on the state of the postsynaptic neuron and is

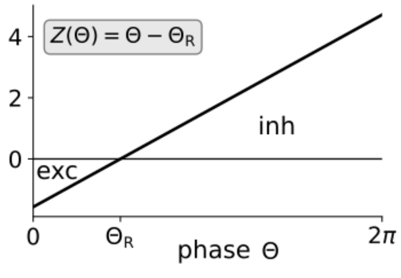

Figure 4.35: Linear phase response curve (PRC).

intended to mimick the effect of an inhibitory reversal potential E_I in the detailed ripple model (Eq. (4.11)): For most of the phase space ($[\theta_R, 2\pi)$) the effect of incoming spikes is inhibitory ($-KZ(\theta_i) < 0$). The closer the neuron is to crossing the spike threshold itself (large phase θ_i corresponding to a membrane potential $v \gg E_I$), the stronger the inhibitory feedback. If, however, the neuron's phase is small ($\theta_i < \theta_R$ corresponding to $v < E_I$) the effect of incoming spikes becomes excitatory ($-KZ(\theta_i) > 0$, see Fig. 4.35).

Varying the external drive in the detailed ripple model corresponds to varying the intrinsic unit firing rate ω in the network of pulse-coupled oscillators (PCO). For increasing intrinsic rate ω the PCO network exhibits a similar range of dynamics as the detailed ripple model, including a transition from sparse to full synchrony (Fig. 4.36A). The (empirical) population rate in a small time interval $[t, t + \Delta t]$ is defined as before as $r_N(t) = \frac{n_{\text{spk}}([t,t+\Delta t])}{N\Delta t}$ (cf. Eq. (4.13)).

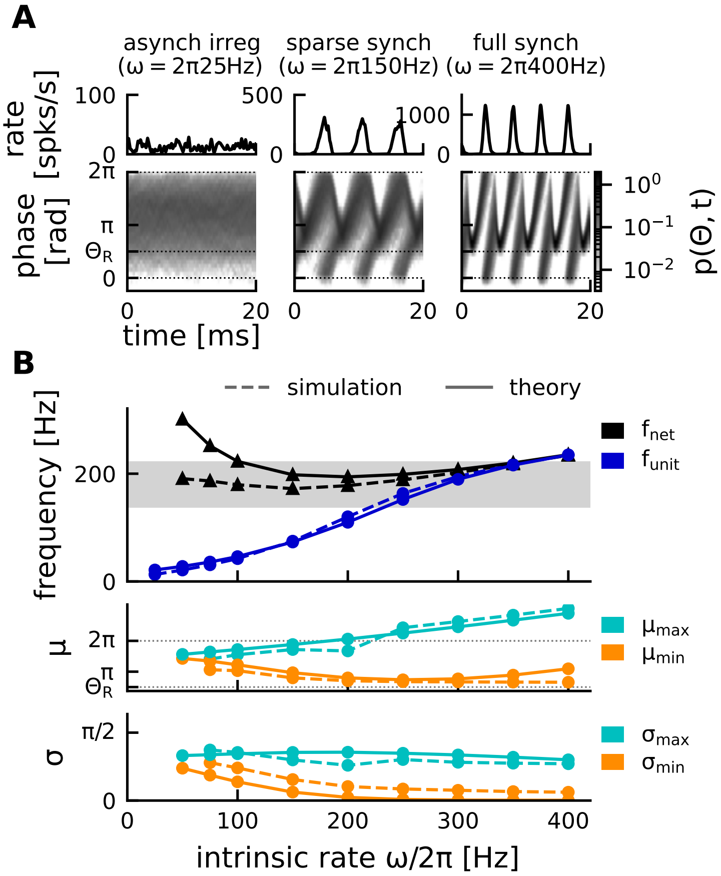

Figure 4.36: Ripple dynamics in a network of pulse-coupled oscillators. **A,** Examplary dynamics in asynchronous irregular state (left), sparse synchrony (middle), full synchrony (right). Top: population rate, bottom: distribution of phases over time. Dotted lines mark phase 0, Θ_R, and the spike threshold 2π. **B,** Oscillation dynamics in spiking network simulation (dashed lines) and approximated analytically (solid lines, Eqs. (4.96), (4.97), (4.98), (4.101)). Top: network frequency f_{net} and mean unit firing rate f_{unit}; middle: periodic maximum $\mu_{\max}$ and minimum $\mu_{\min}$ of mean phase μ; middle: periodic maximum $\sigma_{\max}$ and minimum $\sigma_{\min}$ of the standard deviation of phases σ. Both $\mu_{\max}$ and $\sigma_{\max}$ are theoretical quantities based on a first passage time-approach. They were estimated in the spiking network based on a (circular) Gaussian fit of the distribution of phases $\theta \mod 2\pi$. Parameters see Table 4.5.

Instead of considering the distribution of membrane potentials over time, we can now look at the distribution of phases $p(\theta, t)$. The average phase μ oscillates with an amplitude defined by the two extrema $\mu_{\min}$, $\mu_{\max}$, that becomes larger for larger ω (Fig. 4.36B, middle). The standard deviation of the phase distribution exhibits a clear trend as well: For fixed ω the standard deviation increases in each cycle, from $\sigma_{\min}$ to $\sigma_{\max}$, as the mean phase rises from $\mu_{\min}$ to $\mu_{\max}$. For increasing ω, both $\sigma_{\min}$ and $\sigma_{\max}$ *de*crease, corresponding to a compression of the phase distribution (Fig. 4.36B, bottom).

The PCO network with linear PRC can thus phenomenologically account for the network dynamics observed in an LIF network with inhibitory reversal potential (Fig. 4.12, right).

Parameter	Value	Definition
N	1000	Number of oscillators
Δ	2 ms	Coupling delay
K	5	Coupling strength
D	20 π^2/sec	Noise strength
θ_R	$\pi/2$	Reversal phase

Table 4.5: Default parameters for the PCO network.

4.B.2 Mean-field dynamics of the PCO network

In the mean-field limit ($N \to \infty$) the dynamics of the density of phases $p(\theta, t)$ is described by the following Fokker-Planck equation (see also Abbott and van Vreeswijk, 1993):

$$\partial_t p(\theta,t) = -\partial_\theta J(\theta,t) = -\partial_\theta \Big(\left[\omega - KZ(\theta) r(t-\Delta)\right] p(\theta,t) \Big) + D\partial_\theta^2 p(\theta,t) \ . \tag{4.93a}$$

Since phases that cross the spike threshold of 2π are instantaneously reset to 0, there is an absorbing boundary condition at threshold:

$$p(2\pi, t) = 0 \ . \tag{4.93b}$$

The population rate is defined as the probability current through the threshold:

$$r(t) = J(2\pi, t) \overset{(4.93b)}{=} -D\partial_\theta p(2\pi, t) \ . \tag{4.93c}$$

The fire-and-reset rule introduces a discontinuity of the derivative of p at the reset value 0:

$$\left[\partial_\theta p(\theta,t)\right]_0 = \lim_{\epsilon\to 0} \left[\partial_\theta p(\epsilon,t) - \partial_\theta p(-\epsilon,t)\right] \overset{(4.93c)}{=} -\frac{1}{D} r(t) \ .$$

As for the LIF network, we require that the density of phases decays to zero sufficiently fast as $\theta \to -\infty$:

$$\lim_{\theta\to-\infty} p(\theta,t) = \lim_{\theta\to-\infty} \partial_\theta p(\theta,t) = 0 \tag{4.93d}$$

Since p is a probability density, it is normalized:

$$\int_{-\infty}^{2\pi} p(\theta,t)\,\mathrm{d}\theta = 1 \quad \forall\, t \ .$$

The stationary solution for such a network of pulse-coupled oscillators was derived by Abbott and van Vreeswijk (1993).

Gaussian solutions for natural boundary conditions. Let's neglect the absorbing boundary condition and the derivative discontinuity imposed by the fire-and-reset rule and only assume natural boundary conditions ($\lim_{\theta\to\pm\infty} p(\theta,t) = \lim_{\theta\to\pm\infty} \partial_\theta p(\theta,t) = 0$). Assume further that at time 0, the phases are either all identical to, or Gaussian distributed around an initial phase θ_0. The time-dependent solution of the FPE for an uncoupled population ($K = 0$)

$$\partial_t p(\theta,t) = -\partial_\theta \left(\omega p(\theta,t)\right) + D\partial_\theta^2 p(\theta,t)$$

is then a Gaussian

$$p(\theta,t) = \frac{1}{\sqrt{2\pi}\Sigma(t)} \exp\left[-\frac{\left(\theta - [\theta_0 + \omega t]\right)^2}{2\Sigma^2(t)}\right]$$

with a variance

$$\Sigma(t) := \begin{cases} \sqrt{2Dt} & , \ p(\theta,0) = \delta(\theta-\theta_0) \\ \sqrt{\sigma_0^2 + 2Dt} & , \ p(\theta,0) = \frac{1}{\sqrt{2\pi}\sigma_0}\exp\left[-\frac{(\theta-\theta_0)^2}{2\sigma_0^2}\right] \end{cases} \tag{4.94}$$

that diverges to infinity in the long-time limit (Risken, 1989; Gardiner, 1985). A stationary solution does not exist.

Now assume that the uncoupled population receives a constant amount of (feedforward) inhibition $r_0 > 0$:

$$\partial_t p(\theta,t) = -\partial_\theta \Big(\left[\omega - KZ(\theta) r_0\right] p(\theta,t)\Big) + D\partial_\theta^2 p(\theta,t)$$

In this case a stationary solution of the FPE exists and is given by a Gaussian

$$p(\theta) = \frac{1}{\sqrt{2\pi}\Sigma_\infty} \exp\left[-\frac{\left(\theta - \left[\theta_R + \frac{\omega}{Kr_0}\right]\right)^2}{2\Sigma_\infty^2}\right] , \quad \Sigma_\infty = \sqrt{\frac{D}{Kr_0}} \ .$$

(see Appendix Section 4.D.2). The variance Σ_∞ of the Gaussian density is now finite, due to the opposing effects of noise-induced diffusion, and inhibition-induced compression, brought about by the PRC Z with sign change. This should provide an intuition why, in the recurrently coupled network with feedback inhibition, it is reasonable to assume a Gaussian phase distribution.

4.B.3 Drift-based approximation of ripples and IFA in the PCO network

Based on the same assumptions as in Section 4.5.3, I will approximate the density of phases in the mean-field limit ($N \to \infty$) as a Gaussian

$$p(\theta,t) = \frac{1}{\sqrt{2\pi}\sigma(t)} \exp\left[-\frac{\left(\theta - \mu(t)\right)^2}{2\sigma^2(t)}\right] . \tag{4.95a}$$

The mean phase μ moves depending on the intrinsic firing rate ω and the inhibitory feedback:

$$\dot{\mu} = \omega - KZ(\mu)r(t-\Delta) \tag{4.95b}$$

The standard deviation $\sigma(t)$ changes over time depending on the balance between noise-induced diffusion, and inhibition-induced compression. This is an important difference to the drift-based approximation for the LIF network in Section 4.5.3 where the Gaussian density had fixed width at all times. If the network exhibits oscillations for a constant intrinsic firing rate ω, the mean phase oscillates periodically between two local extrema μ_{min} and μ_{max}. For simplicity I will assume that the standard deviation reaches its local extrema at the same time, *i.e.* noise-induced diffusion dominates while the mean phase μ increases, and inhibition-induced compression dominates as the mean phase decreases. Thus, the Gaussian density oscillates periodically between a narrow Gauss centered around μ_{min}:

$$p_{\text{min}}(\theta) = \frac{1}{\sqrt{2\pi\sigma_{\text{min}}^2}} \exp\left[-\frac{(\theta-\mu_{\text{min}})^2}{2\sigma_{\text{min}}^2}\right]$$

and a wide Gauss ($\sigma_{\text{max}} > \sigma_{\text{min}}$) centered around μ_{max}:

$$p_{\text{max}}(\theta) = \frac{1}{\sqrt{2\pi\sigma_{\text{max}}^2}} \exp\left[-\frac{(\theta-\mu_{\text{max}})^2}{2\sigma_{\text{max}}^2}\right]$$

with a standard deviation evolving as

$$\dot{\sigma}(t) = \begin{cases} \frac{D}{\sigma}\,, & \text{if } \dot{\mu} \geq 0 \quad \text{(diffusion)} \\ -Kr(t-\Delta)\sigma\,, & \text{if } \dot{\mu} < 0 \quad \text{(compression)}\ . \end{cases} \tag{4.95c}$$

The diffusion-mediated increase of the standard deviation during the upstroke of the mean phase is a direct result of the FPE when the absorbing boundary is neglected (see Eq. (4.94)). The ODE describing inhibition-mediated compression will be derived in detail in *Step 4* below. The drift-based population rate is derived as before for the LIF network (cf. Eq. (4.48)):

$$\begin{aligned} r(t) = J(2\pi,t) &\overset{(4.93d)}{=} \int_{-\infty}^{2\pi} \partial_\theta J(\theta,t)\,\mathrm{d}\theta \overset{(4.93a)}{=} -\partial_t \int_{-\infty}^{2\pi} p(\theta,t)\,\mathrm{d}\theta \\ &\overset{(4.95a)}{=} -\partial_t \int_{-\infty}^{2\pi} \frac{1}{\sqrt{2\pi}\sigma(t)} \exp\left[-\frac{(\theta-\mu(t))^2}{2\sigma^2(t)}\right] \mathrm{d}\theta \end{aligned}$$

Substitute $z := \frac{\theta-\mu(t)}{\sqrt{2}\sigma(t)}$, $\frac{\mathrm{d}}{\mathrm{d}\theta}z = \frac{1}{\sqrt{2}\sigma(t)}$

$$\begin{aligned} r(t) &= -\partial_t \int_{-\infty}^{\frac{2\pi-\mu(t)}{\sqrt{2}\sigma(t)}} \exp\left[-z^2\right] \mathrm{d}z = -\partial_t \frac{\sqrt{\pi}}{2} \left[\operatorname{erf}(z)\right]_{-\infty}^{\frac{2\pi-\mu(t)}{\sqrt{2}\sigma(t)}} \\ &= \partial_t \frac{\sqrt{\pi}}{2} \left[-\operatorname{erf}\left(\frac{2\pi-\mu(t)}{\sqrt{2}\sigma(t)}\right) - 1\right] \\ &= \exp\left[-\frac{(2\pi-\mu(t))^2}{2\sigma^2(t)}\right] \frac{\dot{\mu}(t)\sqrt{2}\sigma(t) - (2\pi-\mu(t))\sqrt{2}\dot{\sigma}(t)}{2\sigma^2(t)} \end{aligned}$$

Since a rate shall only be produced during the upstroke of the mean phase, we can assume that the standard deviation is increasing due to diffusion (Eq. (4.95c)):

$$r(t) = \exp\left[-\frac{(2\pi - \mu(t))^2}{2\sigma^2(t)}\right]\left[\frac{\dot{\mu}(t)}{\sqrt{2}\sigma(t)} - \frac{(2\pi - \mu(t))D}{\sqrt{2}\sigma^3(t)}\right]$$

The second term in the second bracket represents diffusion-mediated spiking (Plesser and Gerstner, 2000) and will be neglected, since the mean phase during ripple oscillations undergoes strong transients such that the drift-based term $\mathcal{O}(\dot{\mu})$ dominates over the small concurrent changes in the width $\sigma(t)$ of the phase density. The rate is thus approximated as

$$r(t) \approx \frac{[\dot{\mu}(t)]_+}{\sqrt{2\pi\sigma(t)}} \exp\left[-\frac{(2\pi - \mu(t))^2}{2\sigma(t)}\right] . \tag{4.95d}$$

A periodic solution can be found using the same steps that were described in Methods Section 4.5.4, hence I will keep their description short. Since here both the mean and the standard deviation of the Gaussian density are unknown, the solution has to be found self-consistently by repeating these steps iteratively for various potential choices for the maximal width σ_{max}:
For every σ_{max}:

Step 1: Find the periodic maximum $\mu_{\text{max}} = \mu(t_{\text{off}})$.

Step 2: Find $\mu_{\text{min}} = \mu(t_{\text{off}} + \Delta)$.

Step 3: Infer t_{off} and the network frequency f_{net}.

Step 4: Infer the standard deviation at the beginning and end of the cycle and check if they are the same (self-consistent condition).

Step 1: Approximating μ_{max}. The time t_{off} at which the mean phase reaches its maximum, marks the end of the population spike. We find μ_{max} by solving the local extremum condition:

$$0 = \dot{\mu}(t_{\text{off}}) = \omega - KZ(\mu_{\text{max}})\dot{\mu}(t_{\text{off}} - \Delta)\frac{1}{\sqrt{2\pi}\sigma_{\text{max}}} \exp\left[-\frac{(2\pi - \mu(t_{\text{off}} - \Delta))^2}{2\sigma_{\text{max}}^2}\right]$$

Again, I approximate the trajectory of μ shortly before the local maximum, taking into account only the excitatory drive/the intrinsic firing rate (cf. Eq. (A1)):
$\dot{\mu}(t_{\text{off}} - \Delta) \approx \omega$, and $\mu(t_{\text{off}} - \Delta) \approx \mu_{\text{max}} - \omega\Delta$.
The resulting equation can be solved numerically for μ_{max}:

$$\Leftrightarrow \quad \frac{1}{K(\mu_{\text{max}} - \theta_R)} = \frac{1}{\sqrt{2\pi}\sigma_{\text{max}}} \exp\left[-\frac{(\mu_{\text{max}} - (2\pi + \omega\Delta))^2}{2\sigma_{\text{max}}^2}\right] \tag{4.96}$$

(see Fig. 4.37). As for the LIF network we see that μ_{max} grows with the intrinsic firing rate ω (previously external drive), which predicts the transition from sparse to full synchrony.

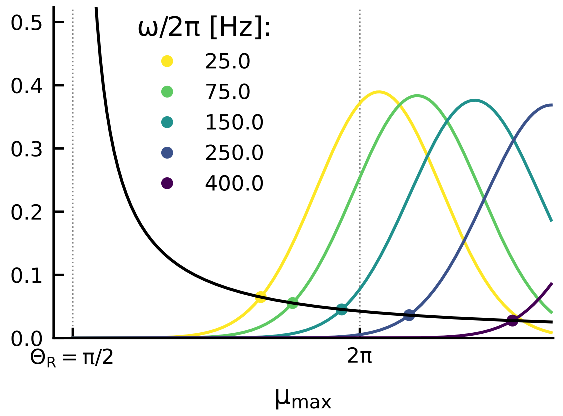

Figure 4.37: Numerical solution for $\mu_{\max}$ in PCO network. Numerical solution of Eq. (4.96). Black line: left-hand side of Eq. (4.96). Colored lines: right-hand side of Eq. (4.96) for various intrinsic firing rates ω. Markers indicate intersections, *i.e.* solutions $\mu_{\max}(\omega)$. Vertical gray lines: reversal phase Θ_R and spike threshold 2π. (RHS curves are shown for self-consistently determined $\sigma_{\max}(\omega)$ (see Step 4, Fig. 4.38).)

Step 2: Approximating $\mu_{\min}$. Using the local maximum $\mu_{\max}$ as initial condition, ODE Eq. (4.95b) is integrated over one delay period Δ, taking into account the feedback inhibition, in order to find the approximate local minimum

$$\begin{aligned}\mu_{\min} &:= \mu(t_{\text{off}} + \Delta) \\ &\approx \theta_R + (\mu_{\max} - \theta_R)\exp(\phi(\Delta) - \phi(0)) + \omega \exp(\phi(\Delta)) \int_0^{\Delta} \exp\left(-\phi(\bar{t})\right) \mathrm{d}\bar{t} \quad (4.97)\end{aligned}$$

with

$$\phi(t) := \frac{K}{2} \operatorname{erf}\left(\frac{2\pi - \mu_{\max} + \omega(\Delta - t)}{\sqrt{2}\sigma_{\max}}\right) .$$

The integration of the inhibitory feedback was simplified by approximating the width of the Gaussian density during the population spike as constant ($\sigma_{\max}$). One could also take into account its widening due to diffusion, and solve the integrals for the inhibitory feedback numerically.

Step 3: Inferring the network frequency. As for the LIF network, the period of the network oscillation is estimated as the sum of the upstroke time, required for the mean phase to rise from $\mu_{\min}$ to $\mu_{\max}$, and the imposed downstroke time of Δ:

$$f_{\text{net}} = (t_{\text{off}} + \Delta)^{-1} \tag{4.98}$$

with

$$t_{\text{off}} \approx \frac{\mu_{\max} - \mu_{\min}}{\omega} \qquad \text{(cf. Eq. (A1))} .$$

The saturation and mean unit firing rate can be inferred as before:

$$f_{\text{unit}} = s \cdot f_{\text{net}} , \quad s = \int_{2\pi}^{\infty} p_{\max}(\theta)\, \mathrm{d}\theta = \frac{1}{2}\left(1 - \operatorname{erf}\left[\frac{2\pi - \mu_{\max}}{\sqrt{2}\sigma_{\max}}\right]\right)$$

Step 4. Inferring $\sigma_{\min}$. At time t_{off} the Gaussian density has reached its maximal width $\sigma_{\max}$. We can now infer the width of the Gaussian density at the beginning and end of the cycle. For a periodic solution these widths should be identical ($\sigma_{\min}$):

Gaussian width at the end of the cycle. Thinking forward in time, we can calculate the compression of the density due to the inhibitory feedback. Consider the upper and lower "edges" of the Gaussian density $\sigma_u(t) = \mu(t) + 3\sigma(t)$ and $\sigma_l(t) = \mu(t) - 3\sigma(t)$. If we ignore diffusion during the downstroke of the mean phase, the trajectory of the edges is described by the same ODE as the mean phase μ (Eq. (4.95b)):

$$\begin{aligned} \dot\sigma_u(t) &= \omega - KZ(\sigma_u)r(t-\Delta)\,, \qquad & \sigma_u(t_{\text{off}}) &= \mu_{\max} + 3\sigma_{\max} \\ \dot\sigma_l(t) &= \omega - KZ(\sigma_l)r(t-\Delta)\,, \qquad & \sigma_l(t_{\text{off}}) &= \mu_{\max} - 3\sigma_{\max} \end{aligned}$$

The standard deviation of the Gaussian during the downstroke is then given by $\sigma(t) = (\sigma_u(t) - \sigma_l(t))/6$ and is described by the following ODE (cf. Eq. (4.95c)):

$$\dot\sigma(t) = \frac{1}{6}\frac{\mathrm{d}}{\mathrm{dt}}(\sigma_u(t) - \sigma_l(t)) = -\frac{1}{6}Kr(t-\Delta)\Big(Z(\sigma_u) - Z(\sigma_l)\Big) = -KZ(\sigma)r(t-\Delta)$$

due to the linearity of the PRC Z. We can thus integrate the trajectory of the standard deviation during the downstroke, starting from the initial value $\sigma(t_{\text{off}}) = \sigma_{\max}$ and find the compressed width of the Gaussian density at the end of the cycle:

$$\sigma(t_{\text{off}} + \Delta) = \sigma_{\max} \exp\Big[\phi(\Delta) - \phi(0)\Big]\ . \tag{4.99}$$

Gaussian width at the beginning of the cycle. Thinking backwards in time, we can calculate how narrow the Gaussian density must have been at the beginning of the cycle (time 0), in order for it to diffuse precisely to width $\sigma_{\max}$ over the time t_{off} of the upstroke:

$$\begin{aligned} & \sigma_{\max} \overset{!}{=} \sqrt{\sigma^2(0) + 2Dt_{\text{off}}} \qquad \text{(see Eq. (4.95c))} \\ \Leftrightarrow \quad & \sigma(0) = \sqrt{\sigma^2_{\max} - 2D\frac{\mu_{\max} - \mu_{\min}}{\omega}} \end{aligned} \tag{4.100}$$

A self-consistent solution must fulfill

$$\sigma(t_{\text{off}} + \Delta) \overset{!}{=} \sigma(0) =: \sigma_{\min}\ . \tag{4.101}$$

Steps 1-4 are thus repeated for various choices of $\sigma_{\max}$, until a self-consistent solution is found (Fig. 4.38).

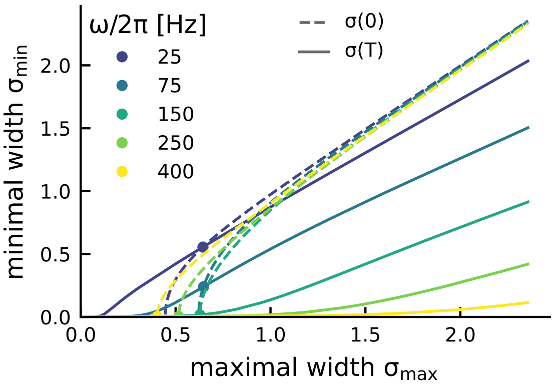

Figure 4.38: Self-consistent solution for the PCO oscillation dynamics. Solid lines: Gaussian width $\sigma(t_{\text{off}} + \Delta)$ at the end of the cycle (Eq. (4.99)). Dashed lines: Gaussian width $\sigma(0)$ at the beginning of the cycle (Eq. (4.100)). Both shown for a range of intrinsic firing rates ω and widths $\sigma_{\max}$. Intersections (round markers) indicate self-consistent solutions $\big(\sigma_{\min}(\omega), \sigma_{\max}(\omega)\big)$ (Eq. (4.101)).

The self-consistent periodic solutions $(\mu_{\max}, \mu_{\min}, \sigma_{\max}, \sigma_{\min}, f_{\text{net}}, f_{\text{unit}})$ for various intrinsic firing rates ω are shown in Fig. 4.36 (solid lines). As in the LIF case, the match with the PCO spiking network simulations is not perfect, due to the simplification of only considering drift-mediated spiking. The qualitative dynamics are however captured well: Both the mean and the standard deviation of the phase density exhibit a clear trend for increasing intrinsic firing rates ω. We can thus expect a similar speed-dependent hysteresis in the PCO network, when the intrinsic firing rate is changed over time (corresponding to transient SPW-like input).

As for the LIF network, the core mechanism of IFA in the PCO network can be illustrated for the case of piecewise constant drive (now: intrinsic rate ω, Fig. 4.39). Since both the mean $\mu_{\min}$ and standard deviation $\sigma_{\min}$ are *de*creasing functions of the intrinsic rate ω (Fig. 4.36), a hysteresis emerges in both variables, when ω changes after each cycle. A typical cycle during the upstroke of ω begins with a phase distribution of slightly *in*creased mean and standard deviation (compared to the asymptotic dynamics, Fig. 4.39A, left, orange markers vs lines), and is thus shorter ($f_{\text{net}}^{\text{inst}} = 192.9$ Hz vs 180.8 Hz). Vice versa, a cycle during the downstroke is slightly longer, since it begins with a phase distribution of lower mean and standard deviation (Fig. 4.39A, right, orange markers vs lines, $f_{\text{net}}^{\text{inst}} = 168.6$ Hz vs 180.8 Hz). A SPW-like drive, that first increases and then decreases the intrinsic rate ω over a short period of time (Fig. 4.39B, bottom), thus induces IFA (Fig. 4.39B, top).

In summary, the drift-based approximation, presented in Section 4.3.2 for a current-based LIF network, can be applied in an analogous way for a PCO network that accounts for inhibitory reversal potentials phenomenologically with a linear phase response curve. The theory predicts the emergence of IFA due to the same, speed-dependent hysteresis, here however in two variables, namely the mean and standard deviation of the phase distribution. I chose to present the LIF network in the main text, as it allows the derivation of closed-form expressions for the network frequency, and membrane potential oscillation amplitude, whereas the PCO network requires a self-consistent solution scheme. The analysis shows that inhibitory reversal potentials are not a necessary ingredient for IFA (see current-based LIF network), but can be incorporated in the theory by taking into account both the mean and the standard deviation of the phase distribution over time and for different levels of drive (PCO network).

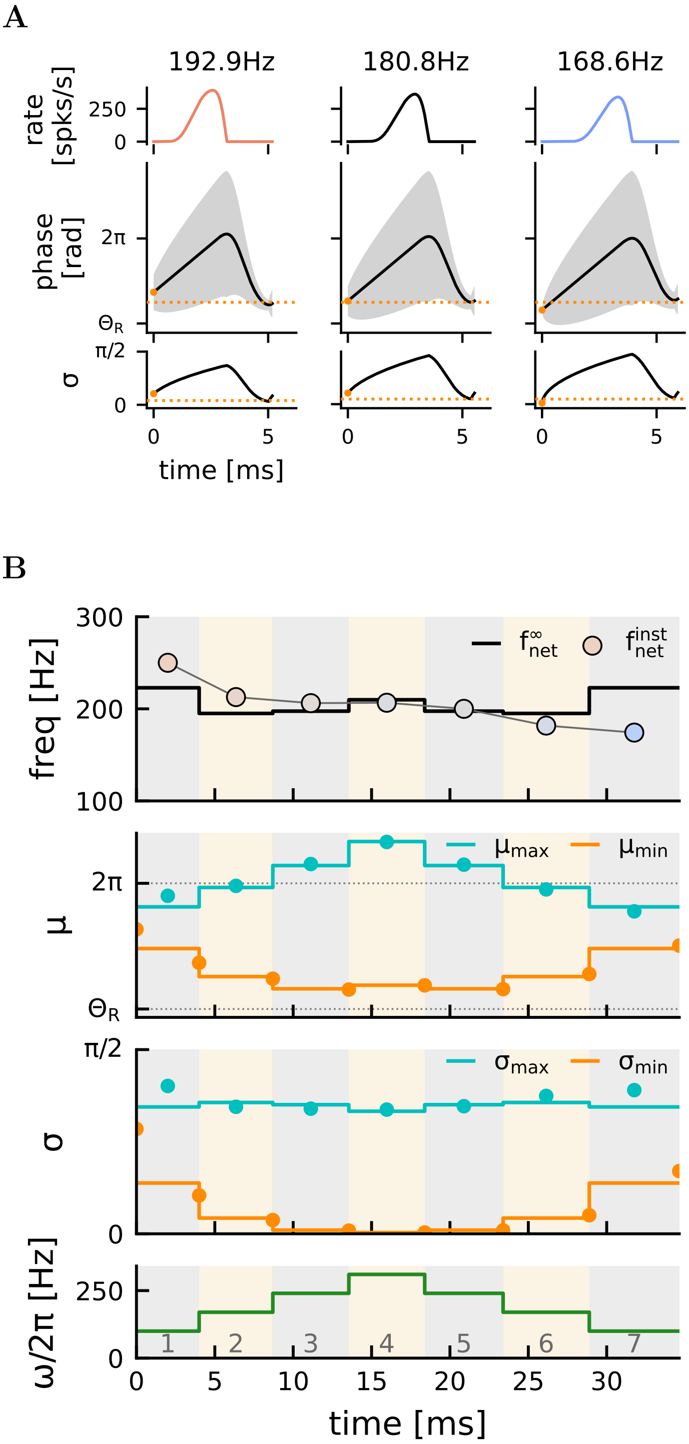

Figure 4.39: Drift-based approximation of IFA in the PCO network. **A,** Dependence of the length of the oscillation cycle on the initial mean and standard deviation of the Gaussian phase distribution (cf. Fig. 4.9A). Top: population rate; middle: Gaussian phase distribution with mean $\mu(t)$ (black); bottom: standard deviation $\sigma(t)$ of the gaussian density shown above (grey area). Note the small differences in the initial phase distributions (time 0): Left: shorter period for $\mu_{\text{min}} > \mu^{\infty}_{\text{min}}(\omega)$, $\sigma_{\text{min}} > \sigma^{\infty}_{\text{min}}(\omega)$ (orange marker vs. dashed line). Middle: asymptotic period for $\mu_{\text{min}} = \mu^{\infty}_{\text{min}}(\omega)$, $\sigma_{\text{min}} = \sigma^{\infty}_{\text{min}}(\omega)$. Right: longer period for $\mu_{\text{min}} < \mu^{\infty}_{\text{min}}(\omega)$, $\sigma_{\text{min}} < \sigma^{\infty}_{\text{min}}(\omega)$. In all examples the intrinsic firing rate was $\omega = 170$ Hz. Traces were integrated numerically (Eqs. (4.95)). **B,** IFA for piecewise constant intrinsic firing rate ω with symmetric step height (cf. Fig. 4.9C). Top to bottom: network frequency, mean phase, standard deviation of Gaussian phase distribution, intrinsic firing rate. Shaded areas mark oscillation cycles. Solid lines indicate asymptotic dynamics associated to the intrinsic firing rate ω of the respective cycle. Markers indicate transient behavior. Cyan: μ_{max}; orange: μ_{min}. Top: the instantaneous network frequency (markers) is first above and then below the resp. asymptotic network frequencies (black line). All quantities are the result of the (semi-) analytical approximation described above.

4.C Auxiliary calculations for piecewise linear drive

4.C.1 Comparison of μ_{max} for constant and linear drive

The transient μ_{max} for piecewise linear drive is found numerically by solving Eq. (4.84) (Fig. 4.40). The solution $\mu_{\text{max}}(\hat{I}_{\text{E}}, m, \mu^i_{\text{min}})$ does not deviate much from the asymptotic $\mu^{\infty}_{\text{max}}(\hat{I}^i_{\text{E}})$, since the left- and right-hand side of Eq. (4.84) are both Gaussian functions centered around the same mean. The solution can be approximated by noting that the denominator of the left-hand side is generally large, if we assume that the network is somewhere between sparse and full synchrony ($s \leq 1$, i.e. $\mu_{\text{max}} \leq V_T + 3\sqrt{D} \ll \hat{I}^i_{\text{E}}$. Hence we can approximate $\hat{I}^i_{\text{E}} - \mu_{\text{max}}$ as a constant $C \geq \hat{I}^i_{\text{E}} - V_T - 3\sqrt{D}$. Eq. (4.84) can then be solved analytically:

$$\frac{m\Delta K p(V_T, t^i_{\text{off}} - \Delta)}{C} = K\, \mathrm{e}^{\frac{\Delta}{\tau_m}}\, p(V_T, t^i_{\text{off}} - \Delta) - 1$$

$$\begin{aligned}
\Leftrightarrow \quad 1 &= \left(\mathrm{e}^{\frac{\Delta}{\tau_m}} - \frac{m\Delta}{C}\right) K p(V_T, t^i_{\text{off}} - \Delta) \\
\overset{(4.83)}{\Leftrightarrow} \quad 0 &= \ln\left(\mathrm{e}^{\frac{\Delta}{\tau_m}} - \frac{m\Delta}{C}\right) + \ln\left(\frac{K}{\sqrt{2\pi D}}\right) - \frac{(V_T - I_{\text{E}}(1 - \mathrm{e}^{\Delta/\tau_m}) - \mu_{\text{max}}\, \mathrm{e}^{\Delta/\tau_m})^2}{2D} \\
\Leftrightarrow \quad \mu_{\text{max}} &= \left(1 - \mathrm{e}^{-\frac{\Delta}{\tau_m}}\right) I_{\text{E}} + \mathrm{e}^{-\frac{\Delta}{\tau_m}} \left(V_T - \sqrt{2D\left[\ln\left(\mathrm{e}^{\frac{\Delta}{\tau_m}} - \frac{m\Delta}{C}\right) + \ln\left(\frac{K}{\sqrt{2\pi D}}\right)\right]}\right) \\
&\begin{cases} = \mu^{\infty}_{\text{max}}(I_{\text{E}}), & m = 0 \quad \text{(cf. Eq. (4.58))} \\ \gtrsim \mu^{\infty}_{\text{max}}(I_{\text{E}}), & m > 0 \\ \lesssim \mu^{\infty}_{\text{max}}(I_{\text{E}}), & m < 0 \end{cases}
\end{aligned}$$

The slope-dependent term appears in the logarithm and thus generally introduces only a small deviation of μ_{max} from the asymptotic $\mu^{\infty}_{\text{max}}(I_{\text{E}})$. An upper bound of the deviation from $\mu^{\infty}_{\text{max}}(I_{\text{E}})$ can be calculated by using $C = I_{\text{E}} - V_T - 3\sqrt{D}$ (Fig. 4.40, blue line).

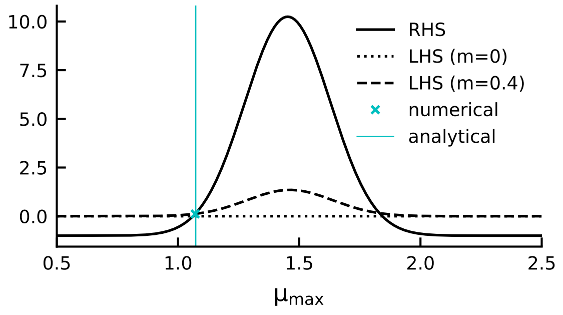

Figure 4.40: Numerical solution for μ_{max} under linear drive. RHS/LHS: right- and left-hand side of Eq. (4.84). Default parameters (Table 4.3), $I_{\text{E}} = 5, m = 0.4/\,\text{ms}$. Deviation of transient $\mu_{\text{max}}(\hat{I}^i_{\text{E}}, m, \mu^i_{\text{min}})$ from the asymptotic $\mu^{\infty}_{\text{max}}(\hat{I}^i_{\text{E}})$ depends on $\text{sgn}(m)$: For positive slope $m > 0$, μ_{max} is slightly larger (as shown here), for negative slope μ_{max} is slightly smaller.

4.C.2 A solvability condition for the initial mean membrane potential

The expression Eq. (4.85) for the length of the upstroke t_{off} in a cycle i with initial value μ_{min}, local maximum μ_{max}, and linear drive $I_{\text{E}}(t) = \hat{I}_{\text{E}} + m(t - t_{\text{off}})$ (superscript i was dropped for readability) contains the Lambert W function, which only has solutions for arguments larger than $-\exp(-1)$. Thus, the following condition must be satisfied (see Eq. (4.85)):

$$-\,\mathrm{e}^{-1} \overset{!}{<} \frac{\hat{I}_{\text{E}} - m\tau_m - \mu_{\text{max}}}{m\tau_m} \exp\left(-1 + \frac{\hat{I}_{\text{E}} - \mu_{\text{min}}}{m\tau_m}\right)$$

For any reference drive $\hat{I}_{\text{E}}$ we can distinguish multiple cases.
Case 1: $m > 0$
1a: If $m\tau_m < \hat{I}_{\text{E}} - \mu_{\text{max}}$, the above condition is equivalent to

$$-1 \overset{!}{<} \underbrace{\left(\frac{\hat{I}_{\text{E}} - \mu_{\text{max}}}{m\tau_m} - 1\right)}_{>0} \mathrm{e}^{\frac{\hat{I}_{\text{E}} - \mu_{\text{min}}}{m\tau_m}} > 0 \quad \text{so solutions exist for all } \mu_{\text{min}}.$$

1b: If $m\tau_m > \hat{I}_{\text{E}} - \mu_{\text{max}}$:

$$-1 \overset{!}{<} \underbrace{\frac{\hat{I}_{\text{E}} - m\tau_m - \mu_{\text{max}}}{m\tau_m}}_{<0} \mathrm{e}^{\frac{\hat{I}_{\text{E}} - \mu_{\text{min}}}{m\tau_m}} \quad \Leftrightarrow \quad \underbrace{-\frac{m\tau_m}{\hat{I}_{\text{E}} - m\tau_m - \mu_{\text{max}}}}_{>0} \overset{!}{>} \mathrm{e}^{\frac{\hat{I}_{\text{E}} - \mu_{\text{min}}}{m\tau_m}}$$

$$\Leftrightarrow \quad \mu_{\text{min}} \overset{!}{>} \hat{I}_{\text{E}} - m\tau_m \log\left(-\frac{m\tau_m}{\hat{I}_{\text{E}} - m\tau_m - \mu_{\text{max}}}\right)$$

(cf. solvability condition Eq. (4.86) for the initial mean membrane potential μ_{min}).
Case 2: $m < 0$

$$-1 \overset{!}{<} \underbrace{\left(\frac{\hat{I}_{\text{E}} - \mu_{\text{max}}}{m\tau_m} - 1\right)}_{<0} \mathrm{e}^{\frac{\hat{I}_{\text{E}} - \mu_{\text{min}}}{m\tau_m}} \quad \Leftrightarrow \quad \underbrace{-\frac{m\tau_m}{\hat{I}_{\text{E}} - m\tau_m - \mu_{\text{max}}}}_{>0} \overset{!}{>} \mathrm{e}^{\frac{\hat{I}_{\text{E}} - \mu_{\text{min}}}{m\tau_m}}$$

$$\Leftrightarrow \quad \mu_{\text{min}} \overset{!}{<} \hat{I}_{\text{E}} \underbrace{-m\tau_m \log\left(-\frac{m\tau_m}{\hat{I}_{\text{E}} - m\tau_m - \mu_{\text{max}}}\right)}_{>0} > \hat{I}_{\text{E}}$$

So solutions exist for all initial values $\mu_{\text{min}} < \hat{I}_{\text{E}}$ (this condition is always satisfied).

4.C.3 Decomposition of total input current under linear drive

Here I derive the seperation of the total current I during the membrane potential downstroke into a stationary part, and a part arising from the linearly changing drive

(Eq. (4.89)). Again $p(V_T, t)$ is abbreviated as $p(t)$ for readability.

$$
\begin{aligned}
I(t+t_{\text{off}}) &\overset{(4.45)}{=} I_{\text{E}}(t+t_{\text{off}}) - K\tau_m r(t+t_{\text{off}}-\Delta)\,, \qquad\qquad 0 \leq t \leq \Delta \\
&\overset{(4.49)}{=} I_{\text{E}}(t+t_{\text{off}}) - K\tau_m \underbrace{[\dot{\mu}(t_{\text{off}}-(\Delta-t))]_+}_{\geq 0 \quad \forall t \in [0,\Delta]} p(t_{\text{off}}-(\Delta-t)) \\
&\overset{(4.44)}{=} I_{\text{E}}(t+t_{\text{off}}) - K\tau_m \frac{1}{\tau_m}[I(t_{\text{off}}-(\Delta-t)) - \mu(t_{\text{off}}-(\Delta-t))]p(t_{\text{off}}-(\Delta-t)) \\
&\overset{(4.45)}{=} I_{\text{E}}(t+t_{\text{off}}) - Kp(t_{\text{off}}-(\Delta-t)) \\
&\quad \cdot [I_{\text{E}}(t_{\text{off}}-(\Delta-t)) - K\tau_m r(t_{\text{off}}-(2\Delta-t)) - \mu(t_{\text{off}}-(\Delta-t))]
\end{aligned}
\tag{4.102}
$$

For the times $t_{\text{off}} - (2\Delta - t) \in [t_{\text{off}} - 2\Delta, t_{\text{off}} - \Delta]$ the rate is approximated as

$$
\begin{aligned}
r(t_{\text{off}}-(2\Delta-t)) &= [\dot{\mu}(t_{\text{off}}-(2\Delta-t))]_+\, p\left(V_T, t_{\text{off}}-(2\Delta-t)\right) \\
&\overset{(\text{A1})}{\approx} \frac{1}{\tau_m}\left[I_{\text{E}}(t_{\text{off}}-(2\Delta-t)) - \mu(t_{\text{off}}-(2\Delta-t))\right] p(t_{\text{off}}-(2\Delta-t))\ .
\end{aligned}
$$

Inserting this approximation in Eq. (4.102) yields:

$$
\begin{aligned}
I(t+t_{\text{off}}) \approx I_{\text{E}}(t+t_{\text{off}}) - Kp(t_{\text{off}}-(\Delta-t))\Big[& I_{\text{E}}(t_{\text{off}}-(\Delta-t)) - \mu(t_{\text{off}}-(\Delta-t)) \\
& - Kp(t_{\text{off}}-(2\Delta-t))\Big[I_{\text{E}}(t_{\text{off}}-(2\Delta-t)) - \mu(t_{\text{off}}-(2\Delta-t))\Big]\Big]
\end{aligned}
\tag{4.103}
$$

We already approximated the trajectory of μ during the upstroke in Step 1 (Eq. (4.83)):

$$
\Rightarrow \quad I_{\text{E}}(t_{\text{off}}-x) - \mu(t_{\text{off}}-x) \overset{(4.83)}{\approx} \left(I_{\text{E}}(t_{\text{off}}) - \mu_{\max}\right) \mathrm{e}^{x/\tau_m} - mx
$$

Using this approximation in Eq. (4.103) (and abbreviating $p(\cdot)$ as $p(\cdot)$ for readability) yields:

$$
\begin{aligned}
I(t+t_{\text{off}}) &\approx I_{\text{E}}(t_{\text{off}}) + mt - Kp(t_{\text{off}}-(\Delta-t))\Big[\left(I_{\text{E}}(t_{\text{off}}) - \mu_{\max}\right)\mathrm{e}^{(\Delta-t)/\tau_m} - m(\Delta-t) \\
&\qquad - Kp(t_{\text{off}}-(2\Delta-t))\Big[\left(I_{\text{E}}(t_{\text{off}}) - \mu_{\max}\right)\mathrm{e}^{(2\Delta-t)/\tau_m} - m(2\Delta-t)\Big]\Big] \\
&= I^{\text{stat}}(t+t_{\text{off}}) + I^m(t+t_{\text{off}})
\end{aligned}
\tag{4.104}
$$

where

$$
\begin{aligned}
I^{\text{stat}}(t+t_{\text{off}}) &= \hat{I}_{\text{E}} - Kp(t_{\text{off}}-(\Delta-t))\left(\hat{I}_{\text{E}} - \mu_{\max}\right)\mathrm{e}^{(\Delta-t)/\tau_m} \\
&\quad + K^2 p(t_{\text{off}}-(\Delta-t))p(t_{\text{off}}-(2\Delta-t))\left(\hat{I}_{\text{E}} - \mu_{\max}\right)\mathrm{e}^{(2\Delta-t)/\tau_m} \\
I^m(t+t_{\text{off}}) &= mt + Kp(t_{\text{off}}-(\Delta-t))m(\Delta-t) \\
&\quad - K^2 p(t_{\text{off}}-(\Delta-t))p(t_{\text{off}}-(2\Delta-t))m(2\Delta-t)\ .
\end{aligned}
$$

4.D Background on Fokker-Planck Equations and linear response

4.D.1 The Fokker-Planck Equation for leaky integrate-and-fire (LIF) neurons

The Langevin Equation

$$\tau_m \dot{x}_i = -x_i + I(t) + \sqrt{2D\tau_m}\xi_i(t) \tag{4.105}$$

has the associated Fokker-Planck Equation (FPE)

$$\tau_m \partial_t p(x,t) = -\partial_x \Big(\big(I(t) - x \big) p(x,t) \Big) + D\partial_x^2 p(x,t) \ . \tag{4.106}$$

The FPE can also be written as a continuity equation

$$\Leftrightarrow \quad \partial_t p(x,t) = -\partial_x J(x,t) \tag{4.107}$$

with the probability current

$$J(x,t) := \Big(\frac{1}{\tau_m} \big(I(t) - x \big) p(x,t) \Big) - \frac{D}{\tau_m} \partial_x p(x,t) \ . \tag{4.108}$$

4.D.1.1 Natural boundary conditions

First, I will solve the FPE Eq. (4.106) with *natural* boundary conditions

$$p(\pm\infty, t) = \partial_x p(x,t)|_{\pm\infty} = 0 \tag{4.109}$$

given either a Dirac Delta or a Gaussian distribution as initial condition:

$$p(x,0) = \delta(x - x_0) \quad \vee \quad p(x,0) = \frac{1}{\sqrt{2\pi}\sigma_0} \exp\left[-\frac{(x-x_0)^2}{2\sigma_0^2} \right] \ .$$

Steady-state solution. The steady-state solution of the FPE Eq. (4.106) with natural boundary conditions is given by:

$$p(x) = \frac{1}{\sqrt{2\pi}\sigma_\infty} \exp\left(-\frac{(x-I)^2}{2\sigma_\infty^2} \right) \quad \text{with } \sigma_\infty^2 := D \ . \tag{4.110}$$

Proof
Setting $\partial_t p(x,t) = 0$ yields

$$\begin{aligned} &\partial_x \Big(-\big(I - x \big) p(x) + D\partial_x p(x) \Big) = 0 \\ \Rightarrow \quad &-\big(I - x \big) p(x) + D\partial_x p(x) = \text{const.} = 0 \ , \quad \text{since } p(\pm\infty) = \partial_x p(x)|_{\pm\infty} = 0 \end{aligned} \tag{4.111}$$

The solution of this ODE is found as

$$\begin{aligned} &\int \frac{1}{p} dp = \frac{1}{D} \int \Big(I - x\Big)\,\mathrm{d}x \\ \Rightarrow \quad &\ln(p) = \frac{1}{D}\left(Ix - \frac{1}{2}x^2\right) + \text{const.} \\ \Rightarrow \quad &p(x) = \exp\left(-\frac{x^2 - 2Ix + \text{const.}}{2D}\right) = c \exp\left(-\frac{(x-I)^2}{2D}\right) \end{aligned}$$

Using the normalization condition of p as a probability density and substituting $\tau := \frac{x-I}{\sqrt{2D}}, \mathrm{d}\tau/\,\mathrm{d}x = \frac{1}{\sqrt{2D}}$, we can find the constant c:

$$\int_{-\infty}^{\infty} p(x)\,\mathrm{d}x = c\sqrt{2D} \int_{-\infty}^{\infty} \exp(-\tau^2)\,\mathrm{d}\tau = c\sqrt{2\pi D} \overset{!}{=} 1 \qquad \Rightarrow \qquad c = \frac{1}{\sqrt{2\pi D}}$$

$$\Rightarrow \qquad p(x) = \frac{1}{\sqrt{2\pi}\sigma_\infty} \exp\left(-\frac{(x-I)^2}{2\sigma_\infty^2}\right), \quad \sigma_\infty = \sqrt{D} \qquad \square$$

Time-dependent solution. If the initial condition is either a Dirac Delta distribution or a Gaussian, the time-dependent solution of the FPE Eq. (4.106) with natural boundary conditions is given by:

$$p(x,t) = \frac{1}{\sqrt{2\pi}\sigma(t)} \exp\left[-\frac{(x - x_{av}(t))^2}{2\sigma^2(t)}\right] \tag{4.112}$$

where

$$\begin{aligned} x_{av}(t) &:= \left(x_0\,\mathrm{e}^{-t/\tau_m} + \frac{1}{\tau_m}\int_0^t \mathrm{e}^{-(t-\bar{t})/\tau_m}\, I(\bar{t})\,\mathrm{d}\bar{t}\right) \\ \sigma^2(t) &:= \begin{cases} D\left(1 - \mathrm{e}^{-2t/\tau_m}\right) & , p(x,0) = \delta(x - x_0) \\ \sigma_0^2\,\mathrm{e}^{-2t/\tau_m} + D\left(1 - \mathrm{e}^{-2t/\tau_m}\right) & , p(x,0) = \frac{1}{\sqrt{2\pi}\sigma_0}\exp\left[-\frac{(x-x_0)^2}{2\sigma_0^2}\right] \end{cases} \end{aligned}$$

(Uhlenbeck and Ornstein, 1930, see also Eqs. (5.22)ff in Risken, 1989, 3.8.4 in Gardiner, 1985).

Proof

At first we will make no assumption on the initial condition $p(x,0)$. We take the Fourier transform on both sides of the FPE:

$$\tilde{p}(\omega,t) := \int_{-\infty}^{\infty} \mathrm{e}^{-i\omega x}\, p(x,t)\,\mathrm{d}x \quad , \text{ initial condition: } \tilde{p}(\omega,0) = \int_{-\infty}^{\infty} \mathrm{e}^{-i\omega x}\, p(x,0)\,\mathrm{d}x$$

$$\begin{aligned} \tau_m \partial_t \tilde{p}(\omega,t) &= \int_{-\infty}^{\infty} \mathrm{e}^{-i\omega x}\,\partial_t p(x,t)\,\mathrm{d}x \overset{(4.107)}{=} -\int_{-\infty}^{\infty} \mathrm{e}^{-i\omega x}\,\partial_x J(x,t)\,\mathrm{d}x \\ &= \underbrace{-\Big[\mathrm{e}^{-i\omega x}\, J(x,t)\Big]_{-\infty}^{\infty}}_{=0 \quad (bc)} - i\omega \int_{-\infty}^{\infty} \mathrm{e}^{-i\omega x}\, J(x,t)\,\mathrm{d}x \\ &= i\omega\Big(-I(t)\underbrace{\int_{-\infty}^{\infty} \mathrm{e}^{-i\omega x}\, p\,\mathrm{d}x}_{=\tilde{p}} + \underbrace{\int_{-\infty}^{\infty} \mathrm{e}^{-i\omega x}\, xp\,\mathrm{d}x}_{=i\partial_\omega \tilde{p} \quad (4.113)} + D\underbrace{\int_{-\infty}^{\infty} \mathrm{e}^{-i\omega x}\,\partial_x p\,\mathrm{d}x}_{=i\omega\tilde{p} \quad (4.114)}\Big) \\ &= -i\omega I(t)\tilde{p} - \omega\partial_\omega\tilde{p} - \omega^2 D\tilde{p} = -\Big(\omega^2 D + i\omega I(t)\Big)\,\tilde{p} - \omega\partial_\omega\tilde{p} \end{aligned}$$

The following auxiliary calculations have been used above:

$$\partial_\omega \tilde{p}(\omega,t) = -i\int_{-\infty}^{\infty} \mathrm{e}^{-i\omega x}\, x p(x,t)\,\mathrm{d}x \tag{4.113}$$

$$\int_{-\infty}^{\infty} \mathrm{e}^{-i\omega x}\,\partial_x p\,\mathrm{d}x = \underbrace{\left[\mathrm{e}^{-i\omega x}\,p\right]}_{=0} + i\omega \underbrace{\int_{-\infty}^{\infty} \mathrm{e}^{-i\omega x}\,p\,\mathrm{d}x}_{=\tilde{p}} = i\omega\tilde{p} \tag{4.114}$$

The PDE in Fourier space is only first order and can be solved by the method of characteristics:

$$\tau_m \partial_t \tilde{p}(\omega,t) + \omega\partial_\omega \tilde{p}(\omega,t) = -\left(\omega^2 D + i\omega I(t)\right)\tilde{p} \tag{4.115}$$

For a parametrisation $(t(s),\omega(s)) = (\tau_m s, \omega_0\,\mathrm{e}^s)$, such that

$$\frac{\mathrm{d}t}{\mathrm{d}s} = \tau_m\,, \quad \frac{\mathrm{d}\omega}{\mathrm{d}s} = \omega$$

a characteristic ODE can be inferred from the PDE as

$$\begin{aligned}\frac{\mathrm{d}}{\mathrm{d}s}\tilde{p}(\omega(s),t(s)) &= \frac{\mathrm{d}t}{\mathrm{d}s}\partial_t\tilde{p}(\omega(s),t(s)) + \frac{\mathrm{d}\omega}{\mathrm{d}s}\partial_\omega\tilde{p}(\omega(s),t(s))\\ &= \tau_m\partial_t\tilde{p}(\omega(s),t(s)) + \omega\partial_\omega\tilde{p}(\omega(s),t(s))\\ &\overset{(4.115)}{=} -\left(\omega^2(s)D + i\omega(s)I(\tau_m s)\right)\tilde{p}(\omega(s),t(s))\end{aligned}$$

This ODE can be solved via variation of the constant:

$$\begin{aligned}\Rightarrow\quad \ln(\tilde{p}) &= -D\int \omega^2(s)ds - i\int \omega(s)I(\tau_m s)ds\\ &= -\frac{D\omega_0^2}{2}\,\mathrm{e}^{2s} - i\omega_0\int e^z I(\tau_m z)\,\mathrm{d}z + \text{const.}\\ \Rightarrow\quad \tilde{p}(s) &= c\exp\left[-\frac{D\omega_0^2}{2}\,\mathrm{e}^{2s} - i\omega_0\int_0^s e^z I(\tau_m z)\,\mathrm{d}z\right]\end{aligned}$$

We find the constant c using the initial condition:

$$\begin{aligned}\tilde{p}(0) &= c\exp\left[-\frac{D\omega_0^2}{2}\right] \overset{!}{=} \tilde{p}(\omega_0,0) \quad\Rightarrow\quad c = \tilde{p}(\omega_0,0)\exp\left[\frac{D\omega_0^2}{2}\right]\\ \Rightarrow\quad \tilde{p}(s) &= \tilde{p}(\omega_0,0)\exp\left[\frac{D\omega_0^2}{2}\left(1-\mathrm{e}^{2s}\right) - i\omega_0\int_0^s \mathrm{e}^z\, I(\tau_m z)\,\mathrm{d}z\right]\end{aligned}$$

Resubstitute $s = t/\tau_m, \omega_0 = \omega\,\mathrm{e}^{-t/\tau_m}$:

$$\tilde{p}(\omega,t) = \tilde{p}(\omega\,\mathrm{e}^{-t/\tau_m},0)\exp\left[\frac{D\omega^2}{2}\left(\mathrm{e}^{-2t/\tau_m}-1\right) - i\omega\underbrace{\frac{1}{\tau_m}\int_0^t \mathrm{e}^{-(t-\bar{t})/\tau_m}\, I(\bar{t})\,\mathrm{d}\bar{t}}_{=:\kappa * I}\right]$$

with membrane filter $\kappa(t) := 1/\tau_m\,\mathrm{e}^{-t/\tau_m}$. Taking the inverse Fourier transform yields

$$\begin{aligned}p(x,t) &= \frac{1}{2\pi}\int_{-\infty}^{\infty} \mathrm{e}^{i\omega x}\,\tilde{p}(\omega,t)\,\mathrm{d}\omega\\ &= \frac{1}{2\pi}\int_{-\infty}^{\infty} \tilde{p}(\omega\,\mathrm{e}^{-t/\tau_m},0)\exp\left[i\omega x + \frac{D\omega^2}{2}\left(\mathrm{e}^{-2t/\tau_m}-1\right) - i\omega\kappa * I(t)\right]\mathrm{d}\omega\end{aligned}$$

One can now distinguish different initial conditions:

1: Dirac Delta

$$\begin{aligned} & p(x,0) = \delta(x-x_0) \\ \Rightarrow \quad & \tilde{p}(\omega,0) = \int_{-\infty}^{\infty} \mathrm{e}^{-i\omega x}\, p(x,0)\,\mathrm{d}x = \mathrm{e}^{-i\omega x_0} \end{aligned}$$

It follows:

$$\begin{aligned} p(x,t) &= \frac{1}{2\pi}\int_{-\infty}^{\infty} \tilde{p}(\omega\,\mathrm{e}^{-t/\tau_m},0)\exp\left[i\omega x + \frac{D\omega^2}{2}\left(\mathrm{e}^{-2t/\tau_m}-1\right) - i\omega\kappa * I(t)\right]\mathrm{d}\omega \\ &= \frac{1}{2\pi}\int_{-\infty}^{\infty} \exp\left[i\omega x + \frac{D\omega^2}{2}\left(\mathrm{e}^{-2t/\tau_m}-1\right) - i\omega\underbrace{\left(x_0\,\mathrm{e}^{-t/\tau_m} + \kappa * I(t)\right)}_{=:x_{\mathrm{av}}(t)}\right]\mathrm{d}\omega \\ &= \frac{1}{2\pi}\int_{-\infty}^{\infty} \exp\left[i\omega x + \frac{D\omega^2}{2}\left(\mathrm{e}^{-2t/\tau_m}-1\right) - i\omega x_{av}(t)\right]\mathrm{d}\omega \\ &= \frac{1}{2\pi}\int_{-\infty}^{\infty} \exp\left[-\underbrace{\frac{D}{2}\left(1-\mathrm{e}^{-2t/\tau_m}\right)}_{a}\omega^2 + i\omega\underbrace{(x - x_{av}(t))}_{b}\right]\mathrm{d}\omega \end{aligned}$$

Use: $\int_{-\infty}^{\infty} e^{-a\omega^2+i\omega b}\,\mathrm{d}\omega = \sqrt{\pi/a}e^{-b^2/4a}$:

$$\begin{aligned} &= \frac{1}{\sqrt{2\pi}\sqrt{D\left(1-\mathrm{e}^{-2t/\tau_m}\right)}}\exp\left[-\frac{(x-x_{av}(t))^2}{2D\left(1-\mathrm{e}^{-2t/\tau_m}\right)}\right] \\ &= \frac{1}{\sqrt{2\pi}\sigma(t)}\exp\left[-\frac{(x-x_{av}(t))^2}{2\sigma^2(t)}\right], \quad \sigma^2(t) = D\left(1-\mathrm{e}^{-2t/\tau_m}\right) \end{aligned} \tag{4.116}$$

2: Gaussian

$$\begin{aligned} & p(x,0) = \frac{1}{\sqrt{2\pi}\sigma_0}\exp\left[-\frac{(x-x_0)^2}{2\sigma_0^2}\right] \\ \Rightarrow \quad & \tilde{p}(\omega,0) = \int_{-\infty}^{\infty} \mathrm{e}^{-i\omega x}\,\frac{1}{\sqrt{2\pi}\sigma_0}\exp\left[-\frac{(x-x_0)^2}{2\sigma_0^2}\right]\mathrm{d}x \\ & \qquad = \frac{1}{\sqrt{2\pi}\sigma_0}\int_{-\infty}^{\infty}\exp\left[-i\omega x - \frac{1}{2\sigma_0^2}x^2 + \frac{2x_0 x}{2\sigma_0^2} - \frac{x_0^2}{2\sigma_0^2}\right]\mathrm{d}x \\ & \qquad = \frac{1}{\sqrt{2\pi}\sigma_0}\,\mathrm{e}^{-\frac{x_0^2}{2\sigma_0^2}}\int_{-\infty}^{\infty}\exp\left[-\frac{1}{2\sigma_0^2}x^2 + ix(-\omega - i\frac{x_0}{\sigma_0^2})\right]\mathrm{d}x \\ & \qquad = \frac{1}{\sqrt{2\pi}\sigma_0}\,\mathrm{e}^{-\frac{x_0^2}{2\sigma_0^2}}\sqrt{\pi 2\sigma_0^2}\exp\left[-\frac{(\omega + i\frac{x_0}{\sigma_0^2})^2}{4}2\sigma_0^2\right] \\ & \qquad = \exp\left[-\frac{x_0^2}{2\sigma_0^2} - \frac{\sigma_0^2}{2}\left(\omega^2 + 2i\omega\frac{x_0}{\sigma_0^2} - \frac{x_0^2}{\sigma_0^4}\right)\right] \\ & \qquad = \exp\left[-\frac{\sigma_0^2}{2}\omega^2 - i\omega x_0\right] \end{aligned}$$

It follows:

$$
\begin{aligned}
p(x,t) &= \frac{1}{2\pi}\int_{-\infty}^{\infty} \tilde{p}(\omega\,\mathrm{e}^{-t/\tau_m},0)\exp\left[i\omega x + \frac{D\omega^2}{2}\left(\mathrm{e}^{-2t/\tau_m}-1\right) - i\omega\kappa * I(t)\right]\mathrm{d}\omega\\
&= \frac{1}{2\pi}\int_{-\infty}^{\infty} \mathrm{e}^{i\omega x}\exp\Big[-\underbrace{\left(\frac{\sigma_0^2}{2}\,\mathrm{e}^{-2t/\tau_m}+\frac{D}{2}\left(1-\mathrm{e}^{-2t/\tau_m}\right)\right)}_{=:\frac{1}{2}\sigma^2(t)}\omega^2\\
&\qquad - i\omega\underbrace{\left(x_0\,\mathrm{e}^{-t/\tau_m}+\kappa*I(t)\right)}_{=:x_{\mathrm{av}}(t)}\Big]\,\mathrm{d}\omega\\
&= \frac{1}{2\pi}\int_{-\infty}^{\infty}\exp\left[-\frac{1}{2}\sigma^2(t)\omega^2 + i\omega(x-x_{\mathrm{av}}(t))\right]\mathrm{d}\omega
\end{aligned}
$$

Use: $\int_{-\infty}^{\infty} e^{-a\omega^2+i\omega b}\,\mathrm{d}\omega = \sqrt{\pi/a}e^{-b^2/4a}$:

$$
= \frac{1}{2\pi}\sqrt{\frac{2\pi}{\sigma^2(t)}}\exp\left[-\frac{(x-x_{\mathrm{av}}(t))^2}{2\sigma^2(t)}\right] = \frac{1}{\sqrt{2\pi}\sigma(t)}\exp\left[-\frac{(x-x_{\mathrm{av}}(t))^2}{2\sigma^2(t)}\right] \qquad \square
$$

General initial condition
The solution for an arbitrary initial condition $p_0(x)$ (that satisfies the normalization condition $\int_{-\infty}^{\infty} p_0(x)\,\mathrm{d}x = 1$) can be found by convolution with the solution $p_\delta(x,t|x_0)$ for initial Dirac delta distribution $\delta(x-x_0)$ (Eq. (4.116)):

$$
\begin{aligned}
p(x,t) &= \int_{-\infty}^{\infty} p_0(x_0)p_\delta(x,t|x_0)\,\mathrm{d}x_0 \qquad (4.117)\\
&= \int_{-\infty}^{\infty} p_0(x_0)\frac{1}{\sqrt{2\pi}\sigma(t)}\exp\left[-\frac{(x-x_{\mathrm{av}}(t))^2}{2\sigma^2(t)}\right]\mathrm{d}x_0
\end{aligned}
$$

Since $x_{\mathrm{av}}^{\infty} := \lim_{t\to\infty} x_{\mathrm{av}}(t)$ is independent of the initial condition x_0, we get the long-time limit:

$$
\lim_{t\to\infty} p(x,t) = \frac{1}{\sqrt{2\pi D}}\exp\left[-\frac{(x-x_{\mathrm{av}}^{\infty})^2}{2D}\right]\underbrace{\int_{-\infty}^{\infty} p_0(x_0)\,\mathrm{d}x_0}_{=1} \qquad (4.118)
$$

So for any "well-behaved" initial condition the solution will become Gaussian density with fixed variance D in the long time limit $t \to \infty$.

4.D.1.2 Absorbing boundary condition and source term

If units are reset to x_R when they reach a threshold x_T (fire-and-reset rule), the following combination of boundary conditions arises for the FPE (4.106):

$$\begin{aligned}
&\lim_{x\to-\infty} p(x,t) &&= \lim_{x\to-\infty} \partial_x p(x,t) = 0 && \text{natural boundary} \quad (4.119a)\\
&p(x_T,t) &&= 0 && \text{absorbing boundary} \quad (4.119b)\\
&\partial_x p(x_T,t) &&= -\frac{\tau_m}{D} r(t) && \text{rate} \quad (4.119c)\\
&[\partial_x p(x,t)]_{x_R} &&:= \lim_{\epsilon\to 0}\Big(\partial_x p(x_R+\epsilon,t) - \partial_x p(x_R-\epsilon,t)\Big) && \\
& &&= -\frac{\tau_m}{D} r(t) && \text{source term in } x_R \quad (4.119d)\\
&\int_{-\infty}^{x_T} p(x,t)\,\mathrm{d}x = 1 \quad \forall\, t\,, && && \text{normalization} \quad (4.119e)
\end{aligned}$$

The population rate is defined as the probability current through the threshold:

$$r(t) := J(x_T,t) \tag{4.119f}$$

I assume here that there is no refractory period.

Steady-state solution The steady-state solution of the FPE Eq. (4.106) with constant current $I(t)\equiv I$ and boundary conditions Eqs. (4.119) is given by:

$$\begin{aligned}
p(x) &= \frac{\tau_m r_0}{D}\,\mathrm{e}^{-\frac{(x-I)^2}{2D}} \int_x^{x_T} \mathrm{e}^{\frac{(s-I)^2}{2D}}\,\Theta(s-x_R)\,\mathrm{d}s \qquad (4.120)\\
&= \begin{cases} \frac{\tau_m r_0}{D}\,\mathrm{e}^{-\frac{(x-I)^2}{2D}} \int_{x_R}^{x_T} \mathrm{e}^{\frac{(s-I)^2}{2D}}\,\mathrm{d}s, & x < x_R \\ \frac{\tau_m r_0}{D}\,\mathrm{e}^{-\frac{(x-I)^2}{2D}} \int_{x}^{x_T} \mathrm{e}^{\frac{(s-I)^2}{2D}}\,\mathrm{d}s, & x > x_R \end{cases}
\end{aligned}$$

with stationary rate

$$r_0 = \left(\sqrt{\pi}\tau_m \int_{\frac{I-x_T}{\sqrt{2D}}}^{\frac{I-x_R}{\sqrt{2D}}} \mathrm{e}^{y^2}\,\mathrm{erfc}(y)\,\mathrm{d}y\right)^{-1} \tag{4.121}$$

(Brunel and Hakim, 1999).

Proof
In the stationary state the population rate r is constant over time:

$$r(t) \equiv r_0$$

To find the stationary solution of the FPE we set the time-derivative of the density of membrane potentials p to zero:

$$\partial_t p(x,t) = -\partial_x J(x) = 0$$

It follows that the probability current J must be constant (with a discontinuous jump at x_R due to the source term, Eq. (4.119d)):

$$J(x) \overset{(4.108)}{=} \left(\frac{1}{\tau_m}\Big(I-x\Big)p(x)\right) - \frac{D}{\tau_m}\partial_x p(x) = \text{const.} \overset{\substack{(4.119f)\\(4.119d)}}{=} \begin{cases} r_0\,, & x > x_R \\ 0\,, & x < x_R \end{cases}$$

The FPE in the steady state is thus reduced to an ODE (from here on I denote the derivative w.r.t. x by $'$):

$$\Leftrightarrow \quad p' - \frac{1}{D}\Big(I-x\Big)p \quad = \begin{cases} -\frac{\tau_m}{D}r_0 & , x > x_R \\ 0 & , x < x_R \end{cases}$$

which can be rewritten using the heaviside function Θ:

$$\Leftrightarrow \quad p' - \frac{1}{D}\Big(I-x\Big)p \quad = -\frac{\tau_m}{D}r_0\Theta(x-x_R)$$

The ODE can be solved by the method of integrating factors: Both sides are multiplied by an integrating factor $u(x)$ which is chosen such that the left hand side of the ODE is equal to $\frac{\mathrm{d}}{\mathrm{d}\,x}(up)$.

$$\Leftrightarrow \quad \underbrace{up' + u\frac{1}{D}\Big(x-I\Big)p}_{\overset{!}{=}\frac{\mathrm{d}}{\mathrm{d}\,x}(up)=u'p+up'} = -\frac{\tau_m}{D}r_0\Theta(x-x_R)u$$

$$\begin{aligned} \Rightarrow \quad u' \quad &= u\frac{1}{D}\Big(x-I\Big) \\ u(x) \quad &= c\exp\left[\frac{\left(x-I\right)^2}{2D}\right] \qquad \text{(The constant is chosen as } c=1.) \end{aligned}$$

The ODE now has the form

$$\frac{\mathrm{d}}{\mathrm{d}\,x}(up) = -\frac{\tau_m}{D}r_0\Theta(x-x_R)u$$

which can be integrated to find p:

$$\begin{aligned} \Leftrightarrow \quad p(x) \quad &= -\frac{1}{u}\frac{\tau_m}{D}r_0\left(\int_0^x u(s)\Theta(s-x_R)\,\mathrm{d}s + C\right) \\ &= -\frac{\tau_m}{D}r_0\exp\left[-\frac{\left(x-I\right)^2}{2D}\right]\left(\int_0^x u(s)\Theta(s-x_R)\,\mathrm{d}s + C\right) \end{aligned}$$

The integration constant C is determined by the absorbing boundary condition at threshold, Eq. (4.119b):

$$\begin{aligned} p(x_T) \quad &= -\frac{\tau_m}{D}r_0\exp\left[-\frac{\left(x_T-I\right)^2}{2D}\right]\left(\int_0^{x_T} u(s)\Theta(s-x_R)\,\mathrm{d}s + C\right) \overset{(4.119b)}{=} 0 \\ \Leftrightarrow \quad C \quad &= -\int_0^{x_T} u(s)\Theta(s-x_R)\,\mathrm{d}s \\ \Leftrightarrow \quad p(x) \quad &= \frac{\tau_m}{D}r_0\exp\left[-\frac{\left(x-I\right)^2}{2D}\right]\int_x^{x_T} u(s)\Theta(s-x_R)\,\mathrm{d}s \qquad \square \end{aligned}$$

(cf. Eq. (3.10) in Brunel and Hakim, 1999).

The stationary rate r_0 is found using the normalization condition (4.119e):

$$\begin{aligned}1 &\overset{!}{=} \int_{-\infty}^{x_T} p(x)\,\mathrm{d}x \\ &= \int_{-\infty}^{x_T} \frac{\tau_m}{D} r_0 \exp\left[-\frac{(I-x)^2}{2D}\right] \left(\int_x^{x_T} u(s)\Theta(s-x_R)\,\mathrm{d}s\right) \mathrm{d}x\end{aligned}$$

Substitute $v := (x-I)/\sqrt{2D}$, $\mathrm{d}v/\,\mathrm{d}x = 1/\sqrt{2D}$:

$$= \sqrt{2}\frac{\tau_m}{\sqrt{D}} r_0 \int_{-\infty}^{\frac{x_T-I}{\sqrt{2D}}} \mathrm{e}^{-v^2} \int_{\sqrt{2D}v+I}^{\frac{x_T-I}{\sqrt{2D}}} \exp\left[\frac{(I-s)^2}{2D}\right] \Theta(s-x_R)\,\mathrm{d}s\,\mathrm{d}v$$

Substitute $y := (s-I)/\sqrt{2D}$, $\mathrm{d}y/\,\mathrm{d}s = 1/\sqrt{2D}$:

$$= 2\tau_m r_0 \int_{-\infty}^{\frac{x_T-I}{\sqrt{2D}}} \int_v^{\frac{x_T-I}{\sqrt{2D}}} \mathrm{e}^{y^2-v^2}\, \Theta\left(y - \frac{x_R-I}{\sqrt{2D}}\right) \mathrm{d}y\,\mathrm{d}v$$

The integration boundaries can be exchanged as shown in Eq. (4.122):

$$\begin{aligned}&= 2\tau_m r_0 \int_{\frac{x_R-I}{\sqrt{2D}}}^{\frac{x_T-I}{\sqrt{2D}}} \int_{-\infty}^{y} \mathrm{e}^{y^2-v^2}\,\mathrm{d}v\,\mathrm{d}y = 2\tau_m r_0 \int_{\frac{I-x_T}{\sqrt{2D}}}^{\frac{I-x_R}{\sqrt{2D}}} \mathrm{e}^{y^2} \int_y^{\infty} \mathrm{e}^{-v^2}\,\mathrm{d}v\,\mathrm{d}y \\ \Leftrightarrow \quad r_0 &= \left(\sqrt{\pi}\tau_m \int_{\frac{I-x_T}{\sqrt{2D}}}^{\frac{I-x_R}{\sqrt{2D}}} \mathrm{e}^{y^2}\,\mathrm{erfc}(y)\,\mathrm{d}y\right)^{-1} \qquad \square\end{aligned}$$

Auxiliary calculation: exchange of integration boundaries

$$\int_{-\infty}^{X_T} \int_v^{X_T} f(y,v)\Theta\left(y - X_R\right) \mathrm{d}y\,\mathrm{d}v = \int_{X_R}^{X_T} \int_{-\infty}^{y} f(y,v)\,\mathrm{d}v\,\mathrm{d}y \tag{4.122}$$

4.D.2 The Fokker-Planck Equation for pulse-coupled oscillators with linear phase response curve

The Langevin Equation

$$\dot{x} = \omega - KZ(x)r_0 + \sqrt{2D}\xi(t)$$

with constant (external) inhibition r_0, scaled by a linear PRC $Z(x) = x - \theta_R$ has the associated Fokker-Planck Equation (FPE)

$$\partial_t p(x,t) = -\partial_x\Big(\left[\omega - KZ(x)r_0\right] p(x,t)\Big) + D\partial_x^2 p(x,t) \ . \tag{4.123}$$

Steady-state solution for natural boundary conditions. The steady-state solution of the FPE (4.123) with natural boundary conditions

$$\lim_{x\to\pm\infty} p(x,t) = \partial_x p(x,t) = 0 \tag{4.124}$$

and normalization condition $\int_{-\infty}^{\infty} p(x,t)\,\mathrm{d}x = 1$, is given by:

$$p(x) = \frac{1}{\sqrt{2\pi}\Sigma_\infty} \exp\left[-\frac{\left(x - \frac{\omega+\theta_0 K r_0}{K r_0}\right)^2}{2\Sigma_\infty^2}\right], \quad \Sigma_\infty = \sqrt{\frac{D}{K r_0}}\,. \tag{4.125}$$

Proof Abbreviating the drift term as $A(x) := \omega - KZ(x)r_0$ and setting $\partial_t p(x,t) = 0$ yields:

$$\partial_x\left(-A(x)p(x) + D\partial_x p(x)\right) = 0$$

$$\Leftrightarrow \quad -A(x)p(x) + D\partial_x p(x) = \text{const.} \overset{(4.124)}{=} 0 \qquad \Leftrightarrow \quad \ln(p) = \frac{1}{D}\int_0^x A(\bar{x})\,\mathrm{d}\bar{x} + \text{const.}$$

$$\begin{aligned}
p(x) &= c\exp\left[\frac{1}{D}\int_0^x A(\bar{x})\,\mathrm{d}\bar{x}\right] = c\exp\left[\frac{1}{D}\int_0^x (\omega - KZ(\bar{x})r_0)\,\mathrm{d}\bar{x}\right] \\
&= c\exp\left[\frac{1}{D}\left(\omega x - K r_0\int_0^x Z(\bar{x})\,\mathrm{d}\bar{x}\right)\right] = c\exp\left[\frac{1}{D}\left(\omega x - K r_0\left(\frac{1}{2}x^2 - \theta_R x\right)\right)\right] \\
&= c\exp\left[-\frac{x^2 - 2\left(\frac{\omega}{K r_0} + \theta_R\right)x}{2D/K r_0}\right] = c\exp\left[-\frac{\left(x - \frac{\omega+\theta_R K r_0}{K r_0}\right)^2 - \left(\frac{\omega+\theta_R K r_0}{K r_0}\right)^2}{2D/K r_0}\right] \\
&=: \tilde{c}\exp\left[-\frac{\left(x - \frac{\omega+\theta_R K r_0}{K r_0}\right)^2}{2D/K r_0}\right]
\end{aligned}$$

The constant $\tilde{c}$ is determined by the normalization condition:

$$p(x) = \frac{1}{\sqrt{2\pi}\Sigma_\infty}\exp\left[-\frac{\left(x - \frac{\omega+\theta_R K r_0}{K r_0}\right)^2}{2\Sigma_\infty^2}\right], \quad \Sigma_\infty = \sqrt{\frac{D}{K r_0}}$$

4.D.3 Linear response

This section follows the derivation in the lecture notes “Neural Noise and Neural Signals” by Benjamin Lindner (2018, Section 6.2). Following their notation, the Fourier transform is defined with a sign change compared to the rest of the dissertation (and Brunel and Hakim (1999)):

$$\tilde{f}(\omega) := \int_{-\infty}^{\infty} f(t)e^{+i\omega t}\,\mathrm{d}t \tag{4.126}$$

Time and frequency are denoted in units of the membrane time constant and its inverse respectively.

Consider a general integrate-and-fire (IF) unit with an unspecified nonlinearity f, that is subject to Gaussian white noise of intensity D, a mean drive μ, and a weak periodic perturbation $s(t) := \epsilon\,\mathrm{e}^{-i\omega t}$ of angular frequency ω ($\epsilon > 0$ small):

$$\dot{V} = f(V) + \mu + \epsilon\,\mathrm{e}^{-i\omega t} + \sqrt{2D}\xi(t)$$

The nonlinearity f and the mean drive μ define a potential $U(v)$ that determines the unit's subthreshold dynamics:

$$= -U'(V) + \epsilon\, \mathrm{e}^{-i\omega t} + \sqrt{2D}\xi(t)$$

The associated Fokker-Planck Equation reads:

$$\begin{aligned}\partial_t P(V,t) &= \partial_V \underbrace{\left[\Big(U'(V) - \epsilon\, \mathrm{e}^{-i\omega t} + D\partial_V \Big) P(V,t) \right]}_{=:-J(V,t)} + r(t-\tau_{\mathrm{ref}})\delta(V-V_R) \\ &= \mathcal{L}P(V,t) - \epsilon\, \mathrm{e}^{-i\omega t}\, \partial_V P(V,t) + r(t-\tau_{\mathrm{ref}})\delta(V-V_R) \qquad (4.127)\end{aligned}$$

with the operator

$$\mathcal{L}[\cdot] := \partial_V \Big(\Big(U'(V) + D\partial_V \Big) [\cdot] \Big) \qquad (4.128)$$

The boundary conditions are given by:

$$P(V_T,t) = 0 \qquad (4.129a)$$

$$r(t) = J(V_T,t) = -D \left.\frac{\partial P}{\partial V}\right|_{V_T} \qquad (4.129b)$$

$$\lim_{V\to-\infty} P(V,t) = 0 \qquad (4.129c)$$

As a probability density $P(V,t)$ is normalized:

$$\int_{-\infty}^{\infty} P(V,t)\,\mathrm{d}V = \int_{-\infty}^{V_T} P(V,t)\,\mathrm{d}V = 1 \quad \forall\, t \qquad (4.129d)$$

The jump discontinuity at the reset potential has been incorporated directly into the FPE as a source term.

Given the periodic drive, both the density P and the rate r will settle into periodic solutions (after initial conditions have been forgotten). Such periodic solutions of angular frequency ω must satisfy:

$$P\left(V, t + \frac{2\pi}{\omega}\right) = P(V,t), \quad r\left(t + \frac{2\pi}{\omega}\right) = r(t)$$

Since the drive is weak ($\sim \mathcal{O}(\epsilon)$) one can expand both the rate and the voltage density in ϵ and consider only the terms up to first order.

Expanding r: For the rate we assume there is an (unknown) function G that describes the linear response to a weak periodic drive s:

$$\begin{aligned} r(t) &\approx r_0 + G * s(t) = r_0 + \int_{-\infty}^{t} G(t-t')s(t')dt' = r_0 + \epsilon \int_{-\infty}^{t} G(t-t')\, \mathrm{e}^{-i\omega t'}\, dt' \\ &= r_0 + \epsilon \int_{-\infty}^{t} G(t-t')\, \mathrm{e}^{i\omega(t-t')}\, dt'\, \mathrm{e}^{-i\omega t} = r_0 + \epsilon \int_{0}^{\infty} G(s)\, \mathrm{e}^{i\omega s}\, \mathrm{d}s\, \mathrm{e}^{-i\omega t}\end{aligned}$$

G should be a causal filter ($G(t<0)=0$), hence one can extend the lower integration boundary to $-\infty$:

$$\begin{aligned}
&= r_0 + \epsilon \int_{-\infty}^{\infty} G(s)\,\mathrm{e}^{i\omega s}\,\mathrm{d}s\,\mathrm{e}^{-i\omega t} \\
&= r_0 + \epsilon \tilde{G}(\omega)\,\mathrm{e}^{-i\omega t}
\end{aligned}$$

Expanding P: The first order linear expansion of the solution of the FPE will in general be given by the stationary solution P_0 plus a term of order ϵ that is ω-periodic in time and has an unknown voltage-dependence:

$$P(V,t) \approx P_0(V) + \epsilon\,\mathrm{e}^{-i\omega t}\,\underbrace{\mathrm{e}^{-\frac{U(V)-U(V_R)}{2D}}}_{=:e_-(V)} q(V)$$

For convenience the voltage-dependent factor is split into an unknown $q(V)$ and a prefactor $e_-(V)$, which will simplify the ODE derived for q in the following.
Inserting the linear expansion into the FPE (Eq. (4.127)) yields:

$$\begin{aligned}
-\epsilon i\omega\,\mathrm{e}^{-i\omega t}\,e_- q = {}& \mathcal{L}P_0 + r_0\delta(V-V_R) \\
&+ \epsilon\,\mathrm{e}^{-i\omega t}\,\mathcal{L}\left(e_- q\right) - \epsilon\,\mathrm{e}^{-i\omega t}\,\partial_V P_0 + \epsilon\tilde{G}(\omega)\,\mathrm{e}^{-i\omega(t-\tau_{\mathrm{ref}})}\,\delta(V-V_R) + \mathcal{O}(\epsilon^2)
\end{aligned} \tag{4.130}$$

Comparing linear terms $\sim \mathcal{O}(\epsilon)$ on both sides leads to an ODE for $q(V)$:

$$\begin{aligned}
i\omega e_- q &= -\mathcal{L}\left(e_- q\right) + \partial_V P_0 - \tilde{G}(\omega)\,\mathrm{e}^{i\omega\tau_{\mathrm{ref}}}\,\delta(V-V_R) \\
\underbrace{\left(\mathcal{L}+i\omega\right)\left(e_-(V)q(V)\right)}_{=:(*)} &= \partial_V P_0(V) - \tilde{G}(\omega)\,\mathrm{e}^{i\omega\tau_{\mathrm{ref}}}\,\delta(V-V_R)
\end{aligned} \tag{4.131}$$

Let's write out the left-hand side $(*)$:

$$\begin{aligned}
(*) &\overset{(4.128)}{=} U''\left(e_- q\right) + U'\left(e_-' q + e_- q'\right) + D\left(e_- q\right)'' + i\omega e_- q \\
&= U''\left(e_- q\right) + U'\left(e_-' q + e_- q'\right) + D\left(e_-'' q + 2e_-' q' + e_- q''\right) + i\omega e_- q
\end{aligned}$$

Sort by order of q:

$$= De_- q'' + \left(U' e_- + 2De_-'\right) q' + \left(U'' e_- + U' e_-' + De_-'' + i\omega e_-\right) q$$

We use $e_-' = -\frac{U'}{2D} e_-$ and $e_-'' = -\frac{U''}{2D} e_- + \frac{(U')^2}{4D^2} e_-$ and multiply by $e_+ := 1/e_-$.

$$\begin{aligned}
\Leftrightarrow \quad e_+(*) &= Dq'' + \left(U' - U'\right) q' + \left(U'' - \frac{(U')^2}{2D} - \frac{U''}{2} + \frac{(U')^2}{4D} + i\omega\right) q \\
&= Dq'' - \underbrace{\left(\frac{(U')^2}{4D} - \frac{U''}{2} - i\omega\right)}_{=:F(V)} q
\end{aligned} \tag{4.132}$$

Eq. (4.131) is thus equivalent to the following ODE for q:

$$\begin{aligned} Dq'' - F(V)q &= e_+(V)\left(P_0'(V) - \tilde{G}(\omega)\,\mathrm{e}^{i\omega\tau_{\mathrm{ref}}}\,\delta(V-V_R)\right) \\ &= H(V) - e_+(V)\tilde{G}(\omega)\,\mathrm{e}^{i\omega\tau_{\mathrm{ref}}}\,\delta(V-V_R) \\ \Leftrightarrow \quad Dq'' - F(V)q &= H(V) - \tilde{G}(\omega)\,\mathrm{e}^{i\omega\tau_{\mathrm{ref}}}\,\delta(V-V_R)\,, \quad \text{since } e_+(V_R)=1 \end{aligned} \tag{4.133}$$

and where

$$H(V) := e_+(V)P_0'(V)\ .$$

Boundary conditions: The boundary conditions of this ODE are inferred from the boundary conditions of the original FPE:

$$\lim_{V\to-\infty} q(V) = 0 \tag{4.134}$$

$$q(V_T) = 0$$

$$[q(V)]_{V_R} = 0$$

$$q'(V_T) = -\frac{\tilde{G}(\omega)}{D}e_+(V_T) \tag{4.135}$$

Eq. (4.135) is derived as follows:

$$\begin{aligned} \partial_V P(V,t)|_{V_T} &= P_0'(V_T) + \epsilon\,\mathrm{e}^{-i\omega t}\left(e_-'(V_T)\underbrace{q(V_T)}_{=0} + e_-(V_T)q'(V_T)\right) \\ &= P_0'(V_T) + \epsilon\,\mathrm{e}^{-i\omega t}\,e_-(V_T)q'(V_T) \end{aligned}$$

The original boundary condition, given the expansion of r, reads:

$$\partial_V P(V,t)|_{V_T} = -\frac{r(t)}{D} = -\frac{r_0}{D} - \epsilon\frac{\tilde{G}(\omega)}{D}\,\mathrm{e}^{-i\omega t}$$

Comparing equal powers of ϵ yields Eq. (4.135).
Solving the ODE Eq. (4.133)*:* First the Green's function is determined, i.e. the solution for a simple delta-source term:

$$Dq'' - F(V)q = -\delta(V-V_s) \tag{4.136}$$

which is equivalent to a homogeneous ODE in the separate regimes $V \lessgtr V_s$ and a jump condition for the derivative q' in V_s:

$$\begin{aligned} & Dq'' - F(V)q = 0 \qquad \text{for } V<V_s \text{ and } V>V_s \text{ resp.} \\ \text{and} \qquad & [q']_{V_s} = -\frac{1}{D}\ ,\ \text{where } [q']_{V_s} := \lim_{\epsilon\to 0}\left(q'(V_s+\epsilon) - q'(V_S-\epsilon)\right) \end{aligned} \tag{4.137}$$

Assume we know two independent solutions q_1, q_2 of the homogeneous ODE $Dq'' - F(V)q = 0$. Then

$$Q := q_1q_2' - q_1'q_2 \overset{*}{=} \text{const.} \overset{**}{=} 1$$

*since: $Q' = q_1 q_2'' - q_1'' q_2 = -q_1 \frac{F(V)}{D} q_2 + \frac{F(V)}{D} q_1 q_2 = 0$.
** with appropriate scaling
A general solution of Eq. (4.136) can be constructed as:

$$q_G(V, V_s) := A \begin{cases} (q_{1s} q_{2T} - q_{1T} q_{2s}) q_1(V), & V < V_s \\ (q_1(V) q_{2T} - q_{1T} q_2(V)) q_{1s}, & V > V_s \end{cases} \tag{4.138}$$

where

$$q_{iT} = q_i(V_T), \qquad q_{is} = q_i(V_s)$$

q_1 is chosen such that $\lim_{V \to -\infty} q_1(V) = 0$ to ensure that boundary condition Eq. (4.134) is met. The prefactor A is chosen such that the jump condition at reset is satisfied (Eq. (4.137)):

$$\begin{aligned} \frac{1}{A}[q_G']_{V_s} &\overset{(4.137)}{=} -\frac{1}{AD} \qquad\qquad (4.139) \\ \frac{1}{A}[q_G']_{V_s} &= \frac{1}{A} q_G'(V_s^+) - \frac{1}{A} q_G'(V_s^-) \\ &\overset{(4.138)}{=} (q_{1s}' q_{2T} - q_{1T} q_{2s}') q_{1s} - (q_{1s} q_{2T} - q_{1T} q_{2s}) q_{1s}' = -q_{1T} q_{2s}' q_{1s} + q_{1T} q_{2s} q_{1s}' \\ &= -q_{1T} \underbrace{\left(q_{1s} q_{2s}' - q_{1s}' q_{2s} \right)}_{=Q=1} \end{aligned}$$

$$\overset{(4.139)}{\Longrightarrow} \qquad A = \frac{1}{D q_{1T}}$$

A particular solution for the ODE Eq. (4.133) is found by convolution of the original source term with the Green's function:

$$\begin{aligned} q(V) &= -\int_{-\infty}^{V_T} q_G(V, V_s) \Big(H(V_s) - \tilde{G}(\omega)\, \mathrm{e}^{i\omega\tau_{\mathrm{ref}}}\, \delta(V_s - V_R) \Big)\, \mathrm{d}V_s \\ &= -\int_{-\infty}^{V_T} q_G(V, V_s) H(V_s)\, \mathrm{d}V_s + q_G(V, V_R) \tilde{G}(\omega)\, \mathrm{e}^{i\omega\tau_{\mathrm{ref}}} \\ &= q_G(V, V_R) \tilde{G}(\omega)\, \mathrm{e}^{i\omega\tau_{\mathrm{ref}}} - \int_{-\infty}^{V_T} q_G(V, V_s) H(V_s)\, \mathrm{d}V_s \end{aligned} \tag{4.140}$$

Using the boundary condition at the threshold (Eq. (4.135)) one obtains a closed expression for the susceptibility $\tilde{G}(\omega)$:

$$q'(V_T) = \underbrace{q_G'(V_T, V_R)}_{=-\frac{q_{1R}}{D q_{1T}}} \tilde{G}(\omega)\, \mathrm{e}^{i\omega\tau_{\mathrm{ref}}} - \int_{-\infty}^{V_T} \underbrace{q_G'(V_T, V_s)}_{=-\frac{q_{1s}}{D q_{1T}}} H(V_s)\, \mathrm{d}V_s \overset{(4.135)}{=} -\frac{\tilde{G}(\omega)}{D} e_+(V_T) \tag{4.141}$$

where we have used the derivative of the Green's function:

$$q_G'(V_T, V_s) = A \underbrace{(q_{1T}' q_{2T} - q_{1T} q_{2T}')}_{=-Q=-1} q_{1s} = -\frac{q_{1s}}{D q_{1T}}\ .$$

Eq. (4.141) is thus equivalent to:

$$\begin{aligned}
&\left(\frac{q_{1R}}{q_{1T}}\,\mathrm{e}^{i\omega\tau_\mathrm{ref}} - e_+(V_T)\right)\tilde{G}(\omega) = \frac{1}{q_{1T}}\int_{-\infty}^{V_T} q_1(V_s)e_+(V_s)P_0'(V_s)\,\mathrm{d}V_s \\
\Leftrightarrow\quad &\frac{\mathrm{e}^{i\omega\tau_\mathrm{ref}}\, e_-(V_T)q_{1R} - q_{1T}}{q_{1T}e_-(V_T)}\tilde{G}(\omega) = \frac{1}{q_{1T}}\int_{-\infty}^{V_T} q_1(V_s)e_+(V_s)P_0'(V_s)\,\mathrm{d}V_s \\
\Leftrightarrow\quad &\tilde{G}(\omega) = -\frac{e_-(V_T)\int_{-\infty}^{V_T} q_1(v)e_+(v)P_0'(v)\,\mathrm{d}v}{q_{1T} - \mathrm{e}^{i\omega\tau_\mathrm{ref}}\, e_-(V_T)q_{1R}} \qquad (4.142)
\end{aligned}$$

This is the general susceptibility for any IF unit under Gaussian white noise and still needs to be evaluated for a concrete potential $U(V)$. In the following I will derive the susceptibility specifically for the LIF unit with potential $U(V) = \frac{1}{2}V^2 - \mu V$.

4.D.3.1 Linear response of the LIF unit under Gaussian white noise

The LIF unit has potential $U(V) = \frac{1}{2}V^2 - \mu V$ and hence the membrane potential under periodic drive is described by the following ODE:

$$\begin{aligned}
\dot{V} &= -U'(V) + \epsilon\,\mathrm{e}^{-i\omega t} + \sqrt{2D}\xi(t) \\
&= -V + \mu + \epsilon\,\mathrm{e}^{-i\omega t} + \sqrt{2D}\xi(t)
\end{aligned}$$

Again time is given in units of the membrane time constant and the voltage has been shifted such that the leak potential is at 0 ($V(t) \mapsto V(\tau_m t) - E_L$).
The homogeneous ODE $Dq'' - F(V)q = 0$ for

$$F(V) = \frac{(U')^2}{4D} - \frac{U''}{2} - i\omega = \frac{(V-\mu)^2}{4D} - \frac{1}{2} - i\omega$$

becomes

$$0 = Dq'' - \left(\frac{(V-\mu)^2}{4D} - \frac{1}{2} - i\omega\right)q \qquad (4.143)$$

We subtract the mean drive from the membrane potential and rescale w.r.t. the noise standard deviation:

$$x(V) := \frac{V-\mu}{\sqrt{D}}$$

For this rescaled voltage x we get:

$$\begin{aligned}
F(V) &= \bar{F}(x) = \frac{1}{4}x^2 + a\,, \qquad a := -\frac{1}{2} - i\omega \\
q(V) &= \bar{q}(x(V)) \\
q' &= \frac{\mathrm{d}q}{\mathrm{d}V} = \frac{\mathrm{d\bar{q}}}{\mathrm{dx}}\frac{\mathrm{dx}}{\mathrm{dV}} = \frac{\mathrm{d\bar{q}}}{\mathrm{dx}}\frac{1}{\sqrt{D}} = \frac{1}{\sqrt{D}}\bar{q}' \qquad (\text{now } ' \text{ denotes } \frac{\mathrm{d}}{\mathrm{dx}}) \\
q'' &= \frac{\mathrm{d}}{\mathrm{d}V}\frac{\mathrm{d}\bar{q}}{\mathrm{d}V} = \frac{\mathrm{d}}{\mathrm{d}V}\left(\frac{1}{\sqrt{D}}\frac{\mathrm{d\bar{q}}}{\mathrm{dx}}\right) = \frac{1}{\sqrt{D}}\frac{\mathrm{d^2\bar{q}}}{\mathrm{dx}^2}\frac{\mathrm{d}x}{\mathrm{d}V} = \frac{1}{D}\frac{d^2\bar{q}}{\mathrm{d}x^2} = \frac{1}{D}\bar{q}''
\end{aligned}$$

The ODE Eq. (4.143) in terms of $\bar{q}(x)$ reads:

$$0 = \bar{q}''(x) - \bar{F}(x)\bar{q}(x) = \bar{q}''(x) - \left[\frac{1}{4}x^2 + a\right]\bar{q}(x)$$

The solutions of this ODE can be expressed in terms of parabolic cylinder functions (Abramowitz and Stegun (1965)(19.1.2)):

$$\begin{aligned}\bar{q}_1(x) &= \mathcal{U}(a,-x) = \mathcal{D}_{-a-\frac{1}{2}}(-x) = \mathcal{D}_{i\omega}(-x)\\ \bar{q}_2(x) &= \mathcal{U}(a,x) = \mathcal{D}_{i\omega}(x)\end{aligned}$$

The notations $\mathcal{U}$ (used in Abramowitz and Stegun (1965) and auxiliary calculation 1) and $\mathcal{D}$ (used in Lindner and Schimansky-Geier (2001)) are interchangeable. The two independent solutions of the original ODE in terms of V are:

$$\begin{aligned}q_1(V) &= \mathcal{U}\left(-i\omega - \frac{1}{2}, \frac{\mu - V}{\sqrt{D}}\right) = \mathcal{D}_{i\omega}\left(\frac{\mu - V}{\sqrt{D}}\right)\\ q_2(V) &= \mathcal{U}\left(-i\omega - \frac{1}{2}, \frac{V - \mu}{\sqrt{D}}\right) = \mathcal{D}_{i\omega}\left(\frac{V - \mu}{\sqrt{D}}\right)\end{aligned} \tag{4.144}$$

The solution q_1 was chosen such that $\lim_{V\to-\infty} q_1(V) = 0$ as required above. The expression for the susceptibility derived above for a general IF unit (Eq. (4.142)) can now be evaluated specifically for the LIF unit:

$$\tilde{G}(\omega) \overset{(4.142)}{=} -\frac{e_-(V_T)\int_{-\infty}^{V_T} q_1(v)e_+(v)P_0'(v)\,\mathrm{d}v}{q_{1T} - \mathrm{e}^{i\omega\tau_{\text{ref}}}\,e_-(V_T)q_{1R}}$$

First the integral is solved with integration by parts (see auxiliary calculation 1):

$$\begin{aligned}\tilde{G}(\omega) &\overset{(4.153)}{=} -\frac{e_-(V_T)\frac{r_0}{\sqrt{D}}\frac{i\omega}{i\omega-1}\left[\hat{q}_1(V_R) - e_+(V_T)\hat{q}_1(V_T)\right]}{q_{1T} - \mathrm{e}^{i\omega\tau_{\text{ref}}}\,e_-(V_T)q_{1R}}\\ &= \frac{r_0}{\sqrt{D}}\frac{i\omega}{i\omega - 1}\frac{\hat{q}_1(V_T) - e_-(V_T)\hat{q}_1(V_R)}{q_{1T} - \mathrm{e}^{i\omega\tau_{\text{ref}}}\,e_-(V_T)q_{1R}}\end{aligned}$$

For the LIF potential U the factor $e_-(V)$ can be evaluated explicitly (see auxiliary calculation 2). Following the notation in Lindner et al. (2005) I abbreviate $e_-(V_T) =: \mathrm{e}^{\delta}$ where $\delta = \frac{V_R^2 - V_T^2 + 2\mu(V_T - V_R)}{4D}$.

$$\tilde{G}(\omega) = \frac{r_0}{\sqrt{D}}\frac{i\omega}{i\omega - 1}\frac{\hat{q}_1(V_T) - e^{\delta}\hat{q}_1(V_R)}{q_{1T} - \mathrm{e}^{i\omega\tau_{\text{ref}}}\,e^{\delta}q_{1R}}$$

Recalling that both q_1 and $\hat{q}_1$ are parabolic cylinder functions (Eqs. (4.144), (4.148)), we get:

$$\boxed{\tilde{G}(\omega) = \frac{r_0}{\sqrt{D}}\frac{i\omega}{i\omega - 1}\frac{\mathcal{D}_{i\omega-1}\left(\frac{\mu - V_T}{\sqrt{D}}\right) - e^{\delta}\mathcal{D}_{i\omega-1}\left(\frac{\mu - V_R}{\sqrt{D}}\right)}{\mathcal{D}_{i\omega}\left(\frac{\mu - V_T}{\sqrt{D}}\right) - e^{\delta}\,\mathrm{e}^{i\omega\tau_{\text{ref}}}\,\mathcal{D}_{i\omega}\left(\frac{\mu - V_R}{\sqrt{D}}\right)}} \tag{4.145}$$

(cf. Lindner and Schimansky-Geier (2001), Eq. (5), Lindner et al. (2005), Eq.(41)). Since the rest of this thesis uses the opposite sign convention for the Fourier transform (cf. Eq. (4.126)), the complex argument of the LIF susceptibility under Gaussian white noise will be reported as $-\arg\left(\tilde{G}(\omega)\right)$ (see for example Fig. 6.4).

Auxiliary calculation 1: The integral is solved with integration by parts:

$$\int_{-\infty}^{V_T} q_1(v)e_+(v)P_0'(v)\,\mathrm{d}v = \underbrace{\left[P_0(v)e_+(v)q_1(v)\right]_{-\infty}^{V_T}}_{=0\ \text{(Eqs. (4.129a), (4.129c))}} - \int_{-\infty}^{V_T} P_0(v)\underbrace{\left[e_+(v)q_1(v)\right]'}_{(*)}\mathrm{d}v \tag{4.146}$$

The term $(*)$ can be evaluated as follows:

$$\begin{aligned}
\left[e_+(v)q_1(v)\right]' &\overset{(4.144)}{=} \frac{v-\mu}{2D}e_+(v)q_1(v) + e_+(v)\frac{\mathrm{d}}{\mathrm{d}v}\mathcal{U}\left(-i\omega-\frac{1}{2},\frac{\mu-v}{\sqrt{D}}\right)\\
&= \frac{v-\mu}{2D}e_+(v)q_1(v) - \frac{e_+(v)}{\sqrt{D}}\,\frac{\mathrm{d}}{\mathrm{d}x}\mathcal{U}\left(-i\omega-\frac{1}{2},x\right)\Bigg|_{\frac{\mu-v}{\sqrt{D}}}\\
&\overset{(4.144)}{=} -\frac{e_+(v)}{\sqrt{D}}\left[\frac{1}{2}x\mathcal{U}\left(-i\omega-\frac{1}{2},x\right)+\frac{\mathrm{d}}{\mathrm{d}x}\mathcal{U}\left(-i\omega-\frac{1}{2},x\right)\right]_{x=\frac{\mu-v}{\sqrt{D}}}
\end{aligned}$$

Use the following recurrence relation from Abramowitz and Stegun (1965) Eq. (19.6.1): $\frac{1}{2}x\mathcal{U}(a,x)+\frac{\mathrm{d}}{\mathrm{d}x}\mathcal{U}(a,x) = -(a+\frac{1}{2})\mathcal{U}(a+1,x)$

$$= -i\omega\frac{e_+(v)}{\sqrt{D}}\mathcal{U}\left(\frac{1}{2}-i\omega,\frac{\mu-v}{\sqrt{D}}\right) = -i\omega\frac{e_+(v)}{\sqrt{D}}\hat{q}_1 \tag{4.147}$$

where function

$$\hat{q}_1 := \mathcal{U}\left(\frac{1}{2}-i\omega,\frac{\mu-v}{\sqrt{D}}\right) \tag{4.148}$$

solves the ODE:

$$D\hat{q}_1'' - \hat{F}(V)\hat{q}_1 = 0\,, \qquad \text{with } \hat{F}(V) = \frac{1}{4}\frac{(V-\mu)^2}{D} - i\omega + \frac{1}{2}$$

Adding $-(i\omega-1)\hat{q}_1$ to both sides the ODE can be rewritten as:

$$D\hat{q}_1'' - F_0(V)\hat{q}_1 = -(i\omega-1)\hat{q}_1\,, \quad \text{with } \hat{F}_0(V) := \hat{F}_{\omega=0}(V) = \frac{1}{4}\frac{(V-\mu)^2}{D} - \frac{1}{2} \tag{4.149}$$

which will be useful in the following.
So far we have simplified the integral as follows:

$$\int_{-\infty}^{V_T} q_1(v)e_+(v)P_0'(v)\,\mathrm{d}v \overset{\substack{(4.146)\\(4.147)}}{=} \frac{i\omega}{\sqrt{D}}\int_{-\infty}^{V_T}\underbrace{P_0(v)e_+(v)}_{=:q_0(v)}\hat{q}_1(v)\,\mathrm{d}v \tag{4.150}$$

Starting from the ODE for the stationary solution $P_0 = e_-(v)q_0(v)$ of the FPE (cf. Eq. (4.130)), we can infer an ODE for the rescaled function q_0:

$$-r_0\delta(v - V_R) \overset{(4.130)}{=} \mathcal{L}P_0(v) = \mathcal{L}\Big[e_-(v)q_0(v)\Big]$$

Applying the operator $\mathcal{L}$ to $e_-(v)q_0(v)$ as before (see Eq. (4.132)) yields:

$$= e_-(v)\left(Dq_0'' - \left(\frac{(U')^2}{4D} - \frac{U''}{2}\right)q_0\right) \overset{(4.149)}{=} e_-(v)\Big(Dq_0'' - \hat{F}_0(v)q_0\Big)$$

$$\Leftrightarrow \quad Dq_0'' - F_0(v)q_0 = -r_0\delta(v - V_R) \tag{4.151}$$

The boundary conditions are easily inferred from P_0

$$q_0(V_T) = 0 \tag{4.152a}$$

$$q_0'(V_T) = -\frac{r_0}{D}e_+(V_T) \tag{4.152b}$$

$$\lim_{v\to-\infty} q_0(v) = \lim_{v\to-\infty} q_0'(v) = 0 \tag{4.152c}$$

Now solve the integral:

$$\int_{-\infty}^{V_T} q_1(v)e_+(v)P_0'(v)\,\mathrm{d}v$$

$$\overset{(4.150)}{=} \frac{i\omega}{\sqrt{D}}\int_{-\infty}^{V_T} q_0(v)\hat{q}_1(v)\,\mathrm{d}v \overset{(4.149)}{=} -\frac{i\omega}{\sqrt{D}(i\omega-1)}\int_{-\infty}^{V_T} q_0(v)\Big[D\hat{q}_1'' - F_0(v)\hat{q}_1\Big]\,\mathrm{d}v$$

Integration by parts for the first summand yields:

$$= -\frac{i\omega}{\sqrt{D}(i\omega-1)}\Bigg[\underbrace{\Big[Dq_0(v)\hat{q}_1'\Big]_{-\infty}^{V_T}}_{\substack{=0\\((4.152\text{a}),\ (4.152\text{c}))}} - \int_{-\infty}^{V_T} Dq_0'(v)\hat{q}_1' + F_0(v)q_0(v)\hat{q}_1\,\mathrm{d}v\Bigg]$$

Another integration by parts resolves the integral:

$$= -\frac{i\omega}{\sqrt{D}(i\omega-1)}\Bigg[-\underbrace{\Big[Dq_0'(v)\hat{q}_1\Big]_{-\infty}^{V_T}}_{\substack{=-r_0e_+(V_T)\hat{q}_1(V_T)\\((4.152\text{b}),\ (4.152\text{c}))}} + \int_{-\infty}^{V_T}\underbrace{\Big[Dq_0''(v) - F_0(v)q_0(v)\Big]}_{=-r_0\delta(v-V_R)\ (\text{Eq. }(4.151))}\hat{q}_1\,\mathrm{d}v\Bigg]$$

$$= -\frac{i\omega}{\sqrt{D}(i\omega-1)}\left[r_0e_+(V_T)\hat{q}_1(V_T) - r_0\hat{q}_1(V_R)\right]$$

$$= \frac{r_0}{\sqrt{D}}\frac{i\omega}{i\omega-1}\left[\hat{q}_1(V_R) - e_+(V_T)\hat{q}_1(V_T)\right] \tag{4.153}$$

Auxiliary calculation 2:
For the LIF potential U the factor $e_-(V)$ can be evaluated as follows:

$$e_-(V) = \mathrm{e}^{-\frac{U(V)-U(V_R)}{2D}} = \mathrm{e}^{-\frac{\frac{1}{2}V^2-\mu V-\frac{1}{2}V_R^2+\mu V_R}{2D}} = \mathrm{e}^{\frac{V_R^2-V^2+2\mu(V-V_R)}{4D}}$$

$$\Rightarrow \quad e_-(V_T) = e^{\delta}$$

where

$$\delta = \frac{V_R^2 - V_T^2 + 2\mu(V_T - V_R)}{4D} \tag{4.154}$$

(cf. Eq. (40) in Lindner et al., 2005).

4.D.4 Two “flavors” of linear stability analysis

In this section I want to briefly comment on two slightly different ways of formulating the linear stability analysis, that can be found in the literature. I will refer to them here as the *single unit perspective* (Eq. (4.36) in Section 4.5.2.4 (see also Brunel and Hansel, 2006)), and the *network perspective* (Eq. (A.29) in Brunel and Hakim, 1999). I will show their equivalence explicitly for the case of a fully connected network. In short, the equivalence follows from the relation Eq. (4.161) between confluent hypergeometric functions and parabolic cylinder functions.

The single unit perspective
(Brunel and Hansel, 2006; Lindner and Schimansky-Geier, 2001)
The linear response ansatz that I described in Section 4.5.2.4 starts from the perspective of a single unit. The linear response of a single LIF unit under Gaussian white noise is calculated for a weakly sinusoidally modulated drive by solving the FPE for an uncoupled population (which can be thought of as many realizations of the same single unit stimulation). The resulting Fourier transform of the linear response function ("susceptibility") is expressed in terms of parabolic cylinder functions (cf. Eq. (4.145)):

$$\begin{aligned}\tilde{G}(\omega) &= \frac{\tau_m r_0}{\sqrt{D}} \frac{i\omega}{i\omega - 1} \frac{\mathcal{D}_{i\omega-1}\left(\frac{I_0-V_T}{\sqrt{D}}\right) - e^{\delta}\mathcal{D}_{i\omega-1}\left(\frac{I_0-V_R}{\sqrt{D}}\right)}{\mathcal{D}_{i\omega}\left(\frac{I_0-V_T}{\sqrt{D}}\right) - e^{\delta}\,\mathrm{e}^{i\omega\tau_{\mathrm{ref}}}\,\mathcal{D}_{i\omega}\left(\frac{I_0-V_R}{\sqrt{D}}\right)} \\ \delta &:= \frac{V_R^2 - V_T^2 + 2I_0(V_T - V_R)}{4D}\end{aligned}$$

(Lindner and Schimansky-Geier, 2001, cf. Brunel et al. (2001)). The delayed inhibitory feedback is only taken into account later, by noting that in the recurrent network the rate resulting from linear response determines the input drive and vice versa, which leads to a self-consistent condition.

$$\begin{aligned}&1 = -K\tilde{G}(\omega)\,\mathrm{e}^{i\omega\Delta/\tau_m} \qquad \text{(see Eq. (4.36))} \\ \Leftrightarrow\quad &\boxed{1 = -\frac{K\tau_m r_0}{\sqrt{D}} \frac{i\omega}{i\omega - 1} \frac{\mathcal{D}_{i\omega-1}\left(\frac{I_0-V_T}{\sqrt{D}}\right) - e^{\delta}\mathcal{D}_{i\omega-1}\left(\frac{I_0-V_R}{\sqrt{D}}\right)}{\mathcal{D}_{i\omega}\left(\frac{I_0-V_T}{\sqrt{D}}\right) - e^{\delta}\,\mathrm{e}^{i\omega\tau_{\mathrm{ref}}}\,\mathcal{D}_{i\omega}\left(\frac{I_0-V_R}{\sqrt{D}}\right)}\,\mathrm{e}^{i\omega\Delta/\tau_m}} \qquad (4.155)\end{aligned}$$

(time t and frequency ω are given in units of τ_m and $1/\tau_m$ respectively.)

The network perspective (Brunel and Hakim, 1999)
Brunel and Hakim (1999) analyze the FPE for the complete network, including the delayed inhibitory coupling. Thus the population rate, defined as the probability current through the threshold, appears also in the drift-term (and in the diffusion term in case of sparse coupling, $H \gneqq 0$)[3]. Conceptually the ansatz is the same: they search for a solution of the FPE with a rate and a membrane potential density that are weakly sinusoidally modulated. Both the rate and the membrane potential density are expanded linearly around their steady state and the FPE is then solved in Fourier space, which

---

[3] Please refer to the *Note on network architecture* in Section 4.5.2.5 for a quick introduction into the notation used in (Brunel and Hakim, 1999).

leads to a solvability condition in terms of confluent hypergeometric functions (Eq. (A.29) in (Brunel and Hakim, 1999)). In the case of all-to-all connectivity ($H = 0$), this solvability condition is indeed equivalent to the phase-/amplitude-condition resulting from the self-consistent linear response ansatz (Eq. (4.36)/Eq. (4.155) above).

In Brunel and Hakim (1999) the linear stability analysis is done from the network perspective and a solvability condition for the FPE is derived in terms of confluent hypergeometric functions (contained in $\phi_{1,2}$ as shown below):

$$\boxed{\left(\tilde{\phi}_2(y_\Theta) - \tilde{\phi}_2(y_r)\right)(1 - H\,\mathrm{e}^{-\lambda\delta/\tau}) = \tilde{W}_2[\hat{Q}_1^p](y_\Theta) - \left[\tilde{W}_2[\hat{Q}_1^p](y)\right]_{y_r^-}^{y_r^+}} \tag{4.156}$$

(Eq. (A.29) in Brunel and Hakim (1999)). Individual terms will be explained below.

Proof of equivalence

I will start from Brunel and Hakim's solvability condition Eq. (4.156) and demonstrate that for my reduced ripple model network ($H = 0$) it is equivalent to (4.155). Auxiliary calculations are summarized in Section 4.D.4.1 and will be referenced along the way. Note that the solvability condition Eq. (4.156) is given in the original notation from Brunel and Hakim (1999), while Eq. (4.155) follows the notation of this thesis. To facilitate comparison with the original paper I will start the derivation in the notation of Brunel and Hakim (1999) and only switch to my notation in the final step towards recovering Eq. (4.155). The switch of notation is summarized in Section 4.D.4.2. I start by writing out all the abbreviated terms in Eq. (4.156) explicitly:

The functions ϕ_1, ϕ_2 are (combinations of) confluent hypergeometric functions (Eq. (A.17) and (A.22) in Brunel and Hakim (1999)) that arise from the linear stability analysis: They are two independent solutions of the homogeneous part of the ODE that is derived for the linearly expanded FPE solution in Fourier space (Eq. (A.14) in Brunel and Hakim (1999)). $\tilde{\phi}_{1,2}$ denotes the scaling of these functions $\phi_{1,2}$ by their Wronskian

$$\begin{aligned}\tilde{\phi}_{1,2} &= \frac{\phi_{1,2}}{\mathrm{Wr}}\\ \mathrm{Wr} &= \phi_1\phi_2' - \phi_1'\phi_2 = \frac{2\sqrt{\pi}}{\Gamma(\lambda/2)}\exp(-y^2) \quad \text{(Eq. (A.25) in Brunel and Hakim (1999)).}\end{aligned}$$

$\hat{Q}_1^p$ is the particular solution of the complete, inhomogeneous ODE (Eq. (A.14) Brunel and Hakim (1999)). Its Wronskian with one of the homogeneous solutions ϕ_j ($j \in \{1, 2\}$), normalized by Wr, is denoted as

$$\tilde{W}_j[\hat{Q}_1^p] = \frac{\hat{Q}_1^p\phi_j' - \left(\hat{Q}_1^p\right)'\phi_j}{\mathrm{Wr}}\ .$$

Inserting these expressions in Eq. (4.156) yields:

$$\begin{aligned}
&\frac{\Gamma(\lambda/2)}{2\sqrt{\pi}}\left(\phi_2(y_\Theta)\,\mathrm{e}^{y_\Theta^2}-\phi_2(y_r)\,\mathrm{e}^{y_r^2}\right)(1-H\,\mathrm{e}^{-\lambda\delta/\tau})\\
&=\frac{\Gamma(\lambda/2)}{2\sqrt{\pi}}\,\mathrm{e}^{y_\Theta^2}\left(\hat{Q}_1^p\phi_2'-\left(\hat{Q}_1^p\right)'\phi_2\right)(y_\Theta)-\frac{\Gamma(\lambda/2)}{2\sqrt{\pi}}\,\mathrm{e}^{y_r^2}\left[\hat{Q}_1^p\phi_2'-\left(\hat{Q}_1^p\right)'\phi_2\right]_{y_r^-}^{y_r^+}\\
\Leftrightarrow\quad&\left(\phi_2(y_\Theta)\,\mathrm{e}^{y_\Theta^2}-\phi_2(y_r)\,\mathrm{e}^{y_r^2}\right)(1-H\,\mathrm{e}^{-\lambda\delta/\tau})\\
&=\mathrm{e}^{y_\Theta^2}\left(\hat{Q}_1^p\phi_2'-\left(\hat{Q}_1^p\right)'\phi_2\right)(y_\Theta)-\mathrm{e}^{y_r^2}\left[\hat{Q}_1^p\phi_2'-\left(\hat{Q}_1^p\right)'\phi_2\right]_{y_r^-}^{y_r^+}\\
\overset{\cdot\,\mathrm{e}^{\lambda\delta/\tau}}{\Leftrightarrow}\quad&\left(\phi_2(y_\Theta)\,\mathrm{e}^{y_\Theta^2}-\phi_2(y_r)\,\mathrm{e}^{y_r^2}\right)(\mathrm{e}^{\lambda\delta/\tau}-H)\\
&=\mathrm{e}^{\lambda\delta/\tau}\,\mathrm{e}^{y_\Theta^2}\left(\hat{Q}_1^p\phi_2'-\left(\hat{Q}_1^p\right)'\phi_2\right)(y_\Theta)-\mathrm{e}^{\lambda\delta/\tau}\,\mathrm{e}^{y_r^2}\left[\hat{Q}_1^p\phi_2'-\left(\hat{Q}_1^p\right)'\phi_2\right]_{y_r^-}^{y_r^+}\\
\Leftrightarrow\quad&\left(\phi_2(y_\Theta)\,\mathrm{e}^{y_\Theta^2}-\phi_2(y_r)\,\mathrm{e}^{y_r^2}\right)\mathrm{e}^{\lambda\delta/\tau}\\
&=\mathrm{e}^{\lambda\delta/\tau}\,\mathrm{e}^{y_\Theta^2}\left(\hat{Q}_1^p\phi_2'-\left(\hat{Q}_1^p\right)'\phi_2\right)(y_\Theta)-\mathrm{e}^{\lambda\delta/\tau}\,\mathrm{e}^{y_r^2}\left[\hat{Q}_1^p\phi_2'-\left(\hat{Q}_1^p\right)'\phi_2\right]_{y_r^-}^{y_r^+}\\
&\quad+H\left(\phi_2(y_\Theta)\,\mathrm{e}^{y_\Theta^2}-\phi_2(y_r)\,\mathrm{e}^{y_r^2}\right)
\end{aligned}\tag{4.157}$$

For the sake of readability the left- and right-hand side will be treated separately:

Left-hand side of Eq. (4.157)
The combination of confluent hypergeometric functions ϕ_2 can be expressed in terms of parabolic cylinder functions as shown in auxiliary calculation Eq. (4.162):

$$\begin{aligned}
\mathrm{LHS}&=\left(\phi_2(y_\Theta)\,\mathrm{e}^{y_\Theta^2}-\phi_2(y_r)\,\mathrm{e}^{y_r^2}\right)\mathrm{e}^{\lambda\delta/\tau}\\
&\overset{(4.162)}{=}2^{\frac{\lambda}{2}}\left(\mathrm{e}^{\frac{1}{2}y_\Theta^2}\,\mathcal{D}_{-\lambda}\left(-\sqrt{2}y_\Theta\right)-\mathrm{e}^{\frac{1}{2}y_r^2}\,\mathcal{D}_{-\lambda}\left(-\sqrt{2}y_r\right)\right)\mathrm{e}^{\lambda\delta/\tau}\\
&=2^{\frac{\lambda}{2}}\,\mathrm{e}^{\frac{1}{2}y_\Theta^2}\left(\mathcal{D}_{-\lambda}\left(-\sqrt{2}y_\Theta\right)-\mathrm{e}^{\frac{1}{2}(y_r^2-y_\Theta^2)}\,\mathcal{D}_{-\lambda}\left(-\sqrt{2}y_r\right)\right)\mathrm{e}^{\lambda\delta/\tau}
\end{aligned}\tag{4.158}$$

Right-hand side of Eq. (4.157)

$$\begin{aligned}
\mathrm{RHS}&=\mathrm{e}^{\lambda\delta/\tau}\,\mathrm{e}^{y_\Theta^2}\left(\hat{Q}_1^p\phi_2'-\left(\hat{Q}_1^p\right)'\phi_2\right)(y_\Theta)-\mathrm{e}^{\lambda\delta/\tau}\,\mathrm{e}^{y_r^2}\left[\hat{Q}_1^p\phi_2'-\left(\hat{Q}_1^p\right)'\phi_2\right]_{y_r^-}^{y_r^+}\\
&\quad+H\left(\phi_2(y_\Theta)\,\mathrm{e}^{y_\Theta^2}-\phi_2(y_r)\,\mathrm{e}^{y_r^2}\right)
\end{aligned}$$

First I insert the explicit terms for the particular solution $\hat{Q}_1^p$ and its derivatives (see auxiliary calculations Eqs. (4.166), (4.167), (4.171)):

$$\begin{aligned}
\mathrm{RHS} = {} & \mathrm{e}^{y_\Theta^2}\left(\left(-\frac{G}{1+\lambda}+\frac{H}{(2+\lambda)}y_\Theta\right)\phi_2'(y_\Theta)-2\left(\frac{G}{1+\lambda}y_\Theta+\frac{H}{2+\lambda}\left(1-y_\Theta^2\right)\right)\phi_2(y_\Theta)\right)\\
& -\mathrm{e}^{y_r^2}\left(\left(-\frac{G}{1+\lambda}+\frac{H}{(2+\lambda)}y_r\right)\phi_2'(y_r)-2\left(\frac{G}{1+\lambda}y_r+\frac{H}{2+\lambda}\left(1-y_r^2\right)\right)\phi_2(y_r)\right)\\
& +H\left(\phi_2(y_\Theta)\,\mathrm{e}^{y_\Theta^2}-\phi_2(y_r)\,\mathrm{e}^{y_r^2}\right)
\end{aligned}$$

The terms depending on threshold y_Θ and reset y_r can be separated as

$$= T(y_\Theta) - T(y_r)$$

with:

$$\begin{aligned}
T(y) := {} & \mathrm{e}^{y^2}\left(\left(\frac{H}{2+\lambda}y-\frac{G}{1+\lambda}\right)\phi_2'(y)+2\left(\frac{H}{2+\lambda}\left(y^2-1\right)-\frac{G}{1+\lambda}y+\frac{H}{2}\right)\phi_2(y)\right)\\
= {} & \mathrm{e}^{y^2}\left(\left(\frac{H}{2+\lambda}y-\frac{G}{1+\lambda}\right)\phi_2'(y)+\left(\frac{H}{2+\lambda}y-\frac{G}{1+\lambda}\right)2y\phi_2(y)+\frac{\lambda H}{2+\lambda}\phi_2(y)\right)\\
= {} & \frac{H}{2+\lambda}\left(y\left[\mathrm{e}^{y^2}\phi_2'(y)+2y\,\mathrm{e}^{y^2}\phi_2(y)\right]+\lambda\,\mathrm{e}^{y^2}\phi_2(y)\right)-\frac{G}{1+\lambda}\left[\mathrm{e}^{y^2}\phi_2'(y)+2y\,\mathrm{e}^{y^2}\phi_2(y)\right]\\
\overset{\substack{(4.164)\\(4.165)}}{=} {} & \frac{H}{2+\lambda}\lambda 2^{\frac{\lambda}{2}}\,\mathrm{e}^{\frac{1}{2}y^2}\,(\lambda+1)\,\mathcal{U}\left(\lambda+\frac{3}{2},-\sqrt{2}y\right)-\frac{G}{1+\lambda}2^{\frac{\lambda+1}{2}}\,\mathrm{e}^{\frac{1}{2}y^2}\,\lambda\mathcal{U}\left(\lambda+\frac{1}{2},-\sqrt{2}y\right)\\
= {} & \lambda 2^{\frac{\lambda}{2}}\,\mathrm{e}^{\frac{1}{2}y^2}\left[\frac{H}{2+\lambda}(\lambda+1)\,\mathcal{U}\left(\lambda+\frac{3}{2},-\sqrt{2}y\right)-\frac{G}{1+\lambda}\sqrt{2}\mathcal{U}\left(\lambda+\frac{1}{2},-\sqrt{2}y\right)\right]\\
= {} & \lambda 2^{\frac{\lambda}{2}}\,\mathrm{e}^{\frac{1}{2}y^2}\left[\frac{H}{2+\lambda}(\lambda+1)\,\mathcal{D}_{-\lambda-2}\left(-\sqrt{2}y\right)-\frac{G}{1+\lambda}\sqrt{2}\mathcal{D}_{-\lambda-1}\left(-\sqrt{2}y\right)\right] \qquad (4.159)
\end{aligned}$$

The right-hand side can thus be written in terms of parabolic cylinder functions:

$$\begin{aligned}
\mathrm{RHS} = {} & T(y_\Theta) - T(y_r)\\
\overset{(4.159)}{=} {} & \lambda 2^{\frac{\lambda}{2}}\Bigg[\frac{H}{2+\lambda}(\lambda+1)\,\mathrm{e}^{\frac{1}{2}y_\Theta^2}\,\mathcal{D}_{-\lambda-2}\left(-\sqrt{2}y_\Theta\right)-\frac{G}{1+\lambda}\sqrt{2}\,\mathrm{e}^{\frac{1}{2}y_\Theta^2}\,\mathcal{D}_{-\lambda-1}\left(-\sqrt{2}y_\Theta\right)\\
& -\frac{H}{2+\lambda}(\lambda+1)\,\mathrm{e}^{\frac{1}{2}y_r^2}\,\mathcal{D}_{-\lambda-2}\left(-\sqrt{2}y_r\right)+\frac{G}{1+\lambda}\sqrt{2}\,\mathrm{e}^{\frac{1}{2}y_r^2}\,\mathcal{D}_{-\lambda-1}\left(-\sqrt{2}y_r\right)\Bigg]
\end{aligned}$$

Group w.r.t. G and H:

$$\begin{aligned}
= {} & -2^{\frac{\lambda}{2}}\sqrt{2}\,\mathrm{e}^{\frac{1}{2}y_\Theta^2}\,G\frac{\lambda}{1+\lambda}\left[\mathcal{D}_{-\lambda-1}\left(-\sqrt{2}y_\Theta\right)-\mathrm{e}^{\frac{1}{2}(y_r^2-y_\Theta^2)}\,\mathcal{D}_{-\lambda-1}\left(-\sqrt{2}y_r\right)\right]\\
& +2^{\frac{\lambda}{2}}\,\mathrm{e}^{\frac{1}{2}y_\Theta^2}\,H\lambda\frac{1+\lambda}{2+\lambda}\left[\mathcal{D}_{-\lambda-2}\left(-\sqrt{2}y_\Theta\right)-\mathrm{e}^{\frac{1}{2}(y_r^2-y_\Theta^2)}\,\mathcal{D}_{-\lambda-2}\left(-\sqrt{2}y_r\right)\right] \qquad (4.160)
\end{aligned}$$

Back to Eq. (4.157)
Going back to Eq. (4.157) I equate the left-hand side and right-hand side terms:

$$\begin{aligned}
& \text{LHS} \overset{(4.157)}{=} \text{RHS} \\
\overset{(4.158)}{\overset{(4.160)}{\Leftrightarrow}} \quad & 2^{\frac{\lambda}{2}}\, \mathrm{e}^{\frac{1}{2}y_\Theta^2} \left(\mathcal{D}_{-\lambda}\left(-\sqrt{2}y_\Theta\right) - \mathrm{e}^{\frac{1}{2}(y_r^2-y_\Theta^2)}\, \mathcal{D}_{-\lambda}\left(-\sqrt{2}y_r\right) \right) \mathrm{e}^{\lambda\delta/\tau} \\
& = -2^{\frac{\lambda}{2}}\sqrt{2}\,\mathrm{e}^{\frac{1}{2}y_\Theta^2}\, G \frac{\lambda}{1+\lambda}\left[\mathcal{D}_{-\lambda-1}\left(-\sqrt{2}y_\Theta\right) - \mathrm{e}^{\frac{1}{2}(y_r^2-y_\Theta^2)}\, \mathcal{D}_{-\lambda-1}\left(-\sqrt{2}y_r\right)\right] \\
& \quad + 2^{\frac{\lambda}{2}}\, \mathrm{e}^{\frac{1}{2}y_\Theta^2}\, H\lambda \frac{1+\lambda}{2+\lambda}\left[\mathcal{D}_{-\lambda-2}\left(-\sqrt{2}y_\Theta\right) - \mathrm{e}^{\frac{1}{2}(y_r^2-y_\Theta^2)}\, \mathcal{D}_{-\lambda-2}\left(-\sqrt{2}y_r\right)\right] \\
\Leftrightarrow \quad & \left(\mathcal{D}_{-\lambda}\left(-\sqrt{2}y_\Theta\right) - \mathrm{e}^{\frac{1}{2}(y_r^2-y_\Theta^2)}\, \mathcal{D}_{-\lambda}\left(-\sqrt{2}y_r\right) \right) \mathrm{e}^{\lambda\delta/\tau} \\
& = -\sqrt{2} G \frac{\lambda}{1+\lambda}\left[\mathcal{D}_{-\lambda-1}\left(-\sqrt{2}y_\Theta\right) - \mathrm{e}^{\frac{1}{2}(y_r^2-y_\Theta^2)}\, \mathcal{D}_{-\lambda-1}\left(-\sqrt{2}y_r\right)\right] \\
& \quad + H\lambda \frac{1+\lambda}{2+\lambda}\left[\mathcal{D}_{-\lambda-2}\left(-\sqrt{2}y_\Theta\right) - \mathrm{e}^{\frac{1}{2}(y_r^2-y_\Theta^2)}\, \mathcal{D}_{-\lambda-2}\left(-\sqrt{2}y_r\right)\right] \\
\Leftrightarrow \quad 1 & = -\sqrt{2} G \frac{\lambda}{1+\lambda} \frac{\mathcal{D}_{-\lambda-1}\left(-\sqrt{2}y_\Theta\right) - \mathrm{e}^{\frac{1}{2}(y_r^2-y_\Theta^2)}\, \mathcal{D}_{-\lambda-1}\left(-\sqrt{2}y_r\right)}{\mathcal{D}_{-\lambda}\left(-\sqrt{2}y_\Theta\right) - \mathrm{e}^{\frac{1}{2}(y_r^2-y_\Theta^2)}\, \mathcal{D}_{-\lambda}\left(-\sqrt{2}y_r\right)}\, \mathrm{e}^{-\lambda\delta/\tau} + \mathcal{O}(H)
\end{aligned}$$

In my fully connected network with synaptic strength scaled as $1/N$ the fluctuations of the inhibitory feedback vanish in the mean-field limit ($H \to 0$ as $N \to \infty$), hence the last term can be neglected. Rewriting also the remaining terms in the notation of this thesis (see Section 4.D.4.2), the above equation becomes:

$$1 = -K \underbrace{\frac{\tau_m r_0}{\sqrt{D}} \frac{i\omega}{i\omega - 1} \frac{\mathcal{D}_{i\omega-1}\left(\frac{I_0-V_T}{\sqrt{D}}\right) - \mathrm{e}^{\delta}\, \mathcal{D}_{i\omega-1}\left(\frac{I_0-V_R}{\sqrt{D}}\right)}{\mathcal{D}_{i\omega}\left(\frac{I_0-V_T}{\sqrt{D}}\right) - \mathrm{e}^{\delta}\, \mathcal{D}_{i\omega}\left(\frac{I_0-V_R}{\sqrt{D}}\right)}}_{\tilde{G}(\omega) \text{ for } \tau_{\mathrm{ref}}=0} \underbrace{\mathrm{e}^{i\omega\Delta/\tau_m}}_{\tilde{\kappa}^{\delta}_{\Delta}} \qquad \square$$

I have thus recovered the solvability condition Eq. (4.155) in terms of parabolic cylinder functions as it results from the self-consistent linear response approach to linear stability analysis.

4.D.4.1 Auxiliary calculations

Relating parabolic cylinder and confluent hypergeometric functions
The following relation holds between parabolic cylinder functions $\mathcal{U}$ and confluent hypergeometric functions $\mathcal{M}$ (Abramowitz and Stegun, 1965, Eq. 19.12.3):

$$\begin{aligned}
& \mathcal{U}(a, \pm x) \\
& = \frac{\sqrt{\pi} 2^{-\frac{1}{4}-\frac{1}{2}a}\, \mathrm{e}^{-\frac{1}{4}x^2}}{\Gamma(\frac{3}{4}+\frac{1}{2}a)} \mathcal{M}\left(\frac{1}{2}a + \frac{1}{4}, \frac{1}{2}, \frac{1}{2}x^2\right) \mp \frac{\sqrt{\pi} 2^{\frac{1}{4}-\frac{1}{2}a} x\, \mathrm{e}^{-\frac{1}{4}x^2}}{\Gamma(\frac{1}{4}+\frac{1}{2}a)} \mathcal{M}\left(\frac{1}{2}a + \frac{3}{4}, \frac{3}{2}, \frac{1}{2}x^2\right) \\
& = \sqrt{\pi}\, \mathrm{e}^{-\frac{1}{4}x^2} \left[\frac{2^{-\frac{1}{4}-\frac{1}{2}a}}{\Gamma(\frac{3}{4}+\frac{1}{2}a)} \mathcal{M}\left(\frac{1}{2}a + \frac{1}{4}, \frac{1}{2}, \frac{1}{2}x^2\right) \mp \frac{2^{\frac{1}{4}-\frac{1}{2}a}}{\Gamma(\frac{1}{4}+\frac{1}{2}a)} x \mathcal{M}\left(\frac{1}{2}a + \frac{3}{4}, \frac{3}{2}, \frac{1}{2}x^2\right) \right]
\end{aligned}$$

Set $A := \frac{1}{2}a + \frac{1}{4}, y = x/\sqrt{2}$:

$$\begin{aligned}
&= \sqrt{\pi}\,\mathrm{e}^{-\frac{1}{2}y^2}\left[\frac{2^{-A}}{\Gamma(A+\frac{1}{2})}\mathcal{M}\left(A,\frac{1}{2},y^2\right) \mp \frac{2^{-A}}{\Gamma(A)}\sqrt{2}x\mathcal{M}\left(A+\frac{1}{2},\frac{3}{2},y^2\right)\right]\\
&= 2^{-A}\sqrt{\pi}\,\mathrm{e}^{-\frac{1}{2}y^2}\left[\frac{1}{\Gamma(A+\frac{1}{2})}\mathcal{M}\left(A,\frac{1}{2},y^2\right) \mp \frac{1}{\Gamma(A)}2y\mathcal{M}\left(A+\frac{1}{2},\frac{3}{2},y^2\right)\right] \qquad (4.161)
\end{aligned}$$

Brunel and Hakim's ϕ_2 in terms of the parabolic cylinder function $\mathcal{U}$:

$$\phi_2(y)\,\mathrm{e}^{y^2} = \mathrm{e}^{y^2}\,\frac{\sqrt{\pi}}{\Gamma\left(\frac{1+\lambda}{2}\right)}\mathcal{M}\left(\frac{1-\lambda}{2},\frac{1}{2},-y^2\right) + \mathrm{e}^{y^2}\,\frac{\sqrt{\pi}}{\Gamma\left(\frac{\lambda}{2}\right)}2y\mathcal{M}\left(1-\frac{\lambda}{2},\frac{3}{2},-y^2\right)$$

I use the relation $\mathrm{e}^{z}\,\mathcal{M}(b-a,b,-z) = \mathcal{M}(a,b,z)$ (Eq. (13.1.27) in Abramowitz and Stegun (1965)):

$$= \frac{\sqrt{\pi}}{\Gamma\left(\frac{1+\lambda}{2}\right)}\mathcal{M}\left(\frac{\lambda}{2},\frac{1}{2},y^2\right) + \frac{\sqrt{\pi}}{\Gamma\left(\frac{\lambda}{2}\right)}2y\mathcal{M}\left(\frac{1+\lambda}{2},\frac{3}{2},y^2\right)$$

For $A = \frac{\lambda}{2}$:

$$\begin{aligned}
&= 2^{A}\,\mathrm{e}^{\frac{1}{2}y^2}\,\underbrace{2^{-A}\sqrt{\pi}\,\mathrm{e}^{-\frac{1}{2}y^2}\left[\frac{1}{\Gamma\left(A+\frac{1}{2}\right)}\mathcal{M}\left(A,\frac{1}{2},y^2\right) + \frac{1}{\Gamma\left(A\right)}2y\mathcal{M}\left(A+\frac{1}{2},\frac{3}{2},y^2\right)\right]}_{=U\left(2A-\frac{1}{2},-\sqrt{2}y\right),\,\text{Eq. (4.161)}}\\
&= 2^{\frac{\lambda}{2}}\,\mathrm{e}^{\frac{1}{2}y^2}\,\mathcal{U}\left(\lambda-\frac{1}{2},-\sqrt{2}y\right) = 2^{\frac{\lambda}{2}}\,\mathrm{e}^{\frac{1}{2}y^2}\,\mathcal{D}_{-\lambda}\left(-\sqrt{2}y\right) \qquad (4.162)
\end{aligned}$$

Derivative of Brunel and Hakim's ϕ_2 in terms of the parabolic cylinder function $\mathcal{U}$:

$$\begin{aligned}
&\phi_2(y) \overset{(4.162)}{=} 2^{\frac{\lambda}{2}}\,\mathrm{e}^{-\frac{1}{2}y^2}\,\mathcal{U}\left(\lambda-\frac{1}{2},-\sqrt{2}y\right)\\
\Rightarrow\qquad &\phi_2'(y) = -y\phi_2(y) - \sqrt{2}2^{\frac{\lambda}{2}}\,\mathrm{e}^{-\frac{1}{2}y^2}\,\frac{\mathrm{d}}{\mathrm{d}x}U\left(\lambda-\frac{1}{2},x\right)\Bigg|_{-\sqrt{2}y}
\end{aligned}$$

According to Abramowitz and Stegun (1965) Eq. (19.6.1): $\frac{\mathrm{d}}{\mathrm{d}x}\mathcal{U}\left(a,x\right) = -\frac{1}{2}x\mathcal{U}(a,x) - (a+\frac{1}{2})\mathcal{U}(a+1,x)$.

$$\begin{aligned}
&= -y\phi_2(y) - \sqrt{2}2^{\frac{\lambda}{2}}\,\mathrm{e}^{-\frac{1}{2}y^2}\left(\frac{1}{\sqrt{2}}y\mathcal{U}\left(\lambda-\frac{1}{2},-\sqrt{2}y\right) - \lambda\mathcal{U}\left(\lambda+\frac{1}{2},-\sqrt{2}y\right)\right)\\
&= -y\phi_2(y) - y\underbrace{2^{\frac{\lambda}{2}}\,\mathrm{e}^{-\frac{1}{2}y^2}\,\mathcal{U}\left(\lambda-\frac{1}{2},-\sqrt{2}y\right)}_{=\phi_2(y)} + 2^{\frac{\lambda+1}{2}}\,\mathrm{e}^{-\frac{1}{2}y^2}\,\lambda\mathcal{U}\left(\lambda+\frac{1}{2},-\sqrt{2}y\right)\\
&= -2y\phi_2(y) + 2^{\frac{\lambda+1}{2}}\,\mathrm{e}^{-\frac{1}{2}y^2}\,\lambda\mathcal{U}\left(\lambda+\frac{1}{2},-\sqrt{2}y\right) \qquad (4.163)
\end{aligned}$$

RHS auxiliary calculation 1:

$$2y\,\mathrm{e}^{y^2}\,\phi_2(y)+\mathrm{e}^{y^2}\,\phi_2'(y)\overset{(4.163)}{=}2y\,\mathrm{e}^{y^2}\,\phi_2(y)-2y\,\mathrm{e}^{y^2}\,\phi_2(y)+2^{\frac{\lambda+1}{2}}\,\mathrm{e}^{\frac{1}{2}y^2}\,\lambda\mathcal{U}\left(\lambda+\frac{1}{2},-\sqrt{2}y\right)$$

$$=2^{\frac{\lambda+1}{2}}\,\mathrm{e}^{\frac{1}{2}y^2}\,\lambda\mathcal{U}\left(\lambda+\frac{1}{2},-\sqrt{2}y\right)\tag{4.164}$$

RHS auxiliary calculation 2:

$$\begin{aligned}&y\left[\mathrm{e}^{y^2}\,\phi_2'(y)+2y\,\mathrm{e}^{y^2}\,\phi_2(y)\right]+\lambda\,\mathrm{e}^{y^2}\,\phi_2(y)\\&\overset{(4.164)}{=}y2^{\frac{\lambda+1}{2}}\,\mathrm{e}^{\frac{1}{2}y^2}\,\lambda\mathcal{U}\left(\lambda+\frac{1}{2},-\sqrt{2}y\right)+\lambda2^{\frac{\lambda}{2}}\,\mathrm{e}^{\frac{1}{2}y^2}\,\mathcal{U}\left(\lambda-\frac{1}{2},-\sqrt{2}y\right)\\&=\lambda2^{\frac{\lambda}{2}}\,\mathrm{e}^{\frac{1}{2}y^2}\left[\sqrt{2}y\mathcal{U}\left(\lambda+\frac{1}{2},-\sqrt{2}y\right)+\mathcal{U}\left(\lambda-\frac{1}{2},-\sqrt{2}y\right)\right]\end{aligned}$$

According to Abramowitz and Stegun (1965) Eq. (19.6.4):
$-x\mathcal{U}(a,x)+\mathcal{U}(a-1,x)=\left(a+\frac{1}{2}\right)\mathcal{U}\left(a+1,x\right)$.

$$=\lambda2^{\frac{\lambda}{2}}\,\mathrm{e}^{\frac{1}{2}y^2}\,(\lambda+1)\,\mathcal{U}\left(\lambda+\frac{3}{2},-\sqrt{2}y\right)\tag{4.165}$$

Brunel and Hakim's particular solution $\hat{Q}_1^p$-terms written out fully:
Equation references (A.xx) refer to Brunel and Hakim (1999). For brevity I write f' instead of $\partial_y f$.
The particular solution at threshold is given by:

$$\begin{aligned}\hat{Q}_1^p(y_\Theta)&\overset{(A.16)}{=}\mathrm{e}^{-\lambda\delta/\tau}\left(\frac{G}{1+\lambda}Q_0'(y_\Theta)+\frac{H}{2(2+\lambda)}Q_0''(y_\Theta)\right)\\&\overset{(*)}{=}\mathrm{e}^{-\lambda\delta/\tau}\left(-\frac{G}{1+\lambda}+\frac{H}{(2+\lambda)}y_\Theta\right)\end{aligned}\tag{4.166}$$

$(*)$ The first derivative of the stationary solution at threshold $Q_0'(y_\Theta)=-1$ is given as a boundary condition (A.7). The second derivative is computed using the recurrence relation (A.9): $Q_0''(y_\Theta)=-2y_\Theta Q_0'(y_\Theta)-2Q_0(y_\Theta)=2y_\Theta$.
The same recurrence relation (A.9) is used to compute the derivative of $\hat{Q}_1^p$.

$$\begin{aligned}\left(\hat{Q}_1^p\right)'&=\mathrm{e}^{-\lambda\delta/\tau}\left(\frac{G}{1+\lambda}Q_0''+\frac{H}{2(2+\lambda)}Q_0'''\right)\\&\overset{(A.9)}{=}\mathrm{e}^{-\lambda\delta/\tau}\left(\frac{G}{1+\lambda}\left(-2yQ_0'(y)-2Q_0(y)\right)+\frac{H}{2(2+\lambda)}\left(-2yQ_0''(y)-4Q_0'(y)\right)\right)\\&=\mathrm{e}^{-\lambda\delta/\tau}\left(\frac{2G}{1+\lambda}\left(-yQ_0'(y)-Q_0(y)\right)+\frac{H}{2+\lambda}\left(-yQ_0''(y)-2Q_0'(y)\right)\right)\\&\overset{(A.9)}{=}\mathrm{e}^{-\lambda\delta/\tau}\left(\frac{2G}{1+\lambda}\left(-yQ_0'(y)-Q_0(y)\right)+\frac{H}{2+\lambda}\left(-y\left(-2Q_0-2yQ_0'\right)-2Q_0'(y)\right)\right)\\&=2\,\mathrm{e}^{-\lambda\delta/\tau}\left(-\frac{G}{1+\lambda}\left(yQ_0'(y)+Q_0(y)\right)+\frac{H}{2+\lambda}\left(yQ_0+(y^2-1)Q_0'\right)\right)\end{aligned}$$

At threshold the boundary conditions yield:

$$\left(\hat{Q}_1^p\right)'(y_\Theta) = 2\,\mathrm{e}^{-\lambda\delta/\tau}\left(\frac{G}{1+\lambda}y_\Theta + \frac{H}{2+\lambda}\left(1-y_\Theta^2\right)\right) \tag{4.167}$$

Next I evaluate the following discontinuities at the reset potential:

$$\left[Q_0''\right]_{y_r^-}^{y_r^+} = \underbrace{\left[-2Q_0\right]_{y_r^-}^{y_r^+}}_{0} - 2y_r\left[Q_0'\right]_{y_r^-}^{y_r^+} \overset{(A.7)}{=} 2y_r \tag{4.168}$$

$$\begin{aligned}\left[\hat{Q}_1^p\right]_{y_r^-}^{y_r^+} &= \mathrm{e}^{-\lambda\delta/\tau}\left(\frac{G}{1+\lambda}\left[Q_0'\right]_{y_r^-}^{y_r^+} + \frac{H}{2(2+\lambda)}\left[Q_0''\right]_{y_r^-}^{y_r^+}\right)\\ &\overset{\substack{(A.7)\\(4.168)}}{=} \mathrm{e}^{-\lambda\delta/\tau}\left(-\frac{G}{1+\lambda} + \frac{H}{(2+\lambda)}y_r\right)\end{aligned} \tag{4.169}$$

$$\begin{aligned}\left[\left(\hat{Q}_1^p\right)'\right]_{y_r^-}^{y_r^+} &= \left[2\,\mathrm{e}^{-\lambda\delta/\tau}\left(-\frac{G}{1+\lambda}\left(yQ_0'(y)+Q_0(y)\right) + \frac{H}{2+\lambda}\left(yQ_0 + (y^2-1)Q_0'\right)\right)\right]_{y_r^-}^{y_r^+}\\ &\overset{(A.7)}{=} 2\,\mathrm{e}^{-\lambda\delta/\tau}\left(\frac{G}{1+\lambda}y_r + \frac{H}{2+\lambda}\left(1-y_r^2\right)\right)\end{aligned} \tag{4.170}$$

The above results are used to infer:

$$\begin{aligned}&\left[\hat{Q}_1^p\phi_2' - \left(\hat{Q}_1^p\right)'\phi_2\right]_{y_r^-}^{y_r^+}\\ &= \lim_{y\searrow y_r}\hat{Q}_1^p\phi_2' - \lim_{y\searrow y_r}\left(\hat{Q}_1^p\right)'\phi_2 - \lim_{y\nearrow y_r}\hat{Q}_1^p\phi_2' + \lim_{y\nearrow y_r}\left(\hat{Q}_1^p\right)'\phi_2\\ &= \left[\hat{Q}_1^p\right]_{y_r^-}^{y_r^+}\phi_2'(y_r) - \left[\left(\hat{Q}_1^p\right)'\right]_{y_r^-}^{y_r^+}\phi_2(y_r) \qquad (\phi_2 \text{ is smooth everywhere})\\ &\overset{\substack{(4.169)\\(4.170)}}{=} \mathrm{e}^{-\frac{\lambda\delta}{\tau}}\left(-\frac{G}{1+\lambda} + \frac{H}{(2+\lambda)}y_r\right)\phi_2'(y_r) - 2\,\mathrm{e}^{-\frac{\lambda\delta}{\tau}}\left(\frac{G}{1+\lambda}y_r + \frac{H}{2+\lambda}\left(1-y_r^2\right)\right)\phi_2(y_r)\\ &= \mathrm{e}^{-\frac{\lambda\delta}{\tau}}\left(\left(-\frac{G}{1+\lambda} + \frac{H}{(2+\lambda)}y_r\right)\phi_2'(y_r) - 2\left(\frac{G}{1+\lambda}y_r + \frac{H}{2+\lambda}\left(1-y_r^2\right)\right)\phi_2(y_r)\right)\end{aligned} \tag{4.171}$$

4.D.4.2 Notation

Time t and frequency ω/λ are denoted in units of τ_m and $1/\tau_m$ resp. in both Eqs. (4.156) and (4.155), hence I keep this notation. To stay consistent with the notation in the rest of the thesis I still denote the average population rate r_0 in units of spks/s. Due to the different sign convention for the Fourier transform used for the linear response function Eq. (4.126) (Lindner and Schimansky-Geier, 2001), the frequency mapping between Brunel and Hakim (1999) and the linear response ansatz I described in Section 4.D.3 is as follows:

$$\lambda \mapsto -i\omega$$

The synaptic delay is

$$\delta \mapsto \Delta$$

Brunel and Hakim used a rescaled voltage variable

$$y \mapsto \frac{V - I_0}{\sqrt{2D}}$$

where $I_0 = I_\mathrm{E} - K\tau_m r_0$ is the total average input.
It follows:

$$\frac{1}{2}(y_r^2 - y_\Theta^2) \mapsto \frac{V_R^2 - V_T^2 + 2I_0(V_T - V_R)}{4D} = \delta$$

Note: δ is now *not* the synaptic delay in the Brunel and Hakim (1999) notation, but the auxiliary constant introduced in the calculation of the LIF susceptibiltity Eq. (4.154) Lindner et al. (2005)!
The relative strength of the average inhibitory feedback is given by

$$G \mapsto \frac{K\tau_m r_0}{\sqrt{2D}} \qquad (r_0 \text{ in units of Hz!})$$

The fluctuations in the recurrent inhibitory input vanish in the mean-field limit of my fully connected network in which the synaptic strength scales as K/N:

$$H \mapsto \frac{N(K/N)^2\tau_m r_0}{\sqrt{2D}} = \frac{K^2\tau_m r_0}{\sqrt{2D}N} \xrightarrow{N\to\infty} 0 \ .$$

4.E Supplementary figures

This section contains supplementary figures that are referenced in the main text.

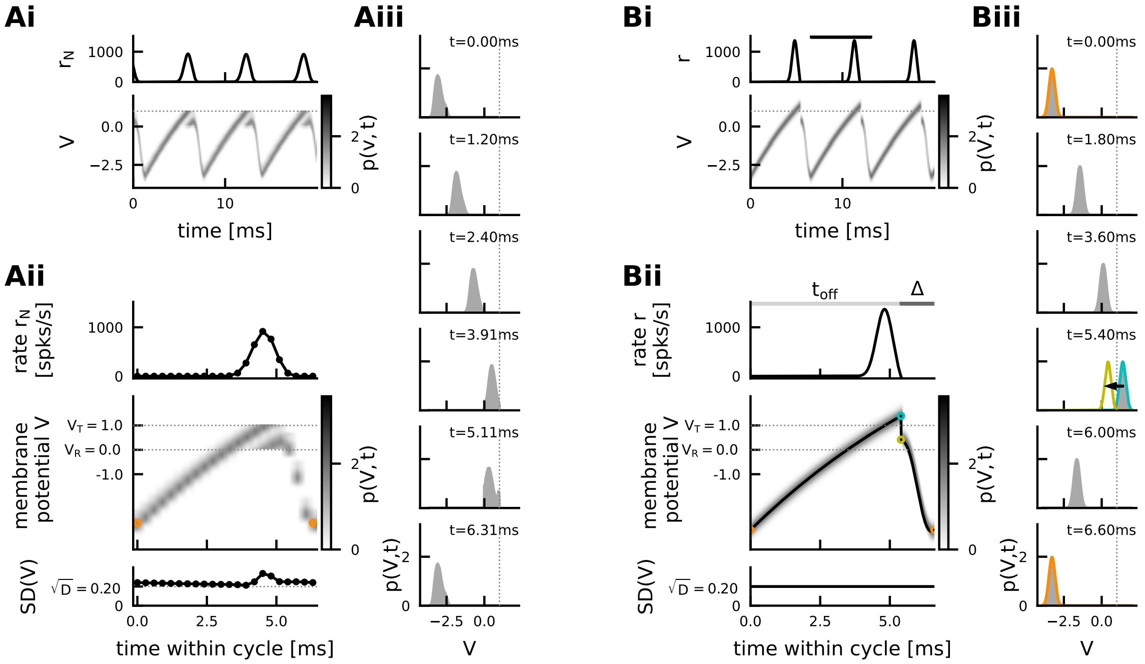

Figure 4.41: Spiking network vs drift-based approximation close to full synchrony. Same outline and parameters as Fig. 4.7, but strong external drive $I_\mathrm{E} = 7.92$. For strong coupling and strong drive the membrane potential distribution is pushed far below threshold inbetween population spikes (A). The drift-based approximation (B) is thus especially good (compare Aii-iii and Bii-iii).

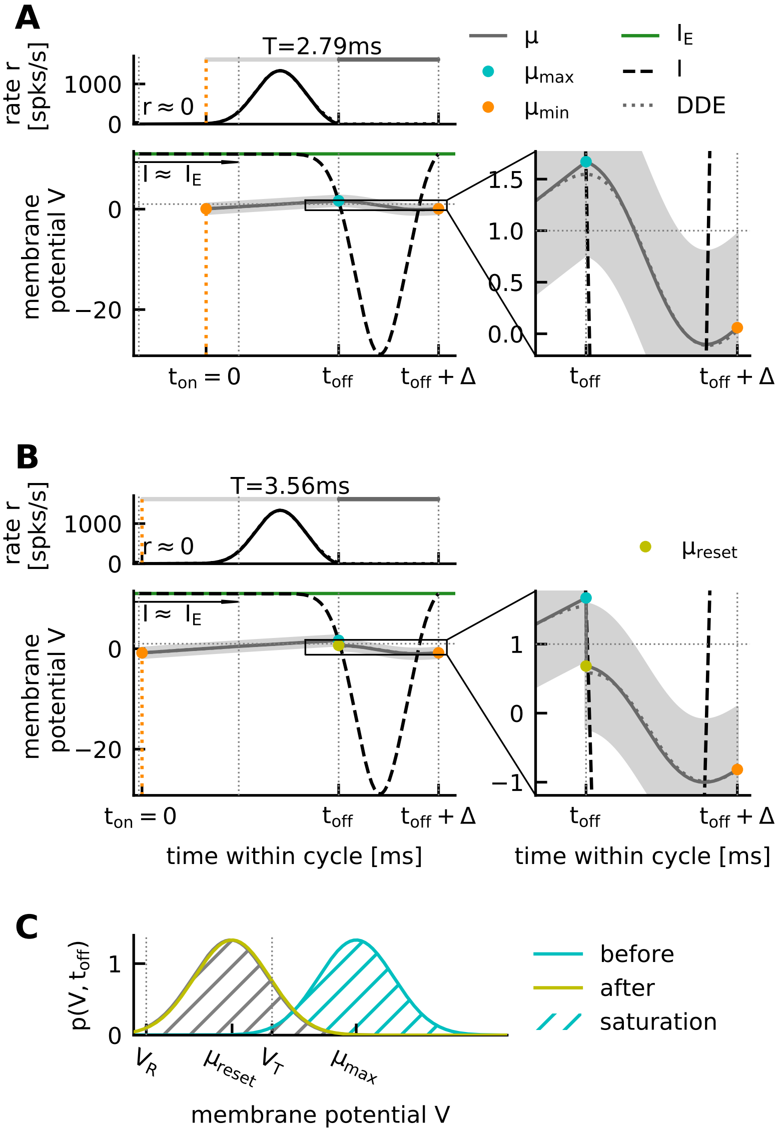

Figure 4.42: Illustration of difference between μ_{min} and the true periodic minimum of the mean membrane potential. Same outline as Fig. 4.24. Larger noise $\sqrt{D} = 0.3$, weaker coupling $K = 3$, strong drive $I_{\text{E}} = 11$, otherwise default parameters (Table 4.3). Here the difference between $\mu_{\text{min}} = \mu(t_{\text{off}} + \Delta)$ and the real local minimum of the trajectory μ, occuring at the second intersection of μ and I, is more obvious (see Zoom in A and B). This only happens at strong drive, close to the point of full synchrony (note the high saturation in C). The estimate of the period T is not affected, since μ_{min} determines both the end and the beginning of each cycle.

5 | The perturbation-based inhibitory ripple model

5.1 Introduction

There is one alternative "inhibition-first" ripple model that also relies on interneurons as the main pacemaker (Malerba et al., 2016). It is based on a transient synchronization ("ringing") effect that can be induced in a heterogeneous population of oscillators (CA1 interneurons) by a strong common external drive (sharp wave-associated input from CA3) (Gerstner, 2000; Fourcaud-Trocmé and Brunel, 2005; Gerstner et al., 2014). The main difference to the bifurcation-based inhibition-first ripple model discussed in Chapter 4 is that the network does not undergo a bifurcation into a state of persistent oscillations. Instead, the external perturbation merely moves the stable focus in state space and the population rate relaxes towards the new focus in transient oscillations. I thus distinguish the two inhibition-first ripple models as *bifurcation-based* and *perturbation-based.*

In this chapter I replicate and analyze the perturbation-based model (Malerba et al., 2016) to understand the role of the various parameters and their influence on the ripple oscillation (Section 5.2). I will then study the instantaneous frequencies within a ripple event and demonstrate that, in the perturbation-based model, an IFA asymmetry only occurs for asymmetric external drive (Section 5.3). Finally I will delineate the boundary between the two inhibition-first models and highlight experimental possibilities to dissociate them (Section 5.4).

5.2 Analysis of the perturbation-based inhibitory ripple model

The perturbation-based model (Malerba et al., 2016) consists of 160 putative CA1 interneurons that are modeled as adaptive exponential integrate-and-fire units (aEIF). The units are all-to-all connected by inhibitory synapses and driven by independent colored noise as well as a common (sharp wave-associated) drive. The network is heterogeneous w.r.t. the excitability of individual cells and the inhibitory coupling strengths between them. A detailed model description and summary of all parameters is given in Methods Section 5.6.1. A note on the replication of the results from the original publication (Malerba et al., 2016) can be found in Appendix Section 5.A.

5.2.1 The default ripple event

If the network is stimulated with a strong step current, a “ringing effect” is triggered and the units transiently synchronize while settling into their new stationary firing rate associated to the amplitude of the step current (here $I_{\max} = 700$ pA, Fig. 5.1).

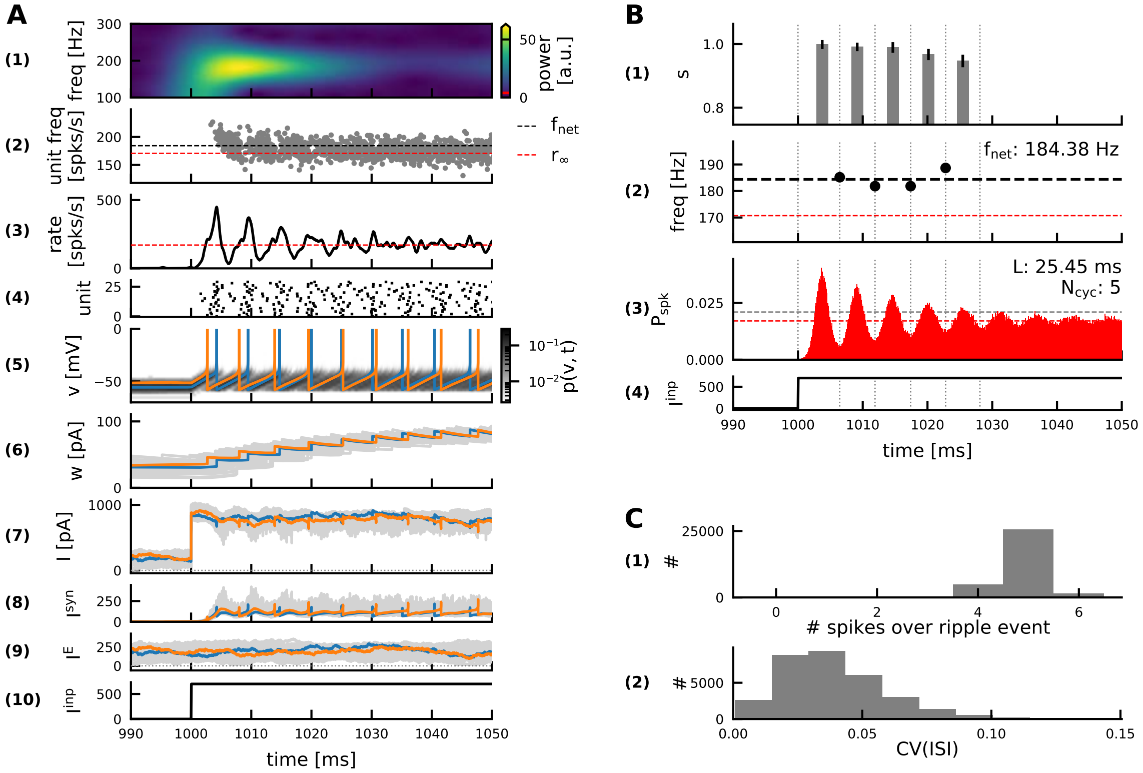

Figure 5.1: Ripples in the perturbation-based inhibitory model: single trial vs. average. A, Illustration of a single trial. (1) wavelet spectrogram quantifying instantaneous frequency and power of the population rate; (2) instantaneous unit firing rates derived from interspike intervals. Dashed lines indicate the asymptotic (constant) population rate $r_\infty = 10^4 \cdot P_{\text{spk}}^{\infty}$ that is reached after a ripple event (red), and the average network frequency as determined in B (black); (3) population rate; (4) raster plot (30/160 interneurons); (5) membrane potentials v_i, traces of two example units (orange, blue); (6) adaptation current w_i; (7) the total current I_i (sum of panels 8-10, Eq.(5.5)); (8) inhibitory synaptic feedback current $I_i^{\text{syn}}(t)$; (9) excitatory background current $I_i^E = I_i^{\text{DC}} + \sigma\beta\eta_i(t)$; (10) step current of 700 pA turned on after an initialization period of 1 s. **B,** Average over 200 trials. Bottom to top: (4) step current (cf. A10); (3) average spike probability P_{spk} in bins of 0.1 ms (see Fig. 5.16 for original result from Malerba et al., 2016). Red dashed line: asymptotic spike probability P_{spk}^{∞}. Grey dashed line: peak significance threshold P_{thr}; (2) discrete estimates of instantaneous ripple frequency (black marker). Averaging yields network frequency (black dashed line). (1) saturation, cyclewise and averaged over trials, errorbars indicate ±1 SD. **C,** Spike statistics. (1) total number of spikes during a ripple event (histogram over all units of all trials). Most units fire 5 spikes, i.e. one spike per cycle; (2) low coefficient of variation of interspike intervals illustrates that unit firing is regular.

Fig. 5.1A illustrates the network dynamics in a single trial. After an initialization period of 1 second, during which the units receive only colored noise and their respective bias currents (see Methods Section 5.6.1), a strong step current of amplitude $I_{\mathrm{max}} = 700\ \mathrm{pA}$ is applied to the whole network. This brings all units to the spike threshold within a narrow time window. Subsequent spikes happen synchronously as well, leading to an oscillatory population rate or “ripple” (Fig. 5.1 A1,3). This ripple oscillation is inherently transient, since the noise and heterogeneity desynchronize the network over time.

The properties of the transient ripple oscillation are characterized by averaging over many events (Fig. 5.1B,C). I followed the analysis described in (Malerba et al., 2016), see also Methods Section 5.6.2. The transient ripple event has an average ripple frequency of ∼184 Hz and a duration of ∼25.45 ms (∼5 cycles) (Fig. 5.1 B2,3). A discrete estimate of instantaneous ripple frequency per cycle, based on the inverse of the peak-to-peak distance in the population rate, indicates that there is no IFA: the instantaneous frequencies of all cycles are close to the mean network frequency, with only a small jitter and no clear trend over the course of the event (Fig. 5.1 B2, black circular markers). The saturation is computed as the integral over the average population rate in each cycle. It decays slightly over the course of the event but is always close to 1, indicating that in every ripple cycle there are approx. as many spikes as cells in the network (Fig. 5.1 B1). The spike statistics shown in Fig. 5.1C confirm that every cell contributes about one spike per cycle: The average number of spikes per cell and ripple event equals the number of ripple cycles (C1) and the interspike intervals are highly regular (low CV, (C2)).

5.2.2 Parameter dependencies

The model by Malerba et al. (2016) contains a lot of biologically-inspired detail, not all of which seems necessary for the core mechanism of ripple generation. In the following, I will analyse the role of the various parameters separately and derive the maximally reduced form of the perturbation-based inhibitory ripple model.

5.2.2.1 The role of adaptation

The adaptive EIF neuron model can exhibit a range of different firing patterns depending on the three parameters describing the adaptation current (Eq. (5.4)): the conductance a, the spike-triggered increase in adaptation current b, and the adaptation time constant τ_w (Gerstner et al., 2014). Malerba et al. (2016) chose the adaptation parameters such that the interneurons are in a tonic firing regime with only negligible adaptation (see Table 5.3, Fig. 5.2). This matches the behavior of PV^+ basket cells, which are known to fire regularly without much adaptation (Pawelzik et al., 2002).

Most likely, Malerba et al. (2016) only chose the adaptive EIF neuron model because their full model also included pyramidal cells, which do exhibit adaptation. In the reduced interneuron-only model, on which I focus here, it seems unnecessary to include adaptation. In Supplementary Fig. 5.23 this is confirmed in a simulation of the network without adaptation. As expected, the ripple dynamics are qualitatively unaltered. The network frequency is slightly higher than in the reference simulation with adaptation (193 vs. 184 Hz, see Fig.5.1). Without adaptation the network frequency coincides

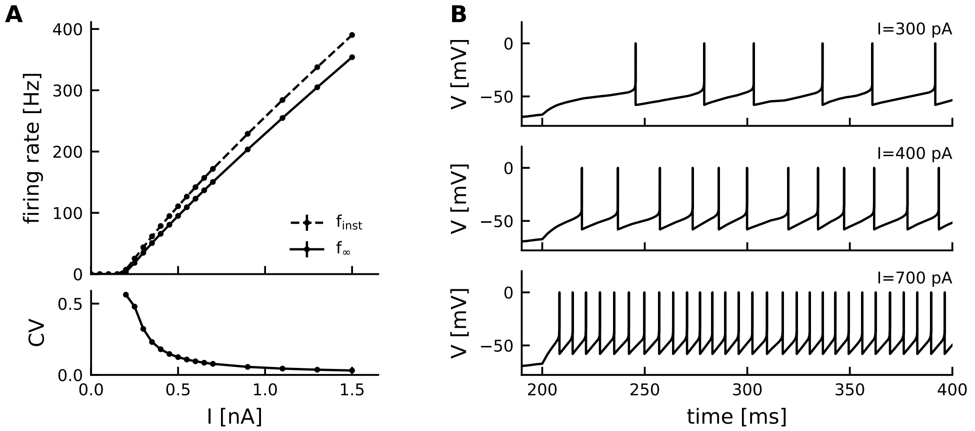

Figure 5.2: f-I curve of an uncoupled aEIF unit under colored noise. A, Top: firing rate of an aEIF unit under colored noise (Table 5.3) for a range of constant external currents I. The instantaneous firing rate f_{inst} is given by the inverse of the first interspike interval. The asymptotic firing rate f_{∞} was estimated over a time window of one second, starting 2 seconds after the onset of the step current. All firing rates were averaged over 200 noise realizations. Standard deviations indicated by errorbars are too small to see. Bottom: average coefficient of variation of the interspike intervals. **B,** Example voltage traces for a step current I applied at time 200ms. Step current amplitude increases from top to bottom.

with the asymptotic firing rate into which the network settles after the initial transient (Supplementary Fig. 5.23 A2,B2, black vs red dashed line). This will be discussed in more detail in Section 5.2.3.1.

5.2.2.2 The role of heterogeneity

There are two sources of heterogeneity in this model: The normally distributed bias currents impose a different level of excitability for each cell (Eq. (5.6)). The normally distributed peak conductances, 6% of which are clipped to 0, introduce heterogeneity in the network connectivity with some connections effectively missing (Eq. (5.10)).

I simulated the network without adaptation ($a = 0\,\mathrm{nS},\ b = 0\,\mathrm{pA}$) and without heterogeneity ($g_{\mathrm{cv}}^{\mathrm{peak}} = 0,\ I_{\mathrm{cv}}^{\mathrm{DC}} = 0$) and find that neither are crucial ingredients (Fig. 5.3). The homogeneous network still exhibits a transient ripple. The ripple event is slightly longer in the absence of heterogeneity (7 cycles, Fig. 5.3 B2 vs. 5 cycles, Fig. 5.1 B2), but is eventually terminated by noise-induced desynchronization (Fig. 5.3A,B).

Figure 5.3: Ripple dynamics without adaptation and without heterogeneity. Network simulation without heterogeneity ($g_{\mathrm{cv}}^{\mathrm{peak}} = 0,\ I_{\mathrm{cv}}^{\mathrm{DC}} = 0$) and without adaptation ($a = 0\,\mathrm{nS},\ b = 0\,\mathrm{pA}$), all other parameters as in Fig. 5.1, Table 5.3. There are only minor changes in the ripple dynamics: Due to the omission of adaptation the network frequency coincides with the asymptotic rate (black vs red dashed line in A2, B2). The ripple event is longer, but still finite (note that the network activity is shown here over 100 ms). For a detailed description of all panels see Fig. 5.1.

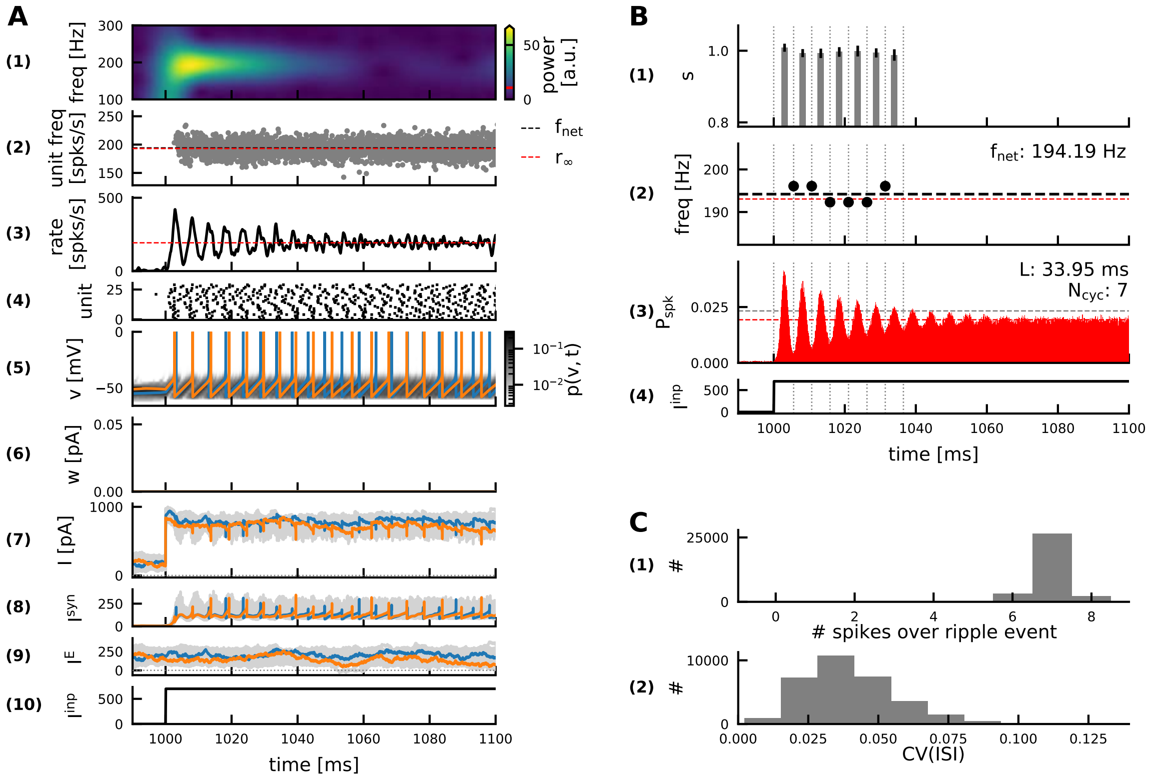

Figure 5.3: Ripple dynamics without adaptation and without heterogeneity. Caption on previous page.

5.2.2.3 The role of inhibitory synaptic coupling

The role of the inhibitory synaptic coupling was already investigated by Malerba et al. (2016) who varied the inhibitory coupling strength by changing either the scaling factor α of the synaptic peak conductance or the synaptic decay time constant τ_D (see Eq. (5.9)). In both cases an increase in inhibitory strength leads to a decrease in the network frequency. Interestingly, ripple oscillations persist even in the absence of synaptic coupling ($\alpha = 0$), which is an important prediction of the perturbation-based inhibitory ripple model. I replicated this parameter exploration as part of the control of my model implementation (see Fig. 5.19).

Note that the parameter exploration by Malerba et al. (2016) only covers a small range of peak conductances ($\alpha g^{\text{peak}} \in [0, 0.2]$ nS). This is true even after accounting for the fact that synaptic strength was likely downscaled in the perturbation-based model due to the full connectivity of the network: If the peak conductance for full connectivity (indegree of 160) was set to $g^{\text{peak}} = 0.0234$ nS, the peak conductance in a sparsely connected network of indegree 40 (as estimated for CA1 PV$^+$ basket cells *in vitro*, Sik et al., 1995; Bezaire and Soltesz, 2013; Donoso et al., 2018), would be $g^{\text{peak}} = 4 \cdot 0.0234$ nS $= 0.0936$ nS. This is still orders of magnitude lower than the experimentally measured coupling strength between CA1 PV$^+$ basket cells (∼5 nS in Bartos et al., 2002). For strong coupling with a peak conductance of 5 nS (1.25 nS in the fully connected network), the network frequency in the perturbation-based model drops below ripple range. I thus conclude:

> To account for ripple-range oscillations the perturbation-based model requires *weak* (or no) inhibitory coupling.

5.2.2.4 The role of noise

A reduction of noise has no effect on the network frequency but prolongs the ripple event (shown in Malerba et al., 2016, and replicated here in Fig. 5.21). This is intuitive since noise facilitates the desychronization of the network, which ultimately terminates the transient oscillation.

In summary, the perturbation-based inhibitory ripple model can be reduced to a homogeneous, uncoupled population of non-adapting integrate-and-fire neurons receiving a small amount of noise and a strong, common external drive.

5.2.3 Ripple properties summarized

I will now summarize the parameter dependencies of the most important ripple properties in this model, i.e. ripple frequency and duration.

5.2.3.1 The ripple frequency

The fact that ripples occur even in the absence of synaptic coupling ($\alpha = 0$ in Fig. 5.19) shows that ripples in the perturbation-based model are not a network phenomenon. Instead, the “network” here can be thought of as a (weakly coupled) group of (adapting) oscillators, each with a slightly different intrinsic frequency due to the heterogeneity in the bias currents I_i^{DC}. The spikes of these oscillators are transiently synchronized due to a strong common excitatory drive I^{inp}. The frequency of the resulting transient in the population activity directly reflects the firing rate of the underlying units (see network frequency (black dashed line) vs. instantaneous unit firing rates (grey dots) in Fig. 5.1A(2)).

One can hence infer the network frequency from the single unit firing rates: Using the numerically estimated f-I curve of a single neuron (Fig. 5.4A) the distribution of total currents that the neurons receive (including the average inhibitory feedback, Fig. 5.4B, left) can be mapped onto a distribution of intrinsic firing rates (Fig. 5.4B, right). Due to adaptation, one can define two distributions of intrinsic firing rates: the instantaneous rates, based on the first interspike interval (Fig. 5.4, grey curve in A, grey histogram in B), and the asymptotic rates, into which the units settle after a few spikes (Fig. 5.4, yellow curve in A, yellow histogram in B). Since adaptation in this model is weak, the two distributions are not far apart. The network frequency (black dashed line in Fig. 5.1, Fig. 5.4B), which is measured during the transient event right after stimulus onset (i.e. while the single units are still adapting) lies between the average instantaneous and asymptotic single unit rates. This is true for any step current amplitude $I_{\max}$ (Fig. 5.4B,C). Since the unit firing rates increase for increasing drive, so does the network frequency (Fig. 5.4C, cf. Fig. S4c in (Malerba et al., 2016)). This implies two important predictions of the perturbation-based inhibitory model:

The ripple frequency reflects the single unit firing rate.

The ripple frequency is proportional to the amplitude of the external drive.

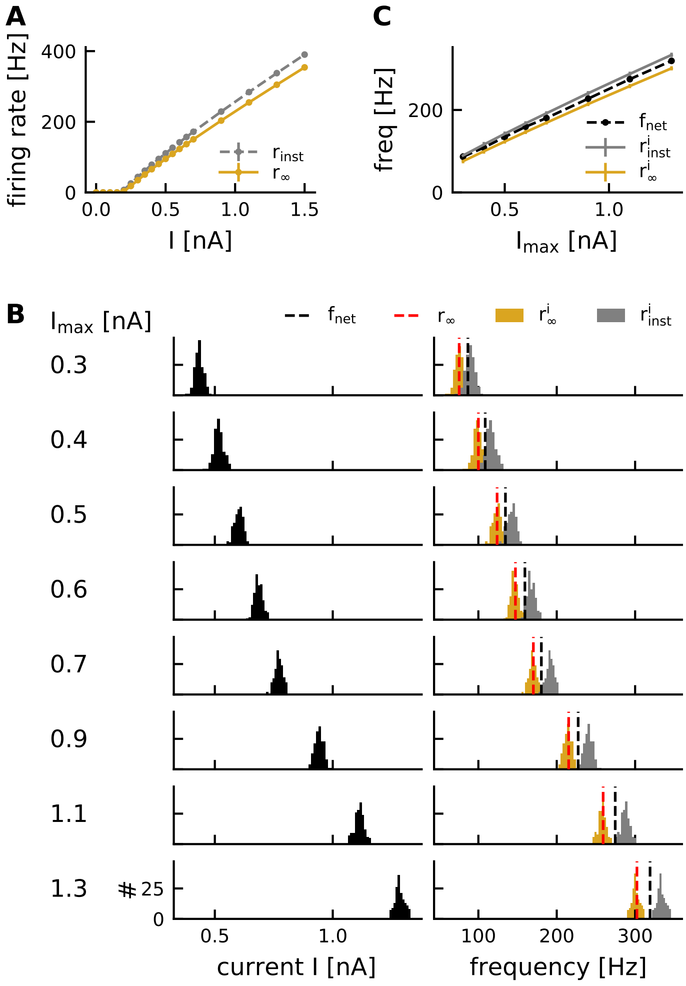

Figure 5.4: Relating unit firing rate and network frequency. **A,** f-I curve of a single aEIF unit receiving a step input of amplitude I and colored noise of intensity $\beta = 45\,\text{pA}$ (cf. Fig. 5.2). Grey: inverse of first interspike interval. Yellow: asymptotic firing rate. **B,** Left: Distribution of average asymptotic input current $I = I_{\text{max}} + I_i^{\text{DC}} - \langle I_i^{\text{syn}}(t)\rangle_t$, that units receive 500 ms after the onset of the step stimulus, shown for various step current amplitudes I_{max} ($I_{\text{max}} = 0.7\,\text{nA}$ corresponds to the default simulation shown in Fig. 5.1). Right: Corresponding distribution of intrinsic firing rates (grey: instantaneous, yellow: asymptotic, as in A). Vertical lines mark the asymptotic population rate (red) and the network frequency (black). **C,** Summary comparing network frequency and intrinsic unit firing rates for different levels of step current input I_{max}. The network frequency always lies between the mean instantaneous and asymptotic intrinsic firing rate. Grey and yellow errorbars indicate ± 1 SD of the single unit rate distributions shown in B (mostly too small to see).

We can now understand the earlier finding that the network frequency decreases with increasing inhibitory coupling strength (Section 5.2.2.3): Since adaptation is weak, the ripple frequency (black line in Fig. 5.4C) is close to the steady-state firing rate r_∞ associated to the external drive I_{max} (yellow line in Fig. 5.4C). This steady-state firing rate can be inferred analytically (see also Chapter 4, Section 4.5.2.3):

Ignoring the conductance-based nature of the synapses, we can approximate the total current that a unit in the recurrent network receives as

$$I_0 \approx I_{\text{max}} - J r_\infty$$

with constant synaptic weight $J > 0$.
Rearranging the terms one sees that the steady-state firing rate must be a linearly decreasing function of the total current I_0, due to the inhibitory nature of the synapses:

$$r_\infty(I_0) = \frac{I_{\max} - I_0}{J} \tag{5.1}$$

On the other hand, the firing rate of a single, uncoupled unit is a monotonically *in*creasing function of the current I_0, described by the f-I curve (Fig. 5.4A):

$$r_\infty(I_0) = f_{\mathrm{EIF}}(I_0) \tag{5.2}$$

The steady-state rate r_∞ is thus given by the intersection of Eqs. (5.1) and (5.2). Clearly the intersection appears at lower firing rates if the inhibitory coupling J is stronger (see sketch in Fig. 5.5).

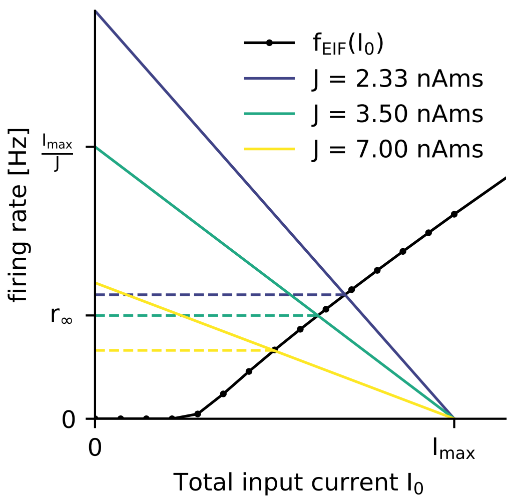

Figure 5.5: Strong inhibition decreases unit firing rate and hence ripple frequency. Sketch of the analytical solution for the mean unit firing rate in a network with inhibitory coupling of strength J. Black line: asymptotic firing rate of EIF unit $f_{\mathrm{EIF}}(I_0)$ (numerical estimate, cf. Fig. 5.2A). Solid colored lines: Eq. (5.1) for increasing synaptic strength J. Dashed colored lines mark the resp. solutions r_∞ given by the intersection of Eqs. (5.1) and (5.2). Note that r_∞ decreases as the coupling strength increases.

5.2.3.2 The ripple duration

The parameter explorations above have uncovered two distinct causes for the termination of the ripple event: the network can desynchronize either due to noise or due to heterogeneity. In a network without noise the heterogeneity causes desynchronization and effectively ends the ripple event (finite durations in Fig. 5.21 for $\sigma = 0$). Vice versa, in a network without heterogeneity it is the noise that terminates the ripple event (Fig. 5.3).

In either case, the duration of the ripple oscillation is inherently finite, even though the step stimulus remains “on” indefinitely. This is an important difference to the bifurcation-based model.

If there is neither heterogeneity nor noise, the network enters a pathological state where all units are essentially identical after the random initial conditions have been forgotten. The “network” then exhibits pathological persistent oscillatory activity, with all neurons firing the same tonic spike train. This can be considered a transition from the perturbation-based to the bifurcation-based model, albeit to a pathological form of the latter (Supplementary Fig. 5.24, see also Section 5.4).

5.3 IFA in the perturbation-based model

We have seen above that in its default configuration (Fig. 5.1) the perturbation-based inhibitory ripple model does *not* exhibit intra-ripple frequency accommodation. The discrete, cycle-wise estimates of instantaneous frequency are all close to the average network frequency and show no clear trend (de- or increasing) (Fig. 5.1 B2).

5.3.1 IFA for asymmetric ramp input

I showed in Section 5.2.3.1 and Fig. 5.4 that the network frequency is proportional to the amplitude of the external step current. One can thus predict that given an external drive that *changes over time*, the instantaneous network frequency will follow this drive, i.e. increases as the drive increases and decreases as the drive decreases.

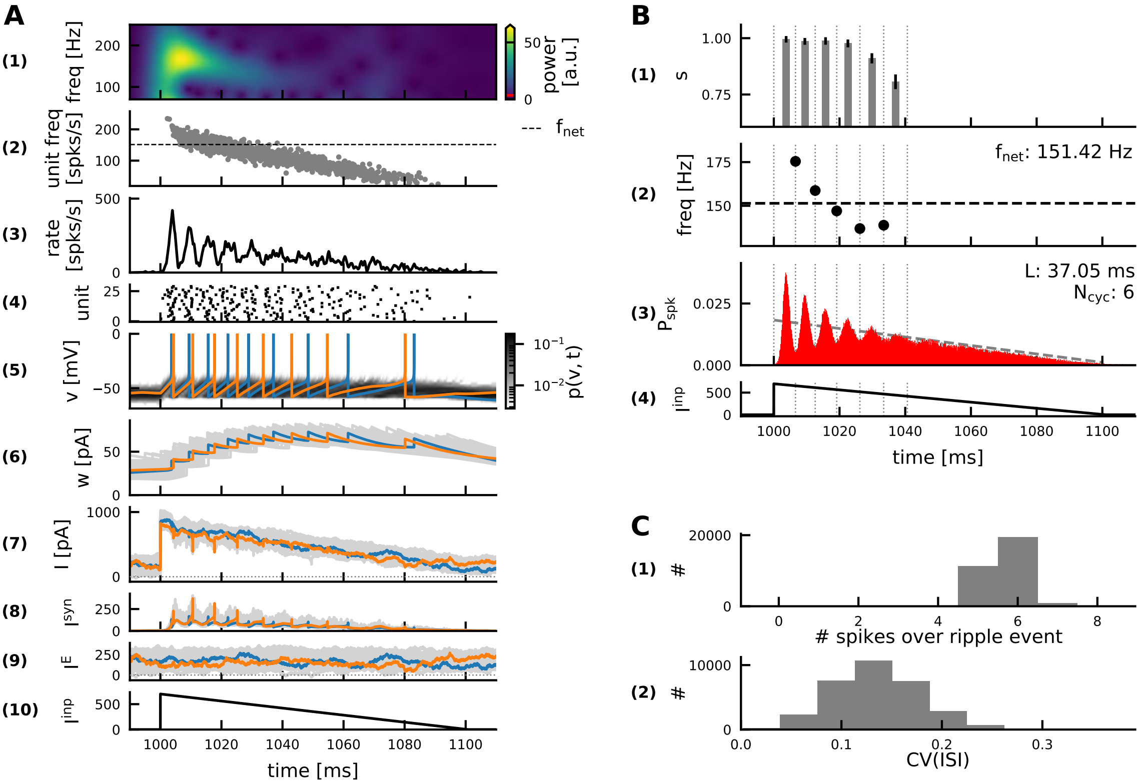

Figure 5.6: IFA in response to asymmetric drive.
The external drive I^{inp} jumps up to 700pA and then linearly decreases back to 0 over a time of 100 ms. The instantaneous network frequency decreases in an IFA-like manner, which can be seen in the wavelet spectrogram of a single trial (A1), as well as in the discrete, instantaneous frequency estimated for the average ripple event (B2). For a detailed description of all panels see Fig. 5.1.

Thus, to achieve an IFA-like decrease in the instantaneous frequency, one would need to apply an asymmetric external drive that first jumps up to a high value and then decreases monotonically from there. I confirmed in a network simulation with an asymmetric ramp current, that this is indeed the case (Fig. 5.6).

5.3.2 "Anti-IFA" for symmetric input

For symmetric drive (here a double-ramp, as in Chapter 4), the instantaneous frequency is symmetric as expected (Fig. 5.7 B2). The instantaneous power, however, is asymmetric and decreases monotonically, since the network progressively desynchronizes over the course of the event (Fig. 5.7 A1). Thus the initial period of increasing frequency is the one with the highest power, and we observe "anti-IFA" (Fig. 5.7 A1).

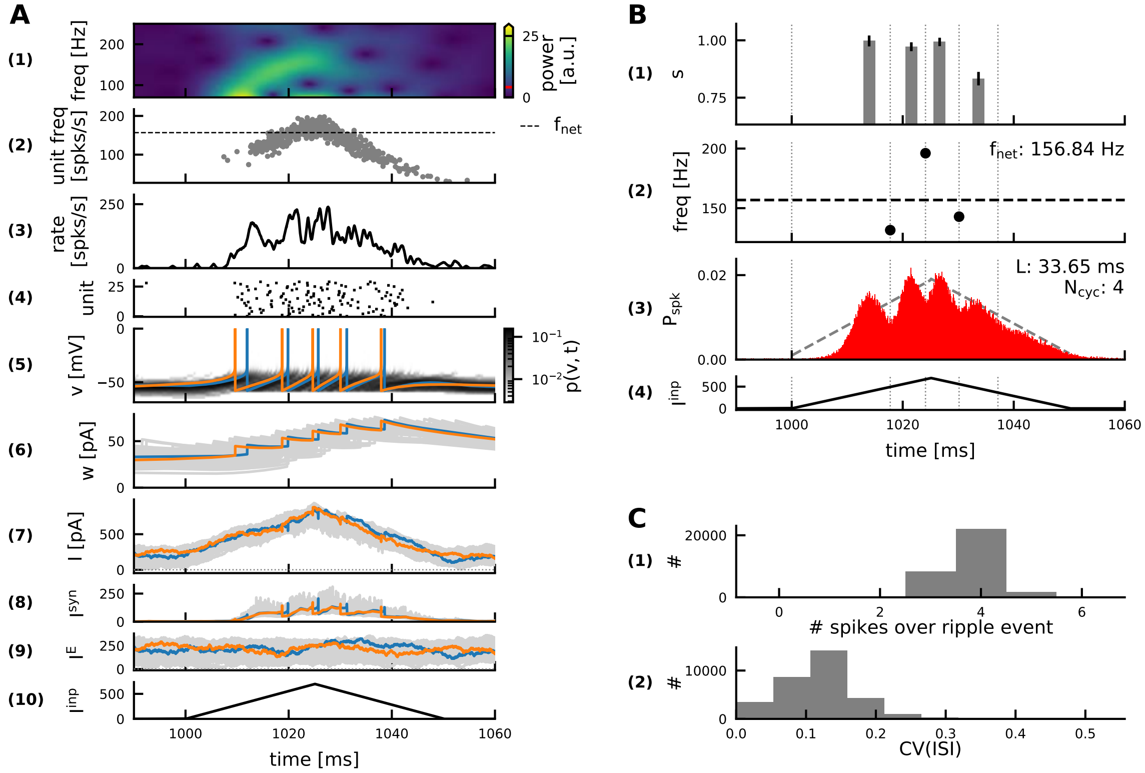

Figure 5.7: No IFA (or "anti-IFA") in response to symmetric drive. The instantaneous frequency of the average event follows the same symmetry as the input (B2). The single trial wavelet spectrogram however reveals an asymmetry in the power giving most weight to the initial period of *in*creasing frequency (A1).

Overall I have derived a new testable prediction:

> The perturbation-based inhibitory ripple model can only generate IFA in response to *asymmetric* external drive. Symmetric drive leads to anti-IFA.

5.3.3 IFA via adaptation

In principle, the perturbation-based inhibitory ripple model could also account for IFA based on spike frequency adaptation. If individual units exhibit significant spike frequency adaptation (e.g. $b = 100$ pA, $\tau_w = 100$ ms), the default step current stimulation evokes IFA (Fig. 5.8). However, such strong adaptation is an unrealistic assumption for CA1 PV$^+$ basket cells, which are known to fire tonically without significant adaptation (Pawelzik et al., 2002).

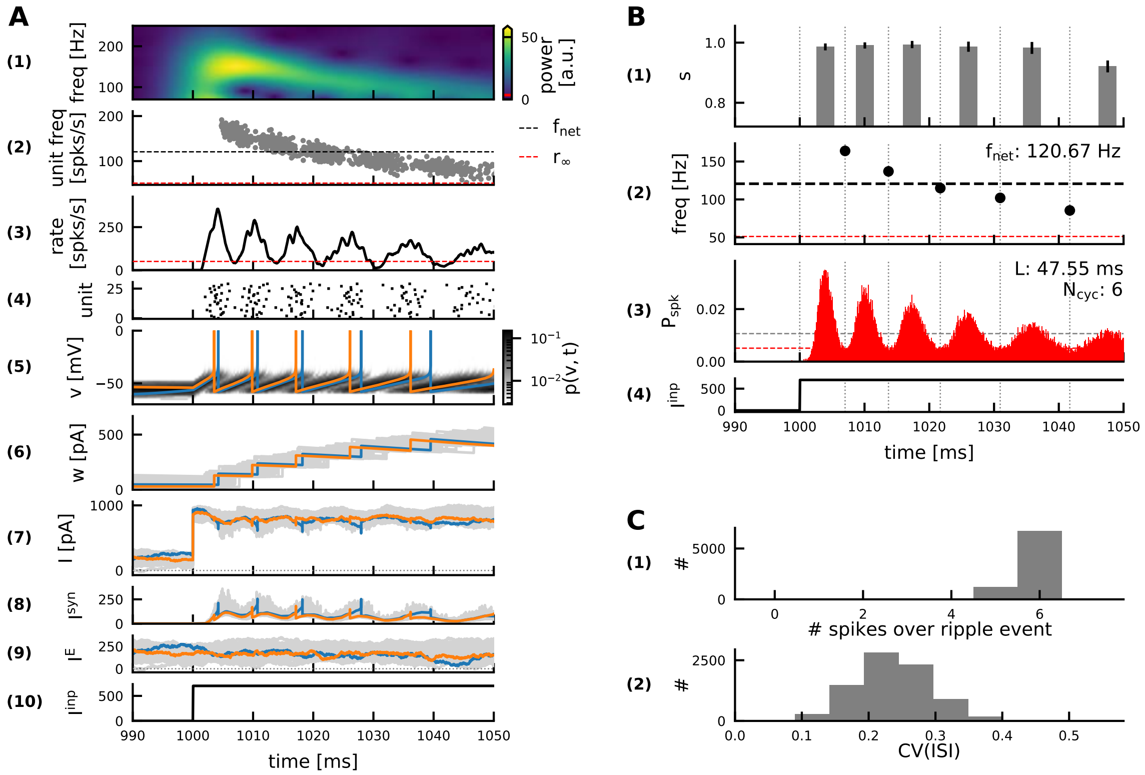

Figure 5.8: IFA via adaptation.
Same default network as in Fig. 5.1 but with significant adaptation ($b = 100$ pA, $\tau_w = 100$ ms, see A6). The default step current of amplitude 700 pA is applied (A10/B4). The adapting firing pattern of individual units (A5) leads to a transient ripple oscillation in the population rate (example in A3, average in B3) with a strongly decreasing instantaneous frequency (IFA, example in A1, average in B2).

5.4 Differentiation of inhibition-first ripple models

In this section I want to delineate the boundary between the two inhibition-first ripple models: perturbation-based (Chapter 5) and bifurcation-based (Chapter 4). Both models assume that the CA1 interneuron network generates ripples, still they differ significantly in their predictions about multiple features of ripple oscillations (Table 5.1). So what are the defining differences between the two models and are they mutually exclusive?

	Perturbation-based model	Bifurcation-based model
ripple frequency set by	• unit firing rate, drive • (coupling strength)	• synaptic time constants • (drive, noise intensity, coupling strength)
interneuron firing	• at ripple frequency	• sparse irregular or up to ripple frequency
ripple duration	• always finite • indep. of stimulation length • set by noise, heterogeneity	• could be infinite in theory • set by stimulation length
IFA	• only for asymmetric drive	• for any fast "up/down" drive
ripples despite GABA block?	• yes	• no

Table 5.1: Properties and predictions of the perturbation-based and the bifurcation-based inhibitory model. Short overview of the model predictions regarding the following questions (top to bottom): What determines the ripple frequency; At what rate do individual interneurons fire; What determines ripple duration; Under which assumptions can the model account for IFA; Does ripple generation rely on inhibitory synaptic coupling or could ripples persist when $\mathrm{GABA_A}$receptors are blocked. Parentheses indicate weak parameter dependencies.

The parameter space of potential network configurations spanned by the degree of heterogeneity, the coupling strength, the noise level and the shape and amplitude of the external drive is large. Thus, in general, the transient ringing effect described by the perturbation-based ripple model (Malerba et al., 2016), and the persistent oscillations described by the bifurcation-based ripple model (Brunel and Hakim, 1999; Donoso et al., 2018) may likely coexist in some portions of this parameter space; especially when considering the network dynamics purely qualitatively (transient vs. persistent oscillation), regardless of whether a given oscillation has ripple frequency or not. It is beyond the scope of this thesis to explore this vast parameter space.

In the context of SPW-Rs, the question can be narrowed down by assuming that the CA1 interneuron network during SPW-R states is characterized by a fixed amount of heterogeneity, coupling strength, and background noise. One can then ask if the typical amount of excitatory drive generated by a CA3 sharp wave triggers a transient ringing at ripple frequency, as described by the perturbation-based model, or a persistent oscillation at ripple frequency, as posited by the bifurcation-based model. In the following, I will delineate a number of changes in network configuration that transform the perturbation-based model by Malerba et al. (2016) into the bifurcation-based model. Finally, I summarize these changes in Table 5.2.

5.4.1 No persistent oscillations in the perturbation-based ripple model.

The first step from the perturbation-based towards the bifurcation-based model is the removal of adaptation and heterogeneity. The analysis in Section 5.2 has already shown that neither adaptation, nor heterogeneity are crucial ingredients of the perturbation-based model. Their removal thus yields a reduced version of the perturbation-based models, in which ripples can still be triggered as a transient ringing effect that is terminated by noise (second column in Table 5.2).

The reduced perturbation-based model, without adaptation and without heterogeneity, does *not* exhibit persistent oscillations. In order to confirm this in simulations, I need to modify the analysis as it was done so far. The ripple analysis by Malerba et al. (2016) (Fig. 5.3B) is based on an average of the population activity over many noise realizations and is thus not suitable to detect the presence of persistent oscillations: Since these oscillations are stochastic and subject to phase diffusion due to the finite size of the network, an average over many noise realizations would always yield a constant, non-oscillatory population activity in the long-time limit, even if coherent stochastic oscillations were present in single trials. I thus repeat the single trial simulation shown in Fig. 5.3A for a longer simulation time, and with an input current that ramps up slowly in order to avoid the transient ringing effect and let the network settle into steady-state quickly (Fig. 5.9A). The steady-state behavior of the reduced perturbation-based model is then quantified by computing the power spectral density of the population activity over the course of this single, long simulation (Fig. 5.9A). The population rate exhibits no coherent oscillation, but only transient periods of “accidental” synchrony due to the finite size of the network (Fig. 5.9 B1,3). These finite size fluctuations cause the weak peak in the power spectral density of the population rate (Fig. 5.9C), which is located precisely at the mean unit firing rate.

We can conclude that the perturbation-based model does *not* exhibit persistent stochastic oscillations, even in its reduced form and for strong drive.

5.4.2 From perturbation- to bifurcation-based ripples

So what prevents the emergence of persistent stochastic oscillations? In the non-reduced perturbation-based model (column 1 in Table 5.2) it is the heterogeneity that ensures the stability of the asynchronous irregular state: persistent oscillations cannot be maintained if the heterogeneity in the network is too large (Brunel and Hakim, 1999). For a *homogeneous* EIF network — such as the reduced perturbation-based model (column 2 in Table 5.2) — a linear stability analysis by Brunel and Hansel (2006) has shown that a bifurcation towards persistent oscillations *exists* in the parameter space, spanned by coupling strength, noise intensity and excitatory input (“n=1” line separating the “asynchronous stable state” from “fast oscillation” regime in Fig. 5.10B).

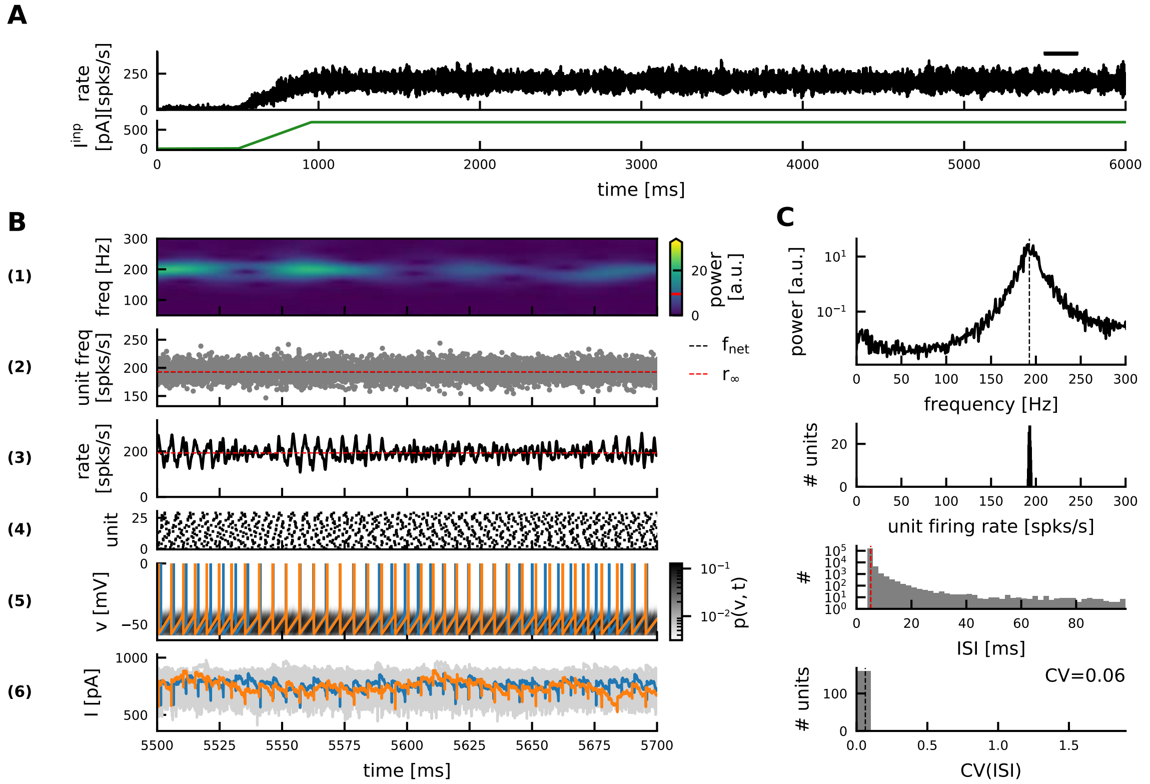

Figure 5.9: No persistent oscillations in the perturbation-based model network without heterogeneity and adaptation for default parameters.
Same network as in Fig. 5.3. **A, :** Population rate (top) of the default network without heterogeneity and without adaptation (for remaining parameters, see Table 5.3) when driven by constant external drive (700 pA, bottom) over 5 seconds. During an initialization period of 1 second the drive was ramped up slowly to prevent strong transients. Horizontal bar marks zoom shown in B. **B, :** Zoom into the network activity shown in A (same outline as Fig. 5.1A, except for adaptation current ($w \equiv 0$) and the detailed composition of the total current I, which have been removed here). Units fire very regularly at ∼193 Hz (panel 5, membrane potentials of two example units are marked in blue and orange). There are transient periods of (accidental) synchrony (panels 3–5) with increased power in the population rate around the mean unit firing rate (panel 1), but there is no collective oscillation. The inhibitory feedback is weak and the total current thus excitatory at all times (panel 6). **C, :** The power spectral density of the population rate (panel 1) exhibits a weak peak at the mean unit firing rate (panel 2). The unit firing is highly regular (panels 3 and 4, average coefficient of variation (CV) of ISIs: 0.06).

However, the default parameter setting of Malerba et al. (2016) (Table 5.3) with weak noise and weak coupling puts the network into the regime where the asynchronous irregular state is stable (mark (1) in Fig. 5.10B).

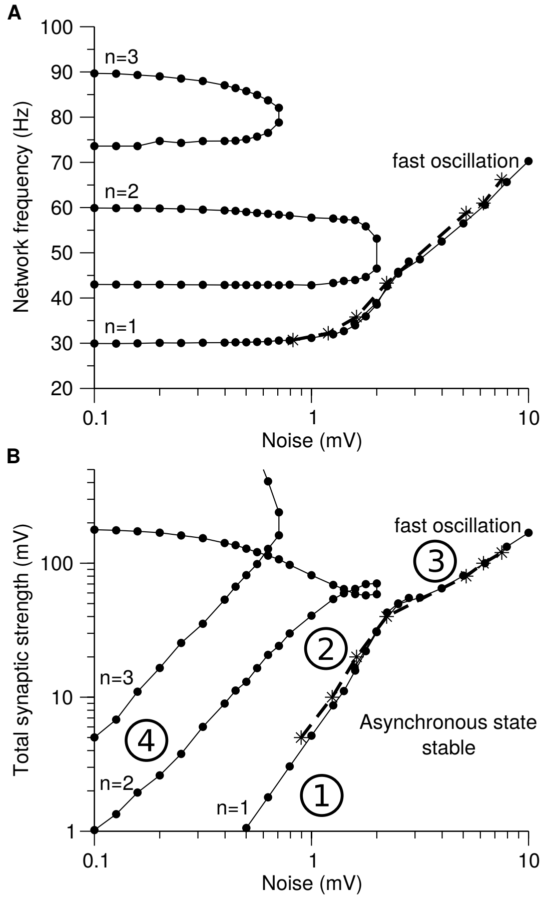

Figure 5.10: Bifurcation diagram of an EIF network with inhibitory coupling.
(adapted from Brunel and Hansel, 2006, with permission from MIT Press). Bifurcation diagram based on a numerical linear stability analysis (see Chapter 4, Section 4.5.2.4 for background on linear response and linear stability). **A,** Frequency of the emerging oscillation, **B,** Location of bifurcations (lines) w.r.t. noise and synaptic strength. Note that the parameter exploration shown here is in fact three-dimensional, since for every combination of noise and synaptic strength the external drive was adjusted to keep the average unit firing rate constant (here $r_0 \equiv 30$ spks/s). Lines indicate solutions of the phase- and amplitude-condition (Eq. (4.36)) and are based on a numerical estimate of the EIF linear response. Solutions at low noise occur close to n-multiples of the mean unit firing rate. Here the $n = 1$ branch marks the bifurcation between the stable asynchronousstate and the regime of persistent oscillations. The network oscillation frequency is thus close to the mean unit firing rate, unless the noise is very strong (see $n = 1$ branch in A). Branches with $n > 1$ mark *clustering instabilites.* I added the markers to illustrate *symbolically* the dynamical regimes discussed below and the parameter changes required to get there: (1) the asynchronous irregular state is stable (Fig. 5.9); (2) persistent, stochastic oscillations with highly synchronized unit firing (Supplementary Fig. 5.25); (3) persistent, stochastic oscillations comparable to sparse synchrony state in Chapter 4 (Fig. 5.11); (4) persistent oscillations with two distinct clusters (Supplementary Fig. 5.26). There is no 1:1 correspondence between this bifurcation diagram and my network simulations, since my network has different parameters, and I only varied noise and coupling strength, while keeping the external drive constant (700 pA).

How can the reduced perturbation-based model be changed such that a realistic amount of SPW-associated drive moves the network across the bifurcation towards persistent oscillations? In fact, a *single* parameter change can “do the trick”, as suggested by the bifurcation diagram by Brunel and Hansel (2006) (mark (2) in Fig. 5.10): If the inhibitory coupling strength is increased, an external drive of $I_{\max} = 700$ pA can induce persistent stochastic oscillations (see Supplementary Fig. 5.25). The resulting oscillations however are overly synchronized due to the then comparably low noise level.

If both noise and coupling strength are increased (mark (3) in Fig. 5.10), the EIF network exhibits persistent, yet sparsely synchronized oscillations with irregular unit firing in response to a drive of 700 pA (Fig. 5.11). This dynamics closely resembles the dynamics of the LIF network of the bifurcation-based model (Chapter 4, Fig. 4.3). I hence refer to the homogeneous EIF network with increased noise and coupling strength as the EIF-version of the bifurcation-based model (column 3 in Table 5.2).

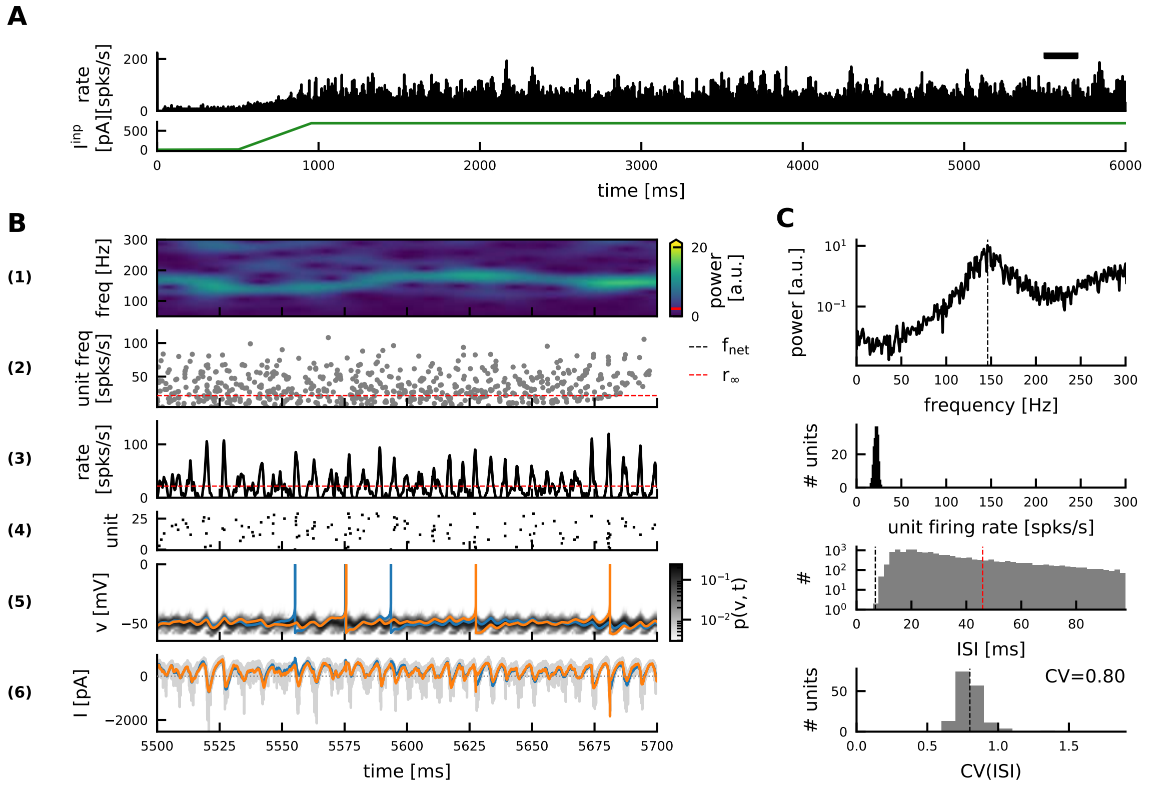

Figure 5.11: Sparse synchrony in a homogeneous EIF network with increased noise and coupling strength. Same network and outline as in Fig. 5.9, but with increased noise ($\sigma = 1.5$, $\sigma\beta = 67.5$ pA) and coupling strength ($\alpha = 100$, $\alpha g_i^{\text{peak}} = 2.34$ nS). **A,** Oscillation amplitude fluctuates over time, but the oscillations are persistent. **B,** Units fire sparsely (4) and the membrane potentials display subthreshold oscillations locked to the population rhythm (5). **C,** The power spectral density of the population rate has a significant peak at ∼146 Hz. In contrast to the peak in Fig. 5.9C, this peak will *not* decrease when the network size is increased, *i.e.* it is not a result of finite size effects. Units fire at a much lower rate (∼21 spks/s) and irregularly (CV=0.8).

Note that the network in Fig. 5.11 has no synaptic delay (Table 5.3). The finite rise time $\tau_R = 0.3$ ms of the postsynaptic potentials (Eq. (5.9)) is sufficient to introduce delayed negative-feedback oscillations (Brunel and Hansel, 2006). Adding a synaptic delay leads to more pronounced oscillations (Fig. 5.12), but also reduces the network frequency to the gamma rather than ripple range (∼82 Hz, Fig. 5.12C). The network frequency can be slightly raised by increasing the noise level (Supplementary Fig. 5.27) or by increasing the sharpness of spike initiation (Δ_{thr}), but it is difficult to achieve ripple range frequencies with realistic synaptic delays in a network of EIF units (but see Taxidis et al., 2012).

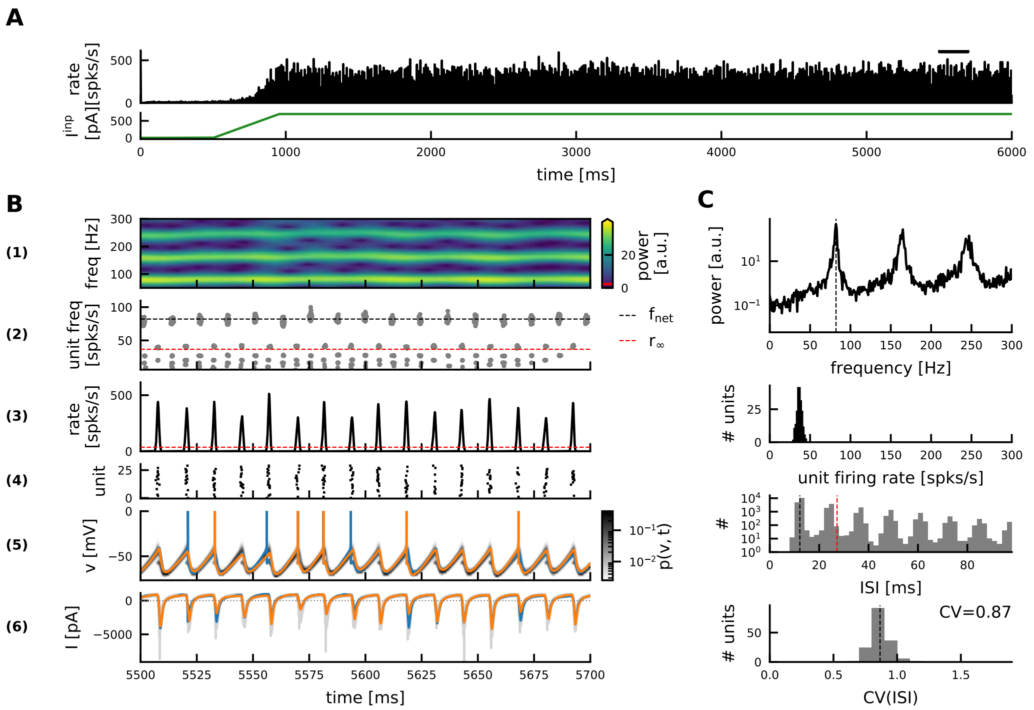

Figure 5.12: Sparse synchrony in gamma range in the homogeneous EIF network with increased noise and coupling strength and finite synaptic delay. Same network as in Fig. 5.11, but a synaptic delay of 0.5 ms was introduced. Oscillatory power increases since units fire more synchronously, but the network frequency drops to ∼82 Hz (C). Increasing the noise in this network can raise the network frequency (Supplementary Fig. 5.27). For a detailed description of all panels see Fig. 5.9.

	PI default Fig. 5.1	PI reduced Fig. 5.9	BI EIF (γ) Fig. 5.11 / 5.12	BI reduced Fig. 4.3
heterogeneity	✓	✗	✗	✗
inh coupling	weak	weak	strong	strong
noise	weak	weak	strong	strong
neuron model	EIF	EIF	EIF	LIF
adaptation	(✓)	✗	✗	✗
synaptic delay	✗	✗	✗/ ✓	✓
	perturbation-based		bifurcation-based	

Table 5.2: From perturbation- to bifurcation-based ripple generation. Summary of how the model parameters (heterogeneity, coupling, noise) affect the occurrence of ripple oscillations (transient ringing or persistent oscillation). All networks were stimulated by the same external drive ($I_{\text{max}} = 700$ pA). PI default: original perturbation-based model (Malerba et al., 2016). BI reduced: reduced bifurcation-based model (Chapter 4). The model transition (PI to BI) is primarily mediated by the removal of heterogeneity and an increase in noise and coupling strength. The neuron model, adaptation and the synaptic delay are only listed as modulatory factors.

Apart from the difference in oscillation frequency, the EIF-version of the bifurcation-based model (column 3 in Table 5.2) exhibits the same dynamics as the LIF model (column 4 in Table 5.2) analyzed in Chapter 4: For increasing external drive there is a transition from sparse to full synchrony (Fig. 5.13). Note that for a synaptic delay of 0.5 ms and an EIF threshold sharpness of $\Delta = 2\,\mathrm{mV}$ the network frequencies are consistently below ripple range (Fig. 5.13B, black line vs grey area).

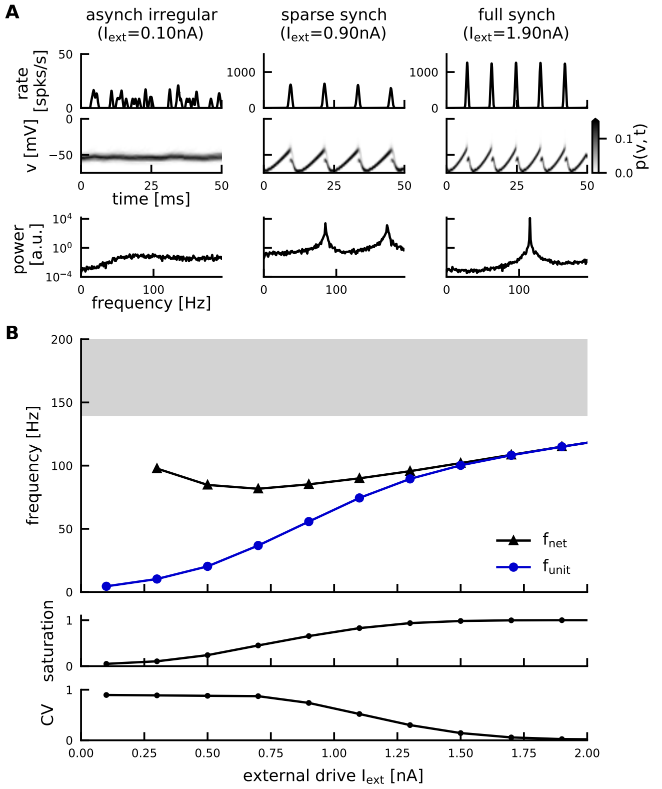

Figure 5.13: Ripple dynamics of the homogeneous EIF network with increased coupling strength, noise level and synaptic delay. Same panel outline as Fig. 4.3. Dynamics of the EIF version of the bifurcation-based model with a synaptic delay 0.5 ms for various levels of external drive (otherwise same parameters as in Fig. 5.12: no heterogeneity, no adaptation, increased noise: $\sigma = 1.5$, $\sigma\beta = 67.5$ pA, and increased coupling strength: $\alpha = 100$, $\alpha g_i^{\mathrm{peak}} = 2.34$ nS). For increasing drive the EIF network exhibits the same transition from sparse to full synchrony as the LIF bifurcation-based model (Chapter 4 Fig. 4.3, Donoso et al., 2018).

In summary, the perturbation-based ripple model can be transformed into the bifurcation-based setting by removing heterogeneity from the network and increasing noise and coupling strength (Table 5.2).

5.5 Discussion

In this chapter I analyzed the perturbation-based inhibition-first ripple model by Malerba et al. (2016). I outlined its parameter dependencies and demonstrated how one can transition from the perturbation-based to the bifurcation-based model. In the following, I will summarize the main differences between the two inhibition-first model classes and relate them to experimental data:

Ripple duration. In the perturbation-based model the ripple is inherently transient, while the bifurcation-based model produces ripple oscillations that persist for as long as the drive is above the critical bifurcation level. Although fundamental, this difference is difficult to test experimentally. Long optogenetic stimulation of CA1 PV$^+$ basket cells is problematic because of side effects such as opsin desensitization (Chater et al., 2010). Schlingloff et al. (2014) varied the length of an optogenetic drive to PV$^+$ basket cells in CA3 in a small range between 5–50 ms and found indeed that ripple duration correlates with stimulus duration, when all other synaptic excitation is blocked. This is in support of the bifurcation-based model. A prolongation of SPW-Rs by stimulation was also shown by Fernández-Ruiz et al. (2019), albeit using optogenetic stimulation of pyramidal cells. It would be interesting to quantify a possible correlation between sharp wave and ripple duration in spontaneous SPW-R events. This may be challenging, since both the sharp wave and the ripple have stereotypical durations with small variability (Malerba et al., 2016; Sullivan et al., 2011), and an assessment of their duration depends heavily on the choice of filters and thresholding.

Ripple frequency. The ripple frequency in the perturbation-based model equals the single unit firing rate and is thus proportional to the external drive. Some studies have indeed shown that the ripple frequency correlates with the amplitude of the sharp wave, which is an indicator for the magnitude of excitatory input reaching CA1 (Sullivan et al., 2011; Stark et al., 2014). The bifurcation-based model, however, has been shown to account for this finding as well, when the indirect drive to CA1 interneurons via local CA1 pyramidal cells dominates over the direct drive via the Schaffer collaterals (Donoso et al., 2018).

Interneuron firing rate. The perturbation-based ripple model is not truly "inhibition-based", in the sense that its mechanism relies on synaptic inhibition. On the contrary: The model works in the absence of synaptic coupling, and strong inhibitory coupling is even detrimental, as it decreases the mean firing rate of neurons and thus the ripple frequency. The ripple frequency is set by the mean unit firing rate, hence this model requires a cell population that is able to fire spikes at ripple frequency. The only CA1 cells that may satisfy this assumption are interneurons, and it is only in this sense that the perturbation-based model is inhibition-based. The bifurcation-based model, on the other hand, can account for a ripple-range oscillation in the population rate, even when individual interneurons fire sparsely at lower rates (sparse synchrony).

There have been reports of CA1 interneurons spiking at ripple frequency (Ylinen et al., 1995, TORO cells: Szabo et al., 2022, bistratified cells: Katona et al., 2014, PV$^+$ BCs: Lapray et al., 2012). The number of such neurons, relative to the overall CA1 interneuron population, and hence their influence on the LFP signal remains to be determined. Many studies have reported interneuron firing rates below ripple frequency, in line with the bifurcation-based model (Csicsvari et al., 1999b; Klausberger et al., 2003; Lapray et al., 2012; Varga et al., 2012, 2014; Stark et al., 2015).

Inhibitory coupling strength. My analysis in Sections 5.2.2.3 and 5.4 highlighted the importance of the inhibitory synaptic strength as a separating factor between the two inhibition-first models: Strong inhibitory coupling lowers the oscillation frequency in the perturbation-based model below ripple range, and can even lead to a transition towards the bifurcation-based model when heterogeneity is omitted.

Paired recordings between PV$^+$ basket cells in CA1 (Bartos et al., 2002) suggest that the inhibitory synaptic connections are much stronger than assumed by Malerba et al. (2016). The bifurcation-based model is further supported by the finding that ripple oscillations do *not* persist, when inhibitory synaptic transmission is blocked by GABA$_\mathrm{A}$-receptor antagonists (Ellender et al., 2010; Schlingloff et al., 2014; Stark et al., 2014) — unlike what is predicted by the perturbation-based model.

Heterogeneity. I pointed out that adaptation and heterogeneity are not crucial ingredients of the perturbation-based model. It is worth noting however, that the perturbation-based model *can* work in a heterogeneous network, while heterogeneity can pose a challenge to the bifurcation-based model. In the perturbation-based model heterogeneity was incorporated in the synaptic coupling strengths and the neuronal excitability. There are various other sources for heterogeneity in the brain, such as non-random connectivity patterns or variability in the various time constants governing neuronal dynamics. Exactly how much and what kind of heterogeneity characterizes the CA1 population of PV$^+$ interneurons, and whether it prevents the emergence of persistent oscillations as posited by the bifurcation-based model, should be investigated in future research. Previous work has shown for example that heterogeneity in the synaptic delays can strongly reduce or even completely abolish the parameter regime for which persistent oscillations emerge (Brunel and Hakim, 1999). If heterogeneity merely *limits* the duration of the otherwise persistent oscillations, the bifurcation-based model could still account for biological ripples, which are naturally transient.

Intra-ripple frequency accommodation. The analysis of the instantaneous ripple frequency in the perturbation-based model is novel and yields promising new insights that might advance model selection: I established that the perturbation-based model in its default configuration with step-current input does *not* exhibit IFA. If the input changes over time, the instantaneous ripple frequency follows these changes, since it is entirely determined by the single unit firing rate. Thus, the perturbation-based model can only account for IFA in response to a strongly *asymmetric* drive — such as a sudden step followed by a monotonic decrease. The bifurcation-based model, on the other hand, produces IFA for any input that rises and falls with sufficient speed, regardless of its symmetry (see Chapter 4).

Excitatory currents measured during spontaneous SPW-Rs can exhibit some asymmetry due to synaptic filtering (Maier et al., 2011), but generally have a non-zero rise time (CA1 pyramidal cell: Maier et al., 2011; Donoso et al., 2018, CA3 PV$^+$ BC: Hajos et al., 2013; Schlingloff et al., 2014). This provides strong evidence for the bifurcation-based model, which can account for IFA independent of the exact (a)symmetry of the SPW-associated drive, whereas the perturbation-based model predicts “anti-IFA” during the rising phase of the external drive.

5.6 Methods

5.6.1 Model summary

In its reduced (interneuron-only) form the perturbation-based inhibitory ripple model consists of a heterogeneous network of 160 interneurons (Malerba et al., 2016). The interneurons are modeled as adaptive exponential integrate-and-fire (aEIF) units with the voltage v_i of neuron i given by:

$$C_m \dot{v}_i = -g_L(v_i - E_L) + g_L \Delta \exp\left[\frac{v_i - V_t}{\Delta}\right] - w_i + I_i(t) \ . \tag{5.3}$$

All model parameters are summarized in Table 5.3. The exponential term mimicks the nonlinear spike generation due to fast sodium currents. Its sharpness is regulated by the parameter Δ. Whenever the voltage v_i reaches the threshold $V_{\text{thr}} = 0\,\text{mV}$, it is reset to $V_{\text{reset}} = -58\,\text{mV}$ and the adaptation current w_i is increased by $b = 10\,\text{pA}$. The adaptation current obeys the differential equation

$$\tau_w \dot{w}_i = a(v_i - E_L) - w_i \ . \tag{5.4}$$

The total input current to cell i is given by

$$I_i(t) = I_i^{\text{DC}} + \sigma\eta_i(t) - I_i^{\text{syn}}(t) + I^{\text{inp}}(t) \ . \tag{5.5}$$

Every cell receives a constant bias current I_i^{DC} drawn from a normal distribution with mean $\bar{I}^{\text{DC}} = 180$ pA and a standard deviation of 10% of the mean ($I_{\text{cv}}^{\text{DC}} = 0.1$):

$$I_i^{\text{DC}} \sim \mathcal{N}\left(\bar{I}^{\text{DC}},\, I_{\text{cv}}^{\text{DC}}\bar{I}^{\text{DC}}\right) \ . \tag{5.6}$$

To model background noise, each cell receives an input η_i generated by an independent Ornstein-Uhlenbeck process

$$\tau_\eta \frac{\mathrm{d}}{\mathrm{d}\,t}\eta_i(t) = -\eta_i + \sqrt{2\tau_\eta}\beta\xi_i(t) \ , \qquad \text{with } \langle\xi_i\rangle = 0,\ \langle\xi_i(t)\xi_j(t')\rangle = \delta_{ij}\delta(t-t') \tag{5.7}$$

with standard deviation β that can be scaled with the scaling factor σ (see Eq. (5.5)). The synaptic current is given by

$$I_i^{\text{syn}}(t) = g_i^I(t)(v_i - E_I) \tag{5.8}$$

with a double-exponential inhibitory conductance

$$g_i^I(t) = \alpha \sum_{j=1}^{N}\sum_{k}^{n_j} g_{ij}^{\text{peak}} s \left(\exp\left[-\frac{t-t_j^k}{\tau_D}\right] - \exp\left[-\frac{t-t_j^k}{\tau_R}\right]\right)\Theta\left(t - t_j^k\right) \tag{5.9}$$

with heaviside function $\Theta(\cdot)$. The sum here is taken over all presynaptic units j and their spike times $\{t_j^k\}_{k\in[1,n_j]}$. The normalizing factor s is chosen such that the inhibitory conductance resulting from a single presynaptic spike at a synapse from unit j to unit i has a peak of g_{ij}^{peak}. The peak conductances are drawn randomly from a normal distribution with mean $\bar{g}^{\text{peak}} = 0.0234$ nS and a standard deviation of 65% of the mean ($g_{\text{cv}}^{\text{peak}} = 0.65$) (see Appendix Section 5.A.1.1). Negative conductances are clipped to 0:

$$g_{ij}^{\text{peak}} \sim \max\left[\mathcal{N}\left(\bar{g}^{\text{peak}},\, \bar{g}^{\text{peak}}g_{\text{cv}}^{\text{peak}}\right),0\right]\text{nS} \ . \tag{5.10}$$

The synaptic coupling strength can be scaled with the scaling factor α.
The input current I^{inp} is the same for all neurons and typically consists of a step current, jumping up from 0 to $I_{\max}$ after an initialization period of 1 second:

$$I^{\text{inp}}(t) = I_{\max}\Theta(t - 1\,\text{sec}) \ . \tag{5.11}$$

Further parameter definitions and all default parameter values are summarized in Table 5.3. Note that compared to the parameters reported in (Malerba et al., 2016) I made two adjustments: larger variability of coupling strength ($g_{\text{cv}}^{\text{peak}} = 0.65$) and lower noise intensity ($\beta = 45\,\text{pA}$) (marked in Table 5.3 and explained in Appendix Section 5.A). Based on the evidence presented in Appendix Section 5.A I assume that my implementation of the perturbation-based ripple model including these parameter corrections faithfully replicates the findings presented in (Malerba et al., 2016).

Parameter	Value	Definition
N	160	Number of interneurons
τ_m	20 ms	Membrane time constant
C_m	200 pF	Membrane capacitance
g_L	10 nS	Leak conductance
E_{leak}	-70 mV	Resting potential
V_{thr}	0 mV	Spike threshold
V_t	-50 mV	Rheobase threshold
Δ	2 mV	Sharpness of threshold
V_{reset}	- 58 mV	Reset potential
E_I	-80 mV	Reversal potential for inhibition
a	2 nS	Subthreshold adaptive coupling
b	10 pA	Spike-triggered adaptation current
τ_w	30 ms	Adaptation time constant
τ_η	10 ms	Noise correlation time constant
β	45 pA	Standard deviation of colored noise input (*)
τ_R	0.3 ms	Synaptic rise time constant
τ_D	2 ms	Synaptic decay time constant
$\bar{g}^{\text{peak}}$	0.0234 nS	Average inhibitory peak conductance
$g_{\text{cv}}^{\text{peak}}$	0.65	Coefficient of variation of peak conductances (**)
$\bar{I}^{\text{DC}}$	180 nA	Average DC input current
$I_{\text{cv}}^{\text{DC}}$	0.1	Coefficient of variation of DC input currents
$I_{\max}$	700 pA	Amplitude of step current
α	2	Scaling factor for synaptic strength
σ	1	Scaling factor for noise

Table 5.3: Default parameters of the perturbation-based inhibition-first ripple model. All parameters as in (Malerba et al., 2016), except for: (*) corrected as described in Section 5.A.1.2, (**) corrected as described in Section 5.A.1.1.

5.6.2 Simulation and analysis

I implemented the network using the spiking network simulator Brian2 (Goodman and Brette, 2009). All simulations were done with a time step of 0.01 ms (after confirming that decreasing the time step to 0.001 ms did not change the results in any significant way).

To assure full comparability, the analysis of network dynamics is done as described in (Malerba et al., 2016): For any given parameter setting, 100–200 independent realizations of the network are simulated and the resulting population activities averaged across trials and in bins of 0.1 ms. In accordance with (Malerba et al., 2016) I translate the average binned population rate (in units of spikes/s) into a spike probability P_{spk} ($\in [0, 1]$) by multiplying with the width of the time bin (Fig. 5.17B). Peaks are detected after smoothing P_{spk} slightly with a gaussian window of standard deviation 0.3 ms. The asymptotic spike probability P_{spk}^{∞} ($\sim r^{\infty}$), which the network reaches after the end of the transient ripple, is found by taking the average over the time window [1500, 2000] ms, i.e. 500 ms after the onset of the step current stimulus. A significance threshold for ripple peaks was defined by Malerba et al. (2016) as

$$P_{\text{thr}} := P_{\text{spk}}^{\infty} + 0.2 \left(p_1 - P_{\text{spk}}^{\infty} \right)$$

where p_1 is the first (and highest) of the peaks detected in the spike probability. All peaks above this threshold are considered significant, and the number of significant peaks equals the number N_{cyc} of cycles of a given ripple event. The inverse of the peak-to-peak distances yields $N_{\text{cyc}} - 1$ discrete estimates of the instantaneous ripple frequency. The average of these instantaneous estimates is defined as the network frequency. The duration of a ripple event is defined as the time from stimulus onset (1 s) until the location of the last significant peak[1].

Up to this point my analysis is exactly the same as described in (Malerba et al., 2016). I introduced a few additional measures to get a better insight into the network dynamics. From each unit's interspike interval I derive a discrete measure of instantaneous unit firing rate (Fig.5.17A2). I define the boundaries of an oscillation cycle as the location of the valleys between the significant peaks of the spike probability. In every cycle I count the number of spikes that each interneuron emitted. Thus I can estimate the saturation in each cycle, i.e. the fraction of cells that have spiked (averaged over trials, Fig. 5.17B1). Also I show the distribution of the total number of spikes that cells have fired over the course of an entire ripple event (Fig. 5.17C1), as well as the distribution of the coefficients of variation of the interspike intervals of all units in all trials (Fig. 5.17C1). For time-dependent stimuli (see Sec.5.3) I define a time-dependent significance-threshold $P_{\text{thr}}(t)$ based on a piecewise-linear fit of the (oscillatory) spike probability (see Figs. 5.6, 5.7).

---

[1] This seems to be what the authors did in (Malerba et al., 2016), so I adopted it to enable direct comparison. Conceptually, since one starts counting ripple cycles in a "valley" at stimulus onset, it seems more reasonable to define the end of the ripple event as the valley after the last significant peak.

5.A Appendix: Replicating (Malerba et al., 2016)

5.A.1 Parameter corrections

5.A.1.1 Variability of peak conductances ($g_{\mathrm{cv}}^{\mathrm{peak}}$)

According to Materials and Methods in (Malerba et al., 2016) the synaptic peak conductances are distributed normally with a mean $\bar{g}^{\mathrm{peak}} = 0.0234$ nS and a standard deviation of 10% of the mean, corresponding to a coefficient of variation $g_{\mathrm{cv}}^{\mathrm{peak}} = 0.1$. All negative conductances are clipped to 0. I argue here that, probably due to a coding error, the actual coefficient of variation used in the simulations underlying the distribution of peak conductances shown in Fig. 2c of (Malerba et al., 2016) (reprinted here as Fig. 5.14) was $g_{\mathrm{cv}}^{\mathrm{peak}} = 0.65$.

In the following I will omit the superscript "peak" to enhance readability. For a normal distribution $\mathcal{N}\left(\bar{g}, \bar{g} \cdot g_{\mathrm{cv}}\right)$ with mean $\bar{g}$ and standard deviation $\bar{g} \cdot g_{\mathrm{cv}}$ the fraction of negative values can be expressed in terms of the cumulative distribution function Φ of the standard normal distribution:

$$\begin{aligned}
\mathrm{P}\left(g \leq 0\right) &= \frac{1}{\sqrt{2\pi} g_{\mathrm{cv}} \bar{g}} \int_{-\infty}^{0} \exp\left[-\frac{\left(g-\bar{g}\right)^2}{\left(2 g_{\mathrm{cv}} \bar{g}\right)^2}\right] \mathrm{d}g = \Phi\left(\frac{0-\bar{g}}{g_{\mathrm{cv}}\bar{g}}\right) = \Phi\left(-\frac{1}{g_{\mathrm{cv}}}\right) \\
&= \frac{1}{2}\left(1 + \operatorname{erf}\left(-\frac{1}{\sqrt{2} g_{\mathrm{cv}}}\right)\right) \qquad (5.12)
\end{aligned}$$

(see Fig. 5.15A). We see that the fraction of negative conductances that will be clipped to 0 depends exclusively on the coefficient of variation g_{CV} and not the mean $\bar{g}$. For a CV of 10% we would expect $\Phi(-10) \sim \mathcal{O}(10^{-24}) \approx 0$ negative conductances. This clearly does not match the original distribution of peak conductances used by Malerba et al. (2016) (see Fig. 5.14), which shows a significant portion of conductances clipped to 0.

Parts of the code by Malerba et al. (2016) are published on ModelDB (McDougal et al., 2017, accession number 188977). I found a presumable typo that explains the inconsistency: When generating the random synaptic peak conductances the authors set the variance to $g_{\mathrm{var}} = g_{\mathrm{CV}}^2 \cdot \bar{g}$ instead of $g_{\mathrm{var}} = g_{\mathrm{CV}}^2 \cdot \bar{g}^2$ (file NetworkRunSeqt.m, line 108). This means that *effectively* they were using a CV of $\hat{g}_{\mathrm{CV}} = \sqrt{g_{\mathrm{var}}}/\bar{g} = g_{\mathrm{CV}}/\sqrt{\bar{g}} = 0.1/\sqrt{0.0234} \approx 0.65$.

For a CV of 65% we know analytically that 6.2% of the conductances should be negative and hence clipped to 0 (Eq. (5.12): $\Phi(-1/0.65) \approx 0.062$). Fig. 5.15 shows the distribution of synaptic conductances for a CV of 65%, after clipping negative conductances to 0. It seems to match the distribution shown in (Malerba et al., 2016) Fig. 2c (here Fig. 5.14) very well.

Note that the code published on ModelDB is an implementation of the full network model including both inhibitory and excitatory cells. The code for the reduced, inhibition-only model is not available (personal communication with Malerba et al. (2016)). Hence we can only assume that the same parameters were used for the reduced model and the same coding error occured, introducing the effectively higher variability of the peak conductances.

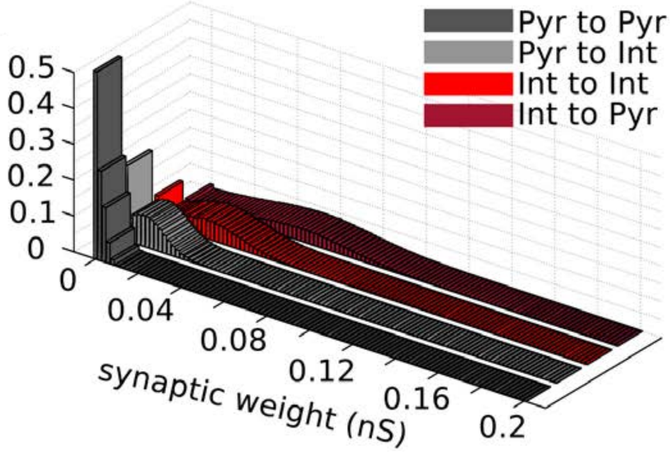

Figure 5.14: Distribution of peak conductances in the perturbation-based inhibition-first model. (adapted from Malerba et al., 2016, CC BY 4.0). Light red histogram shows the distribution of peak conductances for the synapses between inhibitory neurons.

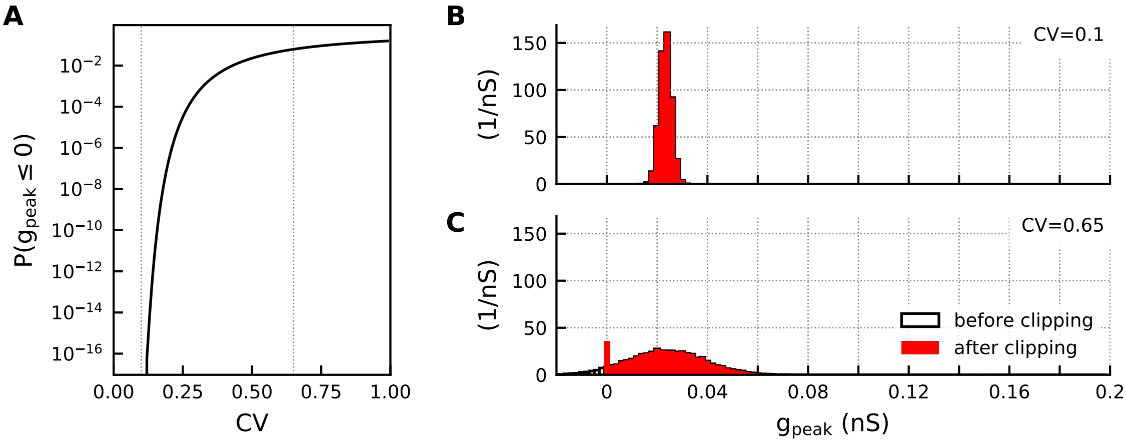

Figure 5.15: Distribution of peak conductances for different coefficients of variations. A, Fraction of peak conductances that will be clipped to 0 depending on the CV (Eq. (5.12)). Vertical lines mark CV 0.1 and 0.65 respectively. **B,** Distribution of peak conductances for CV = 0.1, which was reported by Malerba et al. (2016). **C,** Distribution of peak conductances for CV = 0.65, which seems to be the value that was actually used in (Malerba et al., 2016) (cf. Fig. 5.14). Black: Normal distribution with mean $\bar{g}^{\text{peak}} = 0.0234$ and standard deviation $\bar{g}^{\text{peak}} \cdot \text{CV}$. Red: Same distribution with negative peak conductances mapped to 0.

5.A.1.2 Noise intensity (β)

When adjusting only $g^{\text{peak}}_{\text{cv}}$ as described in the previous section, my network simulation still does *not* yield the same quantitative results that were shown in Fig. 5b of the original paper (here Fig. 5.16). In the following I will discuss the differences and demonstrate how the disparity might be due to an error in the reported noise intensity.

For a synaptic strength scaling of $\alpha = 2$ and a synaptic decay time constant of $\tau_D = 2$ ms Malerba et al. (2016) reported a transient ripple event with 6 cycles at a frequency of ∼180 Hz, amounting to an overall duration of ∼32 ms (Fig. 5b, top left in Malerba et al., 2016, reprinted here as Fig. 5.16).

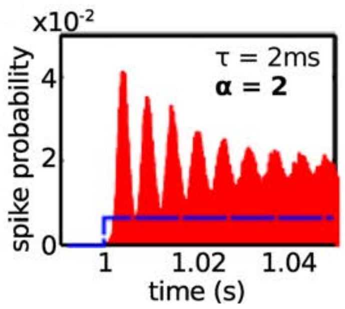

Figure 5.16: Original reference simulation. (Fig. 5b, top left, adapted from Malerba et al., 2016, CC BY 4.0). Red: spike probability averaged over multiple trials. Blue: step current stimuliation of amplitude 700 pA.

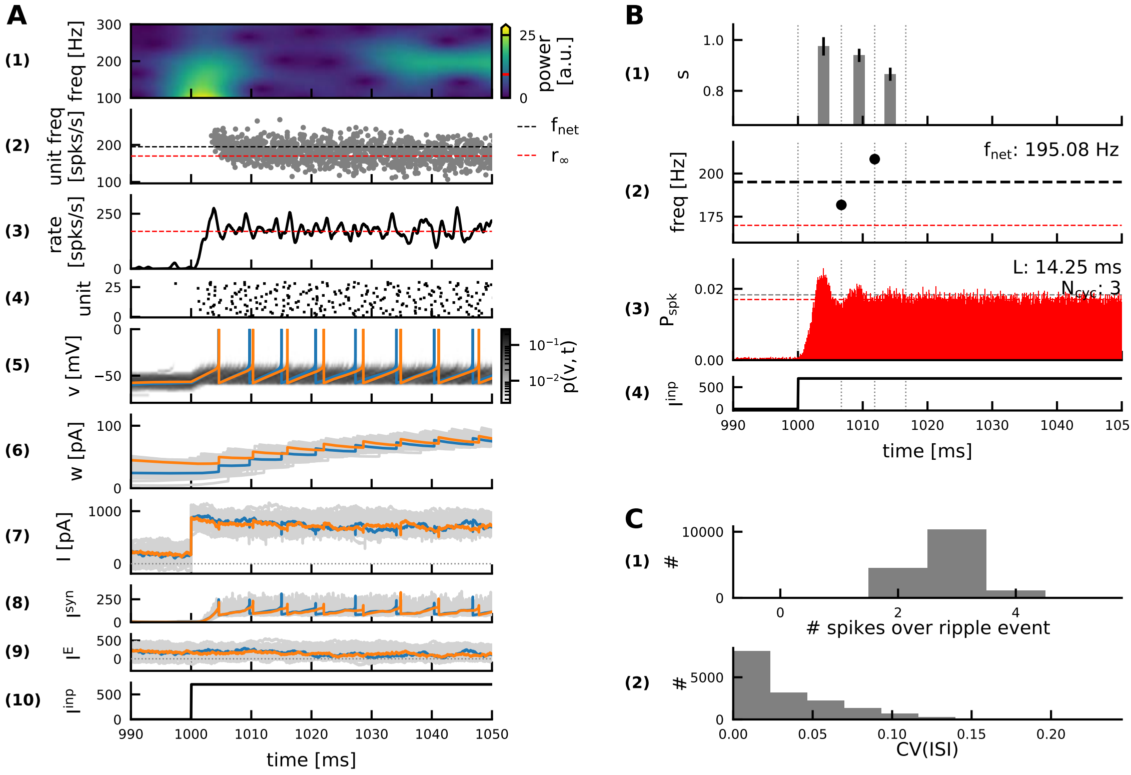

Figure 5.17: Weak ripple in my implementation with original parameters. Parameters as reported by Malerba et al. (2016), see Table 5.3. Same outline as Fig. 5.1. **A,** Single trial. (10) step current of 700 pA (9) excitatory background current $I_i^E = I_i^{\mathrm{DC}} + \sigma\beta\eta_i(t)$; (8) inhibitory feedback current $I_i^{\mathrm{syn}}(t)$; (7) the total current I_i (sum of the bottom 3 panels, Eq. (5.5)); (6) adaptation current w_i; (5) membrane potentials; (4) raster plot (30/160 interneurons); (3) population rate; (2) instantaneous unit firing rates (1/ISI). (1) wavelet spectrogram quantifying instantaneous frequency and power of the population rate. **B,** Average over 100 trials. (4) step current I^{inp}. (3) spike probability P_{spk} in bins of 0.1 ms with significant peaks marked (black stars). (2) discrete estimates of instantaneous ripple frequency (black marker), and average frequency (black dashed line). (1) saturation, ±1 SD. **C,** Spike statistics. (1) total number of spikes per unit per event. (2) coefficient of variation of interspike intervals.

In my implementation the network does exhibit a transient oscillation as well, with a frequency in ripple range (195 Hz). However the event is much shorter (14.25 ms) with only 3 cycles (Fig. 5.17B). Visual comparison of the averaged spike probabilities (Fig. 5.17B vs Fig. 5.16) shows that the activity of my network is much noisier. This is not surprising given the strong colored noise input that every unit receives. Looking at the excitatory background current $I_i^E = I_i^{\mathrm{DC}} + \sigma\eta_i$ of individual cells (Fig. 5.17A, panel 9), we see that it spans up to 500 pA, which is comparable to the incoming "signal", i.e. the step current I^{inp} of amplitude 700 pA.

Malerba et al. (2016) showed that the oscillatory modulation of the spike probability gets more pronounced for lower noise intensities (smaller noise scaling factor σ, their Fig. 6c–d, reprinted here as Fig. 5.22). I hence hypothesized that maybe the noise intensity used for the simulations of the reduced model in Figs. 5 and 6 of (Malerba et al., 2016) was different from the one reported in the Methods section, which was written for the complete model which also includes pyramidal cells.

Further support for this hypothesis comes from the observation that the asymptotic spike probability into which the network settles after the ripple event, matches the published result quite well ($P_{\mathrm{spk}}^{\infty} \approx 0.02$, Fig. 5.17B, second panel). This means that the average currents that the cells receive are comparable. Only the fluctuations around this mean are too strong.

When I reduce the noise amplitude by a factor of 1/2, i.e. $\beta = 45\,\mathrm{pA}$, my network simulation matches the originally published results very well (Fig. 5.1B vs. Fig. 5.16). The averaged spike probability exhibits a pronounced ripple oscillation with 5 cycles at 184 Hz over a total of 25.45 ms.

I demonstrate in the next section that the slight deviation in ripple duration compared to the original (5 instead of 6 cycles, with the 6th peak just below threshold) might be due to the significance criterion for ripple peaks, which is highly sensitive to the details of the averaging procedure (number of trials, presence or absence of quenched variability in the network connectivity.).

5.A.2 The role of random connectivity

Since it was not clear from the original publication whether the network architecture had been fixed or varied across trials, I briefly investigated the effect of random connectivity on the average network dynamics. The network architecture is determined by the distribution of peak conductances (Eq.(5.10)). Not only do peak conductances vary across synapses, but around 6% of them are clipped to 0 (see 5.A.1.1), effectively introducing *structural* heterogeneity to the network with some synapses missing.

In Fig. 5.18 I averaged 100 trials of the default ripple network simulation (shown in Fig. 5.1), once keeping the network architecture the same across trials (i) and once using a new random connectivity matrix in each trial (ii). I observe that although both cases produce very similar results, keeping the network architecture constant increases the estimated ripple duration by 1 cycle ($\sim$ 6 ms) (see Fig. 5.18 C, i vs. ii). This discrepancy disappears if I average more trials (200), in which case both cases yield an average of 5 ripple cycles (not shown).

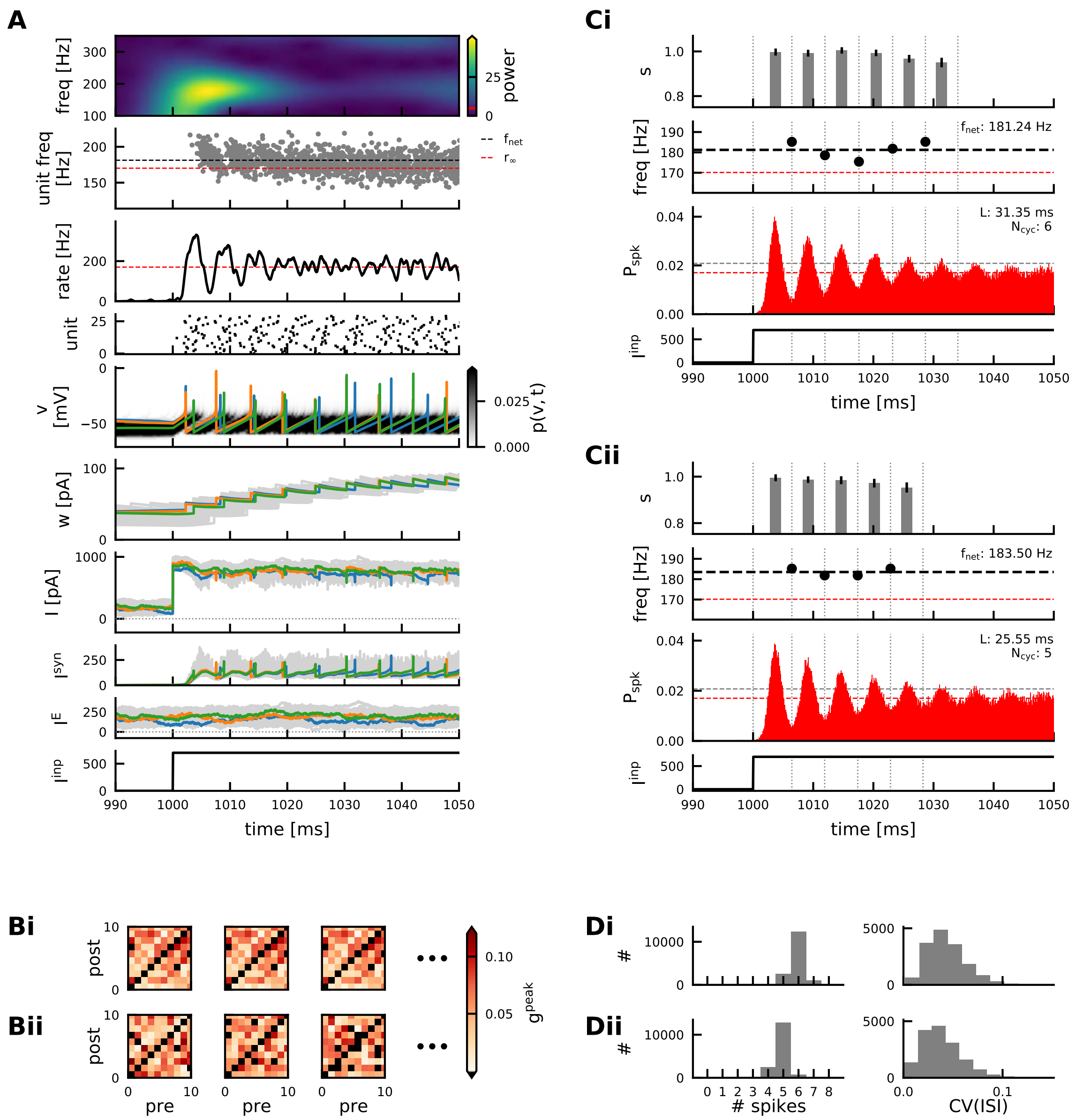

Figure 5.18: Fixed vs variable network architecture.
A, Ripple dynamics in a single trial. **B,** Distribution of peak conductances across trials: fixed (i) or random (ii). For visibility only the connections between the first 10 interneurons are shown here. **C,** Ripple dynamics averaged over 100 trials with either fixed (i) or variable (ii) network architecture. Note the difference in detected ripple duration. **D,** Spiking statistics for both cases.

If the previous parameter adjustments indeed brought us to the exact same point in parameter space used by Malerba et al. (2016) (which we cannot safely assume of course), this could be one possible explanation for why I find 5 instead of their 6 ripple cycles (Fig. 5.1).

If I average 100 trials for a *fixed* network architecture I recover quite precisely the results shown in the original Fig. 5b, top left, i.e. a ripple at 181 Hz with 6 cycles and an overall duration of 31 ms (Fig. 5.18 Ci). Another potential source for discrepancies in estimated ripple duration could be the method used for peak detection. The average spike probability over 100-200 trials in bins of 0.1 ms is still noisy, so I applied a narrow gaussian smoothing window before detecting peaks. If Malerba et al. (2016) used a slightly different method for peak detection this might explain why they find one more peak that passes the significance threshold.

For my further simulations shown in the main text I decided to average not only over noise realizations but also network architectures. This should yield the most meaningful quantification of the ripple dynamics of this model, given that we are not interested in the (small) effect that a particularity in any given connectivity matrix might have. Also I will get better averaging results already at lower trial numbers.

The most important take-away from this section is that the estimate of the duration and number of cycles of a ripple event in this model is highly sensitive to noise and the somewhat arbitrary choice of the significance threshold for the peaks in the spike probability. This should be kept in mind when evaluating the comparisons with the original paper.

5.A.3 Parameter explorations

To further probe my implementation of the model I replicated parts of the parameter exploration shown in (Malerba et al., 2016).

5.A.3.1 Variation of inhibitory coupling strength

Malerba et al. (2016) varied the strength of the inhibitory synapses by changing either the peak conductance, using the scaling factor α, or the synaptic decay time constant τ_D (their Fig. 5, reprinted here as Fig. 5.20). They found that both parameters have similar effects: Increasing either α or τ_D increases the overall amount of inhibitory feedback, which leads to a decrease of the network frequency. They also observe a decrease in ripple cycles. The resulting duration is a combination of both frequency and number of cycles and hence shows mixed trends. Most importantly, ripples in this model occur even in the absence of synaptic coupling ($\alpha = 0$).

My implementation of the network model replicates all of these qualitative findings and also fits the results quantitatively (see Fig. 5.19 vs. Fig. 5.20).

5.A.3.2 Variation of noise strength

Malerba et al. (2016) varied the amplitude of the colored noise input that the interneurons receive using the scaling factor σ (their Fig. 6c-d, reprinted here as Fig. 5.22). Note that based on the arguments presented in Section 5.A.1.2 I assume here that the baseline of $\sigma = 100\%$ corresponds to a noise standard deviation of $\beta = 45\,\mathrm{pA}$. Malerba et al. (2016) find that a reduction of the noise has no effect on the network frequency but prolongs the ripple event (Fig. 5.22).

My implementation of the network replicates the same qualitative findings (Fig. 5.21 vs. Fig. 5.22).

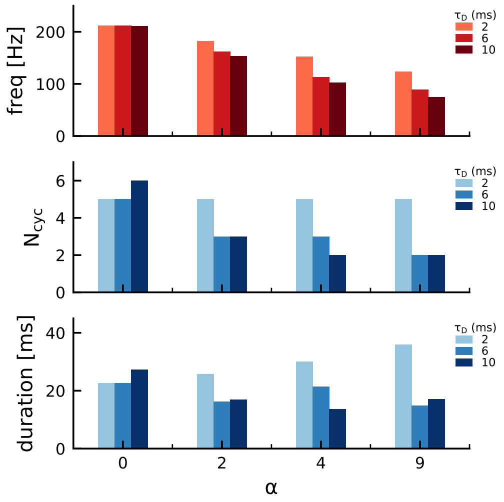

Figure 5.19: Parameter exploration: inhibitory coupling strength. Synaptic strength was varied via the scaling factor α and/or the decay time constant τ_D. The resulting ripple dynamics are quantified in terms of network frequency, number of ripple cycles and duration of the ripple event (from top to bottom). The deviations across different τ_D values for $\alpha = 0$ are due to the beforementioned noise-sensitivity of the measure for ripple duration. All results are in agreement with Fig. 5c-e in (Malerba et al., 2016) (Fig. 5.20)

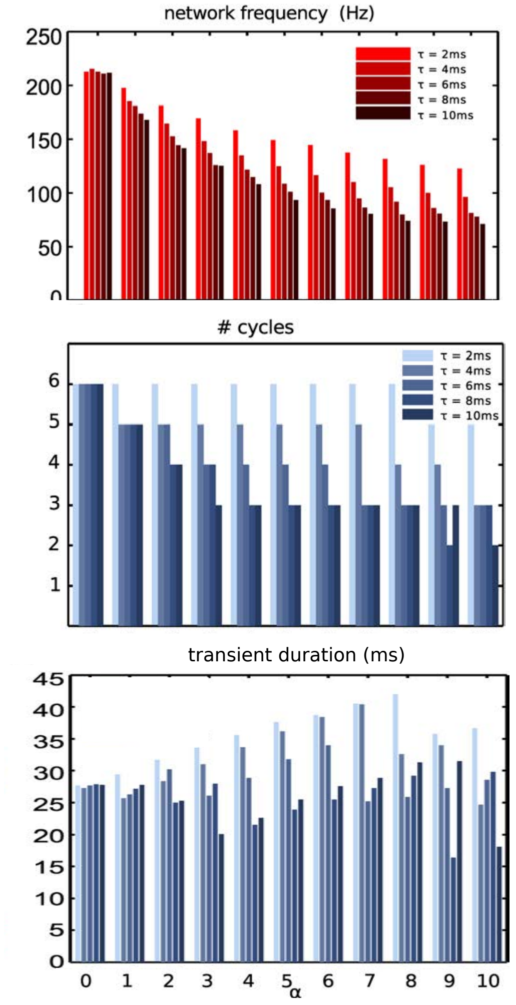

Figure 5.20: Original parameter exploration: inhibitory coupling strength. Same layout as Fig. 5.19 (adapted from Malerba et al., 2016, CC BY 4.0).

A direct *quantitative* comparison between Fig. 5.21 and Fig. 5.22 is not possible due to an inconsistency in the original paper between their Figs. 5 and 6d. According to Malerba et al. (2016) the noise strength was kept constant at $\sigma = 100\%$ when α and τ_D were varied in their Fig. 5. In their Fig. 6 on the other hand σ and α were varied, while τ_D was supposedly at its default value of 2 ms. Hence the network frequency for $\alpha = 2$, $\tau_D = 2\,\text{ms}$ in their Fig. 5d (here Fig. 5.20, light red bar, ~180 Hz) should be the same as the network frequency for $\alpha = 2$, $\sigma = 100\%$ in their Fig. 6d (here Fig. 5.22, dark green bar, ~225 Hz), which is however *not* the case. This seems to suggest that either τ_D or other parameters were varied in the simulations for their Fig. 6 compared to their Fig. 5. I decided not to pursue this further, since it does not affect the overall qualitative finding.

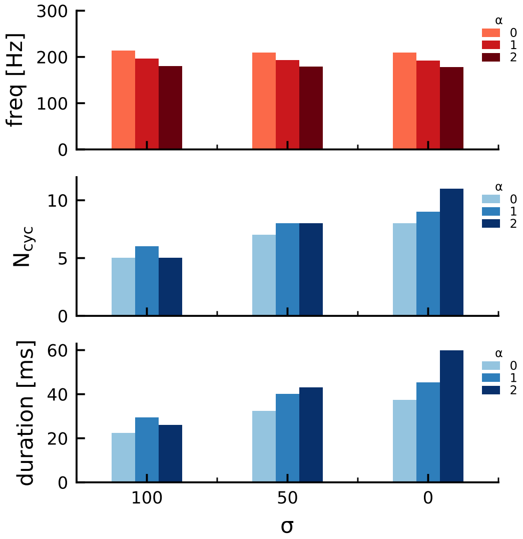

Figure 5.21: Parameter exploration: inhibitory coupling strength and noise intensity. Synaptic strength and the amplitude of the colored noise input are scaled by α and σ resp. The resulting ripple dynamics are quantified in terms of network frequency, number of ripple cycles and duration of the ripple event (from top to bottom). Results agree qualitatively with Fig. 5.22.

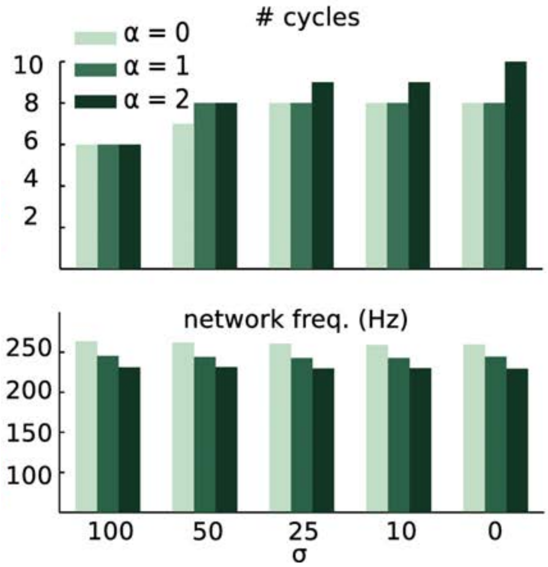

Figure 5.22: Original parameter exploration: inhibitory coupling strength and noise intensity. Top: number of cycles, bottom: network frequency. Note that the default bars here ($\sigma = 100$) do not match the default bars of Fig. 5.20 ($\tau = 2\,\text{ms}$) (adapted from Malerba et al., 2016, CC BY 4.0).

Overall, the above parameter explorations demonstrate that my parameter choice of $g_{\text{cv}}^{\text{peak}} = 0.65$ and $\beta = 45\,\text{pA}$ brings me very close to the point in parameter space that must have been used in the original publication by Malerba et al. (2016). My network exhibits the same ripple dynamics in terms of frequency and duration, quantitatively and qualitatively.

5.B Supplementary figures

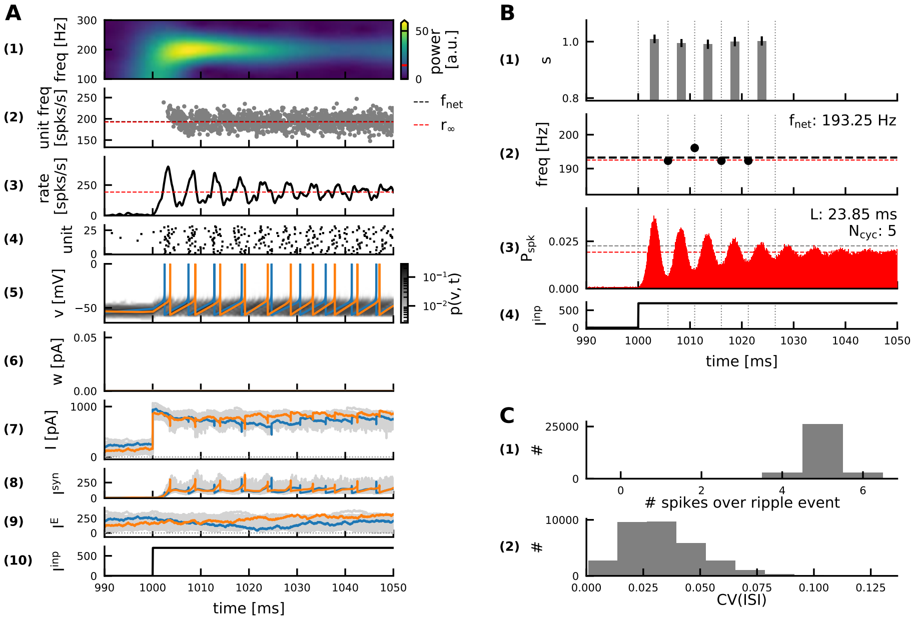

Figure 5.23: Ripple dynamics without adaptation. Same outline as Fig. 5.1. Network simulation without adaptation ($a = 0\,\text{nS}$, $b = 0\,\text{pA}$, hence no adaptation current w (A6), all other parameters as in Fig. 5.1). Qualitatively the same ripple dynamics as in Fig. 5.1. Here the network frequency coincides with the asymptotic rate (black vs red dashed line in A2, B2).

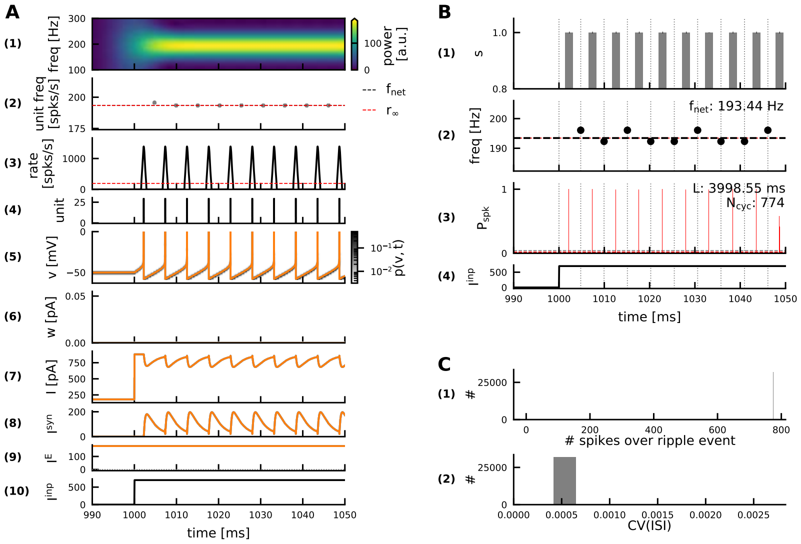

Figure 5.24: Pathological persistent ripple without adaptation, heterogeneity and noise. Same outline as Fig. 5.1. Network simulation without adaptation, heterogeneity or noise ($g_{\text{cv}}^{\text{peak}} = 0$, $I_{\text{cv}}^{\text{DC}} = 0$, $a = 0\,\text{nS}$, $b = 0\,\text{pA}, \sigma = 0$, hence no adaptation current w (A), all other parameters as in Fig. 5.1). The network behaves like a single unit.

Figure 5.25: Introducing persistent oscillations with a single parameter change. Same outline as Fig. 5.9, only the coupling strength is increased (here $\alpha = 200$, $\alpha g_i^{\text{peak}} = 4.58$ nS). Spikes occur highly synchronized (B4) due to the strong inhibitory feedback (B7) compared to the noise.

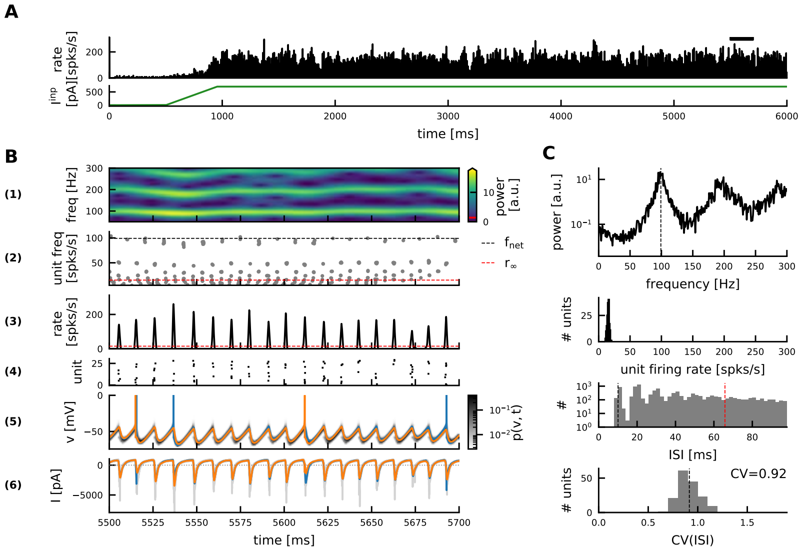

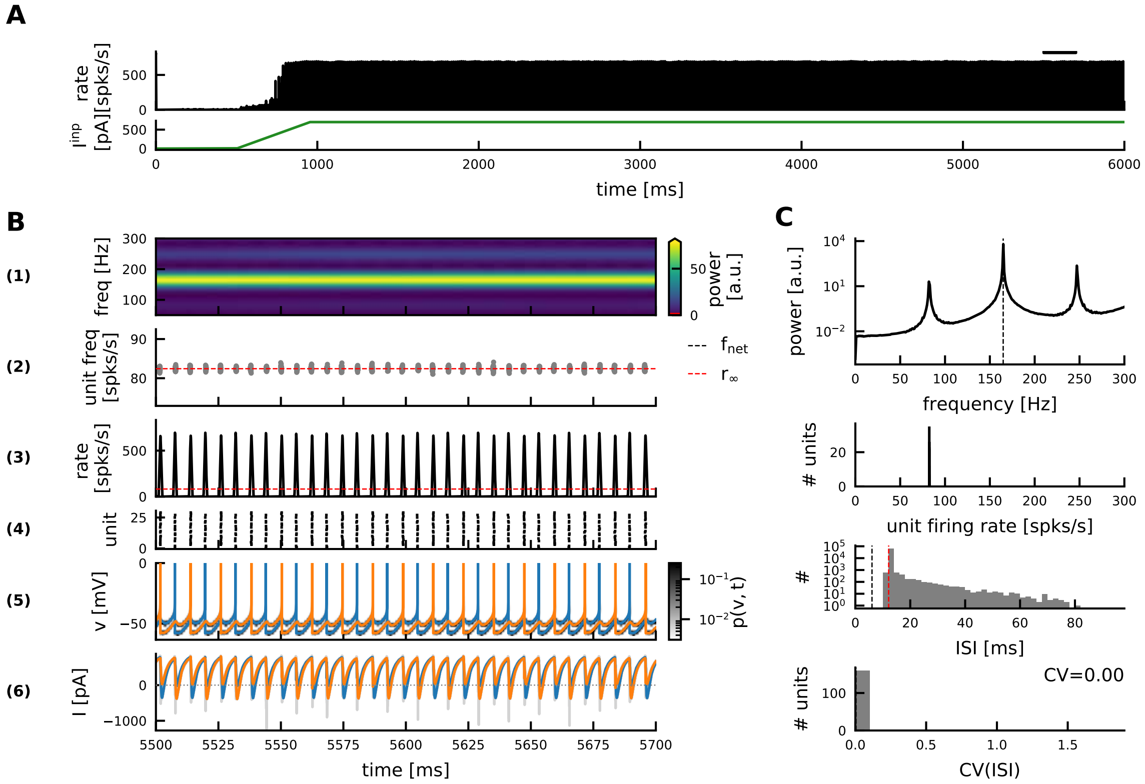

Figure 5.26: Clustering instability in the homogeneous EIF network. Same outline as in Fig. 5.9. At low noise (here $\sigma = 0.1\ \sigma\beta = 4.5\,\text{pA}$) the homogeneous EIF network undergoes a clustering instability when the synaptic coupling strength is increased (here $\alpha = 20$, $\alpha g_i^{\text{peak}} = 0.458\,\text{nS}$) (Brunel and Hansel, 2006, cf. mark (4) in Fig. 5.10B). The network splits into two clusters of units that fire regularly in every second cycle resp. (see orange vs blue unit in B(5)). The network frequency is thus exactly twice the unit firing rate.

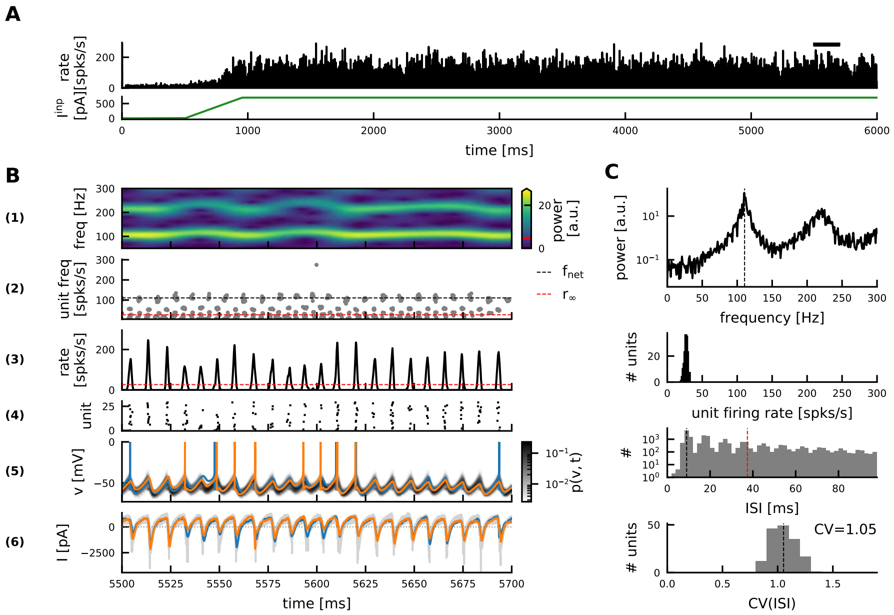

Figure 5.27: Network frequency increases with noise strength. Same as Fig. 5.12, but with increased noise strength ($\sigma = 3$, $\sigma\beta = 135\,\mathrm{pA}$). CV(ISI) and network frequency increase (110.6 Hz).

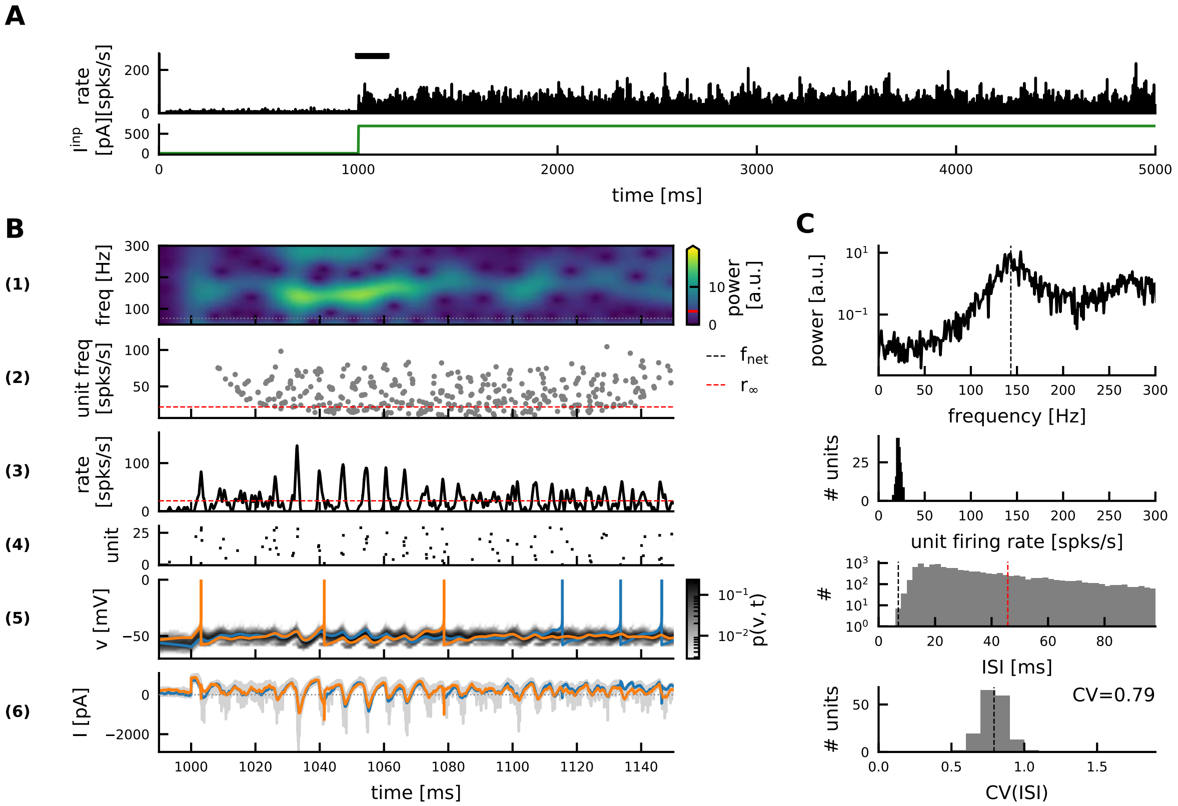

Figure 5.28: No transient ringing effect with strong coupling and noise. Same network as Fig. 5.11. A step current stimulation does not trigger a transient ringing effect. Instead the network enters the same persistent oscillations described in Fig. 5.11.

6 | Mesoscopic models of ripple oscillations

6.1 Introduction

Current evidence suggests that sharp wave-ripples can be generated in local networks of regions like CA3, CA1, the subiculum or the amygdala (Buzsáki, 1986; Ponomarenko et al., 2003; Imbrosci et al., 2021), but also propagate within and across regions (Csicsvari et al., 2000; Maier et al., 2003; Both et al., 2008; Nitzan et al., 2020; Oliva et al., 2016),(but see Ellender et al., 2010). This may be relevant for the transfer of information across regions. Understanding such potential function in the future will likely require a larger-scale model of sharp wave-ripple dynamics (and replay) across multiple regions.

In Chapter 4 I studied the bifurcation-based inhibitory ripple model on micro- and on macroscopic scale. The gap between the two levels of description is large: Simulating the activity of a spiking neural network on a microscopic scale requires an integration of the membrane potential dynamics of a large number of neurons over many small time steps. This can become computationally expensive when studying very large networks, multiple coupled networks, or the evolution of the dynamics over longer time windows. On the other hand, I have shown that the most important qualitative features of the interneuron-generated ripples, such as the transition from sparse to full synchrony or IFA, are preserved on a macroscopic, mean-field scale. While such a macroscopic approach is very efficient in determining the population rate expected in the mean-field limit, it completely neglects finite-size effects. Real interneuron networks are of course finite ($\sim$200 PV$^+$ basket cells in a mouse hippocampal slice, $\sim$5530 PV$^+$ BCs in the entire hippocampus; Bezaire and Soltesz, 2013; Donoso et al., 2018) and the resulting finite-size effects (*e.g.* fluctuations) can influence the ripple dynamics quantitatively, in terms of frequency and synchrony (Holzbecher and Kempter, 2018), and are needed to eventually account for the spontaneous emergence of SPW-Rs (Evangelista et al., 2020).

Recently an intermediate *mesoscopic* modeling approach has been developed (Schwalger et al., 2017). It combines efficient integration of the population dynamics on a macroscopic scale with a correction factor that accounts for finite-size effects. An important prerequisite for the mesoscopic ansatz is a switch from a neuron model with noisy input to an escape-noise model with stochastic spiking (*i.e.* „noisy output“). This switch involves the choice of a hazard function governing stochastic spiking. In this chapter I will show that in a recurrently coupled network, such as the bifurcation-based inhibitory ripple model, the choice of hazard function has a significant impact on the network dynamics, not only at the mesoscopic level but already on the microscopic level.

The chapter is organized as follows: First I briefly introduce a microscopic reference network of LIF neurons exhibiting ripple oscillations (Section 6.2). It is the goal of this chapter to model the ripple dynamics of this network on a mesoscopic scale. In Section 6.3 I briefly introduce escape-noise models and two potential hazard functions (Section 6.3.1) that I will compare throughout the chapter. I derive a high-frequency limit for the linear response of escape-noise models depending on the hazard function (Section 6.3.2). Simulations of networks of escape-noise models on the microscopic level will illustrate how the differences in linear response due to the hazard function translate into different ripple oscillation frequencies in a recurrent network (Section 6.3.3). In Section 6.4 the mesoscopic scheme by Schwalger et al. (2017) is introduced and applied to the LIF ripple network. The resulting dynamics are compared to the microscopic simulations of the LIF reference network and the network of escape-noise units.

6.2 Microscopic reference model with noisy input

It will be the goal of this chapter to approximate the dynamics of the bifurcation-based inhibitory ripple model discussed in Chapter 4 on a mesoscopic scale. Thus, one of the network configurations discussed in Chapter 4 is chosen as a microscopic reference model and will be briefly reviewed here (cf. Fig. 4.17B). The membrane potential v_i of an LIF neuron i is described by a stochastic differential equation:

$$\dot{v}_i(t) = \frac{1}{\tau_m}(E_{\text{leak}} - v_i(t)) + \frac{1}{C}\left(I_{\text{ext}} - I_{\text{inh}}(t)\right) + \sqrt{\frac{2}{\tau_m}}\sigma_V \xi_i(t) \tag{6.1a}$$

$$I_{\text{inh}}(t) = I_I^{\text{peak}}\left(\kappa_\Delta^{\text{2exp}} * \sum_{j=1}^{N_I}\sum_k \delta(t_j^k - t)\right) \tag{6.1b}$$

with membrane time constant τ_m, leak potential E_{leak}, and capacitance C. Whenever the membrane potential v_i reaches a spike thresold V_{thr}, a spike is fired and the membrane potential is reset to V_{reset} where it remains for an absolute refractory period of τ_{ref}. The network is fully connected with current-based, inhibitory synapses. The postsynaptic response to an input spike begins after a delay Δ and is modeled as the difference of two exponential functions (filter $\kappa_\Delta^{\text{2exp}}$, Eq. (4.11f)). The peak synaptic current is scaled down to account for the increased indegree in the fully connected network: $I_I^{\text{peak}} = 0.2 \cdot 83$ pA. All neurons receive an independent Gaussian white noise ξ_i with $\langle \xi_i \rangle = 0$, $\langle \xi_i(t)\xi_j(t') \rangle = \delta_{ij}\delta(t - t')$. The noise intensity is fixed to $\sigma_V = 7.3$ mV. All other parameters are taken from the detailed ripple model (see Table 4.2 and Donoso et al., 2018).

As discussed in Chapter 4, this network exhibits ripple oscillations when driven by sufficient excitatory input I_{ext} (Fig. 6.1). For increasing drive we observe a transition from sparse to full synchrony.

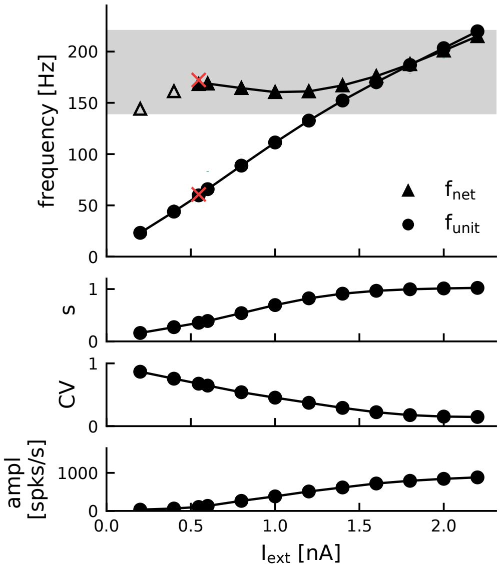

Figure 6.1: Ripple dynamics in a microscopic LIF network under Gaussian white noise input. Network frequency f_{net} and mean unit firing rate f_{unit}; saturation $s = f_{\text{unit}}/f_{\text{net}}$; coefficient of variation (CV) of interspike intervals; and average amplitude of population rate depending on the constant, excitatory drive I_{ext}. All measures were introduced in Chapter 4, Methods Section 4.5.1. Red crosses: network frequency and the mean unit rate at oscillation onset (see Linear stability analysis in Chapter 4, Methods Section 4.5.2.4 Brunel and Hakim, 1999). Empty triangles mark the (small) peak in the power spectral density of the population rate before the bifurcation.

It is the goal of this chapter to investigate whether this range of dynamics in a microscopic simulation of a network of LIF units under Gaussian white noise can be captured in a mesoscopic simulation (Schwalger et al., 2017). In a first step this requires replacing the LIF neuron model with noisy input by an escape-noise model.

6.3 Escape-noise models: Mapping input to output noise

There are many sources of noise in the brain, such as stochastic ion channels, noisy background activity from other cells or stochasticity in synaptic transmission. Standard integrate-and-fire models of neuronal activity, such as the LIF neuron introduced above (Eq. (6.1a)), account for such noise by adding a noisy input current (*e.g.* Gaussian white noise). The membrane potential inbetween spike times is thus described by an Ornstein-Uhlenbeck process. The noisy trajectory of the membrane potential is compared to a deterministic spike threshold V_{thr} in order to determine when the neuron fires a spike.

Instead of incorporating noise in the input, one can also account for noise in the output of a neuron. In the following I will refer to such neuron models as *generalized integrate-and-fire* (GIF) neurons (following the nomenclature in Schwalger et al., 2017; Gerstner et al., 2014; Pozzorini et al., 2015)[1]. The membrane potential u of a GIF neuron is described by an ordinary differential equation (ODE):

$$\frac{\partial}{\partial t}u(t,\hat{t}) = \frac{1}{\tau_m}\Big(E_{\text{leak}} - u(t,\hat{t})\Big) + I(t) \quad , \qquad u(\hat{t},\hat{t}) = V_{\text{reset}} \tag{6.2}$$

---

[1] In the literature GIF often denotes a wider class of neuron models that can have a dynamic, history-dependent firing threshold. In that sense I refer here to a subclass of GIF neurons with static threshold.

and, given some input current $I(t)$, is a deterministic function of time t and the neuron's last spike time $\hat{t}$ at which u was set to the reset potential V_{reset}. The GIF neuron fires spikes stochastically according to a *hazard rate*

$$H(t,\hat{t}) = f\left(u(t,\hat{t}), \dot{u}(t,\hat{t})\right)\, \Theta(t-\hat{t}-\tau_{\text{ref}}) \ . \tag{6.3}$$

The probability that a neuron fires a spike in a small[2] time window $[t, t+\Delta t]$ is given by $H(t,\hat{t})\Delta t$. If a spike is fired, the membrane potential is reset. If there is an absolute refractory period τ_{ref}, the hazard rate remains zero for the time τ_{ref} after the last spike. The hazard function f typically depends on the distance of the momentary membrane potential u from the spike threshold. Additionally it might depend on the time-derivative $\dot{u}$ (more details in the next section).

The hazard rate H can be understood as the *conditional* probability density for firing a spike at time t, given that no spike was fired since the last spike at time $\hat{t}$. The probability of *not* firing, or *survival probability*, is described by

$$S(t,\hat{t}) = P\Big(\text{no spike in } [\hat{t},t]\Big) = \exp\left[-\int_{\hat{t}}^{t} H(s,\hat{t})\,\mathrm{d}s\,\Theta(t-\hat{t})\right] . \tag{6.4}$$

Thus, the survival probability decreases exponentially over time according to the hazard rate:

$$\frac{\partial}{\partial t}S(t,\hat{t}) = -H(t,\hat{t})S(t,\hat{t}) \tag{6.5}$$

The first-passage-time (FPT) density of a GIF unit is thus given by

$$P(t,\hat{t}) = S(t,\hat{t})H(t,\hat{t}) \ . \tag{6.6}$$

6.3.1 Hazard functions

An ideal mapping from an LIF neuron model with noisy input to a GIF escape-noise model would require a hazard function that preserves the first-passage-time (FPT) density. Unfortunately the FPT density of an LIF neuron under Gaussian white noise for general, time-dependent input $I(t)$ is not known. Instead, hazard functions have been chosen either purely phenomenologically or based on various approximations of the LIF FPT density (Plesser and Gerstner, 2000; Goedeke and Diesmann, 2008; Chizhov and Graham, 2007, 2008; Schwalger, 2021).

In the following I will compare two hazard functions: the common, phenomenological exponential hazard, and the Chizhov-Graham hazard, which is based on an approximate solution of the LIF FPT problem and depends not only on the membrane potential but also on its slope (Chizhov and Graham, 2007, 2008).

---

[2] In a simulation with finite time step Δt the spike probability is instead defined as $P_{\text{spk}}(t,\hat{t}) = 1 - \exp\left[-\int_{t}^{t+\Delta t} H(s,\hat{t})\,\mathrm{d}s\,\Theta(t-\hat{t})\right] \leq 1 \quad \forall\, \Delta t$ to ensure that it never exceeds 1, even for larger time steps. For small $H(t,\hat{t})\Delta t$ this is approximately equal to the simpler definition above ($P_{\text{spk}}(t,\hat{t}) \approx H(t,\hat{t})\Delta t$).

6.3.1.1 The exponential hazard

The exponential hazard is based on a simple exponential function of the distance of the momentary membrane potential u from the spike threshold V_{thr}:

$$f(u) = r \exp\left[\frac{u - V_{\text{thr}}}{\Delta_{\text{thr}}}\right] . \tag{6.7}$$

It is independent of the the derivative $\dot{u}$, and it has two parameters: the threshold-softness parameter Δ_{thr} and the instantaneous firing rate at threshold r, which can be fitted to experimental data or to the spike train of a neuron model with noisy input (Gerstner and Naud, 2009; Mensi et al., 2012; Pozzorini et al., 2015; Jolivet et al., 2006).

I fitted r and Δ_{thr} such that the mean firing rate of the GIF unit matches the mean firing rate of the LIF unit under Gaussian white noise (Eq. (6.1a), see Fig. 6.2). The fit was restricted to the input range of 0–0.3 nA (see inset in Fig. 6.2), for which the LIF unit fires at up to ~150 spikes/s, which is the range of unit firing rates observed during ripple oscillations (Fig. 6.1, top). For higher input currents the firing rate of the GIF unit is lower than the LIF rate (Fig. 6.2). The GIF neuron fires more regularly than the LIF neuron at low inputs, and slightly less at high input (Fig. 6.2, bottom).

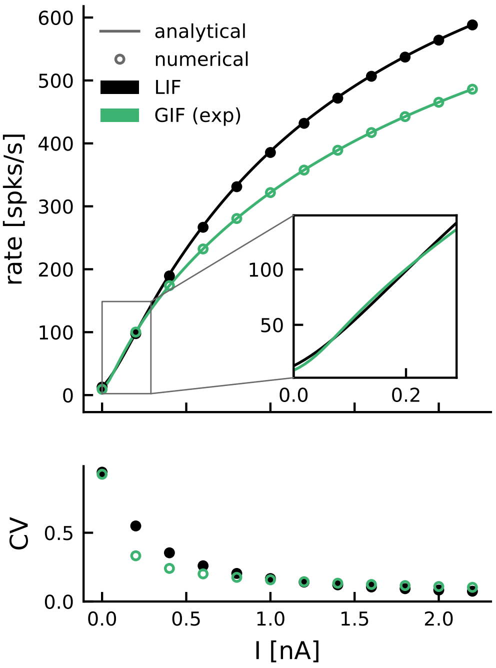

Figure 6.2: Firing properties of a GIF neuron with exponential hazard fitted to match the f-I curve of an LIF neuron.
Mean firing rate (top) and coefficient of variation of the interspike intervals (bottom) as a function of input current for an LIF neuron under Gaussian white noise (black) and for a GIF neuron with exponential hazard (green, $r = 409.96$ spikes/s, $\Delta_{\text{thr}} = 3.45$ mV). Inset shows the fitted range. Solid lines: analytical f-I curves (LIF: Eq. (6.28), GIF: Eq. (6.29)). Markers: numerical estimates from a spiking network simulation.

6.3.1.2 The Chizhov-Graham hazard

Chizhov and Graham (2007) defined a hazard based on the FPT density of an LIF neuron under Gaussian white noise in the two limiting cases of subthreshold input (hazard A) and strong suprathreshold input (hazard B). They approximate the hazard f for general input as the sum of the two independent limit cases:

$$f\Big(u(t, \hat{t}), \dot{u}(t, \hat{t})\Big) = A\Big(T(t, \hat{t})\Big) + B\Big(T(t, \hat{t}), \dot{T}(t, \hat{t})\Big) . \tag{6.8a}$$

On the right-hand side I am following the original notation from Chizhov and Graham (2007). Their function

$$T(t,\hat{t}) = \frac{V_{\text{thr}} - u(t,\hat{t})}{\sqrt{2}\sigma_V} \tag{6.8b}$$

is a moving threshold that arises from a rescaling of the LIF FPT problem. For a detailed derivation please refer to Appendix Section 6.A. For the moment it is sufficient to note, that by inserting the expression for T, both hazards A and B can be rewritten as functions of the mean membrane potential u (and its slope).
Hazard A was derived by Chizhov and Graham (2007) as the purely diffusion-mediated firing rate of an LIF unit under Gaussian white noise in the limit of a slowly changing mean membrane potential for subthreshold input (slow changes in T):

$$A(T) \approx \frac{1}{\tau_m} \exp(6.1 \times 10^{-3} - 1.12T - 0.257T^2 - 0.072T^3 - 0.0117T^4). \tag{6.8c}$$

Hazard B describes drift-mediated spiking in the limit of fast transients in the mean membrane potential due to suprathreshold input (fast changes in T):

$$B(T,\dot{T}) = -\frac{2}{\sqrt{\pi}} \frac{\exp\left[-T^2\right]}{1+\operatorname{erf}(T)} \left[\dot{T}\right]_- = \begin{cases} \frac{2}{\sqrt{\pi}} \frac{\exp\left[-T^2\right]}{1+\operatorname{erf}(T)} |\dot{T}| > 0\,, & \text{if } \dot{T} < 0 \Leftrightarrow \dot{u} > 0 \\ 0, & \text{if } \dot{T} \geq 0 \Leftrightarrow \dot{u} \leq 0 \end{cases} \tag{6.8d}$$

Hazard B depends on $\dot{T}$, and thus the slope $\dot{u}$ of the mean membrane potential. Whenever the mean membrane potential decays (T *in*creases), the hazard rate is clipped to zero by virtue of the linear rectifier function $[x]_- := (x - |x|)/2$ (see also Goedeke and Diesmann, 2008, and Chapter 4). For a detailed derivation of the Chizhov-Graham hazard see Appendix Section 6.A.

The Chizhov-Graham hazard has interesting parallels to the Gaussian approximation of the mean-field ripple dynamics developed in Chapter 4. Note that the rate definition in the Gaussian approximation in Chapter 4 is equivalent to the Chizhov-Graham hazard B (Eq. (6.8d)) derived for the limit of fast transients in the membrane potential due to strong suprathreshold input. The Chizhov-Graham hazard

$$B(t) = -\frac{2}{\sqrt{\pi}} \frac{\exp(-T(t)^2)}{1+\operatorname{erf}(T(t))} \left[\dot{T}\right]_-$$

corresponds to a survival probability

$$S(t) = \frac{1}{2}\Big(1 + \operatorname{erf}\left[T(t)\right]\Big)$$

(see Eq. (6.27)), and yields a first passage time density

$$\begin{aligned} P(t) &\overset{(6.6)}{=} B(t)S(t) = -\frac{1}{\sqrt{\pi}} \exp(-T(t)^2) \left[\dot{T}(t)\right]_- \overset{(6.8b)}{=} -\frac{1}{\sqrt{\pi}} \exp\left[-\frac{(V_{\text{thr}} - u(t))^2}{2\sigma_V^2}\right] \left[-\frac{\dot{u}(t)}{\sqrt{2}\sigma_V}\right]_- \\ &= \left[\dot{u}(t)\right]_+ \frac{1}{\sqrt{2\pi}\sigma_V} \exp\left[-\frac{(V_{\text{thr}} - u(t))^2}{2\sigma_V^2}\right] . \end{aligned}$$

$P(t)$ is equivalent to the rate r defined in Eq. (4.7c) of Chapter 4.

6.3.1.3 Non-stationary extension of the Chizhov-Graham hazard

The hazard function estimated by Chizhov and Graham (2007) is based on the assumption that the membrane potential v of the LIF reference unit is distributed around its expected value u according to the stationary Gaussian distribution of fixed variance σ_V^2 (see Appendix Section 6.A). This assumption can be justified if the average interspike interval is large such that the stationary distribution is reached before the next spike is elicited.

Schwalger (2021) recently proposed a straight-forward extension of the Chizhov-Graham hazard that takes into account the non-stationarity of the membrane potential fluctuations around the mean. After the last spike at time $\hat{t}$ the membrane potential is deterministic during the absolute refractory period: $v(t) \equiv V_{\text{reset}} \quad \forall\, t \in [\hat{t}, \hat{t} + \tau_{\text{ref}}]$. When released from absolute refractoriness the membrane potentials for different noise realizations diffuse into a Gaussian distribution around the mean with a time-dependent variance $\sigma^2(t, \hat{t})$ approaching σ_V^2 exponentially:

$$\sigma^2(t, \hat{t}) = \sigma_V^2 \left(1 - \exp\left[-2\frac{t - \hat{t} - \tau_{\text{ref}}}{\tau_m}\right]\right) \Theta(t - \hat{t} - \tau_{\text{ref}}) \tag{6.9a}$$

(see also Eq. (4.46) in Chapter 4). The time-dependent variance is taken into account in the definition of the rescaled threshold

$$T(t, \hat{t}) = \frac{V_{\text{thr}} - u(t, \hat{t})}{\sqrt{2\sigma^2(t, \hat{t})}} \; . \tag{6.9b}$$

The hazard thus depends not only on the momentary membrane potential and its slope, but also directly on the time $t - \hat{t}$ since the last spike:

$$f\Big(u(t, \hat{t}), \dot{u}(t, \hat{t}), t - \hat{t}\Big) = A\Big(T(t, \hat{t})\Big) + B\Big(T(t, \hat{t}), \dot{T}(t, \hat{t})\Big). \tag{6.9c}$$

Note that, unlike the exponential hazard, the Chizhov-Graham hazards do not contain any parameters that need to be chosen arbitrarily. The firing statistics of a GIF neuron with Chizhov-Graham hazard match the LIF firing statistics much better and across a large range of input currents (Fig. 6.3). The non-stationary extension by Schwalger (2021) enhances the fit of the spike regularity (see red vs. blue CV of interspike intervals in Fig. 6.3).

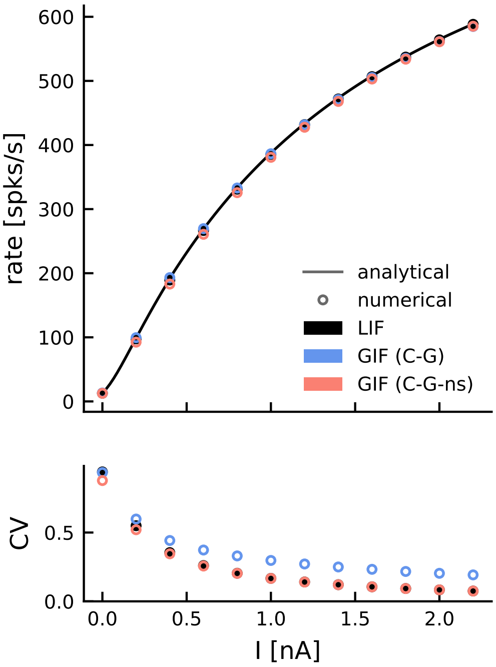

Figure 6.3: Firing properties of a GIF neuron with Chizhov-Graham hazard. Mean firing rate (top panel) and coefficient of variation of the interspike intervals (bottom panel) as a function of input current for an LIF neuron under Gaussian white noise (black), and a GIF neuron with either the original Chizhov-Graham hazard (C-G, blue), or the non-stationary extension (C-G-ns, red). Solid black line shows the analytical solution for the LIF firing rate (Eq. (6.28)). Markers are numerical estimates from spiking network simulations (LIF and GIF).

6.3.2 Dependence of the linear response on the hazard

The linear response of a single unit to weak oscillatory input largely determines the dynamics of a network of such units, when they are coupled by delayed inhibition — at least around the onset of collective oscillations (Brunel and Hakim, 1999; Lindner and Schimansky-Geier, 2001; Brunel et al., 2001; Fourcaud-Trocmé et al., 2003; Brunel and Hansel, 2006, see also Chapter 4). Since it is the goal of this chapter to approximate the oscillation dynamics of an inhibitory LIF network using a network of GIF units, it is relevant to study the linear response of GIF units and how it depends on the choice of hazard function.

The linear response of an integrate-and-fire-type neuron to weakly sinusoidal input $I(t) = I_0 + I_1 \cos(\omega t)$, $I_1 > 0$ small, can be approximated as

$$r_N(t) = r_0 + |\tilde{G}(\omega)| I_1 \cos\left(\omega t + \arg\left(\tilde{G}(\omega)\right)\right)$$

with a phase lag $\arg\left(\tilde{G}(\omega)\right) \leq 0$ and amplitude $|\tilde{G}(\omega)|$ given by the complex argument and absolute value of the susceptibility $\tilde{G}$ respectively (see also Chapter 4, Appendix Section 4.D.3).

The susceptibility of an LIF neuron under Gaussian white noise is known analytically (Lindner and Schimansky-Geier, 2001; Brunel et al., 2001, see Eq. (4.145) in Chapter 4, Appendix Section 4.D.3). The amplitude $|\tilde{G}(\omega)|$ and phase lag $\arg\left(\tilde{G}(\omega)\right)$ of the LIF linear response for a range of input frequencies ω are shown in Fig. 6.4 (black lines in Ai, Aii). The susceptibility of a GIF neuron can be derived for a general hazard $f(u, \dot{u})$ (Gerstner et al., 2014, see Appendix Section 6.C, Eq. (6.38)). For the exponential hazard the resulting closed form expression can be evaluated numerically (Eqs. (6.46), green lines in Fig. 6.4, Ai, Aii). Numerical estimates of the linear response based on a spiking network simulation (Methods Section 6.6.1) agree well with the analytical expressions — both for the LIF unit under Gaussian white noise and the GIF unit with exponential hazard (markers vs lines in Fig. 6.4A). For the more involved Chizhov-Graham hazard even a numerical evaluation of the analytical expression for the susceptibility (Eq. (6.38)) becomes a difficult task. In Fig. 6.4 I am hence just showing the numerical estimates from a spiking network simulation (blue and red markers in Fig. 6.4A).

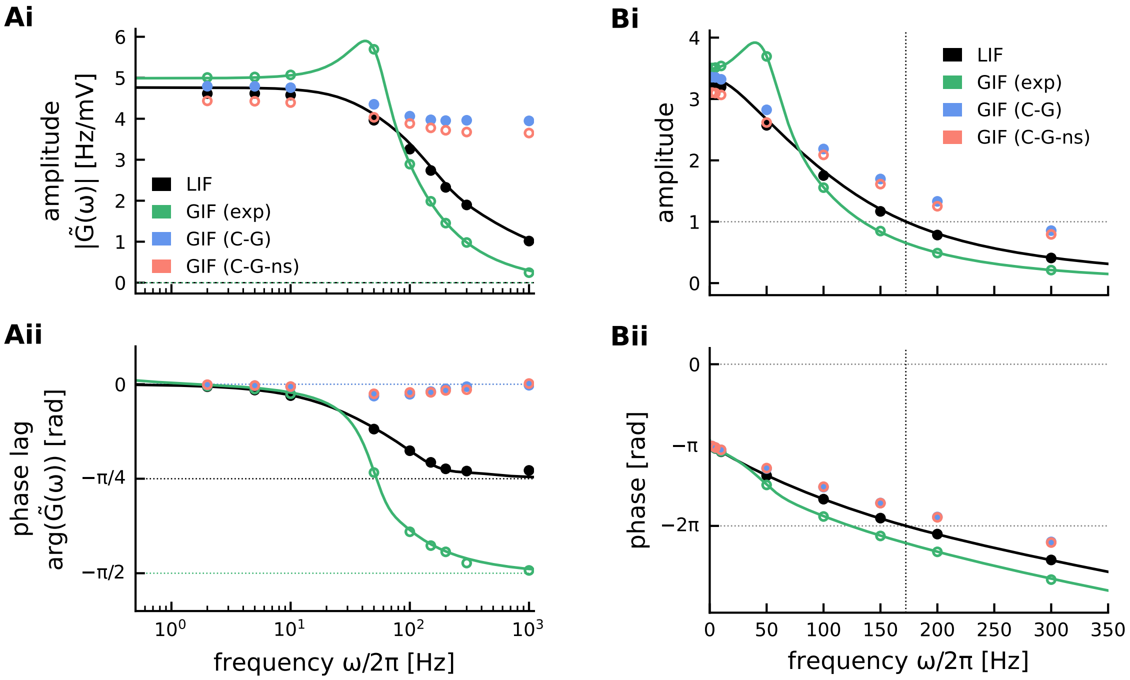

Figure 6.4: Linear response of LIF vs GIF neurons.
A, Linear response $r(t) = r_0 + |\tilde{G}(\omega)| I_1 \cos(\omega t + \arg(\tilde{G}(\omega))$ of a single neuron to sinusoidal input $I(t) = I_0 + I_1 \cos(\omega t)$ (with $(I_0 = I_0^{\text{crit}} \sim 122$ pA, Section 4.5.2.4, $I_1 = I_0/10)$. **Ai**, amplitude $|\tilde{G}(\omega)|$; **Aii**, phase lag $\arg(\tilde{G}(\omega))$. Solid lines: (semi-)analytical solutions: Eq. (4.145) for LIF, Eq. (6.46) for GIF with exponential hazard. Dots: numerical estimates (see Methods Section 6.6.1). Dotted lines: high frequency limits. **B,** Amplitude (i) and phase condition (ii) (Chapter 4, Eq. (4.36)) determining linear stability of the stationary state in a network of the respective LIF or GIF neurons, synaptically coupled via the filter $\kappa_{\Delta}^{\text{2exp}}$ (see Eqs. (6.1), (6.10)). The dotted vertical line indicates the network frequency $\omega_{\text{crit}}/2\pi = 172$ Hz of the LIF network in its mean-field bifurcation. Since the linear response was computed for the mean input level in the LIF bifurcation point, the LIF linear response satisfies both the phase condition $(\text{phase}(I_0^{\text{crit}}, \omega_{\text{crit}}) = 0 \bmod 2\pi)$ and the amplitude condition $(\text{amplitude}(I_0^{\text{crit}}, \omega_{\text{crit}}) = 1)$. The bifurcations of the GIF networks are closeby, hence the amplitude and phase conditions are almost satisfied for the GIF neurons as well.

Fig. 6.4A illustrates that the linear response changes drastically when input noise (in LIF neurons) is mapped to output noise (in GIF neurons) and that the linear response depends strongly on the choice of the hazard function. The GIF with exponential hazard has a much larger phase lag at high frequencies than the LIF unit, while the opposite is the case for the Chizhov-Graham hazard (Fig. 6.4Aii). These differences in linear response already suggest that, when connected into an inhibitory network, the "slowly reacting" GIF units with an exponential hazard will produce a slower population rhythm than LIFs, while the "fast reacting" GIFs with a Chizhov-Graham hazard produce faster oscillations.

The linear responses shown in Fig. 6.4A were calculated for an input $I(t) = I_0 + \frac{I_0}{10}\cos(\omega t)$. The drive I_0 was chosen as the analytically calculated mean drive that units in the LIF network (Eqs. (6.1)) receive in the mean-field bifurcation ($I_0 = (I_{\mathrm{ext}}^{\mathrm{crit}} - I_{\mathrm{inh}}^{\mathrm{crit}})/g_{\mathrm{leak}} = 10\,\mathrm{mV}$). Recall that the frequency of the network oscillation emerging in the bifurcation point can be estimated by solving a phase and amplitude condition derived self-consistently from the single unit linear response (see Chapter 4, Methods Section 4.5.2.4, Eq. (4.36)). Fig. 6.4B illustrates the amplitude and phase terms for the linear response at mean drive I_0. A solution of the phase and amplitude condition is found when both the amplitude and the phase term intersect with the respectively indicated horizontal lines at a common frequency ω_{crit}. The mean drive I_0 was chosen such that the phase and amplitude condition for the LIF network (black lines) have a joint solution, indicated by the vertical dotted line ($\omega_{\mathrm{crit}}/2\pi = 172$ Hz). Since the bifurcation in the GIF networks occurs at a slightly different total drive I_0, the GIF neurons do not have a joint solution for amplitude and phase condition for mean drive I_0. One can guess that the solution appears at a lower frequency for the GIF neuron with exponential hazard due to its consistently larger phase lag. Vice versa, the network of GIF neurons with the Chizhov-Graham hazard generates oscillations at a higher frequency than the LIF network due to the smaller phase lag of the single neuron response.

In the following section this prediction will be confirmed in numerical simulations of spiking networks of LIF and GIF neurons.

6.3.3 Ripple oscillations in networks of escape-noise units at microscopic level

In this section I will demonstate how the mapping from input to output noise in a single unit (*i.e.* the choice of the hazard function) influences the dynamics in a recurrently coupled network. I will compare the dynamics of the LIF reference network (Section 6.2, Eq. (6.1)) to the dynamics of a GIF network. The dynamics of the membrane potentials u_i of the GIF neurons is described by an ODE (same as Eq. (6.1) for v_i but without the noise term):

$$\dot{u}_i(t) = \frac{1}{\tau_m}(E_{\mathrm{leak}} - u_i(t)) + \frac{1}{C}\left(I_{\mathrm{ext}} - I_{\mathrm{inh}}(t)\right) \tag{6.10a}$$

$$I_{\mathrm{inh}}(t) = I_I^{\mathrm{peak}}\left(\kappa_\Delta^{\mathrm{2exp}} * \sum_{j=1}^{N_I}\sum_k \delta(t_j^k - t)\right) \tag{6.10b}$$

All parameters are set as described for the LIF reference network in Section 6.2. Spikes are fired stochastically according to a hazard function $f[u_i(t), \dot{u}_i(t)]$ (see Eq. (6.3)). When unit i fires a spike, its membrane potential is reset.

In Fig. 6.5 the GIF network dynamics are compared to the LIF reference, depending on the different hazard functions introduced in Section 6.3.1. The dynamics of the recurrently coupled network depends strongly on the choice of hazard function. As predicted by the analysis of the linear response (Section 6.3.2), the network of GIF units with exponential hazard (green, Fig. 6.5) oscillates at a much lower frequency than the LIF reference network and reaches full synchrony earlier ($I_{\text{ext}}^{\text{full}} \sim 1$ nA vs ~ 2 nA for LIF). On the other hand, the network of GIF units with the Chizhov-Graham hazard (red and blue symbols in Fig. 6.5) oscillates at higher frequencies than the LIF reference. The non-stationary extension (red symbols) leads to a better match with the LIF reference at strong drive, close to the point of full synchrony, but not in the regime of sparse synchrony (red vs blue). Nevertheless, the non-stationary Chizhov-Graham hazard yields an overall much better fit of the oscillation dynamics than the exponential hazard, capturing quite accurately both the onset of oscillations, and the point of full synchrony. In the sparse-synchrony regime inbetween, the (ir)regularity of the single unit spike trains is very similar to the LIF reference (see CV of ISIs in Fig. 6.5). Since a linear stability analysis for the complex Chizhov-Graham hazard is numerically challenging, the onset of oscillations was simply estimated here from the increase in amplitude (Fig. 6.5, bottom), and the peak in the power spectral density of the population activity (not shown).

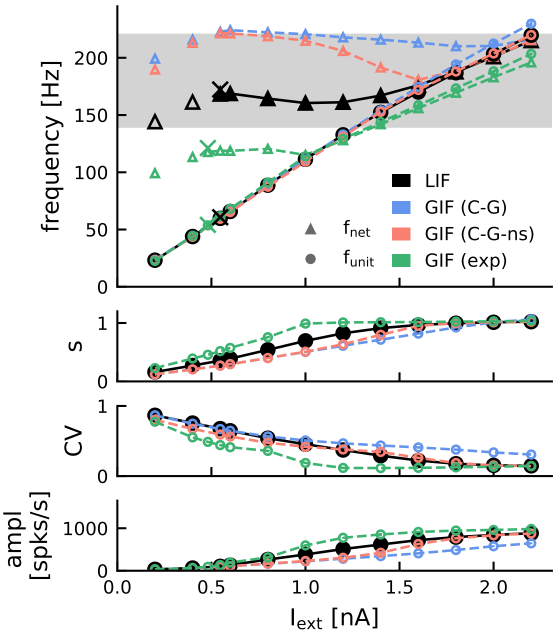

Figure 6.5: Ripple dynamics depending on hazard function. Network frequency f_{net}, mean unit firing rate f_{unit}, saturation ($s = f_{\text{unit}}/f_{\text{net}}$), average CV of interspike intervals, and average amplitude of population activity depending on drive I_{E}. Black lines: LIF network under Gaussian white noise (cf. Fig. 6.1). Colored lines: networks of GIF neurons with: exponential hazard (Eq. (6.7), $r = 409.96$ Hz, $\Delta_{\text{thr}} = 3.45$ mV, green), Chizhov-Graham hazard (Eq. (6.8), blue), or non-stationary Chizhov-Graham hazard (Eq. (6.9), red). Crosses (top): analytical estimate of bifurcation (black: LIF, green: GIF with exponential hazard).

I confirmed that fitting the parameters r and Δ_{thr} of the exponential hazard (Eq. (6.7)) to a wider range of the LIF f-I curve does not bring the dynamics of the GIF network with exponential hazard closer to the LIF dynamics (Supplementary Fig. 6.8). The bifurcation of the GIF network with exponential hazard can be determined (semi-) analytically in a linear stability analysis as described in Chapter 4, Methods Section 4.5.2.4 (using Eqs. (6.30) and (6.46) for the stationary firing rate and the susceptibility of the GIF unit respectively). The numerical simulations are in close agreement with the predicted location of the bifurcation and the respective network frequency and mean unit firing rate at oscillation onset (green crosses in Fig. 6.5, top).

6.4 Mesoscopic models of network dynamics

Schwalger et al. (2017) developed a mesoscopic ansatz that allows an efficient integration of the network activity of one or several populations of neurons, accounting for finite-size effects. I want to give here only a short account for how the mesoscopic integration of the network dynamics works. For a detailed derivation please refer to (Schwalger et al., 2017).

We start by considering the activity $A(t) = \lim_{N\to\infty} \frac{1}{N}\sum_i \sum_k \delta(t - t_i^k)$ of a population of GIF neurons i with spike times $\{t_i^k\}_{k=1,2,...}$ in the mean-field limit ($N \to \infty$, Fig. 6.6A,B). Thanks to the mapping from input to output noise discussed in Section 6.3 each neuron's firing probability at any given time t is entirely determined by its last spike time $\hat{t}$ (quasi-renewal approximation, Naud and Gerstner, 2012, see hazard function sketched in Fig. 6.6A). The state of the population can thus be completely described by the refractory density $\rho(t, \hat{t})$, *i.e.* the distribution of last spike times $\hat{t}$ of all the neurons in the network, at a given time t (Fig. 6.6B, curve above blue area). The refractory density is given by the product of the (past) population activity A and the corresponding survival probability S:

$$\rho(t, \hat{t}) = S(t, \hat{t})A(\hat{t}) \tag{6.11}$$

The refractory density is normalized:

$$\int_{-\infty}^{t} \rho(t, \hat{t}) \,\mathrm{d}\hat{t} = \int_{-\infty}^{t} S(t, \hat{t})A(\hat{t}) \,\mathrm{d}\hat{t} = 1 \ . \tag{6.12}$$

Differentiation of the normalization condition with respect to time t (and using Eq. (6.5) as well as $S(t, t) = 1$) yields an integral equation describing the network activity A:

$$A(t) = \int_{-\infty}^{t} H(t, \hat{t})\rho(\hat{t}) \,\mathrm{d}\hat{t} = \int_{-\infty}^{t} H(t, \hat{t})S(t, \hat{t})A(\hat{t}) \,\mathrm{d}\hat{t} \ . \tag{6.13}$$

This integral equation can be understood intuitively (see Fig. 6.6B): The fraction of neurons that fired a spike in a small past time bin $[\hat{t}, \hat{t} + \Delta\hat{t}]$ is approximately given by $A(\hat{t})\Delta\hat{t}$. Of these cells, a fraction $S(t, \hat{t})$ has "survived", *i.e.* not fired another spike up to the present time t. The fraction $S(t, \hat{t})A(\hat{t})\Delta\hat{t}$ of units that had their last spike time in the history bin $[\hat{t}, \hat{t} + \Delta\hat{t}]$ all have the same membrane potential at time t, and will thus fire with the same rate $H(t, \hat{t})$. The population activity at time t can thus be inferred by integrating the spike contributions $H(t, \hat{t})S(t, \hat{t})A(\hat{t})$ over the entire history of last spike times $\hat{t}$. The integral equation Eq. (6.13), together with the ODE (6.5) describing the survival probability, can be solved in an iterative scheme forward in time to infer the mean-field network activity A for arbitrary external drive.

In a *finite* network ($N < \infty$) the population activity $A_N(t) = \frac{1}{N}\sum_i \sum_k \delta(t - t_i^k)$ and survival probability S_N exhibit finite-size fluctuations due to the stochasticity of spike emission (Fig. 6.6C). Schwalger et al. (2017) assume that the total number of spikes in a time bin $[t, t + \Delta t]$ is Poisson distributed with mean $\bar{n}(t) = \bar{A}(t)N\Delta t$ where

$$\begin{aligned}\bar{A}(t) &= \int_{-\infty}^{t} H(t, \hat{t})S_N(t, \hat{t})A_N(\hat{t}) \,\mathrm{d}\hat{t} \\ &= \underbrace{\int_{-\infty}^{t} H(t, \hat{t})S(t, \hat{t})A_N(\hat{t}) \,\mathrm{d}\hat{t}}_{\text{mesoscopic}} + \underbrace{\int_{-\infty}^{t} H(t, \hat{t})\delta S(t, \hat{t})A_N(\hat{t}) \,\mathrm{d}\hat{t}}_{\text{microscopic}}\end{aligned}$$

denotes the expected population activity. Here the survival probability was split into its expected value and the microscopic fluctuations around it ($S_N(t,\hat{t}) = S(t,\hat{t}) + \delta S(t,\hat{t})$) to emphasize that the expected population activity $\bar{A}$ still depends on microscopic fluctuations. Schwalger et al. (2017) replace the microscopic terms by introducing a mesoscopic correction factor $\Lambda(t)$:

$$\begin{aligned}\bar{A}(t) &\approx \int_{-\infty}^{t} H(t,\hat{t})S(t,\hat{t})A_N(\hat{t})\,\mathrm{d}\hat{t} + \Lambda(t)\int_{-\infty}^{t} \delta S(t,\hat{t})A_N(\hat{t})\,\mathrm{d}\hat{t} \\ &= \underbrace{\int_{-\infty}^{t} H(t,\hat{t})S(t,\hat{t})A_N(\hat{t})\,\mathrm{d}\hat{t} + \Lambda(t)\left(1 - \int_{-\infty}^{t} S(t,\hat{t})A_N(\hat{t})\,\mathrm{d}\hat{t}\right)}_{\text{mesoscopic}} \; . \end{aligned} \tag{6.14}$$

In the last step the normalization condition

$$1 = \int_{-\infty}^{t} S_N(t,\hat{t})A_N(\hat{t})\,\mathrm{d}\hat{t} = \int_{-\infty}^{t} [S(t,\hat{t}) + \delta S(t,\hat{t})]A_N(\hat{t})\,\mathrm{d}\hat{t} \tag{6.15}$$

was used to eliminate the dependence on the microscopic fluctuations. The correction factor

$$\Lambda(t) = \frac{\int_{-\infty}^{t} H(t,\hat{t})v(t,\hat{t})\,\mathrm{d}\hat{t}}{\int_{-\infty}^{t} v(t,\hat{t})\,\mathrm{d}\hat{t}} \tag{6.16}$$

is found as an “effective hazard rate” accounting for the average effect of the past microscopic fluctuations in the survival probability on the present population activity. It results from a weighting of the hazard function with a “variance function” v that evolves as

$$\partial_t v(t,\hat{t}) = -2H(t,\hat{t})v + H(t,\hat{t})S(t,\hat{t})A_N(\hat{t})\,, \qquad v(\hat{t},\hat{t}) = 0 \; . \tag{6.17}$$

The variance v accounts for the magnitude of the microscopic fluctuations in the survival probability in the past (see Schwalger et al., 2017, and Fig. 6.6C).
Together, the mesoscopic Eqs. (6.14), (6.16), (6.17), (6.5) can be used to efficiently integrate the finite size population activity forward in time, without tracking the microscopic fluctuations in the activity of individual units. In every time step the activity of the finite network is inferred as

$$A_N(t) = \frac{n(t)}{N\Delta t}\,, \quad n(t) \sim \mathrm{Poi}\Big(\bar{A}N\Delta t\Big) \; . \tag{6.18}$$

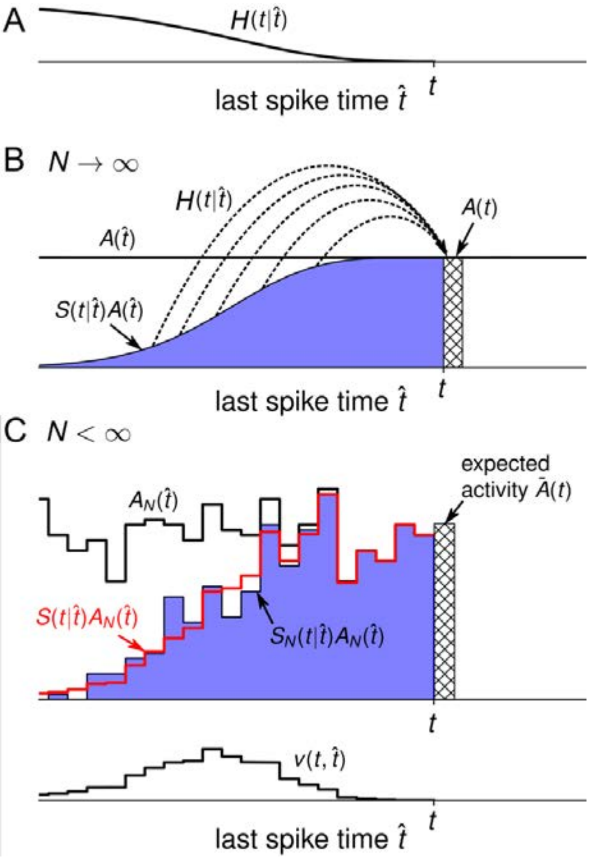
A
$H(t|\hat{t})$
last spike time $\hat{t}$
t
B $N \to \infty$
$H(t|\hat{t})$
$A(\hat{t})$
$A(t)$
$S(t|\hat{t})A(\hat{t})$
last spike time $\hat{t}$
t
C $N < \infty$
expected activity $\bar{A}(t)$
$A_N(\hat{t})$
$S(t|\hat{t})A_N(\hat{t})$
$S_N(t|\hat{t})A_N(\hat{t})$
t
$v(t,\hat{t})$
last spike time $\hat{t}$
t

Figure 6.6: Illustration of the mesoscopic integration scheme by Schwalger et al. (2017).
A, Hazard rate H as a function of last spike time $\hat{t}$, given fixed time t. **B,** Illustration of the forward integration of the population activity A using the integral equation Eq. (6.13), which is exact in the mean-field limit. **C,** Forward integration of the population activity including finite size fluctuations. Red line shows the expected refractory density based on the past, fluctuating activity A_N and the mean-field survival probability S. Blue area/black line shows the actual refractory density resulting from finite size fluctuations in the survival probability S_N. The deviations from the expected refractory density are quantified by the variance function v (bottom). Figure adapted from Schwalger et al., 2017, CC BY 4.0.

6.4.1 Ripples in networks of escape-noise units on mesocopic level

I implemented the mesoscopic model by Schwalger et al. (2017) and used it to integrate the activity of the GIF networks that were already analyzed on a microscopic level in Section 6.3.3, Fig. 6.5. In Fig. 6.7 I compare the dynamics of the GIF networks at mesoscopic level to the GIF network dynamics at microscopic level, as well as to the dynamics of the microscopic LIF reference network with Gaussian white noise input. For any choice of hazard function the mesoscopic dynamics closely matches the dynamics of the microscopic GIF network (exponential hazard: dark vs light green in Fig. 6.7A; Chizhov-Graham hazard: dark vs light blue/red in Fig. 6.7B). The difference between the mesoscopic population activity and the dynamics of the LIF network is significant, but entirely due to the imperfect mapping from input to output noise via a hazard function that has been discussed in the previous chapters.

Figure 6.7: Ripple dynamics on micro- and mesoscopic levels.
Ripples in a GIF network, simulated at micro- or mesoscopic level (light dashed, vs dark dotted lines), for the exponential hazard (**A,** green), and the Chizhov-Graham hazards (**B,** blue and red). Same panel outline as in Fig. 6.1 and Fig. 6.5. The microscopic LIF simulations (black, Fig. 6.5) are repeated here for comparison. Note that the CV of interspike intervals cannot be estimated on the mesoscopic level.

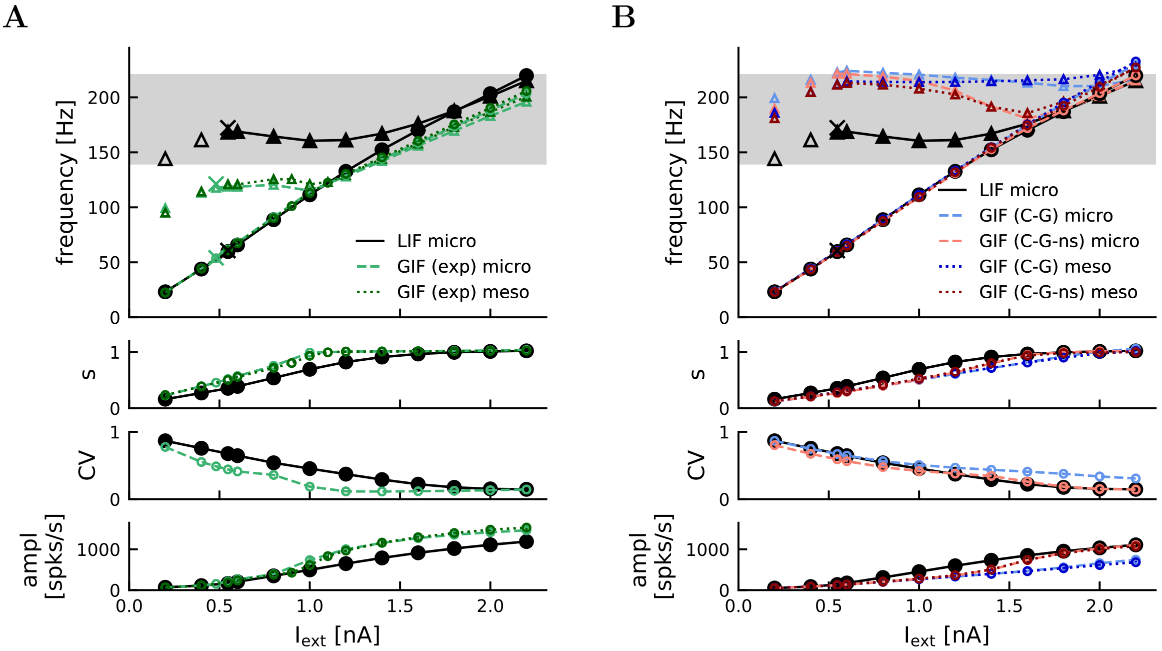

Figure 6.7: Ripple dynamics on micro- and mesoscopic levels. Caption on previous page.

6.4.2 A note on computational efficiency

In a microscopic simulation of length T_{sim} the membrane potential of N individual neurons is integrated over $T_{\mathrm{sim}}/\Delta t$ time steps, resulting in a total of $N \cdot T_{\mathrm{sim}}/\Delta t$ updates. Furthermore, in every time step N random numbers have to be drawn to model either the Gaussian white noise input, or the stochastic spiking in case of GIF neurons.

In the mesoscopic simulation, the hazard rate needs to be computed as a function of last spike time (see Fig. 6.6A), which requires knowledge of the membrane potential depending on last spike time. It is sufficient to track a finite history of potential last spike times of length T_{hist}. For each potential last spike time $\hat{t} \in [t - T_{\mathrm{hist}}, t]$, a representative membrane potential is integrated in every time step. I used a history buffer of $T_{\mathrm{hist}} = 50$ ms. In the above ripple oscillation regimes (Fig. 6.7), where units spike at a mean rate of ∼20 Hz or more, it is a reasonable assumption that 50 ms after its last spike time, a unit's membrane potential is no longer affected by that last reset event[3]. The membrane potential of units with last spike times further in the past ($\hat{t} < t - T_{\mathrm{hist}}$) are assumed to follow the *free* membrane potential, which is also updated iteratively. Thus, in every time step, $1 + T_{\mathrm{hist}}/\Delta t$ updates are computed, resulting in a total of $(1 + T_{\mathrm{hist}}/\Delta t) \cdot T_{\mathrm{sim}}/\Delta t$ updates. The mesoscopic integration scheme allows for a larger numerical time step, which can speed up simulation time, especially in combination with a short history buffer. For small networks however, in a dynamical regime that requires keeping track of a long history buffer, the mesoscopic scheme may not be much faster than the microscopic integration. A general advantage of the mesoscopic scheme comes from the fact that only one random number (not N) has to be drawn per time step, in order to determine the population activity in the next time step.

---

[3] I confirmed that the mesoscopic simulation results do not change if I increase the length of the history buffer.

For a simulation of ripple oscillations in a single network, the increase in efficiency due to the mesoscopic integration scheme is limited. Since ripples are fast and governed by short time constants ($\tau_r = 0.45$ ms in Fig. 6.7), the mesoscopic integration time step cannot be chosen as large as in other use cases. In fact I had to use a time step as small as $\Delta t = 0.1$ ms in the mesoscopic simulation with exponential hazard shown in Fig. 6.7A, in order to achieve a good match between meso- and microscopic dynamics of the GIF network. Efficiency can be increased by decreasing the length of the history buffer, and will be more prominent in larger scale simulations involving several populations.

6.5 Discussion

In this chapter I investigated the applicability of a recently proposed mesoscopic integration scheme (Schwalger et al., 2017) for the efficient simulation of ripple oscillation dynamics in a recurrent inhibitory network. The mesoscopic theory is based on a refractory density approach and thus requires a microscopic reference network of homogeneous units with membrane potentials uniquely determined by the last spike time. Applying the mesoscopic theory to the bifurcation-based ripple model discussed in Chapter 4 thus requires an initial mapping from Gaussian white noise input to escape noise, mediated by a hazard function. I showed that the choice of this hazard function can affect the network dynamics significantly.

My results can be taken as a note of caution regarding modeling the effect of noisy input by a phenomenological hazard function. The performance of hazard functions as a mapping from input to output noise is often assessed in simulations of uncoupled populations receiving feedforward input (Plesser and Gerstner, 2000; Chizhov and Graham, 2007). Here I demonstrate that the dynamics of recurrently coupled networks can be strongly altered when noisy input is replaced by stochastic output.

The exponential hazard is already challenged by approximating the mean firing rate of an uncoupled unit over a larger range of drives. With parameters fitted to match the mean firing rate of an LIF unit under Gaussian white noise, a GIF unit with an exponential hazard can approximate the mean firing rate of an LIF unit in a limited regime, but produces spike trains that are more regular than the LIF reference (lower CV of ISIs in Fig. 6.2).

The Chizhov-Graham hazard performs much better and can closely approximate both the mean rate and the regularity of the spike train of an uncoupled unit under constant drive (Fig. 6.3). Importantly, the Chizhov-Graham hazard can be entirely derived from the reference LIF model and requires no arbitrary parameter choices.

Nevertheless, neither of the two hazards provides an accurate approximation of the ripple oscillation dynamics in a recurrently coupled network of LIF neurons with noisy input: A GIF network with exponential hazard oscillates at much lower frequencies and reaches full synchrony earlier. A GIF network with Chizhov-Graham hazard fits the LIF dynamics qualitatively, but oscillates at higher frequencies. This is due to differences in the linear response of a single GIF neuron, depending on its hazard. We have seen that the high frequency limit of the neuronal phase lag changes drastically when input noise is replaced by output noise (0 for Chizhov-Graham hazard, $-\pi/2$ for exponential hazard, instead of $-\pi/4$ for LIF reference model). I outlined in Chapter 4 how the single neuron linear response determines the oscillation frequency in a recurrent network (Methods Section 4.5.2.4). Of course we cannot draw precise conclusions based only on the high frequency limit. For high noise however, we could assume that the phase lag decreases rather smoothly from 0 towards the respective high frequency limit. In this case, the neuronal phase lag would be consistently larger for GIF neurons with exponential hazard than for LIF neurons under white noise, even for input signals of finite frequency. That explains the onset of network oscillations at a lower frequency than in the LIF network. Vice versa, networks of GIF neurons with Chizhov-Graham hazard, that respond to oscillatory input with a much shorter phase lag, can oscillate at higher frequencies than LIF networks.

It is not surprising that the network dynamics are affected by a switch from input to output noise. Neither of the hazard functions preserves the first passage time density of an LIF neuron under Gaussian white noise perfectly. The exponential hazard is purely phenomenological. The Chizhov-Graham hazard is based on exact derivations of the FPT density in the two limiting cases of constant or infinitely fast changing input, but makes an approximation by assuming that the hazards of the two limiting cases can simply be added to account for the spiking activity under arbitrary time-dependent input. Recently, a novel hazard function was proposed, based on a level-crossing approach, taking into account correlations of interspike intervals under colored noise input Schwalger (2021). It would be interesting to compare its performance in approximating ripple oscillations under Gaussian noise with the hazards studied here.

It is worth noting that, despite the quantitative differences in oscillation frequency w.r.t. the LIF reference, the GIF network with Chizhov-Graham hazard *can* account for ripple oscillations, including a transition from sparse to full synchrony, and IFA (not shown here), at micro- and mesoscopic level. If the goal is to model ripple oscillations efficiently, and phenomenologically, this can be achieved with the Chizhov-Graham hazard. The oscillation frequency can easily be tuned by adjusting the synaptic time constants. It is interesting that a population level description of fast ripple oscillations, with a large regime of sparse synchrony, requires a hazard function that takes into account the slope with which the membrane potential approaches the threshold (such as the Chizhov-Graham hazard). This finding is in line with the mean-field approximations in Chapter 4, which captured ripple dynamics in an approximation of the drift-based population activity, that also depends on the speed with which the mean membrane potential approaches the spike threshold (see comment in Section 6.3.1.2). The analytical expression for the susceptibility of a GIF unit with arbitrary hazard (Eq. (6.38), Gerstner et al., 2014) should allow a systematic analysis of the neuronal phase lag depending on whether or not a given hazard function contains a dependence of the slope (see function $\beta = \partial f / \partial \dot{U}$ in Eq. (6.37)). In future work, I would like to derive an analytical approximation of the GIF neuronal phase lag in the limit of high frequencies, in order to substantiate the numerical observation shown here, that hazard functions with slope-dependence provide a more accurate approximation of the oscillation dynamics in recurrent networks under noisy input.

6.6 Methods

6.6.1 Numerical estimate of linear response

To estimate the linear response of a neuron model numerically, an uncoupled population of N identical units is stimulated with a weak sinusoidal current $I(t) = I_0 + I_1 \cos(\omega t)$ where $I_1 > 0$ is small. The linear response is expected to be sinusoidal as well:

$$r_N(t) = r_0 + |\tilde{G}(\omega)| I_1 \cos\left(\omega t + \arg\left(\tilde{G}(\omega)\right)\right)$$

with a phase lag $\arg\left(\tilde{G}(\omega)\right)$ and an amplitude modulation $|\tilde{G}(\omega)|$ corresponding to the complex argument and the absolute value of the susceptibility $\tilde{G}$, respectively. Recall that the Fourier transform of a cosine $s(t) = a\cos(\omega t + \phi)$ is given by

$$\tilde{s}(\Omega) = \frac{a}{2}\, \mathrm{e}^{i\phi}\, \delta(\Omega - \omega) + \text{c.c.}$$

The phase lag and the amplitude modulation of the population activity $r_N(t)$ can thus be estimated by taking the Fourier transform (after subtracting the mean r_0) at the input-frequency ω:

$$\begin{aligned} \arg\left(\tilde{G}(\omega)\right) &= \arg\left(\tilde{r}_N(\omega)\right) \\ |\tilde{G}(\omega)| &= 2\left|\tilde{r}_N(\omega)\right| / I_1 \ . \end{aligned}$$

(see markers in Fig. 6.4).

6.A Derivation of Chizhov-Graham hazard

Consider an LIF neuron under Gaussian white noise:

$$\dot{v}(t) = \frac{1}{\tau_m}(E_{\text{leak}} - v(t)) + \frac{1}{C} I(t) + \sqrt{\frac{2}{\tau_m}} \sigma_V \xi(t) \tag{6.19}$$

For a given initial membrane potential $v(0) < V_{\text{thr}}$ and a realization of the Gaussian white noise ξ one can integrate the SDE Eq. (6.19) and determine the neuron's first spike time, *i.e.* the time when v reaches the threshold V_{thr}. Repeating this process for infinitely many noise realizations yields the first-passage-time density $P(t)$. In the mean-field limit of infinitely many noise realizations (or an infinitely large population of identical, uncoupled neurons) the dynamics of the probability density of membrane potentials $p(v,t)$ is described by a Fokker-Planck equation

$$\partial_t p(v,t) = \underbrace{-\partial_v \left(\frac{1}{\tau_m}\Big(E_{\text{leak}} + \frac{\tau_m}{C} I(t) - v\Big) p(v,t)\right)}_{\text{drift}} + \underbrace{\frac{\sigma_V^2}{\tau_m} \partial_v^2 p(v,t)}_{\text{diffusion}} = -\partial_v J(v,t) \tag{6.20}$$

with boundary conditions $\lim_{v\to-\infty} p(v,t) = p(V_{\mathrm{thr}},t) = 0\,\forall t$. The membrane potentials can cross the threshold either due to the drift set by the input $I(t)$ or due to noise-induced diffusion. When a unit's membrane potential crosses the threshold, the unit is taken out of the population. Hence there is an absorbing boundary condition at threshold and the integral over the (pseudo-)density p decreases over time:

$$S(t) = \int_{-\infty}^{V_{\mathrm{thr}}} p(v,t)\,\mathrm{d}v \begin{cases} = 1\,, & t = 0 \\ < 1\,, & t > 0 \end{cases}$$

It is denoted as S, since it represents the survival probability, *i.e.* the probability of a unit *not* having crossed the threshold up to time t. The probability current through the threshold corresponds to the first-passage-time density and is often denoted as a rate

$$P(t) = r(t) = J(V_{\mathrm{thr}},t) = -\frac{\sigma_V^2}{\tau_m}\frac{\partial p}{\partial v}\bigg|_{v=V_{\mathrm{thr}}} .$$

Note the time-dependence in the drift-term of the FPE Eq. (6.20) due to the time-dependent input. This problem can be reformulated as an FPE with moving absorbing boundary:

Consider the dynamics of the fluctuations $x(t) := (v(t)-u(t))/\sqrt{2}\sigma_V$ of the membrane potential v around its expected value u, relative to the noise level. The mean membrane potential evolves according to the ODE $\dot{u} = (E_{\mathrm{leak}} - u)/\tau_m + I(t)/C$, hence the fluctuations are described by a simple Langevin Equation:

$$\tau_m \dot{x} = -x + \sqrt{2\tau_m}\sigma_V \xi(t) .$$

The dynamics of the probability density $\tilde{\rho}(x,t)$ is described by the FPE

$$\partial_t \tilde{\rho} = -\partial_x \frac{1}{\tau_m}\left(-x\tilde{\rho} - \frac{1}{2}\partial_x \tilde{\rho}\right) = -\partial_x J(x,t) \tag{6.21}$$

with boundary conditions $\lim_{x\to-\infty} \tilde{\rho}(x,t) = \tilde{\rho}(T(t),t) = 0\,\forall t$. Note that the drift-term is now independent of time. Instead the absorbing boundary moves, since the rescaled threshold for the fluctuations is time-dependent:

$$T(t) = \frac{V_{\mathrm{thr}} - u(t)}{\sqrt{2}\sigma_V} \tag{6.22}$$

The rate/FPT density and survival probability are redefined as

$$P(t) = J(T(t),t) = -\frac{1}{2\tau_m}\frac{\partial \tilde{\rho}}{\partial x}\bigg|_{x=T(t)} \tag{6.23}$$

$$\text{and} \quad S(t) = \int_{-\infty}^{T(t)} \tilde{\rho}(x,t)\,\mathrm{d}x$$

respectively. Rescaling $\tilde{\rho}$ by the survival probability yields a probability density

$$p(x,t) := \frac{\tilde{\rho}(x,t)}{S(t)} \tag{6.24}$$

that is normalized at all times. Chizhov and Graham (2007) refer to p as the *shape* of the probability density $\tilde{\rho}$. The FPE for p is derived from Eq. (6.21) and has an additional source term, proportional to the hazard $H(t)$, ensuring the normalization:

$$\partial_t p(x,t) + \partial_x \frac{1}{\tau_m}\left(-xp(x,t) - \frac{1}{2}\partial_x p(x,t)\right) = -\frac{\dot{S}(t)}{S(t)} p(x,t) \overset{(6.5)}{=} H(t)p(x,t) \qquad (6.25)$$

Note that

$$H(t) = \frac{P(t)}{S(t)} \overset{(6.23)}{=} -\frac{1}{2\tau_m}\frac{1}{S(t)}\frac{\partial\tilde{\rho}}{\partial x}\bigg|_{x=T(t)} \overset{(6.24)}{=} -\frac{1}{2\tau_m}\frac{\partial p}{\partial x}\bigg|_{x=T(t)}$$

i.e. p is the only unknown in the above PDE and the hazard could be infered from the solution p.

Solving this FPE with moving boundary exactly is difficult (Bulsara et al., 1996; Schindler et al., 2004; Lindner, 2004). Instead Chizhov and Graham (2007) solved the problem in two limiting cases.

6.A.1 Subthreshold regime ($H = A$)

If the neuron receives subthreshold input, the distance T between mean membrane potential and threshold, relative to the noise, changes only slowly. In the limit case $T(t) \equiv T$, the shape p of the distribution $\tilde{\rho}(x,t)$ remains constant and a rate $P(t)$ is produced solely due to diffusion-mediated flux through the threshold. The stationary solution $p_0(x)$ of the FPE Eq. (6.25) can be found analytically and expressed in terms of confluent hypergeometric functions. Chizhov and Graham (2008) approximated the lengthy analytical expression for the resulting hazard as

$$A(T) = -\frac{1}{2\tau_m}\frac{\partial p_0}{\partial x}\bigg|_{x=T(t)} \approx \frac{1}{\tau_m}\exp(6.1\cdot 10^{-3} - 1.12T - 0.257T^2 - 0.072T^3 - 0.0117T^4)\ .$$

6.A.2 Subthreshold regime ($H = B$)

If the input is strongly superthreshold, the mean membrane potential rises towards the threshold fast. The concurrent change in the shape of the fluctuations around this fast changing mean due to noise is negligible. In the rescaled system this corresponds to a sudden drop of the threshold T towards the distribution $\tilde{\rho}(x,0)$. The survival probability can be directly inferred as the portion of the initial distribution $\tilde{\rho}(x,0)$ that remains subthreshold:

$$S(t) = \int_{-\infty}^{T(t)} \tilde{\rho}(x,0)\,\mathrm{d}x$$

Chizhov and Graham (2007) assume as intitial condition the stationary (Gaussian) solution of the FPE Eq. (6.21) without the absorbing boundary condition:

$$\tilde{\rho}(x,0) = \frac{1}{\sqrt{\pi}}\exp\left[-x^2\right] \qquad (6.26)$$

This implies the assumption that the average interspike interval is long enough such that the fluctuations x of the membrane potentials around the average trajectory have reached their stationary, Gaussian distribution before the next spike is elicited. This assumption has been relaxed in the non-stationary extension by Schwalger (2021). Under the stationary assumption the survival probability is given by

$$S(t) = \int_{-\infty}^{T(t)} \tilde{\rho}(x,0)\,\mathrm{d}x \overset{(6.26)}{=} \frac{1}{2}\Big(1 + \mathrm{erf}\,[T(t)]\Big) \tag{6.27}$$

and the hazard can be inferred directly as

$$B \overset{(6.5)}{=} -\frac{1}{S}\frac{dS}{dt} = -\frac{2}{\sqrt{\pi}}\frac{\exp(-T^2)}{1+\mathrm{erf}(T)}\frac{dT}{dt}$$

Note that an upwards movement of the mean membrane potential u towards the threshold V_{thr} corresponds to a downwards movement of the rescaled threshold $T(t)$ (Eq. (6.22)). Since only upwards-crossings of the threshold ($\dot{T} < 0$) should contribute to the rate, a sign dependence $[X]_- := (X - |X|)/2$ is added:

$$B(T,\dot{T}) = -\frac{2}{\sqrt{\pi}}\frac{\exp(-T(t)^2)}{1+\mathrm{erf}(T(t))}\left[\frac{dT}{dt}\right]_-$$

This hazard function was also derived by Goedeke and Diesmann (2008).

6.B f-I curves

6.B.1 f-I curve for LIF units

Consider an LIF unit with membrane potential V described by the SDE

$$\tau_m \dot{V}(t) = -V(t) + I + \sqrt{2D\tau_m}\xi(t)$$

with membrane time constant τ_m and Gaussian white noise ξ with $\langle\xi\rangle = 0$, $\langle\xi(t)\xi(t')\rangle = \delta(t-t')$ and intensity D. The neuron fires a spike whenever V reaches a threshold V_T. It is then reset to a reset potential V_R where it remains for an absolute refractory period τ_{ref}. The firing rate in response to constant drive I is given by

$$r(I) = \left(\sqrt{\pi}\tau_m \int_{\frac{I-V_T}{\sqrt{2D}}}^{\frac{I-V_R}{\sqrt{2D}}} \mathrm{e}^{x^2}\,\mathrm{erfc}(x)\,\mathrm{d}x + \tau_{\mathrm{ref}}\right)^{-1} \tag{6.28}$$

(Holden, 1976, see also Chapter 4, Appendix Section 4.D.1.2).

6.B.2 f-I curve for GIF neurons

Consider a GIF unit with membrane potential U described by the ODE

$$\tau_m \dot{U}(t) = -U(t) + I$$

with membrane time constant τ_m, that fires stochastically according to a hazard function

$$H(t,\hat{t}) = f(U,\dot{U})\Theta(t-\hat{t}-\tau_{\text{ref}})$$

and is reset to V_R after each spike. Its mean firing rate is given by

$$r_0 = \frac{1}{\langle P_0(\tau)\rangle} = \frac{1}{\int_0^\infty S_0(\tau)\,\mathrm{d}\tau} \tag{6.29}$$

where $P_0(\tau) = H_0(\tau)S_0(\tau)$ denotes the stationary interval distribution ($\tau = t-\hat{t}$: age, time since last spike). This can be easily seen via integration of parts in the normalization condition, using that $\dot{S}_0 = -H_0S_0 = -P_0$:

$$1 = r_0\int_0^\infty S_0(\tau)\,\mathrm{d}\tau = r_0\Big(\underbrace{[sS_0(s)]_0^\infty}_{=0} + \int_0^\infty sP_0(s)ds\Big) = r_0\langle P_0(t)\rangle$$

6.B.2.1 f-I curve for a GIF neuron with exponential hazard

Consider as an example the exponential hazard function

$$f(U) = r\exp\left(\frac{U-V_T}{\Delta}\right)\,.$$

Under constant input I the trajectory of the membrane potential at time $\tau = t-\hat{t} \geq 0$ is given by

$$U_0(\tau) = I-(I-V_R)\exp\left[-\frac{\tau}{\tau_m}\Theta(\tau)\right]\,.$$

Hence the hazard H_0 and survival probability S_0 evolve over time as:

$$\begin{aligned} H_0(\tau) &= f(U_0(\tau))\Theta(\tau) = r\exp\left(\frac{U_0(\tau)-V_T}{\Delta}\right)\Theta(\tau) \\ &= r\exp\left(\frac{I-(I-V_R)\exp\left[-\frac{\tau}{\tau_m}\Theta(\tau)\right]-V_T}{\Delta}\right)\Theta(\tau) \\ S_0(\tau) &= \exp\left[-\int_0^\tau H_0(s)\,\mathrm{d}s\Theta(\tau)\right] \end{aligned}$$

The firing rate can be computed as:

$$\begin{aligned} r_0(I) &\overset{(6.29)}{=} \left(\int_0^\infty S_0(\tau)\,\mathrm{d}\tau\right)^{-1} = \left(\int_0^\infty \exp\left[-\int_0^\tau H(s)\,\mathrm{d}s\right]\mathrm{d}\tau\right)^{-1} \\ &= \left(\int_0^\infty \exp\left[-\int_0^\tau r\exp\left(\frac{I-(I-V_R)\exp\left[-\frac{s}{\tau_m}\right]-V_T}{\Delta}\right)\mathrm{d}s\right]\mathrm{d}\tau\right)^{-1} \end{aligned} \tag{6.30}$$

6.C Susceptibility for GIF units

Consider a GIF neuron with membrane potential U that is uniquely determined by the unit's last spike time $\hat{t}$ and the current time t:

$$\tau_m \partial_t U(t,\hat{t}) = -U(t,\hat{t}) + I(t)\,, \qquad U(\hat{t},\hat{t}) = V_R \tag{6.31}$$

The GIF unit fires spikes stochastically according to a hazard rate

$$H(t,\hat{t}) = f\Big(U(t), \dot{U}(t)\Big)\Theta(t-\hat{t}-\tau_{\mathrm{ref}})$$

with an arbitrary hazard function $f(U,\dot{U})$, that may depend on the momentary membrane potential U, and/or on its slope $\dot{U}$. After each spike the membrane potential is reset to V_R, where it remains for an absolute refractory period of τ_{ref}. The linear response of the GIF unit to a weak perturbation

$$I(t) = I_0 + \epsilon I_1(t)$$

is given by convolution with the linear response function G:

$$A(t) = (G * I)(t) = A_0 + \epsilon \int_0^\infty G(s) I_1(t-s)\,\mathrm{d}s =: A_0 + \epsilon A_1(t)\ . \tag{6.32}$$

(The stationary firing rate A_0 is given by Eq. (6.29).)
Fourier transformation on both sides yields

$$\tilde{A}(\omega) = \epsilon \tilde{A}_1(\omega) = \epsilon \tilde{G}(\omega) \cdot \tilde{I}_1(\omega) \tag{6.33}$$

In the following I will derive the Fourier transform of the linear response function, or *susceptibility*, $\tilde{G}(\omega)$ starting from the integral equation Eq. (6.14) as described in (Gerstner, 2000; Gerstner et al., 2014, Chapter 14). Alternatively it can also be derived starting from the continuity equation for the refractory density.
Recall the normalization condition of the refractory density:

$$1 = \int_{-\infty}^{t} S(t,\hat{t})A(\hat{t})\,\mathrm{d}\hat{t} = \int_{-\infty}^{t-\tau_{\mathrm{ref}}} S(t,\hat{t})A(\hat{t})\,\mathrm{d}\hat{t} + \int_{t-\tau_{\mathrm{ref}}}^{t} A(\hat{t})\,\mathrm{d}\hat{t}\ ,$$

The second equality holds because the survival probability is one during the absolute refractory period: $S(t,\hat{t}) = 1 \quad \forall\, \hat{t} \in [t-\tau_{\mathrm{ref}}, t]$.
Taking the derivative w.r.t. time on both sides yields:

$$0 = \frac{\mathrm{d}}{\mathrm{d}t} \int_{-\infty}^{t-\tau_{\mathrm{ref}}} S(t,\hat{t})A(\hat{t})\,\mathrm{d}\hat{t} + A(t) - A(t-\tau_{\mathrm{ref}}) \tag{6.34}$$

The hazard and survival probability can be expanded linearly in ϵ as:

$$\begin{aligned} H(t) &= H_0(t-\hat{t}) + \epsilon H_1(t,\hat{t}) \\ S(t) &= S_0(t-\hat{t}) + \epsilon S_1(t,\hat{t}) \end{aligned} \tag{6.35}$$

For constant drive I_0, the hazard H_0 and survival probability S_0 depend only on the neuron's *age*, *i.e.* the time $\tau := t - \hat{t}$ since its last spike, which uniquely determines the membrane potential:

$$
\begin{aligned}
U_0(\tau) &= I_0 - (I_0 - V_R)\exp\left[-\frac{\tau - \tau_\mathrm{ref}}{\tau_m}\Theta(\tau - \tau_\mathrm{ref})\right] \\
H_0(\tau) &= f\left(U_0(\tau), \dot{U}_0(\tau)\right)\Theta(\tau - \tau_\mathrm{ref}) \\
S_0(\tau) &= \exp\left[-\int_0^\tau H_0(s)\,\mathrm{d}s\right] = \exp\left[-\int_{\tau_\mathrm{ref}}^\tau f\left(U_0(s), \dot{U}_0(s)\right)\mathrm{d}s\;\Theta(\tau - \tau_\mathrm{ref})\right]
\end{aligned}
$$

Inserting the linear expansions Eqs. (6.32), (6.35) in Eq. (6.34) yields:

$$
\begin{aligned}
0 = &\underbrace{\frac{\mathrm{d}}{\mathrm{dt}}A_0\int_{-\infty}^{t-\tau_\mathrm{ref}} S_0(t-\hat{t})\,\mathrm{d}\hat{t}}_{=\frac{\mathrm{d}}{\mathrm{dt}}(1 - A_0\tau_\mathrm{ref}) = 0} + \epsilon\frac{\mathrm{d}}{\mathrm{dt}}\int_{-\infty}^{t-\tau_\mathrm{ref}} S_0(t-\hat{t})A_1(\hat{t})\,\mathrm{d}\hat{t} + \epsilon A_0\frac{\mathrm{d}}{\mathrm{dt}}\left[\int_{-\infty}^{t-\tau_\mathrm{ref}} S_1(t,\hat{t})\ \mathrm{d}\hat{t}\right] \\
&\underbrace{+\,\epsilon^2\frac{\mathrm{d}}{\mathrm{dt}}\left[\int_{-\infty}^{t-\tau_\mathrm{ref}} S_1(t,\hat{t})A_1(\hat{t})\ \mathrm{d}\hat{t}\right]}_{\sim\mathcal{O}(\epsilon^2)} + \epsilon(A_1(t) - A_1(t - \tau_\mathrm{ref}))
\end{aligned}
$$

$$
\Leftrightarrow \quad 0 = \frac{\mathrm{d}}{\mathrm{dt}}\int_{-\infty}^{t-\tau_\mathrm{ref}} S_0(t-\hat{t})A_1(\hat{t})\,\mathrm{d}\hat{t} + A_0\frac{\mathrm{d}}{\mathrm{dt}}\left[\int_{-\infty}^{t-\tau_\mathrm{ref}} S_1(t,\hat{t})\ \mathrm{d}\hat{t}\right] + A_1(t) - A_1(t - \tau_\mathrm{ref})
$$

Using: $\partial_w \int_{a(w)}^{b(w)} f(x,w)\,\mathrm{d}x = \int_{a(w)}^{b(w)} \partial_w f(x,w)\,\mathrm{d}x + f(b(w),w)\frac{\mathrm{d}}{\mathrm{dw}}b(w) - f(a(w),w)\frac{\mathrm{d}}{\mathrm{dw}}a(w)$ yields

$$
\begin{aligned}
\Leftrightarrow \quad 0 = &\int_{-\infty}^{t-\tau_\mathrm{ref}} \underbrace{\frac{\mathrm{d}}{\mathrm{dt}}S_0(t-\hat{t})}_{=-P_0(t-\hat{t})} A_1(\hat{t})\,\mathrm{d}\hat{t} + \underbrace{S_0(\tau_\mathrm{ref})}_{=1} A_1(t - \tau_\mathrm{ref}) + A_0\frac{\mathrm{d}}{\mathrm{dt}}\left[\int_{-\infty}^{t-\tau_\mathrm{ref}} S_1(t,\hat{t})\ \mathrm{d}\hat{t}\right] \\
&+ A_1(t) - A_1(t - \tau_\mathrm{ref})
\end{aligned}
$$

Rearranging the terms yields a self-consistent integral equation for the first order modulation A_1 of the population activity:

$$
A_1(t) = \int_{-\infty}^{t-\tau_\mathrm{ref}} P_0(t-\hat{t})A_1(\hat{t})\,\mathrm{d}\hat{t} - A_0\frac{\mathrm{d}}{\mathrm{dt}}\left[\int_{-\infty}^{t-\tau_\mathrm{ref}} S_1(t,\hat{t})\ \mathrm{d}\hat{t}\right]
$$

The second integral can be rewritten as a convolution of the current I_1 with a kernel $\mathcal{L}$ (see Section 6.C.1):

$$
A_1(t) \overset{(6.41)}{=} \int_{-\infty}^{t-\tau_\mathrm{ref}} P_0(t-\hat{t})A_1(\hat{t})\,\mathrm{d}\hat{t} + A_0\frac{\mathrm{d}}{\mathrm{dt}}\left[\int_{-\infty}^{\infty} \mathcal{L}(x)I_1(t-x)\ \mathrm{d}x\right] \tag{6.36}
$$

where

$$
\begin{aligned}
\mathcal{L}(x) &= -\Theta(x)\int_{\tau_\mathrm{ref}}^\infty \chi(x+y,y)\,\mathrm{d}y \qquad (6.37) \\
\chi(t,s) &= -\frac{1}{\tau_m}S_0(t)\left[\int_s^t \left(\alpha(x) - \frac{1}{\tau_m}\beta(x)\right)\exp\left[-\frac{x-s}{\tau_m}\right]\mathrm{d}x + \beta(s)\right] \\
\alpha(t) &= \left.\frac{\partial f}{\partial U}\right|_{(U_0(t),\dot{U}_0(t))}, \qquad \beta(t) = \left.\frac{\partial f}{\partial \dot{U}}\right|_{(U_0(t),\dot{U}_0(t))}
\end{aligned}
$$

Taking the Fourier transform on both sides of Eq. (6.36) yields:

$$\begin{aligned} &\tilde{A}_1(\omega) = \tilde{P}_0(\omega)\tilde{A}_1(\omega) + A_0 i\omega\tilde{\mathcal{L}}(\omega)\tilde{I}_1(\omega) \\ \Leftrightarrow\quad &\tilde{A}_1(\omega) = \frac{i\omega A_0\tilde{\mathcal{L}}(\omega)}{1-\tilde{P}_0(\omega)}\tilde{I}_1(\omega) \end{aligned}$$

By comparison with Eq. (6.33) the susceptibility is inferred as:

$$\boxed{\tilde{G}(\omega) = \frac{i\omega A_0\tilde{\mathcal{L}}(\omega)}{1-\tilde{P}_0(\omega)}} \tag{6.38}$$

6.C.1 Derivation of kernel $\mathcal{L}$

Here I derive the kernel $\mathcal{L}$ used above. Auxiliary calculations are listed in 6.C.1.1 and will be referenced where needed.

The survival probability can be thought of as a functional on the set of all possible input potentials $I(x)$:

$$S : I(x) \mapsto S_{I(x)}(t, \hat{t})$$

We define a current pulse at time s as:

$$I_\delta(s) : x \mapsto \delta(x-s)$$

The functional derivative of the survival probability w.r.t. a delta-pulse of small amplitude $\epsilon > 0$, delivered at time s, in addition to a constant input I_0, is given by:

$$\left.\frac{\delta S(t,\hat{t})}{\delta I_\delta(s)}\right|_{I_0} = \lim_{\epsilon\to 0}\frac{1}{\epsilon}\left(S_{I_0+\epsilon I_\delta(s)}(t,\hat{t}) - S_0(t,\hat{t})\right)$$

where $S_0(t,\hat{t})$ $(= S_0(t-\hat{t})$ in notation above) refers to the survival probability of a unit receiving only constant input I_0 and $S_{I_0+\epsilon I_\delta(s)}(t,\hat{t})$ refers to the survival probability of a unit receiving the additional, weak delta-pulse at time s.

The first order term of the linear expansion of the survival probability (Eq. (6.35)) can then be written as

$$\begin{aligned} S_1(t,\hat{t}) &= \int_{\hat{t}+\tau_{\text{ref}}}^{t} \left.\frac{\delta S(t,\hat{t})}{\delta I_\delta(s)}\right|_{I_0} I_1(s)\,\mathrm{d}s = \int_{\hat{t}+\tau_{\text{ref}}}^{t} \left.\frac{\delta S(t-\hat{t},0)}{\delta I_\delta(s-\hat{t})}\right|_{I_0} I_1(s)\,\mathrm{d}s \\ &= \int_{\hat{t}+\tau_{\text{ref}}}^{t} \chi(t-\hat{t}, s-\hat{t}) I_1(s)\,\mathrm{d}s \end{aligned} \tag{6.39}$$

for

$$\chi(t,s) := \left.\frac{\delta S(t,0)}{\delta I_\delta(s)}\right|_{I_0} = \lim_{\epsilon\to 0}\frac{1}{\epsilon}\left(S_{I_0+\epsilon I_\delta(s)}(t,0) - S_0(t,0)\right)$$

Linear expansion of the disturbed survival probability ((6.45)) yields

$$\begin{aligned}
\chi(t,s) &\approx \lim_{\epsilon\to 0}\frac{1}{\epsilon}\left(S_0(t,0) - \epsilon S_0(t,0)\int_0^t H_1(x-s)\,\mathrm{d}x + \mathcal{O}(\epsilon^2) - S_0(t,0)\right)\\
&= \lim_{\epsilon\to 0}\left(-S_0(t,0)\int_0^t H_1(x-s)\,\mathrm{d}x + \mathcal{O}(\epsilon)\right)\\
&= -S_0(t,0)\int_0^t H_1(x-s)\,\mathrm{d}x\\
&\overset{(6.42)}{=} -S_0(t,0)\int_0^t \left[\alpha(x)U_1(x-s)+\beta(x)\dot{U}_1(x-s)\right]\mathrm{d}x\\
&\overset{(6.44)}{=} -S_0(t,0)\int_0^t\left[\alpha(x)U_1(x-s)+\beta(x)\frac{1}{\tau_m}\left(\delta(x-s)-U_1(x-s)\right)\right]\mathrm{d}x\\
&= -\frac{1}{\tau_m}S_0(t,0)\left[\int_0^t(\tau_m\alpha(x)-\beta(x))U_1(x-s)\,\mathrm{d}x + \int_0^t\beta(x)\delta(x-s)\,\mathrm{d}x\right]\\
&\overset{(6.43)}{=} -\frac{1}{\tau_m}S_0(t,0)\left[\int_0^t(\tau_m\alpha(x)-\beta(x))\frac{1}{\tau_m}\,\mathrm{e}^{-\frac{x-s}{\tau_m}}\,\Theta(x-s)\,\mathrm{d}x+\beta(s)\right]\\
&= -\frac{1}{\tau_m}S_0(t,0)\left[\int_s^t\left(\alpha(x)-\frac{1}{\tau_m}\beta(x)\right)\mathrm{e}^{-\frac{x-s}{\tau_m}}\,\mathrm{d}x+\beta(s)\right]
\end{aligned}\tag{6.40}$$

We can thus write the integral over the first order term of the survival probability as

$$\begin{aligned}
\int_{-\infty}^{t-\tau_{\text{ref}}} S_1(t,\hat{t})\,\mathrm{d}\hat{t} &\overset{(6.39)}{=} \int_{-\infty}^{t-\tau_{\text{ref}}}\int_{\hat{t}+\tau_{\text{ref}}}^{t}\chi(t-\hat{t},s-\hat{t})I_1(s)\,\mathrm{d}s\,\mathrm{d}\hat{t}\\
&= \int_{-\infty}^{t}\int_{-\infty}^{t}\chi(t-\hat{t},s-\hat{t})I_1(s)\Theta(s-\hat{t}-\tau_{\text{ref}})\,\mathrm{d}s\,\mathrm{d}\hat{t}\\
&= \int_{-\infty}^{t}\int_{-\infty}^{t}\chi(t-\hat{t},s-\hat{t})\Theta(s-\hat{t}-\tau_{\text{ref}})\,\mathrm{d}\hat{t}\,I_1(s)\,\mathrm{d}s
\end{aligned}$$

Substitute $x := t-s$:

$$= \int_0^{\infty}\int_{-\infty}^{t}\chi(t-\hat{t},t-x-\hat{t})\Theta(t-x-\hat{t}-\tau_{\text{ref}})\,\mathrm{d}\hat{t}\,I_1(t-x)\,\mathrm{d}x$$

Substitute $y = t-x-\hat{t}$:

$$\begin{aligned}
&= \int_0^{\infty}\int_{-x}^{\infty}\chi(x+y,y)\Theta(y-\tau_{\text{ref}})\,\mathrm{d}y\,I_1(t-x)\,\mathrm{d}x\\
&= \int_0^{\infty}\underbrace{\int_{\tau_{\text{ref}}}^{\infty}\chi(x+y,y)\,\mathrm{d}y}_{=:-L(x)}\;I_1(t-x)\,\mathrm{d}x\\
&= -\int_0^{\infty}L(x)I_1(t-x)\,\mathrm{d}x
\end{aligned}$$

which can be written as as convolution

$$= -\int_{-\infty}^{\infty}\mathcal{L}(x)I_1(t-x)\,\mathrm{d}x = -(\mathcal{L}*I_1)(t)\tag{6.41}$$

with the kernel

$$\mathcal{L}(x) := -\Theta(x)\int_{\tau_{\text{ref}}}^{\infty}\chi(x+y,y)\,\mathrm{d}y$$

6.C.1.1 Auxiliary calculations:

Assume the GIF neuron with membrane potential described by Eq. (6.31) has fired its last spike at time $\hat{t} = 0$ and receives an input $I(t) = I_0 + \epsilon I_\delta(s)$, $s \geq \tau_{\mathrm{ref}}$. Its membrane potential is given by:

$$\begin{aligned} U_s(t) &= I_0 - (I_0 - V_r)\,\mathrm{e}^{-\frac{t-\tau_{\mathrm{ref}}}{\tau_m}\Theta(t-\tau_{\mathrm{ref}})} + \frac{\epsilon}{\tau_m}\int_{\tau_{\mathrm{ref}}}^{t} \underbrace{I_\delta(s)(x)}_{\delta(x-s)}\,\mathrm{e}^{-\frac{t-x}{\tau_m}}\,\mathrm{d}x\,\Theta(t-\tau_{\mathrm{ref}}) \\ &=: U_0(t) + \epsilon U_1(t-s) \end{aligned} \tag{6.42}$$

with

$$\begin{aligned} U_0(t) &:= I_0 - (I_0 - V_r)\,\mathrm{e}^{-\frac{t-\tau_{\mathrm{ref}}}{\tau_m}\Theta(t-\tau_{\mathrm{ref}})} \\ U_1(t-s) &:= \frac{1}{\tau_m}\,\mathrm{e}^{-\frac{t-s}{\tau_m}}\,\Theta(t-s)\Theta(t-\tau_{\mathrm{ref}}) \overset{(*)}{=} \frac{1}{\tau_m}\,\mathrm{e}^{-\frac{t-s}{\tau_m}}\,\Theta(t-s) \end{aligned} \tag{6.43}$$

$(*)$ since $s \geq \tau_{\mathrm{ref}}$.
The derivative of the membrane potential can be split similarly:

$$\dot{U}_s(t) = \frac{1}{\tau_m}\left(-U_s(t) + I_0 + \epsilon I_\delta(s)(t)\right) = \dot{U}_0(t) + \epsilon \dot{U}_1(t-s)$$

with

$$\begin{aligned} \dot{U}_0(t) &= \frac{1}{\tau_m}\left(-U_0(t) + I_0\right) \\ \dot{U}_1(t-s) &= \frac{1}{\tau_m}\left(\delta(t-s) - U_1(t-s)\right) \end{aligned} \tag{6.44}$$

The hazard function for this neuron can be expanded linearly in ϵ:

$$\begin{aligned} H_s(t) &= f(U_0(t), \dot{U}_0(t))\Theta(t-\tau_{\mathrm{ref}}) \\ &\quad + \epsilon\left[\left.\frac{\partial f}{\partial u}\right|_{(U_0(t),\dot{U}_0(t))} U_1(t-s) + \left.\frac{\partial f}{\partial \dot{U}}\right|_{(U_0(t),\dot{U}_0(t))} \dot{U}_1(t-s)\right]\Theta(t-\tau_{\mathrm{ref}}) \end{aligned}$$

The second heaviside function can be dropped, since we assumed $s \geq \tau_{\mathrm{ref}}$ and the U_1 and $\dot{U}_1$ terms are only non-zero for $t \geq s$. We thus arrive at

$$H_s(t) = H_0(t) + \epsilon H_1(t-s)$$

where

$$\begin{aligned} H_0(t) &= f(U_0(t), \dot{U}_0(t))\Theta(t-\tau_{\mathrm{ref}}) \\ H_1(t-s) &= \alpha(t)U_1(t-s) + \beta(t)\dot{U}_1(t-s) \\ \alpha(t) &= \left.\frac{\partial f}{\partial U}\right|_{(U_0(t),\dot{U}_0(t))}, \qquad \beta(t) = \left.\frac{\partial f}{\partial \dot{U}}\right|_{(U_0(t),\dot{U}_0(t))} \end{aligned}$$

The linear expansion of the hazard yields a linear approximation of the survival probability:

$$
\begin{aligned}
S_0(t,0) &= \exp\left[-\int_0^t H_0(x)\,\mathrm{d}x\right] \\
S_{I_0+\epsilon I_\delta(s)}(t,0) &= \exp\left[-\int_0^t H_0(x)+\epsilon H_1(x-s)\,\mathrm{d}x\right] = S_0(t,0)\exp\left[-\epsilon\int_0^t H_1(x-s)\,\mathrm{d}x\right] \\
&\approx S_0(t,0)\left(1-\epsilon\int_0^t H_1(x-s)\,\mathrm{d}x+\mathcal{O}(\epsilon^2)\right) \\
&= S_0(t,0)-\epsilon S_0(t,0)\int_0^t H_1(x-s)\,\mathrm{d}x+\mathcal{O}(\epsilon^2) \qquad (6.45)
\end{aligned}
$$

6.C.2 Susceptibility for exponential hazard

For a GIF neuron with exponential hazard function

$$
f(U) = r\exp\left[\frac{U-V_T}{\Delta}\right]
$$

we can evaluate the individual components of the susceptibility

$$
\tilde{G}(\omega) = \frac{i\omega A_0\tilde{\mathcal{L}}(\omega)}{1-\tilde{P}_0(\omega)}
$$

(Eq. (6.38)) derived above for general hazard. The kernel $\mathcal{L}(x)$ is given by

$$
\begin{aligned}
\mathcal{L}(x) &= -\Theta(x)\int_{\tau_{\mathrm{ref}}}^{\infty}\chi(x+y,y)\,\mathrm{d}y \\
&= \frac{r}{I_0-V_r}\int_{\tau_{\mathrm{ref}}}^{\infty}\exp\left[-r\int_{\tau_{\mathrm{ref}}}^{x+y}\exp\left[\frac{U_0(t)-V_T}{\Delta}\right]\mathrm{d}t\right]\mathrm{e}^{\frac{y-\tau_{\mathrm{ref}}}{\tau_m}} \\
&\quad\cdot\left(\exp\left[\frac{U_0(x+y)-V_T}{\Delta}\right]-\exp\left[\frac{U_0(y)-V_T}{\Delta}\right]\right)\mathrm{d}y\ . \qquad (6.46\mathrm{a}) \\
\tilde{\mathcal{L}}(\omega) &= \int_0^\infty \mathrm{e}^{-i\omega x}\,\mathcal{L}(x)\,\mathrm{d}x
\end{aligned}
$$

and the interval distribution as

$$
\begin{aligned}
P_0(t) &= r\exp\left[\frac{U_0(t)-V_T}{\Delta}\right]\exp\left[-r\int_0^t\exp\left[\frac{U_0(x)-V_T}{\Delta}\right]\mathrm{d}x\right]\Theta(t-\tau_{\mathrm{ref}}) \qquad (6.46\mathrm{b}) \\
\tilde{P}_0(\omega) &= \int_0^\infty \mathrm{e}^{-i\omega x}\,P_0(x)\,\mathrm{d}x
\end{aligned}
$$

(see auxiliary calculations below). The mean firing rate A_0 is given by Eq. (6.30). All expressions can be evaluated numerically.

Auxiliary calculations Let $\tau = t - \hat{t}$ denote the time since the neuron's last spike. The undisturbed membrane potential and its derivative are given by

$$\begin{aligned} U_0(\tau) &= I_0 - (I_0 - V_r)\,\mathrm{e}^{-\frac{\tau-\tau_{\mathrm{ref}}}{\tau_m}\Theta(\tau-\tau_{\mathrm{ref}})} \\ \dot{U}_0(\tau) &= \frac{1}{\tau_m}(I_0 - V_R)\,\mathrm{e}^{-\frac{\tau-\tau_{\mathrm{ref}}}{\tau_m}\Theta(\tau-\tau_{\mathrm{ref}})}\,\Theta(\tau - \tau_{\mathrm{ref}}) \qquad \text{only defined for } \tau > 0 \end{aligned} \tag{6.47}$$

For any hazard function that does *not* depend on the slope of the membrane potential ($\beta = \partial f/\partial\dot{U} \equiv 0$) one can first derive a simplified expression for the integrand χ of kernel $\boldsymbol{\mathcal{L}}$:

$$\begin{aligned} \chi(t,s) &= -\frac{1}{\tau_m}S_0(t)\left[\int_s^t (\alpha(x) - \frac{1}{\tau_m}\beta(x))\exp\left[-\frac{x-s}{\tau_m}\right]\mathrm{d}x + \beta(s)\right] \\ &= -\frac{1}{\tau_m}S_0(t)\int_s^t \alpha(x)\exp\left[-\frac{x-s}{\tau_m}\right]\mathrm{d}x \quad \text{, since } \beta(x) = \left.\frac{\partial f}{\partial\dot{U}}\right|_{(U_0(x),\dot{U}_0(x))} = 0 \end{aligned}$$

Function $\alpha = \left.\frac{\partial f}{\partial U}\right|_{(U_0(x),\dot{U}_0(x))}$ can be thought of as a function on $U_0(x)$. So instead of integrating over time, we can integrate directly over the mean membrane potential trajectory $U_0(x)$ ($x \geq s \geq \tau_{\mathrm{ref}}$):

$$\begin{aligned} \chi(t,s) &\overset{(6.47)}{=} -\frac{1}{\tau_m}S_0(t)\int_{U_0(s)}^{U_0(t)} \tilde{\alpha}(U_0)\exp\left[-\frac{x-s}{\tau_m}\right]\frac{\tau_m}{I_0 - V_R}\,\mathrm{e}^{\frac{x-\tau_{\mathrm{ref}}}{\tau_m}}\,\mathrm{d}U_0 \\ &= -\frac{1}{I_0 - V_R}S_0(t)\,\mathrm{e}^{\frac{s-\tau_{\mathrm{ref}}}{\tau_m}}\int_{U_0(s)}^{U_0(t)} \tilde{\alpha}(U_0)\,\mathrm{d}U_0 \\ &= -\frac{1}{I_0 - V_R}S_0(t)\,\mathrm{e}^{\frac{s-\tau_{\mathrm{ref}}}{\tau_m}}\left[f\big(U_0(t)\big) - f\big(U_0(s)\big)\right] \\ &= -\frac{1}{I_0 - V_R}S_0(t)\,\mathrm{e}^{\frac{s-\tau_{\mathrm{ref}}}{\tau_m}}\left[H_0(t) - H_0(s)\right] \quad \text{for } t \geq s \geq \tau_{\mathrm{ref}} \end{aligned} \tag{6.48}$$

For the exponential hazard in particular, the hazard, survival probability, and interval distribution for constant drive are given as:

$$\begin{aligned} H_0(\tau) &= f(U_0(\tau))\Theta(\tau - \tau_{\mathrm{ref}}) = r\exp\left[\frac{U_0(\tau) - V_T}{\Delta}\right]\Theta(\tau - \tau_{\mathrm{ref}}) \\ S_0(\tau) &= \exp\left[-\int_0^\tau H_0(x)\,\mathrm{d}x\,\Theta(\tau)\right] = \exp\left[-r\int_0^\tau \exp\left[\frac{U_0(x) - V_T}{\Delta}\right]\mathrm{d}x\,\Theta(\tau - \tau_{\mathrm{ref}})\right] \\ P_0(\tau) &= H_0(\tau)S_0(\tau) \\ &= r\exp\left[\frac{U_0(\tau) - V_T}{\Delta}\right]\exp\left[-r\int_0^\tau \exp\left[\frac{U_0(x) - V_T}{\Delta}\right]\mathrm{d}x\right]\Theta(\tau - \tau_{\mathrm{ref}}) \\ \alpha(\tau) &= \left.\frac{\partial f}{\partial U}\right|_{(U_0(\tau),\dot{U}_0(\tau))} = \frac{r}{\Delta}\exp\left[\frac{U_0(\tau) - V_T}{\Delta}\right] = \frac{1}{\Delta}H_0(\tau) \quad \text{if } \tau \geq \tau_{\mathrm{ref}} \end{aligned}$$

So the kernel $\mathcal{L}$ is given by:

$$\begin{aligned}
\mathcal{L}(x) &= -\Theta(x)\int_{\tau_\mathrm{ref}}^{\infty}\chi(x+y,y)\,\mathrm{d}y \\
&\overset{(6.48)}{=} \frac{r}{I_0 - V_r}\int_{\tau_\mathrm{ref}}^{\infty}\exp\left[-r\int_{\tau_\mathrm{ref}}^{x+y}\exp\left[\frac{U_0(t)-V_T}{\Delta}\right]\mathrm{d}t\right]\mathrm{e}^{\frac{y-\tau_\mathrm{ref}}{\tau_m}} \\
&\qquad\cdot\left(\exp\left[\frac{U_0(x+y)-V_T}{\Delta}\right]-\exp\left[\frac{U_0(y)-V_T}{\Delta}\right]\right)\mathrm{d}y\ .
\end{aligned}$$

6.D Supplementary figures

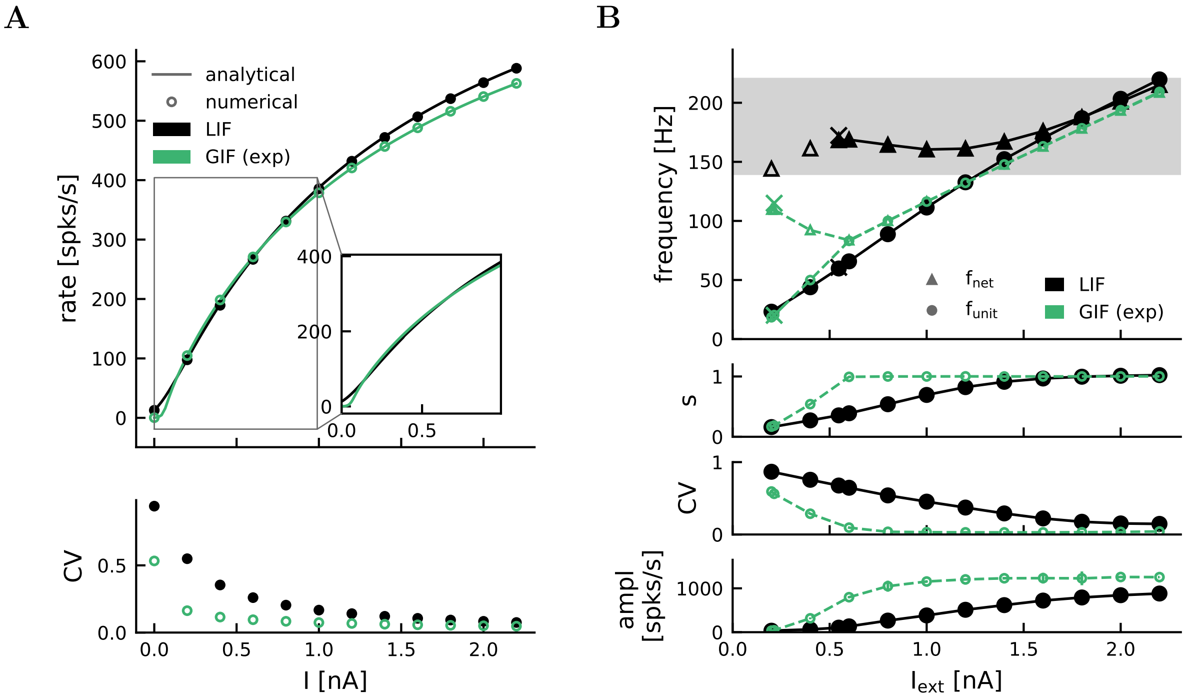

Figure 6.8: Firing properties of a GIF neuron with exponential hazard fitted to match the f-I curve of an LIF neuron (wider fitting range).
A, Mean firing rate (top panel) and coefficient of variation of the interspike intervals (bottom panel) as a function of input current for an LIF neuron under white noise (black), and a GIF neuron with exponential hazard (green). Inset shows the range of the LIF f-I curve used to fit the exponential hazard parameters ($r = 2648$ Hz$, \Delta = 1.37$ mV). For higher inputs the firing rate of the GIF unit differs from the LIF rate. Note that for the large fitting range the smooth onset of firing close to $I = 0$ nA could not be captured by the GIF neuron. The GIF unit fires much more regular than the LIF unit (see low CV of interspike intervals in bottom panel). Solid lines show the analytical solution for the firing rate of an LIF (Eq. (6.28)) or a GIF neuron (Eq. (6.29)). Markers are numerical estimates from a spiking network simulation. **B,** Dynamics of the respective inhibitory networks of LIF or GIF neurons. The different hazard fit does not yield a closer match of the GIF dynamics with the LIF reference.

7 | Discussion and outlook

7.1 Summary of the thesis

The goal of this thesis was to enhance our understanding of the generation of ripple oscillations — an important hippocampal rhythm that has been implicated in cognitive functions such as memory consolidation. In Chapter 2 I summarized current literature regarding brain rhythms and memory consolidation in general, highlighting in particular the potential functional role of sharp wave-ripples. I then introduced in detail the dynamical features of sharp wave-ripples, and the anatomy and neuronal circuitry of the hippocampus as the main site of origin of this rhythm. After introducing the various models that have been put forward to explain the emergence of the ripple oscillation I discussed current experimental evidence and why it has so far been inconclusive regarding which is the most like generating mechanism. Intra-ripple frequency accommodation (IFA) was introduced as a promising feature of the transient ripple events that may advance model selection.

In Chapter 4 I set out to explain the recent observation of IFA in the bifurcation-based inhibition-first model (Donoso et al., 2018). I developed an analytical approximation of the drift-based oscillation dynamics in the mean-field limit under strong drive. The theory provides an estimate of the ripple frequency, mean unit firing rate, and oscillation amplitude of the mean membrane potential as a function of the (constant or time-dependent) external drive. For constant drive, the oscillation amplitude of the mean membrane potential increases monotonically with the level of drive. Thus for fast, time-dependent drive, mimicking transient excitatory input to CA1 due to a sharp wave event in CA3, a speed-dependent hysteresis occurs in the mean membrane potential dynamics, leading to instantaneous ripple frequencies that decay over the course of the event (IFA). The speed-dependence of IFA is a novel prediction that can be tested in optogenetic experiments. My analysis demonstrates that a fast changing drive is the only prerequisite for IFA in the bifurcation-based inhibition-first model. Since spontaneously occurring sharp waves are always short events (∼50–100 ms), generating a fast changing excitatory drive to CA1, IFA can thus be regarded an intrinsic feature of the bifurcation-based model.

In Chapter 5 I showed that the alternative, perturbation-based inhibition-first model by Malerba et al. (2016) requires an asymmetric drive to account for IFA: ideally a sudden onset of excitatory input followed by a decay over ∼50–100 ms. Experimental measurements of the LFP or excitatory postsynaptic currents during a sharp wave suggests that the SPW-associated drive to CA1 has a finite rise time (Maier et al., 2011; Donoso et al., 2018), in which case the perturbation-based model would predict an initial *in*crease in ripple frequency (“anti-IFA”). The analysis of the mechanism of IFA can thus advance model selection and provides new evidence in favor of the bifurcation-based inhibition-first model. In Section 5.5 I discussed additional factors that can be used to dissociate the two inhibition-first ripple models, such as the inhibitory coupling strength, the dependence of the ripple duration on the length of external stimulation, a detailed quantification of the heterogeneity of the CA1 interneuron network active during ripples, or the spike-initiation current/action potential waveform of a single interneuron.

In Chapter 6 I analyzed how a switch of the noise model — from a Gaussian white noise input, to stochastic spiking according to a hazard function — affects the ripple dynamics in the bifurcation-based inhibition-first model. I compared two potential choices of hazard functions, that depend either only on the momentary membrane potential, or also on its slope. While neither of the hazard functions provides a perfect fit of the network dynamics to the reference network under Gaussian white noise input, a slope-dependence of the hazard clearly enhances the fit of the network dynamics qualitatively. This finding is in agreement with the theoretical approach in Chapter 4, where the key ripple dynamics were captured in a redefined population rate that depends not only on the distance of the mean membrane potential from threshold, but also on the slope with which it approaches the threshold. Finding a mapping from input to output noise, that preserves the core aspects of the ripple dynamics, is a prerequisite for modeling ripple oscillations on a mesoscopic scale (Schwalger et al., 2017).

7.2 Outlook and future research

7.2.1 Understanding ripple generation

7.2.1.1 IFA in other ripple models

Having demonstrated that IFA can be used to dissociate inhibition-first ripple models, a natural next step is an analysis of the transient dynamics and IFA in excitation-first ripple models. In both excitation-based ripple models, the ripple frequency depends on the average spike propagation delay among pyramids — either orthodromically via supralinear dendrites (Memmesheimer, 2010; Jahnke et al., 2015) or antidromically via axo-axonal gap junctions (Traub et al., 1999a; Traub and Bibbig, 2000). A preliminary analysis of the model by Memmesheimer (2010), based on supralinear dendritic integration, suggests that the instantaneous ripple frequency is rather stable, but may exhibit a weak IFA or anti-IFA depending on a variety of factors, such as dendritic refractoriness (Nunez del Toro, 2022). The axonal GJ model (Traub et al., 1999a; Traub and Bibbig, 2000) may be able to account for IFA by assuming an increase in the spike propagation delay over the course of a ripple event. Such an increase in latency might occur due to increasing somatic depolarization, which has been shown to decrease the action potential amplitude (Shu et al., 2006, 2007). Future work should investigate in more depth whether and under which conditions excitation-first models can generate IFA.

7.2.1.2 Further evaluation of the bifurcation-based inhibition-first model

My analysis of IFA in inhibition-first models supports the bifurcation-based inhibition-first model as a likely candidate for ripple generation. It is worth noting that, in general, this model faces less severe contradictory evidence than the other ripple models (Table 2.1, yellow highlights). The perturbation-based inhibition-first model crucially relies on weak inhibitory coupling and high interneuron firing rates, for which there is no or limited experimental support (Bartos et al., 2002; Csicsvari et al., 1999b; Klausberger et al., 2003; Lapray et al., 2012; Varga et al., 2012, 2014, but see Szabo et al., 2022). Supralinear dendritic integration is challenged by the seemingly sparse connectivity between CA1 pyramidal cells and the fact that ripples can still be evoked when AMPA excitatory synaptic transmission is blocked (Deuchars and Thomson, 1996; Schlingloff et al., 2014). The very existence of gap junctions and antidromic spike propagation between CA1 pyramidal cell axons is still debated (see Section 2.7.1). The bifurcation-based inhibition-first model has been challenged by the ongoing debate of whether interneuron stimulation can evoke ripples (Schlingloff et al., 2014, but see Stark et al., 2014), and by CA1 pyramidal cell activity as an apparently necessary condition for ripples (Stark et al., 2014). Both these challenges may be resolved by taking into account the potential confounding factor arising from the interpretation of the LFP signal (see Section 2.5.1): I argued in Section 2.8 that current experimental evidence can be interpreted *in favor* of ripple generation by interneuron stimulation, when ripple modulation is not only quantified in the LFP, but also in the spiking activity. Future experiments should clearly establish whether or not a stimulation of interneurons (potentially PV^+ BCs) can indeed evoke ripple oscillations in the neuronal circuit. To avoid the confounding factor arising from the LFP interpretation, it would be helpful to record intracellular inhibitory currents or large scale inhibitory spiking activity as an additional signal that can be analyzed for ripple modulation. The same goes for experiments probing the role of pyramidal cells in ripple generation.

A combined effort of theoretical and experimental analysis of the bifurcation-based inhibition-first model will be needed, to make more precise predictions about the ripple dynamics in the real CA1 circuit, including local CA1 pyramidal cells, heterogeneity, and realistic spike initiation:

Local CA1 pyramidal cells. Throughout this thesis, I analyzed the inhibition-first ripple models in their core form, *i.e.* in a purely inhibitory network, neglecting the local pyramidal cell population in CA1. Including an excitatory population in the bifurcation-based model introduces a competition between two potential oscillation generators: the ripple generating delayed inhibitory feedback loop among the interneurons, and the gamma generating disynaptic feedback loop between pyramidal cells and interneurons (PING, Traub et al., 1996). The resulting network dynamics has been shown to depend on many factors: the relative coupling strengths within and across populations, local E/I balance in each population, the synaptic time scales, the sparsity of synaptic connections between pyramidal cells, and the balance between the excitatory feedforward drive to the two populations (Brunel and Wang, 2003; Melonakos et al., 2018; Donoso et al., 2018; Braun and Memmesheimer, 2022). Predicting the result of optogenetic experiments that activate or silence local CA1 pyramidal cells thus requires a careful analysis of the model, combined with precise experimental estimates of the factors listed above.

Heterogeneity. Heterogeneity can decrease the parameter regime for which the bifurcation-based model exhibits persistent stochastic oscillations (Brunel and Hakim, 1999). Future work could study whether the bifurcation-based model can still produce persistent oscillations, or at least account for *transient* ripple oscillations in the presence of heterogeneity. Heterogeneity in different model parameters may affect the stability of oscillations differentially. A general, experimental quantification of the heterogeneity of the CA1 interneuron population is difficult as long as it has not been clarified which interneuron types are involved in ripple generation. Inhibition-first models have so far focused on PV^+ basket cells as the main pacemaker of ripple oscillations. PV^+ bistratified cells are also known to increase their firing rate during ripples and are connected to basket cells (Fig. 2.6; Klausberger et al., 2004; Varga et al., 2014). Hence, as a first step, one could investigate how the heterogeneity in a mixed network of basket and bistratified cells affects the ripple dynamics.

Single neuron spike generation mechanism. The comparison of the two inhibition-first models in Section 5.4 has once again highlighted the importance of the single neuron spike generation mechanism for the ripple frequency (Fourcaud-Trocmé et al., 2003; Geisler et al., 2005). The increased phase lag of the linear response of EIF neurons, compared to LIF neurons, leads to slower network oscillations in EIF compared to LIF networks (Fig. 5.13). It would thus be of interest to quantify the spike generation mechanism of CA1 PV^+ basket cells in detail, in order to estimate whether a realistic single neuron model for CA1 interneurons can account for ripple-range oscillations in the bifurcation-based inhibitory network model.

7.2.1.3 Towards finding the true mechanism of ripple generation

It may seem counterintuitive, that a detail such as IFA may be necessary to dissociate inhibition- and excitation-first ripple models, that rely on so vastly different assumptions. In Section 2.8 I summarized a number of optogenetic and pharmacological experiments that tried to dissociate the two model classes based on their core differences regarding excitatory and inhibitory contributions to ripple generation. There are two main reasons why these experiments have so far remained inconclusive: One is our incomplete understanding of the LFP signal as discussed above. The other is a more fundamental, conceptual problem: We have seen in Section 2.7 that the basic ingredients of all ripple models seem to be present in CA1 (with the potential exception of axonal gap junctions). Let's assume for a moment that all proposed mechanisms can, in principle, work and generate ripple oscillations. This means that if an experimental manipulation takes out one potential ripple generator, another mechanism might take over. Whatever mechanism generates a ripple-like event in the manipulated circuit may not be the same mechanism that causes ripples in the intact brain. Optogenetic and pharmacological manipulations of the circuit may therefore never allow a clear conclusion about ripple generation in the healthy brain.

For this reason, IFA may be a promising marker for model selection. It is a feature that can be observed in spontaneous ripple events and it may be possible to study its properties, such as a dependence on the time course of sharp wave-associated excitation, without severe manipulations of the circuit.

Ultimately, the real question is of course: If we combine all potential ripple generators into one complex network, which mechanism “wins”? Unfortunately, it is hard to address this question from a modeling perspective, since the multitude of parameter dependencies of all models combined makes a meaningful analysis very difficult. It is also possible that there is no single, true generation mechanism of ripples, but that different classes of (sharp wave-)ripples originate in different circuits and brain states by different mechanisms (Ramirez-Villegas et al., 2015; Yamamoto and Tonegawa, 2017; Oliva et al., 2016, 2020; Navas-Olive et al., 2022).

7.2.2 Mesoscopic models of ripple oscillations

The analysis in Chapter 6 has demonstrated that ripples can, in principle, be modeled on a mesoscopic scale. The efficient mesoscopic integration scheme by Schwalger et al. (2017) could facilitate setting up larger scale models to study the propagation of sharp wave-ripples within and across brain regions, and their coordination with other thalamo-cortical rhythms. An extension of the mesoscopic approach incorporating short-term synaptic plasticity (Schmutz et al., 2020) was recently used to model hippocampal replay on a mesoscopic level (Pietras et al., 2022). Combining models of replay and ripple generation may be the next step towards understanding the potential functional role of the sharp wave-ripple rhythm for cognitive processes such as memory consolidation.

Bibliography

Abbott, L. F. and van Vreeswijk, C. (1993). Asynchronous states in networks of pulse-coupled oscillators. *Phys. Rev. E*, 48(2):1483–1490.

Abramowitz, M. and Stegun, I. (1965). *Handbook of Mathematical Functions: With Formulas, Graphs, and Mathematical Tables.* Dover Publications, New York.

Adrian, E. D. (1942). Olfactory reactions in the brain of the hedgehog. *J. Physiol.*, 100(4):459–473.

Amaral, D. and Witter, M. (1989). The three-dimensional organization of the hippocampal formation: A review of anatomical data. *Neuroscience*, 31(3):571–591.

Ambrose, R. E., Pfeiffer, B. E., and Foster, D. J. (2016). Reverse Replay of Hippocampal Place Cells Is Uniquely Modulated by Changing Reward. *Neuron*, 91(5):1124–1136.

Andersen, P., Bliss, T., and Skrede, K. (1971). Lamellar organization of hippocampal excitatory pathways. *Exp. Brain Res.*, 13:222–238.

Andersen, P., Morris, R., Amaral, D. G., Bliss, T., and O'Keefe, J. (2006). *The hippocampus book.* Oxford University Press.

Ariav, G., Polsky, A., and Schiller, J. (2003). Submillisecond precision of the input-output transformation function Mediated by Fast Sodium Dendritic Spikes in Basal Dendrites of CA1 Pyramidal Neurons. *J. Neurosci.*, 23(21):7750–7758.

Axmacher, N., Elger, C. E., and Fell, J. (2008). Ripples in the medial temporal lobe are relevant for human memory consolidation. *Brain*, 131(7):1806–1817.

Badel, L. (2011). Firing statistics and correlations in spiking neurons: A level-crossing approach. *Phys. Rev. E*, 84(4):041919.

Bähner, F., Weiss, E. K., Birke, G., Maier, N., Schmitz, D., Rudolph, U., Frotscher, M., Traub, R. D., Both, M., and Draguhn, A. (2011). Cellular correlate of assembly formation in oscillating hippocampal networks in vitro. *Proc. Natl. Acad. Sci.*, 108(35):E607–E616.

Barron, H., Vogels, T. P., Behrens, T., and Ramaswami, M. (2017). Inhibitory engrams in perception and memory. *Proc. Natl. Acad. Sci.*, 114(26):6666–6674.

Bartlett, F. C. and Kintsch, W. (1995). *Remembering.* Cambridge University Press.

Bartos, M., Vida, I., Frotscher, M., Meyer, A., Monyer, H., Geiger, J. R. P., and Jonas, P. (2002). Fast synaptic inhibition promotes synchronized gamma oscillations in hippocampal interneuron networks. *Proc. Natl. Acad. Sci.*, 99(20):13222–13227.

Battaglia, F. P., Sutherland, G. R., and McNaughton, B. L. (2004). Hippocampal sharp wave bursts coincide with neocortical "up-state" transitions. *Learn. Mem.*, 11(6):697–704.

Baude, A., Bleasdale, C., Dalezios, Y., Somogyi, P., and Klausberger, T. (2007). Immunoreactivity for the GABAA receptor $\alpha1$ subunit, somatostatin and connexin36 distinguishes axoaxonic, basket, and bistratified interneurons of the rat hippocampus. *Cereb. Cortex*, 17(9):2094–2107.

Behrens, C. J., ul Haq, R., Liotta, A., Anderson, M. L., and Heinemann, U. (2011). Nonspecific effects of the gap junction blocker mefloquine on fast hippocampal network oscillations in the adult rat in vitro. *Neuroscience*, 192:11–19.

Berger, H. (1933). Über das Elektrenkephalogramm des Menschen. *Arch. Psychiatr. Nervenkr.*, 98(1):231–254.

Bezaire, M. J. and Soltesz, I. (2013). Quantitative assessment of CA1 local circuits: Knowledge base for interneuron-pyramidal cell connectivity. *Hippocampus*, 23(9):751–785.

Bi, G. Q. and Poo, M. M. (1998). Synaptic modifications in cultured hippocampal neurons: dependence on spike timing, synaptic strength, and postsynaptic cell type. *J. Neurosci.*, 18(24):10464–10472.

Blasco-Ibáñez, J. M. and Freund, T. F. (1995). Synaptic Input of Horizontal Interneurons in Stratum Oriens of the Hippocampal CA1 Subfield: Structural Basis of Feed-back Activation. *Eur. J. Neurosci.*, 7(10):2170–2180.

Borbély, A. A. (2001). From slow waves to sleep homeostasis: New perspectives. *Arch. Ital. Biol.*, 139(1-2):53–61.

Börgers, C. and Kopell, N. (2003). Synchronization in networks of excitatory and inhibitory neurons with sparse, random connectivity. *Neural Comput.*, 15(3):509–538.

Börgers, C. and Kopell, N. (2005). Effects of noisy drive on rhythms in networks of excitatory and inhibitory neurons. *Neural Comput.*, 17(3):557–608.

Born, J., Rasch, B., and Gais, S. (2006). Sleep to remember. *Neurosci.*, 12(5):410–424.

Both, M., Bähner, F., Von Bohlen Und Halbach, O., and Draguhn, A. (2008). Propagation of specific network patterns through the mouse hippocampus. *Hippocampus*, 18(9):899–908.

Bragin, A., Engel, J., Wilson, C. L., Fried, I., and Buzsáki, G. (1999). High-frequency oscillations in human brain. *Hippocampus*, 9(2):137–142.

Bragin, A., Jando, G., Nadasdy, Z., Van Landeghem, M., and Buzsáki, G. (1995). Dentate EEG spikes and associated interneuronal population bursts in the hippocampal hilar region of the rat. *J. Neurophysiol.*, 73(4):1691–1705.

Bramham, C. R. and Srebro, B. (1989). Synaptic plasticity in the hippocampus is modulated by behavioral state. *Brain Res.*, 493(1):74–86.

Braun, W. and Memmesheimer, R.-M. (2022). High-frequency oscillations and sequence generation in two-population models of hippocampal region CA1. *PLoS Comput. Biol.*, 18(2):e1009891.

Broadbent, N. J. and Clark, R. E. (2013). Remote context fear conditioning remains hippocampus-dependent irrespective of training protocol, training-surgery interval, lesion size, and lesion method. *Neurobiol. Learn. Mem.*, 106:300–308.

Brunel, N. (2000). Dynamics of sparsely connected networks of excitatory and inhibitory neurons. *J. Comput. Neurosci.*, 8:183–208.

Brunel, N., Chance, F. S., Fourcaud, N., and Abbott, L. F. (2001). Effects of synaptic noise and filtering on the frequency response of spiking neurons. *Phys. Rev. Lett.*, 86(10):2186–2189.

Brunel, N. and Hakim, V. (1999). Fast Global Oscillations in Networks of Integrate-and-Fire Neurons with Low Firing Rates. *Neural Comput.*, 11(7):1621–1671.

Brunel, N., Hakim, V., and Richardson, M. J. (2003). Firing-rate resonance in a generalized integrate-and-fire neuron with subthreshold resonance. *Phys. Rev. E*, 67(5):051916.

Brunel, N. and Hansel, D. (2006). How Noise Affects the Synchronization Properties of Recurrent Networks of Inhibitory Neurons. *Neural Comput.*, 18(5):1066–1110.

Brunel, N. and Wang, X.-J. (2003). What determines the frequency of fast network oscillations with irregular neural discharges? I. Synaptic dynamics and excitation-inhibition balance. *J. Neurophysiol.*, 90(1):415–430.

Buhl, D. L. and Buzsáki, G. (2005). Developmental emergence of hippocampal fast-field "ripple" oscillations in the behaving rat pups. *Neuroscience*, 134(4):1423–1430.

Buhl, D. L., Harris, K. D., Hormuzdi, S. G., Monyer, H., and Buzsáki, G. (2003). Selective impairment of hippocampal gamma oscillations in connexin-36 knock-out mouse in vivo. *J. Neurosci.*, 23(3):1013–1018.

Buhl, E. H., Halasy, K., and Somogyi, P. (1994a). Diverse sources of hippocampal unitary inhibitory postsynaptic potentials and the number of synaptic release sites. *Nature*, 368(6474):823–828.

Buhl, E. H., Han, Z.-S., Lörinczi, Z., Stezhka, V., Karnup, S., and Somogyi, P. (1994b). Physiological properties of anatomically identified axo-axonic cells in the rat hippocampus. *J. Neurophysiol.*, 71(4).

Buhl, E. H., Szilágyi, T., Halasy, K., and Somogyi, P. (1996). Physiological properties of anatomically identified basket and bistratified cells in the CA1 area of the rat hippocampus in vitro. *Hippocampus*, 6(3):294–305.

Bulsara, A. R., Elston, T. C., Doering, C. R., Lowen, S. B., and Lindenberg, K. (1996). Cooperative behavior in periodically driven noisy integrate-and-fire models of neuronal dynamics. *Phys. Rev. E*, 53(4).

Buzsáki, G. (1986). Hippocampal Sharp Waves: Their Origin and Significance. *Brain Res.*, 398(2):242–253.

Buzsáki, G. (1989). Two-stage model of memory trace formation: A role for “noisy” brain states. *Neuroscience*, 31(3):551–570.

Buzsáki, G. (2006). *Rhythms of the brain.* Oxford University Press.

Buzsáki, G. (2015). Hippocampal sharp wave-ripple: A cognitive biomarker for episodic memory and planning. *Hippocampus*, 25(10):1073–1188.

Buzsáki, G. (2019). *The brain from inside out.* Oxford University Press.

Buzsáki, G., Anastassiou, C. A., and Koch, C. (2016). The origin of extracellular fields and currents - EEG, ECoG, LFP and spikes. *Nat. Rev. Neurosci.*, 13(6):407–420.

Buzsáki, G. and Chrobak, J. J. (1995). Temporal structure in spatially organized neuronal ensembles: a role for interneuronal networks. *Curr. Opin. Neurobiol.*, 5(4):504–510.

Buzsáki, G., Haas, H. L., and Anderson, E. G. (1987). Long-term potentiation induced by physiologically relevant stimulus patterns. *Brain Res.*, 435(1-2):331–333.

Buzsáki, G., Horvath, Z., Urioste, R., Hetke, J., and Wise, K. (1992). High-frequency network oscillation in the hippocampus. *Science*, 256(5059):1025–1027.

Buzsáki, G., Leung, L. W., and Vanderwolf, C. H. (1983). Cellular bases of hippocampal EEG in the behaving rat. *Brain Res.*, 287(2):139–171.

Buzsáki, G. and Wang, X. J. (2012). Mechanisms of gamma oscillations. *Annu. Rev. Neurosci.*, 35:203–225.

Cajal, S. R. y. (1902). Sobre un ganglio especial de la corteza esfeno-occipital. *Trab. del Lab. Investig. Biológicas la Univ. Madrid*, 1:189–206.

Canolty, R. T., Edwards, E., Dalal, S. S., Soltani, M., Nagarajan, S. S., Kirsch, H. E., Berger, M. S., Barbare, N. M., and Knight, R. T. (2006). High gamma power is phase-locked to theta oscillations in human neocortex. *Science*, 313(5793):1626–1628.

Canto, C. B., Wouterlood, F. G., and Witter, M. P. (2008). What does the anatomical organization of the entorhinal cortex tell us? *Neural Plast.*, 2008:381243.

Carr, M. F., Jadhav, S. P., and Frank, L. M. (2011). Hippocampal replay in the awake state: A potential substrate for memory consolidation and retrieval. *Nat. Neurosci.*, 14(2):147–153.

Carr, M. F., Karlsson, M. P., and Frank, L. M. (2012). Transient slow gamma synchrony underlies hippocampal memory replay. *Neuron*, 75(4):700–713.

Cenquizca, L. A. and Swanson, L. W. (2007). Spatial organization of direct hippocampal field CA1 axonal projections to the rest of the cerebral cortex. *Brain Res. Rev.*, 56(1):1–26.

Chamberland, S. and Topolnik, L. (2012). Inhibitory control of hippocampal inhibitory neurons. *Front. Neurosci.*, 6:1–13.

Chater, T. E., Henley, J. M., Brown, J. T., and Randall, A. D. (2010). Voltage- and temperature-dependent gating of heterologously expressed channelrhodopsin-2. *J. Neurosci. Methods*, 193(1):7–13.

Chizhov, A. V. and Graham, L. J. (2007). Population model of hippocampal pyramidal neurons, linking a refractory density approach to conductance-based neurons. *Phys. Rev. E*, 75(1):011924.

Chizhov, A. V. and Graham, L. J. (2008). Efficient evaluation of neuron populations receiving colored-noise current based on a refractory density method. *Phys. Rev. E - Stat. Nonlinear, Soft Matter Phys.*, 77(1):011910.

Chizhov, A. V., Sanchez-Aguilera, A., Rodrigues, S., and De La Prida, L. M. (2015). Simplest relationship between local field potential and intracellular signals in layered neural tissue. *Phys. Rev. E - Stat. Nonlinear, Soft Matter Phys.*, 92(6):62704.

Chrobak, J. J. and Buzsaki, G. (1996). High-Frequency Oscillations in the Output Networks of the Hippocampal-Entorhinal Axis of the Freely Behaving Rat. *J. Neurosci.*, 76(9):3056–3066.

Church, J. and Baimbridge, K. G. (1991). Exposure to high-pH medium increases the incidence and extent of dye coupling between rat hippocampal CA1 pyramidal neurons in vitro. *J. Neurosci.*, 11(10):3289–3295.

Clemens, Z., Mölle, M., Eross, L., Jakus, R., Rásonyi, G., Halász, P., and Born, J. (2011). Fine-tuned coupling between human parahippocampal ripples and sleep spindles. *Eur. J. Neurosci.*, 33(3):511–520.

Cobb, S. R., Halasy, K., Vida, I., Nyíri, G., Tamás, G., Buhl, E. H., and Somogyi, P. (1997). Synaptic effects of identified interneurons innervating both interneurons and pyramidal cells in the rat hippocampus. *Neuroscience*, 79(3):629–648.

Colbert, C. M. and Levy, W. B. (1992). Electrophysiological and pharmacological characterization of perforant path synapses in CA1: Mediation by glutamate receptors. *J. Neurophysiol.*, 68(1):1–8.

Colgin, L. L. (2016). Rhythms of the hippocampal network. *Nat. Rev. Neurosci.*, 17(4):239–249.

Colgin, L. L., Jia, Y., Sabatier, J. M., and Lynch, G. (2005). Blockade of NMDA receptors enhances spontaneous sharp waves in rat hippocampal slices. *Neurosci. Lett.*, 385(1):46–51.

Condorelli, D. F., Belluardo, N., Trovato-Salinaro, A., and Mudò, G. (2000). Expression of Cx36 in mammalian neurons. *Brain Res. Rev.*, 32(1):72–85.

Cox, R., Rüber, T., Staresina, B. P., and Fell, J. (2019). Heterogeneous profiles of coupled sleep oscillations in human hippocampus. *Neuroimage*, 202:116178.

Crick, F. and Mitchison, G. (1983). The function of dream sleep. *Nature*, 304:111–114.

Csicsvari, J., Hirase, H., Czurkó, A., Mamiya, A., and Buzsáki, G. (1999a). Fast network oscillations in the hippocampal CA1 region of the behaving rat. *J. Neurosci.*, 19(16):RC20–RC20.

Csicsvari, J., Hirase, H., Czurkó, A., Mamiya, A., and Buzsáki, G. (1999b). Oscillatory coupling of hippocampal pyramidal cells and interneurons in the behaving rat. *J. Neurosci.*, 19(1):274–287.

Csicsvari, J., Hirase, H., Mamiya, A., and Buzsáki, G. (2000). Ensemble patterns of hippocampal CA3-CA1 Neurons during Sharp Wave-Associated Population Events. *Neuron*, 28:585–594.

Csicsvari, J., O'Neill, J., Allen, K., and Senior, T. (2007). Place-selective firing contributes to the reverse-order reactivation of CA1 pyramidal cells during sharp waves in open-field exploration. *Eur. J. Neurosci.*, 26(3):704–716.

Cutsuridis, V., Graham, B. P., Cobb, S., and Vida, I. (2010). *Hippocampal Microcircuits*. Springer Cham.

Czarnecki, A., Birtoli, B., and Ulrich, D. (2007). Cellular mechanisms of burst firing-mediated long-term depression in rat neocortical pyramidal cells. *J. Physiol.*, 578(2):471–479.

D'Antuono, M., De Guzman, P., Kano, T., and Avoli, M. (2005). Ripple activity in the dentate gyrus of dishinibited hippocampus-entorhinal cortex slices. *J. Neurosci. Res.*, 80(1):92–103.

Davidson, T. J., Kloosterman, F., and Wilson, M. A. (2009). Hippocampal Replay of Extended Experience. *Neuron*, 63(4):497–507.

Deuchars, J. and Thomson, A. (1996). CA1 pyramid-pyramid connections in rat hippocampus in vitro: Dual intracellular recordings with biocytin filling. *Neuroscience*, 74(4):1009–1018.

Diba, K. and Buzsáki, G. (2007). Forward and reverse hippocampal place-cell sequences during ripples. *Nat. Neurosci.*, 10(10):1241–1242.

Diekelmann, S. and Born, J. (2010). The memory function of sleep. *Nat. Rev. Neurosci.*, 11(2):114–126.

Dolorfo, C. L. and Amaral, D. G. (1998). Entorhinal cortex of the rat: Organization of intrinsic connections. *J. Comp. Neurol.*, 398(1):49–82.

Donoso, J. R., Schmitz, D., Maier, N., and Kempter, R. (2018). Hippocampal Ripple Oscillations and Inhibition-First Network Models: Frequency Dynamics and Response to GABA Modulators. *J. Neurosci.*, 38(12):3124–3146.

Dragoi, G. and Tonegawa, S. (2012). Preplay of future place cell sequences by hippocampal cellular assemblies. *Nature*, 469(7330):397–401.

Draguhn, A., Traub, R. D., Schmitz, D., and Jefferys, J. G. R. (1998). Electrical coupling underlies high-frequency oscillations in the hippocampus in vitro. *Nature*, 394(6689):189–192.

Droste, F. and Lindner, B. (2017). Up-down-like background spiking can enhance neural information transmission. *eNeuro*, 4(6).

Dudai, Y., Karni, A., and Born, J. (2015). The Consolidation and Transformation of Memory. *Neuron*, 88(1):20–32.

Dugladze, T., Schmitz, D., Whittington, M. A., Vida, I., and Gloveli, T. (2012). Segregation of axonal and somatic activity during fast network oscillations. *Science*, 336(6087):1458–1461.

Dupret, D., O'Neill, J., Pleydell-Bouverie, B., and Csicsvari, J. (2010). The reorganization and reactivation of hippocampal maps predict spatial memory performance. *Nat. Neurosci.*, 13(8):995–1002.

Ecker, A., Bagi, B., Vértes, E., Steinbach-Németh, O., Karlócai, M. R., Papp, O. I., Miklós, I., Hájos, N., Freund, T. F., Gulyás, A. I., and Káli, S. (2022). Hippocampal sharp wave-ripples and the associated sequence replay emerge from structured synaptic interactions in a network model of area CA3. *Elife*, 11:e71850.

Ego-Stengel, V. and Wilson, M. A. (2010). Disruption of ripple-associated hippocampal activity during rest impairs spatial learning in the rat. *Hippocampus*, 20(1):1–10.

Ellender, T. J., Nissen, W., Colgin, L. L., Mann, E. O., and Paulsen, O. (2010). Priming of hippocampal population bursts by individual perisomatic- targeting interneurons. *J. Neurosci.*, 30(17):5979–5991.

Empson, R. M. and Heinemann, U. (1995). Perforant path connections to area CA1 are predominantly inhibitory in the rat hippocampal-entorhinal cortex combined slice preparation. *Hippocampus*, 5(2):104–107.

English, D. F., Peyrache, A., Stark, E., Roux, L., Vallentin, D., Long, M. A., and Buzsáki, G. (2014). Excitation and inhibition compete to control spiking during hippocampal ripples: intracellular study in behaving mice. *J. Neurosci.*, 34(49):16509–17.

Epsztein, J., Lee, A. K., Chorev, E., and Brecht, M. (2010). Impact of spikelets on hippocampal CA1 pyramidal cell activity during spatial exploration. *Science*, 327(5964):474–477.

Erdös, P. and Rényi, A. (1960). On the evolution of random graphs. *Publ. Math. Inst. Hung. Acad. Sci*, 5:17–61.

Eschenko, O., Ramadan, W., Mölle, M., Born, J., and Sara, S. J. (2008). Sustained increase in hippocampal sharp-wave ripple activity during slow-wave sleep after learning. *Learn. Mem.*, 15(4):222–228.

Evangelista, R., Cano, G., Cooper, C., Schmitz, D., Maier, N., and Kempter, R. (2020). Generation of sharp wave-ripple events by disinhibition. *J. Neurosci.*, 40(41):7811–7836.

Fayyaz, Z., Altamimi, A., Zoellner, C., Klein, N., Wolf, O. T., Cheng, S., and Wiskott, L. (2022). A model of semantic completion in generative episodic memory. *Neural Comput.*, 34(9):1841–1870.

Fernández-Ruiz, A., Oliva, A., de Oliveira, E. F., Rocha-Almeida, F., Tingley, D., and Buzsáki, G. (2019). Long-duration hippocampal sharp wave ripples improve memory. *Science*, 364(6445):1082–1086.

Ferraguti, F., Cobden, P., Pollard, M., Cope, D., Shigemoto, R., Watanabe, M., and Somogyi, P. (2004). Immunolocalization of metabotropic glutamate receptor 1α (mGluR1α) in distinct classes of interneuron in the CA1 region of the rat hippocampus. *Hippocampus*, 14(2):193–215.

Ferraris, M., Cassel, J. C., Pereira de Vasconcelos, A., Stephan, A., and Quilichini, P. P. (2021). The nucleus reuniens, a thalamic relay for cortico-hippocampal interaction in recent and remote memory consolidation. *Neurosci. Biobehav. Rev.*, 125:339–354.

Fink, C. G., Gliske, S., Catoni, N., and Stacey, W. C. (2015). Network Mechanisms Generating Abnormal and Normal Hippocampal High-Frequency Oscillations: A Computational Analysis. *eNeuro*, 2(3):1–19.

Foster, D. J. (2017). Replay Comes of Age. *Annu. Rev. Neurosci.*, 40:581–602.

Foster, D. J. and Wilson, M. A. (2006). Reverse replay of behavioural sequences in hippocampal place cells during the awake state. *Nature*, 440(7084):680–683.

Fourcaud-Trocmé, N. and Brunel, N. (2005). Dynamics of the instantaneous firing rate in response to changes in input statistics. *J. Comput. Neurosci.*, 18(3):311–321.

Fourcaud-Trocmé, N., Hansel, D., van Vreeswijk, C., and Brunel, N. (2003). How spike generation mechanisms determine the neuronal response to fluctuating inputs. *J. Neurosci.*, 23(37):11628–11640.

Freund, T. and Buzsáki, G. (1996). Interneurons of the hippocampus. *Hippocampus*, 6(4):347–470.

Freund, T. F. (2003). Interneuron Diversity series: Rhythm and mood in perisomatic inhibition. *Trends Neurosci.*, 26(9):489–495.

Freund, T. F. and Antal, M. (1988). GABA-containing neurons in the septum control inhibitory interneurons in the hippocampus. *Nature*, 336(6195):170–173.

Fries, P. (2005). A mechanism for cognitive dynamics: Neuronal communication through neuronal coherence. *Trends Cogn. Sci.*, 9(10):474–480.

Fries, P. (2015). Rhythms for Cognition: Communication through Coherence. *Neuron*, 88(1):220–235.

Froemke, R. C. (2015). Plasticity of Cortical Excitatory-Inhibitory Balance. *Annu. Rev. Neurosci.*, 38:195–219.

Fuentealba, P., Begum, R., Capogna, M., Jinno, S., Márton, L. F., Csicsvari, J., Thomson, A., Somogyi, P., and Klausberger, T. (2008). Ivy Cells: A population of nitric-oxide-producing, slow-spiking GABAergic neurons and their involvement in hippocampal network activity. *Neuron*, 58(2):295.

Fukuda, T. and Kosaka, T. (2000). Gap junctions linking the dendritic network of GABAergic interneurons in the hippocampus. *J. Neurosci.*, 20(4):1519–1528.

Galarreta, M. and Hestrin, S. (2001a). Electrical synapses between GABA-releasing interneurons. *Nat. Rev. Neurosci.*, 2:425–433.

Galarreta, M. and Hestrin, S. (2001b). Spike transmission and synchrony detection in networks of GABAergic interneurons. *Science*, 292(5525):2295–2299.

Gardiner, C. (1985). *Handbook of Stochastic Methods for Physics, Chemistry and the Natural Sciences.* Springer, second edition.

Gasparini, S. and Magee, J. C. (2006). State-dependent dendritic computation in hippocampal CA1 pyramidal neurons. *J. Neurosci.*, 26(7):2088–2100.

Gasparini, S., Migliore, M., and Magee, J. C. (2004). On the initiation and propagation of dendritic spikes in CA1 pyramidal neurons. *J. Neurosci.*, 24(49):11046–11056.

Geisler, C., Brunel, N., and Wang, X.-J. (2005). Contributions of intrinsic membrane dynamics to fast network oscillations with irregular neuronal discharges. *J. Neurophysiol.*, 94(6):4344–4361.

Gerstner, W. (2000). Population dynamics of spiking neurons: fast transients, asynchronous states, and locking. *Neural Comput.*, 12:43–89.

Gerstner, W., Kempter, R., Hemmen, J. L. V., and Wagnert, H. (1996). A neuronal learning rule for sub-millisecond temporal coding. *Nature*, 383(6595):76–78.

Gerstner, W. and Kistler, W. M. (2002). *Spiking Neuron Models.* Cambridge University Press.

Gerstner, W., Kistler, W. M., Naud, R., and Paninski, L. (2014). *Neuronal Dynamics: From single neurons to networks and models of cognition and beyond.* Cambridge University Press.

Gerstner, W. and Naud, R. (2009). How good are neuron models? *Science*, 326(5951):379–380.

Girardeau, G., Benchenane, K., Wiener, S. I., Buzsáki, G., and Zugaro, M. B. (2009). Selective suppression of hippocampal ripples impairs spatial memory. *Nat. Neurosci.*, 12(10):1222–1223.

Girardeau, G., Cei, A., and Zugaro, M. (2014). Learning-induced plasticity regulates hippocampal sharp wave-ripple drive. *J. Neurosci.*, 34(15):5176–5183.

Girardeau, G. and Lopes-dos Santos, V. (2021). Brain neural patterns and the memory function of sleep. *Science*, 374(6567):560–564.

Girardeau, G. and Zugaro, M. (2011). Hippocampal ripples and memory consolidation. *Curr. Opin. Neurobiol.*, 21(3):452–459.

Glass, L. and Mackey, M. (1988). *From clocks to chaos: The rhythms of life.* Princeton University Press, Princeton, NJ.

Glickfeld, L. L., Roberts, J. D., Somogyi, P., and Scanziani, M. (2009). Interneurons hyperpolarize pyramidal cells along their entire somatodendritic axis. *Nat. Neurosci.*, 12(1):21–23.

Gliske, S. V., Stacey, W. C., Lim, E., Holman, K. A., and Fink, C. G. (2017). Emergence of narrowband high frequency oscillations from asynchronous, uncoupled neural firing. *Int J Neural Syst*, 27(1):1650049.

Goedeke, S. and Diesmann, M. (2008). The mechanism of synchronization in feed-forward neuronal networks. *New J. Phys.*, 10(1):015007.

Goodman, D. F. and Brette, R. (2009). The brian simulator. *Front. Neurosci.*, 3(2):192–197.

Goswamee, P., Leggett, E., and McQuiston, A. R. (2021). Nucleus reuniens afferents in hippocampus modulate CA1 network function via monosynaptic excitation and polysynaptic inhibition. *Front. Cell. Neurosci.*, 15.

Gray, C. M. and Singer, W. (1989). Stimulus-specific neuronal oscillations in orientation columns of cat visual cortex. *Proc. Natl. Acad. Sci. USA*, 86(5):1698–1702.

Grosmark, A. D. and Buzsáki, G. (2016). Diversity in neural firing dynamics supports both rigid and learned hippocampal sequences. *Science*, 351(6280):1440–1443.

Gulyás, A. I., Megías, M., Emri, Z., and Freund, T. F. (1999). Total number and ratio of excitatory and inhibitory synapses converging onto single interneurons of different types in the CA1 area of the rat hippocampus. *J. Neurosci.*, 19(22):10082–10097.

Gupta, A. S., van der Meer, M. A., Touretzky, D. S., and Redish, A. D. (2010). Hippocampal replay is not a simple function of experience. *Neuron*, 65(5):695–705.

Hafting, T., Fyhn, M., Molden, S., Moser, M. B., and Moser, E. I. (2005). Microstructure of a spatial map in the entorhinal cortex. *Nature*, 436(7052):801–806.

Hájos, N., Ellender, T. J., Zemankovics, R., Mann, E. O., Exley, R., Cragg, S. J., Freund, T. F., and Paulsen, O. (2009). Maintaining network activity in submerged hippocampal slices: Importance of oxygen supply. *Eur. J. Neurosci.*, 29(2):319–327.

Hajos, N., Karlocai, M. R., Nemeth, B., Ulbert, I., Monyer, H., Szabo, G., Erdelyi, F., Freund, T. F., and Gulyas, A. I. (2013). Input-output features of anatomically identified CA3 neurons during hippocampal sharp wave/ripple oscillation in vitro. *J. Neurosci.*, 33(28):11677–11691.

Halasy, K., Buhl, E. H., Lörinczi, Z., Tamás, G., and Somogyi, P. (1996). Synaptic target selectivity and input of GABAergic basket and bistratified interneurons in the CA1 area of the rat hippocampus. *Hippocampus*, 6(3):306–329.

Hamam, B. N., Amaral, D. G., and Alonso, A. A. (2002). Morphological and electrophysiological characteristics of layer V neurons of the rat lateral entorhinal cortex. *J. Comp. Neurol.*, 451(1):45–61.

Hamzei-Sichani, F., Kamasawa, N., Janssen, W. G., Yasumura, T., Davidson, K. G., Hof, P. R., Wearne, S. L., Stewart, M. G., Young, S. R., Whittington, M. A., Rash, J. E., and Traub, R. D. (2007). Gap junctions on hippocampal mossy fiber axons demonstrated by thin-section electron microscopy and freeze-fracture replica immunogold labeling. *Proc. Natl. Acad. Sci. USA*, 104(30):12548–12553.

Harris, K. D. and Thiele, A. (2011). Cortical state and attention. *Nat. Rev. Neurosci.*, 12(9):509–523.

Hasselmo, M. E. and McClelland, J. L. (1999). Neural models of memory. *Curr. Opin. Neurobiol.*, 9(2):184–188.

Hemmer, P. and Steyvers, M. (2009). A bayesian account of reconstructive memory. *Top. Cogn. Sci.*, 1(1):189–202.

Hodgkin, A. and Huxley, A. (1952). A quantitative description of membrane current and its application to conductance and excitation in nerve. *J. Physiol.*, 117(4):500–544.

Hofer, K. T., Kandrács, Á., Ulbert, I., Pál, I., Szabó, C., Héja, L., and Wittner, L. (2015). The hippocampal CA3 region can generate two distinct types of sharp wave-ripple complexes, in vitro. *Hippocampus*, 25(2):169–186.

Holden, A. (1976). *Models of the Stochastic Activity of Neurones*. Springer-Verlag, Berlin.

Hollnagel, J. O., Maslarova, A., ul Haq, R., and Heinemann, U. (2014). GABAB receptor dependent modulation of sharp wave-ripple complexes in the rat hippocampus in vitro. *Neurosci. Lett.*, 574:15–20.

Holzbecher, A. and Kempter, R. (2018). Interneuronal gap junctions increase synchrony and robustness of hippocampal ripple oscillations. *Eur. J. Neurosci.*, 48(12):3446–3465.

Holzbecher, A. J. (2018). *Function of interneuronal gap junctions in hippocampal sharp wave-ripples.* PhD thesis, Humboldt-Universität zu Berlin.

Hormuzdi, S. G., Pais, I., LeBeau, F. E., Towers, S. K., Rozov, A., Buhl, E. H., Whittington, M. A., and Monyer, H. (2001). Impaired electrical signaling disrupts gamma frequency oscillations in connexin 36-deficient mice. *Neuron*, 31(3):487–495.

Huber, R., Mäki, H., Rosanova, M., Casarotto, S., Canali, P., Casali, A. G., Tononi, G., and Massimini, M. (2013). Human cortical excitability increases with time awake. *Cereb. Cortex*, 23(2):332–338.

Hulse, B. K., Moreaux, L. C., Lubenov, E. V., and Siapas, A. G. (2016). Membrane Potential Dynamics of CA1 Pyramidal Neurons during Hippocampal Ripples in Awake Mice. *Neuron*, 89(4):800–813.

Hunt, D. L., Linaro, D., Si, B., Romani, S., and Spruston, N. (2018). A novel pyramidal cell type promotes sharp-wave synchronization in the hippocampus. *Nat. Neurosci.*, 21(7):985–995.

Imbrosci, B., Nitzan, N., McKenzie, S., Donoso, J. R., Swaminathan, A., Böhm, C., Maier, N., and Schmitz, D. (2021). Subiculum as a Generator of Sharp Wave-Ripples in the Rodent Hippocampus. *Cell Rep.*, 35(3):109021.

Ishikawa, D., Matsumoto, N., Sakaguchi, T., Matsuki, N., and Ikegaya, Y. (2014). Operant conditioning of synaptic and spiking activity patterns in single hippocampal neurons. *J. Neurosci.*, 34(14):5044–5053.

Isomura, Y., Sirota, A., Özen, S., Montgomery, S., Mizuseki, K., Henze, D. A., and Buzsáki, G. (2006). Integration and segregation of activity in entorhinal-hippocampal subregions by neocortical slow oscillations. *Neuron*, 52(5):871–882.

Jadhav, S. P., Kemere, C., German, P. W., and Frank, L. M. (2012). Awake hippocampal sharp-wave ripples support spatial memory. *Science*, 336(6087):1454–1458.

Jadhav, S. P., Rothschild, G., Roumis, D. K. K., and Frank, L. M. M. (2016). Coordinated excitation and inhibition of prefrontal ensembles during awake hippocampal sharp-wave ripple events. *Neuron*, 90(1):113–127.

Jahnke, S., Timme, M., and Memmesheimer, R.-M. (2015). A unified dynamic model for learning, replay, and sharp-wave/ripples. *J. Neurosci.*, 35(49):16236–16258.

Jay, T. M. and Witter, M. P. (1991). Distribution of hippocampal CA1 and subicular efferents in the prefrontal cortex of the rat studied by means of anterograde transport of Phaseolus vulgaris-leucoagglutinin. *J. Comp. Neurol.*, 313(4):574–586.

Jefferys, J. G., Traub, R. D., and Whittington, M. A. (1996). Neuronal networks for induced '40 Hz' rhythms. *Trends Neurosci.*, 19(5):202–208.

Jiang, X., Shamie, I., Doyle, W. K., Friedman, D., Dugan, P., Devinsky, O., Eskandar, E., Cash, S. S., Thesen, T., and Halgren, E. (2017). Replay of large-scale spatio-temporal patterns from waking during subsequent NREM sleep in human cortex. *Sci. Rep.*, 7(1):1–17.

Jolivet, R., Rauch, A., Lüscher, H. R., and Gerstner, W. (2006). Predicting spike timing of neocortical pyramidal neurons by simple threshold models. *J. Comput. Neurosci.*, 21(1):35–49.

Josselyn, S. A., Köhler, S., and Frankland, P. W. (2017). Heroes of the engram. *J. Neurosci.*, 37(18):4647–4657.

Josselyn, S. A. and Tonegawa, S. (2020). Memory engrams: Recalling the past and imagining the future. *Science*, 367(6473):eaaw4325.

Juszczak, G. R. and Swiergiel, A. H. (2009). Properties of gap junction blockers and their behavioural, cognitive and electrophysiological effects: Animal and human studies. *Prog. Neuro-Psychopharmacology Biol. Psychiatry*, 33(2):181–198.

Kaefer, K., Nardin, M., Blahna, K., and Csicsvari, J. (2020). Replay of Behavioral Sequences in the Medial Prefrontal Cortex during Rule Switching. *Neuron*, 106(1):154–165.e6.

Kajikawa, K., Hulse, B. K., Siapas, A. G., and Lubenov, E. V. (2021). Inhibition is the hallmark of CA3 intracellular dynamics around awake ripples. *bioRxiv*.

Kamondi, A., Acsády, L., and Buzsáki, G. (1998). Dendritic spikes are enhanced by cooperative network activity in the intact hippocampus. *J. Neurosci.*, 18(10):3919–3928.

Kandel, E. R., Dudai, Y., and Mayford, M. R. (2014). The molecular and systems biology of memory. *Cell*, 157(1):163–186.

Karlsson, M. P. and Frank, L. M. (2009). Awake replay of remote experiences in the hippocampus. *Nat. Neurosci.*, 12(7):913–918.

Kastner, D. B., Schwalger, T., Ziegler, L., and Gerstner, W. (2016). A model of synaptic reconsolidation. *Front. Neurosci.*, 10.

Katona, I., Acsády, L., and Freund, T. F. (1999). Postsynaptic targets of somatostatin-immunoreactive interneurons in the rat hippocampus. *Neuroscience*, 88(1):37–55.

Katona, L., Lapray, D., Viney, T. J., Oulhaj, A., Borhegyi, Z., Micklem, B. R., Klausberger, T., and Somogyi, P. (2014). Sleep and movement differentiates actions of two types of somatostatin-expressing GABAergic interneuron in rat hippocampus. *Neuron*, 82(4):872–886.

Kemp, N. and Bashir, Z. I. (2001). Long-term depression: A cascade of induction and expression mechanisms. *Prog. Neurobiol.*, 65(4):339–365.

Kempter, R., Gerstner, W., and Van Hemmen, J. (1999). Hebbian learning and spiking neurons. *Phys. Rev. E*, 59(4):4498–4514.

Khodagholy, D., Gelinas, J. N., and Buzsáki, G. (2017). Learning-enhanced coupling between ripple oscillations in association cortices and hippocampus. *Science*, 358(6361):369–372.

Kim, S., Guzman, S. J., Hu, H., and Jonas, P. (2012). Active dendrites support efficient initiation of dendritic spikes in hippocampal CA3 pyramidal neurons. *Nat. Neurosci.*, 15(4):600–606.

King, C., Henze, D. A., Leinekugel, X., and Buzsáki, G. (1999). Hebbian modification of a hippocampal population pattern in the rat. *J. Physiol.*, 521(1):159–167.

Kirst, C., Timme, M., and Battaglia, D. (2016). Dynamic information routing in complex networks. *Nat. Commun.*, 7(11061).

Kiss, J., Buzsaki, G., Morrow, J. S., Glantz, S. B., and Leranth, C. (1996). Entorhinal cortical innervation of parvalbumin-containing neurons (basket and chandelier cells) in the rat ammon's horn. *Hippocampus*, 6(3):239–246.

Kitamura, T., Ogawa, S. K., Roy, D. S., Okuyama, T., Morrissey, M. D., Smith, L. M., Redondo, R. L., and Tonegawa, S. (2017). Engrams and circuits crucial for systems consolidation of a memory. *Science*, 356(6333):73–78.

Klausberger, T. (2009). GABAergic interneurons targeting dendrites of pyramidal cells in the CA1 area of the hippocampus. *Eur. J. Neurosci.*, 30(6):947–957.

Klausberger, T., Magill, P. J., Márton, L., Roberts, J., Cobden, P. M., Buzsáki, G., and Somogyi, P. (2003). Brain-state- and cell-type- specific firing of hippocampal interneurons in vivo. *Nature*, 421:844–848.

Klausberger, T., Márton, L. F., Baude, A., Roberts, J. D. B., Magill, P. J., and Somogyi, P. (2004). Spike timing of dendrite-targeting bistratified cells during hippocampal network oscillations in vivo. *Nat. Neurosci.*, 7(1):41–47.

Klausberger, T., Marton, L. F., O'Neill, J., Huck, J. H., Dalezios, Y., Fuentealba, P., Suen, W. Y., Papp, E., Kaneko, T., Watanabe, M., Csicsvari, J., and Somogyi, P. (2005). Complementary roles of cholecystokinin- and parvalbumin-expressing GABAergic neurons in hippocampal network oscillations. *J. Neurosci.*, 25(42):9782–9793.

Klausberger, T. and Somogyi, P. (2008). Neuronal diversity and temporal dynamics: The unity of hippocampal circuit operations. *Science*, 321(5885):53–57.

Klinzing, J. G., Niethard, N., and Born, J. (2019). Mechanisms of systems memory consolidation during sleep. *Nat. Neurosci.*, 22:1598–1610.

Knowles, W. D. and Schwartzkroin, P. A. (1981). Local circuit synaptic interactions in hippocampal brain slices. *J. Neurosci.*, 1(3):318–322.

Köhler, C. (1985). A projection from the deep layers of the entorhinal area to the hippocampal formation in the rat brain. *Neurosci. Lett.*, 56(1):13–19.

Koniaris, E., Drimala, P., Sotiriou, E., and Papatheodoropoulos, C. (2011). Different effects of zolpidem and diazepam on hippocampal sharp wave-ripple activity in vitro. *Neuroscience*, 175:224–234.

Kopell, N. and Ermentrout, B. (2004). Chemical and electrical synapses perform complementary roles in the synchronization of interneuronal networks. *Proc. Natl. Acad. Sci.*, 101(43):15482–15487.

Kopell, N. and Gwendal, L. (1994). Rhythmogenesis, Amplitude Modulation, and Multiplexing in a Cortical Architecture. *Proc. Natl. Acad. Sci. USA*, 91(22):10586–10590.

Lamothe-Molina, P. J., Franzelin, A., Auksutat, L., Fieblinger, T., Laprell, L., Alhbeck, J., Gee, C. E., Kneussel, M., Engel, A. K., Hilgetag, C. C., Morellini, F., and Oertner, T. G. (2020). cFos ensembles in the dentate gyrus rapidly segregate over time and do not form a stable map of space. *bioRxiv*.

Lapray, D., Lasztoczi, B., Lagler, M., Viney, T. J., Katona, L., Valenti, O., Hartwich, K., Borhegyi, Z., Somogyi, P., and Klausberger, T. (2012). Behavior-dependent specialization of identified hippocampal interneurons. *Nat. Neurosci.*, 15(9):1265–1271.

Lasztóczi, B., Tukker, J. J., Somogyi, P., and Klausberger, T. (2011). Terminal field and firing selectivity of cholecystokinin-expressing interneurons in the Hippocampal CA3 Area. *J. Neurosci.*, 31(49):18073–18093.

Le Van Quyen, M., Bragin, A., Staba, R., Crépon, B., Wilson, C. L., and Engel, J. (2008). Cell type-specific firing during ripple oscillations in the hippocampal formation of humans. *J. Neurosci.*, 28(24):6104–6110.

Lee, A. K. and Wilson, M. A. (2002). Memory of sequential experience in the hippocampus during slow wave sleep. *Neuron*, 36(6):1183–1194.

Leinekugel, X., Khazipov, R., Cannon, R., Hirase, H., Ben-Ari, Y., and Buzsáki, G. (2002). Correlated bursts of activity in the neonatal hippocampus in vivo. *Science*, 296(5575):2049–2052.

Levenstein, D., Buzsáki, G., and Rinzel, J. (2019). NREM sleep in the rodent neocortex and hippocampus reflects excitable dynamics. *Nat. Commun.*, 10(1):1–12.

Li, X., Somogyi, P., Tepper, J., and Buzsáki, G. (1992). Axonal and dendritic arborization of an intracellularly labeled chandelier cell in the CA1 region of rat hippocampus. *Exp. Brain Res.*, 90:519–525.

Lindner, B. (2004). Moments of the first passage time under external driving. *J. Stat. Phys.*, 117(3-4):703–737.

Lindner, B., Doiron, B., and Longtin, A. (2005). Theory of oscillatory firing induced by spatially correlated noise and delayed inhibitory feedback. *Phys. Rev. E*, 72(6):061919.

Lindner, B. and Schimansky-Geier, L. (2001). Transmission of noise coded versus additive signals through a neuronal ensemble. *Phys. Rev. Lett.*, 86(14):2934–2937.

Liu, X., Ramirez, S., Pang, P. T., Puryear, C. B., Govindarajan, A., Deisseroth, K., and Tonegawa, S. (2012). Optogenetic stimulation of a hippocampal engram activates fear memory recall. *Nature*, 484(7394):381–385.

Llorens-Martín, M., Blazquez-Llorca, L., Benavides-Piccione, R., Rabano, A., Hernandez, F., Avila, J., and DeFelipe, J. (2014). Selective alterations of neurons and circuits related to early memory loss in Alzheimer's disease. *Front. Neuroanat.*, 8.

Logothetis, N. K., Eschenko, O., Murayama, Y., Augath, M., Steudel, T., Evrard, H. C., Besserve, M., and Oeltermann, A. (2012). Hippocampal-cortical interaction during periods of subcortical silence. *Nature*, 491(7425):547–553.

Loomis, A., Harvey, E., and Hobart, G. (1935). Potential rhythms of the cerebral cortex during sleep. *Science*, 81:597–598.

Maccaferri, G. (2005). Stratum oriens horizontal interneurone diversity and hippocampal network dynamics. *J. Physiol.*, 562(1):73–80.

Maccaferri, G., David, J., Roberts, B., Szucs, P., Cottingham, C. A., and Somogyi, P. (2000). Cell surface domain specific postsynaptic currents evoked by identified GABAergic neurones in rat hippocampus in vitro. *J. Physiol.*, 524(1):91–116.

MacVicar, B. A. and Dudek, F. E. (1981). Electrotonic coupling between pyramidal cells: a direct demonstation in rat hippocampal slices. *Science*, 213:782–785.

Maier, N., Güldenagel, M., Söhl, G., Siegmund, H., Willecke, K., and Draguhn, A. (2002). Reduction of high-frequency network oscillations (ripples) and pathological network discharges in hippocampal slices from connexin 36-deficient mice. *J. Physiol.*, 541(2):521–528.

Maier, N. and Kempter, R. (2017). Hippocampal Sharp Wave/Ripple Complexes—Physiology and Mechanisms. In Axmacher, N. and Rasch, B., editors, *Cogn. Neurosci. Mem. Consol.*, pages 227–249. Springer International Publishing Switzerland.

Maier, N., Morris, G., Johenning, F. W., and Schmitz, D. (2009). An approach for reliably investigating hippocampal sharpwave-ripples in vitro. *PLoS One*, 4(9):e6925.

Maier, N., Nimmrich, V., and Draguhn, A. (2003). Cellular and Network Mechanisms Underlying Spontaneous Sharp Wave–Ripple Complexes in Mouse Hippocampal Slices. *J. Physiol.*, 550(3):873–887.

Maier, N., Tejero-Cantero, Á., Dorrn, A. L., Winterer, J., Beed, P. S., Morris, G., Kempter, R., Poulet, J. F., Leibold, C., and Schmitz, D. (2011). Coherent phasic excitation during hippocampal ripples. *Neuron*, 72(1):137–152.

Maingret, N., Girardeau, G., Todorova, R., Goutierre, M., and Zugaro, M. (2016). Hippocampo-cortical coupling mediates memory consolidation during sleep. *Nat. Neurosci.*, 19(7):959–964.

Makara, J. K. and Magee, J. C. (2013). Variable dendritic integration in hippocampal CA3 pyramidal neurons. *Neuron*, 80(6):1438–1450.

Malerba, P., Krishnan, G. P., Fellous, J.-M., and Bazhenov, M. (2016). Hippocampal CA1 ripples as inhibitory transients. *PLOS Comput. Biol.*, 12(4):e1004880.

McBain, C. J., DiChiara, T. J., and Kauer, J. A. (1994). Activation of metabotropic glutamate receptors differentially affects two classes of hippocampal interneurons and potentiates excitatory synaptic transmission. *J. Neurosci.*, 14(7):4433–4445.

McClelland, J. L., McNaughton, B., and O'Reilly, R. (1995). Why there are complementary learning systems in the hippocampus and neocortex: insights from the success and failures of connectionist models of learning and memory. *Psychol. Rev.*, 102(3):419–457.

McDougal, R. A., Morse, T. M., Carnevale, T., Marenco, L., Wang, R., Migliore, M., Miller, P. L., Shepherd, G. M., and Hines, M. L. (2017). Twenty years of ModelDB and beyond: building essential modeling tools for the future of neuroscience. *J. Comput. Neurosci.*, 42(1):1–10.

McKenzie, S., Huszár, R., English, D. F., Kim, K., Christensen, F., Yoon, E., and Buzsáki, G. (2021). Preexisting hippocampal network dynamics constrain optogenetically induced place fields. *Neuron*, 109(6):1–15.

Megías, M., Emri, Z., Freund, T. F., and Gulyás, A. I. (2001). Total number and distribution of inhibitory and excitatory synapses on hippocampal CA1 pyramidal cells. *Neuroscience*, 102(3):527–540.

Meier, K., Merseburg, A., Isbrandt, D., Marguet, S. L., and Morellini, F. (2020). Dentate gyrus sharp waves, a local field potential correlate of learning in the dentate gyrus of mice. *J. Neurosci.*, 40(37):7105–7118.

Melonakos, E. D., White, J. A., and Fernandez, F. R. (2018). A model of cholinergic suppression of hippocampal ripples through disruption of balanced excitation/inhibition. *Hippocampus*, 29(9):1–14.

Memmesheimer, R.-M. (2010). Quantitative prediction of intermittent high-frequency oscillations in neural networks with supralinear dendritic interactions. *Proc. Natl. Acad. Sci.*, 107(24):11092–11097.

Memmesheimer, R. M. and Timme, M. (2006). Designing complex networks. *Phys. D Nonlinear Phenom.*, 224(1-2):182–201.

Mensi, S., Naud, R., Pozzorini, C., Avermann, M., Petersen, C. C., and Gerstner, W. (2012). Parameter extraction and classification of three cortical neuron types reveals two distinct adaptation mechanisms. *J. Neurophysiol.*, 107(6):1756–1775.

Mercer, A., Bannister, A. P., and Thomson, A. M. (2006). Electrical coupling between pyramidal cells in adult cortical regions. *Brain Cell Biol.*, 35(1):13–27.

Merhav, M., Karni, A., and Gilboa, A. (2015). Not all declarative memories are created equal: Fast Mapping as a direct route to cortical declarative representations. *Neuroimage*, 117:80–92.

Merker, B. (2013). Cortical gamma oscillations: The functional key is activation, not cognition. *Neurosci. Biobehav. Rev.*, 37(3):401–417.

Meyer, R. and Obermayer, K. (2016). Pypet: A python toolkit for data management of parameter explorations. *Front. Neuroinform.*, 10:38.

Michalikova, M., Remme, M. W., and Kempter, R. (2017). Spikelets in Pyramidal Neurons: Action Potentials Initiated in the Axon Initial Segment That Do Not Activate the Soma. *PLoS Comput. Biol.*, 13(1):1–25.

Michalikova, M., Remme, M. W., Schmitz, D., Schreiber, S., and Kempter, R. (2019). Spikelets in pyramidal neurons: Generating mechanisms, distinguishing properties, and functional implications. *Rev. Neurosci.*, 31(1):101–119.

Michon, F., Sun, J. J., Kim, C. Y., Ciliberti, D., and Kloosterman, F. (2019). Post-learning Hippocampal Replay Selectively Reinforces Spatial Memory for Highly Rewarded Locations. *Curr. Biol.*, 29(9):1436–1444.

Mirollo, R. and Strogatz, S. H. (1990). Synchronization of pulse-coupled biological oscillators. *SIAM J. Appl. Math.*, 50(6):1645–1662.

Mitzdorf, U. (1985). Current source-density method and application in cat cerebral cortex: Investigation of evoked potentials and EEG phenomena. *Physiol. Rev.*, 65(1):37–100.

Mizuseki, K. and Buzsáki, G. (2013). Preconfigured, skewed distribution of firing rates in the hippocampus and entorhinal cortex. *Cell Rep.*, 4(5):1010–1021.

Montbrió, E. and Pazó, D. (2018). Kuramoto Model for Excitation-Inhibition-Based Oscillations. *Phys. Rev. Lett.*, 120(24):244101.

Naber, P. A., Lopes Da Silva, F. H., and Witter, M. P. (2001). Reciprocal connections between the entorhinal cortex and hippocampal fields CA1 and the subiculum are in register with the projections from CA1 to the subiculum. *Hippocampus*, 11(2):99–104.

Nádasdy, Z., Hirase, H., Czurkó, A., Csicsvari, J., and Buzsáki, G. (1999). Replay and time compression of recurring spike sequences in the hippocampus. *J. Neurosci.*, 19(21):9497–9507.

Nadel, L. and Moscovitch, M. (1997). Memory consolidation, retrograde amnesia and the hippocampal complex. *Curr. Opin. Neurobiol.*, 7(2):217–227.

Nader, K. (2015). Reconsolidation and the dynamic nature of memory. *Cold Spring Harb. Perspect. Biol.*, 7(10):a021782.

Nagy, D. G., Török, B., and Orbán, G. (2020). Optimal forgetting: Semantic compression of episodic memories. *PLoS Comput. Biol.*, 16(10):e1008367.

Nagy, J. I. (2012). Evidence for connexin36 localization at hippocampal mossy fiber terminals suggesting mixed chemical/electrical transmission by granule cells. *Brain Res.*, 1487:107–122.

Nakashiba, T., Buhl, D. L., McHugh, T. J., and Tonegawa, S. (2009). Hippocampal CA3 output is crucial for ripple-associated reactivation and consolidation of memory. *Neuron*, 62(6):781–787.

Naud, R. and Gerstner, W. (2012). Coding and Decoding with Adapting Neurons: A Population Approach to the Peri-Stimulus Time Histogram. *PLoS Comput. Biol.*, 8(10).

Navas-Olive, A., Amaducci, R., Jurado-Parras, M.-T., Sebastian, E. R., and de la Prida, L. M. (2022). Deep learning based feature extraction for prediction and interpretation of sharp-wave ripples in the rodent hippocampus. *Elife*, 11::e77772.

Nguyen, D. P., Kloosterman, F., Barbieri, R., Brown, E. N., and Wilson, M. A. (2009). Characterizing the dynamic frequency structure of fast oscillations in the rodent hippocampus. *Front. Integr. Neurosci.*, 3.

Nguyen, Q. A. and Rubchinsky, L. L. (2021). Temporal patterns of synchrony in a pyramidal-interneuron gamma (PING) network. *Chaos*, 31(4):043134.

Nimmrich, V., Maier, N., Schmitz, D., and Draguhn, A. (2005). Induced sharp wave-ripple complexes in the absence of synaptic inhibition in mouse hippocampal slices. *J. Physiol.*, 563(3):663–670.

Nitzan, N., McKenzie, S., Beed, P., English, D. F., Oldani, S., Tukker, J. J., Buzsáki, G., and Schmitz, D. (2020). Propagation of hippocampal ripples to the neocortex by way of a subiculum-retrosplenial pathway. *Nat. Commun.*, 11:1947.

Norimoto, H., Makino, K., Gao, M., Shikano, Y., Okamoto, K., Ishikawa, T., Sasaki, T., Hioki, H., Fujisawa, S., and Ikegaya, Y. (2018). Hippocampal ripples downregulate synapses. *Science*, 359(6383):1524–1527.

Nunez del Toro, A. I. (2022). *Hippocampal ripple oscillations in an excitation-first network model with supralinear dendritic interactions.* Master thesis, Humboldt-Universität zu Berlin.

O'Keefe, J. (1976). Place units in the hippocampus of the freely moving rat. *Exp. Neurol.*, 51(1):78–109.

O'Keefe, J., Dostrovsky, J., and J. O'Keefe, J. D. (1971). Short Communications The hippocampus as a spatial map . Preliminary evidence from unit activity in the freely-moving rat. *Brain Res.*, 34(1):171–175.

Ólafsdóttir, H. F., Barry, C., Saleem, A. B., Hassabis, D., and Spiers, H. J. (2015). Hippocampal place cells construct reward related sequences through unexplored space. *Elife*, 4:e06063.

Ólafsdóttir, H. F., Bush, D., and Barry, C. (2018). The role of hippocampal replay in memory and planning. *Curr. Biol.*, 28:R37–R50.

Ólafsdóttir, H. F., Carpenter, F., and Barry, C. (2016). Coordinated grid and place cell replay during rest. *Nat. Neurosci.*, 19(6):792–794.

Ólafsdóttir, H. F., Carpenter, F., and Barry, C. (2017). Task demands predict a dynamic switch in the content of awake hippocampal replay. *Neuron*, 96(4):925–935.

Oliva, A., Fernández-Ruiz, A., Buzsáki, G., and Berényi, A. (2016). Role of hippocampal CA2 region in triggering sharp-wave ripples. *Neuron*, 91(6):1342–1355.

Oliva, A., Fernández-Ruiz, A., Leroy, F., and Siegelbaum, S. A. (2020). Hippocampal CA2 sharp-wave ripples reactivate and promote social memory. *Nature*, 587:264–269.

Orman, R., Von Gizycki, H., Lytton, W. W., and Stewart, M. (2008). Local axon collaterals of area CA1 support spread of epileptiform discharges within CA1, but propagation is unidirectional. *Hippocampus*, 18(10):1021–1033.

Ostojic, S., Brunel, N., and Hakim, V. (2009). Synchronization properties of networks of electrically coupled neurons in the presence of noise and heterogeneities. *J. Comput. Neurosci.*, 26(3):369–392.

Oyanedel, C. N., Durán, E., Niethard, N., Inostroza, M., and Born, J. (2020). Temporal associations between sleep slow oscillations, spindles and ripples. *Eur. J. Neurosci.*, 52(12):4762–4778.

Pais, I., Hormuzdi, S. G., Monyer, H., Traub, R. D., Wood, I. C., Buhl, E. H., Whittington, M. A., and LeBeau, F. E. (2003). Sharp wave-like activity in the hippocampus in vitro in mice lacking the gap junction protein connexin 36. *J. Neurophysiol.*, 89(4):2046–2054.

Palmigiano, A., Geisel, T., Wolf, F., and Battaglia, D. (2017). Flexible information routing by transient synchrony. *Nat. Neurosci.*, 20(7):1014–1022.

Pangalos, M., Donoso, J. R., Winterer, J., Zivkovic, A. R., Kempter, R., Maier, N., and Schmitz, D. (2013). Recruitment of oriens-lacunosum-moleculare interneurons during hippocampal ripples. *Proc. Natl. Acad. Sci. USA*, 110(11):4398–4403.

Papatheodoropoulos, C. (2007). NMDA receptor-dependent high-frequency network oscillations (100-300 Hz) in rat hippocampal slices. *Neurosci. Lett.*, 414(3):197–202.

Papatheodoropoulos, C. (2008). A possible role of ectopic action potentials in the in vitro hippocampal sharp wave-ripple complexes. *Neuroscience*, 157(3):495–501.

Papatheodoropoulos, C. and Kostopoulos, G. (2002). Spontaneous GABAA-dependent synchronous periodic activity in adult rat ventral hippocampal slices. *Neurosci. Lett.*, 319(1):17–20.

Pawelzik, H., Hughes, D. I., and Thomson, A. M. (2002). Physiological and morphological diversity of immunocytochemically defined parvalbumin- and cholecystokinin-positive interneurones in CA1 of the adult rat hippocampus. *J. Comp. Neurol.*, 443(4):346–367.

Penttonen, M. and Buzsáki, G. (2003). Natural logarithmic relationship between brain oscillators. *Thalamus Relat. Syst.*, 2(2):145–152.

Perez-Velazquez, J. L., Valiante, T. A., and Carlen, P. L. (1994). Modulation of gap junctional mechanisms during calcium-free induced field burst activity: A possible role for electrotonic coupling in epileptogenesis. *J. Neurosci.*, 14(7):4308–4317.

Perumal, M. B., Latimer, B., Xu, L., Stratton, P., Nair, S., and Sah, P. (2021). Microcircuit mechanisms for the generation of sharp-wave ripples in the basolateral amygdala: A role for chandelier interneurons. *Cell Rep.*, 35(6):109106.

Peyrache, A., Battaglia, F. P., and Destexhe, A. (2011). Inhibition recruitment in prefrontal cortex during sleep spindles and gating of hippocampal inputs. *Proc. Natl. Acad. Sci. USA*, 108(41):17207–17212.

Peyrache, A., Khamassi, M., Benchenane, K., Wiener, S. I., and Battaglia, F. P. (2009). Replay of rule-learning related neural patterns in the prefrontal cortex during sleep. *Nat. Neurosci.*, 12(7):919–926.

Pfeiffer, B. E. (2020). The content of hippocampal “replay”. *Hippocampus*, 30(1):6–18.

Pfeiffer, B. E. and Foster, D. J. (2013). Hippocampal place-cell sequences depict future paths to remembered goals. *Nature*, 497(7447):74–79.

Pietras, B., Schmutz, V., and Schwalger, T. (2022). Mesoscopic description of hippocampal replay and metastability in spiking neural networks with short-term plasticity. *PLoS Comput. Biol.*, 18(12):e1010809.

Plesser, H. E. and Gerstner, W. (2000). Noise in Integrate-and-Fire Neurons: From Stochastic Input to Escape Rates. *Neural Comput.*, 12(2):367–384.

Ponomarenko, A. A., Korotkova, T. M., and Haas, H. L. (2003). High frequency (200 Hz) oscillations and firing patterns in the basolateral amygdala and dorsal endopiriform nucleus of the behaving rat. *Behav. Brain Res.*, 141(2):123–129.

Ponomarenko, A. A., Korotkova, T. M., Sergeeva, O. A., and Haas, H. L. (2004). Multiple GABAA receptor subtypes regulate hippocampal ripple oscillations. *Eur. J. Neurosci.*, 20(8):2141–2148.

Pöschel, B., Heinemann, U., and Draguhn, A. (2003). High frequency oscillations in the dentate gyrus of rat hippocampal slices induced by tetanic stimulation. *Brain Res.*, 959(2):320–327.

Poulet, J. F. and Crochet, S. (2019). The cortical states of wakefulness. *Front. Syst. Neurosci.*, 12:64.

Pozzorini, C., Mensi, S., Hagens, O., Naud, R., Koch, C., and Gerstner, W. (2015). Automated High-Throughput Characterization of Single Neurons by Means of Simplified Spiking Models. *PLoS Comput. Biol.*, 11(6):e1004275.

Ramirez-Villegas, J. F., Logothetis, N. K., and Besserve, M. (2015). Diversity of sharp-wave–ripple LFP signatures reveals differentiated brain-wide dynamical events. *Proc. Natl. Acad. Sci.*, 112(46):E6379–E6387.

Ramirez-Villegas, J. F., Willeke, K. F., Logothetis, N. K., and Besserve, M. (2018). Dissecting the synapse- and frequency-dependent network mechanisms of in vivo hippocampal sharp wave-ripples. *Neuron*, 100(5):1224–1240.e13.

Rash, J. E., Duffy, H. S., Dudek, F. E., Bilhartz, B. L., Whalen, L. R., and Yasumura, T. (1997). Grid-mapped freeze-fracture analysis of gap junctions in gray and white matter of adult rat central nervous system, with evidence for a 'panglial syncytium' that is not coupled to neurons. *J. Comp. Neurol.*, 388(2):265–292.

Richardson, M. J. (2008). Spike-train spectra and network response functions for non-linear integrate-and-fire neurons. *Biol. Cybern.*, 99:381–392.

Richardson, M. J. E. (2007). Firing-rate response of linear and nonlinear integrate-and-fire neurons to modulated current-based and conductance-based synaptic drive. *Phys. Rev. E - Stat. Nonlinear, Soft Matter Phys.*, 76(2):021919.

Risken, H. (1989). *The Fokker-Planck Equation: Methods of solution and applications.* Springer, second edition.

Rosanova, M. and Ulrich, D. (2005). Pattern-specific associative long-term potentiation induced by a sleep spindle-related spike train. *J. Neurosci.*, 25(41):9398–9405.

Roux, L., Hu, B., Eichler, R., Stark, E., and Buzsáki, G. (2017). Sharp wave ripples during learning stabilize the hippocampal spatial map. *Nat. Neurosci.*, 20:845–853.

Roy, D. S., Park, Y. G., Kim, M. E., Zhang, Y., Ogawa, S. K., DiNapoli, N., Gu, X., Cho, J. H., Choi, H., Kamentsky, L., Martin, J., Mosto, O., Aida, T., Chung, K., and Tonegawa, S. (2022). Brain-wide mapping reveals that engrams for a single memory are distributed across multiple brain regions. *Nat. Commun.*, 13:1799.

Rudoy, J. D., Voss, J. L., Westerberg, C. E., and Paller, K. A. (2009). Strengthening individual memories by reactivating them during sleep. *Science*, 326(5956):1079.

Sadowski, J. H., Jones, M. W., and Mellor, J. R. (2016). Sharp-Wave Ripples Orchestrate the Induction of Synaptic Plasticity during Reactivation of Place Cell Firing Patterns in the Hippocampus. *Cell Rep.*, 14(8):1916–1929.

Schindler, M., Talkner, P., and Hänggi, P. (2004). Firing time statistics for driven neuron models: Analytic expressions versus numerics. *Phys. Rev. Lett.*, 93(4):048102.

Schlingloff, D., Kali, S., Freund, T. F., Hajos, N., and Gulyas, A. I. (2014). Mechanisms of Sharp Wave Initiation and Ripple Generation. *J. Neurosci.*, 34(34):11385–11398.

Schmalbruch, H. and Jahnsen, H. (1981). Gap junctions on CA3 pyramidal cells of guinea pig hippocampus shown by freeze-fracture. *Brain Res.*, 217(1):175–178.

Schmitz, D., Schuchmann, S., Fisahn, A., Draguhn, A., Buhl, E. H., Petrasch-Parwez, E., Dermietzel, R., Heinemann, U., and Traub, R. D. (2001). Axo-axonal coupling: A novel mechanism for ultrafast neuronal communication. *Neuron*, 31(5):831–840.

Schmutz, V., Gerstner, W., and Schwalger, T. (2020). Mesoscopic population equations for spiking neural networks with synaptic short-term plasticity. *J. Math. Neurosc.*, 10(5).

Schomburg, E. W., Anastassiou, C. A., Buzsáki, G., and Koch, C. (2012). The spiking component of oscillatory extracellular potentials in the rat hippocampus. *J. Neurosci.*, 32(34):11798–11811.

Schönberger, J., Draguhn, A., and Both, M. (2014). Lamina-specific contribution of glutamatergic and GABAergic potentials to hippocampal sharp wave-ripple complexes. *Front. Neural Circuits*, 8.

Schuck, N. W. and Niv, Y. (2019). Sequential replay of nonspatial task states in the human hippocampus. *Science*, 364(6447).

Schwalger, T. (2021). Mapping input noise to escape noise in integrate-and-fire neurons: a level-crossing approach. *Biol. Cybern.*, 115(5):539–562.

Schwalger, T., Deger, M., and Gerstner, W. (2017). Towards a theory of cortical columns: From spiking neurons to interacting neural populations of finite size. *PLoS Comput. Biol.*, 13(4):e1005507.

Seenivasan, P., Basak, R., and Narayanan, R. (2022). Conjunctive theta- and ripple-frequency oscillations across hippocampal strata of foraging rats. In *Cosyne Conf. Poster*, Lisbon.

Seibt, J., Richard, C. J., Sigl-Glöckner, J., Takahashi, N., Kaplan, D. I., Doron, G., De Limoges, D., Bocklisch, C., and Larkum, M. E. (2017). Cortical dendritic activity correlates with spindle-rich oscillations during sleep in rodents. *Nat. Commun.*, 8(1):1–12.

Semon, R. (1921). *The Mneme.* Allen, Unwin, London.

Sharon, T., Moscovitch, M., and Gilboa, A. (2011). Rapid neocortical acquisition of long-term arbitrary associations independent of the hippocampus. *Proc. Natl. Acad. Sci. USA*, 108(3):1146–1151.

Shu, Y., Hasenstaub, A., Duque, A., Yu, Y., and McCormick, D. A. (2006). Modulation of intracortical synaptic potentials by presynaptic somatic membrane potential. *Nature*, 441(7094):761–765.

Shu, Y., Hasenstaub, A., and McCormick, D. A. (2003). Turning on and off recurrent balanced cortical activity. *Nature*, 423(6937):288–293.

Shu, Y., Yu, G., Yang, J., and McCormick, D. A. (2007). Selective control of cortical axonal spikes by a slowly inactivating K+ current. *Proc. Natl. Acad. Sci. USA*, 104(27):11453–11458.

Siapas, A. G. and Wilson, M. A. (1998). Coordinated interactions between hippocampal ripples and cortical spindles during slow-wave sleep. *Neuron*, 21(5):1123–1128.

Sik, A., Penttonen, M., Ylinen, A., and Buzsáki, G. (1995). Hippocampal CA1 interneurons: An in vivo intracellular labeling study. *J. Neurosci.*, 15(10):6651–6665.

Simbürger, E., Stang, A., Kremer, M., and Dermietzel, R. (1997). Expression of connexin36 mRNA in adult rodent brain. *Histochem Cell Biol.*, 107:127–137.

Singer, A. C. and Frank, L. M. (2009). Rewarded outcomes enhance reactivation of experience in the hippocampus. *Neuron*, 64(6):910–921.

Singer, W. (2018). Neuronal oscillations: unavoidable and useful? *Eur. J. Neurosci.*, 48(7):2389–2398.

Sirota, A. and Buzsáki, G. (2005). Interaction between neocortical and hippocampal networks via slow oscillations. *Thalamus Relat. Syst.*, 3(4):245–259.

Sirota, A., Csicsvari, J., and Buhl, D. (2003). Communication between neocortex and hippocampus. *Proc. Natl. Acad. Sci.*, 100(4):2065–2069.

Sirota, A., Montgomery, S., Fujisawa, S., Isomura, Y., Zugaro, M., and Buzsáki, G. (2008). Entrainment of neocortical neurons and gamma oscillations by the hippocampal theta rhythm. *Neuron*, 60(4):683–697.

Somogyi, P. (1977). A specific 'axo-axonal' interneuron in the visual cortex of the rat. *Brain Res.*, 136:345–350.

Somogyi, P., Katona, L., Klausberger, T., Lasztóczi, B., and Viney, T. J. (2014). Temporal redistribution of inhibition over neuronal subcellular domains underlies state-dependent rhythmic change of excitability in the hippocampus. *Philos. Trans. R. Soc. B*, 369:20120518.

Somogyi, P., Nunzi, M. G., Gorio, A., and Smith, A. D. (1983). A new type of specific interneuron in the monkey hippocampus forming synapses exclusively with the axon initial segments of pyramidal cells. *Brain Res.*, 259(1):137–142.

Squire, L. R. (2004). Memory systems of the brain: A brief history and current perspective. *Neurobiol. Learn. Mem.*, 82(3):171–177.

Staresina, B. P., Bergmann, T. O., Bonnefond, M., Van Der Meij, R., Jensen, O., Deuker, L., Elger, C. E., Axmacher, N., and Fell, J. (2015). Hierarchical nesting of slow oscillations, spindles and ripples in the human hippocampus during sleep. *Nat. Neurosci.*, 18(11):1679–1686.

Stark, E., Roux, L., Eichler, R., and Buzsáki, G. (2015). Local generation of multineuronal spike sequences in the hippocampal CA1 region. *Proc. Natl. Acad. Sci. USA*, 112(33):10521–10526.

Stark, E., Roux, L., Eichler, R., Senzai, Y., Royer, S., and Buzsáki, G. (2014). Pyramidal cell-interneuron interactions underlie hippocampal ripple oscillations. *Neuron*, 83(2):467–480.

Steriade, M. and Deschenes, M. (1984). The thalamus as a neuronal oscillator. *Brain Res. Rev.*, 8(1):1–63.

Steriade, M., Domich, L., Oakson, G., and Deschenes, M. (1987). The deafferented reticular thalamic nucleus generates spindle rhythmicity. *J. Neurophysiol.*, 57(1):260–273.

Steriade, M., Nunez, A., and Amzica, F. (1993). A novel slow (< 1 Hz) oscillation of neocortical neurons in vivo: Depolarizing and hyperpolarizing components. *J. Neurosci.*, 13(8):3252–3265.

Sterpenich, V., van Schie, M. K., Catsiyannis, M., Ramyead, A., Perrig, S., Yang, H. D., Van De Ville, D., and Schwartz, S. (2021). Reward biases spontaneous neural reactivation during sleep. *Nat. Commun.*, 12:4162.

Straube, B. (2012). An overview of the neuro-cognitive processes involved in the encoding, consolidation, and retrieval of true and false memories. *Behav. Brain Funct.*, 8:35.

Sullivan, D., Csicsvari, J., Mizuseki, K., Montgomery, S., Diba, K., and Buzsáki, G. (2011). Relationships between hippocampal sharp waves, ripples, and fast gamma oscillation: Influence of dentate and entorhinal cortical activity. *J. Neurosci.*, 31(23):8605–8616.

Sürmeli, G., Marcu, D. C., McClure, C., Garden, D. L. F., Pastoll, H., and Nolan, M. F. (2015). Molecularly defined circuitry reveals input-output segregation in deep layers of the medial entorhinal cortex. *Neuron*, 88:1040–1053.

Sutherland, R. J. and Lehmann, H. (2011). Alternative conceptions of memory consolidation and the role of the hippocampus at the systems level in rodents. *Curr. Opin. Neurobiol.*, 21(3):446–451.

Sutherland, R. J., O'Brien, J., and Lehmann, H. (2008). Absence of systems consolidation of fear memories after dorsal, ventral, or complete hippocampal damage. *Hippocampus*, 18(7):710–718.

Suzuki, S. S. and Smith, G. K. (1988). Spontaneous EEG spikes in the normal hippocampus. IV. Effects of medial septum and entorhinal cortex lesions. *Electroencephalogr. Clin. Neurophysiol.*, 70(1):73–83.

Swaminathan, A., Wichert, I., Schmitz, D., and Maier, N. (2018). Involvement of mossy cells in sharp wave-ripple activity in vitro. *Cell Rep.*, 23(9):2541–2549.

Swanson, L. W. (1981). A direct projection from Ammon's horn to prefrontal cortex in the rat. *Brain Res.*, 217(1):150–154.

Szabadics, J., Varga, C., Molnár, G., Oláh, S., Barzó, P., and Tamás, G. (2006). Excitatory effect of GABAergic axo-axonic cells in cortical microcircuits. *Science*, 311(5758):233–235.

Szabo, G. G., Farrell, J. S., Dudok, B., Hou, W.-h., Ortiz, A. L., Varga, C., Dimidschstein, J., Capogna, M., and Soltesz, I. (2022). Ripple-selective GABAergic projection cells in the hippocampus. *Neuron*, 110(12):1959–1977.e9.

Takács, V. T., Klausberger, T., Somogyi, P., Freund, T. F., and Gulyás, A. I. (2012). Extrinsic and local glutamatergic inputs of the rat hippocampal CA1 area differentially innervate pyramidal cells and interneurons. *Hippocampus*, 22(6):1379–1391.

Tamamaki, N. and Nojyo, Y. (1993). Projection of the entorhinal layer II neurons in the rat as revealed by intracellular pressure-injection of neurobiotin. *Hippocampus*, 3(4):471–480.

Tamás, G., Buhl, E., Lörincz, A., and Somogyi, P. (2000). Proximally targeted GABAergic synapses and gap juctions synchronize cortical interneurons. *Nat. Neurosci.*, 3(4):366–371.

Taube, J. S., Muller, R. U., and Ranck, J. B. (1990). Head-direction cells recorded from the postsubiculum in freely moving rats. I. Description and quantitative analysis. *J. Neurosci.*, 10(2):420–435.

Taxidis, J., Coombes, S., Mason, R., and Owen, M. R. (2012). Modeling sharp wave-ripple complexes through a CA3-CA1 network model with chemical synapses. *Hippocampus*, 22:995–1017.

Terada, S., Geiller, T., Liao, Z., O'Hare, J., Vancura, B., and Losonczy, A. (2021). Adaptive stimulus selection for consolidation in the hippocampus. *Nature*, 601:204–244.

Terman, D., Kopell, N. J., and Bose, A. (1998). Dynamics of two mutually coupled slow inhibitory neurons. *Phys. D*, 117:241–275.

Teubner, B., Odermatt, B., Güldenagel, M., Söhl, G., Degen, J., Bukauskas, F. F., Kronengold, J., Verselis, V. K., Jung, Y. T., Kozak, C. A., Schilling, K., and Willecke, K. (2001). Functional expression of the new gap junction gene connexin47 transcribed in mouse brain and spinal cord neurons. *J. Neurosci.*, 21(4):1117–1126.

Thome, C., Kelly, T., Yanez, A., Schultz, C., Engelhardt, M., Cambridge, S. B., Both, M., Draguhn, A., Beck, H., and Egorov, A. V. (2014). Axon-carrying dendrites convey privileged synaptic input in hippocampal neurons. *Neuron*, 83(6):1418–1430.

Todorova, R. and Zugaro, M. (2020). Hippocampal ripples as a mode of communication with cortical and subcortical areas. *Hippocampus*, 30(1):39–49.

Tokunaga, A., Akert, K., Sandri, C., and Bennett, M. V. (1980). Cell types and synaptic organization of the medullary electromotor nucleus in a constant frequency weakly electric fish, Sternarchus albifrons. *J. Comp. Neurol.*, 192(3):407–426.

Tonegawa, S., Liu, X., Ramirez, S., and Redondo, R. (2015a). Memory Engram Cells Have Come of Age. *Neuron*, 87(5):918–931.

Tonegawa, S., Morrissey, M. D., and Kitamura, T. (2018). The role of engram cells in the systems consolidation of memory. *Nat. Rev. Neurosci.*, 19(8):485–498.

Tonegawa, S., Pignatelli, M., Roy, D. S., and Ryan, T. J. (2015b). Memory engram storage and retrieval. *Curr. Opin. Neurobiol.*, 35:101–109.

Tononi, G. and Cirelli, C. (2003). Sleep and synaptic homeostasis: A hypothesis. *Brain Res. Bull.*, 62(2):143–150.

Traub, R. D. (1995). Model of synchronized population bursts in electrically coupled interneurons containing active dendritic conductances. *J. Comput. Neurosci.*, 2(4):283–289.

Traub, R. D. and Bibbig, A. (2000). A model of high-frequency ripples in the hippocampus based on synaptic coupling plus axon-axon gap junctions between pyramidal neurons. *J. Neurosci.*, 20(6):2086–2093.

Traub, R. D., Cunningham, M. O., Gloveli, T., LeBeau, F. E., Bibbig, A., Buhl, E. H., and Whittington, M. A. (2003). GABA-enhanced collective behavior in neuronal axons underlies persistent gamma-frequency oscillations. *Proc. Natl. Acad. Sci. USA*, 100(19):11047–11052.

Traub, R. D., Jefferys, J. G., and Whittington, M. A. (1997). Simulation of gamma rhythms in networks of interneurons and pyramidal cells. *J. Comput. Neurosci.*, 4(2):141–150.

Traub, R. D. and Miles, R. (1991). *Neuronal Networks of the Hippocampus.* Cambridge University Press.

Traub, R. D., Schmitz, D., Jefferys, J. G. R., and Draguhn, A. (1999a). High-frequency population oscillations are predicted to occur in hippocampal pyramidal neuronal networks interconnected by axoaxonal gap junctions. *Neuroscience*, 92(2):407–426.

Traub, R. D., Schmitz, D., Maier, N., Whittington, M. A., and Draguhn, A. (2012). Axonal properties determine somatic firing in a model of in vitro CA1 hippocampal sharp wave/ripples and persistent gamma oscillations. *Eur. J. Neurosci.*, 36(5):2650–2660.

Traub, R. D., Whittington, M. A., Buhl, E. H., Jefferys, J. G., and Faulkner, H. J. (1999b). On the mechanism of the $\gamma \to \beta$ frequency shift in neuronal oscillations induced in rat hippocampal slices by tetanic stimulation. *J. Neurosci.*, 19(3):1088–1105.

Traub, R. D., Whittington, M. A., Colling, S. B., Buzsáki, G., and Jefferys, J. G. (1996). Analysis of gamma rhythms in the rat hippocampus in vitro and in vivo. *J. Physiol.*, 493(2):471–484.

Tuckwell, H. C. (1988). *Introduction to Theoretical Neurobiology.* Cambridge University Press.

Tukker, J. J., Beed, P., Schmitz, D., Larkum, M. E., and Sachdev, R. N. (2020). Up and down states and memory consolidation across somatosensory, entorhinal, and hippocampal cortices. *Front. Syst. Neurosci.*, 14:22.

Tukker, J. J., Lasztóczi, B., Katona, L., Roberts, J. D. B., Pissadaki, E. K., Dalezios, Y., Márton, L., Zhang, L., Klausberger, T., and Somogyi, P. (2013). Distinct dendritic arborization and in vivo firing patterns of parvalbumin-expressing basket cells in the hippocampal area CA3. *J. Neurosci.*, 33(16):6809–6825.

Uhlenbeck, G. and Ornstein, L. (1930). On the Theory of the Brownian Motion. *Phys. Rev.*, 36(5):823–841.

Valero, M., Cid, E., Averkin, R. G., Aguilar, J., Sanchez-Aguilera, A., Viney, T. J., Gomez-Dominguez, D., Bellistri, E., and De La Prida, L. M. (2015). Determinants of different deep and superficial CA1 pyramidal cell dynamics during sharp-wave ripples. *Nat. Neurosci.*, 18(9):1281–1290.

Valiante, T. A., Perez Velazquez, J. L., Jahromi, S. S., and Carlen, P. L. (1995). Coupling potentials in CA1 neurons during calcium-free-induced field burst activity. *J. Neurosci.*, 15(10):6946–6956.

van Haeffen, T., Baks-te Bulte, L., Goede, P. H., Wouterlood, F. G., and Witter, M. P. (2003). Morphological and numerical analysis of synaptic interactions between neurons in deep and superficial layers of the entorhinal cortex of the rat. *Hippocampus*, 13(8):943–952.

van Strien, N. M., Cappaert, N. L. M., and Witter, M. P. (2009). The anatomy of memory: an interactive overview of the parahippocampal-hippocampal network. *Nat. Rev. Neurosci.*, 10(4):272–282.

Van Vreeswijk, C., Abbott, L. F., and Bard Ermentrout, G. (1994). When inhibition not excitation synchronizes neural firing. *J. Comput. Neurosci.*, 1(4):313–321.

Van Vreeswijk, C. and Sompolinsky, H. (1996). Chaos in neuronal networks with balanced excitatory and inhibitory activity. *Science*, 274(5293):1724–1726.

Vandael, D. and Kole, M. (2022). Role of PV+ BC myelination in inhibitory precision in the mouse CA1 hippocampal microcircuit. In *Poster FENS Forum*, Paris.

Vandecasteele, M., Varga, V., Berényi, A., Papp, E., Barthó, P., Venance, L., Freund, T. F., and Buzsáki, G. (2014). Optogenetic activation of septal cholinergic neurons suppresses sharp wave ripples and enhances theta oscillations in the hippocampus. *Proc. Natl. Acad. Sci. USA*, 111(37):13535–13540.

Vanderwolf, C. H. (1969). Hippocampal electrical activity and voluntary movement in the rat. *Electroencephalogr. Clin. Neurophysiol.*, 26:407–418.

Vaney, D. (1993). The coupling pattern of axon-bearing horizontal cells in the mammalian retina. *Proc. R. Soc. B*, 252:93–101.

Varela, F., Lachaux, J.-p., Rodriguez, E., and Martinerie, J. (2001). The brainweb: phase synchronization and large-scale integration. *Nat. Rev. Neurosci.*, 2:229–239.

Varga, C., Golshani, P., and Soltesz, I. (2012). Frequency-invariant temporal ordering of interneuronal discharges during hippocampal oscillations in awake mice. *Proc. Natl. Acad. Sci. USA*, 109(40):E2726–E2734.

Varga, C., Oijala, M., Lish, J., Szabo, G. G., Bezaire, M., Marchionni, I., Golshani, P., and Soltesz, I. (2014). Functional fission of parvalbumin interneuron classes during fast network events. *Elife*, 3:e04006.

Vaz, A. P., Inati, S. K., Brunel, N., and Zaghloul, K. A. (2019). Coupled ripple oscillations between the medial temporal lobe and neocortex retrieve human memory. *Science*, 363(6430):975–978.

Vaz, A. P., Wittig, J. H., Inati, S. K., and Zaghloul, K. A. (2020). Replay of cortical spiking sequences during human memory retrieval. *Science*, 367(6482):1131–1134.

Viereckel, T., Kostic, M., Bähner, F., Draguhn, A., and Both, M. (2013). Effects of the GABA-uptake blocker NNC-711 on spontaneous sharp wave-ripple complexes in mouse hippocampal slices. *Hippocampus*, 23(5):323–329.

Viriyopase, A., Memmesheimer, R.-M., and Gielen, S. (2016). Cooperation and competition of gamma oscillation mechanisms. *J. Neurophysiol.*, 116(2):232–251.

Viriyopase, A., Memmesheimer, R.-M., and Gielen, S. (2018). Analyzing the competition of gamma rhythms with delayed pulse-coupled oscillators in phase representation. *Phys. Rev. E*, 98:022217.

Volgushev, M., Chauvette, S., Mukovski, M., and Timofeev, I. (2006). Precise long-range synchronization of activity and silence in neocortical neurons during slow-wave sleep. *J. Neurosci.*, 26(21):5665–5672.

Vyazovskiy, V. V., Cirelli, C., Pfister-Genskow, M., Faraguna, U., and Tononi, G. (2008). Molecular and electrophysiological evidence for net synaptic potentiation in wake and depression in sleep. *Nat. Neurosci.*, 11(2):200–208.

Wang, X. J. (2010). Neurophysiological and computational principles of cortical rhythms in cognition. *Physiol. Rev.*, 90(3):1195–1268.

Wheeler, D. W., White, C. M., Rees, C. L., Komendantov, A. O., Hamilton, D. J., and Ascoli, G. A. (2015). Hippocampome.org: A knowledge base of neuron types in the rodent hippocampus. *Elife*, 4:e09960.

Whittington, M. A., Jefferys, J. G., and Traub, R. D. (1996). Effects of intravenous anaesthetic agents on fast inhibitory oscillations in the rat hippocampus in vitro. *Br. J. Pharmacol.*, 118(8):1977–1986.

Whittington, M. A., Traub, R. D., and Jefferys, J. G. R. (1995). Synchronized oscillations in interneuron networks glutamate receptor activation. *Nature*, 373:612–615.

Whittington, M. A., Traub, R. D., Kopell, N., Ermentrout, B., and Buhl, E. H. (2000). Inhibition-based rhythms: Experimental and mathematical observations on network dynamics. *Int. J. Psychophysiol.*, 38(3):315–336.

Wierzynski, C. M., Lubenov, E. V., Gu, M., and Siapas, A. G. (2009). State-dependent spike-timing relationships between hippocampal and prefrontal circuits during sleep. *Neuron*, 61(4):587–596.

Wilber, A. A., Skelin, I., Wu, W., and McNaughton, B. L. (2017). Laminar organization of encoding and memory reactivation in the parietal cortex. *Neuron*, 95(6):1406–1419.

Wilson, M. A. and McNaughton, B. L. (1994). Reactivation of hippocampal ensemble memories during sleep. *Science*, 265(5172):676–679.

Winocur, G. and Moscovitch, M. (2011). Memory transformation and systems consolidation. *J. Int. Neuropsychol. Soc.*, 17(5):766–780.

Witter, M. P. (1993). Organization of the entorhinal—hippocampal system: A review of current anatomical data. *Hippocampus*, 3:33–44.

Witter, M. P. and Groenewegen, H. J. (1986). Connections of the parahippocampal cortex in the cat. IV. Subcortical efferents. *J. Comp. Neurol.*, 252(1):51–77.

Woodruff, A. R., McGarry, L. M., Vogels, T. P., Inan, M., Anderson, S. A., and Yuste, R. (2011). State-dependent function of neocortical chandelier cells. *J. Neurosci.*, 31(49):17872–17886.

Woodson, W., Nitecka, L., and Ben-Ari, Y. (1989). Organization of the GABAergic system in the rat hippocampal formation: A quantitative immunocytochemical study. *J. Comp. Neurol.*, 280(2):254–271.

Wouterlood, F. G., Saldana, E., and Witter, M. P. (1990). Projection from the nucleus reuniens thalami to the hippocampal region: light and electron microscopic tracing study in the rat with the anterograde tracer phaseolus vulgaris-leucoagglutinin. *J. Comp. Neurol.*, 296:179–203.

Wu, C., Shen, H., Luk, W. P., and Zhang, L. (2002). A fundamental oscillatory state of isolated rodent hippocampus. *J. Physiol.*, 540(2):509–527.

Xiao-Jing Wang and Buzsáki, G. (1996). Gamma Oscillation by Synaptic Inhibition in a Hippocampal Interneuronal Network Model. *J. Neurosci.*, 16(20):6402–6413.

Yamamoto, J. and Tonegawa, S. (2017). Direct Medial Entorhinal Cortex Input to Hippocampal CA1 Is Crucial for Extended Quiet Awake Replay. *Neuron*, 96(1):217–227.

Yang, S., Yang, S., Moreira, T., Hoffman, G., Carlson, G. C., Bender, K. J., Alger, B. E., and Tang, C. M. (2014). Interlamellar CA1 network in the hippocampus. *Proc. Natl. Acad. Sci. USA*, 111(35):12919–12924.

Yartsev, M. M., Witter, M. P., and Ulanovsky, N. (2011). Grid cells without theta oscillations in the entorhinal cortex of bats. *Nature*, 479(7371):103–107.

Ylinen, A., Bragin, A., Nádasdy, Z., Jandó, G., Szabó, I., Sik, A., and Buzsáki, G. (1995). Sharp wave-associated high-frequency oscillation (200 Hz) in the intact hippocampus: network and intracellular mechanisms. *J. Neurosci.*, 15(1):30–46.

Zhou, S. and Yu, Y. (2018). Synaptic E-I balance underlies efficient neural coding. *Front. Neurosci.*, 12:46.

List of Figures

2.1 Replay. 5
2.2 Rhythmic cortico-hippocampal interactions and replay during slow wave sleep. 9
2.3 Hippocampal anatomy. 11
2.4 Sharp wave-ripples *in vivo* and *in vitro*. 15
2.5 Intra-ripple frequency accommodation (IFA). 17
2.6 Differential recruitment of hippocampal cell types during SPW-Rs. 18

4.1 Constant-drive dynamics of the detailed spiking network. 35
4.2 IFA in the detailed spiking network. 36
4.3 Constant-drive dynamics of the reduced spiking network. 39
4.4 Transient dynamics and IFA in the reduced spiking network. 40
4.5 Stationary network dynamics in simulation and theory. 42
4.6 Linear stability analysis for the detailed ripple model. 43
4.7 Illustration of the drift-based approximation. 47
4.8 Drift-based approximation of ripple dynamics for constant drive. 48
4.9 Transient dynamics and IFA for piecewise constant drive. 51
4.10 Transient dynamics and IFA for piecewise linear drive. 53
4.11 IFA is speed-dependent. 55
4.12 The role of the inhibitory reversal potential. 57
4.13 Absolute refractoriness can induce period-2 oscillations. 58
4.14 Absolute refractoriness has negligible effect on ripple frequency. 59
4.15 Approximating Poisson input spikes by Gaussian white noise. 67
4.16 Ripple dynamics after diffusion approximation in feedforward input. . . . 67
4.17 Ripple dynamics with current-based inhibitory coupling: sparse vs. full connectivity. 69
4.18 Ripple dynamics in fully connected network with delta-pulse coupling. . . 71
4.19 Extracting the average oscillation cycle from the spiking network simulation 76
4.20 Self-consistent solution for the population rate r_0 and the total drive I_0 in steady-state. 79
4.21 Numerical solution of the amplitude and phase condition for the reduced ripple model. 81
4.22 Illustration of the self-consistent phase condition. 82
4.23 Numerical analysis of the drift-based approximation. 90
4.24 Illustration of analytical approximations. 97

4.25 Analytical vs numerical analysis of the drift-based approximation. . . . 99
4.26 Sketch of drift-based approximation for linear drive. 101
4.27 Performance of drift-based approximation depending on noise and coupling strength. 107
4.28 Parameter dependencies of the point of full synchrony. 108
4.29 Performance of drift-based approximation — analytical vs numerical solution. 109
4.30 Multimodal membrane potential density for low noise, weak coupling, low reset potential. 110
4.31 Unimodal membrane potential density for low noise, weak coupling, and increased reset potential. 110
4.32 Drift-based approximation at low noise, depending on coupling strength and reset potential. 111
4.33 Performance of drift-based approximation depending on synaptic delay and coupling strength. 112
4.34 Performance of drift-based approximation depending on synaptic delay and noise intensity. 113
4.35 Linear phase response curve (PRC). 114
4.36 Ripple dynamics in a network of pulse-coupled oscillators. 115
4.37 Numerical solution for $\mu_{\max}$ in PCO network. 120
4.38 Self-consistent solution for the PCO oscillation dynamics. 122
4.39 Drift-based approximation of IFA in the PCO network. 123
4.40 Numerical solution for $\mu_{\max}$ under linear drive. 124
4.41 Spiking network vs drift-based approximation close to full synchrony. . 153
4.42 Illustration of difference between $\mu_{\min}$ and the true periodic minimum of the mean membrane potential. 154

5.1 Ripples in the perturbation-based inhibitory model: single trial vs. average. 156
5.2 f-I curve of an uncoupled aEIF unit under colored noise. 158
5.3 Ripple dynamics without adaptation and without heterogeneity. 159
5.4 Relating unit firing rate and network frequency. 161
5.5 Strong inhibition decreases unit firing rate and hence ripple frequency. . 162
5.6 IFA in response to asymmetric drive. 163
5.7 No IFA (or “anti-IFA”) in response to symmetric drive. 164
5.8 IFA via adaptation. 165
5.9 No persistent oscillations in the perturbation-based model network without heterogeneity and adaptation for default parameters. 168
5.10 Bifurcation diagram of an EIF network with inhibitory coupling. 169
5.11 Sparse synchrony in a homogeneous EIF network with increased noise and coupling strength. 170
5.12 Sparse synchrony in gamma range in the homogeneous EIF network with increased noise and coupling strength and finite synaptic delay. 171
5.13 Ripple dynamics of the homogeneous EIF network with increased coupling strength, noise level and synaptic delay. 172

5.14 Distribution of peak conductances in the perturbation-based inhibition-first model. 179
5.15 Distribution of peak conductances for different coefficients of variations. 179
5.16 Original reference simulation. 180
5.17 Weak ripple in my implementation with original parameters. 180
5.18 Fixed vs variable network architecture. 182
5.19 Parameter exploration: inhibitory coupling strength. 184
5.20 Original parameter exploration: inhibitory coupling strength. 184
5.21 Parameter exploration: inhibitory coupling strength and noise intensity. 185
5.22 Original parameter exploration: inhibitory coupling strength and noise intensity. 185
5.23 Ripple dynamics without adaptation. 186
5.24 Pathological persistent ripple without adaptation, heterogeneity and noise. 186
5.25 Introducing persistent oscillations with a single parameter change. . . . 187
5.26 Clustering instability in the homogeneous EIF network. 187
5.27 Network frequency increases with noise strength. 188
5.28 No transient ringing effect with strong coupling and noise. 188

6.1 Ripple dynamics in a microscopic LIF network under Gaussian white noise input. 191
6.2 Firing properties of a GIF neuron with exponential hazard fitted to match the f-I curve of an LIF neuron. 193
6.3 Firing properties of a GIF neuron with Chizhov-Graham hazard. 196
6.4 Linear response of LIF vs GIF neurons. 197
6.5 Ripple dynamics depending on hazard function. 199
6.6 Illustration of the mesoscopic integration scheme by Schwalger et al. (2017). 202
6.7 Ripple dynamics on micro- and mesoscopic level. 203
6.8 Firing properties of a GIF neuron with exponential hazard fitted to match the f-I curve of an LIF neuron (wider fitting range). 218

List of Tables

2.1 Properties and predictions of ripple models. 26

4.1 IFA in theory and simulation. 55
4.2 Default parameters of the detailed spiking network. 65
4.3 Default parameters of the reduced spiking network. 72
4.4 Default parameters of the hybrid spiking networks. 73
4.5 Default parameters for the PCO network. 116

5.1 Properties and predictions of the perturbation-based and the bifurcation-based inhibitory model. 166
5.2 From perturbation- to bifurcation-based ripple generation. 171
5.3 Default parameters of the perturbation-based inhibition-first ripple model.176

Selbstständigkeitserklärung

Hiermit erkläre ich, dass ich die vorliegende Arbeit selbstständig, ohne unerlaubte fremde Hilfe, und nur unter Verwendung der angegebenen Hilfsmittel und Quellen erstellt habe.

Hereby I declare that I have written this thesis independently, without illicit assistance from third parties, and using solely the aids and references mentioned.

Berlin, 25.10.22

(Natalie Schieferstein)

Acknowledgements

There are many people I want to thank for making this PhD the amazing time that it was! First of all, I want to thank Richard for always being there, for his patience in giving me a chance to dig deep and explore many avenues, for connecting me with the experimental side of neuroscience, and for sharing his overall passion for unraveling the mysteries of the brain. A big thank you also to Benjamin and Tilo for their continued advice and many helpful comments and explanations over the years. I greatly enjoyed the interactions with Dietmar and Nikolaus. Special thanks to Nikolaus for taking the time and teaching me a lot about all the complexities of ripples in real life.

I had the pleasure to work with three amazing BCCN master students during my time here: Saeed Salehinajafabadi, Debapratim Jana, and Ana Toro. Thanks to all of you for your enthusiasm, and your contribution to this work by exploring ripple and sharp wave dynamics in various simulations and data sets!

Thanks also to Farzada for inspiring discussions and helpful advice, and to Rike for saving me from despair with computer issues many times.

In these past weeks, I received great support from Paul, Naomi, Gaspar, Robert, Kris, Andrés, and of course Richard, who proof read many final and not-so-final text passages and provided helpful comments!

I want to thank two eras of office mates: Tiziano and Eric in cosy 013, and Naomi, Gaspar, Paula, Mehnoush, and briefly Mila, in 106. All of you were an integral part of this journey and made everyday life in the office very enjoyable! Along these lines I shall also thank the people beyond our offices: Susana, Roberta, Paul, Meng, Philipp, Robert, Mahraz, Nelson, Martina, José, and many more present and past members of the Schreiber and Kempter lab for fun lunch times, conference trips and Café Flora nights! A special episode was definitely the organization of the ENCODS conference 2018, which I will always remember fondly despite Asana, thanks to the great co-organizers in Berlin and Essen — it was a lot of fun working with you!

Thanks to the ITB, and the BCCN with Margret, Lisa and Robert for creating a beautiful community and many nice memories of barbecues, christmas parties and retreats.

Finally, I want to thank my family and Andrés for always being there and supporting me through all stages of this adventure.

Natalie Schieferstein
Berlin, October 2022